Hydrodynamic Dispersion in Concentrated Sedimenting Suspensions

Thesis by
Julia C. Lester

in Partial Fulfillment of the Requirements
for the Degree of
Doctor of Philosophy

California Institute of Technology
Pasadena, California
1988
(Submitted March 23, 1988)

ABSTRACT

The hydrodynamic dispersion in concentrated sedimenting suspensions is investigated by numerical simulation. The particle Reynolds number is zero, and the Péclet number is infinite(the particles are non-Brownian). Particle trajectories are calculated by Stokesian dynamics. Stokesian dynamics is a molecular-dynamics-like simulation that provides an accurate representation of the suspension hydrodynamics. Detailed in this thesis is a technique that accelerates the convergence of the mobility interactions among particles in an infinite suspension. The simulations are of a monolayer of identical spheres sedimenting in the plane of the monolayer. Relative motion among the spheres arises from hydrodynamic interactions. The displacement related to this relative motion may constitute a random walk, giving rise to diffusive behavior of the spheres. This hydrodynamically induced self-diffusivity has been seen in sheared suspensions of non-Brownian, neutrally buoyant spheres.

Results of the numerical simulations show that the motion of spheres in sedimenting suspensions is also diffusive. The diffusion coefficient is relatively insensitive to the nature of the microstructure, as expressed by the pair-distribution function and the short-time, self-diffusion coefficient. The coefficient of diffusion decreases as the concentration increases for concentrated suspensions (it increases in the shear case). The ratio of the diffusion coefficient to the velocity variance of the spheres should be proportional to the time scale of the diffusive interactions. The diffusion time scale and the diffusion velocity scale (the square root of the velocity variance) both decrease as the concentration increases. In the shear case, the velocity scale (sphere radius multiplied by the shear rate) is independent of concentration, and the time scale (the product of the square of the concentration and the inverse of the shear rate) increases with increasing concentration. At the lowest concentrations, the spheres whose centers are separated by less than 2.05 radii prefer to align in the direction of sedimentation. At the highest concentrations, the preferred alignment is in the perpendicular direction.

Table of Contents

LIST OF FIGURES

Note: This list only includes those figures that occur in the body of the thesis, not in the appendices.

Figure 3.7b A detailed view of the low concentration results in Figure 3.7*b*.

Figure 3.8a The evolution of the short-time, self-diffusion coefficent in time for a non-Ewald sedimentation simulation using the FTS method, $\phi_A = 0.453$ and $N_1 = 25$ (this run is denoted as FTSn1-5 in Chapter 4). The top two curves are the xx and yy components of $\mathbf{D}_o^s$. Note that, as expected, there is no significant directional dependence of these results. The bottom curve is the xy component of $\mathbf{D}_o^s$. The time average of this component is very close to zero.

Figure 3.8b The evolution of the short-time, self-diffusion coefficent in time for a non-Ewald sedimentation simulation using the FT method, $\phi_A = 0.453$ and $N_1 = 25$ (this run is denoted as FTn1 in Chapter 4). See Figure 3.8*a* for explanation of curves.

Figure 3.8c The evolution of the short-time, self-diffusion coefficent in time for a non-Ewald sedimentation simulation using the F method, $\phi_A = 0.453$ and $N_1 = 25$ (this run is denoted as Fn1 in Chapter 4). See Figure 3.8*a* for explanation of curves.

Figure 3.9 The evolution of the short-time, self-diffusion coefficent in time for a non-Ewald sedimentation simulation; the short-time, self-diffusion coefficient has been calculated using the FTS method in all cases, but the configurations are those from the runs shown in Figures 3.8*a-c*. The solid curve with filled circles are for FTS run configurations. The dashed curve with filled stars are for FT run configurations. The dotted curve with filled triangles are for F run configurations. The symbols indicate that D_o^s was calculated for that given configuration, and the curves connect the symbols for each case.

Figure 3.10 The pair-distribution function for the FT run described in Figure 3.8*b*. Only configurations occurring from $t = 150 - 500$ contribute to this distribution.

LIST OF TABLES

Note: This list only includes those figures that occur in the body of the thesis, not in the appendices.

coefficient. Note the stronger increasing degree of anisotropy in the components of the diffusion coefficient as the concentration decreases.

CHAPTER 1: INTRODUCTION

Particles suspended or dispersed in a fluid medium occur in a wide variety of natural and industrial settings, e.g. slurries, porous media, composite materials, colloids, polymers, proteins, etc. Investigators are beginning to understand and predict the macroscopic behavior of such systems from a knowledge of the fundamental microstructural mechanics – that is, from the interactions among the particles and from their distribution in space and time. In this thesis, we are concerned with dispersion of particles in sedimenting suspensions where Brownian forces are negligible. Recent experiments by Leighton & Acrivos (1987) have shown that the dispersion of neutrally-buoyant non-Brownian spheres in simple shear flow is a diffusive process; i.e., at long times the mean-squared displacement of the particles grows linearly with time. Generally, self-diffusion has been considered a property of colloidal suspensions, whose particles are strongly affected by Brownian forces. Our investigation focuses on the hydrodynamic dispersion occurring in sedimenting suspensions of non-Brownian particles; particularly, we seek to answer the question of whether dispersion is or is not diffusive, as well as to provide estimates of the dispersion as a function of the concentration of particles.

Self-diffusion is an important property of colloidal suspensions and has been the subject of theoretical, experimental and numerical studies. Self-diffusion can convey static information through the short-time diffusivity measuring the properties of the local structure, as well as dynamic information in the behavior of the long-time diffusivity, as a particle must wander far from its starting point, deforming the local structure, and exchanging places with its neighbors. The long-time diffusivity in colloidal systems arises from non-deterministic Brownian impulses that give the particles a series of displacements that result in an irreversible random walk. Statistical mechanicians and fluid dynamicists have developed theories to predict the self-diffusion coefficient and its dependence on concentration (Ralli-son & Hinch 1986). Experimentally, measurements of the self-diffusion coefficients by dynamic light scattering are used to infer particle size and/or shape and infor-

mation about the interparticle forces (Berne & Pecora 1976). Recently, Bossis & Brady (1987) have studied the self-diffusion of a concentrated suspension of neutrally buoyant Brownian spheres in a simple shear flow by numerical simulation.

In non-colloidal suspensions, random Brownian forces are negligible and do not affect the dispersion of the particles. If the suspension does not contain Brownian or interparticle forces, the governing equations of motion are linear and the trajectories of the particles should be reversible. The question is how such a suspension can produce long-time dispersion that is diffusive. In the shear system studied by Leighton & Acrivos, the motion of the spheres was shown to be diffusive, despite the fact that the governing Stokes equations demand that the sphere paths be reversible. (For a discussion of this and other types of microscopically reversible diffusion processes, see Leighton & Acrivos 1987, and Okagawa, *et al.* 1978). The diffusive nature of the sphere trajectories resulted from the shear-induced multi-body hydrodynamic interactions. Although the particle trajectories are completely deterministic, the equations of particle motion are highly non-linear, forming a non-linear dynamical system that should display deterministic chaos, and hence, diffusive behavior. Determining whether the dispersion of particles in a sedimenting solution exhibits this type of self diffusion is the goal of this research.

Consider the trajectories of particles in a sedimenting suspension of non-Brownian particles with no non-hydrodynamic interparticle forces. If the particles did not interact hydrodynamically, there would be no relative motion among the particles; they would all fall vertically at the sedimentation velocity. When the particles do interact hydrodynamically, their displacement will no longer simply arise from their sedimentation velocity. Imagine labeling a single particle at a given time and following its trajectory. As it interacts with the other particles and moves to its next position, it will drift laterally from its line of fall in a non-hydrodynamically-interacting suspension. Also, its displacement in the direction of settling may be more or less than the displacement in a non-hydrodynamically interacting suspension, or more or less than that accounted by the average sedimen-

tation velocity in a hydrodynamically interacting suspension. These displacements may constitute a random walk – the time-averaged displacement in the direction perpendicular to gravity will be zero, as will the time-averaged displacement in the direction of gravity minus the displacement owing to the average sedimentation velocity. It is our task to determine if this series of displacements is diffusive. The next question is how we shall accomplish this.

As in the colloid studies, three avenues of study present themselves – theory, experiment, and numerical simulation. The only published studies of non-Brownian systems have dealt with the shear-induced self diffusion of suspensions of neutrally buoyant sphere in shear flow. Both experiments and numerical simulations have shown that the displacement of spheres in these systems is indeed self diffusive (Leighton & Acrivos 1987, Bossis & Brady 1987). Quick analysis of rate of the three-body interactions in these flows (two-body interactions cannot lead to diffusive behavior) show that the long-time self diffusion coefficient should be proportional to $\dot{\gamma}\phi^2 a^2$ as $\phi \rightarrow 0$, where $\dot{\gamma}$ is the shear rate, ϕ is the volume fraction of spheres, and a is the sphere radius. This scaling prediction is supported by the experimental results. There have been no rigorous theoretical analyses of this diffusion process.

To date, no studies of the dispersion in sedimenting suspensions have been reported in the literature. Theoretical studies of long-time dispersion in dilute suspensions are under way. Early work indicates that the long-time dispersion is diffusive and is proportional to the inverse of the volume fraction as the volume fraction goes to zero (Koch & Shaqfeh 1987). We are also aware of experiments in progress by Ham & Homsy (1987) and Davis & Hassen (1987); however, these are still restricted to dilute suspensions. Our approach to this problem is to numerically simulate concentrated sedimenting suspensions. Thus, the particle trajectories are completely available for analysis, and non-hydrodynamic or Brownian forces can be ignored or included in an exact way. We shall use a molecular-dynamics-like approach known as Stokesian dynamics.

Stokesian dynamics is capable of dynamically simulating the behavior of particles in infinite suspensions. In its most general form, the particles may interact through both hydrodynamic and non-hydrodynamic forces, which may be any type or combination of Brownian, interparticle or external forces. The central element of this method is the approximation of the complex hydrodynamic interactions among all particles in the suspension. Since we are interested in hydrodynamic dispersion in suspensions, it is essential that the simulation accurately accounts for the many-body interactions, which are necessary for diffusive displacement of particles. Since it is a dynamic simulation, lubrication forces that prevent the overlap of particles (a physical impossibility) are also essential. Stokesian dynamics includes both of these important elements and has been successfully applied to a variety of finite and infinite systems. Bossis & Brady (1987) used this technique in their study of self-diffusion in sheared suspensions.

In Chapter 2, the basic Stokesian dynamics method is outlined. There are two important features of sedimenting suspensions that need to be recognized. The first is the long-range nature of the hydrodynamic interactions, particularly among particles on which external forces act. In an infinite suspension, these long-range interactions can lead to divergent expressions for the velocity of the particles. In previous simulation studies of infinite suspension, these interactions have been rendered convergent by applying the method of O'Brien (1979). These previous simulations all dealt with neutrally buoyant spheres in simple shear flow, whose long-range interactions decay as $O(r^{-2})$, where r is the distance from the center of the sphere. The long-range interactions in a sedimenting suspension decay as $O(r^{-1})$, so that more particles are required to satisfy the conditions of O'Brien's method. As will be seen, the computational cost increases as the cube of the number of particles in the simulation, and thus an efficient means for calculating the long-range interactions is needed. This has been accomplished by using Ewald sums, as first developed for the hydrodynamic problem by Beenakker (1986). We have applied this technique to all long-range (previously divergent or conditionally convergent) hydrodynamic interactions, drastically reducing the cost of calculating

these interactions.

The importance of reducing the calculation time is clear when the second important feature of sedimenting suspensions is considered. In sheared suspensions, the rate of the interactions of the particles causing relative motion is set by the shear flow forcing them past one other. In sedimenting suspensions, however, only the hydrodynamic interactions among the particles themselves, not the imposed flow, give rise to relative motion. The microstructure changes at a much slower pace than in the sheared suspensions, and thus, longer simulations are needed. It takes longer for the suspension to achieve a steady state, and it takes longer for a particle to experience sufficient uncorrelated interactions for its motion to become diffusive. Chapter 2 details all of the steps we have taken to produce simulations that capture the necessary physics to study dispersion in sedimenting suspensions in reasonable computational times.

We present the results of our investigations in Chapters 3 and 4. In Chapter 3 we compare the short-time, self-diffusion coefficient, which is configuration-dependent only, found in infinite regular arrays of spheres, in random suspensions, and in steady-state sedimenting suspensions. Included in this chapter is the dependence of the short-time, self-diffusion coefficient on concentration in randomly distributed suspensions. In Chapter 4 we present the results of our study of the long-time dispersion in sedimenting suspensions. The effect of repulsive interparticle forces and the concentration dependence are discussed. Chapter 5 presents our overall conclusions, including recommendations for continuing research.

CHAPTER 2: THE STOKESIAN DYNAMICS METHOD

We now take a closer look at the tool we have chosen to investigate the sedimentation-induced, self-diffusion of non-Brownian particles in suspensions of infinite extent. The tool is Stokesian dynamics, a molecular-dynamics-like approach to simulating dynamically the behavior of many particles suspended or dispersed in a fluid medium. The method is very general and is applicable to systems with a finite number of particles or suspensions of infinite extent. The particles may interact through both hydrodynamic and non-hydrodynamic forces, such as Brownian, colloidal, and/or other types of interparticle or external forces. Possible applications of Stokesian dynamics include problems of sedimentation, flocculation, diffusion in many types of suspensions, polymer rheology, transport in porous media, etc. The simulation method is capable of predicting both static (i.e., configuration-specific) and dynamic microstructural properties, as well as macroscopic properties in a variety of systems at all concentrations. This section presents the method at its most general and will clearly show how our present study fits into the larger research area accessible to Stokesian dynamics.

First, we present the evolution equation for the suspension microstructure. The equation will include contributions from Brownian, interparticle, external and hydrodynamic forces acting on the particles. Of course, not all these forces will be present in the particular systems we wish to investigate, so the necessary simplifications of the evolution equation are outlined. The equation is completely general and exact for N particles suspended in a volume, V; the central role of the hydrodynamic interactions in the evolution of the microstructure is explicitly shown. Secondly, we define a variety of macroscopic properties. These definitions involve the appropriate averaging of the microstructural evolution equation or its solution. All of these properties involve, explicitly or implicitly, the averages of hydrodynamic interaction tensors that relate the dynamic properties of the particles to their kinematic conditions.

Approximating the N-body hydrodynamic interactions accurately and quickly

is at the heart of the Stokesian dynamics method. This approximation, which includes both the near-field lubrication forces and the dominant many-body interactions among the particles, is presented in Section 2.31. In Section 2.3.2, we show how the hydrodynamic interactions in unbounded, infinite systems, i.e., the thermodynamic limit $N \to \infty$, $V \to \infty$, with N/V fixed, are simulated. This is not a trivial problem because of the long-range $(1/r)$ nature of the hydrodynamic interactions. Specifically, we introduce the Ewald-sum technique to speed the convergence of the hydrodynamic interactions, after O'Brien's method has insured their convergence.

2.1 The Microstructural Mechanics

For N rigid particles suspended in an incompressible Newtonian fluid of viscosity, η, and density, ρ, the motion of the fluid is governed by the Navier-Stokes equations, and the particle motion is described by the coupled N-body Langevin equation, which can be written

$$\mathbf{m} \cdot \frac{d\mathbf{U}}{dt} = \mathbf{F}_H + \mathbf{F}_P + \mathbf{F}_B, \tag{2.1–1}$$

that simply states the mass times the acceleration equals the sum of the forces. $\mathbf{m}$ is a generalized mass/moment of inertia matrix of dimension $6N \times 6N$, $\mathbf{U}$ is the particle translational/rotational velocity vector of dimension $6N$, and the $6N$ force/torque vectors, $\mathbf{F}$, represent: 1) the hydrodynamic forces, $\mathbf{F}_H$, exerted on the particles due to their motion relative to the fluid, 2) the deterministic non-hydrodynamic forces, $\mathbf{F}_P$, which may be interparticle and/or external, and 3) the stochastic forces, $\mathbf{F}_B$, that give rise to Brownian motion. We will study only suspensions whose motion on the particle scale is such that the LHS of Equation (2.1–1) is zero. Thus, the evolution equation is a linear combination of the forces acting on the particles; of course, in actual practice we would include only those forces relevant for the given problem. From now on, we consider only systems where the Brownian forces are negligible; the infinite Péclet number limit.

When the motion of the particle scale is such that the particle Reynolds

number is small (the exact statement of this condition is given below), the hydrodynamic force/torque exerted on the particles in a suspension undergoing a bulk linear shear flow is

$$\mathbf{F}_H = -\mathbf{R}_{FU} \cdot (\mathbf{U} - \mathbf{U}^\infty) + \mathbf{R}_{FE} : \mathbf{E}^\infty \qquad (2.1\text{–}2)$$

(see Brenner & O'Neill 1972, Kim & Mifflin 1985, Bossis & Brady 1984). $\mathbf{U}^\infty$ is the imposed flow at infinity evaluated at the particle center, i.e., $\mathbf{U}_\alpha^\infty = \mathbf{\Omega}^\infty$ for rotation and $\mathbf{U}_\alpha^\infty = \mathbf{E}^\infty \cdot \mathbf{x}_\alpha$ for translation, where $\mathbf{x}_\alpha$ is the particle postion vector of the α^{th} particle. $\mathbf{E}^\infty$ and $\mathbf{\Omega}^\infty$ are the symmetric (and traceless from continuity) and anti-symmetric parts of the the velocity gradient tensor, respectively. Both are constants in space, but may be arbitrary functions of time. $\mathbf{R}_{FU}(\mathbf{x})$ and $\mathbf{R}_{FE}(\mathbf{x})$ are resistance matrices that give the hydrodynamic force/torque on the particles because of their motion relative to the fluid ($\mathbf{R}_{FU}(\mathbf{x})$) and because of the imposed shear flow ($\mathbf{R}_{FE}(\mathbf{x})$). These matrices depend only on the configuration of the particles since the Reynolds number is zero. $\mathbf{x}$ represents the generalized configuration vector, specifying the location *and* orientation of all N particles, and $\mathbf{U}$ is the particles' translational/rotational velocity vector. Note that the subscripts on the matrices indicate the coupling between the kinematic and dynamic quantities. If there is no imposed shear flow, Equation (2.1–2) reduces to

$$\mathbf{F}_H = -\mathbf{R}_{FU} \cdot (\mathbf{U} - \mathbf{U}^\infty) \qquad (2.1\text{–}3a)$$

$$(\mathbf{U} - \mathbf{U}^\infty) = -\mathbf{M} \cdot \mathbf{F}_H, \qquad (2.1\text{–}3b)$$

where $\mathbf{M}$, the exact mobility matrix, is the inverse of the resistance matrix ($\mathbf{M} = (\mathbf{R}_{FU})^{-1}$). In all problems, this mobility matrix is the central element describing the hydrodynamic interactions among the particles.

The deterministic, non-hydrodynamic force, $\mathbf{F}_P$, can be most any form of interparticle and/or external force. For example, Bossis & Brady(1984) included a pairwise electrostatic repulsive force between neutrally buoyant spheres in a shear flow. For sedimentation problems, $\mathbf{F}_P$ will simply be the buoyancy force. It is also possible to link together some of the particles permanently through

an interparticle force; we would then be able to extract information about the *internal* dynamics of the linked particles and their effect on the bulk properties of the suspension.

Solving Equation (2.1–1) and (2.1–2) for $\mathbf{U}$ and integrating that expression over time produces the evolution equation for the particle positions and orientations with an error of $O(\Delta t^2)$:

$$\Delta \mathbf{x} = \{\mathbf{U}^\infty + (\mathbf{R_{FU}})^{-1} \cdot [\dot{\gamma}^* \, \mathbf{R}_{FE} : \mathbf{E}^\infty + \mathbf{F}_P]\}\Delta t. \qquad (2.1\text{–}4)$$

$\Delta \mathbf{x}$ is the vector representing the change in position and orientation of every particle during the time step Δt. $\mathbf{x}$ has been non-dimensionalized by the particle size a, the time by $6\pi\eta a^2/|\mathbf{F}_P|$, the shear force by $6\pi\eta\dot{\gamma}$ ($\dot{\gamma} = |\mathbf{E}^\infty|$ is the magnitude of the shear rate), and the interparticle and/or external forces by $|\mathbf{F}_P|$. $\dot{\gamma}^* = 6\pi\eta a^2\dot{\gamma}/|\mathbf{F}_P|$ is the non-dimensional shear rate that gives the relative importance of the shear flow and the imposed interparticle and/or external forces.

Equation (2.1–4) simply states that the motion of a particle is composed of two parts, each resulting from the basic forces in Equation (2.1–1). There is a contribution due to the hydrodynamic shear forces, $[\mathbf{U}^\infty + (\mathbf{R}_{FU})^{-1} \cdot \mathbf{R}_{FE} : \mathbf{E}^\infty] \, \Delta t$, and a contribution from the interparticle or external forces, $[(\mathbf{R}_{FU})^{-1} \cdot \mathbf{F}_P] \, \Delta t$. In general, the motion of the particles in a suspension depends on the dimensionless parameters characterizing the suspension and flow conditions: $\dot{\gamma}^*$, and ϕ, the volume fraction of particles. No restriction has been made to particles of identical size and shape. If the particles are not spherical, other dimensionless parameters characterizing their shape must be included. If more than one type of particle is present, there will be a volume fraction, ϕ_i, for each type. If interparticle forces are present, in general, we will need dimensionless parameters to specify their range (as opposed to their amplitude).

For sedimentation of non-Brownian particles in the absence of a shear flow, $\mathbf{F}_H$ is determined from Equation (2.1–1) for the specified external and/or interparticle forces, and then Equation (2.1–3*b*) is solved for the translational and rotational velocities of the particles. For sedimentation, the requirement that

the particle Reynolds number be small takes the form $Re = \rho U_o a/\eta \ll 1$, where $U_o(= 2(\rho_p - \rho)ga^2/(9\eta))$ is the sedimentation velocity of an isolated particle (characteristic length is a and density is ρ_p) in a fluid of density ρ and viscosity η. Equation (2.1–3*b*) is the core of our dynamic simulation of the sedimentation problem. It is an exact description for N particles of arbitrary size and shape suspended in a volume, V. Given an initial configuration and specified external and/or interparticle forces, Equation (2.1–3*b*) is integrated to follow the dynamic evolution of the suspension microstructure. The only task remaining is to approximate the hydrodynamic interaction matrices. The description of our approximation of these matrices is in Section 2.3 and the solution of the evolution equation is in Section 2.4.

The Stokesian dynamics formulation is completely general, describing the motion of N particles suspended in a volume, V, interacting through hydrodynamic, interparticle, or external forces. Simulating specific suspension flows only requires identifying the correct time scale and setting the correct dimensionless parameters, e.g., $\dot{\gamma}^*$, ϕ, etc., in the evolution equation. Thus, the sedimentation problem and the shear problem, are both seen as special cases to the general problem of suspension dynamics. In all of these problems, the central element is the hydrodynamic interaction tensors, and we will see that they are explicitly present in the definitions of important macroscopic properties that characterize the suspension. In the next section we will show how the macroscopic properties of various suspension types are determined from the appropriate averaging of the microscale evolution equation.

2.2 The Macroscopic Properties

We now consider the bulk properties of the suspension, which can be determined from the corresponding averaged expressions of the microscale results. These expression, in general, depend on the property to be investigated, and we shall only discuss a few of them here. Most of the general formulae for the macroscopic properties have been derived by Batchelor (1970, 1972, 1976, 1977), and all

involve (generally explicitly) averages of the hydrodynamic interaction tensors.

For sedimentation relative to zero volume flux axes, $\mathbf{U}^{\infty} = \mathbf{0}$, a macroscopic property of interest is the average velocity of the particles, $\langle \mathbf{U} \rangle$. For identical particles all experiencing the same external force, $\mathbf{F}$, the average sedimentation velocity would be given by

$$\langle \mathbf{U} \rangle = \langle (\mathbf{R}_{FU})^{-1} \cdot \mathbf{F} \rangle = \langle \mathbf{M} \rangle \cdot \mathbf{F}. \tag{2.2–1}$$

This equation can be generalized for suspensions of unlike particles (Batchelor 1982).

Other important macroscopic properties of a suspension are related to the deviatoric stress felt by the individual particles. The anti-symmetric part of the bulk deviatoric stress, $\mathcal{T}_{\times}$, is given as

$$\langle v_o \mathcal{T}_{\times} \rangle = \langle \mathbf{R}_{T\Omega} \cdot (\mathbf{\Omega} - \mathbf{\Omega}^{\infty}) \rangle, \tag{2.2–2}$$

where v_o is the volume of an individual particle, and $\mathbf{R}_{T\Omega}$ is the resistance matrix that gives the hydrodynamic torque on the particles because of their rotational motion relative to the fluid. The symmetric part of the bulk deviatoric stress is known as the bulk stress, $\langle \mathbf{\Sigma} \rangle$, and is defined

$$\langle \mathbf{\Sigma} \rangle = \text{I.T.} + 2\eta \mathbf{E}^{\infty} + \frac{N}{V} \{ \langle \mathbf{S}^H \rangle + \langle \mathbf{S}^P \rangle \}. \tag{2.2–3}$$

This property defines the rheology of the suspension. I.T. stands for an isotropic term of no interest. The particles make two contributions to the bulk stress: a mechanical or contact stress transmitted by the fluid because of the shear flow, $\langle \mathbf{S}^H \rangle$ and an "elastic" stress due to the interparticle forces, $\langle \mathbf{S}^P \rangle$. The particle contributions to the bulk stress are given by

$$\langle \mathbf{S}^H \rangle = -\langle \mathbf{R}_{SU} \cdot (\mathbf{U} - \mathbf{U}^{\infty}) \; - \; \mathbf{R}_{SE} : \mathbf{E}^{\infty} \rangle, \tag{2.2–4a}$$

$$\langle \mathbf{S}^P \rangle = -\langle \mathbf{x} \mathbf{F}_P \rangle. \tag{2.2–4b}$$

$\mathbf{R}_{SU}(\mathbf{x})$ and $\mathbf{R}_{SE}(\mathbf{x})$ are configuration- dependent resistance matrices, similar to $\mathbf{R}_{FU}$ and $\mathbf{R}_{FE}$, relating the particle stresslet, $\mathbf{S}$, to the particle velocities ($\mathbf{R}_{SU}$) and to the imposed rate of strain ($\mathbf{R}_{SE}$).

The general N-particle diffusion tensor for Brownian particles, $\mathbf{D}$, is related to the resistance and mobility matrices as follows:

$$\mathbf{D} \equiv kT(\mathbf{R}_{FU})^{-1} = kT\mathbf{M}, \tag{2.2–5}$$

where T is the temperature and k is Boltzman's constant. Several "particle diffusivities" may be defined. Self-diffusion is a basic property in many types of suspensions and it may be induced a variety of ways. The short-time self-diffusivity, $\mathbf{D}_o^s$, measures the average instantaneous mobility of a particle in its local environment and is defined

$$\mathbf{D}_o^s = \langle \mathbf{D}_{ii} \rangle. \tag{2.2–6}$$

The angle brackets denote an average over all configurations as well as the average over the particles in a given configuration, and $\mathbf{D}_{ii}$ denotes the self-submatrix that relates a particle's kinematic quantities to its own dynamic quantities.

The long-time self-diffusivity, $\mathbf{D}_\infty^s$, measures the ability of a particle to wander far from its starting point and is defined

$$\mathbf{D}_\infty^s = \lim_{t\to\infty} \frac{1}{2}\frac{d}{dt}\langle(\mathbf{x} - \tilde{\mathbf{x}})^2\rangle, \tag{2.2–7}$$

where $\mathbf{x}$ is the vector representing the displacement of the particles from their initial configuration at a given time, and $\tilde{\mathbf{x}}$ is the displacement resulting from the bulk motion. In this case, the angle brackets indicate the average over all initial configurations of the particles as well as the average over all the particles. If the limit in Equation (2.2–7) is a constant, the dispersion of the particles as they wander among their neighbors is diffusive. Both the short- and long-time self-diffusivities are accessible by light scattering techniques, being the long- and short-wave scattering limits, respectively (Rallison & Hinch 1986, van Megen *et al.* 1986).

In addition to these (and other) macroscopic properties, we can also calculate all types of statistical properties, since the complete microstructural dynamics is followed. These statistical properties include all normal particle distribution functions, such as the pair-distribution function, $g(\mathbf{r})$, the triplet-distribution function,

$g(\mathbf{r}_1, \mathbf{r}_2)$, etc., cluster sizes and cluster-distribution functions. One can also calculate particle velocity fluctuations about the average and so define a "suspension temperature", and so on.

In summing up this section, several points need to be emphasized. From the definitions of the macroscopic properties, the fundamental role of the hydrodynamic resistance matrices is obvious. All of the above equations, as written, are exact; all that remains is to approximate the hydrodynamic interactions. The entire evolution of the suspension microstructure *and* the macroscopically observed properties depend on these interactions, so an accurate representation of the N-body resistance matrices is essential. In succeeding section we will discuss the core of the Stokesian dynamics method, the accurate and computationally efficient approximation of the N-body resistance matrices for finite and infinite systems. This approximation, within the context of Stokesian dynamics, has already been applied successfully to a variety of suspension flows. Such investigations include the rheology of concentrated suspensions of neutrally-buoyant non-Brownian spheres in simple shear flow (Brady & Bossis 1985), the self-diffusion of Brownian particles in concentrated suspensions under shear (Bossis & Brady 1987), the sedimentation rate of disordered suspensions (Brady & Durlofsky 1987), among others. Our study focuses on the sedimentation-induced self- diffusivity of non-Brownian spheres in suspension.

2.3 The Hydrodynamic Interactions

In this section, we will describe the general Stokesian dynamics method and its application to the present sedimentation problem. Our object is to study the long-time diffusive behavior of monodisperse, non-Brownian spherical particles settling in an infinite suspension. This problem demands that the method do several tasks well: long-range multi-body hydrodynamic interactions, lubrication interactions, and the computationally efficient calculation of all of the above. Since we are studying diffusive behavior, the importance of including the multi-body hydrodynamic interactions is obvious. Section 2.3.1 describes how the method

includes these important interactions. The inclusion of lubrication forces, which becomes increasingly important as the concentration increases, is also described in this section. This method was developed by Durlofsky, *et al.* (1987) for a finite number of particles, and we start with this basic methodology.

Simulating a suspension of infinite extent is not a simple extension of the finite particle case. A simple summation of hydrodynamic interactions among the particles results in badly divergent expressions; this difficulty is overcome by the method of O'Brien (1979). O'Brien's method allows us to write convergent expressions for the hydrodynamic interactions for a particle in a suspension, yet to deal only with a finite number of its neighbors.

Although O'Brien's method allows us to consider only N particles of the suspension when determining the kinematic behavior of a particle, N may still be too large for practical computation. From O'Brien, we know that the effect of particles outside the volume, V, which contains the N particles, on the velocity of a sedimenting particle at the center of V is zero, within an error of $O(R^{-1})$, where R is the characteristic radius of V. As R increases, the effect of the surrounding particles can be made arbitrarily small. The same effect in systems of neutrally buoyant spheres in a linear shear field is also zero, but the error is of $O(R^{-2})$ (Brady & Bossis 1985). Since increasing the number of spheres is computationally expensive, we opt to speed the convergence of the interaction expressions another way. That way is to choose a smaller number of spheres, N_1, in a smaller volume, V_1, and replicate their images throughout V. By creating a lattice of these images, we can invoke Ewald's method of accelerating the convergence of lattice sums. This technique is common in the study of electrostatic problems and was first applied to the Rotne-Prager tensor by Beenakker(1986). Details of O'Brien's method and further discussion can be found in Section 2.3.2.

2.3.1 The Hydrodynamic Interactions: Finite Particle Systems

We consider the problem of determining the motion of particles subject to a constant body force, such as the buoyancy force. After rewriting Equation (2.1–

3*b*) after solving for the hydrodynamic force in Equation (2.1–1), the motion of the particles in Stokes flow can be calculated from

$$\mathbf{U} - \mathbf{U}^{\infty} = \mathbf{M} \cdot \mathbf{F}_P. \qquad (2.3.1\text{–}1)$$

The mobility matrix depends on the instantaneous configuration of the particles only. The mobility matrix is symmetric, as can be shown from the reciprocal theorem, and positive definite, because of the dissipative nature of the system. Since there is no general solution to the N-body Stokes equation, we must approximate **M**. Durlofsky *et al.* (1987) developed an excellent approximation to the true mobility matrix that preserves the dominant multi-body interactions and lubrication forces among an arbitrary number of spheres. This section is a brief description of the way the exact mobility matrix for a finite number of spheres is approximated in our simulation.

The basic problem is to generate an approximate N-particle mobility matrix, **M**, that relates the particles' translational and rotational velocities to the forces and torques imposed on them. We start with the exact integral representation of the velocity field in Stokes flow, in conjunction with Faxén's laws; the force density on the surface of each particle is expanded in a series of moments about the center of each particle. The monopole, or zeroth moment of the force density, corresponds to the total force on the particle, $\mathbf{F}_t$ (the subscript t indicates that the force is related to the translational motion of the particles). The dipole, or first moment of the force density, has both symmetric and anti-symmetric parts: the anti-symmetric part is the total torque, **L**, and the symmetric part is known as the stresslet, **S**, which in sedimentation problems is an induced quantity resulting from the interaction with the other particles. We can truncate the multipole expansion at any order, depending on the level of accuracy we desire, but to include the effects of lubrication, all moments are necessary. Since we will include the effects of lubrication in the resistance formulation, we truncate the expansion after the first moment. (We also include two higher order multipole contributions that result from the finite size of the particles. A more complete derivation that

considers explicitly the quadrupole contribution to the mobility matrix can be found in Brady *et al.* 1987.) For the sedimentation problem, we approximate the mobility matrix by the $6N \times 6N$ matrix $\mathbf{M_{UF}}$ and write Equation (2.3.1–1) as

$$\begin{pmatrix} \mathbf{U}_t - \mathbf{U}_t^\infty \\ \mathbf{\Omega} - \mathbf{\Omega}^\infty \end{pmatrix} = \begin{pmatrix} \mathbf{M}_{U_t F} & \mathbf{M}_{U_t L} \\ \mathbf{M}_{\Omega F} & \mathbf{M}_{\Omega L} \end{pmatrix} \cdot \begin{pmatrix} \mathbf{F}_t \\ \mathbf{L} \end{pmatrix}, \qquad (2.3.1\text{–}2)$$

where $\mathbf{U}_t$ and $\mathbf{\Omega}$ are the N-particle translational and rotational velocity vectors. When $\mathbf{M}_{U_t F}$ is formed for two particles, it is commonly called the Rotne-Prager tensor.

We can increase the accuracy of our mobility matrix by including the stresslet interactions. This is necessary for problems where there is an imposed linear shear field. We form the grand mobility matrix, $\mathcal{M}$, which includes the stresslet interactions, as follows:

$$\begin{pmatrix} \mathbf{U} - \mathbf{U}^\infty \\ -\mathbf{E}^\infty \end{pmatrix} = \mathcal{M} \cdot \begin{pmatrix} \mathbf{F}^p \\ \mathbf{S} \end{pmatrix}, \qquad (2.3.1\text{–}3)$$

with $\mathcal{M}$ partitioned as

$$\mathcal{M} = \begin{pmatrix} \mathbf{M}_{UF} & \mathbf{M}_{US} \\ \mathbf{M}_{EF} & \mathbf{M}_{ES} \end{pmatrix} \qquad (2.3.1\text{–}4)$$

where the imposed rate of strain, $-\mathbf{E}^\infty$, is zero for sedimentation problems. The grand mobility matrix, $\mathcal{M}$, is written as an $11N \times 11N$ matrix, since the stresslets are traceless and symmetric. The $6N \times 5N$ matrix $\mathbf{M}_{US}$ relates the velocities and the stresslets, the $5N \times 6N$ matrix $\mathbf{M}_{EF}$ relates the rate of strain and forces, and the $5N \times 5N$ matrix $\mathbf{M}_{ES}$ relates the rate of strain and the stresslets. In addition, $\mathbf{E}^\infty$ and $\mathbf{S}$ are written in a compact form, which takes advantage of the fact the stresslets are traceless and symmetric; this is done so that $\mathcal{M}$ is not singular and may be inverted. To include higher order multipole moments, the vector on the RHS is extended by including the irreducible (quadrupole, octupole, etc.) moments, and the kinematical vector on the LHS is extended with zeros, as all higher velocity gradients must be zero. As we construct them, $\mathcal{M}$, $\mathbf{M}_{UF}$ and $\mathbf{M}_{ES}$ are all symmetric and positive definite like $\mathbf{M}$. Details of the construction of these matrices can be found in Durlofsky *et al.* (1987).

In our simulation, these matrices are far-field approximations to the hydrodynamic interactions between spherical particles. Consider the small (as opposed to grand) mobility matrix, $\mathbf{M_{UF}}$, and neglect the stresslets for a moment. Solving Equation (2.3.1–2) for the sphere velocities will sum only the pairwise interactions between spheres. If we attempt to move the spheres based on these velocities, the spheres will overlap since the far-field approximations to the sphere interactions do not include the strong lubrication interactions that will prevent this overlap. To include these lubrication interactions, we first invert $\mathbf{M}_{UF}$. The invert, $(\mathbf{M}_{UF})^{-1}$, is the far-field approximation to the resistance matrix $\mathbf{R}$. More importantly, this invert is a true many-body approximation of $\mathbf{R}$. Whatever elements are included in the mobility matrix – point force, finite size effects, stresslet interactions, etc. – upon inversion, the reflections among all elements and all spheres are summed. The proof of this is in Durlofsky *et al.* (1987).

The invert, $(\mathbf{M}_{UF})^{-1}$, is still only a far-field approximation to the true resistance matrix. Lubrication effects would occur only if all multipole moments were included in the mobility matrix. We include these important near-field interactions in a pairwise fashion to the resistance formulation. To each element of the $(\mathbf{M}_{UF})^{-1}$ we add the known exact two-sphere resistance interactions. This additional two-sphere resistance matrix is known as $\mathbf{R}_{2b}$. However, $(\mathbf{M}_{UF})^{-1}$ already contains the the far-field part of the two-sphere interactions. These far-field interactions, denoted by $\mathbf{R}_{2b}^{\infty}$, must be subtracted from $\mathbf{R}_{2b}$. Our approximation to the exact resistance matrix is

$$\mathbf{R} \approx (\mathbf{M}_{UF})^{-1} + \mathbf{R}_{2b} - \mathbf{R}_{2b}^{\infty}. \qquad (2.3.1\text{–}5)$$

In an actual simulation, we would then solve the equation set in Equation (2.1–3a) for the translational and rotational velocities of the spheres. This is known as the FT formulation and method.

When there is no imposed linear shear flow, Durlofsky *et al.* (1987) have shown that the FT method gives accurate results. If we want more accurate results by including the effect of induced stresslets and if we are willing to pay the

computational costs to obtain them, we form the grand mobility matrix, $\mathcal{M}$. The invert of the grand mobility matrix is the grand resistance matrix $\mathcal{R}$:

$$\begin{pmatrix} \mathbf{F}_p \\ \mathbf{S} \end{pmatrix} = \mathcal{R} \cdot \begin{pmatrix} \mathbf{U} - \mathbf{U}^\infty \\ -\mathbf{E}^\infty \end{pmatrix}, \tag{2.3.1–6}$$

where $\mathcal{R}$ is partitioned as

$$\mathcal{R} = \begin{pmatrix} \mathbf{R}_{FU} & \mathbf{R}_{SU} \\ \mathbf{R}_{FE} & \mathbf{R}_{SE} \end{pmatrix}. \tag{2.3.1–7}$$

The effect of the induced stresslets is obvious when one realizes that $\mathbf{R}_{FU} \neq (\mathbf{M}_{UF})^{-1}$. The approximation for the true resistance matrix is now

$$\mathbf{R} \approx \mathbf{R}_{FU} + \mathbf{R}_{2b} - \mathbf{R}_{2b}^{\infty}. \tag{2.3.1–9}$$

This is the FTS formulation. Note that inverting the larger grand mobility matrix is approximately 6.25 times slower than inverting the small mobility matrix (cf. Section 2.6).

The results of these methods, when applied to several known cases involving the interactions among a finite number of spheres, compare excellently with reported results (cf. Durlofsky *et al.* 1987). The procedure reproduces both the proper near-field lubrication forces and the dominant many-body interactions that occur among a finite number of spheres subject to imposed forces.

2.3.2 The Hydrodynamic Interactions: Infinite Systems

We are interested in the behavior of particles settling in an infinite suspension, i.e., letting the number of particles, $N \rightarrow \infty$, as their containing volume, $V \rightarrow \infty$, keeping the number density, $n = N/V$, fixed. The long-range nature of the hydrodynamic interactions among the particles (for example, the disturbance velocity from a falling sphere decays as $O(r^{-1})$, where r is the distance from the sphere's center) demands that care be taken in simulating suspensions of infinite extent; a simple summation of interactions among the particles produces badly divergent expressions for certain kinematic quantities, such as the particle's translational velocity. This convergence problem can be overcome by several alternative

methods, but only the method of O'Brien (1979) can be applied to dynamic simulations. Although O'Brien's formulation assures us of convergence, it does not promise us speedy convergence. To improve computational efficiency, we rewrite the lattice sums that can occur in O'Brien's method into a rapidly converging form. This recasting of the lattice sums is called Ewald's method. This technique was first applied to the Rotne-Prager tensor by Beenakker (1986); we have applied this technique to the additional mobility matrix elements in our simulation (cf. Appendix A and below). We will discuss, in detail, these methods at the level of point forces; extensions to include finite-size effect, torques, stresslets, etc., are briefly explained.

In O'Brien's method, we start from an integral representation for the solution to Stokes equation for the velocity field $\mathbf{u}(\mathbf{x})$ at the point $\mathbf{x}$ in the suspension in terms of integrals of the force distribution on the surfaces of the N particles, and an integral over a mathematical surface Γ of large radius R and volume V that cuts through the fluid and particles. The exact solution of the velocity field for a suspension of rigid particles is

$$\mathbf{u}(\mathbf{x}) = -\frac{1}{8\pi\eta}\sum_{\alpha=1}^{N}\int_{S_\alpha}\mathbf{J}\cdot\sigma\cdot\mathbf{n}dS - \frac{1}{8\pi\eta}\int_{S_\Gamma}[\mathbf{J}\cdot\sigma+\mathbf{K}\cdot\mathbf{u}]\cdot\mathbf{n}dS, \qquad (2.3.2\text{–}1)$$

where $\mathbf{J}$ is the Green function for Stokes flow, $\mathbf{J} = (\mathbf{I}+\mathbf{rr}/r^2)/r$, $\mathbf{K} = -6\eta\mathbf{rrr}/r^5$, $\mathbf{I}$ is the unit isotropic tensor, $\mathbf{r} = \mathbf{x} - \mathbf{y}$, $\mathbf{y}$ being a point on the surface, σ is the fluid stress tensor, and $\mathbf{n}$ is the outward normal from the particle surfaces S_α and the surface Γ. Only particle surfaces within Γ are included in the sum. This volume V is surrounded by an unbounded statistically homogeneous suspension. If the volume radius is taken to be very large, the variation of $\mathbf{J}$ and $\mathbf{K}$ will be small over a surface element dS_Γ that cuts though many particles and the fluid. At that point we may replace σ and $\mathbf{u}$ in the second integral by their ***suspension*** averages $\langle\sigma\rangle$ and $\langle\mathbf{u}\rangle$. This is the only assumption made in O'Brien's method. $\langle\sigma\rangle$ and $\langle\mathbf{u}\rangle$ are either constant or linear functions of position in a statistically homogeneous suspension.

Invoking the above assumption and using the divergence theorem, Equation (2.3.2–1) becomes

$$\mathbf{u}(\mathbf{x}) - \langle \mathbf{u}(\mathbf{x}) \rangle = \frac{1}{8\pi\eta} \sum_{\alpha=1}^{N} \mathbf{J}(\mathbf{x} - \mathbf{x}_\alpha) \cdot \mathbf{F}^\alpha - \frac{n}{8\pi\eta} \int_0^R \mathbf{J} \cdot \langle \mathbf{F} \rangle dV, \qquad (2.3.2\text{–}2)$$

where $\mathbf{F}^\alpha = -\int_{S_\alpha} \sigma \cdot \mathbf{n} dS$ is the force the α^{th} particle exerts on the fluid, $\langle \mathbf{F} \rangle$ is the average force. It is now permissible to let $R \to \infty$, because at large distances from $\mathbf{x}_\alpha$, the difference between the summation and integral terms in the above equation go to zero; we now have a convergent expression for $\mathbf{u} - \langle \mathbf{u} \rangle$. Physically, the integral term represents a "back flow" of fluid relative to zero volume flux axes $\langle \mathbf{u} \rangle = \mathbf{0}$ caused by the macroscopic pressure gradient that balances the excess weight, $\langle \mathbf{F} \rangle \neq \mathbf{0}$, of the particles. No assumptions have been made about the distribution of the particles within V.

In a similar manner, we manipulate the equations relating the rotational velocity and rate of strain to the torques and stresslets, including the effect of the finite size of the particles. These expressions will have the appropriate volume integrals of the average force $\langle \mathbf{F} \rangle$, torque $\langle \mathbf{L} \rangle$, and stresslet $\langle \mathbf{S} \rangle$, analogous to that appearing in Equation (2.3.2–2). With these expressions, a convergent representation for the grand mobility matrix $\mathcal{M}$ of Equation (2.3.1–4) can be written. In this equation, $\mathbf{U}^\infty$ and $\mathbf{E}^\infty$ must now be interpreted as the suspension average velocity and rate of strain evaluated at the center of particle α, etc.

We return to the point-force expression in Equation (2.3.2–2), which is not yet in a form suitable for simulations. Note that neither the sum nor the integral in Equation (2.3.2–2) converge as R increases; only their difference is finite. In general, many particles are needed before the sum approximates a continuous distribution and convergence is obtained; in simulations, the required computer time increases dramatically as the number of particles increases. In order to reduce the number of particles needed and to accelerate convergence of the elements of the mobility matrix, we take a finite number N_1 particles and replicate them

periodically within the volume V. We rewrite Equation (2.3.2–2) for the velocity of particle α at the center of its periodic cell, as

$$\mathbf{U}^{\alpha} - \langle \mathbf{u}(\mathbf{x}_{\alpha}) \rangle = \frac{1}{8\pi\eta} \sum_{\gamma} {\sum_{\beta=1}^{N_1}}' \mathbf{J}(\mathbf{x}_{\beta} - \mathbf{x}_{\alpha}) \cdot \mathbf{F}^{\beta} - \frac{n}{8\pi\eta} \int_0^{\infty} \mathbf{J} \cdot \langle \mathbf{F} \rangle dV, \qquad (2.3.2\text{–}3)$$

where γ labels the periodic cells, and the $'$ on the sum indicates that for $\alpha = \beta$ in cell $\gamma = 1$, $\mathbf{J}$ is replaced by $\mathbf{I}$, giving the correct self term.

If we use only one periodic cell ($\gamma = 1$), and if N_1 is suitably large, then the contribution to the α^{th} particle velocity from particles outside the periodic cell will cancel the part of the integral from L to ∞, where L is the characteristic length of the periodic cell. A constant contribution from the back-flow integral evaluated from 0 to L will remain. Simulation runs that invoke only one periodic cell will be called non-Ewald runs. Of course, the slow convergence of the difference between the discreet sum and the continuous integral may require that N_1 be prohibitively large in terms of computational time constraints. This problem is particularly acute in sedimentation problems as opposed to problems concerning sheared suspensions of neutrally buoyant spheres. In a force-free system, particles outside of V, *in total*, contribute nothing to the velocity of the particle at the center of the periodic cell within an error of $O(L^{-2})$. In sedimenting suspensions, particles outside of V, *in total*, also contribute nothing to the velocity of a falling particle at the center of the periodic cell, but the error is of $O(L^{-1})$. Whether it is feasible to simulate dynamically settling suspensions depends on how quickly we can obtain convergent expressions for the mobility matrix elements.

Expressions of the type in Equation (2.3.2–3) contain so-called lattice sums, i.e., $\sum_{\gamma}$. The convergence of these sums can be accelerated using a method developed by Ewald (1921), which rewrites the lattice sums into two rapidly converging parts, one in real space and the other in reciprocal space. This technique has been used in electrostatic problems for some time. Beenakker (1986) has recently worked out the Ewald sums for both $\mathbf{J}$ and the more complete Rotne-Prager ten-

sor ($\mathbf{M}_{U_t F}$ from Equation (2.3.1–2)), which includes the effect of finite particle size. Beenakker assumed that the average force on the particles in suspension was zero ($\langle \mathbf{F} \rangle = \mathbf{0}$) in order to remove a singular term from the reciprocal-space lattice sum; this singular term occurs when $\mathbf{k} = \mathbf{0}$, where $\mathbf{k}$ is a reciprocal lattice vector. However, when the average force is non-zero, the back-flow integral in Equation(2.3.2–3) exactly cancels this singular term at $\mathbf{k} = \mathbf{0}$. Thus, Beenakker's Ewald-summed Rotne-Prager tensor is correct whether or not there is a non-zero average force on the particles. This makes intuitive sense – the mobility matrix is a purely geometric quantity, which cannot depend the kinematic or dynamic properties of the system.

We have applied O'Brien's method (which guarantees convergence) and the Ewald-sum procedure (which simply speeds the convergence) to all divergent or conditionally convergent interactions occurring in the grand mobility matrix. A brief description of of this process and explicit expressions for the interactions can be found in Appendix A. Any mobility matrix whose elements have undergone the above procedures will be denoted by a $\star$; i.e., $\mathcal{M}^\star$ will replace $\mathcal{M}$ in Equation (2.3.1–3). It should be noted that the Ewald sums and the periodic boundary conditions are computational conveniences; they accelerate the convergence guaranteed by O'Brien's method, and they speed matrix inversion and solution time by reducing the number of particles we need to consider, but they are not essential. However, at high concentrations and fixed values of N_1, the mobility matrix calculated by the non-Ewald method may lose positive definiteness. The Ewald-summed mobility matrix will not lose positive definiteness, even at high concentrations.

To illustrate that we have correctly constructed the grand mobility matrix $\mathcal{M}^\star$, we test our method against the only known results for particulate systems of infinite extent – spatially periodic suspensions, such as an infinite cubic array of spheres. Periodicity is a highly restrictive microstructure, but it does allow the "exact" solution of the many-body problem on the unit cell. From this solution, we can calculate the bulk properties such as the sedimentation velocity and the spin and shear viscosities. Our method does not depend on the periodicity of the

microstructure as do the "exact" calculations. These results are also discussed in detail in Brady *et al.* (1987).

For us to calculate these bulk properties accurately, the hydrodynamic interactions among the particles must be accurately accounted for in $\mathcal{M}^*$. In Figure 2.1 we show a comparison of the sedimentation velocity of an infinite simple cubic array of spheres as a function of volume fraction ϕ (Brady & Bossis 1988 and Brady *et al.* 1987). The solid curve is the Stokesian dynamics result, the dashed curve is the results of Zick & Homsy (1982), who solved the integral equation for Stokes flow using the periodic Green function, and the dashed curve is the point-force solution of Saffman (1973). Convergent solutions using the periodic Green functions will be termed exact, but it should be noted that it becomes increasingly difficult and time-consuming to obtain convergent solutions as the concentration increases. At low concentrations, the exact and Stokesian dynamics results are indistinguishable. If we form the Ewald-summed mobility matrix at the level of point forces only, we recover the point-force calculation of Saffman exactly. The importance of including the effect of the finite size of the spheres is obvious from Figure 2.1. The point-force solution will diverge significantly from the exact solution for $\phi > 0.1$ and give unrealistic negative sedimentation velocities for $\phi \geq 0.19$; inclusion of finite size effects in $\mathbf{M}^*_{U_t F}$ is sufficient to reproduce the exact results for $\phi \leq 0.1$. At higher concentrations, the agreement between the exact and Stokesian dynamics results is good, but not exact; the agreement worsens as $\phi \rightarrow \phi_{max}$, where ϕ_{max} is the maximum volume fraction ($\phi_{max} = \frac{\pi}{6}$ for a simple cubic array). Physically, there are relatively large channels in a sedimenting periodic array through which the upwardly flowing fluid may pass; we would not expect the effect of lubrication forces between the spheres to influence the sedimentation velocity. Indeed, the inclusion of the near-field lubrication interactions in the resistance matrix has little effect on the results. The deviation of the exact and Stokesian dynamics results for higher concentrations is caused mainly by the truncation of the many-body interactions in the mobility matrix. The preceding results are also discussed in Brady *et al.* (1987), and we would like to acknowledge the contribution of our

colleague Ron Phillips to this work (see also Phillips *et al.* 1988).

Comparisons between "exact" and Stokesian dynamics results for the spin and shear viscosities of spatially periodic suspensions demonstrate the importance of the near-field lubrication interactions in properly approximating the hydrodynamic interactions among the spheres. The spin viscosity of a cubic array (see Equation (2.2–2)) can be written in terms of one scalar, ξ, because of the symmetry of the array geometry. In Figures 2.2, 2.3 and 2.4, we compare our simulation results for the spin viscosity of a variety of cubic arrays to the dilute and close-packed asymptotic results given by Zuzovsky *et al.* (1983) (close-packed asymptotic results for simple cubic arrays only). The solid curves are the Stokesian dynamics results, the dot-dashed curves are the dilute (to $O(\phi^2)$) and close-packed limits calculated by Zuzovsky *et al.*, and the dotted curves are the far-field, many-body results (no additional two-body interactions included). The simulation (without lubrication forces) and the asymptotic results are identical to $O(\phi)$. For the spin viscosity, the far-field interactions included in the mobility matrix are insensitive to array type; the effects of array type first arise at $O(\phi^2)$. In the close-packed limit for the simple cubic array, the asymptotic solution shows a logarithmic rise in the spin viscosity as $\phi/\phi_{max} \rightarrow 1$. Our simulation method reproduces this asymptotic behavior (see Figure 2.2). It is important to note that if we do not include the lubrication forces, the simulation incorrectly predicts the behavior of the spin viscosity as $\phi \rightarrow \phi_{max}$. The close agreement at high and low concentrations is not simply fortuitous, since our approximation to the true resistance matrix is simply the combination of the correct long-range, multi-body interactions for suspensions of infinite extent and near-field "lubrication" interactions. The limitations of our approximation would show up only at moderate concentrations when a sphere's nearest neighbors are neither very close nor very far away. Unfortunately, no "exact" solution for the spin viscosity exists over the whole concentration range.

Nunan & Keller (1984) have determined the shear viscosity for a variety of cubic arrays over the entire concentration range following the procedure of Zick & Homsy (1982); the dilute and close- packed limits were first worked out by

Zuzovsky *et al.* (1983). The particle contribution to the shear viscosity is contained in the fourth-order tensor, $\mathbf{R}_{SE}$ (see Equation(2.2–3,4*a*)). (Note that for a sheared periodic suspension $\mathbf{U} \equiv \mathbf{U}^{\infty}$, and only the second term contributes in Equation(2.2–4*a*).) The shear viscosity can be uniquely written in terms of two scalars, α and β, because of the symmetry of the cubic array geometry. Figure 2.5*a* is representative of the shear viscosity results – in this case , the shear viscosity function α is shown as a function of ϕ for a sheared simple cubic lattice. In Figures 2.5–2.7, the solid curves are the full Stokesian dynamic results, the dotted curves are the far-field Ewald-sum contribution with no lubrication, i.e., $(\mathcal{M}^{\star}_{ES})^{-1}$, and the dashed curves are the "exact" result of Nunan & Keller (1984). Agreement is again seen to be quite good, being exact as to $O(\phi^2)$ in the dilute limit. As $\phi \rightarrow \phi_{max}$, α and β may approach infinity as either a function of $\ln \epsilon$ or a function of $1/\epsilon$ ($\epsilon = 1 - (\phi/\phi_{max})^{\frac{1}{3}}$), depending on the lattice type. Our full simulation exactly reproduces these singularities for all array types. Agreement at moderate concentrations is good, though not exact – errors generally range from 5% to 20% depending on array type and viscosity function except for the face-centered cubic array β viscosity function (cf. Figure 2.7*b*).

The periodicity of these arrays provides an especially strict test of our simulation technique. Remember that we expect our simulation to approximate best the hydrodynamic interactions between spheres for two-sphere center-to-center separations of greater that 4 radii or less than 2.02 radii; the largest error in the resistance interactions will occur when a sphere's nearest neighbors are an intermediate distance of between 2.02 and 4 radii away. In periodic cubic arrays, the error resulting from truncating the many-body interactions is exaggerated at moderate concentrations because of the relatively high percentage of spheres separated by intermediate distances. In a random suspension at the same moderate concentration, we would expect, on average, fewer spheres to be separated by these intermediate distances; the errors seen in the periodic array cases should be seen as fairly high upper bounds of the effect of truncation on the many-body hydrodynamic interactions in the mobility matrix. Further discussion of this subject can

be found in Brady *et al.* (1987).

From the above comparisons, it is evident that our simulation method captures the essential physics of the dominant, many-body interaction among spheres in an infinite suspension and of the lubrication forces between these spheres. Indeed, we achieve not only good qualitative results with our method, but good quantitative results over the entire concentration range. It must be stressed that the method does not depend on the periodicity of the microstructure. Unlike the "exact" calculations, the computation time requirements do not increase as the concentration rises.

In summary, O'Brien's method allows us to obtain exact convergent expressions for the hydrodynamic interactions affecting a particle at the center of a volume V containing N particles; V is immersed in a statistically homogeneous suspension of infinite extent. The use of Ewald's technique to speed the convergence of interactions is of computational importance, but adds concerns about the possible effects of long-range periodicity on simulation results. The only approximations in the method are the calculation of the hydrodynamic interactions and the use of periodic boundary conditions to simulate an unbound medium. These approximations have been quite good when compared against "exact" results for a number of finite and infinite systems of spheres. The approximations can be improved by including more moments in the integral expansions and/or increasing the number of spheres in the periodic cell.

2.4 Integration of the Sphere Trajectories

In this section we shall discuss how the trajectories are determined. From an initial configuration, $(\mathbf{R}_{FU})^{-1}$ is calculated, and then Equation (2.1–3a) is integrated to find the configuration at the next time step. Periodic boundary conditions are used to simulate the infinite suspension. After the particles have been moved, the program checks for any overlap among the particles. During the course of a simulation, spheres spend a large fraction of their time very close to one another, even at low and moderate areal fractions. This is clear from the

pair-distribution functions determined from the simulation data. Lubrication interactions added to the invert of the mobility matrix should, in principle, prevent the spheres from overlapping, but sphere overlap can and does occur since the time step is finite. Of course, we can decrease the time step, but computation costs become large. To avoid taking prohibitively small time steps, we tolerate a small amount of overlap. Typical overlaps are about 10^{-6} or 10^{-7} radii, with the largest overlap being about 10^{-5} radii. Since we cannot calculate the lubrication interactions between spheres less than two radii apart (the calculation would require the evaluation of a logarithm of a negative number), we set the sphere separation to $2+10^{-8}$ radii for the resistance calculations, but leave the actual sphere positions unaffected. If the spheres overlap more than 10^{-2} radii, the program is terminated.

A sphere's position at the next time step is calculated by multiplying a weighted average of its velocity at a given number of previous time steps by the time step. Historically, Stokesian dynamic simulations have used the explicit, fourth-order Adams-Bashforth integrator. In the course of our research we experimented with other types of integrators. The motivation behind this study and its results are explained in this section.

In previous simulations of sheared monolayer suspensions of neutrally buoyant spheres, the explicit, fourth-order Adams-Bashforth intergrator was used, and a typical time step was $O(10^{-3})$ dimensionless time unit. The time step had to be small because the relative motion in sheared suspensions is quite large; the shear flow forces particles past each other on a time scale $\dot{\gamma}^{-1}$. If the time step was too large, the program would terminate because of excessive sphere overlap. In a settling suspension of identical particles, gravity will act equally on all the particles, and relative motion results only from the non-uniform configuration of the particles. This causes the configuration of the particles in a settling suspension to change much more slowly than in a sheared suspension. Program termination due to overlap did not occur in simulations of sedimenting monolayer suspension (at an areal fraction of 0.4), even when the time step was 0.1 dimensionless time

unit.

In our original simulations of monolayer sedimenting suspensions (areal fraction was 0.4), the FT method was used, and the time step was varied from 0.1 to 0.01. The resulting steady-state configurations showed a high degree of non-terminal overlapping and the "clumping" of most of the spheres in the periodic cell. This clumping consisted of a majority of the spheres connected to each other, often in hexagonally packed formations (see Figure 2.8*a*). These clumps often spanned the periodic cell. Decreasing the time step did not change the general characteristics of the steady-state microstructure or other suspension statistics. We included the effect of induced stresslets by using the FTS method, but this merely accelerated and worsened the clumping (see Figure 2.9*b*).

Varying the time step or the level of accuracy had little effect on the degree of clumping or hexagonal packing. Doubling the number of spheres still resulted in clumping at long times; however, doubling the number of spheres only increases the edge of the periodic cell by 40% (see Figures 2.9*a*-*b*). Further increasing the number of spheres becomes prohibitively expensive for dynamic simulation, even in the monolayer. To insure the convergence of the long-range, hydrodynamic interactions, we introduced the Ewald-summed mobility interactions described in Section 2.3. However, as we shall see in Chapter 4, the simulation still results in a high degree of hexagonal packing and clumping in a sedimenting monolayer suspension at steady state.

Still disturbed by the high degree of clumping, we began to experiment with the order and method of the integrator. In addition to the explicit fourth-order, Adams-Bashforth integrator, we have used the fourth-order, Adams-Moulton predictor-corrector, the explicit second-order, Adams-Bashforth integrator, the first-order, Euler predictor-corrector, and the explicit first-order, Euler integrator in simulation runs. All integrators except for the first-order methods led to clumping and "overlap". There was little difference in the suspension properties calculated from these higher-order methods. There was little difference between the explicit and

the predictor-corrector methods. The first-order methods differ from their higher-order cousins in that only the velocity at the present instant in time is used to calculate the position at the next time step. The amount of overlapping seen in runs using the explicit first-order, Euler integrator was an order of magnitude less than in the higher-order methods. The steady-state configurations were free of hexagonal packing and large clusters (see Figure 2.10). The time step could be as large as 0.1 for $\phi_A = 0.4$, and simulations could be carried out to quite long times – 1000-3000 time units. Steady-state statistics and distributions were extracted, and the long-time sphere motion was diffusive. An entire series of simulations at different levels of accuracy and different concentrations was completed over a period of a few months. (See Appendix C for the results of these simulations.)

At this time, simulations of sheared monolayer suspensions of neutrally buoyant spheres using the first-order integrator produced an angular dependence in the pair-distribution function – more particles were found upstream of a test partcle than downstream of it. (These simulations were performed by Dr. Georges Bossis). Without repulsive forces between the spheres, the symmetry of the hydrodynamic forces demands that there be no angular structure. The appearance of angular structure can be understood by considering how an integration method determines the trajectory of two isolated, nearly touching spheres imbedded in a shear flow (see Figure 2.11). The analytic solution to this problem shows that the spheres tumble over each other in constant closed orbits. Dr. Louis Durlofsky solved this problem using Stokesian dynamics with a wide variety of integrators. He found that the fourth-order methods correctly reproduced the closed orbit trajectories of the spheres to within five significant figures. The second- and third-order methods also captured the closed orbit trajectory, although they were slightly less accurate. The first-order method integrator failed miserably; the calculated trajectories are no longer closed, and the spheres quickly wandered away from each other. Even drastically reducing the time step does not eliminate this error.

Analysis of the first-order integrator explains why it fails in the two-sphere case and produces angular structure in the shear problem. Simply put, the first-

order integrator cannot accurately capture the tangential motion of the spheres moving around each other. This is seen by considering the two-sphere problem, which is schematically shown in Figure 2.11. The solid line is the actual trajectory that the sphere should follow. The dashed line shows the tangent to this trajectory. An explicit first-order method will always advance the sphere along this tangent, explaining why the method cannot accurately produce the correct trajectory. Higher-order methods use velocities at previous points on the trajectory and can accurately follow the curved nature of the sphere path. This explains why angular dependence was seen in the shear case when the first-order integrator was used. Spheres approaching from the upstream side were carried away from the spheres they were approaching, instead of following a more semicircular path around them. This results in more spheres being seen upstream of a given sphere and angular dependence when there should be none. This is not seen when the higher-order integrators are used. It should be stressed that the first-order integrator did not produce any unwanted angular dependence in the sedimentation problem. However, the first-order integrator obviously does not capture adequately the trajectories of particles moving relative to one another.

So we come full circle. When appropriate, we will comment on results of the first-order simulations, but in general, an explicit fourth-order integrator is used in all simulations reported in this thesis. Of course, the simulations still produce steady-state microstructures that are characterized by large clusters and a high degree of hexagonal packing (see Figure 2.12). To better gauge the effect of these clusters on the short- and long-time dispersion, we would want to see the results of sedimenting suspensions whose configurations are free of these features. The addition of repulsive forces between the particles can eliminate this clumping and hexagonal packing in the steady-state configurations of the sedimenting suspensions (see Figure 2.13).

2.5 Repulsive Interparticle Forces

In Bossis & Brady (1984), pairwise repulsive forces between the neutrally

buoyant spheres in a shear flow affected the resulting steady-state microstructure. The addition of these repulsive forces inhibited clustering, particularly cell-spanning clusters. Adding these repulsive forces to the simulation of sedimenting suspensions inhibits such cluster formation. We want to see if the change in the microstructure affects the long-time dispersion properties of particles in a sedimenting suspension. Thus, in certain simulation runs we include pairwise repulsive DVLO-type colloidal forces, as was done in Bossis & Brady (1984). The DVLO theory holds that the colloidal forces are of two types – a London-van der Waals attractive force and an electrostatic repulsive force due to the interaction between the particle double layers. In these simulations we have included only the repulsive double-layer forces. We will vary the strength and range of the repulsive force to consider its effect on the local structure and dispersion in sedimenting suspensions.

For particles larger than a micron in size, the double layers are usually small compared with the particle radius, and the pairwise electrostatic repulsive force can be written

$$\mathbf{F}_{rep} = \mathbf{F}_o \frac{\tau e^{-\tau\epsilon}}{1 - e^{-\tau\epsilon}}, \tag{2.5–1}$$

where $\epsilon = r - 2$ is the separation distance between the sphere surfaces, and r is their center-to-center separation. Both have been made dimensionless by the particles' characteristic length scale, a. $\tau = \kappa a$, where κ^{-1} is the Debye length. The amplitude of $\mathbf{F}_o$ (the direction is outward along the line of centers) is given by

$$|\mathbf{F}_0| = 2\pi\varepsilon\psi^2, \tag{2.5–2}$$

where ε is the electrical permittivity of the fluid and ψ is the surface potential of the particles when $\epsilon \to \infty$. The derivation of Equation (2.5–1) assumes that the surface potentials for the two particles are the same, and the surface charge densities remain constant as the particles move relative to each other.

$|\mathbf{F}_0|$ sets the magnitude of the force and τ sets its range in space. The repulsive force varies as $1/\epsilon$ as $\epsilon \to 0$ and decays to $0(10^{-2}|\mathbf{F}_0|\tau)$ when $\epsilon \sim O(4.5\tau^{-1})$. At

separations greater than $4.5\tau^{-1}$, the interparticle force will generally be negligible compared with the hydrodynamic force, and as $\tau \rightarrow \infty$, there is essentially no effect from the interparticle force. The total interparticle force on a particle is built by summing the force calculated from Equation (2.5–1) for the particle paired with all other particles in the simulation.

In our simulations, we set $|\mathbf{F}_0|\tau = 1.0$, so the range, τ, is the only independent parameter. In most simulations that include interparticle forces between the particles, $\tau = 10^5$; one simulation was run where $\tau = 10^3$. The effect of the repulsive forces on the steady-state short-time self-diffusion coefficient in sedimenting suspensions is discussed in Chapter 3. Its effect on the long-time dispersion is discussed in Chapter 4.

2.6 Monolayer Simulations

Despite the decrease in computation time from using lattice sums and Ewald's method, full three-dimensional simulations are still too time consuming. We choose to simulate monolayer suspensions instead of the three-dimensional problem because the computations are much faster and can be accomplished without sacrificing the goal of this research, which is to study the diffusional nature of particle motions in sedimenting suspensions. In a full three-dimensional FTS simulation, each sphere has 11 degrees of freedom (three force, three torque and five stresslet unknowns), resulting in a grand mobility matrix of $11N \times 11N$, where N is the number of spheres in the object cell. In the monolayer problem, this matrix is $6N \times 6N$. Inverting the mobility matrix will be 6.25 $((\frac{11}{6})^3)$ times more costly in the three-dimensional problem than in the monolayer problem. Solving the equation set will be 8 times more costly. In addition, it requires $N_1^{\frac{1}{2}}$ more particles to do a three-dimensional simulation whose periodic cell edge length is the same as the monolayers. Thus, the full three-dimensional problem can be up to $8N_1^{\frac{3}{2}}$ times more expensive than the monolayer problem, per time step. Since an average monolayer simulation requires 25 spheres, an equivalent, three-dimensional run would be $\sim$ 1000 times slower. Since a single simulation run can require in-

verting the mobility matrix from 5,000 to 10,000 times and solving the equation set from 500,000 to 1,000,000 times, simulating the monolayer instead of the full three-dimensional problem results in a substantial reduction in computing time.

We restrict our attention to monolayer simulations – spheres in a monolayer sediment within the plane of the monolayer (see Figure 2.14). Instead of characterizing a suspension by the volume fraction of spheres (ϕ), in the monolayer we define the areal fraction,

$$\phi_A = \frac{N\pi a^2}{A}, \tag{2.5–1}$$

where a is the radius of the spheres, and A is the area enclosing the N spheres. We want to consider the effect of lattice sums on the monolayer formulation. This is not straightforward since the lattice is still fully three-dimensional.

The use of lattice sums (and of Ewald's method to speed their convergence) in calculating the mobility matrix elements needs to be considered in more detail, especially as applied to monolayer suspensions. A lattice of cells of volume V_1 fills a larger convergence volume of V. The shape of the cells is constrained only by the fact that they must fit together to fill V. For ease of explanation, consider a cubic cell of volume V_1 (edge length is H) containing N_1 spheres. The cell has periodic boundary conditions on its edges; each sphere can be considered as being at the center of its own periodic cell. If we do not invoke lattice sums ($\gamma = 1$ in Equation (2.3.2–3)), the suspension outside the cell is considered statistically homogeneous. If we do invoke the lattice sums, the cell will be surrounded by a given number of images of itself, and this finite cluster of cell will itself be surrounded by a statistically homogeneous suspension. Convergence is improved by increasing the volume, V; in the non-Ewald method, we increase N such that N/V is constant; in the Ewald method, we extend the lattice of cells. Extending the lattice is much cheaper than increasing V_1. The cost of inverting the mobility matrix and the solving of the equation set both increase as $(N_1)^3$. The Ewald method involves extra $O((N_1)^2)$ algebraic operations when forming the mobility matrix, but the size of the mobility matrix does not change. Computationally, the use of lattice

sums in conjunction with Ewald's method is clearly favored to produce convergent expressions for the elements of the mobility matrix. Additionally, at higher concentrations the mobility matrix looses positive definiteness when the non-Ewald method is used. Unresolved is the effect of the long-range periodicity that periodic boundary conditions and the lattice sums introduce to the simulation. We have performed simulations both with and without lattice sums.

Although solving the sedimentation problem in a monolayer is computationally advantageous, the use of lattice sums is not as straightforward as in the full three-dimensional problem. The lattice sum remains fully three-dimensional, even though the spheres are confined to a monolayer. Figure 2.15 describes schematically the periodic cell used in monolayer simulations. The area of the cell A is $H_1 \cdot H_2$, where H_1 and H_2 are the cell edges in the x and y directions, respectively. The non-Ewald method (lattice sums are not invoked) explicitly sums only the interactions among the spheres in this object cell. For computational purposes, each sphere is considered at the center of its own periodic cell. This technique to simulate monolayer suspensions has been applied and discussed in Bossis and Brady(1984) and Brady and Bossis(1985). Figure 2.16 describes schematically the application of lattice sums to the monolayer formulation. The object cell is now fully three dimensional with edge lengths of H_1, H_2, and L, in the x, y, and z directions, respectively. The spheres are still confined to a monolayer. Image cells also extend into and out of the plane of the paper. The lattice can be extended indefinitely, although the mobility matrix elements usually converge to within 0.1% of a constant value with about 124 image cells surrounding the object cell. (Elements of all matrices except $\mathbf{M}_{\mathbf{U_t F}}$ usually converge with only 26 image cells around the object cell. This makes intuitive sense considering the long-range nature of the given hydrodynamic interactions.) The sphere at the center of its object cell will be affected by spheres inside *and outside* the monolayer. As long as the lattice is symmetric about the z-axis (object cell monolayer at $z = 0$), the spheres will remain in the monolayer, but there is no doubt that the presence of image spheres outside the $z = 0$ plane will affect the behavior of the spheres in

the monolayer.

Consider the effect of varying the distance between the image planes. For convenience of discussion, we consider the edges of the cell to be of length H in the x and y directions. The edge length in the z direction will be $L = z_l \cdot H$; we vary the distance between the monolayer images by changing z_l. Specifically, we will be judging the effect of varying the monolayer separation on the number-averaged suspension properties, such as $\langle v_x \rangle$, $\langle v_y \rangle$ (the "sedimentation" velocity), $\langle (v_x - \langle v_x \rangle)^2 \rangle$, and $\langle (v_y - \langle v_y \rangle)^2 \rangle$. The object cell contains 25 spheres randomly distributed at an areal fraction of $\phi_A = 0.4$ The sphere velocities are calculated by solving

$$\mathbf{U}_t = \mathbf{M}_{U_t F} \cdot \mathbf{F}, \tag{2.6–1}$$

where $\mathbf{F} = \mathbf{1}$, and velocity interactions are pairwise additive. The monolayer separation factor, z_l, ranged from 0.25 to 16.0. The extent of the lattice varied for different separations, but all values for the suspension-averaged quantities converged to six decimal places.

The dependence of the sedimentation velocity $\langle v_y \rangle$ on the monolayer separation distance is seen in Figure 2.17. The dots (•) are simulation results; the line was calculated independently and will be discussed below. It is obvious from Figure 2.17 that the sedimentation velocity in the monolayer is strongly dependent on the separation distance. This is not necessarily a matter of concern – even without lattice sums, the sedimentation velocity in the monolayer problem is not a well-defined quantity. In a three-dimensional suspension, the fluid that is displaced by the falling particles is called the backflow – the displaced fluid must flow up around the particles since it has nowhere else to go. Thus, the sedimentation velocity in a three-dimensional suspension decreases as the volume fraction of particles increases. In a monolayer suspension, the backflow may flow up around the particles, or it may flow out of the plane of the monolayer. The sedimentation velocity is a function of the backflow returning in the plane of the monolayer; backflow in the monolayer increases the drag on the particles. As the areal fraction

increases, the backflow finds it easier to return outside of the monolayer. Thus, the sedimentation velocity in the monolayer increases as the areal fraction increases.

The behavior of the sedimentation velocity can be rather easily understood by considering the analogous problem of parallel, infinite flat plates, of thickness $2a$, moving at a constant velocity U through an infinite fluid; a zero mass flux plane exists perpendicular to the direction of motion (see Figure 2.18). We can solve this problem by considering one such plate with no-slip conditions on its surfaces and free surfaces a distance of $\frac{1}{2}z_l \cdot H$ from either side of the center of the plate. Solving the equation of motion

$$\mu \frac{\partial^2 u}{\partial x^2} = \frac{\partial p}{\partial y}, \tag{2.6–2}$$

where μ is the fluid viscosity, u is the fluid velocity and p is the pressure, in conjunction with the boundary conditions and mass conservation, we can determine the unit drag force on the plate

$$F_{drag} = \frac{6U\mu A_{xs}}{a(\frac{1}{2}z_l \cdot H - 1)}, \tag{2.6–3}$$

where A_{xs} is the unit cross-sectional area of the plate. The Stokes drag on all the spheres in that unit cross-sectional area is

$$F = \frac{6U_s \mu A_{xs}}{a}\phi_A, \tag{2.6–4}$$

where U_s is Stokes velocity and ϕ_A is the areal fraction of spheres. Equating these two forces gives

$$\frac{U}{U_s} = \frac{1}{2}\phi_A(z_l \cdot H - 2). \tag{2.6–5}$$

This equation is the straight line plotted in Figure 2.17. For $z_l \geq 1$, the difference between the simulation and equation results are less than 1%.

The dependence of $\langle v_x \rangle$ and the velocity variances, $\langle (v_x - \langle v_x \rangle)^2 \rangle$ and $\langle (v_y - \langle v_y \rangle)^2 \rangle$, on the monolayer separation distance is seen in Figure 2.19. The curves merely connect the simulation results for each quantity: a indicates each $\langle v_x \rangle$ result, a $\triangle$ indicates each $\langle (v_x - \langle v_x \rangle)^2 \rangle$ result, and a $\triangledown$ indicates each $\langle (v_y - \langle v_y \rangle)^2 \rangle$

result. For $z_l \geq 1$, all these averaged quantities are constant, $\pm 0.5\%$. This is important since we expect the relative motion of the spheres in suspension to be related to the velocity variances. As long as $z_l \geq 1$, the separation distance between the monolayers should not affect the diffusion of spheres in the monolayer.

To confirm the correct construction of the monolayer problem in terms of the lattice sums, we performed a simple check. Spheres were arranged in a regular array in the monolayer. The factor z_l was set such that the distance between the monolayers was the same as the nearest neighbor distance between spheres in the monolayer – i.e., a simple cubic lattice of spheres was formed from the object and image spheres. Results for the full three-dimensional formulation and the special monolayer formulation were exactly equal, as they should be. We can now use the lattice-sum technique with confidence in the monolayer problem.

2.7 Specific Aspects of the Simulation Programming

This section deals with the actual programming of our Stokesian dynamic simulations of sedimenting suspensions. The method outlined in the last three sections will accurately simulate the dynamic behavior of spheres in a sedimenting suspension. However, several important decisions must be made when we actually implement the method. We can choose the level of approximation of the mobility matrix, the level of acceptable convergence (with or without the lattice-sum technique), how often the far-field and near-field interactions need to be calculated, not to mention the particular suspension conditions to be simulated. All of these choices can affect how well we simulate the true behavior of settling spheres in suspension, and all of them have an effect on computing time. In all cases, increasing the level of accuracy of the simulation increases computing time. The importance of finding the most efficient program is obvious when one considers that determining the long-time displacement of the particles requires relatively long computer runs and large amounts of stored data. Even at the lowest levels of approximation and accuracy, a "short" simulation run will take about 25 CPU hours to complete and produce over 12 million bytes of data on a SUN 3/260 with

a floating point accelerator. Increasing the level of approximation and accuracy can increase these requirements drastically.

We do not invert the mobility matrix as often as we solve the equation set. The elements of the mobility matrix are far-field approximations to sphere-sphere interactions and change significantly only when the relative separation of two particles has changed by an amount comparable to the sphere size. Conversely, the elements of the resistance matrix can change significantly with small changes in the surface separation of two spheres close to one another. Thus, there are two natural length (time) scales, and a multiple time-scale method can be used. Thus, relatively small time steps are used when solving the equation set, and the mobility matrix is formed and inverted less frequently.

For each simulation run, we need to choose the level of approximation in the mobility matrix, the number of spheres in the periodic cell, the step size, how often we will invert the mobility matrix, whether to use lattice sums or not, the extent of the lattice and the spacing between monolayers if we choose to use lattice sums, and how often we will store the simulation data. The effect of these decisions needs to be gauged, since this is the first application of this method to the problem of dynamic settling. Chapter 4 will discuss the effect of the decisions we outline in this section on the long-time dispersion.

We consider three levels of approximation of the mobility matrix. The first level is called the F method and implies that there is no rotation of the spheres. It is the fastest method, but obviously spheres will rotate in real suspensions and probably enhance any diffusive motion in the suspension. The second level of approximation is called the FT method and allows the free rotation of the spheres. Durlofsky *et al.* (1987) have shown that this method performs well for problems that do not involve an imposed shear flow. The third level of approximation is called the FTS method; even though there is no imposed shear flow, the motion of the spheres will give rise to induced stresslets on the spheres that may affect their diffusion. Although it is the most accurate method, it is also the most time-

consuming. In Chapter 4 we discuss the effect of approximation level on variance of the spheres' velocity, their pair-distribution function and their dispersion.

The smallest step size in the simulations is the interval at which two-body, near-field resistance interactions are added to the mobility invert, the equation set is solved, and the new sphere positions are calculated. This step size was reduced until the time-averaged suspension velocities and velocity variances were relatively unaffected by further step-size reduction. The unit time step is (a/U_s), where U_s is the Stokes settling velocity. The equation set was solved every 0.001 time unit. The mobility matrix was formed and inverted every 0.1 time unit.

The Ewald runs set z_l=2, so the monolayers are separated by the twice the distance H (the edge of the object cell in the monolayer). The reasons behind this choice are discussed in Chapter 3. Convergence of the lattice sum is obtained by extending the lattice. Preliminary results for the three-dimensional and monolayer problems indicate that, in general, an acceptable level of convergence (within 5% of final answers) can be obtained if the lattice size is $5 \cdot H$ in all directions (124 image cells) for elements in the $\mathbf{M}_{U_t F}$ matrix, and if the lattice size is $3 \cdot H$ in all directions (26 image cells) for the elements of all the other submatrices. We would expect it to require a larger lattice to obtain convergence in the $\mathbf{M}_{U_t F}$ matrix because the disturbance velocity from a settling sphere decays as $O(r^{-1})$, whereas the disturbance velocities from rotating or sheared spheres decay as $O(r^{-2})$ or faster.

At given time intervals the program will store all sphere velocity and position data. These data are used to calculate time-averaged sphere velocities and velocity variances, pair-distribution functions and mean-squared displacements of the spheres. Although all of these can be calculated as during simulation runs, we often make *a posteriori* decisions on which part of the data we would like to analyze. Storage limitations of the computer disk and core memory make it impossible to store and analyze the data for a complete run if we store the data at every time step. Data were stored every 0.05 time unit (every 50 time steps). In

several simulations, we calculated the time-averaged velocities and variance, as well as the pair-distribution function, while the program was running – data at every time step were included. The difference between the run-time results and the reduced-data results was negligible.

The actual CPU time requirements for different type of simulation runs deserve consideration. Runs were done on a Sun 3/260 computer with floating point accelerator or the CRAY-XMP at the San Diego Supercomputing Center. For conditions cited for the non-Ewald runs at $\phi_A = 0.453$, the F method required about 301 CPU minutes per 100 time units, the FT method, about 837 CPU minutes, and the FTS method, about 1024 CPU minutes on the Sun3/260. An F method Ewald run ($\phi_A = 0.453$) required about 717 CPU minutes. Simulation runs lasted 3 to 6 CPU days, or even more, because the analysis of the long-time diffusion coefficients generally required that data over 500 to 1000 time units be used. Extending the method, as it is now, to three-dimensional systems would require a 50- to 100-fold increase in the CPU time.

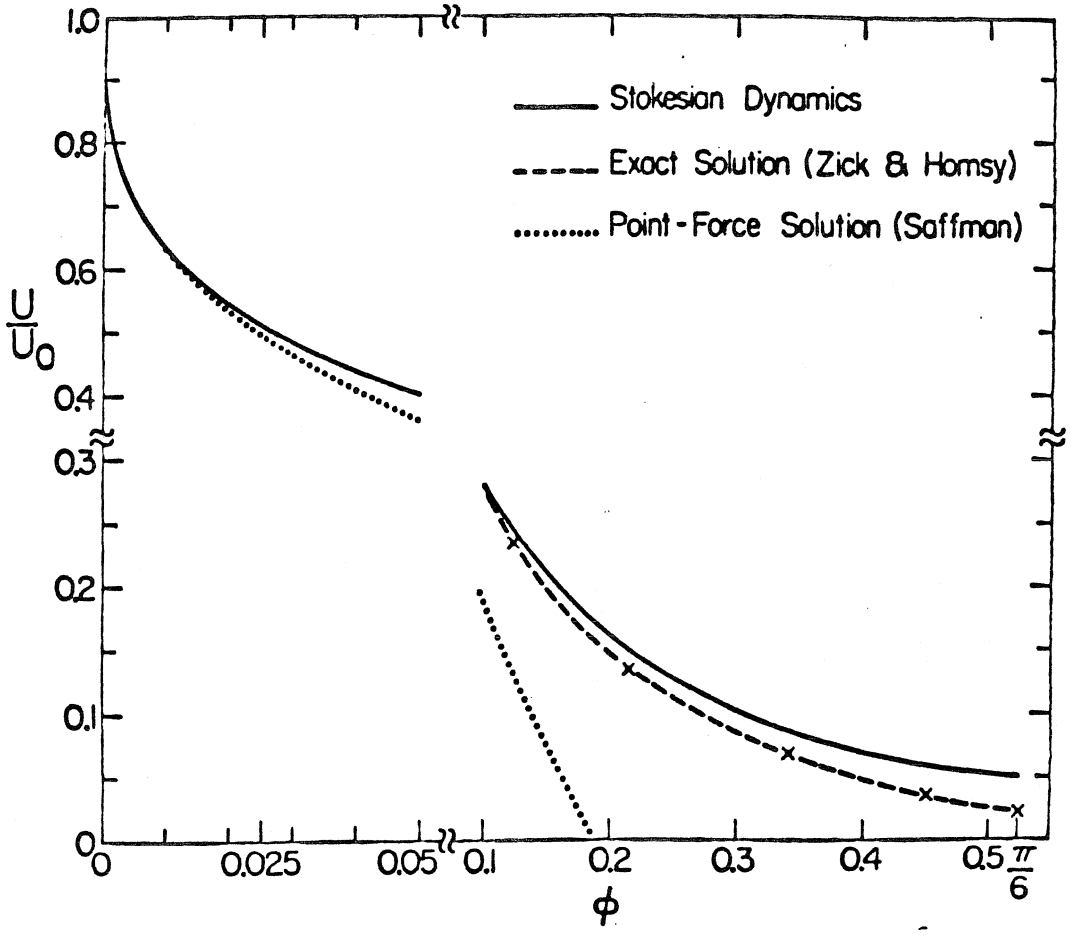

Figure 2.1 Nondimensional sedimentation velocity of a simple cubic array of spheres as a function of volume fraction ϕ. The solid curve is the result of the Stokesian dynamics method, the dashed curve is the exact result of Zick & Homsy (1982), and the dotted curve is the point-force solution of Saffman (1973). To facilitate comparison at high and low ϕ, the ordinate and abscissa scales change for $\phi \geq 0.1$. The exact and Stokesian dynamics results are indistinguishable up to $\phi = 0.1$.

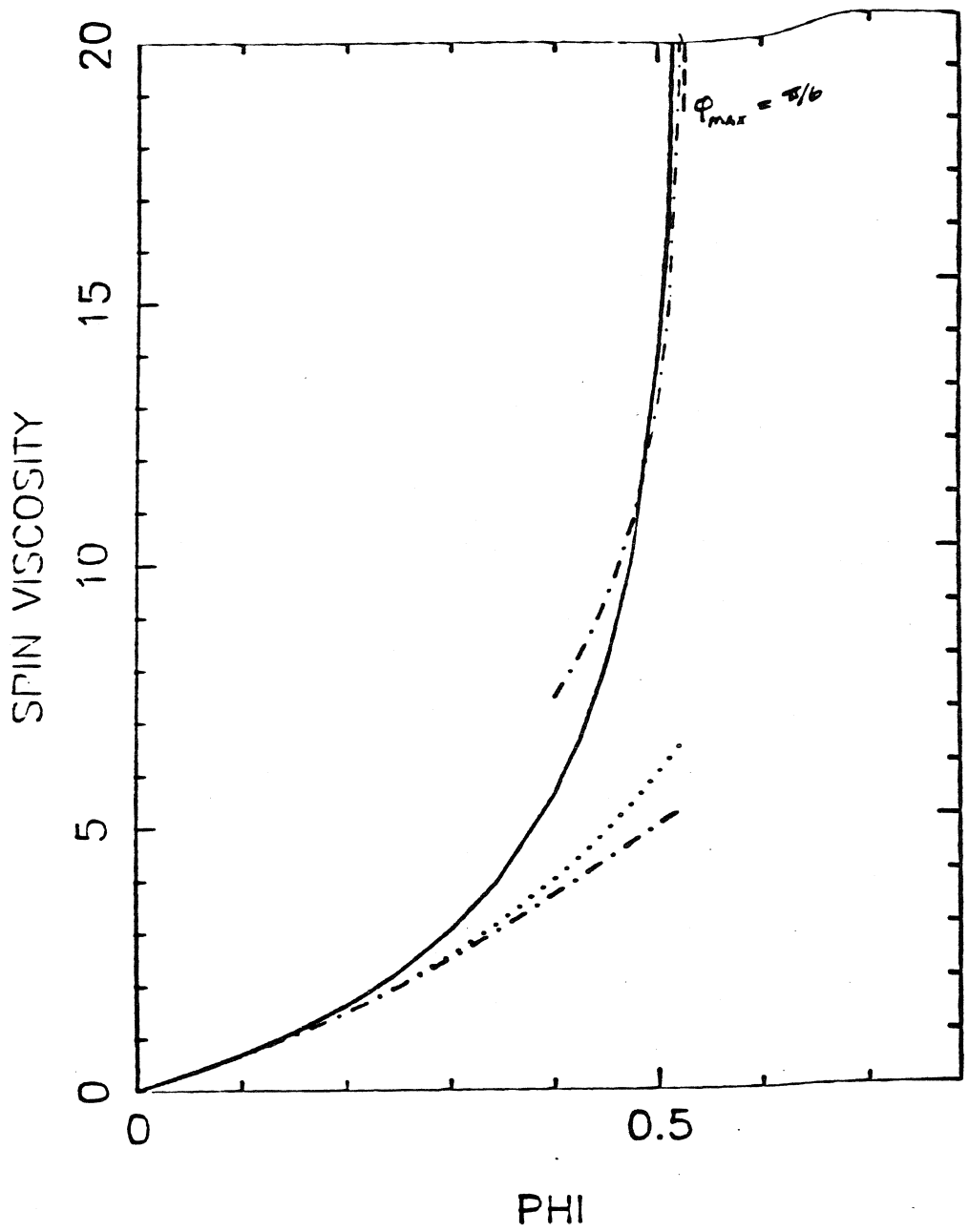

Figure 2.2 The spin viscosity function ξ for a SC lattice as a function of volume fraction. The solid curves are the Stokesian dynamics results, the dotted curves are the far-field results obtained from $\langle \mathbf{M}_{\Omega L}^{*-1} \rangle$, and the dot-dashed curves are the asymptotic forms as $\phi \to \phi_{max}$ and as $\phi \to 0$.

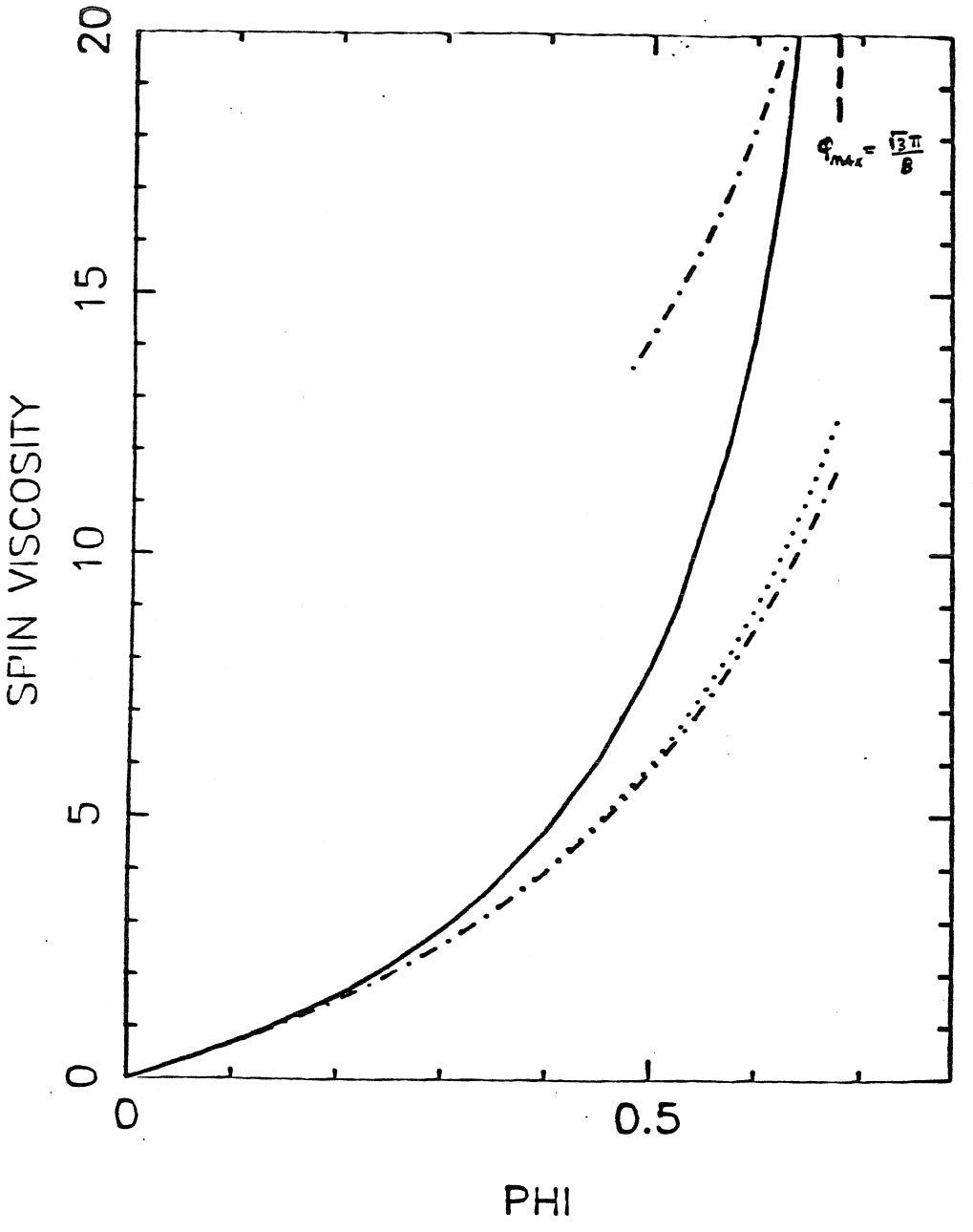

Figure 2.8 The spin viscosity function ξ a BCC lattice as a function of volume fraction. The solid curves are the Stokesian dynamics results, the dotted curves are the far-field results obtained from $\langle \mathbf{M}_{\Omega L}^{*-1} \rangle$, and the dot-dashed curves are the asymptotic forms as $\phi \to \phi_{max}$ and as $\phi \to 0$.

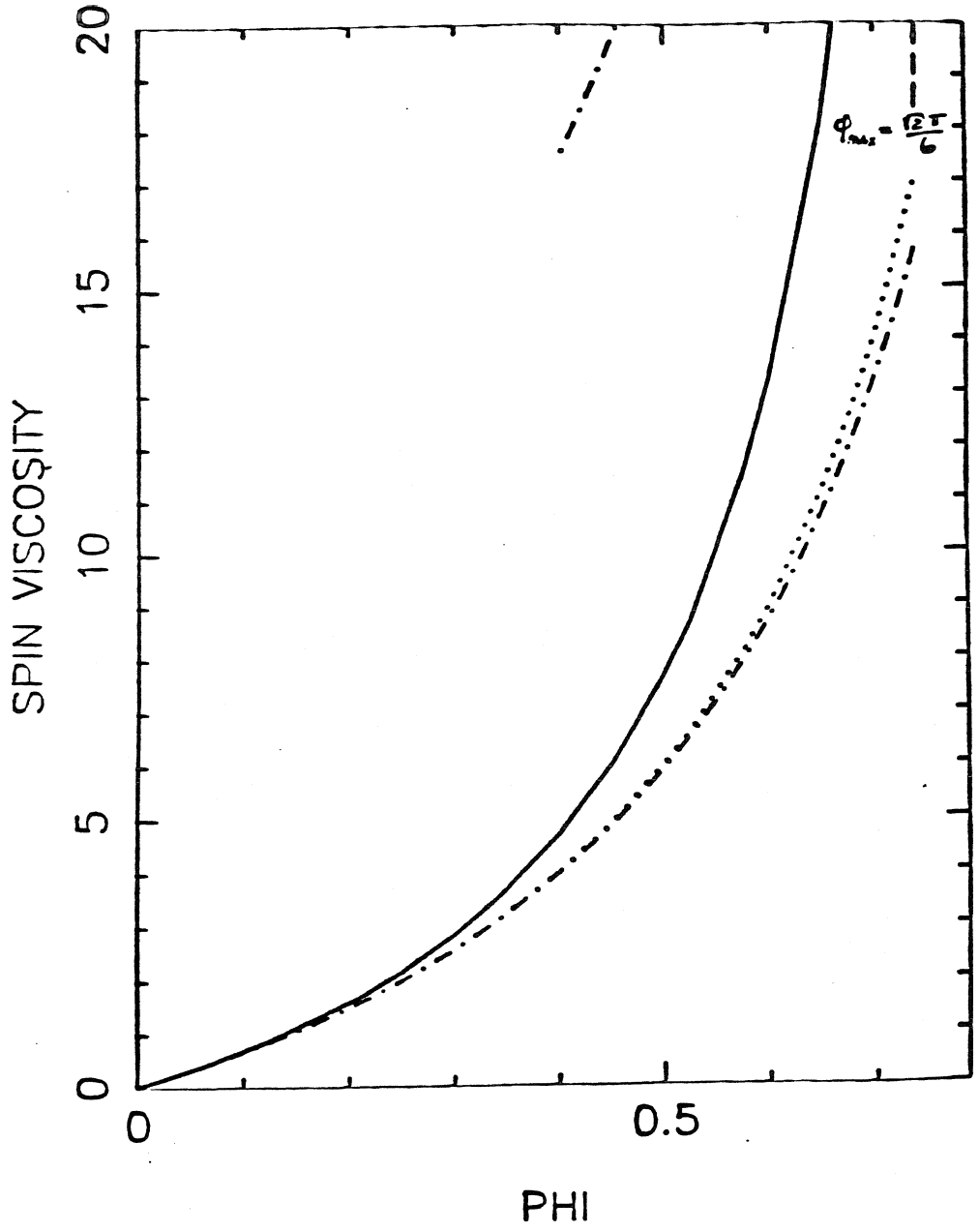

Figure 2.4 The spin viscosity function ξ a FCC lattice as a function of volume fraction. The solid curves are the Stokesian dynamics results, the dotted curves are the far-field results obtained from $\langle \mathbf{M}_{\Omega L}^{*-1} \rangle$, and the dot-dashed curves are the asymptotic forms as $\phi \to \phi_{max}$ and as $\phi \to 0$.

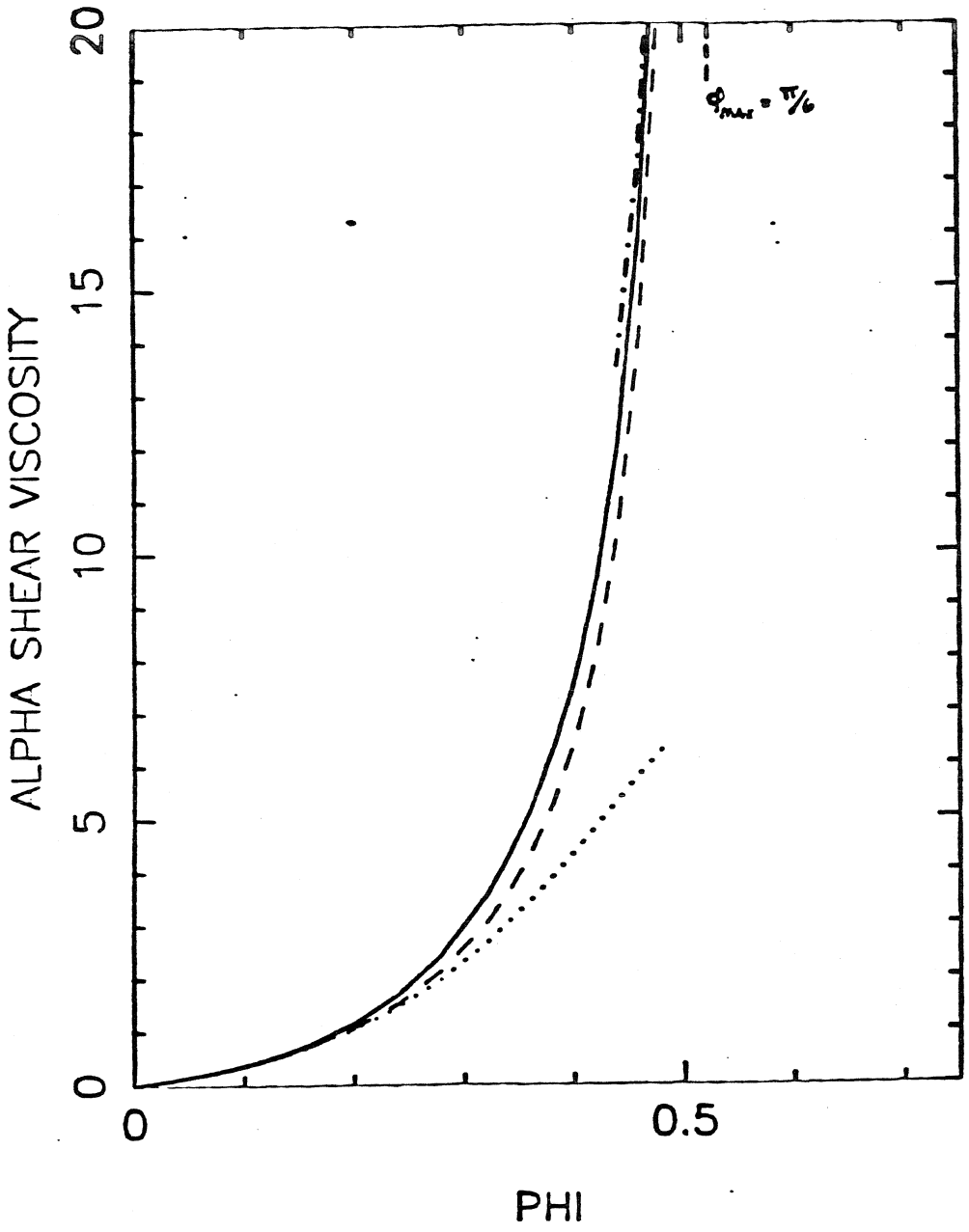

Figure 2.5a The shear viscosity function α for a simple cubic array as a function of volume fraction. The solid curves are the Stokesian dynamics results, the dashed curves are the exact solutions of Nunan & Keller (1984), which terminates at $\phi = 0.48$, the dotted curves are the far-field results obtained from $\langle \mathbf{M}_{ES}^{*-1} \rangle$, i.e. no lubrication, and the dot-dashed curves are the singular form as $\phi \rightarrow \phi_{max}$.

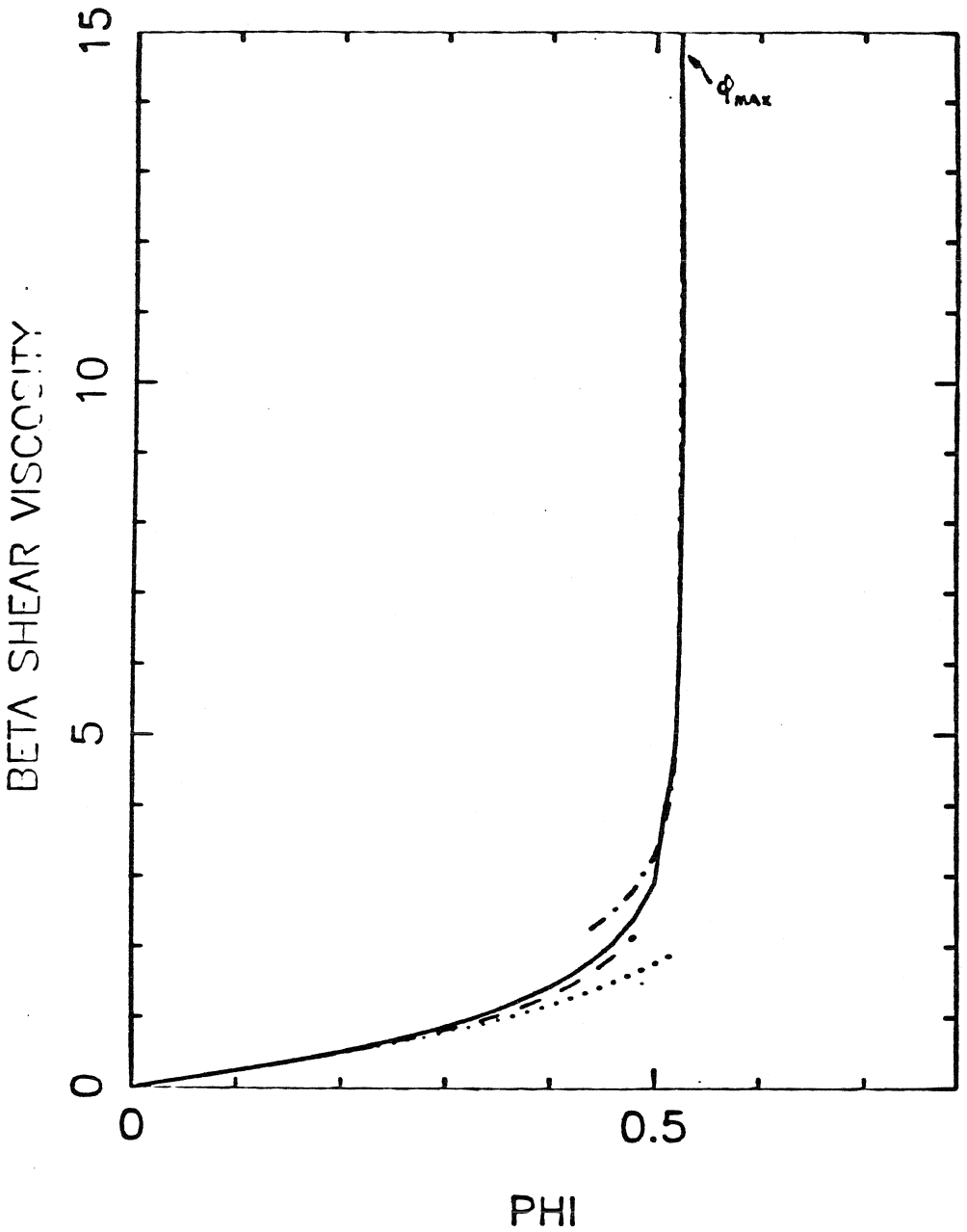

Figure 2.5b The shear viscosity function β for a SC lattice as a function of volume fraction. See Figure 2.5*a* for an explanation of the curves.

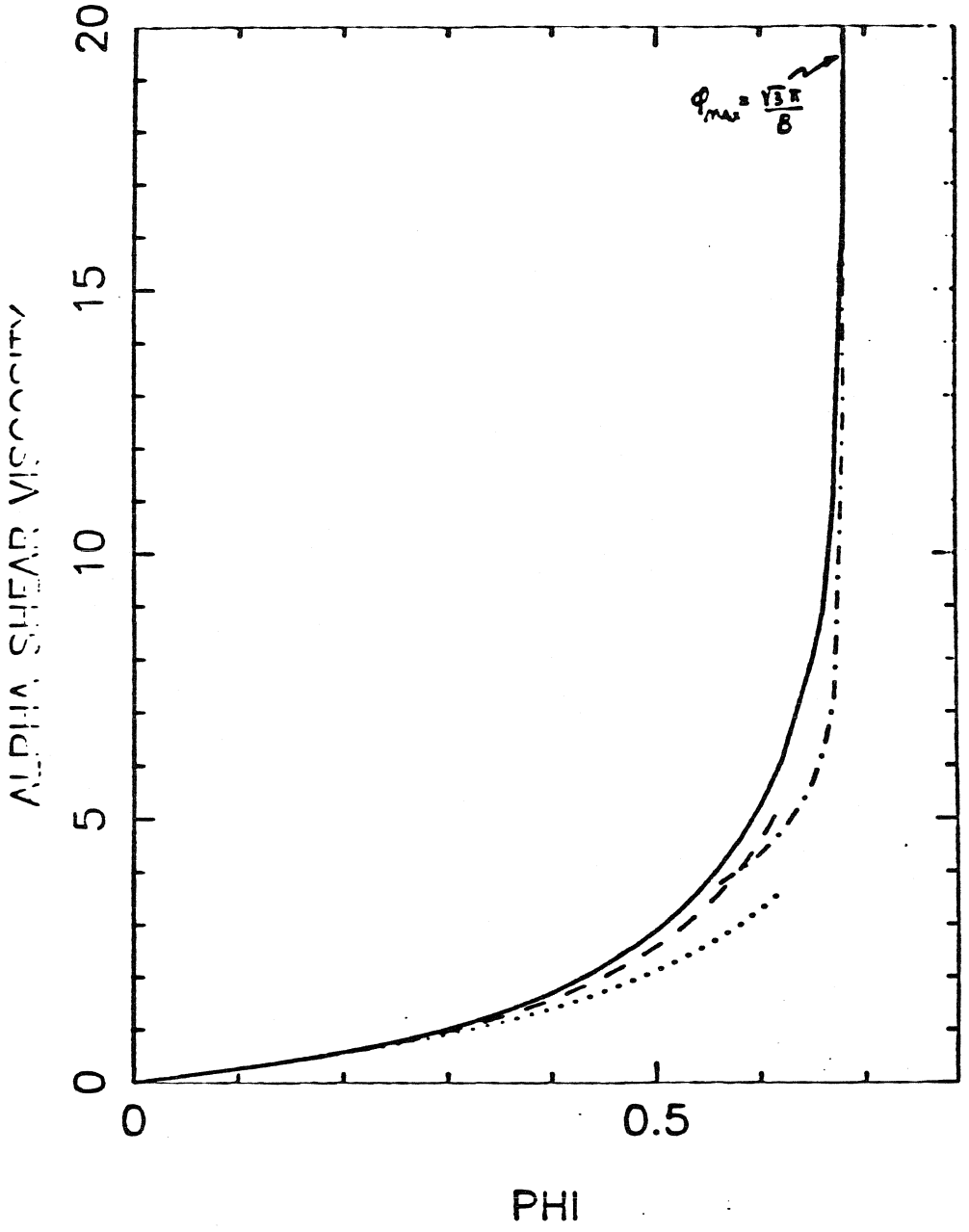

Figure 2.6a The shear viscosity function α for a BCC lattice as a function of volume fraction. See Figure 2.5*a* for an explanation of the curves.

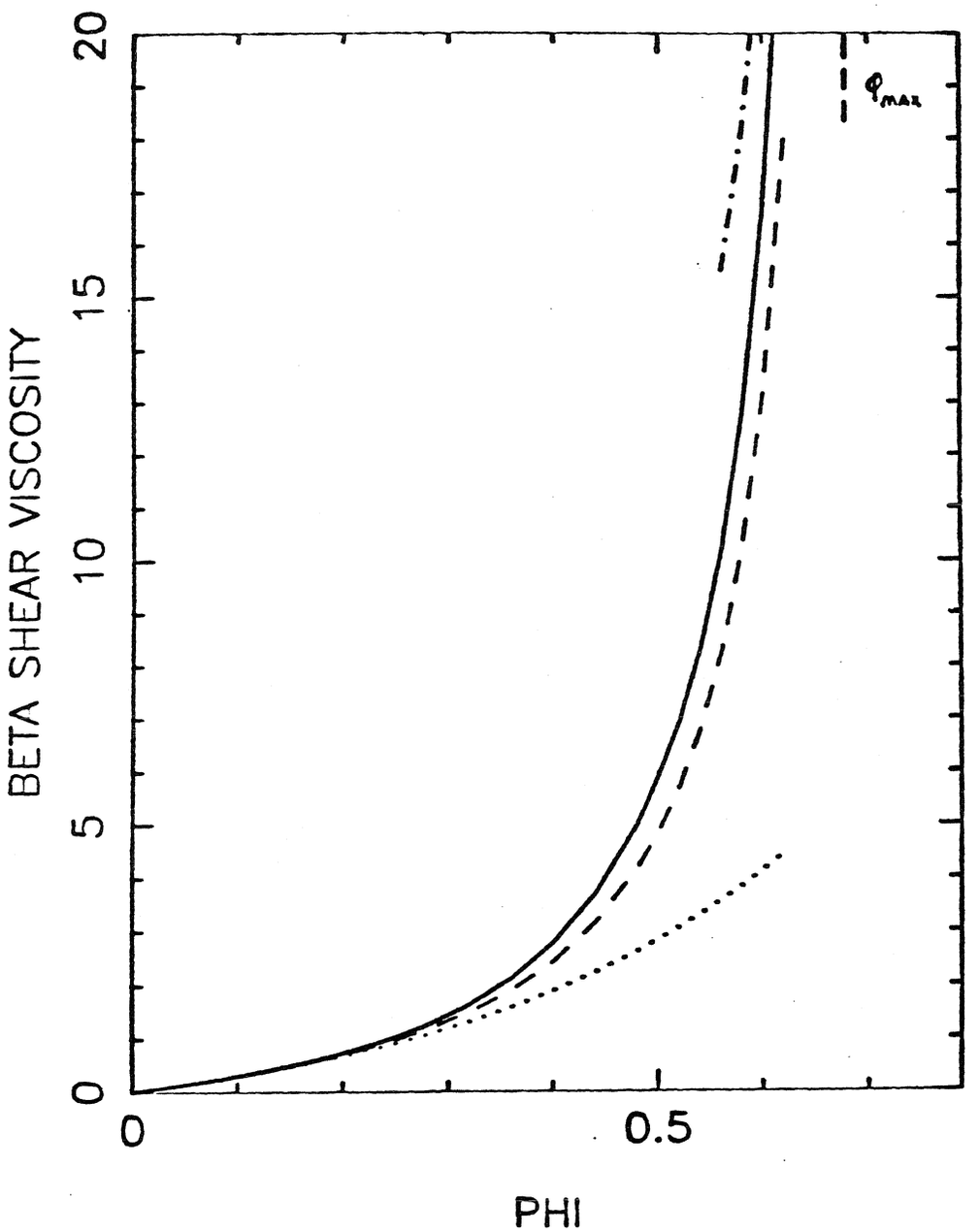

Figure 2.6b The shear viscosity function β for a BCC lattice as a function of volume fraction. See Figure 2.5*a* for an explanation of the curves.

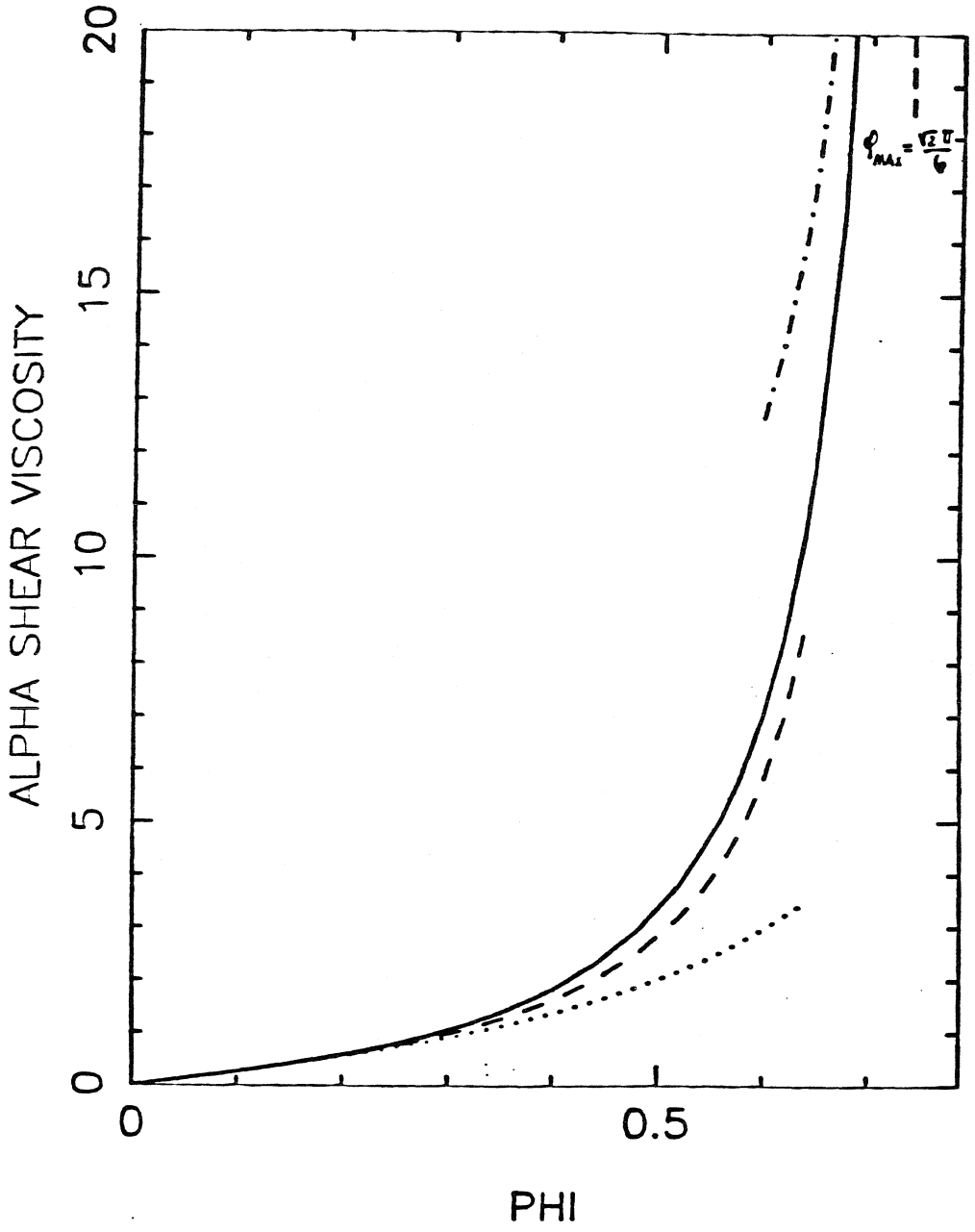

Figure 2.7a The shear viscosity function α for a FCC lattice as a function of volume fraction. See Figure 2.5*a* for an explanation of the curves.

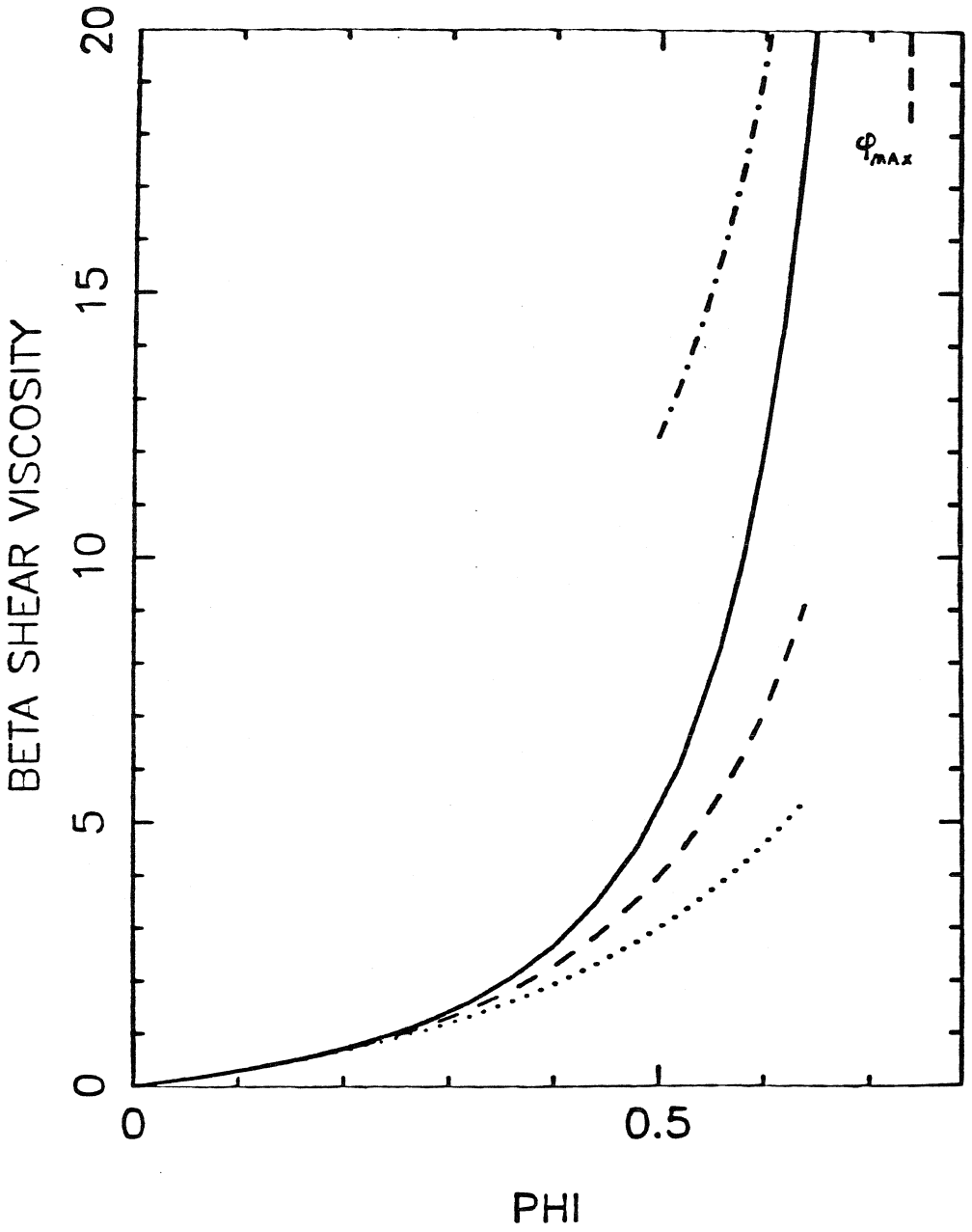

Figure 2.7b The shear viscosity function β for a FCC lattice as a function of volume fraction. See Figure 2.5*a* for an explanation of the curves.

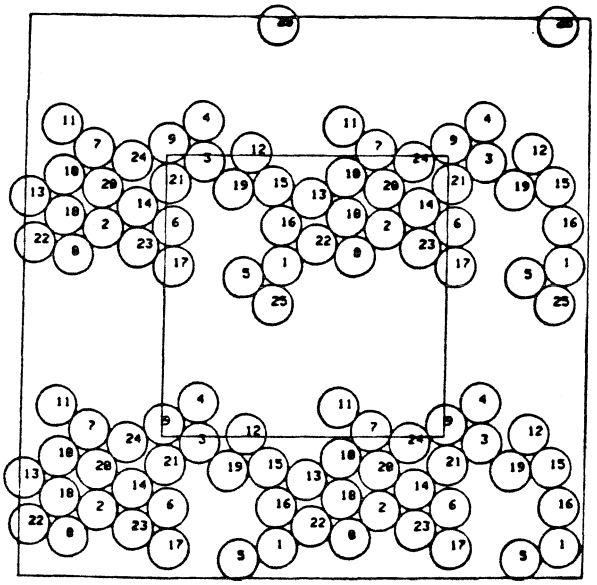

Figure 2.8a A "snapshot" of sphere positions. The inner box is the periodic cell. These are the sphere positions at $t = 490.0$ time units for an FT, non-Ewald simulation. The time step is 0.1 time unit and the mobility matrix is inverted every 10 steps.

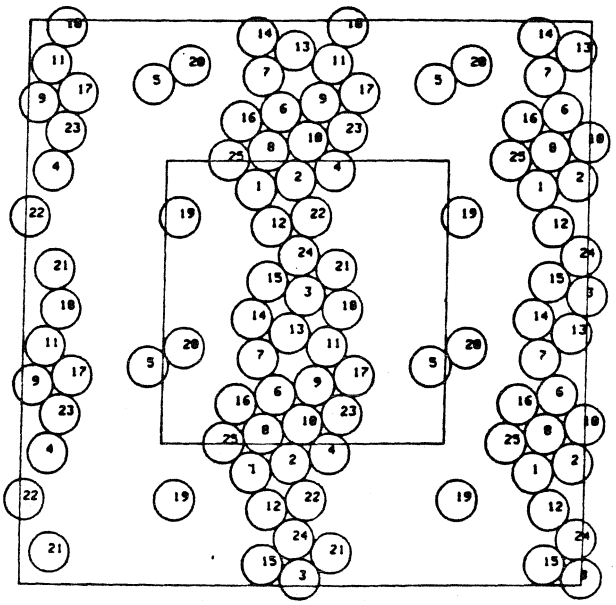

Figure 2.8b A "snapshot" of sphere positions. The inner box is the periodic cell. These are the sphere positions at $t = 1000.0$ time units for an FTS, non-Ewald simulation. The time step is 0.1 time unit and the mobility matrix is inverted every 10 steps.

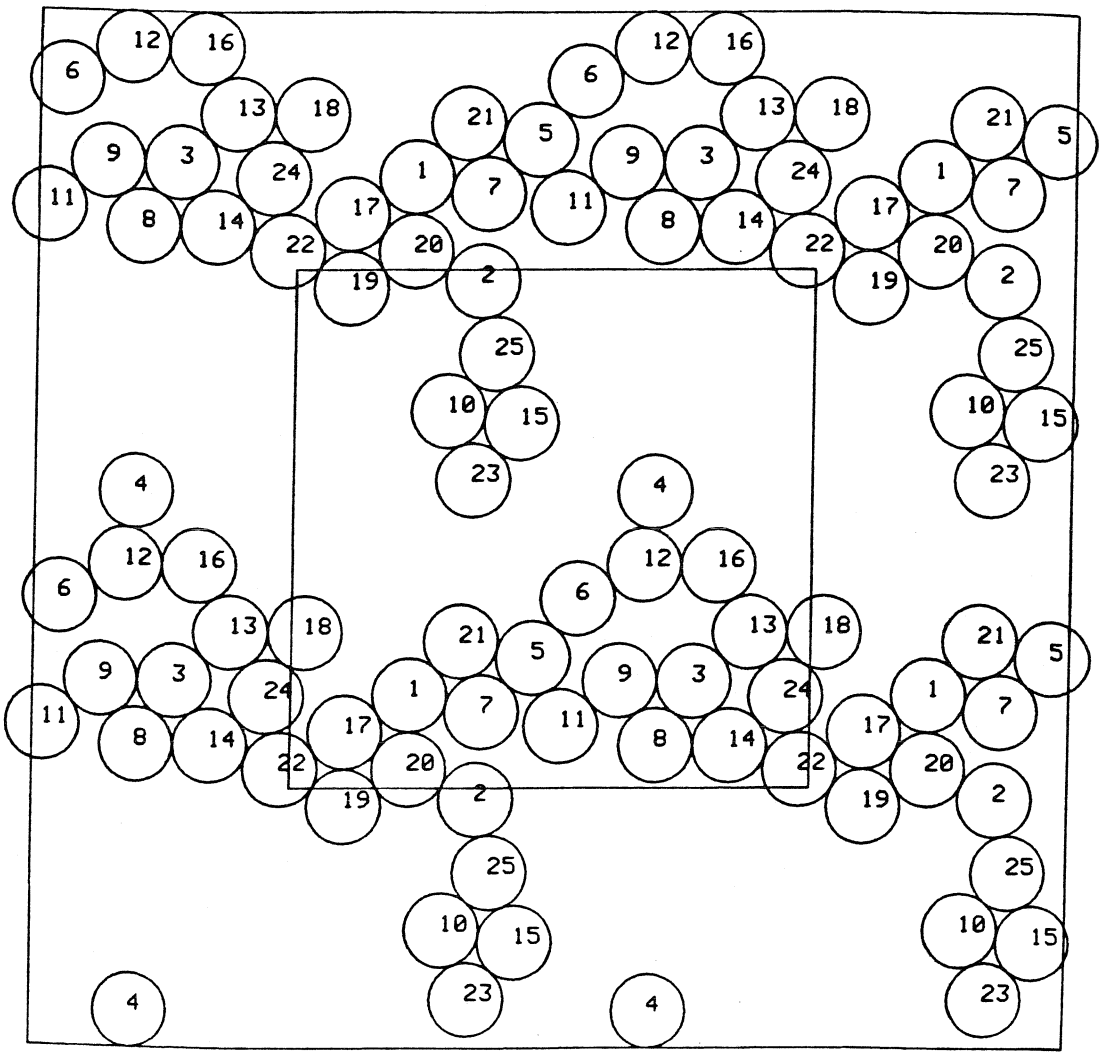

Figure 2.9a A "snapshot" of sphere positions. The inner box is the periodic cell. These are the sphere positions at $t = 300.0$ time units for an F, non-Ewald simulation. The time step is 0.1 time unit and the mobility matrix is inverted every 10 steps.

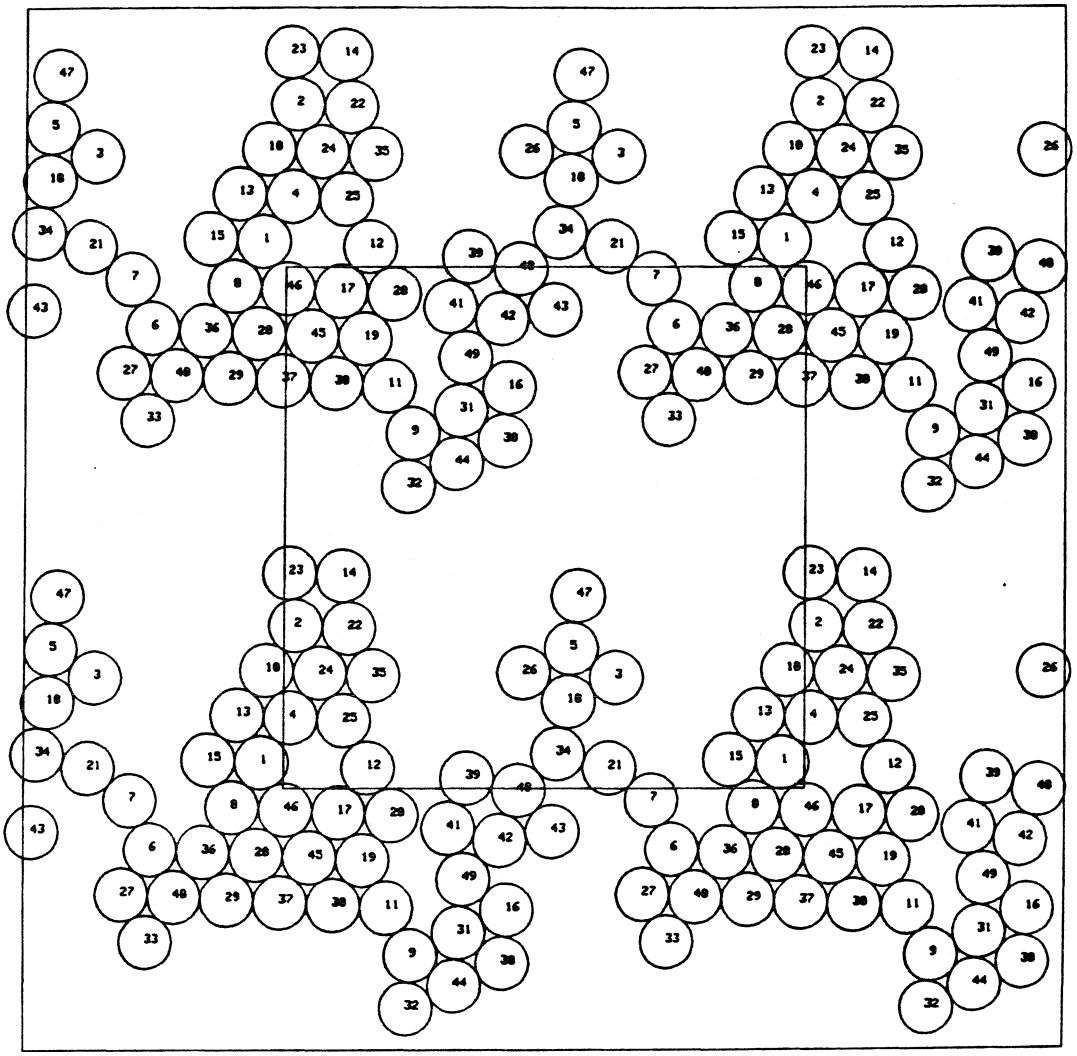

Figure 2.9b A "snapshot" of sphere positions. The inner box is the periodic cell. The specifications are the same as in Figure 2.9*a*, except that the number of spheres in the simulation is 49, instead of 25.

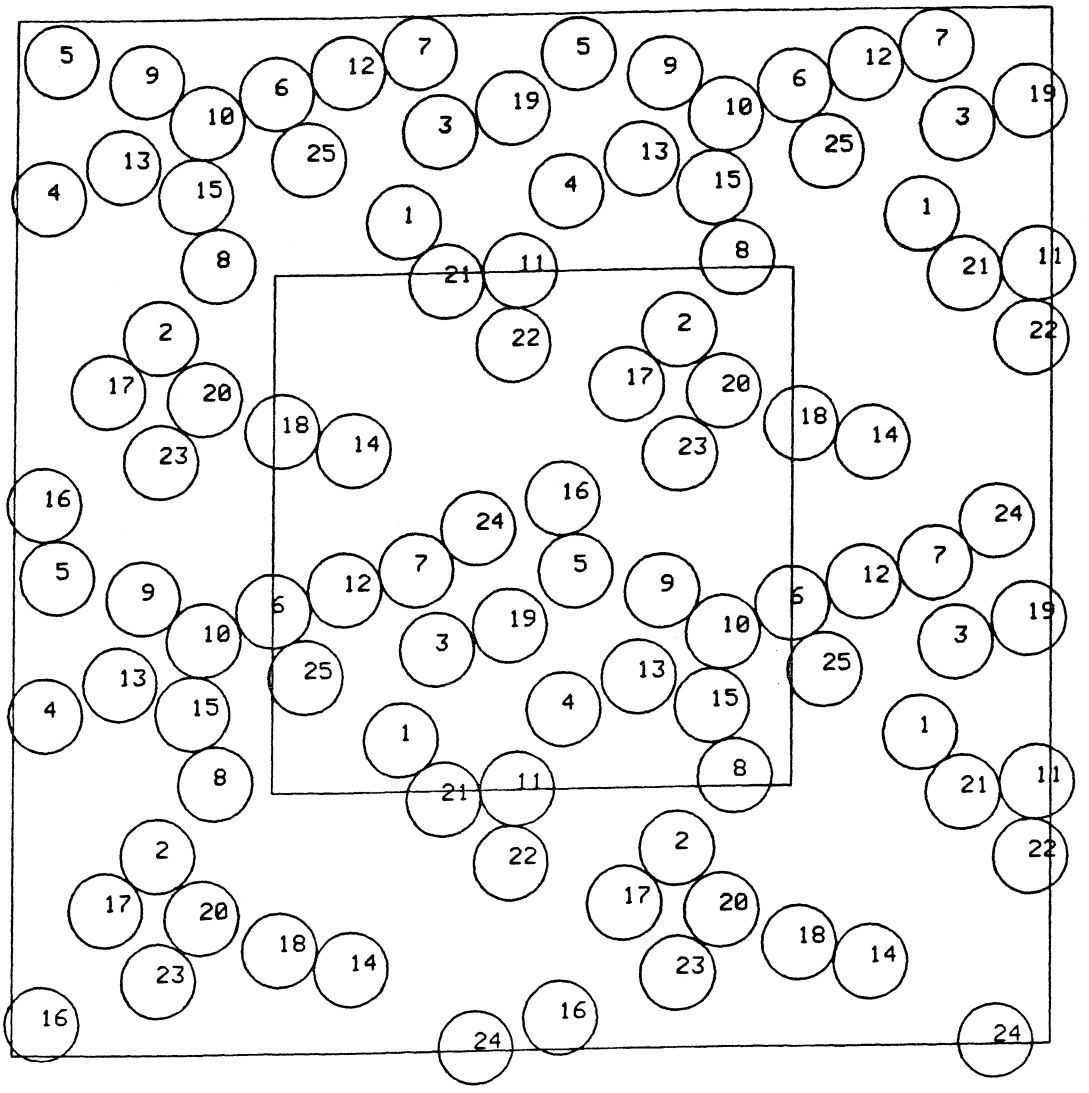

Figure 2.10 A "snapshot" of sphere positions. The inner box is the periodic cell. These are the sphere positions at $t = 299.0$ time units for an F, non-Ewald simulation. However, unlike the previous simulations, the sphere trajectories are integrated using an explicit, first-order, Euler integrator. The time step is 0.005 time unit and the mobility matrix is inverted every 200 steps.

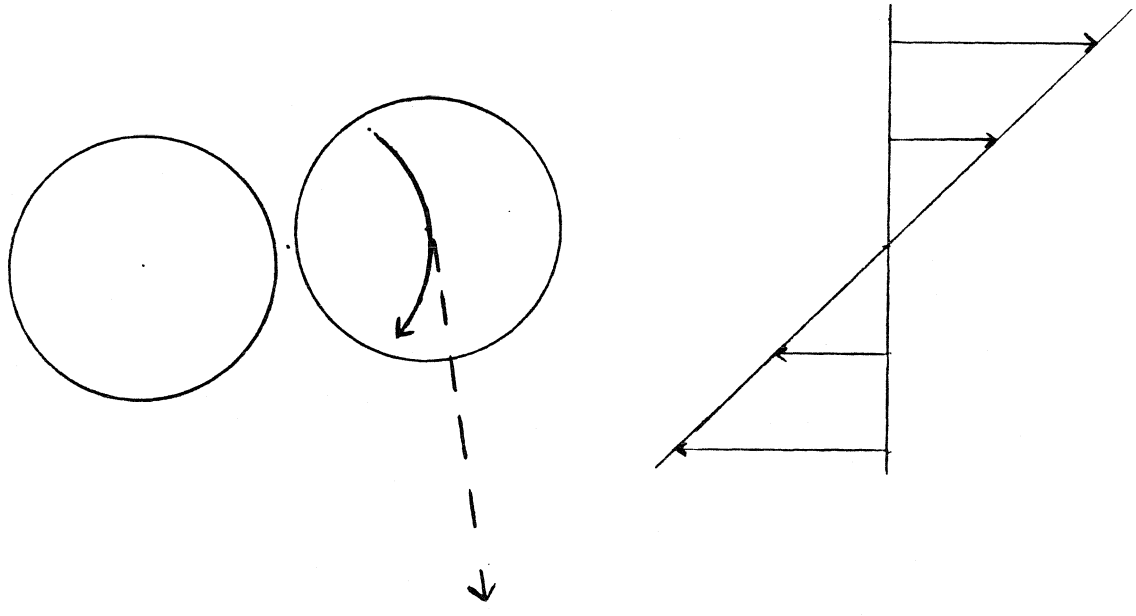

Figure 2.11 Schematic of two spheres in a linear shear field. The solid curve is the actual trajectory and the dashed line is the tangent to this curve.

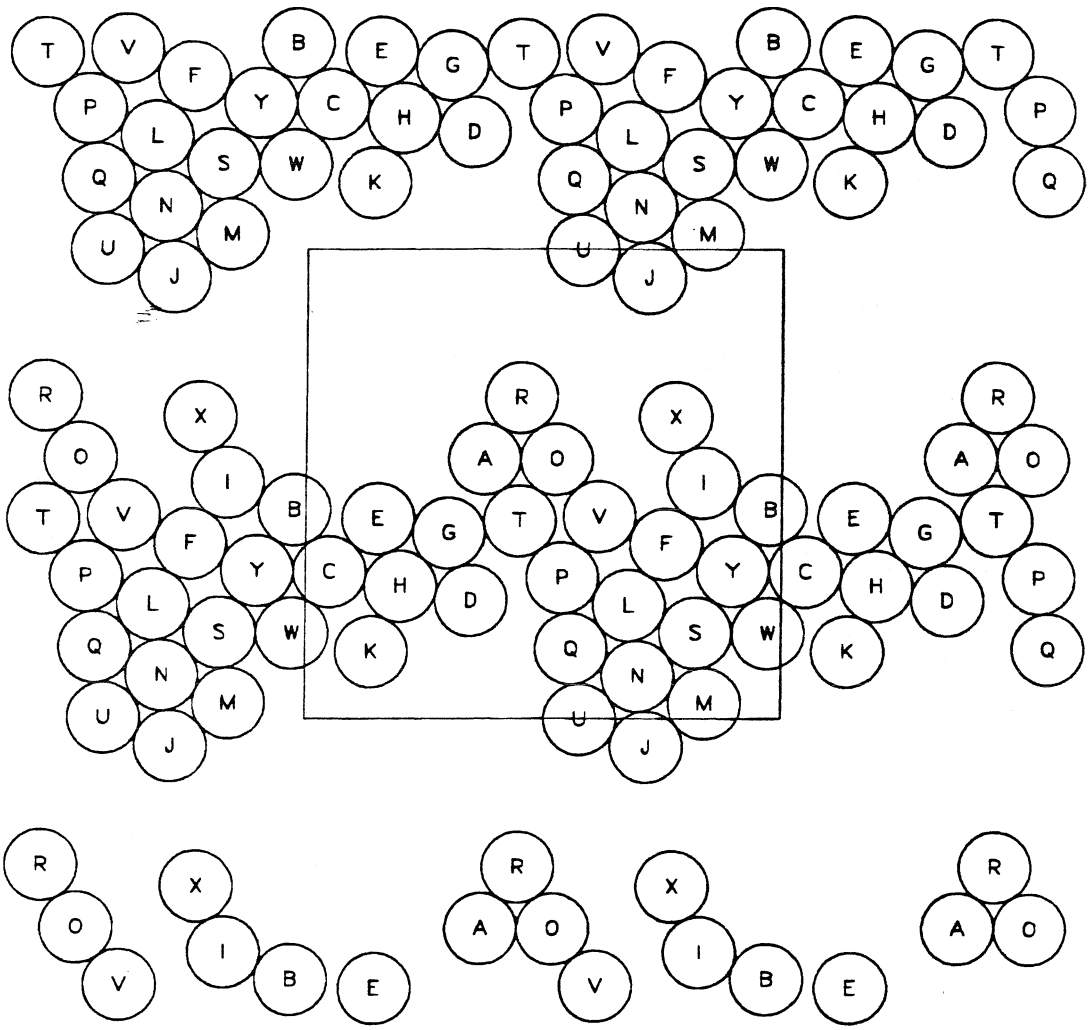

Figure 2.12 A "snapshot" of sphere positions. The box is the periodic cell. These are the sphere positions at $t = 500.0$ time units for an FTS, non-Ewald simulation (referred to as run FTSn5 in Chapter 4). The time step is 0.001 time unit and the mobility matrix is inverted every 100 steps.

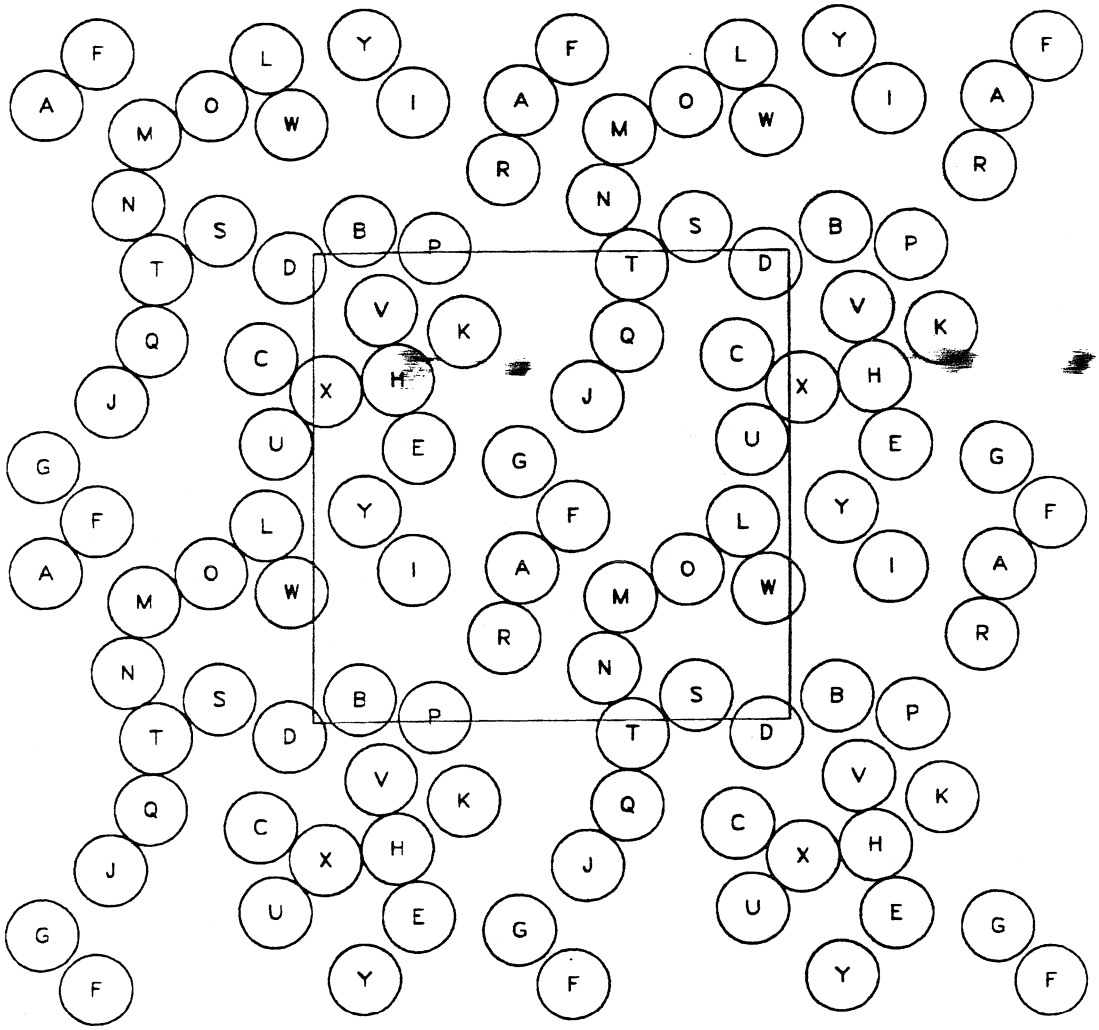

Figure 2.13 A "snapshot" of sphere positions. The box is the periodic cell. These are the sphere positions at $t = 500.0$ time units for an F, non-Ewald simulation when there are repulsive interparticle forces between the spheres (referred to as run nfr1 in Chapter 4). The time step is 0.001 time unit and the mobility matrix is inverted every 100 steps. The range parameter of the interparticle force, τ, is 10^3.

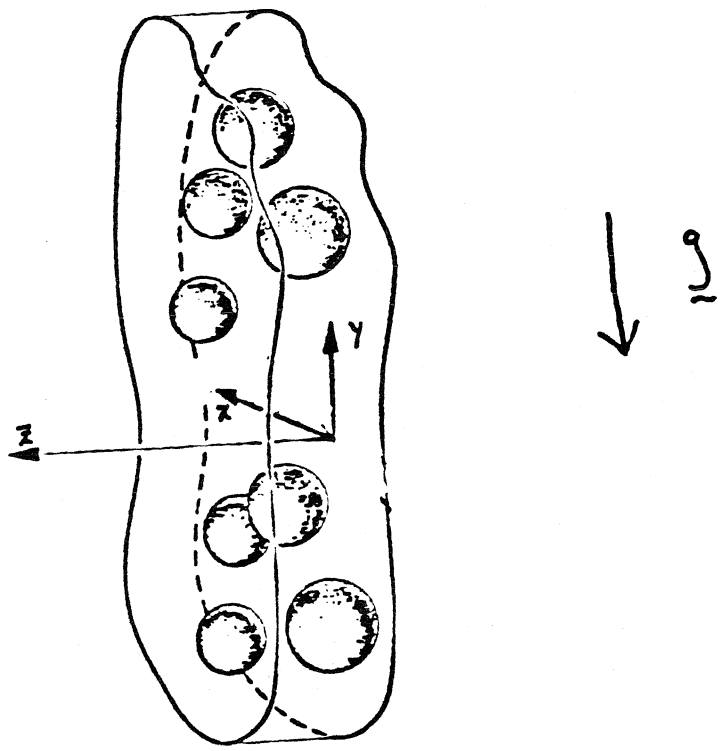

Figure 2.14 Schematic of a monolayer suspension of non-neutrally buoyant spheres.

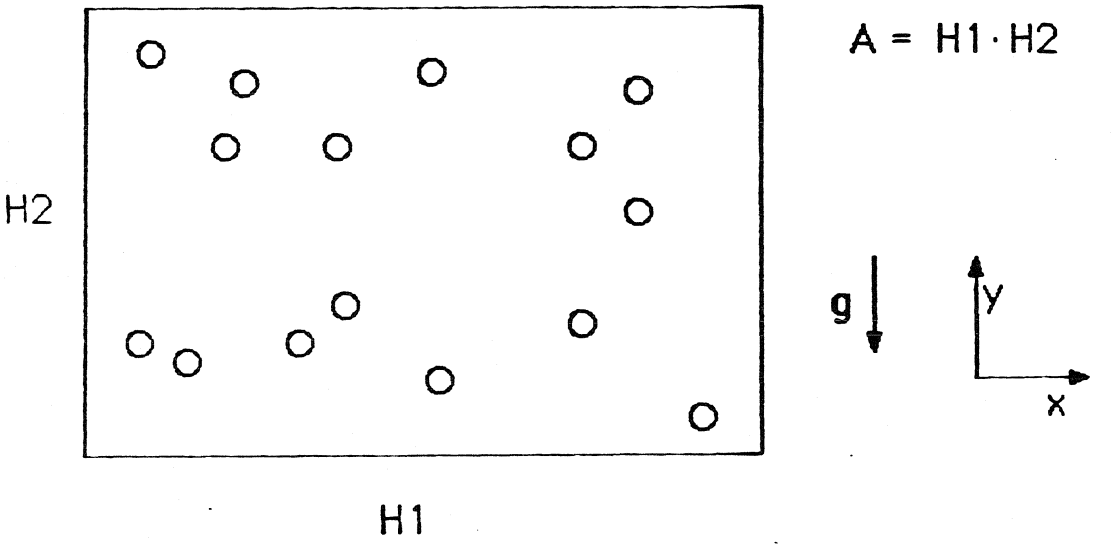

Figure 2.15 The periodic cell in the monolayer.

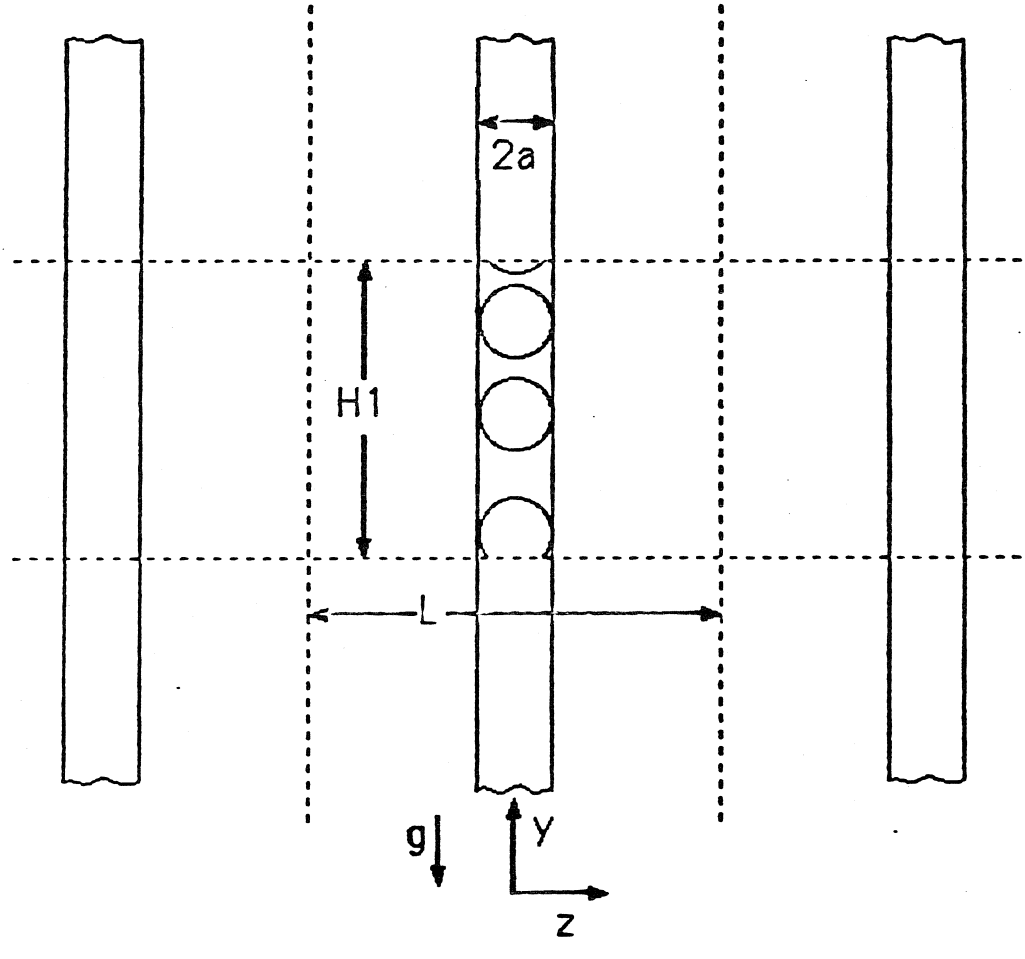

Figure 2.16 Physical representation of the application of Ewald sums to the monolayer problem. The monolayers extend into and out of the plane of the page. The central cell is considered the object cell.

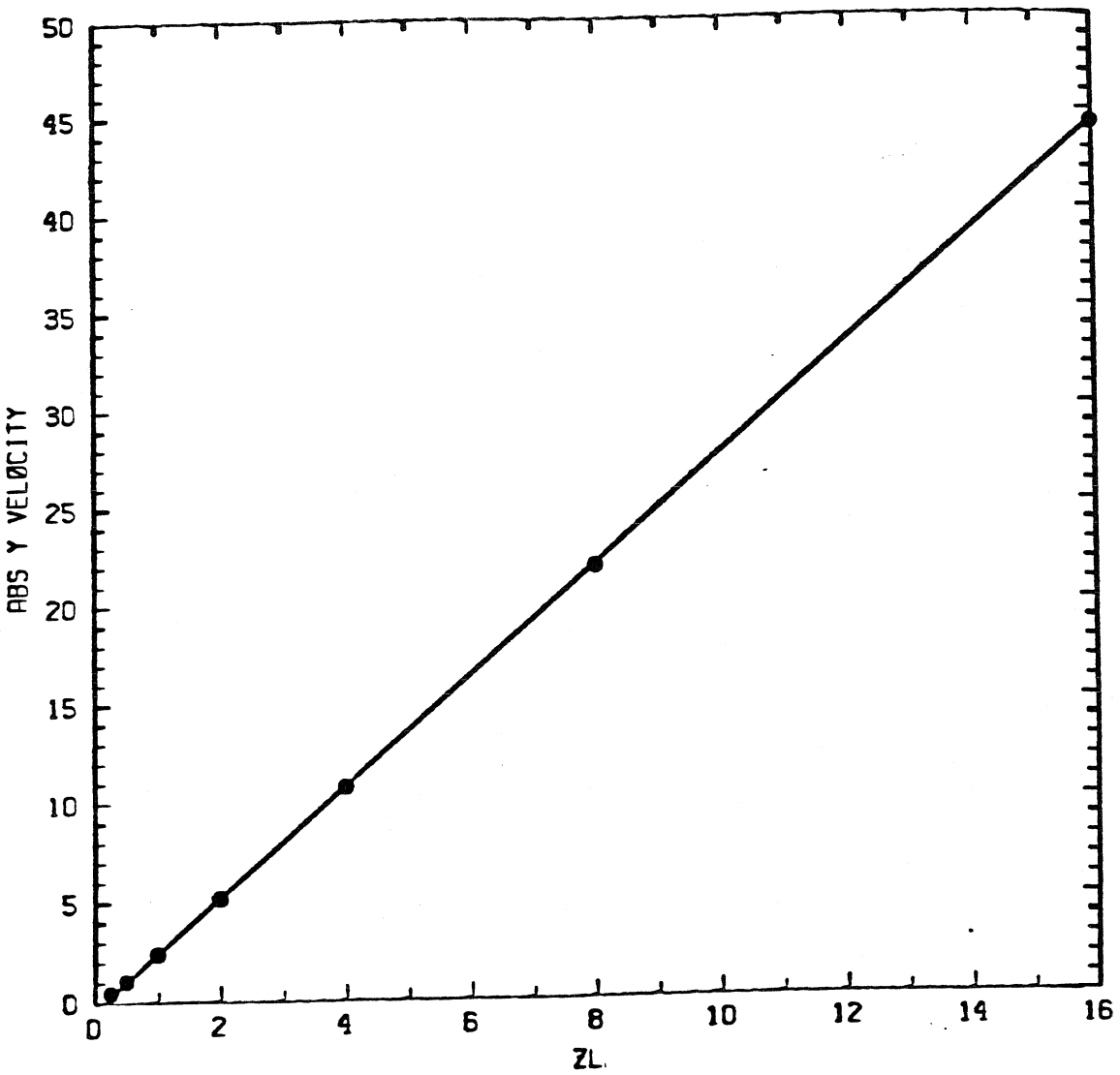

Figure 2.17 The dependence of the "sedimentation" velocity, $\langle v_y \rangle$, on the distance between the monolayers, which is characterized by z_l. The dots (•) are simulation results calculated from Equation (2.6–1). The solid line is a plot of Equation (2.6–5), which results from the falling planes analysis.

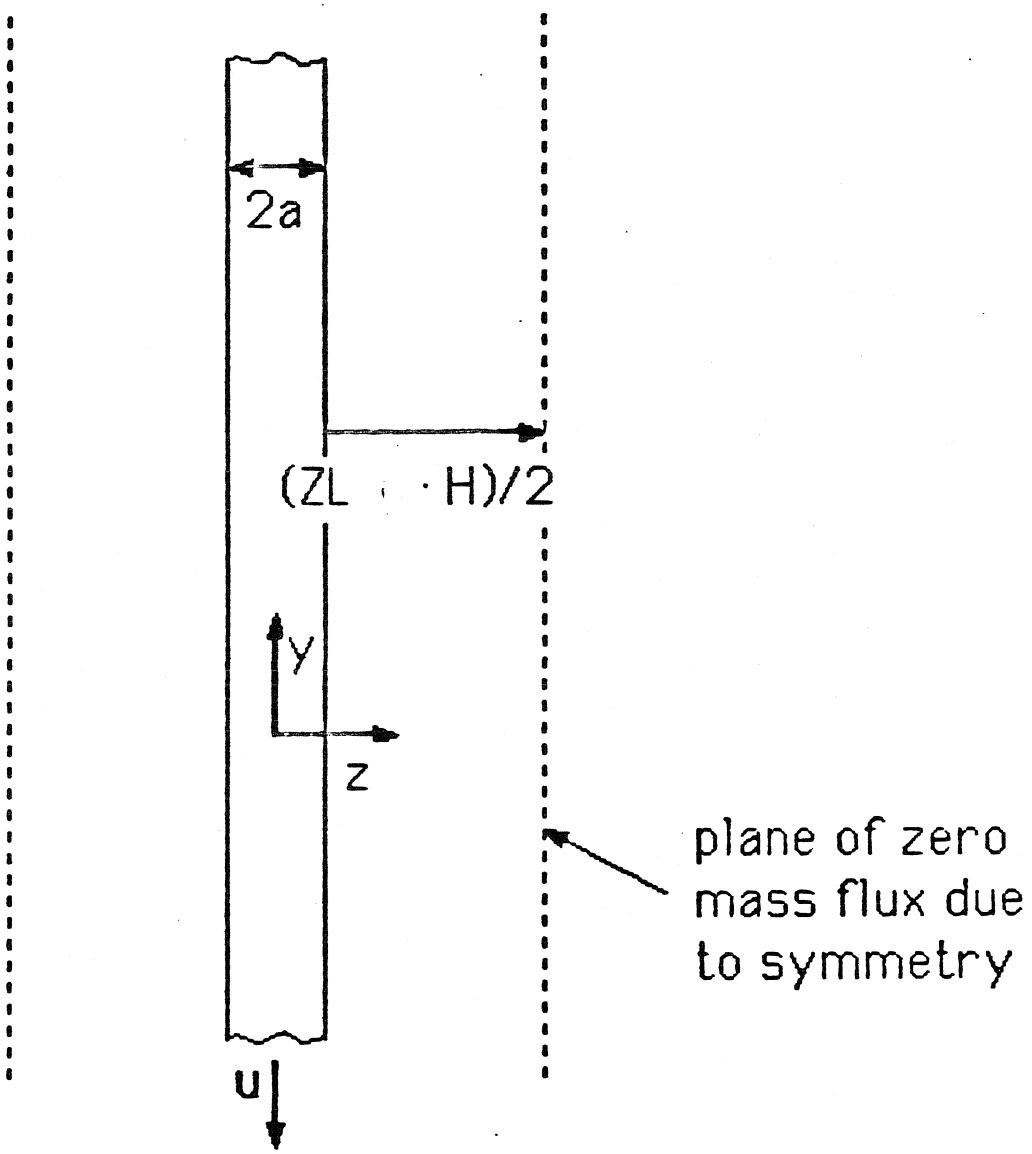

Figure 2.18 The analogous problem of falling parallel planes: a single plane falls at a constant velocity with parallel planes of zero mass flux a distance of $\frac{1}{2}(z_l \cdot H + a)$ on either side of the plane.

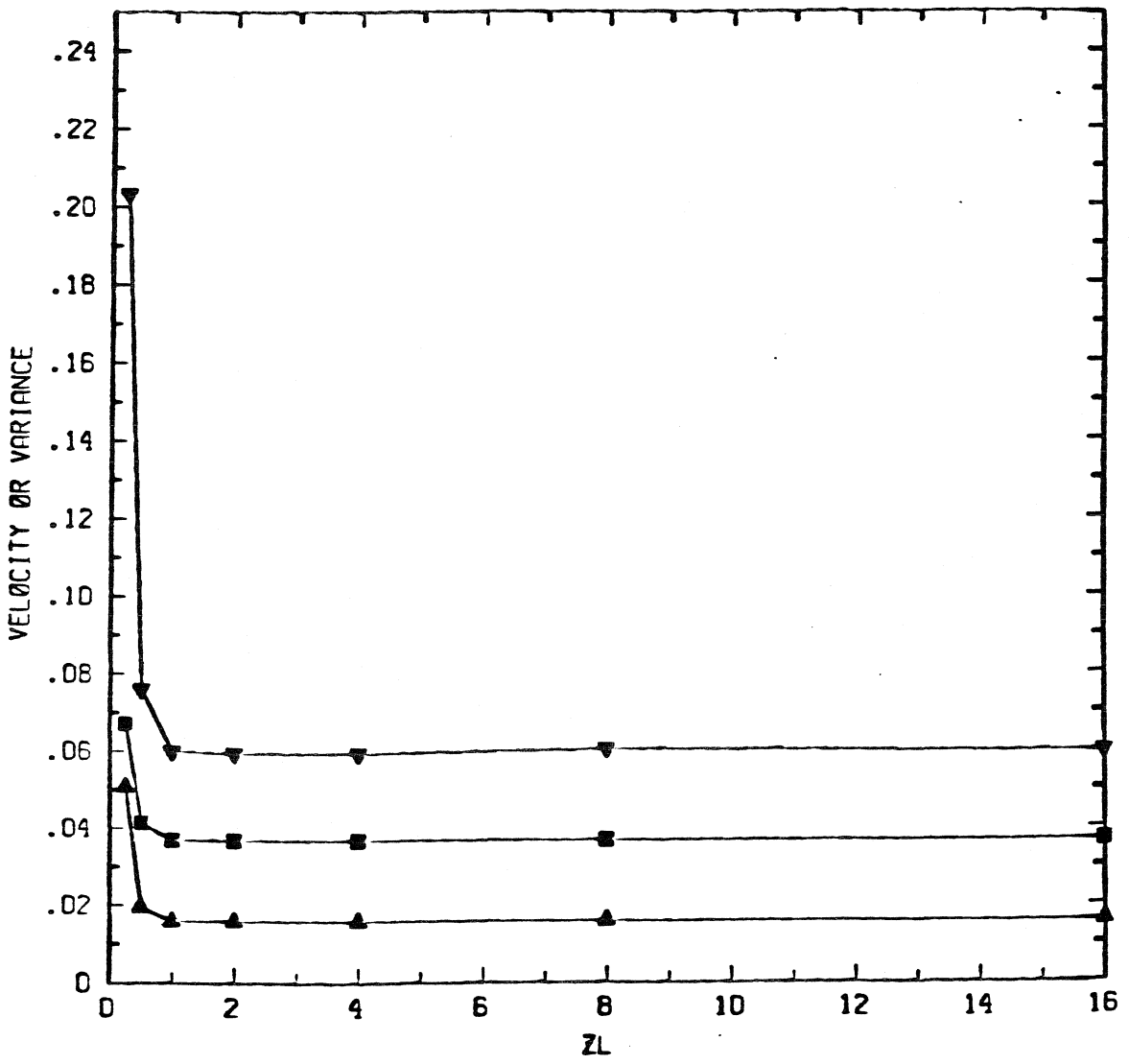

Figure 2.19 Simulation results for $\langle v_x \rangle$ (the filled squares), $\langle (v_y - \langle v_y \rangle)^2 \rangle$ (the filled upside-down triangles), and $\langle (v_x - \langle v_x \rangle)^2 \rangle$ (the filled triangles), as a function of the distance between the monolayers, which is characterized by z_l. The curves connect the simulation results for each case.

CHAPTER 3: SHORT-TIME SELF-DIFFUSION IN A MONOLAYER

The coefficient of short-time self-diffusivity, $\mathbf{D}_o^s$, measures the average instantaneous mobility of a particle in a suspension. Unlike the long-time dispersion, it is independent of the dynamics of the suspension. $\mathbf{D}_o^s$ is the configuration average of the instantaneous mobility of a forced particle when the other particles are considered neutrally buoyant; from a computational viewpoint, it is the number average of the self submatrices in the mobility matrix that couples the translational velocity of the particle to the force on that particle. Clearly, how we approximate the mobility matrix will affect $\mathbf{D}_o^s$, and we will be able to show clearly the effect of the induced stresslets and the near-field, two-body interactions. Since there is no preferred direction in the suspensions we are considering, we report the value of $D_o^s = \frac{1}{2} tr \mathbf{D}_o^s$. In this chapter we consider the effect of concentration and microstructure on this diffusivity for spheres in monolayer suspensions, although the basic analysis is not limited to monolayer suspensions. The distribution of spheres within the monolayer may be a regular square array, a random hard-disk distribution generated by a Monte-Carlo simulation, or a distribution resulting from the dynamic settling simulations of Chapter 4.

The first section of this chapter defines the pair-distribution function, and it tells how this and D_o^s are calculated for the random and sedimenting monolayer suspensions. The second section presents the results of Ewald calculations of D_o^s. The application of Ewald sums to monolayer suspensions requires special consideration. We shall see that the Ewald sums for the monolayer produces effects to be expected in the analogous case of a series of parallel plates, as shown in Section 2.6 for the "sedimentation" velocity. Varying the distance between the image monolayers (keeping the number of spheres in the periodic cell constant) can alter the relative contributions of the far-field pairwise interactions, the multibody and stresslet interactions, and the near-field interactions. Varying the number of particles in the periodic cell (keeping the ration of the distance between the

monolayer to the length of the periodic cell constant) exposes a relationship between the Ewald and non-Ewald results. The third section presents the results of non-Ewald calculations of D_o^s that consider its concentration dependence for random and regular array distributions. The fourth section reports the results of D_o^s for the steady-state configurations of the dynamic simulations of sedimenting monolayers. The concluding section discusses the consistent relationship between the pair-distribution function and short-time, self-diffusion coefficient seen in these results.

3.1 Determination of Configuration-Related Properties

The pair-distribution function, $\mathbf{g(r)}$, is the probability density of finding a second particle a distance $\mathbf{r}$ from the test particle and is, in general, a function of both r and θ (see Figure 3.1). The arc of $\theta = 0°$ to $180°$ is divided into 10 equal wedges, each spanning a $\Delta\theta = 18°$. The first wedge is centered at $9°$ and the last, at $171°$. The radial distance from the test sphere is divided into sections of $\Delta r = 0.05$. The value of $g(r,\theta)$ in a given region of size $\Delta r \Delta\theta$ is determined by considering each sphere at the center of its own periodic cell and by averaging over the configurations the number of sphere centers found in this region. In the dynamic simulations, configurations from each data step, after the system reachs a stationary state, are averaged to determine the pair-distribution function. The value of r in the radial distribution function varies from 2.0 to a distance half the periodic box length. The definition of a near-touching pair of spheres is that the sphere centers are separated by 2.05 sphere radii or less.

For the random distributions, we are not generally interested in the short-time, self-diffusion coefficient for a given configuration. However, in dynamic simulations, it is interesting to consider the time evolution of the short-time self-diffusion coefficient (see Figure 3.8*a*). The upper two curves are the xx and yy components of $\mathbf{D}_o^s$ and, as expected because of symmetry, are roughly equivalent. D_o^s is the average of these two curves. The lowest curve is the xy component of $\mathbf{D}_o^s$, which should be zero because of symmetry. $\mathbf{D}_o^s$ is a run-time calculation and

has been used as a quick measure of the development of the microstructure in a simulation. The reported value of D_o^s for the dynamic simulations is the time average of D_o^s.

3.2 Ewald Results and Discussion

This section contains the results of a series of studies on the effect of the application of the Ewald method on determining D_o^s for spheres in a monolayer. Unless otherwise noted, the configuration within the monolayer will be a regular array with the spheres on the lattice points of a square grid, $\phi_A = 0.453$, and the FTS method is used to approximate the mobility matrix. Just as the application of the Ewald method to the monolayer has certain implications for the velocity and velocity variance of the spheres, it also has implications for the value of D_o^s. In particular, we will discuss the effect of varying z_l (where $L = z_l \cdot H$ is the distance between neighboring monolayers, and H is the length scale of the periodic cell), keeping N_1 fixed and varying N_1, keeping z_l fixed. Since the mobility matrix can be approximated in various ways, we will consider the following contributions to D_o^s: 1) the far-field pairwise mobility interactions in the grand mobility matrix, $\mathbf{M}_{UF}^{\star}$ (this would be 1.0 in the non-Ewald case); 2) the far-field many-body mobility interactions, including the effect of the induced stresslets, in the inverse of the small resistance matrix that has not had the two-body interactions included, $(\mathbf{R}_{FU}^{\star})^{-1}$; and 3) the full approximation to the mobility matrix interactions, $(\mathbf{R})^{-1}$. One of the greatest advantages of the Ewald method is that the mobility matrix will not lose positive definiteness, regardless of concentration or N_1 – this will be discussed at the conclusion of this section. At that time we will also look at the effect of varying the microstructure in the monolayer and general implications of applying the Ewald method to dynamic monolayer sedimentation simulations.

3.2.1 D_o^s vs. z_l, N_1 fixed

We have studied the effect on D_o^s of varying the distance between the monolayers, keeping N_1 fixed. In all cases, $N_1 = 16$, $\phi_A = 0.453$, the spheres are in a

regular array, and convergence in D_o^s is guaranteed to at least 4 significant figures. Using an analysis similar to the one in Section 2.6 (except that $\langle F \rangle \neq 1$, but $\langle F \rangle = 1/N_1$), we might expect that

$$D_o^s \propto \frac{1}{2}\phi_A N_1^{-1} H \cdot z_l, \qquad (3.2.1\text{–}1)$$

when N_1, ϕ_A, and H are fixed (see Equation 2.6–5). Figure 3.2 shows the results of our study; the pluses are the D_o^s results when the mobility matrix has not been inverted ($\mathbf{M}^*$), the dots indicate that the far-field (many-body and induced stresslets) interactions have been added ($(\mathbf{R}_{FU}^*)^{-1}$), and the x's indicate the full approximation results. The dotted line through the direct Ewald contribution results is a least squares fit of those data; it has a slope of 0.1492 and a correlation coefficient of 0.99998. The factor of $\frac{1}{2}\phi_A N_1^{-1} H$ from Equation 3.2.1–1 is 0.1492 for this case. The $(\mathbf{R}_{FU}^*)^{-1}$ results lie along a basically parallel line slightly below the direct Ewald contribution curve. This shows the mobility-reducing effect of the many-body and induced stresslet interactions, which also occurs in the full three-dimensional case (cf. Brady & Durlofsky 1988). When the near-field two-body interactions are not included, the relationship between D_o^s and z_l is as predicted. However, when the full approximation to the mobility matrix is used, D_o^s does not behave as predicted; indeed, D_o^s levels off as $z_l \rightarrow \infty$. Two things clearly need to be discussed: How can D_o^s increase as the apparent three-dimensional concentration decreases (z_l increasing), and why does D_o^s approach a constant value, greater than 1, when the full mobility approximation is used, instead of increasing linearly with z_l as predicted and in the far-field approximations?

The first question can be answered by understanding the nature of the Ewald sums. Theoretically, D_o^s is calculated by applying a force to a given sphere when all other spheres are force-free and then determining the mobility of that particular sphere. However, in invoking the lattice sums and the Ewald method, each sphere at the center of its periodic cell *and* all of its images will feel an applied force on them. Thus, we have a similar situation to the one in Chapter 2.3; monolayer planes with a given average force "move" faster as the distance between them increases (see Equation 3.2.1–1).

The second question is answered by considering the relative contributions of the near-field and Ewald-summed components. Remember that the mobility matrix is constructed as follows:

$$\mathbf{M} = \mathbf{R}^{-1} \approx (\mathbf{R}^{\star}_{FU} + \mathbf{R}_{2b} - \mathbf{R}^{\infty}_{2b})^{-1}, \qquad (3.2.1\text{–}2)$$

where $\mathbf{R}^{\star}_{FU}$ is $(\mathcal{M}^{\star})^{-1}_{FU}$ and $\mathcal{M}^{\star}$ is the Ewald-summed grand mobility matrix. The behavior of the Ewald-summed elements of the mobility matrix coincides with the predicted behavior. The elements of $\mathcal{M}^{\star}$ (especially the important self terms) increase as z_l increases, and the same elements in $\mathbf{R}^{\star}_{FU}$ decrease (they are related to the inverse of the mobility elements). Now, let us include the difference of the two-body terms. This difference is a constant for any given configuration. We have seen that the difference is, in general, quite small (cf. the permeability results in Brady, *et al.* 1987 and Chapter 2.2.2), but as z_l increases, the elements of $\mathbf{R}^{\star}_{FU}$ become as small as, and then smaller than, the difference of the two-body terms. Thus, as $z_l \to \infty$, $\mathbf{M} \sim (\mathbf{R}_{2b} - \mathbf{R}^{\infty}_{2b})^{-1}$, which is independent of z_l.

3.2.2 D^s_o vs. N_1, z_l fixed

We have studied the effect on D^s_o of varying the number of spheres in the periodic cell, N_1, keeping z_l fixed. Although z_l is fixed, the actual distance between the image monolayers, L, will change, since $L = H \cdot z_l$ and H is a function of $N_1^{\frac{1}{2}}$. Again, we predict the behavior of D^s_o from Equation (3.2.1–1), in this case,

$$D^s_o \propto N_1^{-\frac{1}{2}}. \qquad (3.2.2\text{–}1)$$

The areal fraction in all cases is $\phi_A = 0.453$, and the spheres are in a regular array within the monolayer. Figure 3.3 shows D^s_o *vs.* $N_1^{-\frac{1}{2}}$, where D^s_o is calculated from the non-inverted Ewald-summed mobility matrix. Each curve represents a different value of z_l and the pluses indicate actual data points. Figure 3.4 graphs D^s_o *vs.* $N_1^{-\frac{1}{2}}$, where D^s_o is calculated from $(\mathbf{R}^{\star}_{FU})^{-1}$. Figure 3.5 graphs D^s_o *vs.* $N_1^{-\frac{1}{2}}$, where D^s_o is calculated from full mobility matrix approximation. The curves on Figure 3.3 represent the best least-squares fit of the data at that value of z_l. The

curves on Figures 3.4 and 3.5 are lines drawn though the results of the two largest values of N_1. The triangle on the y-axis represents the appropriate D_o^s calculated without Ewald sums ($N_1 = 81$). In general, all the curves on each figure meet approximately at a given y-intercept, close to the non-Ewald result. In all cases, increasing N_1 gives a predicted value of the y-intercept closer to the non-Ewald result. As N_1 increases, the actual distance between the monolayer increases, even though z_l is fixed. The average force on the spheres in each periodic cell, $\langle F \rangle$, decreases as N_1^{-1} as N_1 increases. For finite values of z_l, $N_1 = \inf$ implies that the slope of D_o^s *vs.* z_l will be zero (the slope is $\propto N_1^{-\frac{1}{2}}$; thus, D_o^s will be independent of z_l at $N_1 = \infty$. The effect of the image monolayer can now be neglected and the average force on the spheres in the monolayer will be zero; the Ewald results for D_o^s should be equivalent to the non-Ewald results in the limit as $N_1 \rightarrow \infty$.

3.3 Non-Ewald Results and Discussion

In the preceding section, we only considered regular arrays of spheres. In considering the short-time, self-diffusion coefficient in random suspensions, we form and invert the grand mobility matrix for 50 to 1000 configurations of a fixed number of spheres. Unfortunately, the Ewald method is very time consuming, especially for large values of N_1 and/or z_l; it can require 30 to 100 CPU minutes per configuration or more to obtain convergence in the mobility interaction expressions. A non-Ewald calculation will commonly take 30–50 CPU seconds per configuration. (These comparisons are for $N_1 = 25$ and $\phi = 0.453$). To sample enough configurations to insure a truly random distribution of spheres, time constraints strongly recommend that a non-Ewald method be used to form the grand mobility matrix. The last section implies that the Ewald and non-Ewald methods produce close to the same results for the short-time, self-diffusion coefficient. This section contains the results for non-Ewald calculations ($\gamma = 1$ in Equation 2.3.2–3), and the mobility matrix is approximated using the FTS method, unless otherwise noted. We begin our study of the short-time self diffusivity by investigating the

concentration and cell size dependence of the mobility of spheres in a regular array within a monolayer. The number of spheres in the periodic cell is N_1, and the maximum packing for this microstructure is $\phi_A = 0.785$ $(\frac{\pi}{4})$. The regular array results are presented in Figure 3.6. The solid curve connects the $N_1 = 81$ results, the dotted curve, the $N_1 = 49$ results, and the dashed curve, the $N_1 = 25$ results. Each curve ends when the grand mobility matrix loses positive definiteness. As the periodic cell size decreases (increasing ϕ_A *or* decreasing N_1), the magnitude of the truncation errors, $(O(r^{-6}))$, in the mobility elements will increase, and the mobility matrix will lose positive definiteness. This is one advantage to using the Ewald method since the convergence of the mobility elements (and therefore, positive definiteness) can be guaranteed for any value of N_1. Note that at any given concentration, the addition of other spheres to the periodic cell reduces D_o^s, which is the expected result. The small hump seen at about $\phi_A = 0.19$ is an artifact of our method; the $\mathbf{R}_{2B} - \mathbf{R}_{2B}^{\infty}$ term is truncated at a sphere-sphere distance of 4 radii, and the effect of this will, of course, be exaggerated in a regular array.

Now consider monolayer suspensions of spheres whose average distribution is a random, hard-disk distribution. Bossis & Brady (1987) have shown that the Stokesian dynamic simulation of pure Brownian motion produces this hard-disk distribution. However, we use a Monte-Carlo simulation to produce the configurations in our study. Where possible, we have compared the pair-distribution function of our actual configurations to the hard-disk distributions reported in Chae, Ree & Ree (1969). We used between 100 and 1000 configurations to obtain an average D_o^s. After considering the effect of cell size (number density constant), we will show the relationship between D_o^s and ϕ_A and end this section with a discussion of the effect of microstructure on D_o^s. This last point will include the results from non-Ewald dynamic simulations of sedimenting spheres in a monolayer.

Figure 3.7*a* graphically presents the random distribution results; the regular array results are repeated for comparison. (See Figure 3.7*b* for an expanded view of the small concentration results.) The (•)'s indicate that $N_1 = 16$, the (+)'s

indicate that $N_1 = 25$, and the $(\times)$'s indicate $N_1 = 49$. Bossis & Brady's (1987) result for $Pe = 0$ is denoted by a $\triangle$ (D_o^s is calculated from 30,000 configurations). The most striking feature of Figure 3.7*a* is that the random distribution results all lie beneath the regular array results for $\phi_A < \frac{\pi}{4}$. This clearly shows the dominant mobility-reducing effect of the near neighbors in a random distribution. Consider the decrease in D_o^s as we increase N_1. In the random distribution case the decrease is only 60% of the decrease for the regular array ($N_1 = 25, 49$, $\phi_A = 0.453, 0.5441$). This is another indication of dominant, near-sphere interactions. In general, D_o^s is a monotonically decreasing function of increasing areal fraction for any given type of microstructure. This is expected since the mobility of a particle will decrease as its local environment gets more crowded.

3.4 D_o^s in sedimenting monolayer suspensions

The last microstructure we will consider is that resulting from our dynamic simulation of sedimentation in a monolayer. These runs are at different levels of approximation, may or may not use Ewald sums, and may or may not have repulsive forces between the spheres. All of these variables may affect the steady-state configuration and D_o^s of the suspension. Instead of presenting the pair-distribution functions and the time traces of $\mathbf{D}_o^s$ for all the simulation runs, the next paragraph will illustrate the basic trends we notice in the relationship between the steady-state configuration and D_o^s. The results for these dynamic simulations are presented in Table 3.1 and are discussed below. The complete $\mathbf{D}_o^s$ results for the dynamic simulations are presented in Table 4.5.

Figures 3.8*a-c* show the dynamic evolution of $\mathbf{D}_o^s$ in sedimenting monolayers from the same initial configuration using the FTS, FT, and F methods, respectively, for both the dynamics and diffusivity calculations. The solid curves are the D_{yy} and D_{yy} components of the short-time self diffusivity, and the dotted line its D_{xy} component. The initial condition is a configuration taken from the Monte-Carlo hard-disk simulation. The mobility-reducing effect of the stresslets can be seen by comparing the D_o^s results of each method at $t = 0$. D_o^s is cal-

culated to the level of accuracy of the simulation run, and the actual difference among the steady-state values of D_o^s is misleading if we wish to characterize the microstructure with this coefficient. To remedy this, we calculate D_o^s for certain configurations produced by the F and FT dynamic simulations using the FTS method. This is done at intervals of 50 time units. The results are shown in Figure 3.9. The curves are solid with filled circles for FTS run configurations, dashed with filled stars for FT run configurations, and dotted with filled triangles for F run configurations. In general, the FT configuration results lie above the F configuration results, which, in turn, lie above the FTS configuration results, all of which lie beneath the random distribution result of $D_0^s = 0.72$. These results are easily understood by considering the pair-distribution functions in each case. Figure 3.10 is the pair-distribution function for the FT configurations ($t = 150$ to 500). Figure 3.11 is the pair-distribution function for the F configurations ($t = 250$ to 500). Figures 3.12*a,b* are pair-distribution functions for the FTS configurations (a:$t = 300$ to 400, b:$t = 380$ to 500). These figures have been arranged such that the figure number increases as D_o^s decreases (see Table 3.1). The key feature in this case is the peak at $r = 3.5$; this peak is associated with the presence of hexagonal packing of spheres in the monolayer (see Figure 3.13 for a "snapshot" of the configuration at $t = 500$ for the FTS run). Of course, hexagonal packing will strongly limit the mobility of spheres in such a configuration.

We see similar results when Ewald sums are applied to the mobility approximation ($z_l = 2.0$); the pair-distribution function shows a high degree of hexagonal packing and D_o^s is correspondingly small. Figure 3.14 shows the configuration of the spheres at $t = 750.0$ for an Ewald, F method run. $D_o^s \approx 0.30$ compared to $D_o^s \approx 0.36$ for the non-Ewald result (the F method is used in both runs). The discrepancy is due to the higher degree of hexagonal packing and near-pairs, and to the fact that at this value of z_l and N_1, the Ewald results will be slightly less than the non-Ewald results (see Section 3.2.2 and Figure 3.5).

Now consider the effect of repulsive interparticle forces on the microstructure and short-time self-diffusion coefficient of steady-state sedimenting suspensions.

Remember that as we increase the value of τ, the range of the interparticle force decreases; the interparticle force will generally be negligible compared to the hydrodynamic forces at surface separations greater than $4.5\tau^{-1}$. The most important feature of these results is the absence of hexagonal packing as denoted by the lack of a $g(3.5)$ peak in the radial pair-distribution function. (The absence of hexagonal packing can be seen in Figure 3.15, which is the configuration at $t = 500$ for a non-Ewald, F method simulation where $\tau = 10^3$). This is true for all values of τ that are considered ($\tau = 10^3$ and $\tau = 10^5$). D_o^s is 0.69, 0.60 and 0.36 for $\tau = 10^3$, 10^5 and ∞ (no repulsive forces), respectively; this is for non-Ewald F method simulations, but the trend is the same in the Ewald F method simulations. The value of D_o^s for a random, hard-disk configurations (to this level of approximation) is 0.78. When repulsive forces are present, we see again that the radial pair-distribution function is closely related to D_o^s. As τ decreases, the $g(2)$ and $g(4)$ peaks decrease; this indicates an decrease of near-pairs as the range of the interparticle force increases. The sedimentation of spheres without repulsive forces produces a dense, steady-state microstructure that severely restricts the instantaneous mobility of the spheres. The addition of repulsive interparticle forces increases this instantaneous mobility; as the range of this force increases (τ decreases), the mobility increases, but is still less than that in the random suspension. The evolution of the structures in sedimenting suspensions, with and without repulsive forces, will be discussed in more detail in Chapter 4.

3.5 Conclusions

Other microstructures than the regular arrays, random or steady-state sedimentation distributions are possible; a common suspension flow is a system of neutrally buoyant particles in a linear shear flow. Bossis & Brady (1987) studied the self-diffusivity of Brownian hard spheres within a monolayer subjected to a simple shear flow. The value of the shear Péclet number, which is the ratio of the importance of the shear flow to the Brownian motion, directly affected the sphere distribution and thus, the short-time self-diffusion coefficient. At the areal

fraction they studied, $\phi_A = 0.453$, D_o^s decreased monotonically from 0.74 ($\pm$0.01) to 0.57 ($\pm$0.01) as the Péclet number increased from zero to infinity. The pair-distribution function shows a rapid increase of the $r = 2$ peak, as well as the formation of a significant second near-neighbor peak at $r = 4$, as $Pe \rightarrow \infty$. This occurs as more and more spheres become clustered. This increase in clustering is clearly related to the decrease in D_o^s, as we have seen in comparing the regular array and random distribution results. It must be noted that the pair-distribution function for the $Pe = \infty$ case reported by Bossis & Brady (1987) is very similar to the FT pair-distribution function, with the exception that the small $g(3.5)$ peak ($g(3.5) = 1.01$) is missing in the shear result. We would expect that D_0^s for the shear case would be greater than that in any of the sedimentation cases that do not have repulsive interparticle forces. In a similar vein, the radial pair-distribution function for sedimentation simulations that included repulsive interparticle forces are qualitatively similar to the infinite Pe case for the sheared suspension. The trend here is that D_o^s will decrease as the $g(2)$ and $g(4)$ peaks increase in the radial pair-distribution function; there are a greater number of near pairs in the sheared suspension and the corresponding short-time diffusivity is smaller.

Both types of suspension flows considered here, shear and sedimentation, produce steady-state configurations that reduce the instantaneous mobility of their particles compared to the random Brownian suspension. In the absence of repulsive interparticle forces, sedimentation produces the densest microstructure and, of course, is characterized by the smallest short-time self-diffusion coefficient. With the addition of repulsive interparticle forces, we can essentially set the instantaneous mobility of the particles in the sedimenting suspension. Table 3.1 sums up the relationship among the short-time diffusivity, the microstructure of the monolayer, the suspension character and flow type, and concentration.

Table 3.1 The relation between the microstructure of the monolayer, D_o^s, and the pair-distribution function for runs reported in Chapter 3. $\phi_A = 0.453$ for all cases. The shear results are from Bossis & Brady (1987). The F, FT, and FTS sedimentation runs are non-Ewald simulations and are described in detail in Table 4.1 (they are designated Fn1, FTn1, and FTSn1-5, respectively). ef3 designates an Ewald, F method simulation run (t = 500–700). nfr1 designates a non-Ewald, F method simulation run in which interparticle forces ($\tau = 10^3$) are present (t = 0–500). See Tables 4.4 and 4.5 for the results of all the sedimentation simulations.

Microstructure	D_o^s	g(2.0)	g(3.5)	g(4.0)
regular array	0.801	-	-	-
random hard-disk	0.72	2.68	0.78	0.91
shear ($Pe=\infty$)	0.57	≈ 20	≈ 0.80	≈ 3.0
FT sedimentation	0.50	16.2	1.08	2.74
F sedimentation	0.45	16.3	1.61	3.12
FTS sedimentation	0.35	12.6	4.27	4.82
ef3 sedimentation	0.30	15.4	2.28	4.34
nfr1 sedimentation	0.69	11.5	0.92	1.44

For regular array: g(2.63)=33.6, g(3.75)=23.7

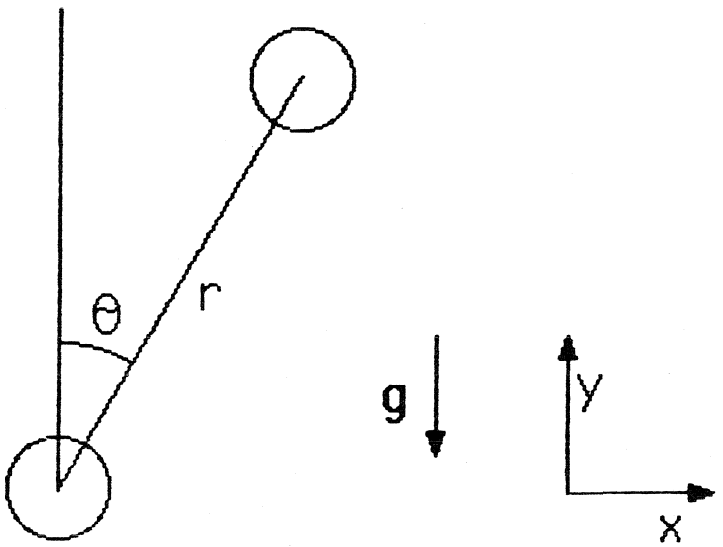

Figure 3.1 Defining sketch for the pair-distribution function.

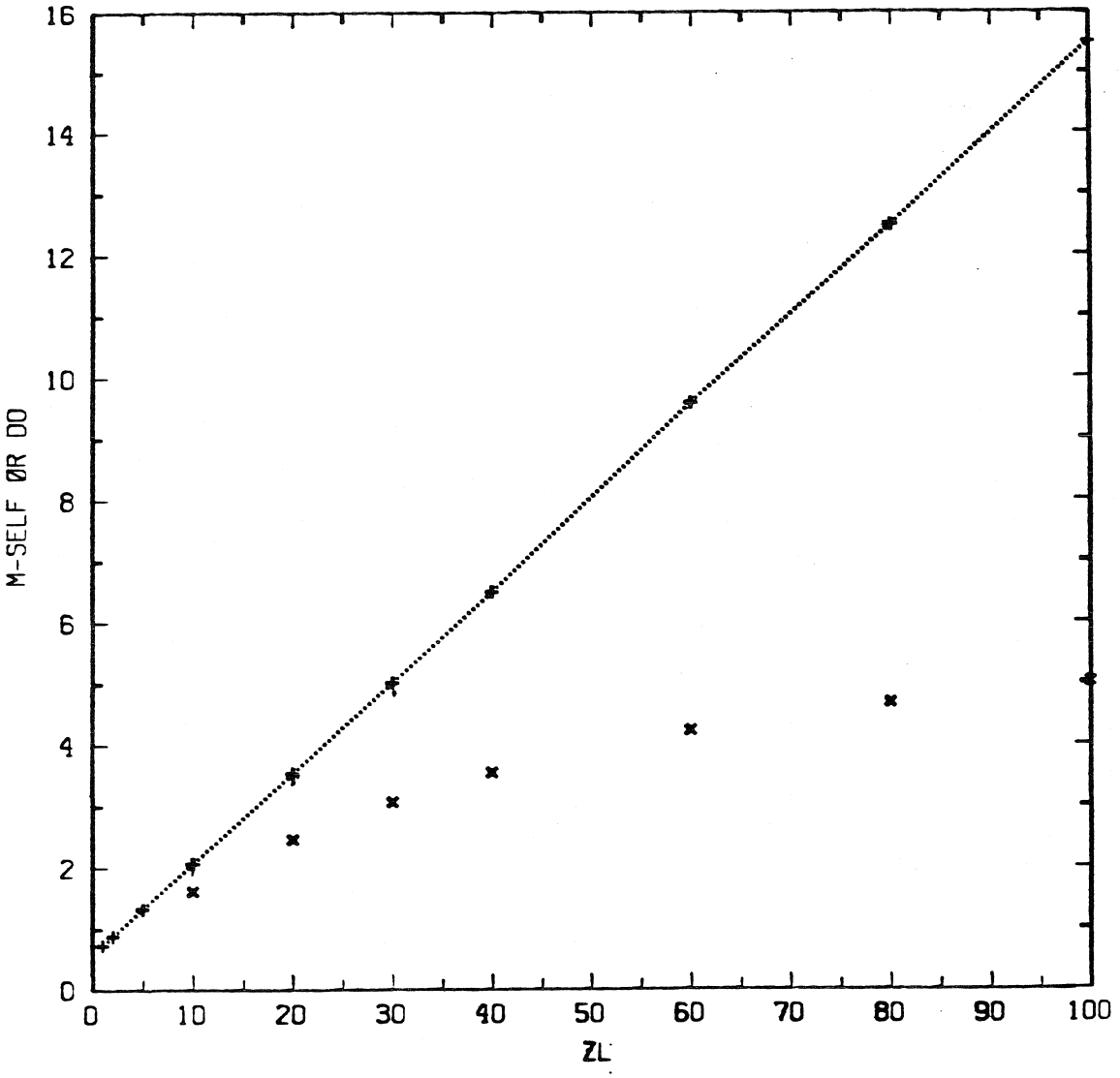

Figure 3.2 Short-time, self-diffusion coefficient as a function of z_l, $N_1 = 16$. The coefficient is calculated from the mobility matrix, which is approximated by $\mathbf{M}^*$ (+) or the full mobility approximation (x).

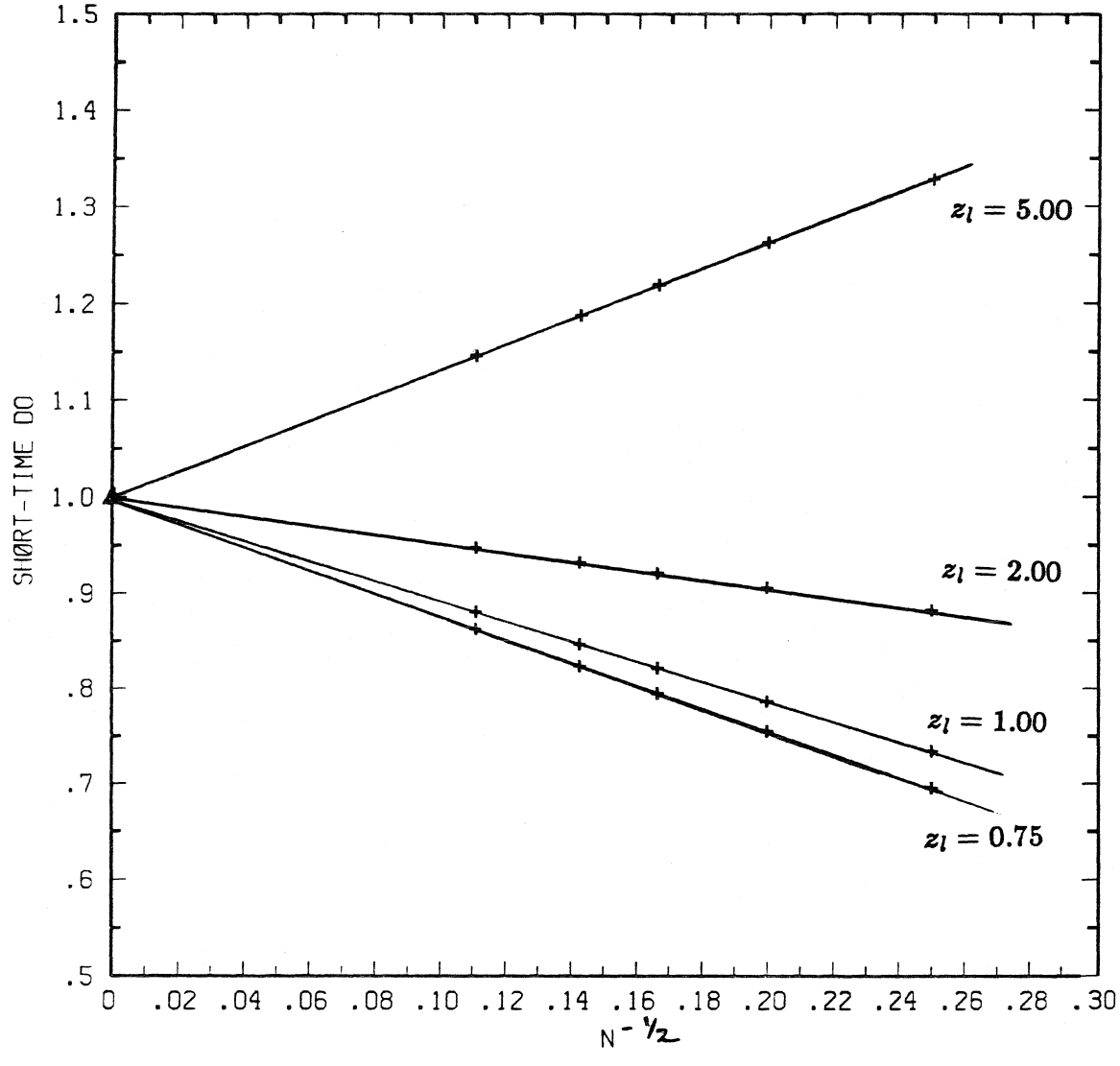

Figure 3.3 D_o^s as a function of $N^{-\frac{1}{2}}$. The mobility matrix is approximated by the uninverted Ewald-summed mobility matrix.

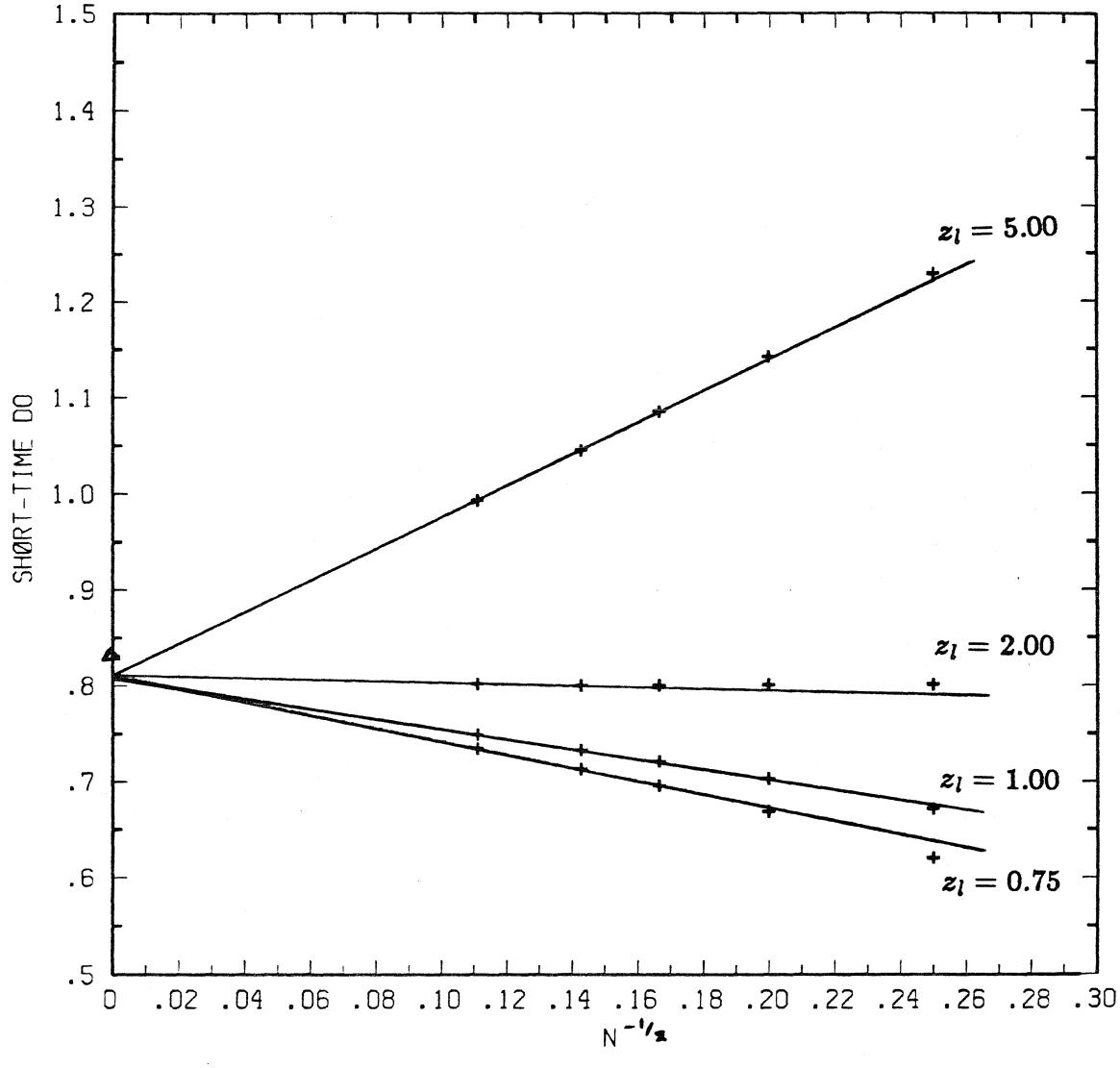

Figure 3.4 D_o^s as a function of $N^{-\frac{1}{2}}$. The mobility matrix is approximated by $(\mathbf{R}_{FU}^*)^{-1}$.

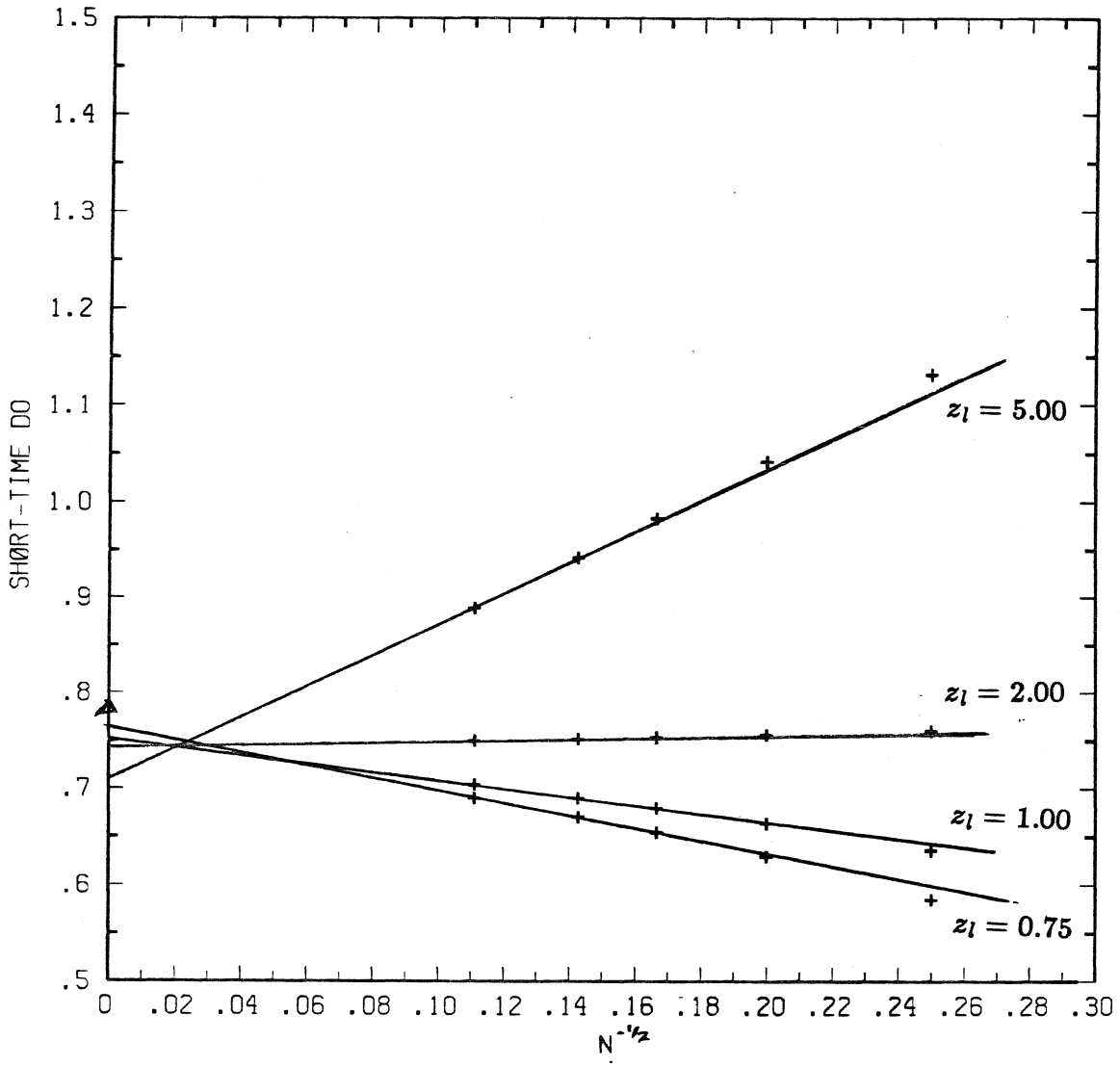

Figure 8.5 D_o^s as a function of $N^{-\frac{1}{2}}$. The mobility matrix is approximated by the full mobility approximation.

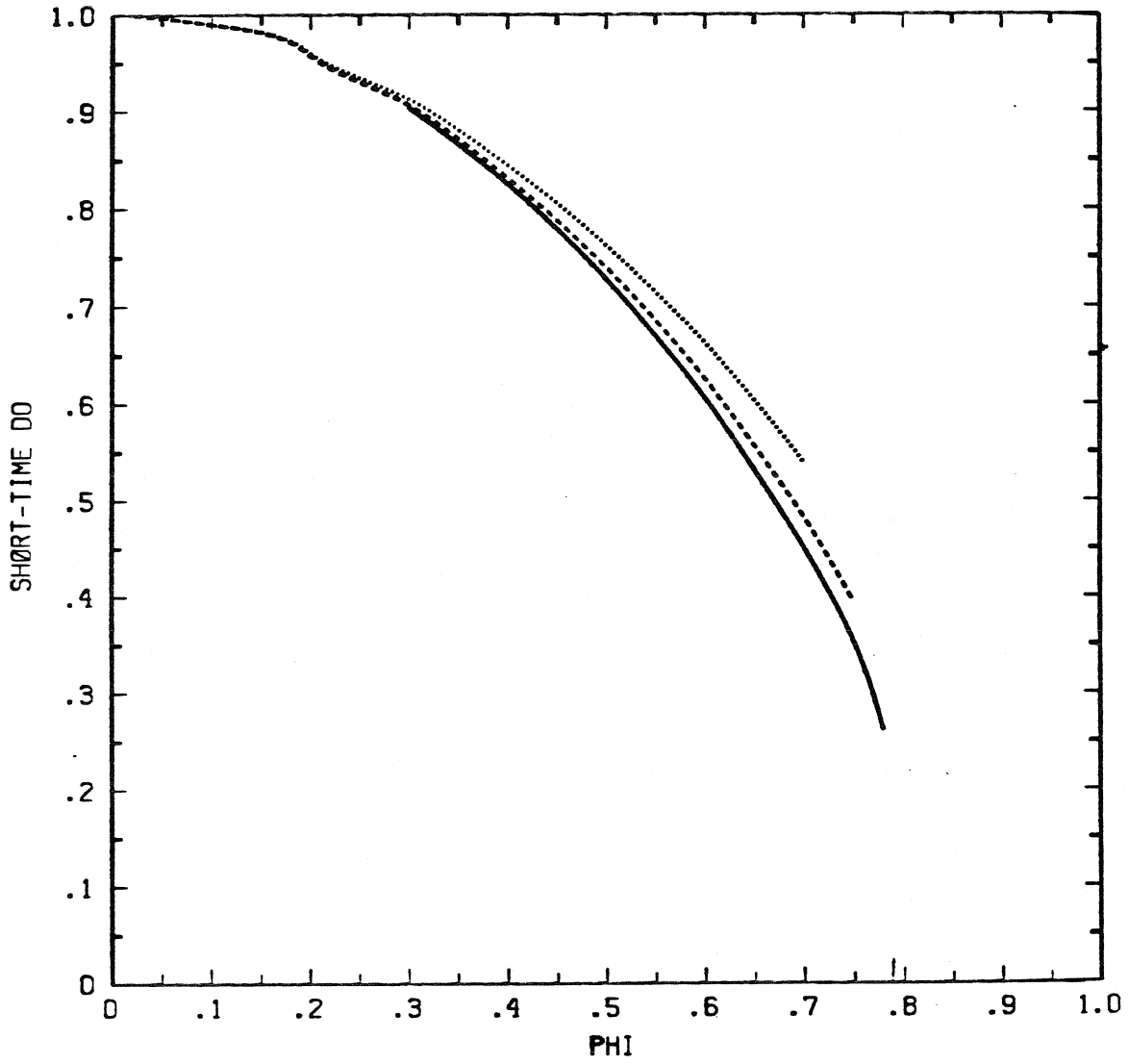

Figure 3.6 Short-time, self-diffusion coefficient as a function of areal fraction for spheres in a regular array in a monolayer (see inset). The number of spheres in the object cell is 81 (solid line), 49 (dashed line), or 25 (dotted line).

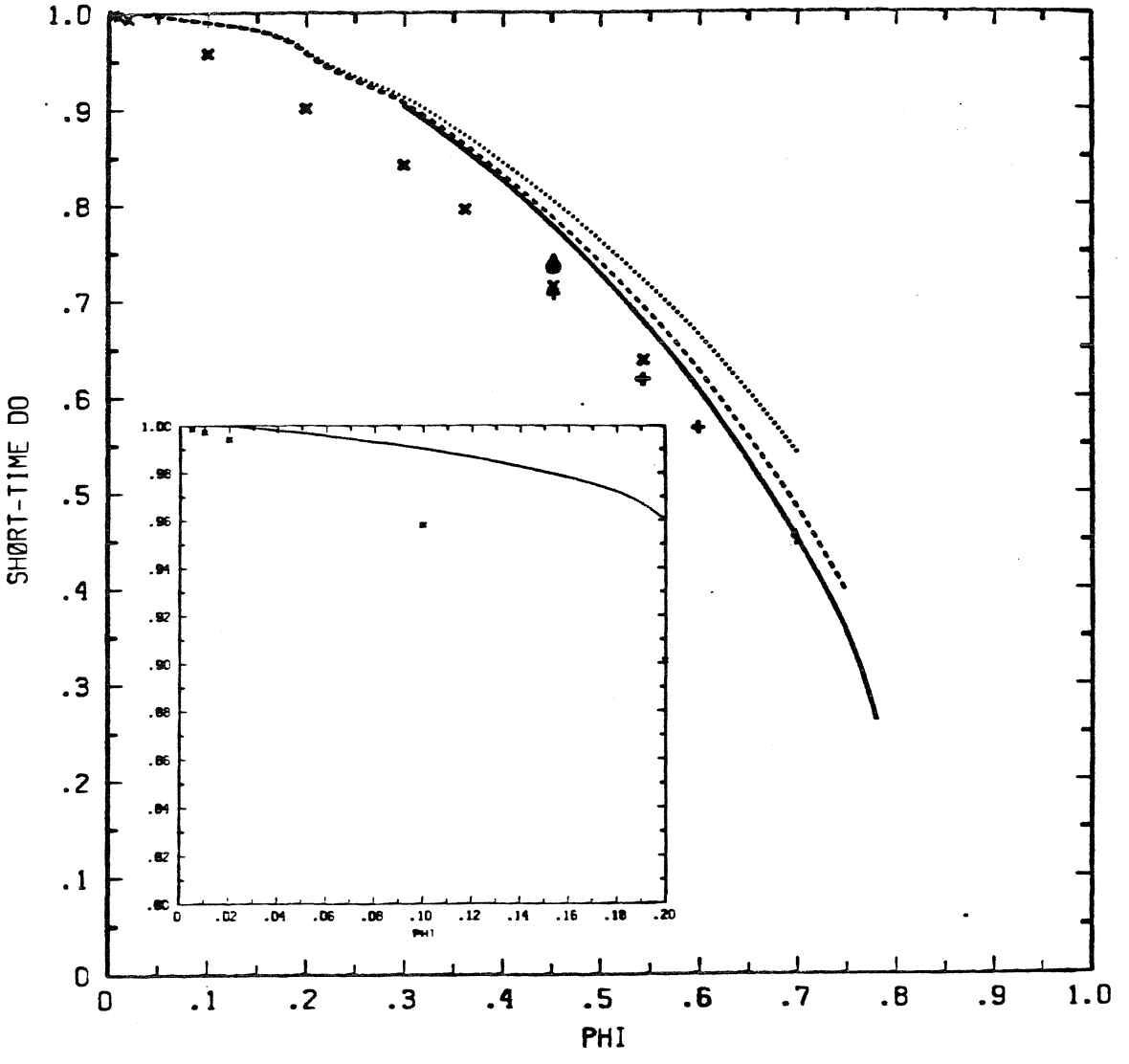

Figure 3.7a Short-time, self-diffusion coefficient as a function of areal fraction for random, hard-disk distributions of spheres in a monolayer. The regular array results from Figure 3.1 are included for comparison. The number of spheres in the object cell is 16 (•), 25 (x), or 49 (+). The result of Bossis & Brady (1987) is denoted by a filled triangle ($\phi_A = 0.453$).

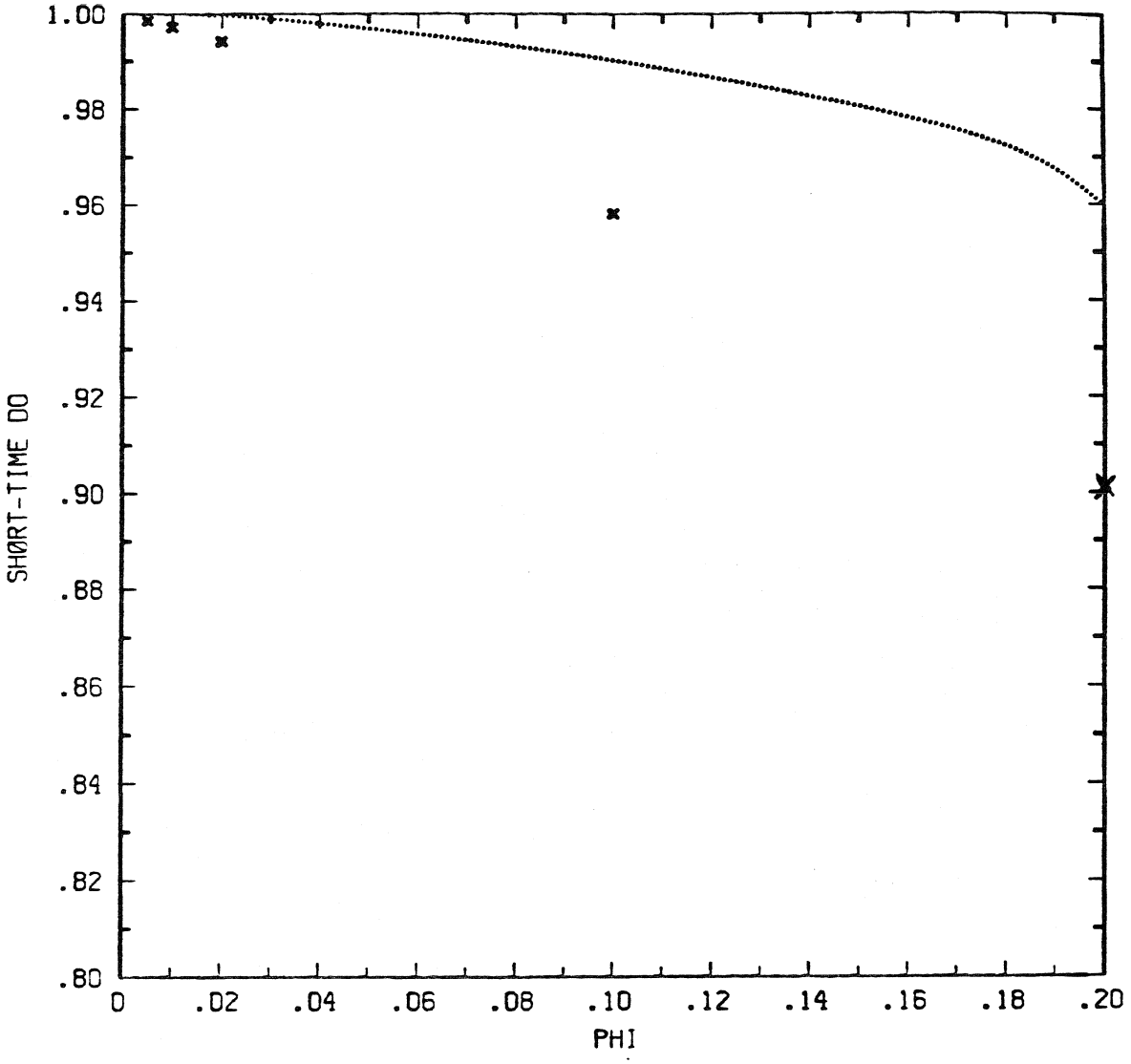

Figure 3.7b A detailed view of the low concentration results in Figure 3.7a

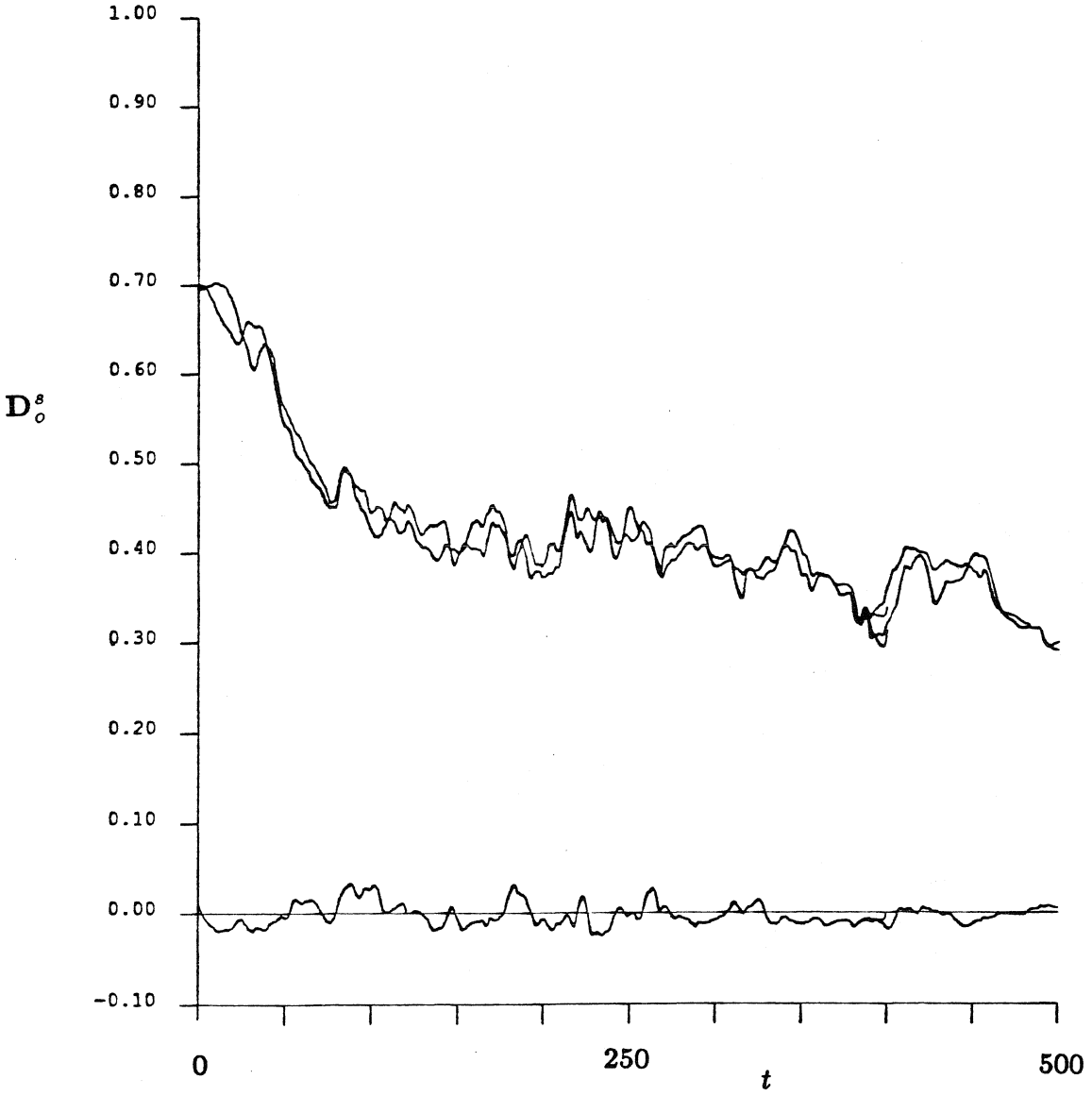

Figure 3.8a The evolution of the short-time, self-diffusion coefficent in time for a non-Ewald sedimentation simulation using the FTS method, $\phi_A = 0.453$ and $N_1 = 25$ (this run is denoted as FTSn1-5 in Chapter 4). The top two curves are the xx and yy components of $\mathbf{D}_o^s$. Note that, as expected, there is no significant directional dependence of these results. The bottom curve is the xy component of $\mathbf{D}_o^s$. The time average of this component is very close to zero.

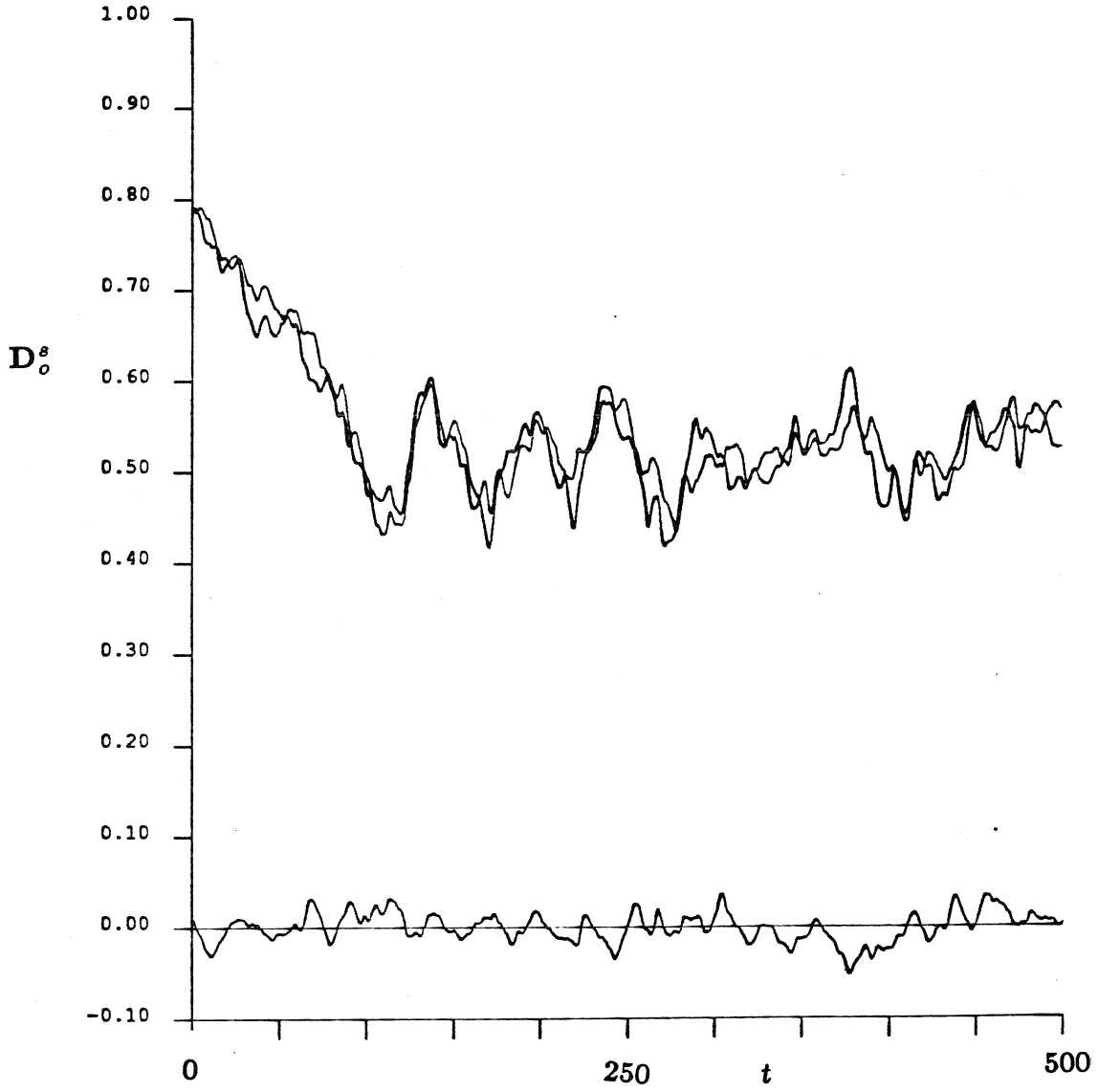

Figure 3.8b The evolution of the short-time, self-diffusion coefficent in time for a non-Ewald sedimentation simulation using the FT method, $\phi_A = 0.453$ and $N_1 = 25$ (this run is denoted as FTn1 in Chapter 4). See Figure 3.8*a* for explanation of curves.

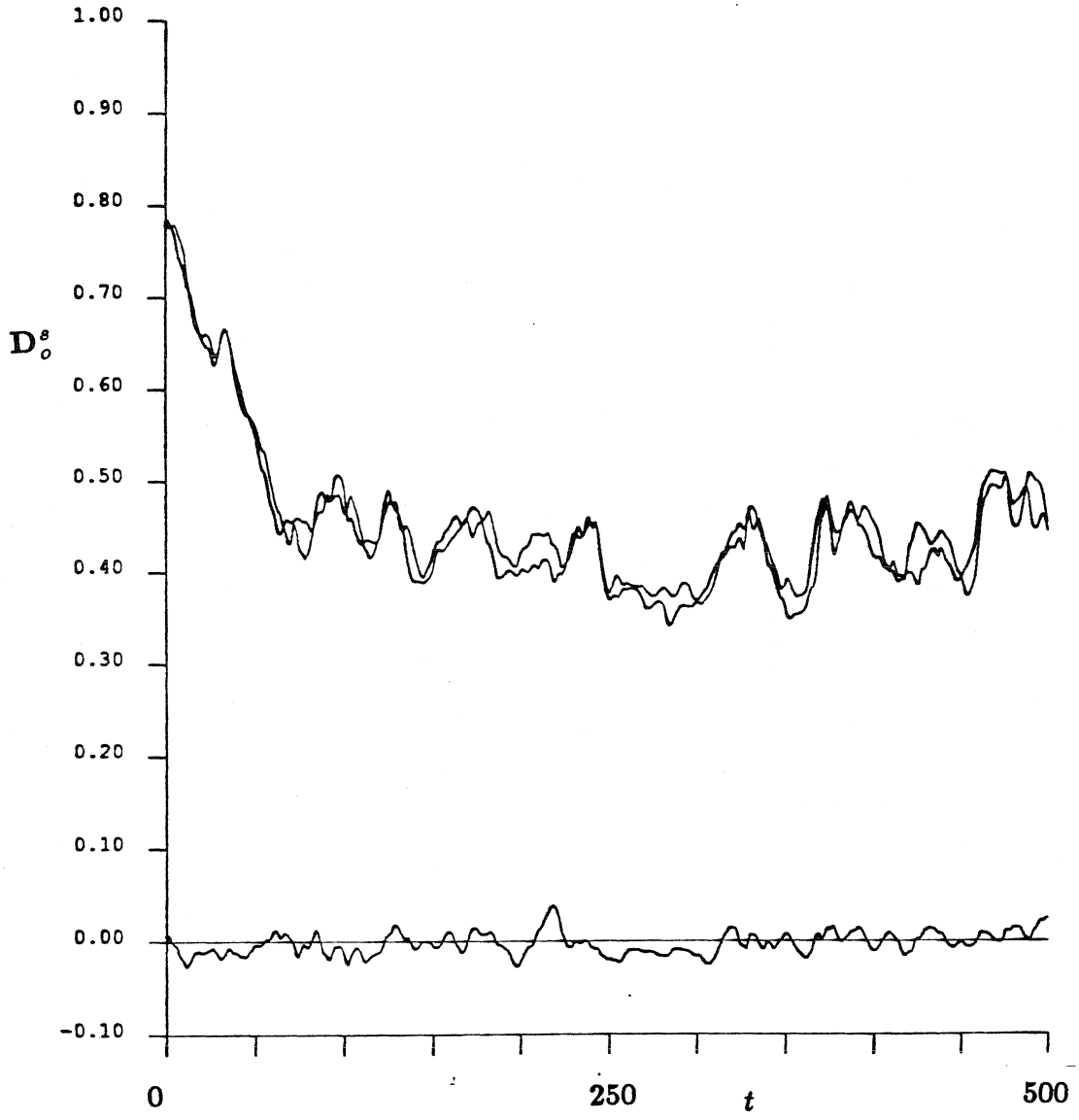

Figure 3.8c The evolution of the short-time, self-diffusion coefficent in time for a non-Ewald sedimentation simulation using the F method, $\phi_A = 0.453$ and $N_1 = 25$ (this run is denoted as Fn1 in Chapter 4). See Figure 3.8*a* for explanation of curves.

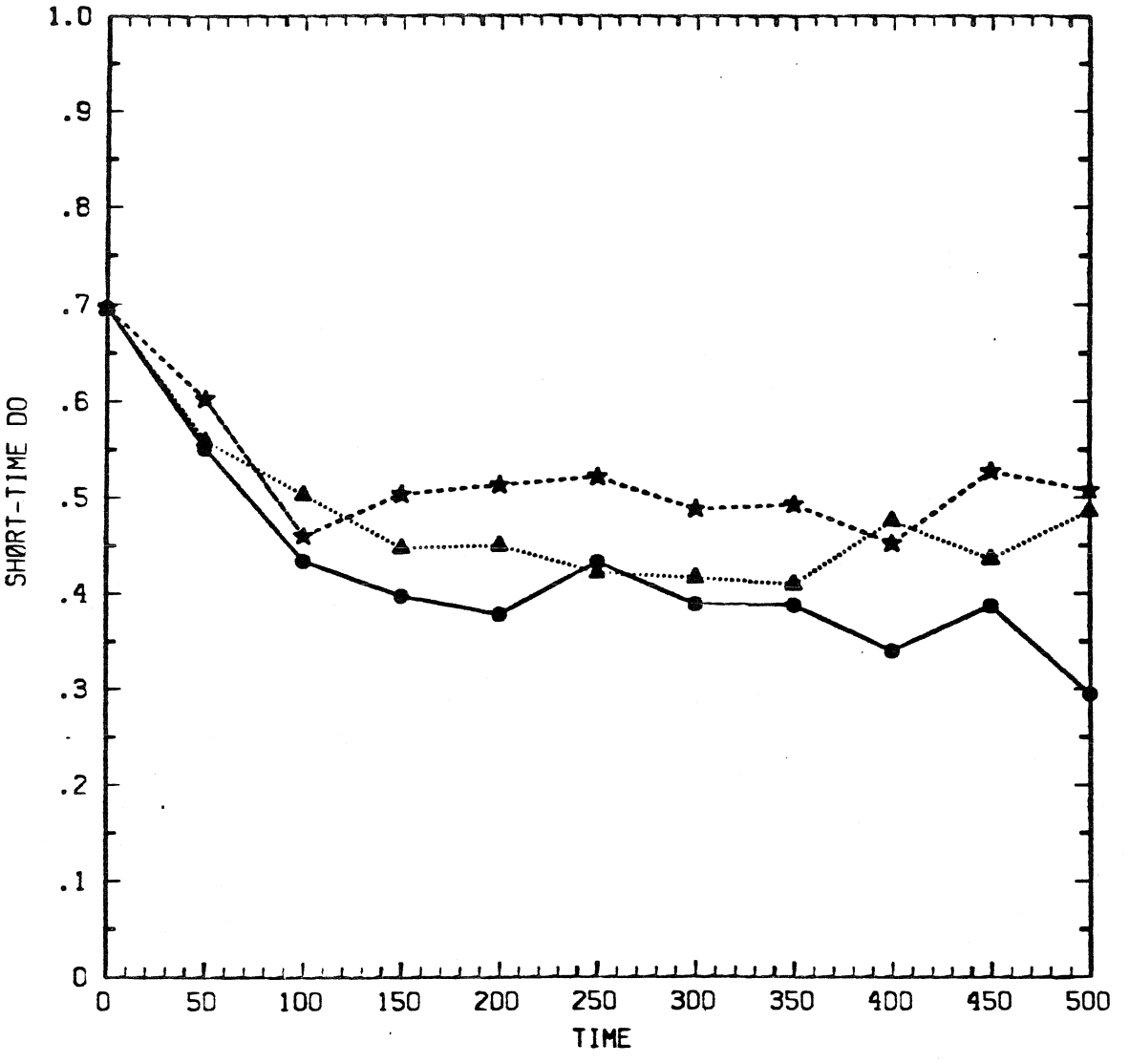

Figure 3.9 The evolution of the short-time, self-diffusion coefficent in time for a non-Ewald sedimentation simulation; the short-time, self-diffusion coefficient has been calculated using the FTS method in all cases, but the configurations are those from the runs shown in Figures 3.8*a-c*. The solid curve with filled circles are for FTS run configurations. The dashed curve with filled stars are for FT run configurations. The dotted curve with filled triangles are for F run configurations. The symbols indicate that D_o^s was calculated for that given configuration, and the curves connect the symbols for each case.

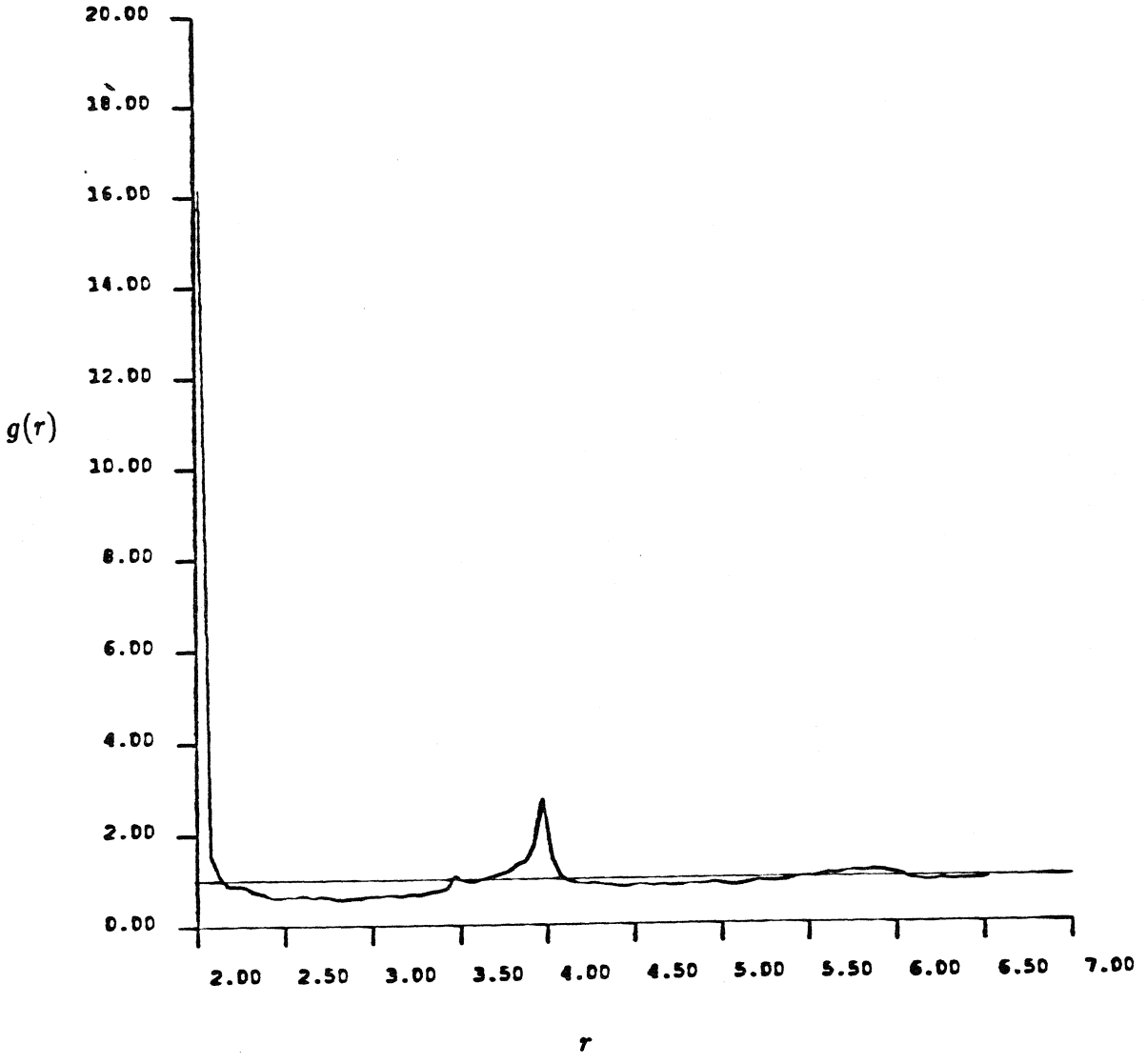

Figure 3.10 The pair-distribution function for the FT run described in Figure 3.8*b*. Only configurations occurring from $t = 150 - 500$ contribute to this distribution.

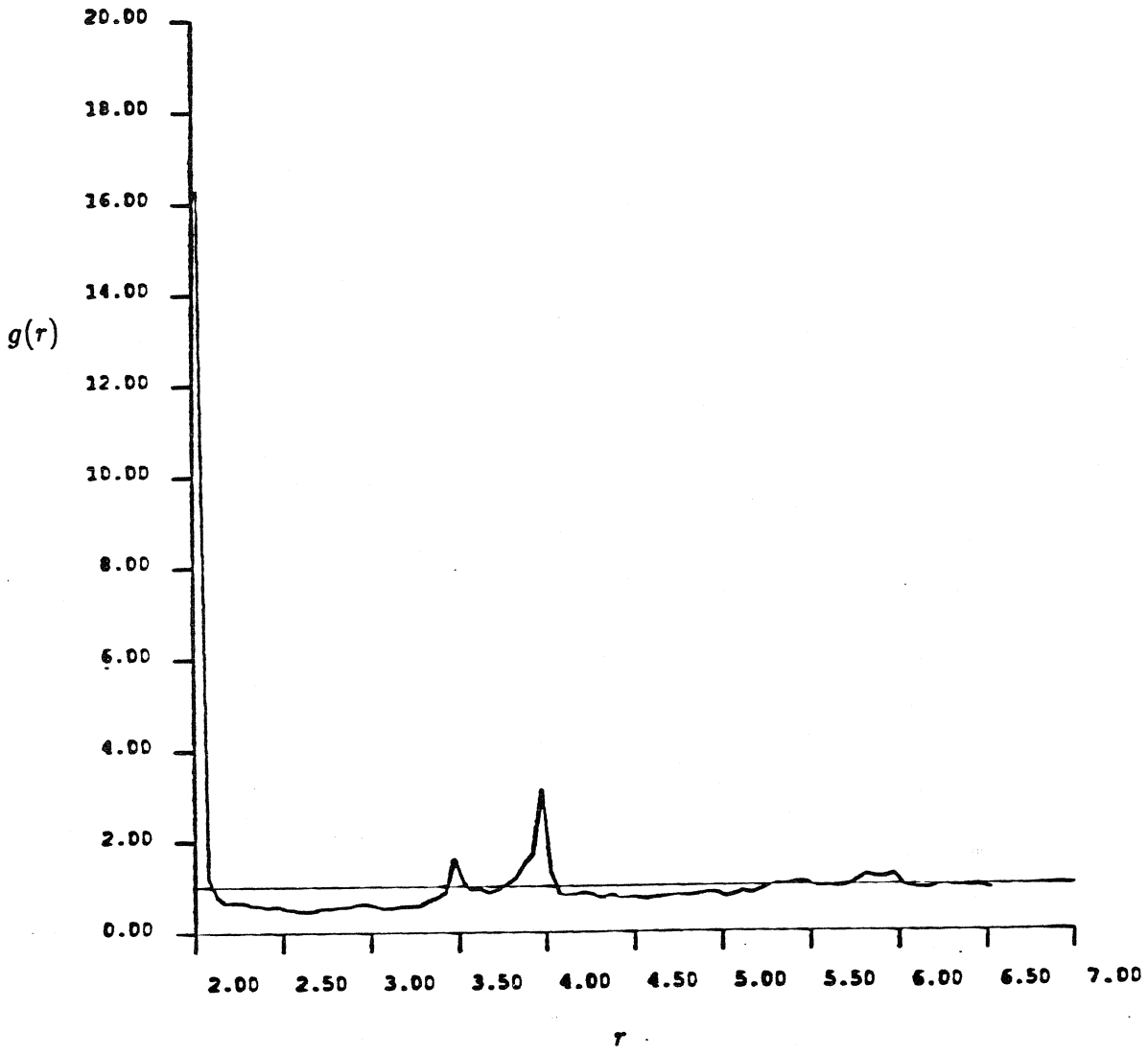

Figure 3.11 The pair-distribution function for the F run described in Figure 3.8*c*. Only configurations occurring from $t = 250 - 500$ contribute to this distribution.

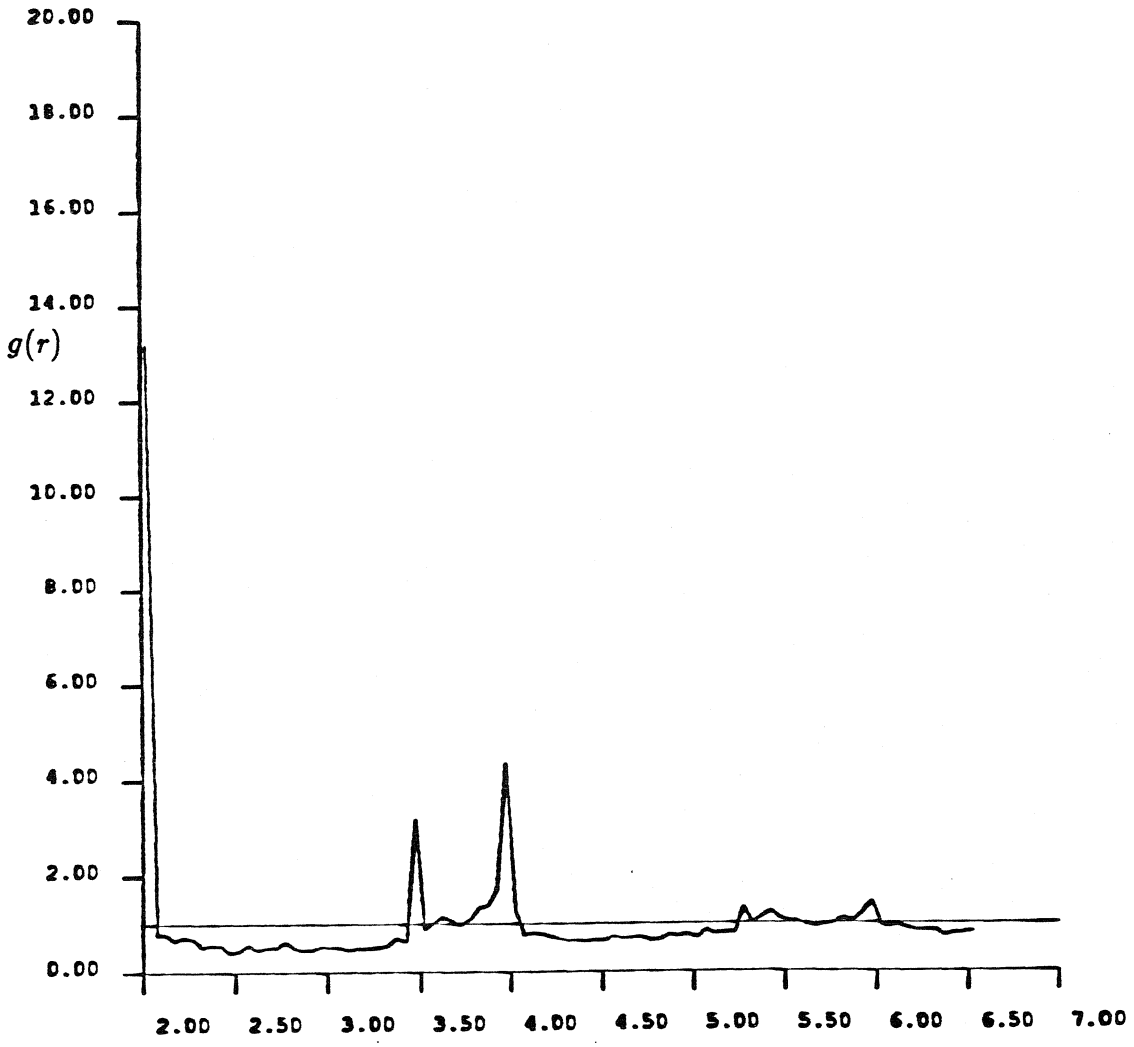

Figure 3.12a The pair-distribution function for the FTS run described in Figure 3.8*a*. Only configurations occurring from $t = 300 - 400$ contribute to this distribution.

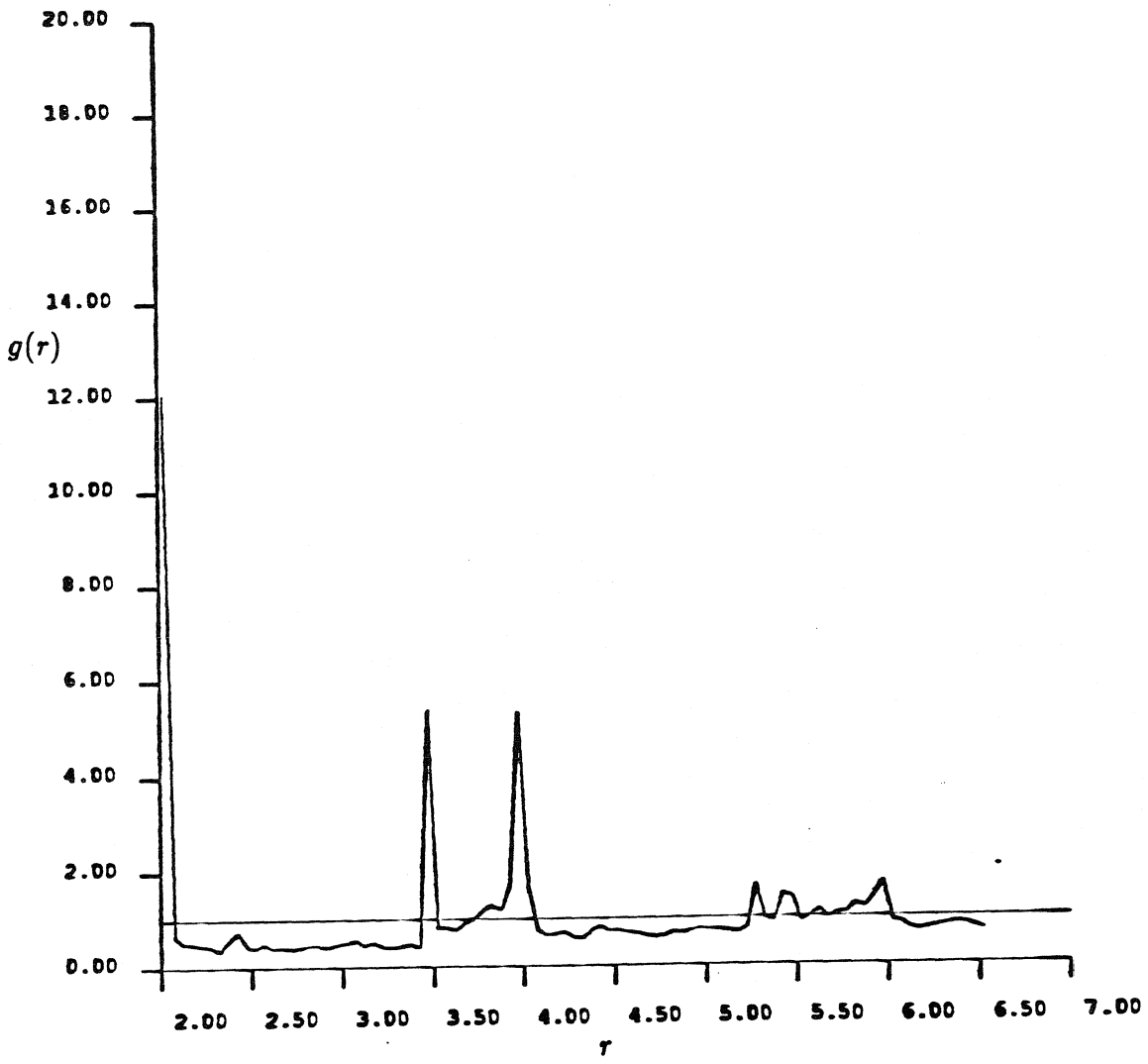

Figure 3.12b The pair-distribution function for the FTS run described in Figure 3.8*a*. Only configurations occurring from $t = 380 - 500$ contribute to this distribution.

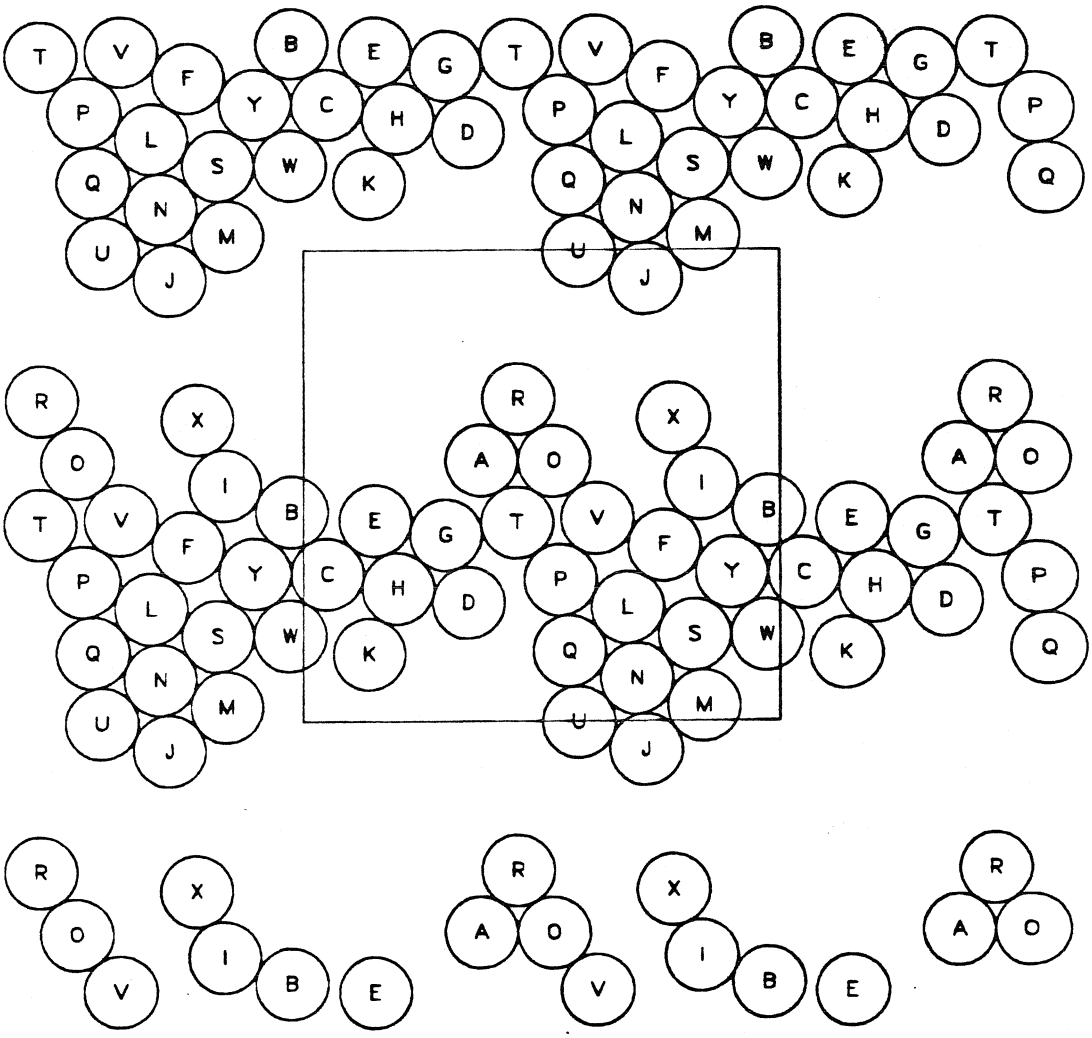

Figure 3.13 A "snapshot" of sphere positions. The box is the periodic cell. These are the sphere positions at $t = 500.0$ time units for an FTS, non-Ewald simulation (referred to as run FTSn5 in Chapter 4).

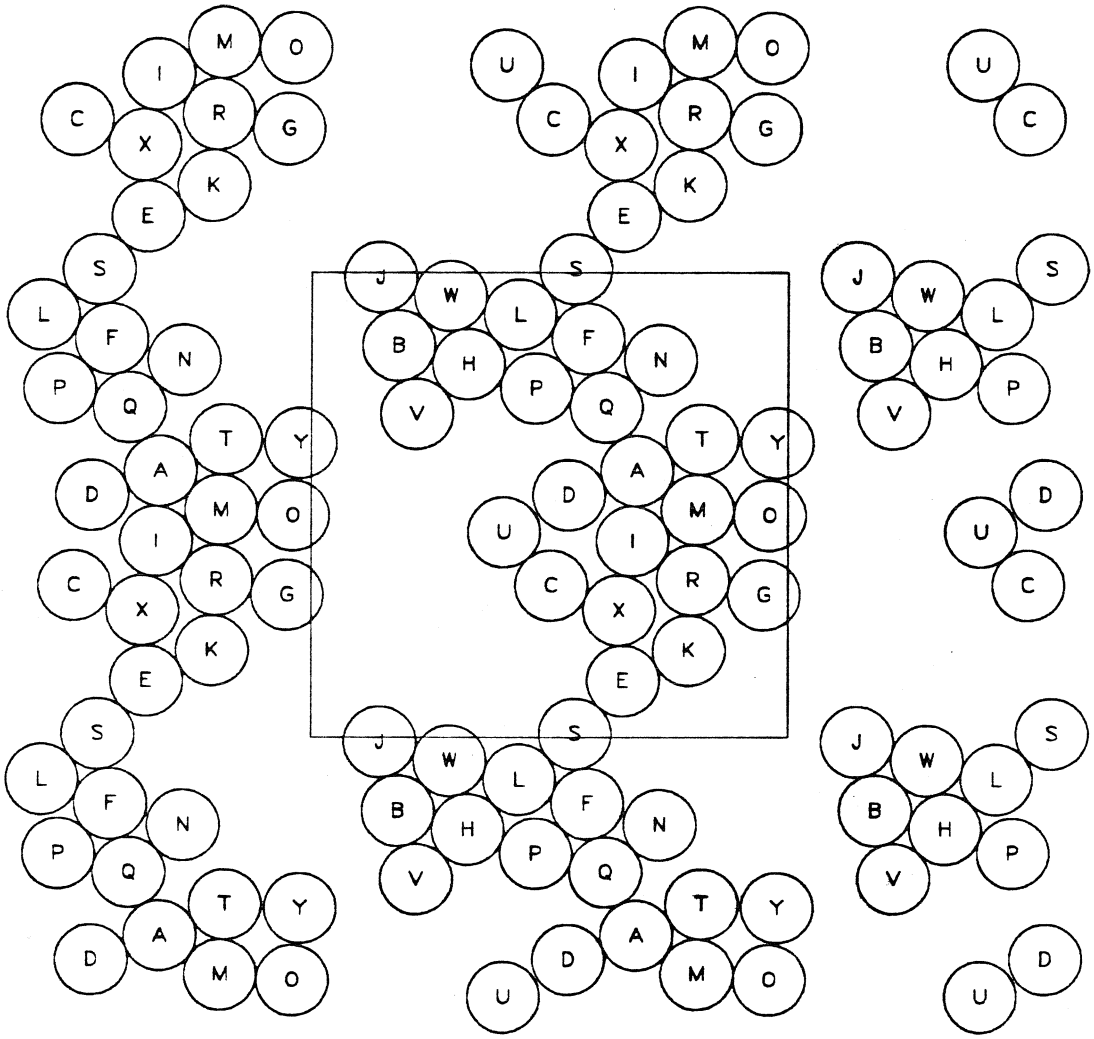

Figure 3.14 A "snapshot" of sphere positions. The box is the periodic cell. These are the sphere positions at $t = 750.0$ time units for an Ewald F simulation (referred to as run ef3 in Chapter 4).

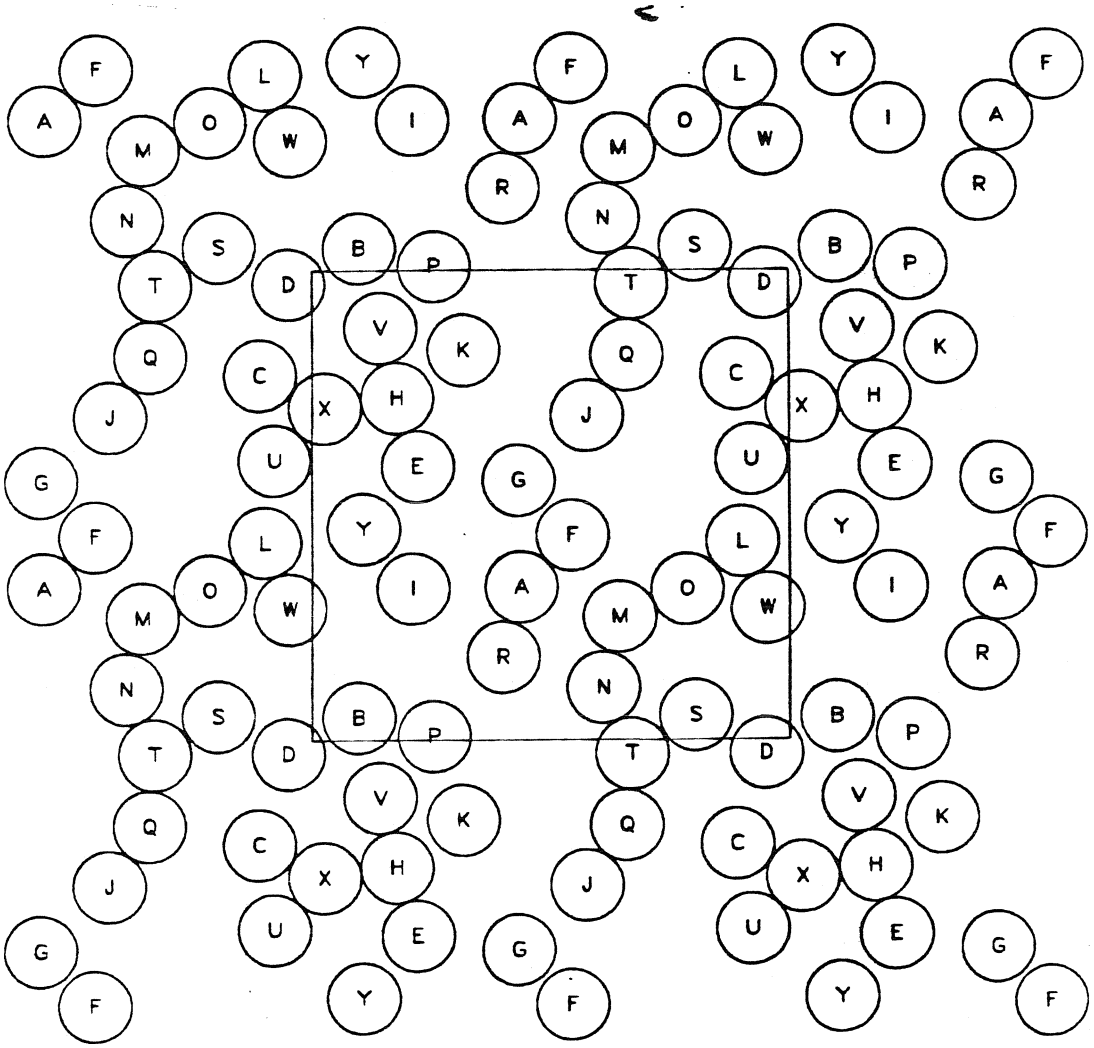

Figure 3.15 A "snapshot" of sphere positions. The box is the periodic cell. These are the sphere positions at $t = 500.0$ time units for an F, non-Ewald simulation when there are repulsive interparticle forces between the spheres (referred to as run nfr1 in Chapter 4). The range parameter of the interparticle force, r, is 10^3.

CHAPTER 4: LONG-TIME DISPERSION IN SEDIMENTING SUSPENSIONS

This chapter reports the results of our investigation of hydrodynamic dispersion in concentrated sedimenting suspensions. We simulate monolayer suspensions of equal-sized spheres falling within the plane of the monolayer. Monolayer simulations are computationally much faster than a full three-dimensional simulation (cf. Chapter 2), but the particle dynamics that could lead to diffusive behavior are preserved. Our focus is a fuller understanding of the basics of hydrodynamic dispersion in sedimenting suspensions and its relation to suspension conditions and simulation variables. The raw data from a simulation run are the positions and velocities (and angular velocities, if the FT or FTS method is used) of the spheres at given time intervals during the run; data are generally recorded every 0.05 time unit, or every 10 to 50 time steps. It is not our intention to inundate the reader with a large number of graphs of simulation run results. Instead, the first section will present the results of one simulation run and will explain how we extract the various statistical, distribution and transport properties from the raw data. Appendix B contains the results of these analyses for all the reported simulation runs. We will refer to this appendix when appropriate. Table 4.1 lists the simulation conditions of all reported runs. In the succeeding sections we discuss how these properties vary (or do not vary) when suspension or simulation conditions change.

In the second section we examine the effect of the level of accuracy in approximating the hydrodynamic interactions on the suspension properties. This consists of comparing results from non-Ewald simulations using the F, FT, and FTS methods. In the third section, the effect of Ewald sums is considered. Based on conclusions from Chapter 3, $z_l = 2.0$ for all Ewald simulations. In the fourth section, we add pairwise electrostatic-type repulsive forces to the simulation and examine how their strength and range affect suspension properties. We will consider the effect of increasing the periodic box size for the runs at an areal fraction

of 0.453 in the fifth section. In the sixth section we will examine the concentration dependence of the suspension properties, particularly the dispersion.

4.1 Sample Analysis of a Simulation Run

Before we derive the properties from a simulation run, we list the suspension conditions and simulation inputs. In the run considered in this section the areal fraction is 0.453 and there are interparticle repulsive forces on the spheres ($\tau = 10^5$ and $F_o = 10^{-5}$). The initial configuration of the spheres in the periodic cell is taken from a Monte-Carlo random, hard-disk simulation. The run goes from $t = 0 - 500$. This run can be continued from this point using a restart file that the simulation periodically produces - the file contains previous velocities and the present configuration needed to continue the the Adams-Moulton integration of the sphere trajectories. The mobility matrix is approximated by the Ewald F method ($z_l = 2.0$), and the short-time diffusion coefficient is also calculated at this level of approximation. The time step is 0.0025, the mobility matrix is inverted every 40 time steps, the short-time self-diffusion coefficient is calculated every 400 time steps and the data is saved every 20 time steps.

4.1.1 Velocity-related Statistics

Let us start with the basic definitions of the particle-averaged velocity and velocity variance. In our general notation, the subscript y refers to the direction parallel to the gravity vector (specifically, gravity is in the negative y direction), and the subscript x refers to the direction perpendicular to the gravity vector. At each time where data are stored, we calculate

the x velocity,
$$\langle v_x \rangle = \frac{1}{N} \sum_{i=1}^{N} (v_x)_i \qquad (4.1.1\text{-}1)$$

the y velocity,
$$\langle v_y \rangle = \frac{1}{N} \sum_{i=1}^{N} (v_y)_i \qquad (4.1.1\text{-}2)$$

the v_x variance,

$$\langle (v_x - \langle v_x \rangle)^2 \rangle = \frac{1}{N} \sum_{i=1}^{N} (v_x)_i^2 - \langle v_x \rangle^2 \qquad (4.1.1\text{–}3)$$

the v_y variance,

$$\langle (v_y - \langle v_y \rangle)^2 \rangle = \frac{1}{N} \sum_{i=1}^{N} (v_y)_i^2 - \langle v_y \rangle^2 \qquad (4.1.1\text{–}4)$$

and the v_{xy} variance,

$$\langle (v_x - \langle v_x \rangle)(v_y - \langle v_y \rangle) \rangle = \frac{1}{N} \sum_{i=1}^{N} (v_x v_y)_i - \langle v_x \rangle \langle v_y \rangle. \qquad (4.1.1\text{–}5)$$

Obviously, the v_x variance and the v_y variance are always positive. Time averages of these quantities (denoted by an overbar) calculated from simulation data sets and calculated during the simulation (data taken at each time step) are indistinguishable when the data are saved every 50 to 100 small time steps. Figures 4.1 – 4.5 are the time traces of the particle-averaged velocity and velocity variance. The absolute value of the time average of $\langle v_x \rangle$ for all runs is ≤ 0.02 and is usually ≤ 0.01. The absolute value of the time average of the v_{xy} variance for all runs is ≤ 0.0008. These near-zero results are consistent with the symmetry imposed by the gravitational force vector. Table 4.2 lists $\overline{\langle v_y \rangle}$ and the time-averaged v_x and v_y variances for all reported simulation runs. Table 4.3 lists $\overline{\langle v_x \rangle}$ and the time-averaged v_{xy} variance for these runs.

4.1.2 Configuration-related Statistics and Properties

As shown in Chapter 3, the pair-distribution function, g(r), is the probability density of finding a second particle a distance r from the test particle and is, in general, a function of both r and θ. The arc of $\theta = 0°$ to 180° is divided into 10 equal wedges, each spanning a $\Delta\theta = 18°$. The first wedge is centered at 9° and the last, at 171°. The radial distance from the test sphere is divided into sections of $\Delta r = 0.05$. The value of $g(r, \theta)$ in a given region of size $\Delta r \Delta\theta$ is determined by averaging over time the number of sphere centers found in this region. The time averaging is done after the system reaches a stationary state. The stationary state is said to begin when the values of y velocity and D_o^s no longer change significantly

with time. Each sphere in the periodic box is taken as the test sphere, so

$$g(r,\theta) = g(r,\theta+\pi). \qquad (4.1.2\text{–}1)$$

We also know that the presence of the external body force parallel to the $\theta = 0°$ axis should mean that $g(r,\theta)$ is symmetric about that axis. Coupled with the symmetry through the origin stated in Equation (4.1.2–1), we would expect that our θ distributions should exhibit a four-fold symmetry – symmetry about the $\theta = 0°$ and the $\theta = 90°$ axes. For each simulation, we report both the radial distribution function, $g(r)$, and the full pair-distribution function for the near-touching spheres; the radial distribution function is the full distribution function integrated over θ. The value of r in the radial distribution function varies from 2.0 to a distance half the periodic box length. The definition of a near-touching pair of spheres is that the sphere centers are separated by 2.05 sphere radii or less. Figure 4.6 shows the radial pair-distribution function for our specified run – only configurations occurring after $t = 150$ are included in this calculation. This is done to insure that only steady-state results are reported. Figure 4.7 is the full pair-distribution function at $r/a = 2.025$. The curve denoted by the filled circles is forced to be symmetric about $\theta = 90°$, allowing us to see how well the simulation actually preserves the symmetry we expect. Because of the finite amount of data and the size of the Δr bins, the error bars in Figure 4.7 are fairly large and may be up to 5 to 10 % of the value of the distribution function. Table 4.4 lists the important radial pair-distribution function information.

The other measure of the microstructure that we consider is the time evolution of the short-time, self-diffusion coefficient (see Figure 4.8). As seen in Chapter 3, the evolution of the microstructure can be followed by considering the time trace of $\mathbf{D}_o^s$. $\mathbf{D}_o^s$ is a run-time calculation and has been used as a quick measure of the development of the microstructure in a simulation. We have noted that the sedimentation velocity of the suspension may reach a steady value at a different time than $\mathbf{D}_o^s$, and in general, we wait for both properties to settle down before beginning to calculate the pair-distribution function and the mean-squared displacement of the spheres. Table 4.5 lists the steady-state values of $\mathbf{D}_o^s$.

4.1.3 Dispersion-related Properties

The long-time coefficient of sedimentation-induced sphere self-diffusion, $\mathbf{D}^s_\infty$, is defined in terms of the mean-squared displacement of spheres from their original positions. It is defined such that

$$\mathbf{D}^s_\infty = \lim_{t\to\infty} \frac{1}{2}\frac{d}{dt}\langle(\mathbf{x}-\tilde{\mathbf{x}})^2\rangle, \qquad (4.1.3\text{–}1)$$

where $\tilde{\mathbf{x}} = \overline{\langle \mathbf{v} \rangle} \cdot t$. The displacement of the spheres is not taken directly from the raw data set because those positions are for sphere positions within the periodic box. Instead, we compute the actual displacement of the N spheres from their positions at chosen time, t_o. This is done by systematically reversing the processes which kept the spheres in the periodic box in the simulation.

The mean-squared displacement is calculated from the above trajectory data. At each time step the effects of bulk motions are removed by subtracting the mean displacement in each direction. Although the time-averaged mean displacement perpendicular to the direction of settling should be zero, the actual mean may be non-zero. In the direction of settling, the largest portion of the actual displacement results from the applied force. In both directions, we subtract off the time-averaged displacement; i.e., the displacement of a single sphere is considered to be $\mathbf{x} - \tilde{\mathbf{x}}$, and the mean displacement $\overline{\langle(\mathbf{x}-\tilde{\mathbf{x}})\rangle}$ will be identically zero for the entire run. Classical self-diffusion processes have a zero-mean displacement, and the long-time coefficient of self-diffusion is found by considering the mean-squared displacement as $t \to \infty$. Any displacement related to local or large-scale concentration gradients, or the bulk motion in response to applied forces, will have non-zero means, and diffusion related to these displacements will not be considered in this thesis.

We report the mean-squared displacement as a function of time in the following way:

$$\frac{1}{2}\frac{\langle(\mathbf{x}-\tilde{\mathbf{x}})^2\rangle}{t} \quad vs \quad t. \qquad (4.1.3\text{–}2)$$

The reason for this is simple. If the motion of the spheres is truly diffusive, we would expect that

$$\langle(\mathbf{x}-\tilde{\mathbf{x}})^2\rangle = 2\,\mathbf{D}^s_\infty \cdot t \text{ as } t \to \infty. \qquad (4.1.3\text{–}3)$$

If the motion is deterministic, we would expect

$$\langle (\mathbf{x} - \tilde{\mathbf{x}})^2 \rangle \sim O(t^2) \text{ as } t \to \infty. \qquad (4.1.3\text{–}4)$$

Therefore, if the graph of the relation in Equation (4.1.3–2) levels off as $t \to \infty$, we conclude that the sedimenting system is self-diffusive, and its long-time coefficient of self-diffusion, $\mathbf{D}^s_\infty$, is the height of the plateau. (Figure 4.9 is an idealized graph of Equation 4.1.3–2 for a diffusive process.).

We use a technique, also used by molecular-dynamicists, to improve the accuracy in finding the long-time coefficient of self-diffusion without additional simulation computation costs. This technique essentially averages the curves of $\frac{1}{2}\frac{\langle (\mathbf{x}-\tilde{\mathbf{x}})^2 \rangle}{t}$ *vs* t calculated from a number of initial configurations. This is not the same as running the simulation from different initial configurations. If the simulation data run from an initial time of t_0, to a final time of t_f, we can just follow the spheres' trajectories from their original configuration to their final configuration. Alternatively, we can choose to follow the trajectories for an interval of time, $\Delta T_I \leq (t_f - t_0)$. Now, we can choose the data at any time before $(t_f - \Delta T_I)$ as the initial configuration for the displacement measurements. Actually, we take the position data from a number of such times, graph the function in Equation(4.1.3–2) and average the resulting curves. The averaged curve is much smoother than the individual curves, making it much easier to determine $\mathbf{D}^s_\infty$. Figure 4.10 schematically shows this data enhancement technique. The time between the start of each ΔT_I interval is 2 to 100 data time steps. The smaller this time is (i.e., the more curves that we average), the smoother the curve is. The error in reading off $\mathbf{D}^s_\infty$ from the unaveraged curves is much greater than the averaged curves, even when the unaveraged curves are much longer than the averaged curves. Regardless of how much time is taken between interval starts, the difference in the values of $\mathbf{D}^s_\infty$ from the averaged curves is much smaller than the error associated with the unaveraged curves.

Figures 4.11 and 4.12 are actual graphs of one-half of the mean-squared displacement divided by time *vs.* time for sphere motion in the y and x direction,

respectively. Data are taken from $t = 100 - 500$. ΔT_I is 150, 200, and 300 time units, where the interval between 'initial' configurations is 2 time steps (except for $\Delta T_I = 400$, which is an unaveraged curve). It is noted that the sphere motion in the x direction resulted consistently in dispersion that is diffusive. The sphere motion in the y direction also shows diffusive behavior, but the behavior is generally more complicated than that seen in the x-direction. Remember that more intervals are used as the length of the interval decreases. In all cases studied, the sphere motion exhibits diffusive behavior; the degree to which the dispersion varies for different suspension conditions and simulation variables will be considered in the succeeding sections. Tables 4.6 and 4.7 list the minimum, maximum and average values of $\mathbf{D}^e_\infty$.

4.2 Approximation-level Dependence

The mobility matrix can be approximated to three different levels of accuracy – the F method, the FT method, and the FTS method. Although the FTS method is the most accurate method, it is also the most computationally expensive. It would be advantageous to use the lowest level of accuracy that preserves the properties of the suspension, particularly those related to the dispersion. We compare non-Ewald F, FT and FTS runs that begin at the same initial configuration and the same simulation run-time inputs. There are no repulsive forces, and the areal fraction, which will be the same in all sections except when we consider the concentration dependence of the long-time dispersion, is 0.453. The F and FT runs are 1000 time units long, and the FTS run is 800 time units long. We conclude that the F method is accurate enough to investigate the long-time dispersion of spheres in a sedimenting suspension. The similarities and differences in the suspension properties resulting from the three types of simulations are discussed in detail below. The first four sections of Appendix B contain the results of the analysis of the raw data for the simulations discussed in this section. The results from the FTS simulation are in Appendix B.1. The results from the FT simulation first discussed are in Appendix B.2. At the end this section, we shall discuss

another FT simulation that starts from a different initial condition; the results from this simulation are in Appendix B.3. The results from the F simulation are in Appendix B.4. These results include relevant "snapshots" of sphere positions that occur during the simulation.

We begin with the velocity-related averages. The "sedimentation" velocity, $\langle v_y \rangle$, reaches a steady value after 400 (FTS), 100 (FT) and 250 (F) time units. The value of $\overline{\langle v_y \rangle}$ for the different methods varies less than 2%. The v_x variance of the F and FTS runs is $\approx 0.0030(\pm 15\%)$; it is ≈ 0.0082 for the FT run. The v_y variance of the F and FTS runs is $\approx 0.010(\pm 15\%)$; it is ≈ 0.030 for the FT run. The prominent feature of the time traces of the v_x and v_y variance in the F and FTS results is that short periods of high variance interrupt generally near-zero variance that occur over most of the time history. In contrast, the variances in the FT run are fairly uniform in time. This behavior is related to microstructure evolution and affects both the configuration-related properties and the dispersion.

The time history of D_o^s shows the evolution of the microstructure from a random, hard-disk distribution. The steady-state distribution function determined for all methods indicates that hexagonal packing and clustering of the spheres occurs. These clusters in the F and FTS cases are fairly dense and very persistent; the time history of D_o^s after steady-state is achieved is relatively smooth and D_o^s is small (≈ 0.30 for the FTS method and ≈ 0.36 for the F method). The pair-distribution function in these two cases shows a high degree of hexagonal packing; the $g(2) \approx 13.0(\pm 0.5)$ and $g(3.5)$ and $g(4.0)$ are $\approx 3.7(\pm 0.5)$ each for the F case and $\approx 9.5(\pm 1.0)$ each for the FTS case. Contrast these results with the FT results. The time history of $\mathbf{D}_o^s$ at steady-state has more high-frequency fluctuations and large (10% of D_o^s) low-frequency (20 – 60 time units) fluctuations. The steady-state value of D_o^s is 0.47, which is greater than in either the F or FTS case. Although the pair-distribution function indicates some hexagonal packing among the spheres ($g(3.5) = 1.4$), the higher $g(2)$(=15.2) peak and the lower $g(3.5)$ and $g(4.0)$ peaks ($\approx 2.3 \pm 0.7$ each) show that there is less hexagonal packing than in the F or FTS case. The θ-distribution of the $g(2)$ peak is fairly level and symmetric around

$\theta = 90°$ for all cases, although the F and FTS results show more variation about the mean value of the peak. This is another indication of the slow dynamics that occurs in these two cases; the relative position spheres changes so slowly that given configurations of spheres have a large impact on the statistics collected for the full pair-distribution function. A slight asymmetry is seen in the FTS case, but this is related to the incredibly slow dynamics and dense hexagonal packing in this case.

The picture emerges that the microstructure in the FT case consists of a loose cluster (or clusters), including many of the spheres in the cell. (Please refer to the microstructure pictures in Appendix B.1, B.2, B.4). This cluster generally spans the cell. There is a good deal of relative motion among the spheres, and the clusters themselves break and reform. In the F and FTS case, the microstructure is characterized by a much denser single cluster of spheres (particularly the FTS case), which includes almost all of the spheres. There is little relative motion among the spheres and the cluster can last 50–200 time units, or more. Most of the time relative motion occurs as the cluster "breathes" – expands and contracts – because ofthe hydrodynamic interactions in the sedimenting suspension. At rare times, the cluster will radically reform itself. This accounts for the short periods of high velocity variance, which are very dramatic in the direction of settling (see above). Our experience has shown that once a suspension evolves into a microstructure with a high degree of hexagonal packing, it becomes locked into this type of microstructure. Although the FT run has not manifested this microstructure by $t = 1000$, analysis of the pair-distribution function indicates an increase in the $g(3.5)$ and $g(4.0)$ peaks and a decrease in $g(2)$ as time increases. It is likely that if the FT run is continued, it would eventually evolve a microstructure similar to that in the F and FTS cases. (The anomalous results from the FT case, especially given the results of later simulations, demand fuller investigation. We have run another FT simulation, starting from a different initial condition. The results of this simulation run are discussed at the end of this section.) In the conclusion of this chapter we shall discuss, in a broader context, the slow dynamics and the dense clustering that occur in sedimenting suspensions.

Finally, we consider the effect of the level of accuracy on the long-time dispersion of the spheres. After calculating the actual displacement, we plot the relation in Equation (4.1.3–2) with and without the averaging technique. These plots tell us whether the motion of spheres in a sedimenting suspension exhibits long-time self-diffusivity. The plots, particularly the unaveraged ones, do not always mimic the idealized curve seen in Figure 4.9. Instead, the curve may level off for a while, then will climb or fall to a new level. Remember that a linear rise or fall indicates deterministic sphere motion. Some plots, particularly the unaveraged curves and those pertaining to the displacement in the direction perpendicular to gravity, show an overshoot at small times.

The diffusive behavior in the x-direction (the direction perpendicular to the gravity vector) is qualitatively similar for all methods. All simulations of sedimenting suspensions exhibit long-time, self-diffusive behavior in the x-direction, regardless of the level of accuracy (or anything else, for that matter). The degree of self-diffusivity, as measured by the long-time self-diffusion coefficient in this direction, $(D^s_\infty)_{xx}$, is relatively independent of method type. $(D^s_\infty)_{xx} \approx 0.022(\pm 0.002)$ for the F and FTS cases. $(D^s_\infty)_{xx} \approx 0.030$ for the FT case, but it should be noted that at earlier times ($t = 300 - 500$), this is the value of $(D^s_\infty)_{xx}$ for the F and FTS methods. All curves in this direction show overshoot at small times, sometimes as much as 100%. The rise time is relatively fast for all cases, $\approx$ 20–40 time units in the initial rise.

The dispersion in the y-direction (the direction parallel to the gravity vector) is, in general, diffusive and an order of magnitude greater than in the perpendicular direction. The plots of the time derivative of the mean-squared displacement *vs.* time are qualitatively and quantitatively similar in the F and FTS cases. The initial rise took $\approx$ 80–100 time units and the average value of $(D^s_\infty)_{yy} \approx 0.13$ in the FTS case, and $(D^s_\infty)_{yy} \approx 0.20$ in the F case. The curves in the y-direction may have several plateaus, ranging from 0.09 to 0.38 (in the FTS case). This is related to the behavior of the v_y variance – long periods of relatively small or near-zero variance interrupted by short bursts of greater variance. The

motion within the cluster is diffusive over a long time, but is characterized by a small diffusion coefficient. When the cluster breaks up or re-forms, this period of time is characterized by greater velocity variance (particularly in the direction of gravity) during which the sphere motion may or may not be diffusive. In the F and FTS cases, this motion (during cluster reformation) is generally diffusive. In the FT case, we see a short period ($\approx$ 100 time units) of diffusive behavior ($(D^s_\infty)_{yy} \approx 0.30$) succeeded by a long ($\approx$ 200 time units) of deterministic behavior. At this time, the results of the FT run are inconclusive since both "long-time" deterministic and diffusive behavior have been observed. However, given the trend in the pair-distribution function, we believe that the FT case has not reached its terminal microstructure. We note that in all cases, a steady "sedimentation" velocity does not guarantee that the microstructure distribution has settled down, though one could still plot the time derivative of the mean-squared displacement *vs.* time.

To establish that the anomalous results of the FT simulation are not because of a particular initial configuration, we did another FT simulation, starting from a different initial configuration. The velocity variance and long-time, self-diffusion coefficient in the direction of settling are slightly closer to the F and FTS results, but are still greater than seen in any other simulation (at this concentration). The velocity variance and long-time, self-diffusion coefficient in the perpendicular to the direction of settling are in the same range as the F and FTS results for both FT simulations. The results of the second FT simulation can be found in Appendix B.3. It would seem that allowing the spheres to rotate increases the diffusivity in the direction of settling, but the affect of the induced stresslets decreases this diffusivity; the net effect is that there is little difference in the resulting diffusivity seen in the F and FTS simulations.

It is our conclusion that the level of accuracy in approximating the mobility interactions has little effect on the long-time dispersion of spheres in sedimenting suspensions. A run of 500 time units took 5150 CPU minutes (the FTS method), 4186 CPU minutes (the FT method), or 1510 CPU minutes (the F method) on a

SUN 3/260 computer with floating-point accelerator. In light of the insensitivity of the long-time microstructure evolution, velocity variance and dispersion to the level of accuracy and the much faster run time, we use the F method in the succeeding runs.

4.3 Ewald vs. non-Ewald

The application of Ewald sums to the mobility interaction insures the convergence of the long-range interactions present in sedimenting suspensions. In this section we shall consider the difference in suspension statistics and properties, particularly the dispersion, when Ewald sums are used to calculate the far-field mobility interactions. As stated above, all the Ewald runs are at the F method level of approximation. The results of the Ewald, F method simulations (no interparticle forces present) are presented in Appendix B.5. This includes selected "snapshots" of the suspension microstructure. The distance between the monolayers in the Ewald analysis is twice the edge length of the periodic cell. This length is chosen based on the relative independence of D_o^s on N_1. To insure convergence, 126 image cells are used. The "sedimentation" velocity, $\overline{\langle v_y \rangle}$, which is a function of z_l, is approximately 20% less than the non-Ewald velocity. The Ewald and non-Ewald runs ($\phi_A = 0.453$) both start at the same initial configuration and end at $t = 1000$.

In general, there are few significant differences between the Ewald and non-Ewald results in the configuration- or dispersion-related properties. The difference in the "sedimentation" velocities is a function of z_l and does not affect the dispersion. The time averages of the velocity variances in the Ewald run are in the same range as the non-Ewald runs, and there are few qualitative differences in the time traces. Figure 4.13 is the time trace of the v_y variance for the non-Ewald, F simulation for t = 500–1000 time units. Figure 4.14 is the time trace of the v_y variance for the Ewald, F simulation for t = 500-1000. In the Ewald run, the periods of near-zero variance in the y-direction are shorter than seen in the non-Ewald runs. The time traces for the Ewald method results do not exhibit the

small, short-time fluctuations seen in the non-Ewald traces. The motion of the spheres in the y-direction is diffusive throughout most of the run for both cases; see the discussion below. The maximum level $(D^s_\infty)_{yy}$ attains is 0.29 ± 0.01 for the two methods. The average value of $(D^s_\infty)_{yy}$ is about 25% smaller in the non-Ewald case due to the periods of near-zero variance in this direction. The Ewald mean-squared displacement curves more closely resemble the idealized curve in Figure 4.9 than do the non-Ewald ones. This is related to the consistency of the variance through time (except as noted below). Both cases have a large increase in the variance between $t = 750 - 950$. The mean-squared displacement during this time is deterministic as a large vertical cluster forms and then returns to the the more common horizontal cluster. Figures 15*a*-*b* show these clusters, which occur at $t = 840$ and $t = 950$ time units in the Ewald simulation. This behavior is seen in the non-Ewald case also.

In the direction perpendicular to the gravity vector, there are no such long periods of deterministic motion. The variance curves are much more qualitatively similar than in the y-direction. $(D^s_\infty)_{xx}$ for both runs is 0.022 ± 0.001, with minimum levels at 0.014 ± 0.002 and maximum levels at 0.033 ± 0.003. The mean-squared displacement curves in the Ewald run are smoother than in the non-Ewald case; there are less fluctuations and the overshoot is small.

The steady-state configurations are relatively insensitive to the application of Ewald sums. The microstructure are still characterized by a high degree of hexagonal packing. The difference in the relative size or the $g(2)$, $g(3.5)$, and $g(4)$ peaks is less than 7%, and the actual difference is less than 14%. Pictures of the microstructure are qualitatively similar.

At the initial condition, $D^s_o = 0.78$ in the non-Ewald case, as compared to $D^s_o = 0.71$ in the Ewald case. In the non-Ewald case, D^s_0 quickly drops to within 0.1 of its steady-state value of ~ 0.35 at $t \approx 100$, though it does not come within 0.05 of its steady-state value until $t \approx 600$. In the Ewald case, D^s_o declined gradually to within 0.05 of its steady-state value of ~ 0.28 by $t \approx 600$. The difference in the

values of D_o^s does not indicate a difference in the steady-state configuration, but simply the difference in calculating the mobility with and without Ewald sums.

All things being equal, the Ewald simulations require more computer time than the non-Ewald ones. For these two cases, a run of 250 time units required 1515 CPU minutes for the non-Ewald, F method simulation, and 3446 CPU minutes for the Ewald, F method simulation. These timings are for a SUN 3/260 computer with a floating point accelerator.

4.4 The Effect of Repulsive Interparticle Forces

To study the dispersion in sedimenting suspensions where the microstructure is not dominated by the hexagonal clumping of the spheres, we add a pairwise repulsive interparticle force, as shown in Section 2.5. As we construct it, the range of the interparticle force, τ^{-1}, is the only adjustable parameter. In the previous simulation runs, τ can be considered infinite. The first two runs with repulsive forces are non-Ewald F method runs; τ is set to 10^3 and 10^5, based on previous work by Dr. Louis Durlofsky. Appendix B.6 contains the results of the $\tau = 10^3$ run, and Appendix B.8 contains the results of the $\tau = 10^5$ run.

The sedimentation velocity is unaffected by the addition of repulsive forces. The velocity variance in both directions decreases as τ increases (more notably in the x-direction). The time traces of the velocity variances are much more regular – the minimum variance is constant and non-zero, and the range between the maximum and minimum variances is smaller in simulations with interparticle forces. There are no periods of intense variance and no periods of deterministic motion (other than that which occurs right after the measurement of the displacement begins). The sphere motion exhibits well-behaved long-time diffusive behavior in both directions when interparticle forces are present. Dispersion in the y-direction is relatively unaffected by the interparticle forces; $(D_\infty^s)_{yy} = 0.17$, 0.21, and 0.20 for $\tau = 10^3$, 10^5, and ∞, respectively. Dispersion in the x-direction is more influenced by the interparticle forces; $(D_\infty^s)_{xx} = 0.065$, 0.084, and 0.021 for $\tau = 10^3$, 10^5, and ∞, respectively. There is minimal or no overshoot in the

mean-squared displacement curves. As τ decreases, the simulation reaches its steady state faster. Additionally, the mean-squared displacement curves are much easier to interpret; the range of values when the averaging length is varied is much smaller when interparticle forces are present. The steady-state microstructure radically changes when repulsive forces are added to the simulation; this is seen in both the coefficient of short-time self diffusion and the radial, pair-distribution function. $D_o^s = 0.69$, 0.61, and 0.35 for $\tau = 10^3$, 10^5, and ∞, respectively. More importantly, a steady value of D_o^s is established much more rapidly as τ decreases. When interparticle forces are absent, the time trace of D_o^s is characterized by a long, slow downward drift as the degree of hexagonal packing increases. There is little or no hexagonal packing when repulsive forces are present (see Figure 4.16). This can be seen by considering the radial, pair-distribution function; the $g(3.5)$ peak characteristic of hexagonal packing is completely absent. The $g(2)$ and $g(4)$ peaks decrease as τ decreases; longer-ranged (smaller τ) repulsive forces reduce the number of near-touching pairs.

The addition of repulsive interparticle forces eliminates the hexagonal packing among the spheres, increases D_o^s, shortens the time a suspension needs to reach a steady-state, and quickens the dynamics of the sphere motion. Its effect on the long-time dispersion is interesting; it eliminates the extremes in the velocity variance, meaning that $\mathbf{D}_\infty^s$ can be calculated more accurately and with less data. However, the actual value of $\mathbf{D}_\infty^s$ (particularly $\mathbf{D}_\infty^s)_{yy}$ is relatively insensitive to the addition of interparticle forces, despite the changes in the microstructure. Thus, further studies of the long-time dispersion will include repulsive interparticle forces ($\tau = 10^5$), because the accuracy and speed of the $\mathbf{D}_\infty^s$ calculations are better and the long-time average value of $\mathbf{D}_\infty^s$ is fairly unaffected.

Our next step is to increase the time step size to see if we can decrease the computational time without affecting accuracy. Increasing the time step from 0.001 to 0.005 results in the mobility matrix losing positive definiteness at $t = 270$. Appendix B.9 contains the results of this simulation. We eliminate the problem of losing positive definiteness by switching to the Ewald-sum method (F level of

approximation). Using this method and a time step of 0.005 results in excessive sphere overlap, causing the simulation to terminate itself at $t = 88$. (Terminal sphere overlap also occurs in the non-Ewald run whose time step is 0.0025 – see Appendix B.10). This sphere overlap does not occur in simulations without interparticle forces, even with a time step as large as 0.1 time unit. Since the buoyancy force acts equally on all the equal-sized, equal-density spheres, the relative motion between two spheres occurs because of the hydrodynamic interactions with the other spheres. The presence of interparticle forces can give rise to a greater degree of relative motion between two particles, leading to a greater degree of overlap. Reducing the time step to 0.0025 for the Ewald-summed F method case ($\phi = 0.453$ still) results in no excessive sphere overlap from $t = 0 - 500$, the complete run time (see Appendix B.11 for the results of this run).

The results of this run confirm that the long-time dispersion in a sedimenting suspension is relatively insensitive to the presence of repulsive interparticle forces. The sphere motion in both directions continues to be diffusive. $(D^s_\infty)_{yy} = 0.22$, which is within 23% of all F method results, regardless of whether there are interparticle forces or whether Ewald sums are invoked. The maximum value of $(D^s_\infty)_{yy}$ is 0.29, compared to 0.28 and 0.30 for the $\tau = \infty$, Ewald and non-Ewald cases, respectively. The average value of $(D^s_\infty)_{xx}$ is 0.027, which is much smaller than in the non-Ewald cases ($\tau \neq \infty$) but within 25% of the $\tau = \infty$ results (Ewald and non-Ewald runs). The Ewald sums appear to reduce the velocity variance in the x-direction, which significantly increases with the addition of interparticle forces to the non-Ewald simulations. The maximum $(D^s_\infty)_{xx}$ differs less than 7% for the Ewald runs, $\tau = 10^5$, and ∞.

The application of Ewald sums to the $\tau = 10^5$ case affects the steady-state microstructure only slightly; D^s_o, $g(2)$, and $g(4)$ decrease less than 3%. In general, the addition of repulsive interparticle forces eliminates the hexagonal packing that had characterized the previous steady-state configurations. The dispersion results show that the addition of repulsive forces has little effect on the long-time coefficient of self-diffusion, although it does affect qualitatively the time traces of the

time derivative of the mean-squared displacement.

4.5 Periodic Cell Size Dependence

A major consideration in the numerical simulation of any infinite system is the effect of periodic cell size – the results of interest should not be dependent on this size. All of the other simulations presented in this thesis use 25 spheres within the periodic cell. We increased the number of spheres in a simulation to 49, which has the effect of increasing the area of the periodic cell by a factor of 1.96. This is a non-Ewald, F method simulation, and $\tau = 10^3$. Except for the number of spheres, this is the same simulation described in the preceding section (see Appendix B.6). It took over 6 times more computer time to complete the $N = 49$ simulation compared to the $N = 25$ simulation (CPU time = 9215 minutes for $t = 0 - 500$ time units). The results of the simulation done with 49 spheres can be found in Appendix B.7. Except for the "sedimentation" velocity, the other reported results are the same for the simulations with 25 or 49 spheres (see Table 4.9). This insensitivity of the diffusion-related properties to the increase in periodic cell size is important; we can have greater confidence in the simulations that employ 25 spheres in the periodic cell. Since the periodic cell size must usually increase as the areal (or volume) fraction decreases, any low concentration study will have to perform similar tests of cell size dependence.

4.6 Concentration Dependence

All previous simulations were done at $\phi_A = 0.453$. In this section we consider the concentration dependence of the long-time dispersion in sedimenting suspensions. Changes in the microstructure, D_o^s, and the velocity-related averages will be noted. Based on the results of the preceding sections, these simulations use an Ewald-sum F method with $\tau = 10^5$. The suspensions have areal fractions of 0.1, 0.25, 0.453, and 0.6. The time step is 0.005 ($\phi_A = 0.1,\ 0.25$), 0.0025 ($\phi_A = 0.453$), and 0.001 ($\phi_A = 0.6$). Appendix B.12 has the $phi_A = 0.1$ results. Appendix B.14

has the $\phi_A = 0.25$ results. As noted before, Appendix B.11 has the $\phi_A = 0.453$ results. Appendix B.15 has the $\phi_A = 0.6$ results. Also included is an older $\phi_A = 0.1$ non-Ewald, F method run with $\tau = \infty$ (see Appendix B.13).

The time-averaged sedimentation velocity increases as the concentration increases. As discussed in Section 2.6, the backflow that occurs outside of the plane of the monolayer increases as the concentration increases. Since less fluid flows back through the monolayer as the concentration increases, the velocity of the spheres increases. The sedimentation velocity in the older, non-Ewald run described in the last paragraph did not reach a constant value; the simulation ended at 1000 time units.

The time-averaged velocity variances in both directions increased as the concentration decreased, although the time-averaged v_x variance levels off for $\phi_A \leq 0.25$ (cf. Figures 4.17 and 4.18). The motion in both directions exhibits long-time diffusive behavior. Figures 4.19*a*-*b* and 4.20 show the concentration dependence of $(D^s_\infty)_{yy}$ and $(D^s_\infty)_{xx}$, respectively. The bar indicates the range of all previous simulation (except the FT non-Ewald case) results ($\phi_A = 0.453$). The FT non-Ewald case results are denoted by a x and the non-Ewald, $\tau = \infty$, $\phi_A = 0.1$ case results are denoted by a +.

As in the random distribution results, D^s_o decreases as the concentration increases (cf. Figure 4.21). $g(2)$ is approximately the same for $\phi_A = 0.25$ and 0.453 and increases slightly for $\phi_A = 0.6$ ($g(2) = 15.7$ compared to 12.1 for $\phi_A = 0.25$, 0.453). The only other interesting feature is the increasing angular dependence of the near-touching spheres as the concentration increases from $\phi_A = 0.453$ to $\phi_A = 0.6$. Figure 4.22 indicates that for $\phi_A = 0.6$ there is a stronger preference for near-touching spheres to spend more time settling with their line of centers perpendicular to the gravity vector (the dashed curve results from forcing the occurs to be symmetric about $\theta = 90°$).

Table 4.1 The simulation conditions for all reported sedimentation runs. The first column is the memnonic case name for that simulation – 'e' implies Ewald, 'r' implies repulsive forces, and 'f', 't', or 's' denotes the level of approximation. 25 spheres are used in all simulations except for the n49 simulations. The mobility matrix was inverted every 0.1 time units in all simulations.

Case	Method	Ewald(?)	dt	Δ T	τ	Comments
ϕ_A=0.453						
FTSn1-6	FTS	no	0.001	0-800	∞	
FTSn6	FTS	no	0.001	500-800	∞	
FTn1	FT	no	0.001	0-500	∞	
FTn2	FT	no	0.001	500-1000	∞	
FTa1	FT	no	0.001	0-500	∞	new initial
FTa2	FT	no	0.001	500-1000	∞	condition
Fn1	F	no	0.001	0-500	∞	
Fn2-3	F	no	0.001	500-1000	∞	
ef1-4	F	z_l=2.0	0.001	0-1000	∞	
ef3	F	z_l=2.0	0.001	500-750	∞	
ef4	F	z_l=2.0	0.001	750-1000	∞	
nfr1	F	no	0.001	0-500	10^3	
n49a	F	no	0.001	0-500	10^3	N=49
n49b	F	no	0.001	500-1000	10^3	N=49
nfr2	F	no	0.001	0-500	10^5	
nfr3	F	no	0.005	0-270	10^5	lost pos. def.
nfr4	F	no	0.0025	0-202	10^5	overlap
efr1	F	z_l=2.0	0.005	0-88	10^5	overlap
efr2	F	z_l=2.0	0.0025	0-500	10^5	
ϕ_A=0.1						
phi1efr1	F	z_l=2.0	0.005	0-500	10^5	
phi1efr2	F	z_l=2.0	0.005	500-1000	10^5	
.1n1-2	F	no	0.001	0-1000	∞	
ϕ_A=0.25						
phi25efr1	F	z_l=2.0	0.005	0-500	10^5	
phi25efr2	F	z_l=2.0	0.005	500-1000	10^5	
ϕ_A=0.6						
phi6efr1	F	z_l=2.0	0.0025	0-126	10^5	overlap
phi6efr2	F	z_l=2.0	0.001	120-250	10^5	
phi6efr3	F	z_l=2.0	0.001	250-500	10^5	

Table 4.2 $\overline{\langle v_y \rangle}$ and the time-averaged v_x and v_y variances for the sedimentation runs.

Case	$\langle v_y \rangle$	$\langle (v_y - \langle v_y \rangle)^2 \rangle$	$\langle (v_x - \langle v_x \rangle)^2 \rangle$
ϕ_A=0.453			
FTSn1-6	-6.2694	0.00582	0.00582
FTSn6	-6.2567	0.00884	0.00287
FTn2	-6.3708	0.03168	0.00847
FTa1	-6.3742	0.02569	0.00893
FTa2	-6.3589	0.01533	0.00704
Fn2-3	-6.3555	0.01156	0.00336
ef3-4	-5.0931	0.01699	0.00210
ef3	-5.0846	0.00854	0.00196
ef4	-5.1015	0.02544	0.00224
nfr1	-6.3849	0.01990	0.00781
n49a	-8.9036	0.02358	0.00622
n49b	-8.9084	0.02087	0.00655
nfr2	-6.3813	0.01785	0.00677
nfr3	-6.3804	0.01344	0.00543
nfr4	-6.3815	0.01426	0.00684
efr1	-5.0020	0.00895	0.00246
efr2	-5.0062	0.01318	0.00274
ϕ_A=0.1			
phi1efr1	-3.2908	0.09987	0.01011
phi1efr2	-3.3023	0.11198	0.01157
.1n1-2	-	-	0.02284
ϕ_A=0.25			
phi25efr1	-4.2552	0.04535	0.00894
phi25efr2	-4.2650	0.05193	0.00998
ϕ_A=0.6			
phi6efr1	-5.3614	0.00330	0.00062
phi6efr2	-5.3407	0.00251	0.00043
phi6efr3	-5.3486	0.00213	0.00062

Table 4.3 $\overline{\langle v_x \rangle}$ and the time-averaged v_{xy} variance for the sedimentation runs.

Case	$\langle v_x \rangle$	$\langle (v_y - \langle v_y \rangle)(v_x - \langle v_x \rangle) \rangle$
ϕ_A=0.453		
FTSn1-6	-0.00277	0.00033
FTSn6	-0.02200	-0.00066
FTn2	0.00351	0.00023
FTa1	0.00392	0.00022
FTa2	-0.00268	-0.00004
Fn2-3	0.00542	0.00043
ef3-4	-0.00489	-0.00017
ef3	-0.01051	0.00008
ef4	0.00074	-0.00042
nfr1	-0.00388	-0.00082
n49a	-0.00188	-0.00047
n49b	-0.00216	-0.00025
nfr2	-0.00886	-0.00014
nfr3	-0.01161	-0.00028
nfr4	-0.00496	0.00002
efr1	-0.00405	-0.00048
efr2	0.00289	-0.00008
ϕ_A=0.1		
phi1efr1	0.00104	-0.00201
phi1efr2	0.00250	0.00075
.1n1-2	0.00822	-
ϕ_A=0.25		
phi25efr1	0.00752	0.00024
phi25efr2	-0.00187	0.00091
ϕ_A=0.6		
phi6efr1	-0.00637	0.00007
phi6efr2	-0.00173	0.00004
phi6efr3	0.00217	0.00001

Table 4.4 Radial pair-distribution results for the sedimentation runs.

Case	g(2.0)	g(3.5)	g(4.0)
ϕ_A=0.453			
FTSn5	12.1	5.38	5.32
FTSn6	12.5	10.8	8.85
FTn1	16.2	1.08	2.74
FTn2	15.2	2.31	3.06
FTa2	15.8	2.44	4.03
Fn1	15.9	1.43	3.03
Fn2-3	13.3	3.36	4.19
ef3-4	15.4	3.55	5.19
ef3	15.4	2.28	4.34
ef4	15.3	4.83	6.04
nfr1	11.5	0.92	1.44
n49b	10.5	.89	1.38
nfr2	15.8	0.83	1.82
efr2	12.1	0.86	1.45
ϕ_A=0.1			
phi1efr2	13.0	0.80	1.07
.1n2	26.4	3.70	3.98
ϕ_A=0.25			
phi25efr2	12.1	0.81	1.11
ϕ_A=0.6			
phi6efr3	15.7	0.78	2.10

Table 4.5 Steady-state values of $\mathbf{D}_o^s$ for the sedimentation runs.

Case	$(D_o^s)_{xx}$	$(D_o^s)_{yy}$	$(D_o^s)_{xy}$
ϕ_A=0.453			
FTSn5	0.355	0.345	-0.0032
FTSn6	0.315	0.299	0.0042
FTn1	0.546	0.544	-0.0004
FTn2	0.478	0.467	-0.0034
FTa1	0.544	0.540	0.0038
FTa2	0.421	0.402	-0.0018
Fn1	0.452	0.453	-0.0025
Fn2-3	0.364	0.364	0.0003
ef3-4	0.289	0.287	0.0019
ef3	0.300	0.294	0.0043
ef4	0.279	0.280	-0.0006
nfr1	0.690	0.695	-0.0045
n49a	0.672	0.682	-0.0012
n49b	0.687	0.693	-0.0031
nfr2	0.615	0.611	0.0076
efr2	0.601	0.603	0.0035
ϕ_A=0.1			
phi1efr2	0.896	0.894	0.0006
ϕ_A=0.25			
phi25efr2	0.772	0.776	-0.0021
ϕ_A=0.6			
phi6efr3	0.416	0.427	0.0006

Table 4.6 The average, minimum, and maximum values of the *yy*-component of $\mathbf{D}^s_\infty$ for the sedimentation runs.

Case	average $(D^s_\infty)_{yy}$	minimum level	maximum level
ϕ_A=0.453			
FTSn5	0.11	0.09	0.13
FTSn6	0.13	0.09	0.38
FTn1	0.46	0.45	0.50
FTn2	-	0.22	-
FTa2	0.34	0.20	0.40
Fn1	0.18	0.17	0.22
Fn2-3	0.20	0.10	0.30
ef3	0.27	0.27	0.28
nfr1	0.17	0.15	0.22
n49b	0.21	0.20	0.23
nfr2	0.21	-	-
efr2	0.22	0.10	0.29
ϕ_A=0.1			
.1n2	-	-	-
phi1efr2	4.77	-	-
ϕ_A=0.25			
phi25efr2	1.05	1.0	1.6
ϕ_A=0.6			
phi6efr3	0.012	0.010	0.023

Table 4.7 The average, minimum, and maximum values of the xx-component of $\mathbf{D}^s_\infty$ for the sedimentation runs.

Case	average $(D^s_\infty)_{xx}$	minimum level	maximum level
ϕ_A=0.453			
FTSn5	0.030	0.025	0.041
FTSn6	0.024	0.011	0.050
FTn1	0.048	0.043	0.050
FTn2	0.030	0.028	0.065
FTa2	0.023	0.022	0.025
Fn1	0.029	0.029	0.042
Fn2-3	0.021	0.012	0.035
ef3	0.023	0.016	0.030
nfr1	0.065	0.062	0.068
n49b	0.068	0.065	0.071
nfr2	0.090	0.090	0.090
efr2	0.027	0.021	0.028
ϕ_A=0.1			
.1n2	0.14	0.14	0.18
phi1efr2	0.11	0.11	0.11
ϕ_A=0.25			
phi25efr2	0.10	0.10	0.17
ϕ_A=0.6			
phi6efr3	0.0075	0.0050	0.0080

Table 4.8 The effect of interparticle forces on the velocity variances. All simulations use the non-Ewald, F method.

Case	τ	$\langle(v_y-\langle v_y\rangle)^2\rangle$	$\langle(v_x-\langle v_x\rangle)^2\rangle$
ϕ_A=0.453			
Fn2-3	∞	0.01156	0.00336
nfr2	10^5	0.01785	0.00677
nfr1	10^3	0.01990	0.00781

Table 4.9 The effect of periodic cell size on the properties of a sedimenting suspension. Increasing the number of spheres from 25 to 49 increases the periodic cell size by a factor of 1.96. Both simulations use the non-Ewald, F method, and τ is 10^3.

ϕ_A=0.453 Result	N=25	N=49
$\langle v_y \rangle$	-6.3849	-8.9084
$\langle v_x \rangle$	-0.00388	-0.00216
$\langle (v_y - \langle v_y \rangle)^2 \rangle$	0.01990	0.02087
$\langle (v_x - \langle v_x \rangle)^2 \rangle$	0.00781	0.00655
$\langle (v_y - \langle v_y \rangle)(v_x - \langle v_x \rangle) \rangle$	-0.00082	-0.00025
$(D^s_\infty)_{yy}$	0.17	0.21
$(D^s_\infty)_{xx}$	0.065	0.068
D^s_o	0.692	0.690
$g(2)$	11.5	10.5
$g(4)$	1.44	1.38

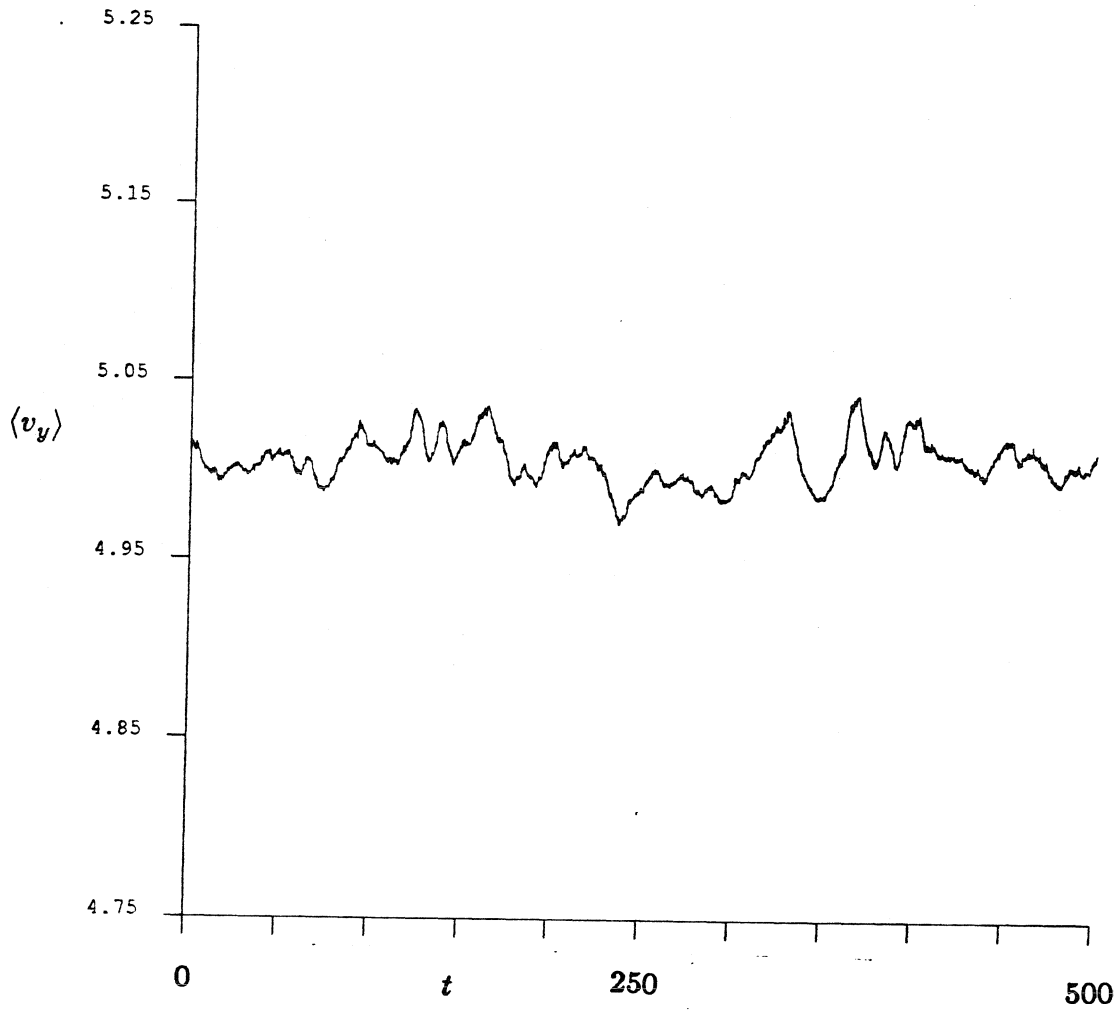

Figure 4.1 The time trace of $\langle v_y \rangle$ for run efr2. This simulation uses the Ewald, F method. The interparticle force variable τ is 10^5. The areal fraction is 0.453, and there are 25 spheres in the periodic cell.

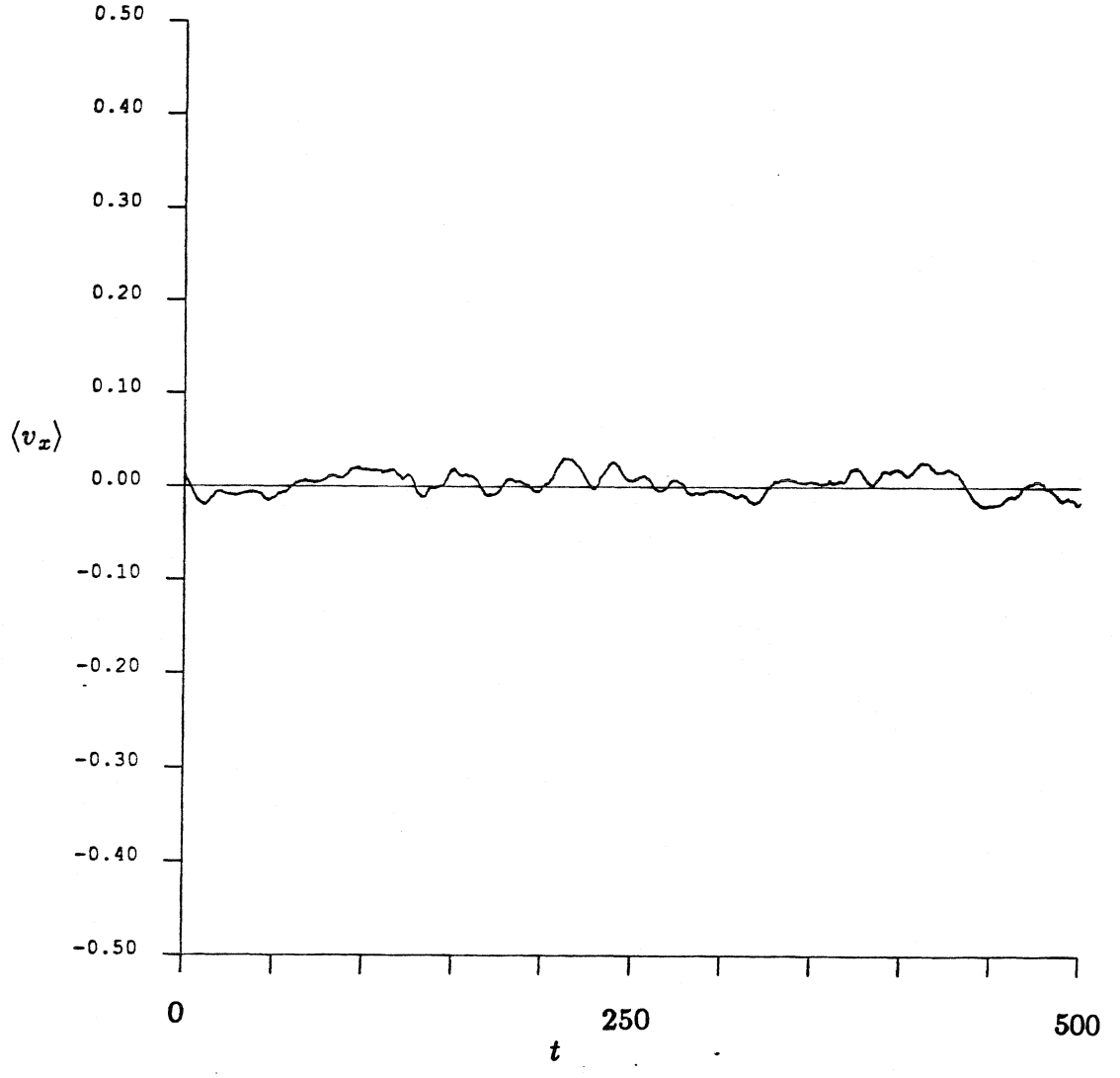

Figure 4.2 The time trace of $\langle v_x \rangle$ for run efr2. This simulation uses the Ewald, F method. The interparticle force variable τ is 10^5. The areal fraction is 0.453, and there are 25 spheres in the periodic cell.

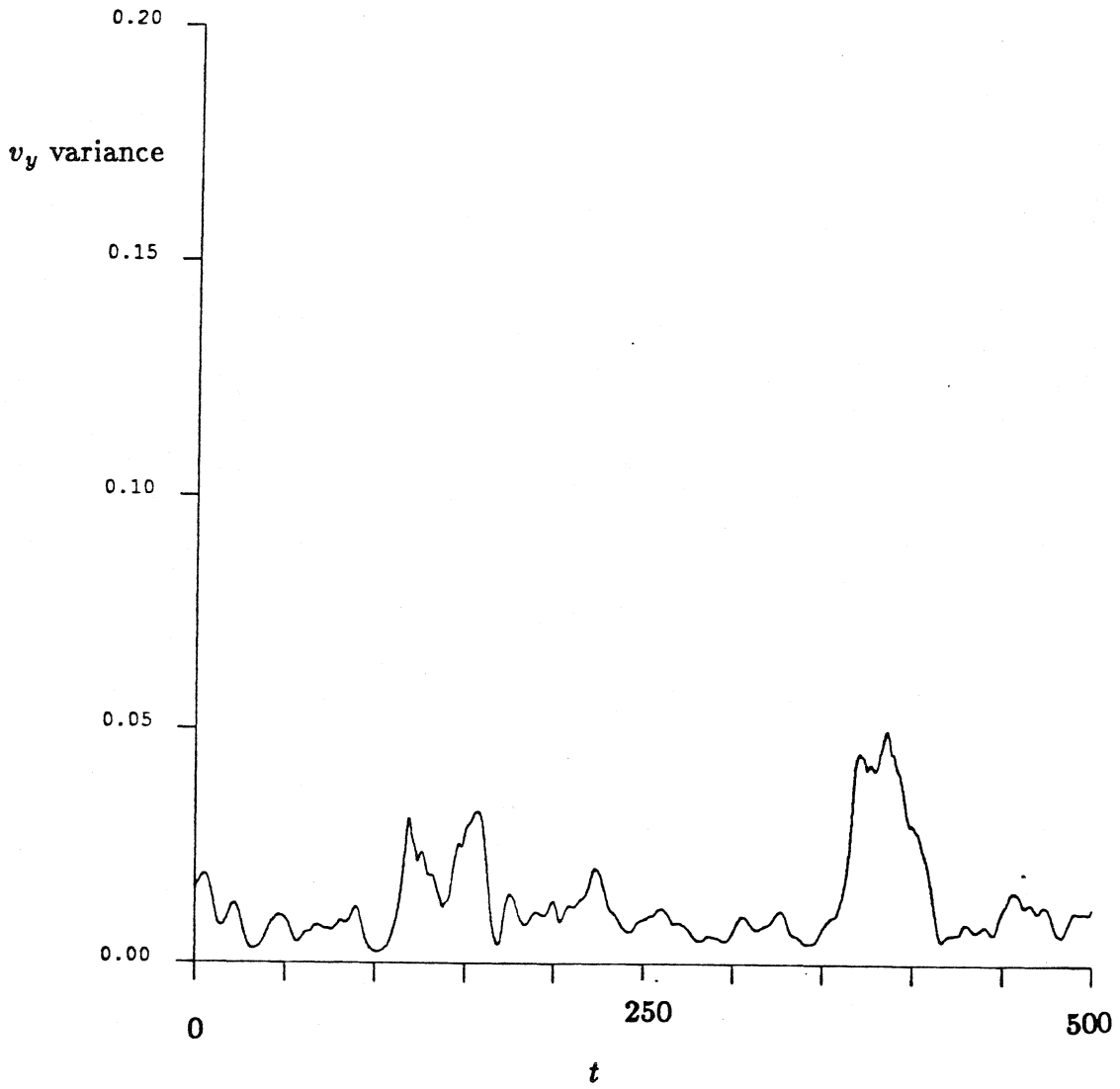

Figure 4.3 The time trace of v_y variance for run efr2. This simulation uses the Ewald, F method. The interparticle force variable τ is 10^5. The areal fraction is 0.453, and there are 25 spheres in the periodic cell.

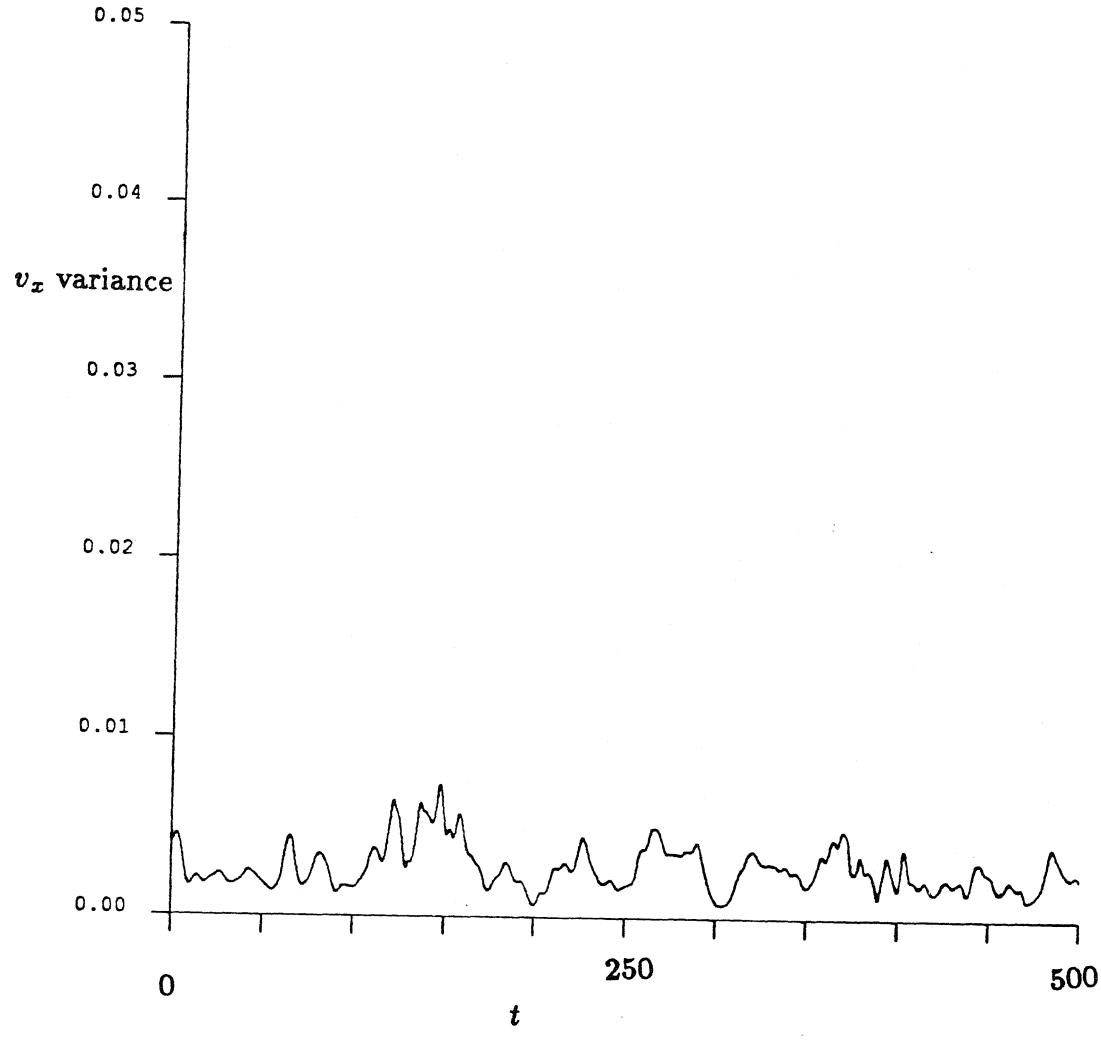

Figure 4.4 The time trace of v_x variance for run efr2. This simulation uses the Ewald, F method. The interparticle force variable τ is 10^5. The areal fraction is 0.453, and there are 25 spheres in the periodic cell.

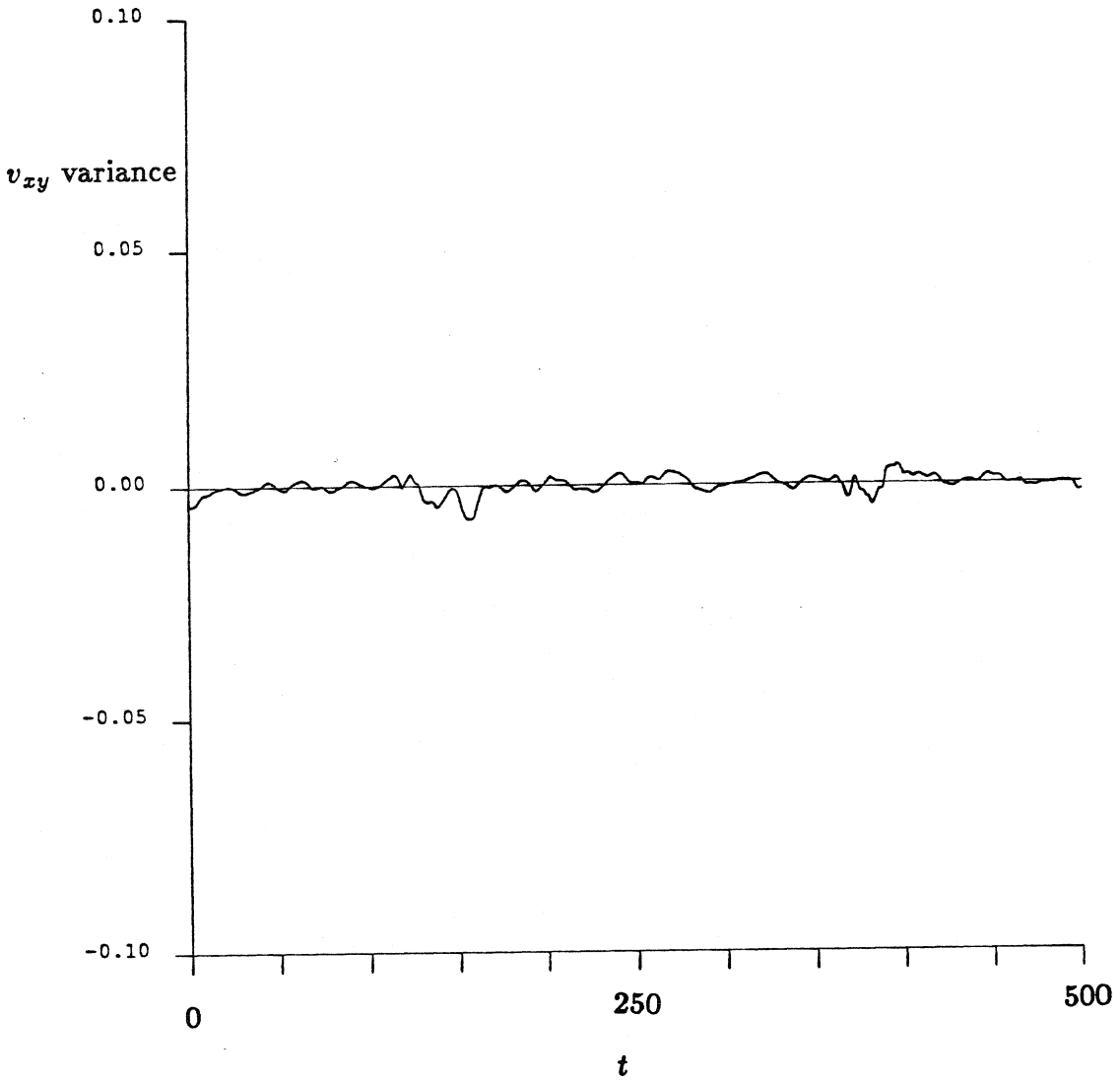

Figure 4.5 The time trace of v_{xy} variance for run efr2. This simulation uses the Ewald, F method. The interparticle force variable τ is 10^5. The areal fraction is 0.453, and there are 25 spheres in the periodic cell.

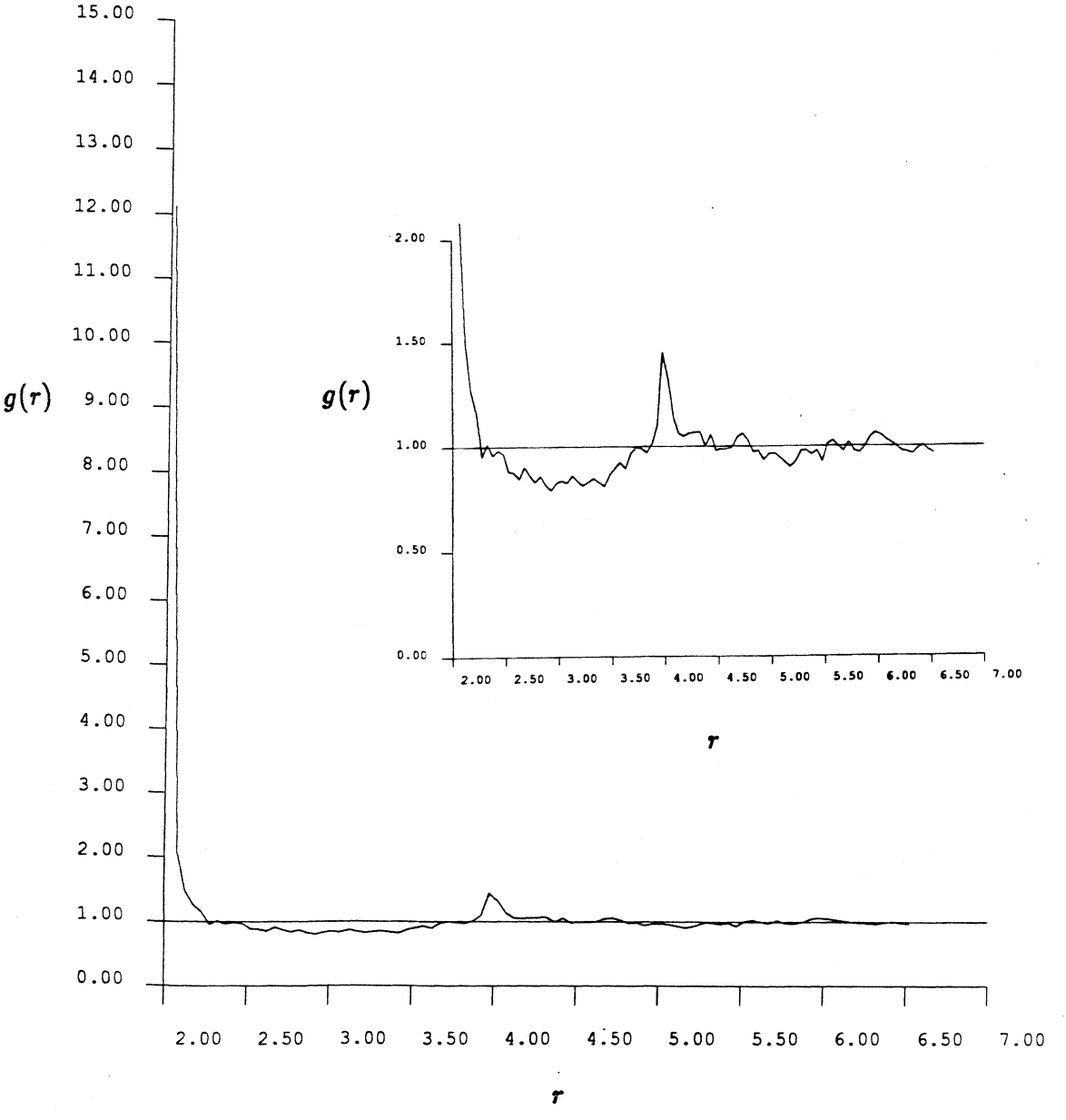

Figure 4.6 The radial pair-distribution function for run efr2. This simulation uses the Ewald, F method. The interparticle force variable τ is 10^5. The areal fraction is 0.453, and there are 25 spheres in the periodic cell. Only configurations that occur after $t = 150$ are averaged into the distribution.

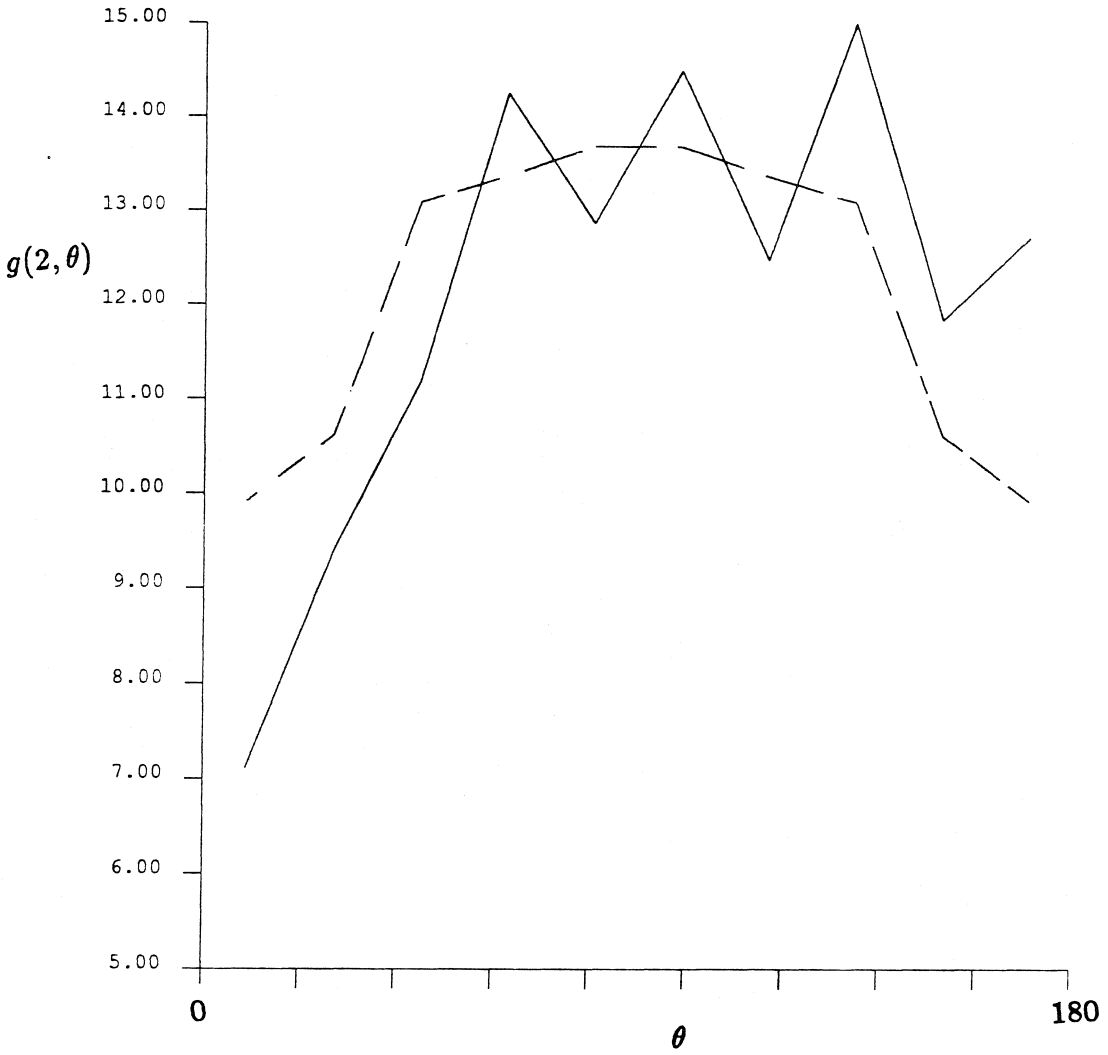

Figure 4.7 The full pair-distribution function for the near-touching spheres in run efr2. This simulation uses the Ewald, F method. The interparticle force variable τ is 10^5. The areal fraction is 0.453, and there are 25 spheres in the periodic cell. Only configurations that occur after $t = 150$ are averaged into the distribution. The dashed curve results when the distribution is forced to be symmetric about $\theta = 90°$.

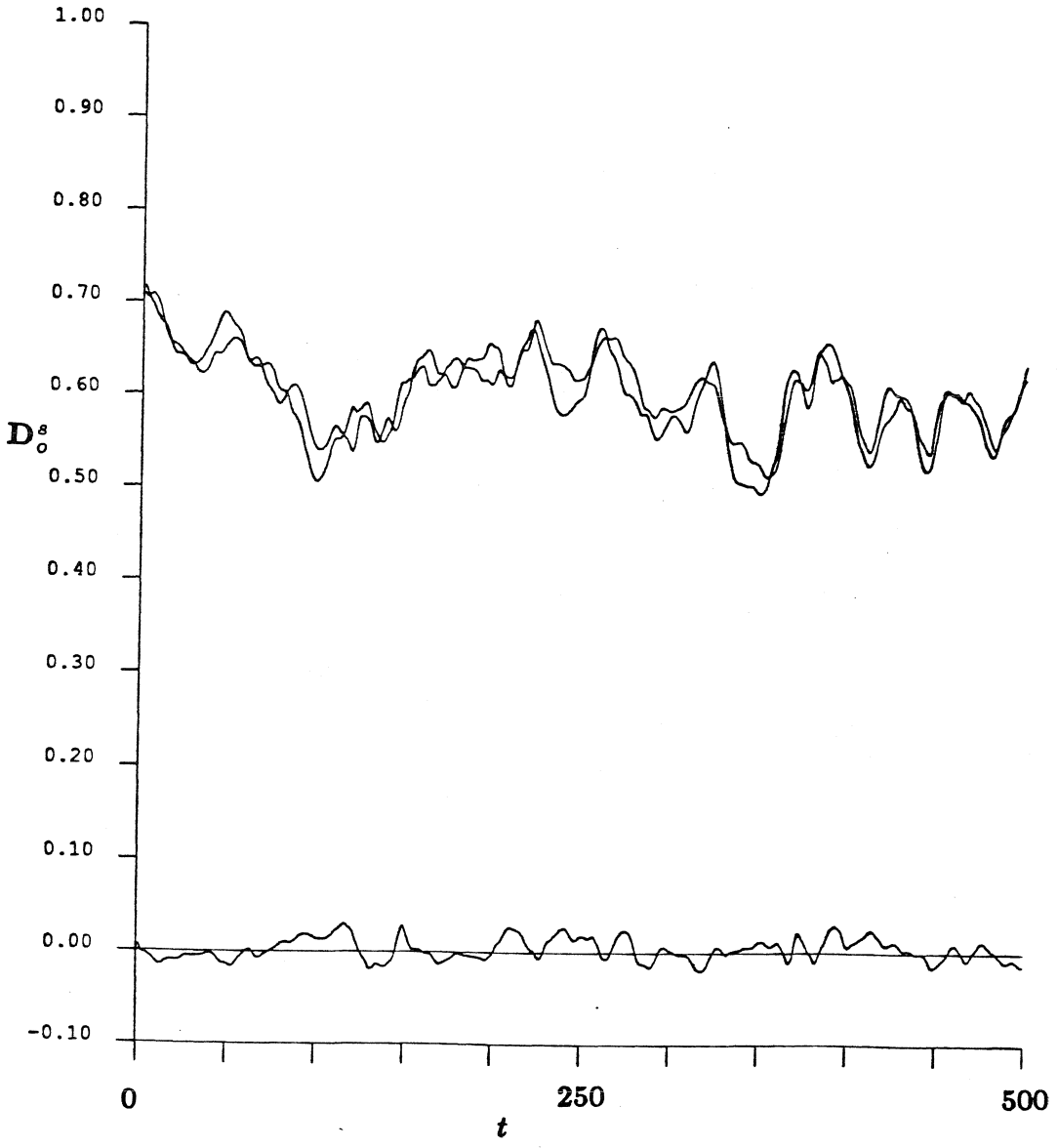

Figure 4.8 The time trace of $\mathbf{D}_o^s$ run efr2. This simulation uses the Ewald, F method. The interparticle force variable τ is 10^5. The areal fraction is 0.453, and there are 25 spheres in the periodic cell. The upper two curves are the xx and yy components of $\mathbf{D}_o^s$. The lower curve is the xy component of $\mathbf{D}_o^s$.

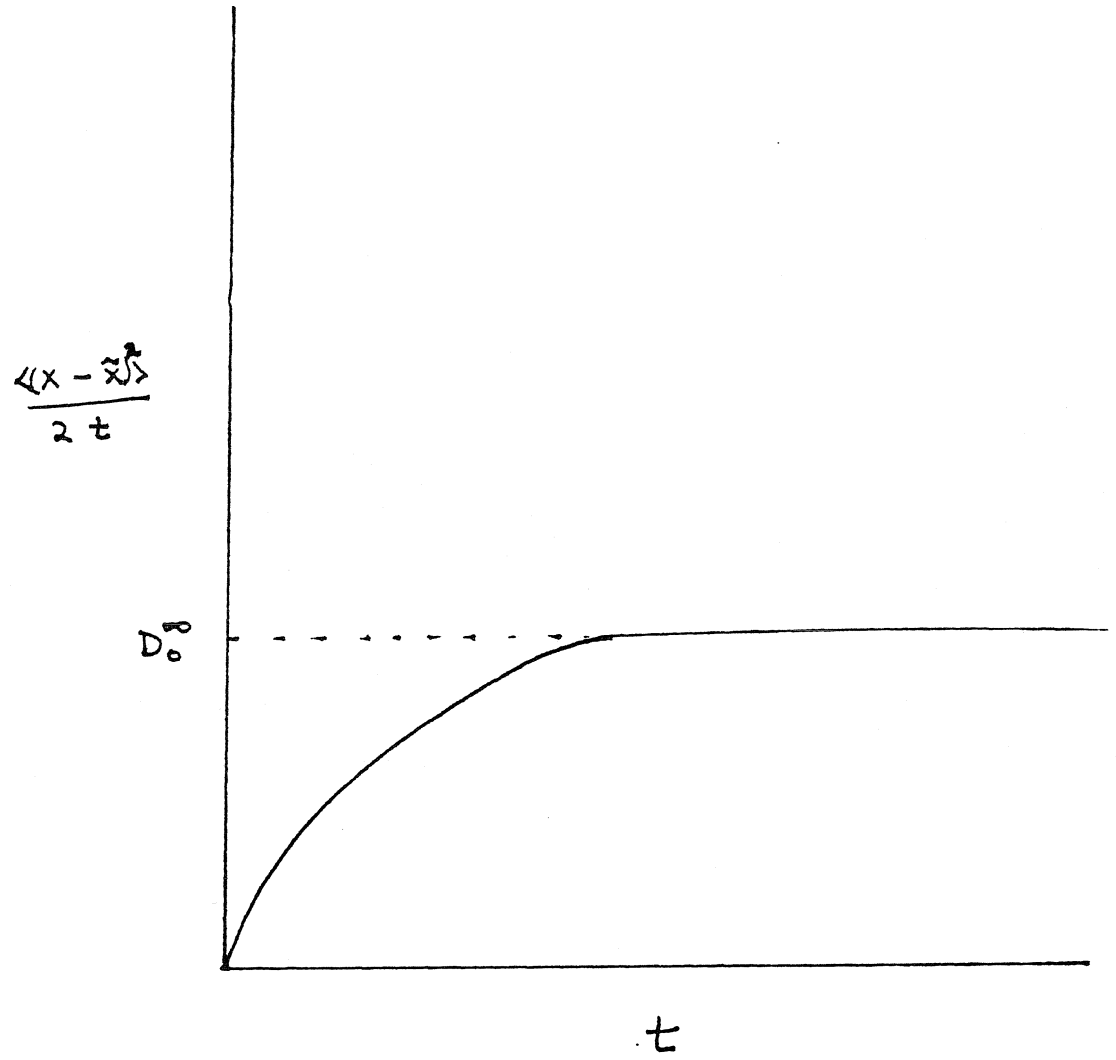

Figure 4.9 An idealized graph of one-half the mean-squared displacement of a sphere divided by time *vs.* time. The plateau in the curve is the definition of D^s_∞.

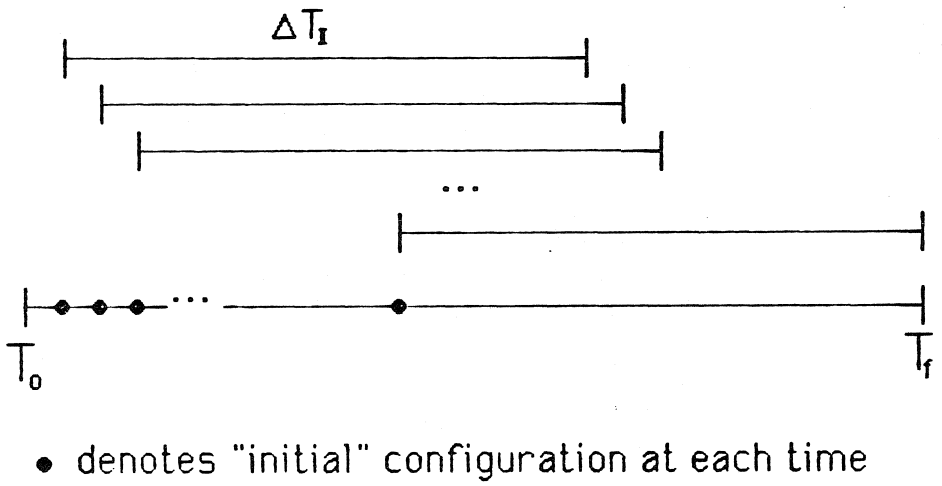

Figure 4.10 Schematic of the data enhancement technique used to calculate the long-time dispersion.

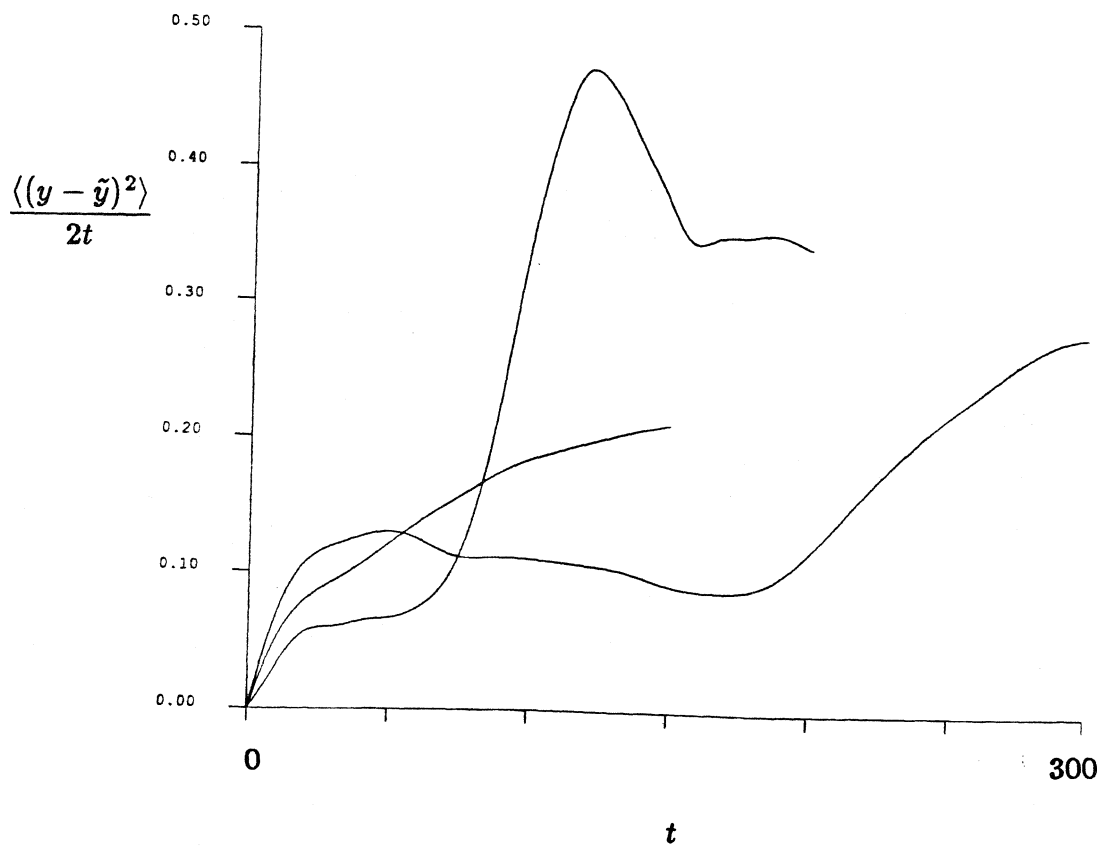

Figure 4.11 $(D^s_\infty)_{yy}$-defining curves for run efr2. This simulation uses the Ewald, F method. The interparticle force variable τ is 10^5. The areal fraction is 0.453, and there are 25 spheres in the periodic cell. Data is taken from $t = 100 - 500$, and the averaging lengths are 150, 200 and 300 time units.

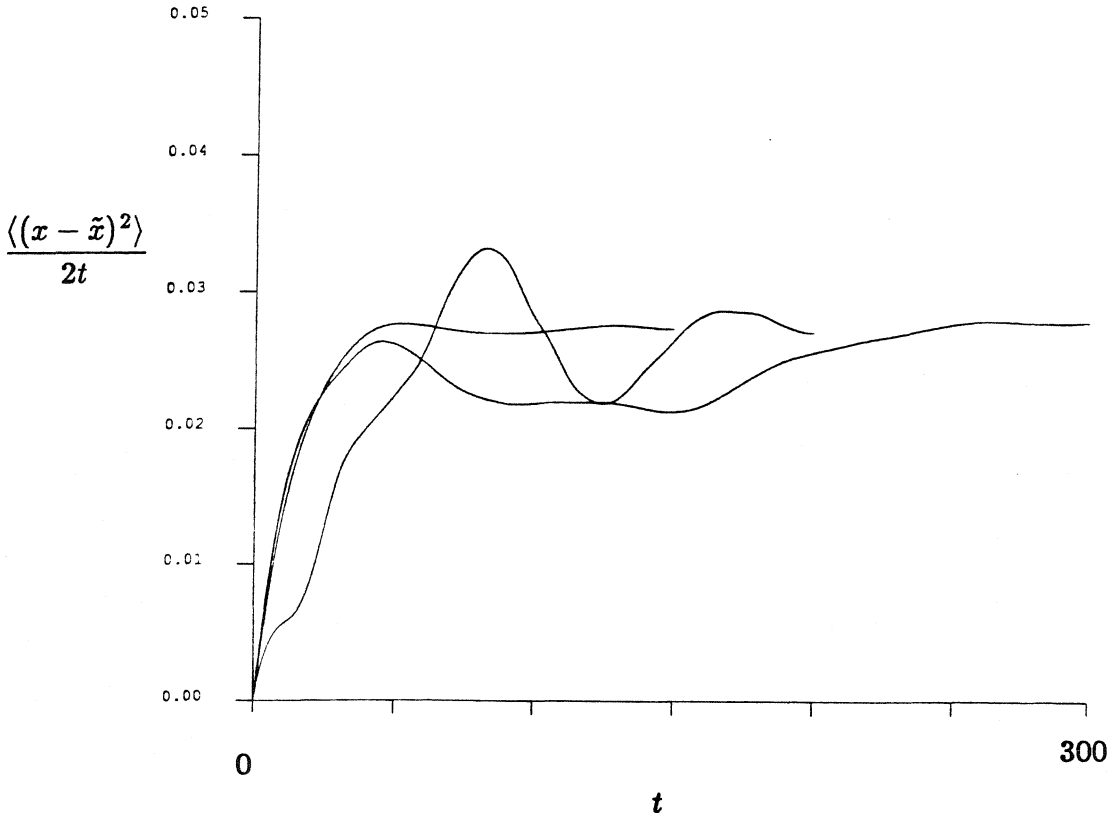

Figure 4.12 $(D^s_\infty)_{xx}$-defining curves for run efr2. This simulation uses the Ewald, F method. The interparticle force variable τ is 10^5. The areal fraction is 0.453, and there are 25 spheres in the periodic cell. Data is taken from $t = 100 - 500$, and the averaging lengths are 150, 200 and 300 time units.

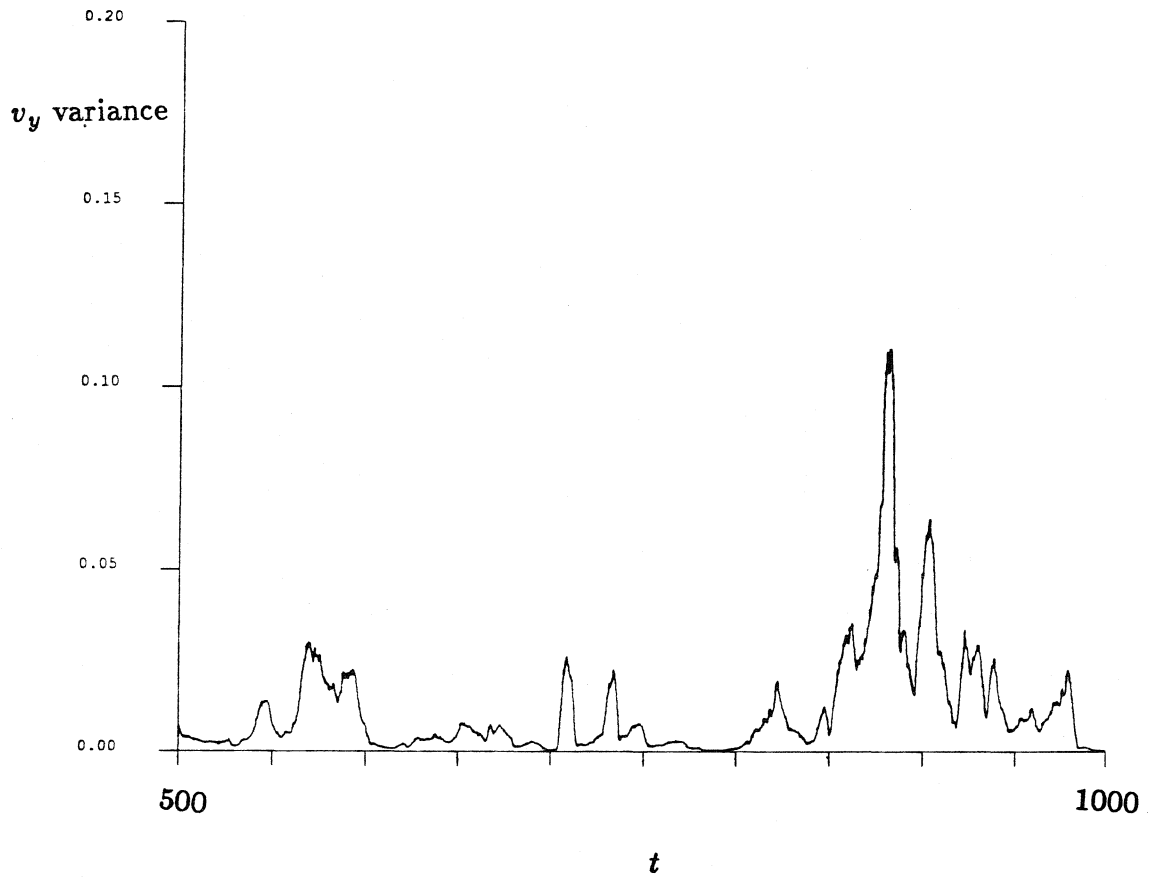

Figure 4.13 The v_y velocity variance trace for a non-Ewald, F method run (Fn2-3). Note the small-scale fluctuations imposed on the the larger-scale fluctuations.

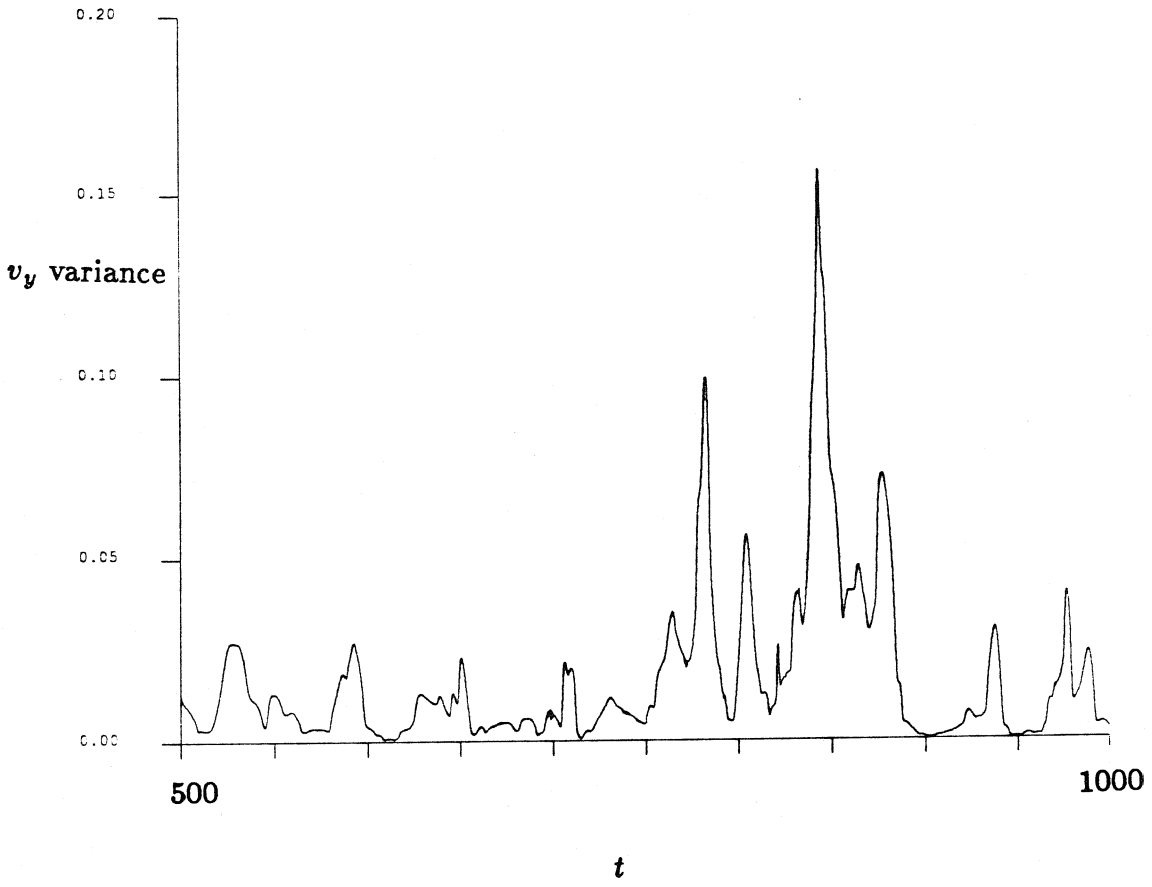

Figure 4.14 The v_y velocity variance trace for an Ewald, F method run (ef3-4).

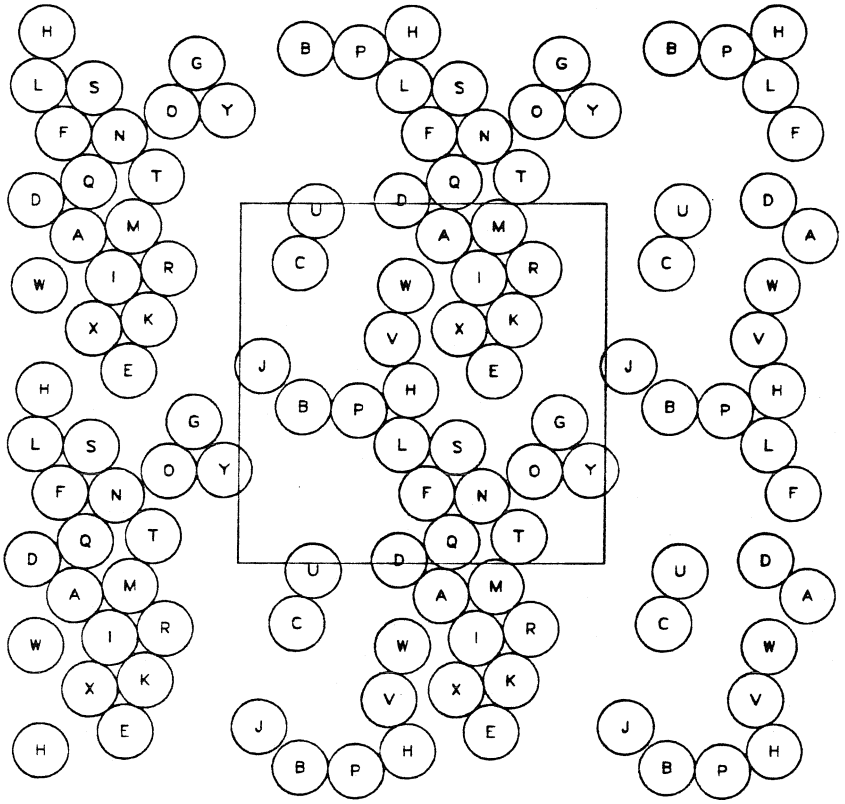

Figure 4.15a A "snapshot" of the sphere positions at $t = 840$ time units in the ef4 simulation. This is an Ewald, F method simulation. Note the presence of hexagonal packing and the vertical nature of the large cluster. The U–C pair of spheres generate an important contribution to the high value of the v_y velocity variance at this time ($v_y = 0.0945$).

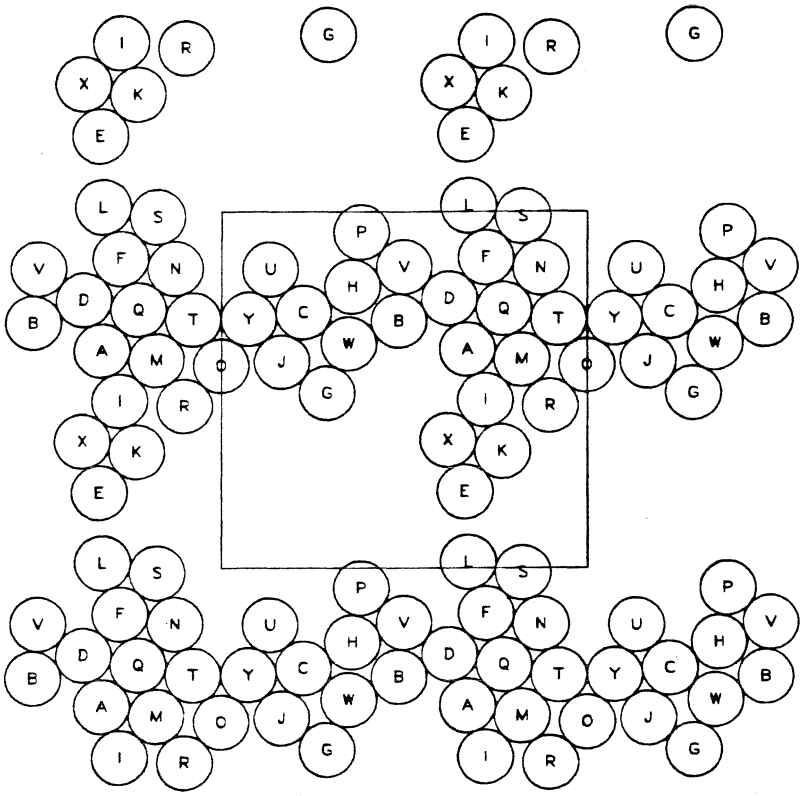

Figure 4.15b A "snapshot" of the sphere positions at $t = 950$ time units in the ef4 simulation. This is an Ewald, F method simulation. Note the increase of hexagonal packing and the horizontal nature of the large cluster. All the spheres in the periodic cell are in the cluster, and the v_y variance is correspondingly small ($v_y = 0.00043$).

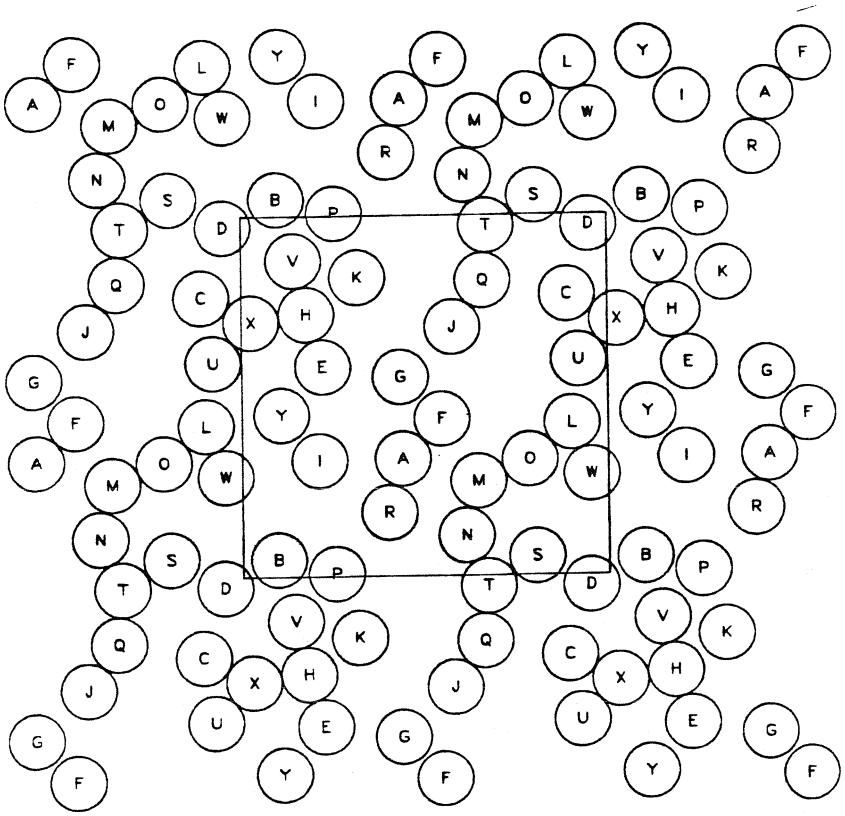

Figure 4.16 A "snapshot" of the sphere positions at $t = 500$ time units in the nfr1 simulation. This is an Ewald, F method simulation, and τ is 10^3. Notice the absence of hexagonal packing and large clusters of spheres.

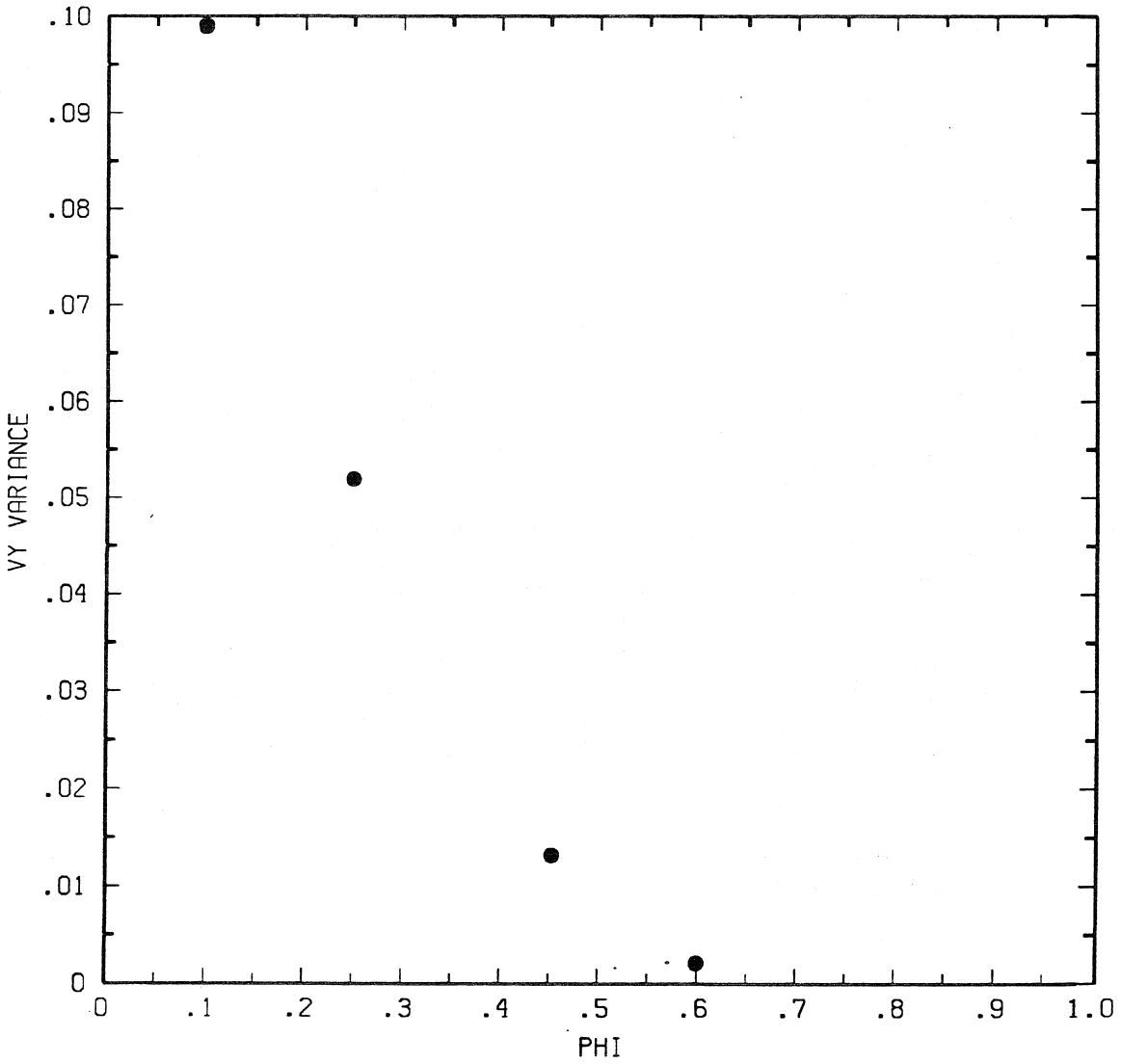

Figure 4.17 The time-averaged v_y variance *vs.* ϕ_A for the Ewald-summed, F method cases ($\tau = 10^5$).

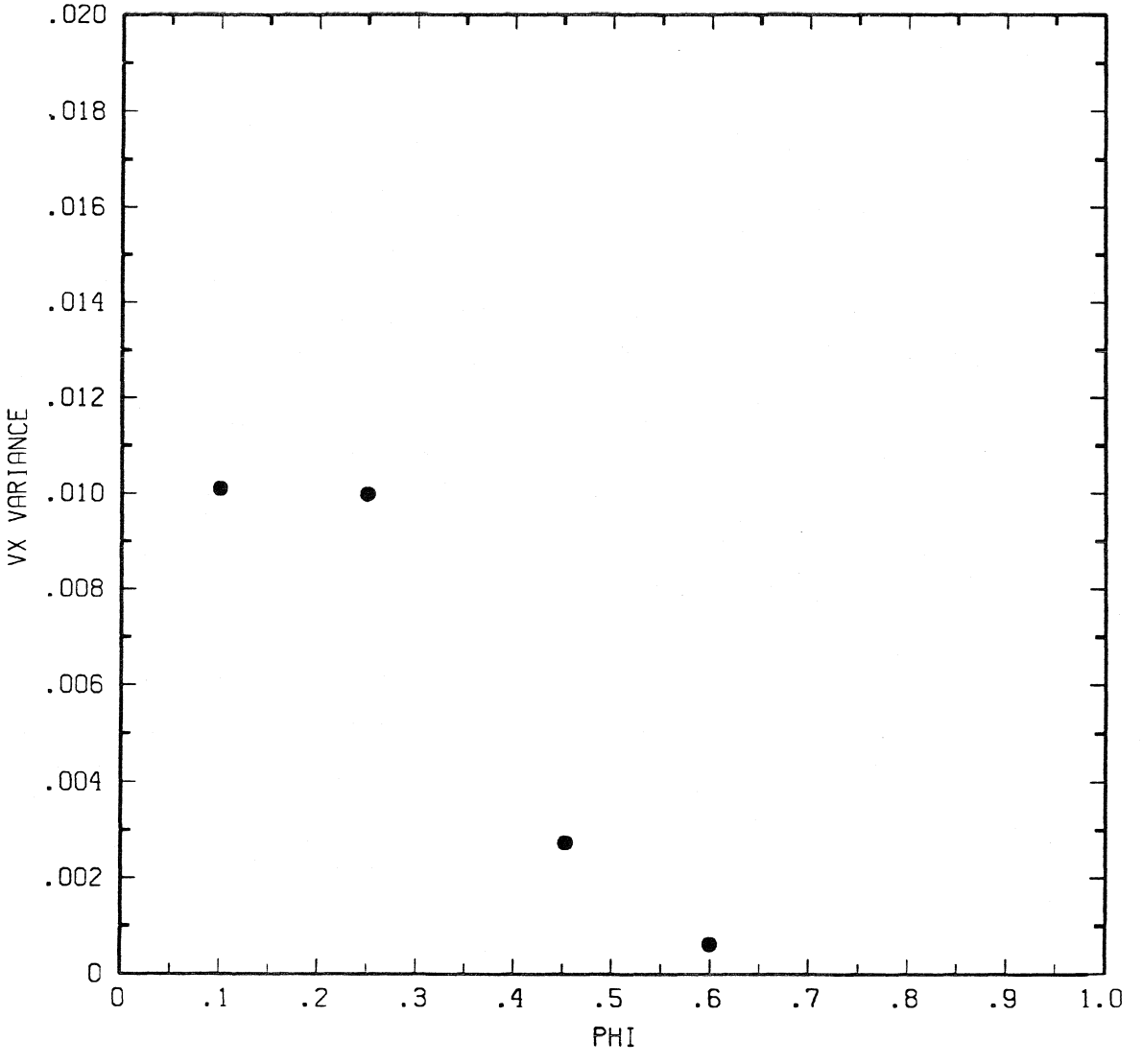

Figure 4.18 The time-averaged v_x variance *vs.* ϕ_A for the Ewald-summed F method cases ($\tau = 10^5$).

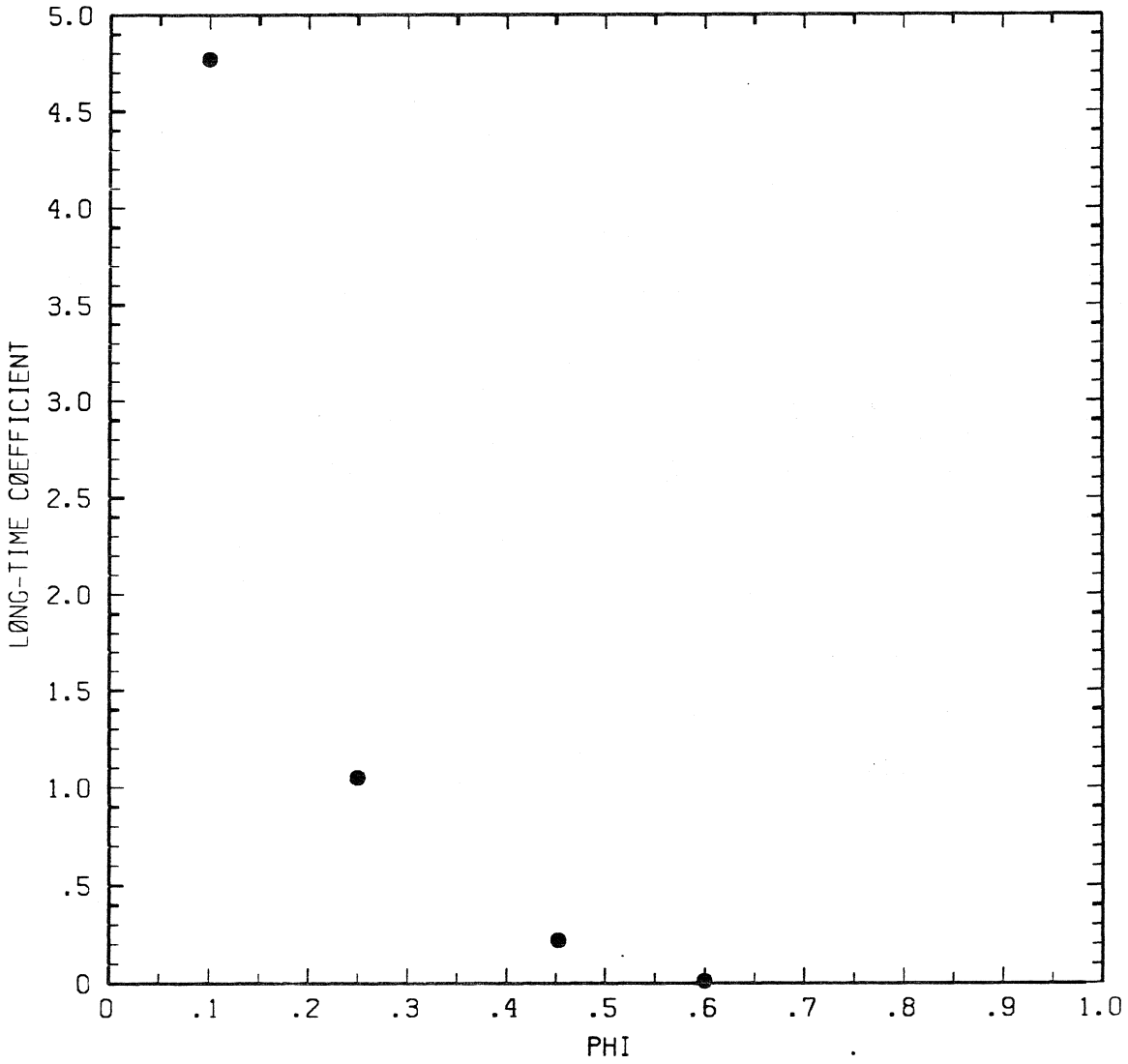

Figure 4.19a $(D^s_\infty)_{yy}$ *vs.* ϕ_A. There are 25 sphere in the periodic cell. The Ewald-summed, F method cases ($\tau = 10^5$) are denoted by filled circles.

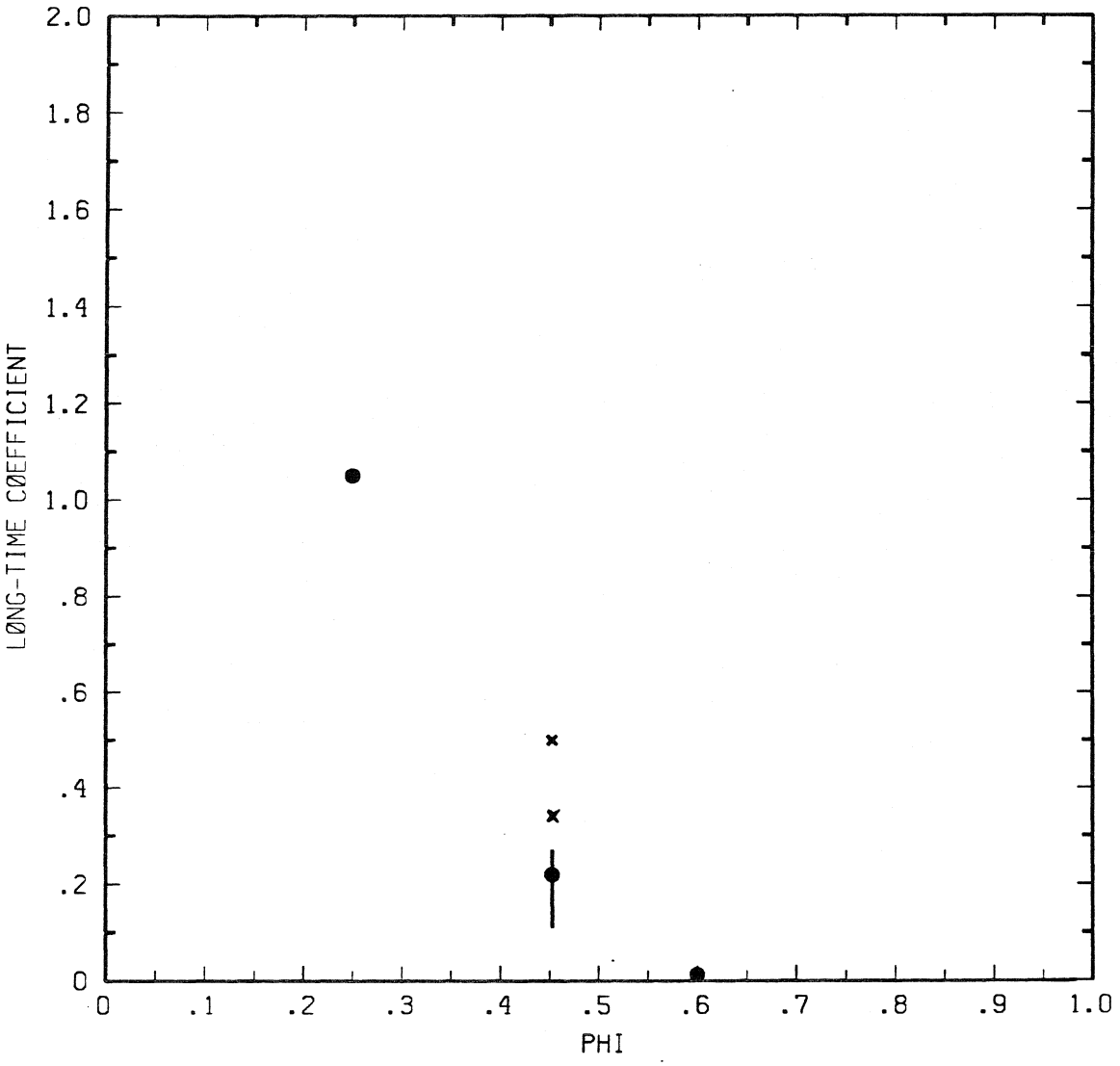

Figure 4.19b $(D^s_\infty)_{yy}$ *vs.* ϕ_A. The Ewald-summed, F method cases ($\tau = 10^5$) are denoted by filled circles. The bar indicates the range of all previous simulations except the FT, non-Ewald cases. They are denoted by the x's.

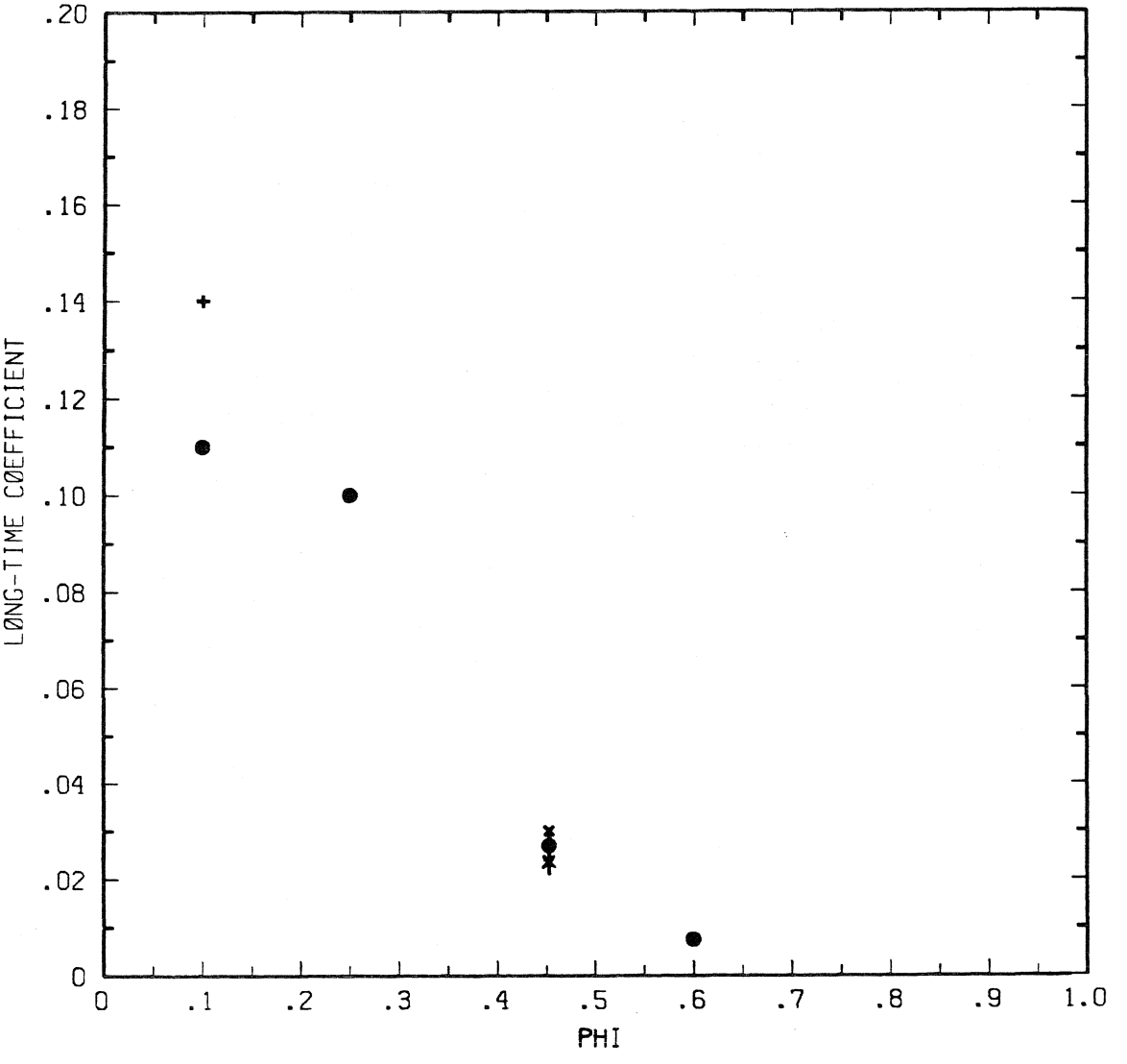

Figure 4.20 $(D^s_\infty)_{xx}$ *vs.* ϕ_A. The Ewald-summed, F method cases ($\tau = 10^5$) are denoted by filled circles. The bar indicates the range of all previous simulations $\tau = \infty$ except the FT, non-Ewald cases. They are denoted by the x's. The non-Ewald, F method, $\phi_A = 0.1$ case is denoted by a +.

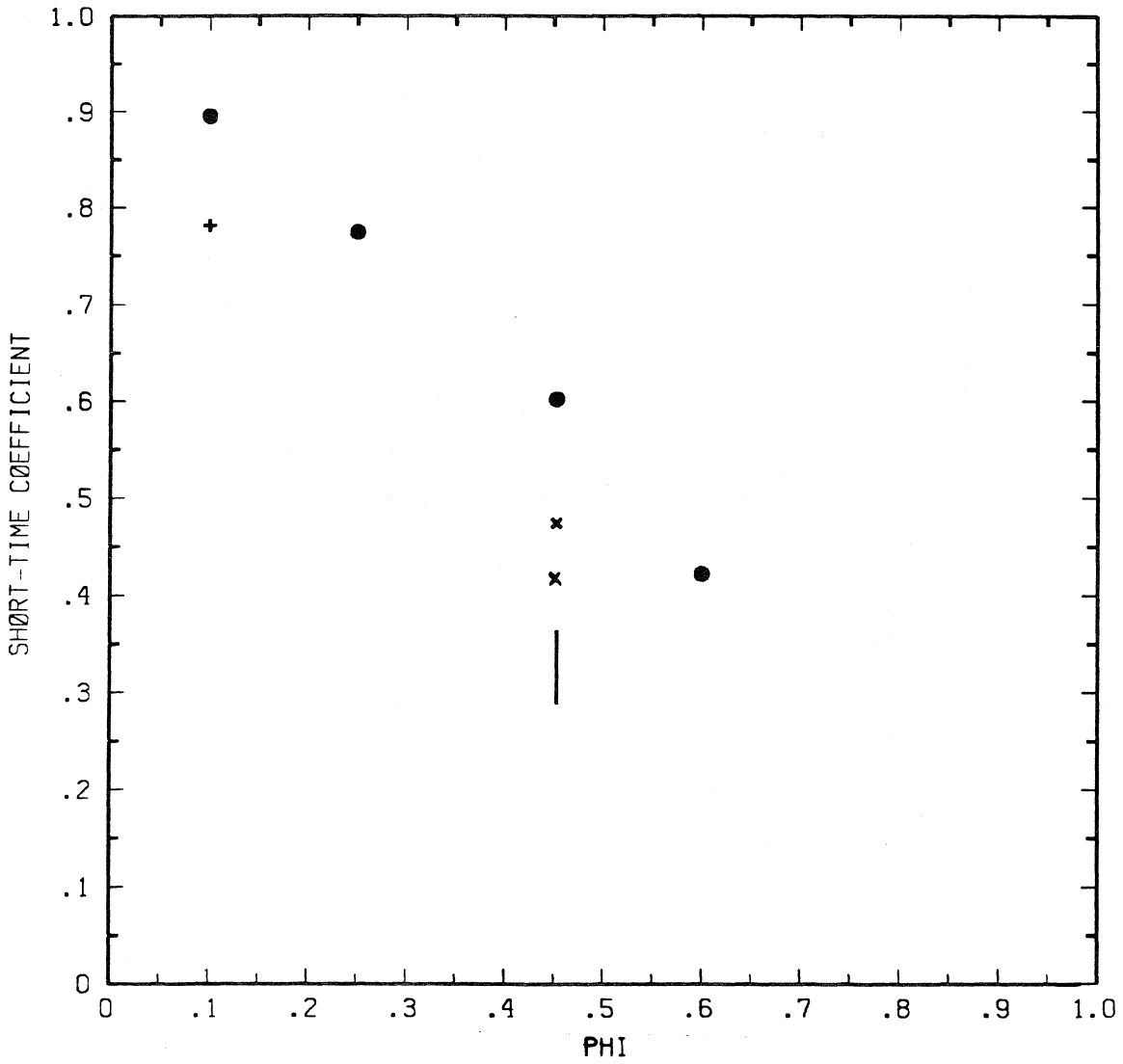

Figure 4.21 (D_o^s) *vs.* ϕ_A. The Ewald-summed, F method cases ($\tau = 10^5$) are denoted by filled circles. The bar indicates the range of all previous simulations $\tau = \infty$ except the FT, non-Ewald cases. The FT, non-Ewald cases are denoted by the x's. The non-Ewald, F method, $\phi_A = 0.1$ case is denoted by a +.

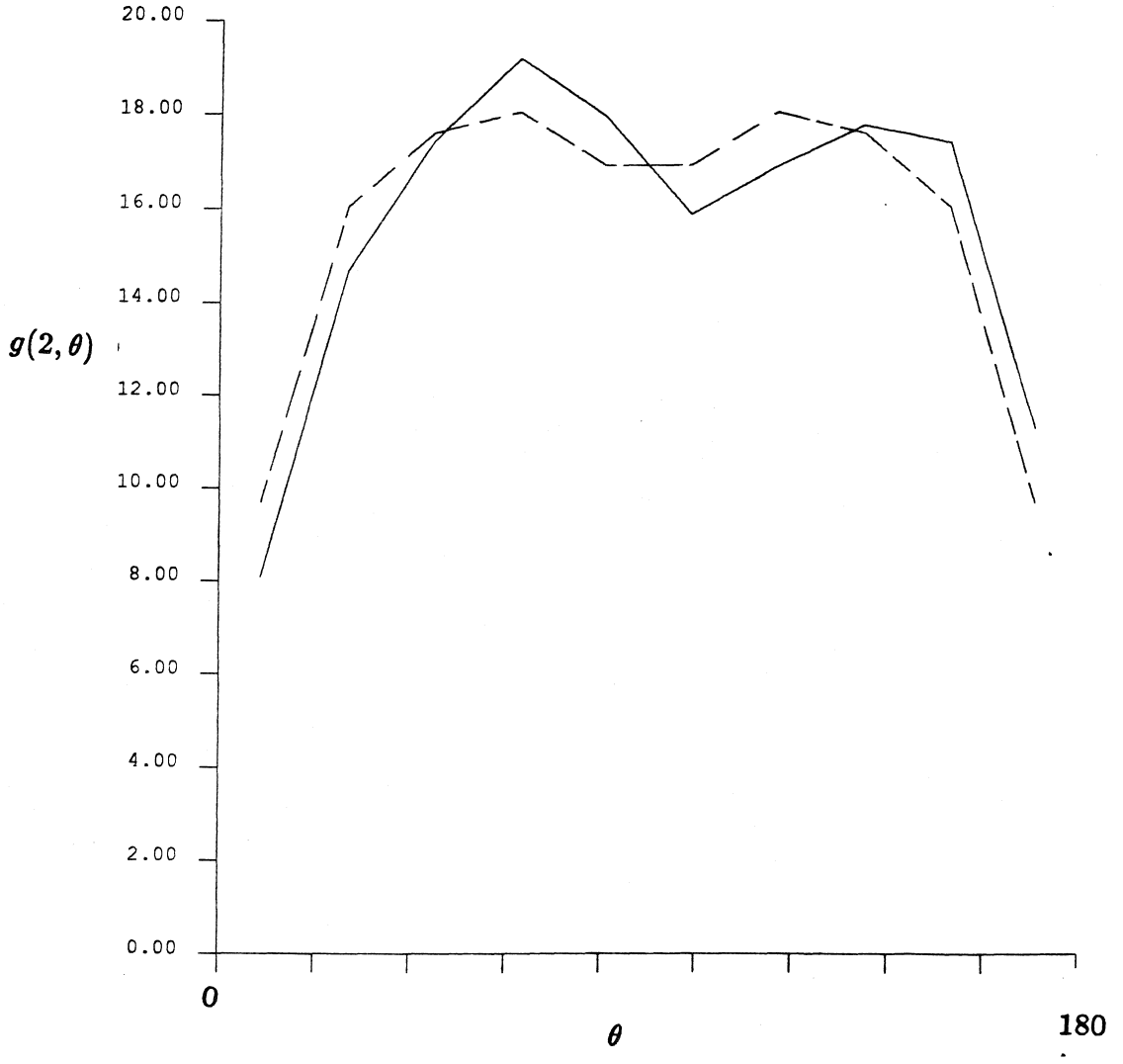

Figure 4.22 The full pair-distribution function at for the near-touching spheres at $\phi_A = 0.6$. Only configurations that occur from $t = 250$–500 are averaged into the distribution. The dashed curve results when the distribution is forced to be symmetric about $\theta = 90°$.

CHAPTER 5: CONCLUDING REMARKS

The behavior of sedimenting, non-Brownian particles in concentrated suspensions is very complex. At this time, neither theory nor experiments have studied the dispersion in these systems. We have studied them using a numerical simulation called Stokesian dynamics. Before discussing the general conclusions of our research, we shall discuss and evaluate both the simulation technique (as applied to this case) and the analysis of the simulation data. This first section will include discussions of the periodic cell size dependence, the level of accuracy in approximating the hydrodynamic interactions, the effect of monolayer *vs.* fully three-dimensional simulations. Further, we shall discuss the implications of deriving the long-time, diffusion coefficients from simulation data.

The second section contains the broad conclusions of this thesis. Leighton & Acrivos (1987) and Bossis & Brady (1988) have shown that the motion of non-Brownian, neutrally buoyant spheres in shear flow is diffusive. We will show that the motion of spheres in a sedimenting suspension is also diffusive. In both cases, the diffusive motion arises from the hydrodynamic interactions among the spheres. The introduction of repulsive interparticle forces alters the microstructure set up in a sedimenting suspension. We consider the effect of microstructure on the dispersion properties.

A simple scaling or dimensional analysis indicates that the diffusion coefficient should be proportional to the product of the square of the velocity scale and the time scale of the diffusive (multi-body) interactions. In the case of sheared suspensions of neutrally buoyant spheres, the relative motion among the spheres is generated by the shear flow. The velocity scale is $a\dot{\gamma}$, where a is the sphere radius and $\dot{\gamma}$ is the shear rate. The time scale of interactions is set by the inverse of the shear rate, and the probability of three-body interactions in proportional to the square of the concentration. Remember that two-sphere interactions do not lead to diffusive motion. The time scale is the time over which the important three-body interactions occur is $\phi^2\dot{\gamma}^{-1}$. In the case of sedimentation, the buoyancy force

does not cause relative motion among the spheres. Therefore, the relevant velocity scale is the square root of the velocity variance, not the sedimentation velocity. We shall see that the velocity variance is a function of concentration. The velocity scale in the shear case ($\dot{\gamma}a$) is independent of concentration. The time scale of three-body interactions is obviously a function of the concentration, but it is not as easily seen as in the shear problem. The time scale of interactions is not set by the sedimentation time scale of a/U_s, where U_s is the Stokes velocity. We shall look more closely at the time scale of the interactions that give rise to dispersion in the second section of this chapter.

Two other findings will be discussed in the second section. First, we consider the concentration dependence of the ratio of the long-time, self-diffusion coefficient in the direction of sedimentation to that in the direction perpendicular to it. Second, we consider the concentration dependence of the angular dependence of the full pair-distribution function for spheres whose centers are separated by less than 2.05 radii.

In the final section, we shall briefly discuss recent studies pertaining to the dispersion on non-Brownian particles in dilute suspensions (volume fractions less than 12 %). Since our results are for more concentrated, monolayer suspensions, comparison is difficult. However, certain conclusions are drawn, and future lines of research are suggested.

5.1 Evaluation of Simulations and Data Analysis

A general evaluation of the accuracy of Stokesian dynamics has been presented in Chapter 2. This includes the newest addition to the simulation – the Ewald formulation that speeds the convergence of mobility interactions. Section 2 of Chapter 4 discusses the effect of increasing the accuracy of the method on the results of a sedimentation simulation. Higher accuracy methods do not significantly change the results of the simulation. In particular, the F and FTS simulation results are very similar. This is a result of the overwhelming effect of the non-zero force vector; the effects of the induced torques and stresslets are

very small compared to the applied force. This is true even for diffusion-related properties. Section 3 of Chapter 4 compares the results of Ewald *vs* non-Ewald methods. There is no significant difference in the diffusion-related properties for the $\tau = \infty$ simulations. However, for cases where repulsive interparticle forces are present, the non-Ewald simulations show a significant increase in $(D^s_\infty)_{xx}$. This phenomena disappears for the Ewald simulations. Section 5 of Chapter 4 shows that the results of the simulations are relatively independent of periodic cell size – the number of spheres is increased from 25 to 49. It is important to note that all these comparisons are done for $\phi_A = 0.453$. Especially for cell size considerations, these conclusions may not be true for other concentration regimes.

All the simulations in this thesis are of monolayer suspensions. Monolayer simulations provide a considerable savings in computer time. A three-dimensional simulation, preserving the edge length of the periodic cell, will increase the run time of the simulation by approximately a factor of 1000 (see Section 6 of Chapter 2). As in previous studies using monolayer simulations (cf. Brady & Bossis 1985 and Bossis & Brady 1987), it is our belief that the interactions that occur among spheres in a monolayer are of the same type that occur in three dimensions. The fundamentals of spheres interacting and moving around each other are preserved. Results from the previous studies yield good qualitative comparison with experimental studies; rough conversions from areal fractions to volume fractions show that the results are in good quantitative agreement also. We do not believe that the sedimenting system will alter this correlation, and that the qualitative behavior exhibited in the monolayer will be seen in three dimensions. The last section of this chapter addresses this point also.

It is clear after reviewing the mean-squared displacement curves in Chapter 4 and in Appendix B that they sometimes do not mimic the idealized curve in Figure 4.9. This type of analysis has also been used to find the long-time, self-diffusion coefficient for sheared systems (Bossis & Brady 1987). For suspensions of non-Brownian spheres, the mean-squared displacement curves showed a considerable overshoot before leveling off. However, only one smooth plateau results.

In the analysis of some sedimentation simulations, we see that the curves may level off at different values at different times. Sedimenting systems are different from sheared systems. The rate of change of the microstructure is much slower in the sedimentation case – the tempo is set by the relative motion arising from the hydrodynamic interactions as opposed to the shear flow forcing the rearrangement of the particles. Coupled with the use of periodic boundary conditions, the environment of a diffusing particle in a sedimenting suspension can remain fairly constant over long periods of time. This explains the change of levels we see in some mean-squared displacement curves. Of course, increasing the number of particles in the periodic cell would increase the types of local environments present and would produce curves that better mimic the idealized curve. Also, by using the data enhancement technique described in Section 1 of Chapter 4, increasing the length of the simulations (keeping the time interval of the curve constant) would have the same effect. It is the slow dynamics of dispersion in sedimenting systems makes this analysis difficult and, in general, more time consuming.

5.2 Conclusions and Discussions

Certainly the major conclusion of this thesis is that the dispersion of non-Brownian, sedimenting spheres in suspension is diffusive. We have considered the dependence of the diffusivity on the accuracy that the simulator approximates the hydrodynamic interactions, the periodic cell size, the range and strength of repulsive interparticle forces, and the concentration. Detailed discussions of these issues is found in Chapter 4.

Of general interest is the insensitivity of method accuracy on the diffusion-related properties. Our crudest approximation of the mobility interactions is the F method – the spheres are not allowed to rotate, as the coupling between the applied force and the rotational velocity is not included at this level. The FT method allows the spheres to rotate (there is no applied torque), and we see a slight, but consistent, increase in the diffusivity in the direction of sedimentation. Obviously, the free rotation of the spheres facilitates their diffusion. The FTS method includes

the effect of the induced stresslets on the motion of the spheres. Induced stresslets on a sphere are caused by the flow field resulting from the relative motion of other spheres. We see that the diffusivity resulting from FTS simulations is similar to that resulting from F simulations. The effect of the induced stresslets is to negate the slight rise in diffusivity caused by the free rotation of the spheres.

An interesting result of this thesis is the relative small effect of large changes in the suspension microstructure on the long-time, self-diffusion coefficient. The diffusivity of spheres is the same whether there is a large degree of hexagonal packing ($\tau = \infty$) or if it is non-existent ($\tau \leq \infty$). Indeed, the short-time, self-diffusion coefficient ranged from 0.31 to 0.69, with relatively small deviation in long-time diffusivity. The one exception is $(D^s_\infty)_{xx}$ for the non-Ewald simulations. We see an dramatic increase in this coefficient for the $\tau = 10^3$ and 10^5 simulations. However, this increase is not seen when the Ewald method is applied in the $\tau = 10^5$ simulation. The independence of the diffusivity on large scale changes in the microstructure is an important phenomena that is not completely understood at this time.

As discussed in Section 6 of Chapter 4, $(D^s_\infty)_{yy}$ is a monotonically decreasing function of increasing concentration for the areal fractions studied. This is also true for the xx-component, although it levels off smaller areal fractions. This basic behavior is also seen in the velocity variances associated with these directions (see Figures 4.17 and 4.19a and Figures 4.18 and 4.20 for the y and x directions, respectively). We shall probe this relation in greater depth. (Remember that the y-direction is the direction parallel to the gravity vector, and the x-direction is perpendicular to this direction). In the shear case, the diffusion coefficient increases as a function of the square of the concentration, and the square of the velocity scale is independent of concentration. The time scale of the interactions that can contribute to diffusive motion is set by the shear rate and the probability of three-body interactions. Although the probability of three-body interactions remains the same in the sedimentation case, the rate of the interactions is no longer imposed externally. The amount of time it takes for a particle to experience

a variety of local environments is obviously a strong function of concentration.

We can not determine the time scale of the hydrodynamic interactions *a priori* for a sedimenting system. Instead, we divide the diffusion coefficient by the velocity variance to give a value that should be proportional to the time scale of the diffusive motion. Tables 5.1 and 5.2 show the ratio of the diffusivity and the velocity variance ($\phi_A = 0.453$ simulations only) for the y- and x-direction, respectively. Tables 5.3 and 5.4 show the concentration dependence of this time scale for the y- and x-direction, respectively. There is a clear decrease in the time scale in the direction of sedimentation as concentration increases (be aware of the large standard of deviation, as seen in Table 5.1). The time scale in the perpendicular direction seems to be independent of concentration. A non-zero force on the particles alters the concentration effect on the time scale of diffusion-causing interactions in the direction of that force. The time scale over which diffusion-causing interactions occur in the direction of sedimentation increases as the concentration decreases. The time scale on particle interactions in general must be growing even faster than that (seen by removing the effect of multiplying this time scale by the probability of three-body interactions). It must be clearly stated that these results only pertain to concentrations within the range of the study.

Consider again the concentration dependence of the velocity variance and the diffusivity. Table 5.5 shows the ratio of the y-component to the x-component of the velocity variance and the diffusion coefficient for the $\phi_A = 0.453$ simulations. Table 5.6 shows the concentration dependence of the ratio of the y-component to the x-component of the velocity variance and the diffusion coefficient. We note a slight concentration dependence in the velocity variance ratio, but it can be considered small compared to the standard deviation shown in the $\phi_A = 0.453$ simulations. In contrast, the concentration dependence in the diffusion coefficient ratio is quite marked at the lowest and highest concentrations. The anisotropy of the diffusion coefficient increases strongly for decreasing concentration. Analysis of these two quantities and the discussion in the preceding paragraph indicate

that it is the time scale of the diffusion-causing interactions that gives rise to this anisotropy.

In this light, consider the angular dependence of the spheres whose centers are separated by less than 2.05 radii, the near-touching spheres. Figures 5.1, 5.2, 5.3 and 5.4 show this angular dependence for $\phi_A = 0.1$, 0.25, 0.453, and 0.6, respectively. As seen in Figure 3.1, $\theta = 90°$ is the direction perpendicular to gravity vector. In Figure 5.1 we see that there is a greater preference for the near-touching spheres to align in the direction of gravity for $\phi_A = 0.1$. In the middle concentration range, there is no real directional preference for the near-touching spheres. There is a slight preference in the $\phi_A = 0.453$ case, but this is not seen in all the $\phi_A = 0.453$ simulations. In Figure 5.4 we see that there is a greater preference for the near-touching spheres to align perpendicular to the direction of gravity at $\phi_A = 0.6$. The direction preference is completely opposite for the highest and lowest concentrations.

We know that for two spheres sedimenting in an infinite fluid, the sedimentation velocity is greater for spheres falling along there line of centers, as opposed to perpendicular to this line. This difference is even greater when the spheres are not allowed to rotate. Whether this effect is important to understanding the concentration dependence of these diffusion-related properties is not clear yet. It is not even clear whether it is a cause, or an effect, or both.

5.3 Comparisons, Future Research Areas

As stated in the introduction of this chapter, we can not compare our results, either qualitatively or quantitatively, to experimental or theoretical results. This is because our simulations are generally of higher concentration, monolayer suspensions. The dilute-limit theory of Koch and Shaqfeh says that the diffusion coefficient in the direction of sedimentation is proportional to the inverse of the concentration (three-dimensional analysis). Results of experiments by Ham and Homsy (1987) indicate that this diffusion coefficient increases at small concentrations, levels off around $\phi = 0.05$, and then begins to decrease as the concentration

continues to increase. The largest volume fraction they consider is 12%. The value of $(D^s_\infty)_{yy}$ at concentrations between 5% and 12% is between 3 and 7. Although comparisons of monolayer and three-dimensional results can be suspect, $(D^s_\infty)_{yy}$ is 4.8 when the areal fraction is 10%.

Many questions still surround the behavior of the diffusivity as the concentration goes to zero. Numerical simulations are one method of probing this regime. An extension of this work to lower concentrations is suggested, but additional care must be taken. In particular, periodic box size dependence must be considered anew and thought must be given to the increasing length of the simulation runs.

Table 5.1 Comparison of $(D^s_\infty)_{yy}$, the v_y variance, and the ratio of the two for the $\phi_A = 0.453$ simulations. The average value of the ratio is 16.6, and the standard deviation is 7.5.

Case	$(D^s_\infty)_{yy}$	v_y variance	$(D^s_\infty)_{yy}$ / v_y variance
ϕ_A=0.453			
FTSn6	0.13	0.00884	14.7
FTa2	0.34	0.01533	22.2
Fn2-3	0.20	0.01156	17.3
ef3	0.27	0.00854	31.6
nfr1	0.17	0.01990	8.5
n49b	0.21	0.02087	10.1
nfr2	0.21	0.01785	11.8
efr2	0.22	0.01318	16.7

Table 5.2 Comparison of $(D^s_\infty)_{xx}$, the v_x variance, and the ratio of the two for the $\phi_A = 0.453$ simulations. The average value of the ratio is 8.3, and the standard deviation is 3.3.

Case	$(D^s_\infty)_{xx}$	v_x variance	$(D^s_\infty)_{xx}$ / v_x variance
ϕ_A=0.453			
FTSn6	0.024	0.00287	8.4
FTn2	0.030	0.00847	3.5
FTa2	0.023	0.00704	3.3
Fn2-3	0.021	0.00336	6.2
ef3	0.023	0.00196	11.7
nfr1	0.065	0.00781	8.3
n49b	0.068	0.00655	8.7
nfr2	0.090	0.00677	13.7
efr2	0.027	0.00274	9.9

Table 5.3 The concentration dependence of $(D^s_\infty)_{yy}$, the v_y variance, and the ratio of the two. Note the decrease in the ratio as the concentration increases.

Case	$(D^s_\infty)_{yy}$	v_y variance	$(D^s_\infty)_{yy}$ / v_y variance
ϕ_A=0.1 phi1efr2	4.77	0.11198	42.6
ϕ_A=0.25 phi25efr2	1.05	0.05193	20.2
ϕ_A=0.453 efr2	0.22	0.01318	16.7
ϕ_A=0.6 phi6efr3	0.012	0.00213	5.63

Table 5.4 The concentration dependence of $(D^s_\infty)_{xx}$, the v_x variance, and the ratio of the two. Note that the ratio is relatively insensitive to the concentration.

Case	$(D^s_\infty)_{xx}$	v_x variance	$(D^s_\infty)_{xx}$ / v_x variance
ϕ_A=0.1 phi1efr2	0.11	0.01157	9.5
ϕ_A=0.25 phi25efr2	0.10	0.00998	10.0
ϕ_A=0.453 efr2	0.027	0.00274	9.9
ϕ_A=0.6 phi6efr3	0.0075	0.00062	12.4

Table 5.5 The ratio of velocity variances (ratio 1) and the ratio of the yy- and xx- components of the long-time, self-diffusion coefficient (ratio 2) for the $\phi_A = 0.453$ simulations. The average value of ratio 1 is 3.3, and the standard deviation is 0.9. The average value of ratio 2 is 7.0, and the standard deviation is 4.1.

Case	(v_y variance) / (v_x variance)	$(D^s_\infty)_{yy}$ / $(D^s_\infty)_{xx}$
ϕ_A=0.453		
FTSn6	3.1	5.4
FTn1		9.6
FTa2	2.2	14.8
Fn1		6.2
Fn2-3	3.4	9.5
ef3	4.4	11.7
nfr1	2.5	2.6
n49b	3.2	3.1
nfr2	2.6	2.3
efr2	4.8	8.1

Table 5.6 The concentration dependence of the ratio of the velocity variances and the ratio of the yy- and xx-components of the long-time, self-diffusion coefficient. Note the stronger increasing degree of anisotropy in the components of the diffusion coefficient as the concentration decreases.

Case	(v_y variance) / (v_x variance)	$(D^s_\infty)_{yy}$ / $(D^s_\infty)_{xx}$
ϕ_A=0.1 phi1efr2	9.6	43.3
ϕ_A=0.25 phi25efr2	5.2	10.5
ϕ_A=0.453 efr2	4.8	8.1
ϕ_A=0.6 phi6efr3	3.4	1.6

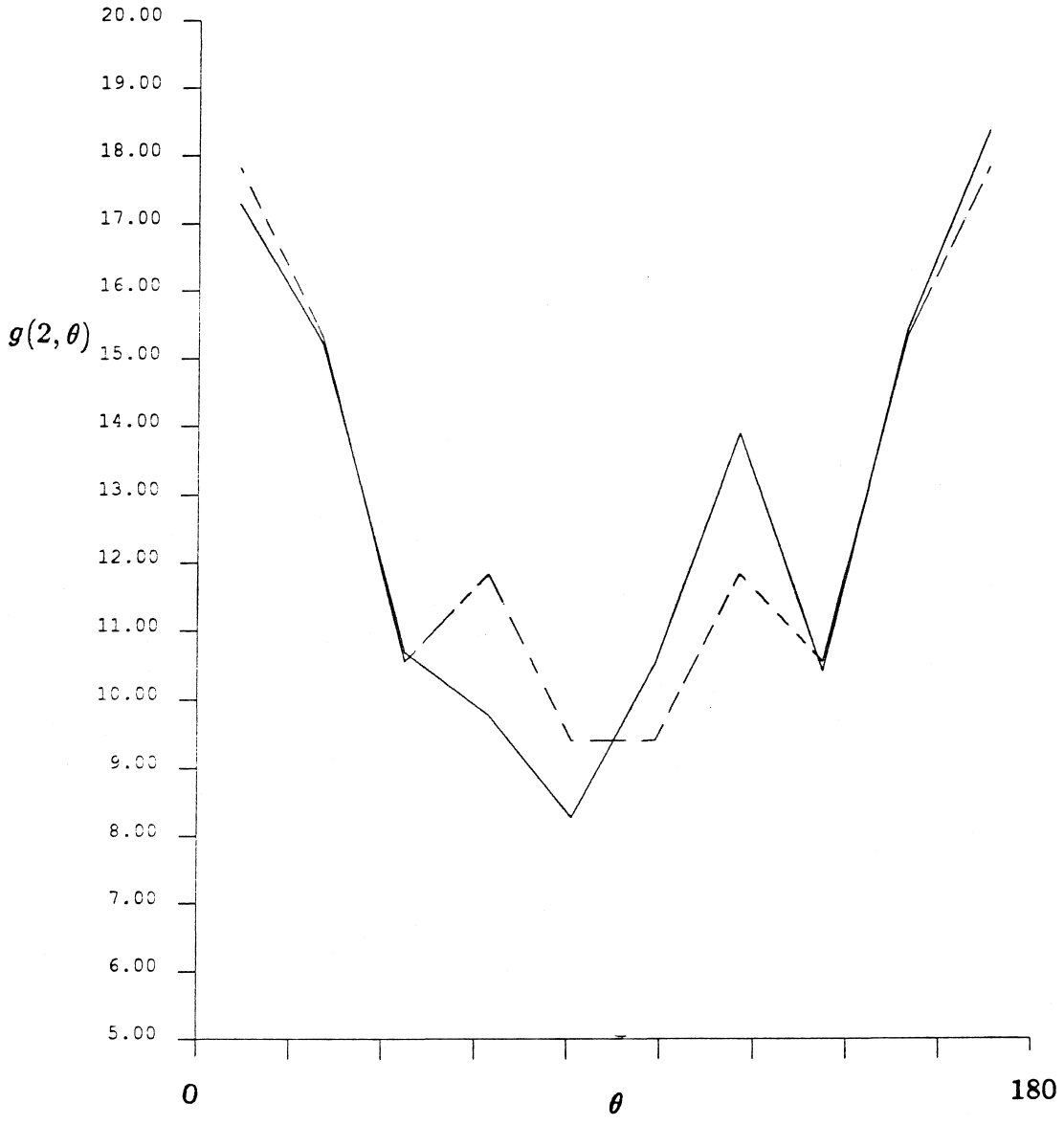

Figure 5.1 The full pair-distribution function for spheres whose surfaces are separated by less than 0.05 radii using data from the phi1efr2 run (t = 500 – 1000). $\phi_A = 0.1$. The dashed curve represents this function when it is forced to be symmetric about $\theta = 90°$.

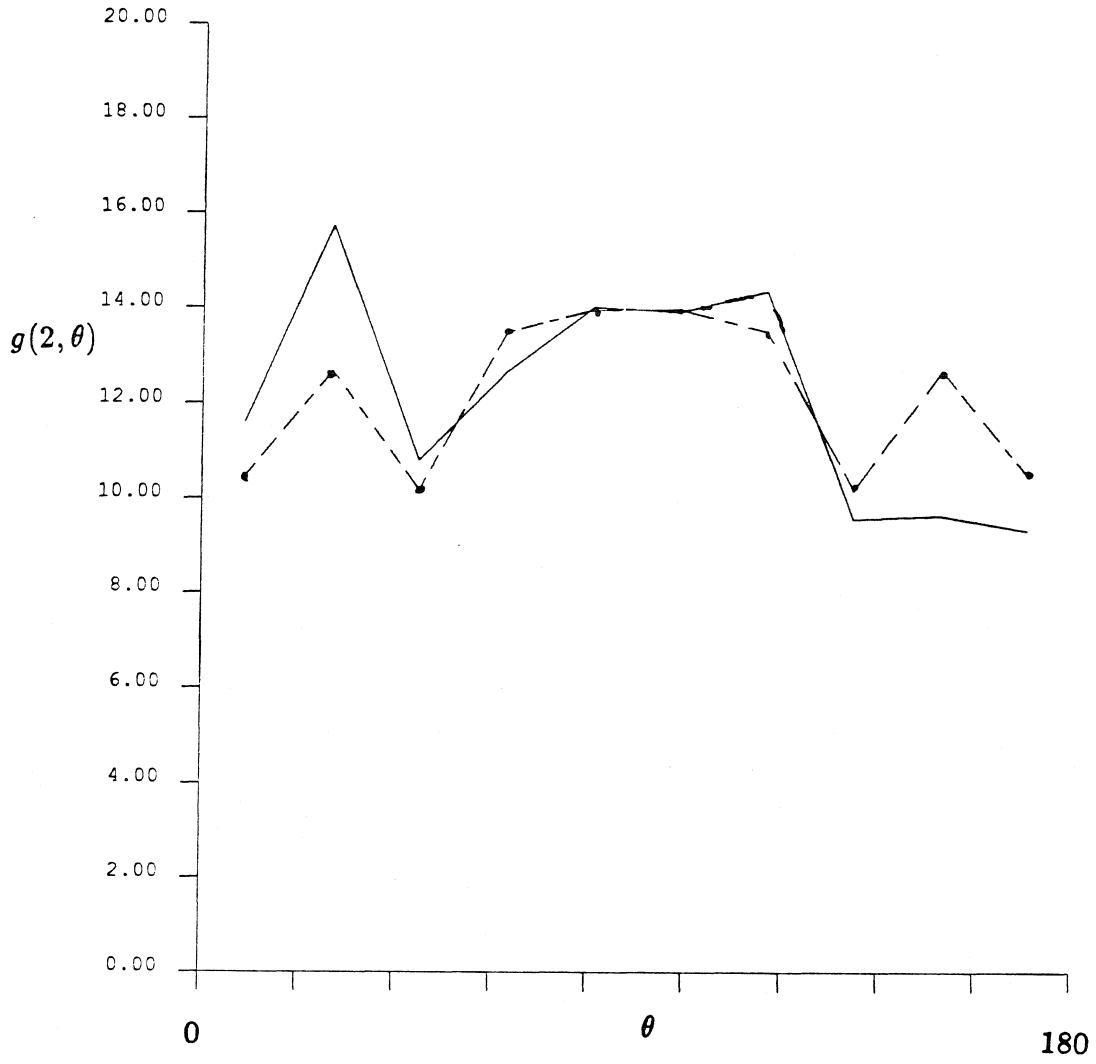

Figure 5.2 The full pair-distribution function for spheres whose surfaces are separated by less than 0.05 radii using data from the phi25efr2 run (t = 500 – 1000). $\phi_A = 0.25$. The dashed curve represents this function when it is forced to be symmetric about $\theta = 90°$.

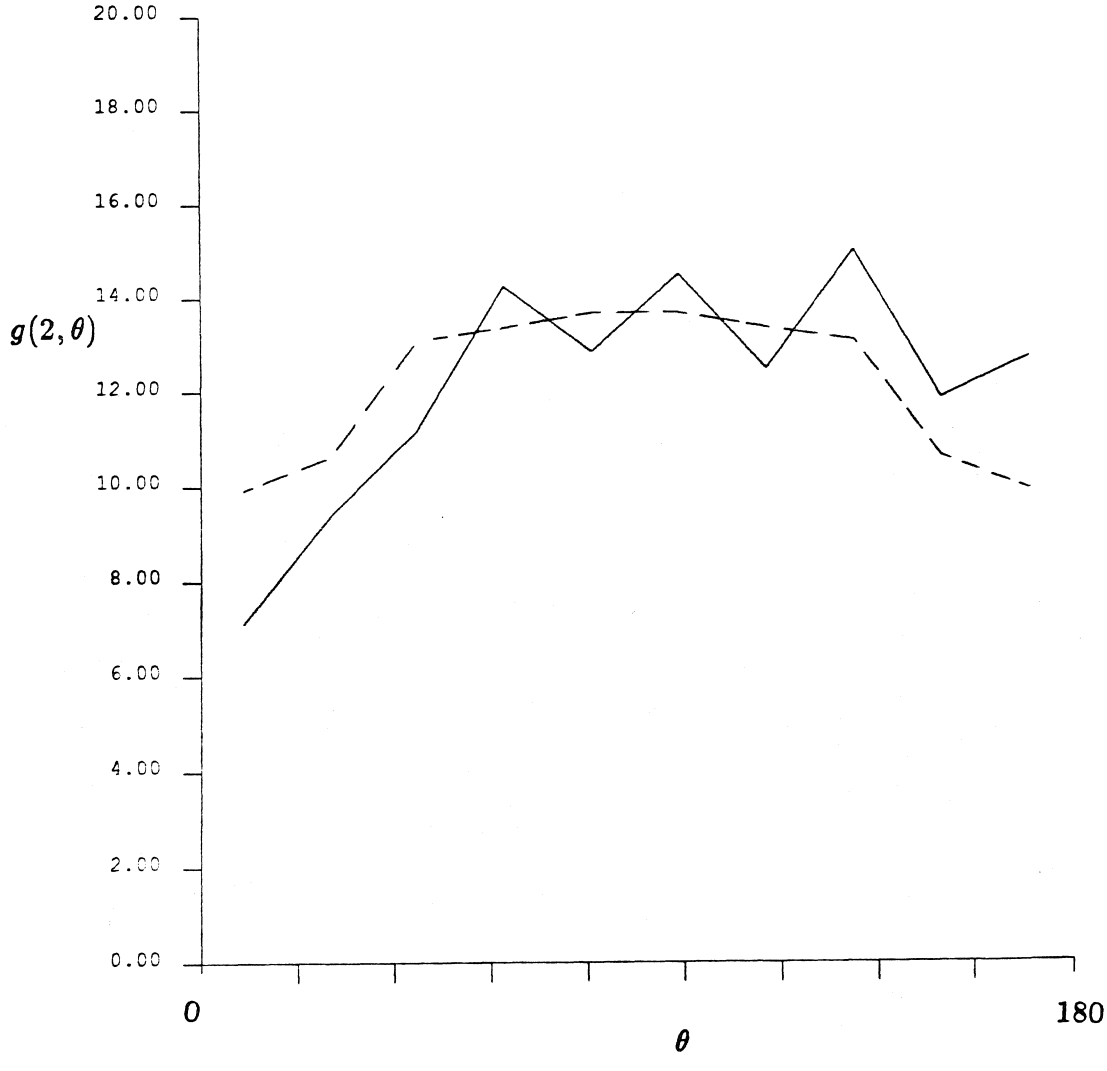

Figure 5.8 The full pair-distribution function for spheres whose surfaces are separated by less than 0.05 radii using data from the efr2 run (t = 100 – 500). $\phi_A = 0.453$. The dashed curve represents this function when it is forced to be symmetric about $\theta = 90°$.

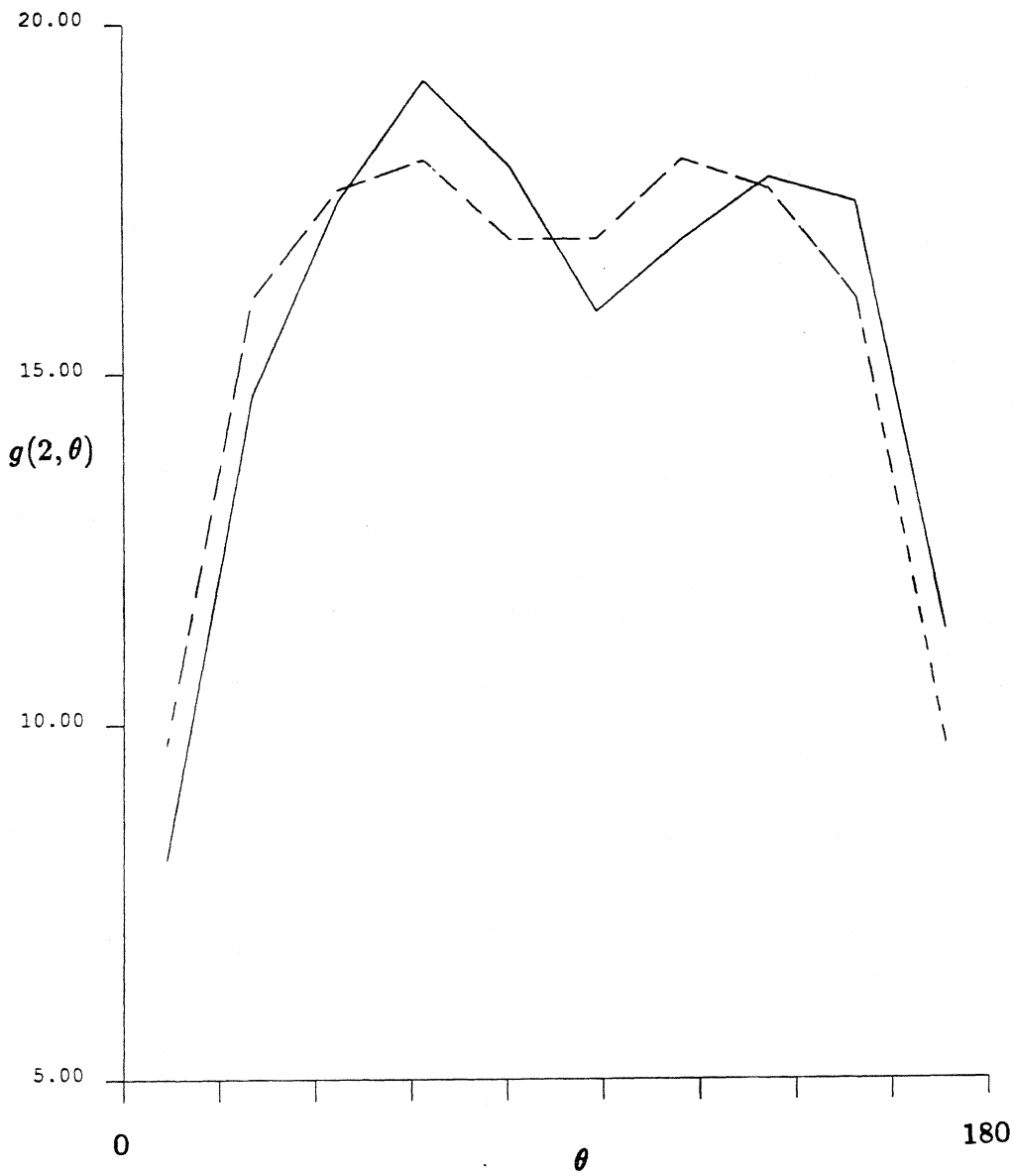

Figure 5.4 The full pair-distribution function for spheres whose surfaces are separated by less than 0.05 radii using data from the phi6efr3 run (t = 250 – 750). $\phi_A = 0.6$. The dashed curve represents this function when it is forced to be symmetric about $\theta = 90°$.

REFERENCES

Batchelor, G.K. 1970 The stress system in a suspension of force-free particles. *J. Fluid Mech.* **41**, 545-570.

Batchelor, G.K. 1972 Sedimentation in a dilute dispersion of spheres. *J. Fluid Mech.* **52**, 245-268.

Batchelor, G.K. 1976 Brownian diffusion of particles with hydrodynamic interaction. *J. Fluid Mech.* **74**, 1-29.

Batchelor, G.K. 1977 The effect of Brownian motion on the bulk stress in a suspension of spherical particles. *J. Fluid Mech.* **83**, 97-117.

Batchelor, G.K. 1982 Sedimentation in a dilute polydisperse system of interacting spheres. Part 1: General Theory. *J. Fluid Mech.* bf 119, 379-408.

Beenakker, C.W.J. and Mazur, P. 1982 Diffusion of spheres in suspension: Three-body hydrodynamic interaction effects. *Phys. Lett. A* **91**, 290-291.

Beenakker, C.W.J. and Mazur, P. 1983 Self-diffusion of spheres in a concentrated suspension. *Physica* **120A**, 338-410.

Beenakker, C.W.J. and Mazur, P. 1984 Diffusion in a concentrated suspension II. *Physica* **126A**, 349.

Beenakker, C.W.J. 1984 The effective viscosity of a concentrated suspension of spheres (and its relation to diffusion). *Physica* **128A**, 48-81.

Beenakker, C.W.J. 1986 Ewald sum of the Rotne-Prager tensor. *J. Chem. Phys.* **85**, 1581-1582.

Berne, B.J. and Pecora, R. 1976 *Dynamic Light Scattering* Wiley, N.Y.

Bossis, G. and Brady, J.F. 1984 Dynamic simulation of sheared suspensions. I. General Method. *J. Chem. Phys.* **80**, 5141-5154.

Bossis, G. and Brady, J.F. 1987 Self-diffusion of Brownian particles in concentrated suspensions under shear. *J. Chem. Phys.* (to appear).

Brady, J.F. and Bossis, G. 1985 The rheology of concentrated suspensions of spheres in simple shear flow by numerical simulation. *J. Fluid Mech.* **155** 105-129.

Brady, J.F. and Bossis, G. 1988 Stokesian dynamics. *Ann. Rev. Fluid Mech.* **20**, 111-157.

Brady, J.F. and Durlofsky, L. 1988 On the sedimentation rate of disordered suspensions. *Phys. Fluid* (to appear).

Brady, J.F., Phillips, R.J., Lester, J.C. and Bossis G. 1987 Dynamic simulation of hydrodynamically interacting suspensions. *J. Fluid Mech.* (submitted).

Brenner, H. and O'Neill, M.E. 1972 On the Stokes resistance of multiparticle systems in a linear shear field. *Chem. Eng. Sci.* **27**, 1421-1439

Chae, D.G., Ree, F.H., and Ree, J. 1969 Radial distribution functions and equation of state of the hard-disk fluid. *J. Chem. Phys.* **50**, 1581-1589.

Durlofsky, L., Brady, J.F. and Bossis G. 1987 Dynamic simulation of hydrodynamically interacting particles. *J. Fluid Mech.* **180**, 21-49.

Ermak, D.L. and McCammon, J.A. 1978 Brownian dynamics with hydrodynamic interactions. *J. Chem. Phys.* **69**, 1352-1360.

Ewald, P.P. 1921 Die berechnung optischa und elektrostatischer Gitterpotentiale. *Annalen Phys.* **64**, 253-287.

Glendinning, A.B. and Russel, W.B. 1982 A pairwise additive description of sedimentation and diffusion in concentrated suspensions of hard spheres. *J. Colloid Interface Sci.* **89**, 124-143.

Ham, J. and Homsy, G. 1987 APS conference.

Kim, S. and Mifflin, R.T. 1985 The resistance and mobility functions of two equal spheres in low-Reynolds-number flow. *Phys. Fluids* **28**, 2033-2045.

Koch, D. and Shaqfeh, E. 1987 AIChE conference.

Leighton, D. and Acrivos, A. 1987 Measurement of shear-induced self-diffusion in concentrated suspensions of spheres. *J. Fluid Mech.* **177**, 109-131.

Nunan, K.C. and Keller, J.B. 1984 Effective viscosity of a periodic suspension. *J. Fluid Mech.* **142**, 269-287.

O'Brien, R.W. 1979 A method for the calculation of the effective transport properties of suspensions of interacting particles. *J. Fluid Mech.* **56**, 401-427.

Okagawa, A., Ennis, G.J. and Mason, S.G. 1978 Memory impairment in flowing suspensions. I. Some theoretical considerations. *Can. J. Chem.* **56**, 2815.

Phillips, R.J., Brady, J.F. and Bossis, G. 1988 Hydrodynamic transport properties of hard-sphere dispersions. (in preparation).

Rallison, J.M. and Hinch, J. 1986 The effect of particle interactions on dynamic light scattering from a dilute suspension. *J. Fluid Mech.* **167**, 131-168.

Saffman, P.G. 1973 On the settling speed of free and fixed suspensions. *Studies Appl. Math.* **52**, 115-127.

Zick, A. and Homsy, G.M. 1982 Stokes flow through periodic arrays of spheres. *J. Fluid Mech.* **115**, 13-26.

Zuzovsky, M., Adler, P.M. and Brenner, H. 1983 Spatially periodic suspensions of convex particles in linear shear flows. III. Dilute arrays of spheres suspended in Newtonian fluids. *Phys. Fluids* **26**, 1714-1723.

APPENDIX A: EWALD SUM OF THE MOBILITY INTERACTIONS

We record here the real ($\mathbf{M}^{(1)}(\mathbf{r})$) and reciprocal ($\mathbf{M}^{(2)}(\mathbf{k})$) space parts of the Ewald summed mobility interactions. Use has been made of Faxén formulae for the velocities of the particles to include the finite size of the particles. The translational velocity/force coupling was first derived by Beenakker (1986); the remaining can be worked out by straightforward, but tedious, calculus. ξ is an inverse length that regulates the speed of convergence of the two sums, $\mathbf{e}$ is a unit vector along the line connecting the particle centers, r is the interparticle separation distance, and $\hat{\mathbf{k}}$ is a unit vector in the reciprocal lattice. All lengths have been nondimensionalized by the particle radius a, and a common normalization of $6\pi\eta a^{\mathrm{n}}$ has been used, where $\mathrm{n} = 1, 2$ or 3 depending on the mobility coupling.

(a) Translational velocity/force, $U - F$, coupling:

$$\begin{aligned} M_{ij}^{(1)}(\mathbf{r}) = \delta_{ij}\Bigg\{ & \left(\frac{3}{4}\frac{1}{r} + \frac{1}{2}\frac{1}{r^3}\right)\mathrm{erfc}(\xi r) + \frac{1}{\sqrt{\pi}}(4\xi^7 r^4 + 3\xi^3 r^2 \\ & - 20\xi^5 r^2 - \frac{9}{2}\xi + 14\xi^3 + \xi/r^2)e^{-\xi^2 r^2}\Bigg\} \\ & + e_i e_j\Bigg\{\left(\frac{3}{4}\frac{1}{r} - \frac{3}{2}\frac{1}{r^3}\right)\mathrm{erfc}(\xi r) + \frac{1}{\sqrt{\pi}}(-4\xi^7 r^4 - 3\xi^3 r^2 \\ & + 16\xi^5 r^2 + \frac{3}{2}\xi - 2\xi^3 - 3\xi/r^2)e^{-\xi^2 r^2}\Bigg\}, \end{aligned} \tag{A1}$$

$$\begin{aligned} M_{ij}^{(2)}(\mathbf{k}) = (\delta_{ij} - \hat{k}_i\hat{k}_j)(1 - k^2/3)(1 + \frac{1}{4}k^2/\xi^2 + \frac{1}{8}k^4/\xi^4)6\pi k^{-2} \\ \mathrm{x}\ \exp(-\frac{1}{4}k^2/\xi^2), \end{aligned} \tag{A2}$$

$$M_{ij}^{(2)}(\mathbf{r} = 0) = \frac{1}{\sqrt{\pi}}(6\xi - \frac{40}{3}\xi^3). \tag{A3}$$

(b) Translational velocity/torque, $U - L$, coupling:

$$\begin{aligned} M_{ij}^{(1)}(\mathbf{r}) = -\frac{3}{8}\epsilon_{lkj}\Bigg\{ & \left[-\frac{1}{r^3}\mathrm{erfc}(\xi r) + \frac{2}{\sqrt{\pi}}\xi\left(-\frac{1}{r^2} + 10\xi^2 - 4\xi^4 r^2\right)e^{-\xi^2 r^2}\right]e_k\delta_{il} \\ & + \left[\frac{1}{r^3}\mathrm{erfc}(\xi r) + \frac{2}{\sqrt{\pi}}\xi(\frac{1}{r^2} - 2\xi^2)e^{-\xi^2 r^2}\right]e_l\delta_{ik}\Bigg\}, \end{aligned} \tag{A4}$$

$$M_{ij}^{(2)}(\mathbf{k}) = 3\pi(\epsilon_{ikj}\hat{k}_k)(\frac{1}{k} + \frac{1}{4}k/\xi^2 + \frac{1}{8}k^3/\xi^4)\exp(-\frac{1}{4}k^2/\xi^2), \tag{A5}$$

$$M_{ij}^{(2)}(\mathbf{r}=0) = 0. \tag{A6}$$

(c) Rotational velocity/torque, $\Omega - L$, coupling:

$$M_{ij}^{(1)}(\mathbf{r}) = \delta_{ij}\left\{-\frac{3}{8}\frac{1}{r^3}\mathrm{erfc}(\xi r) - \frac{3}{\sqrt{\pi}}(\xi/r^2 + 14\xi^3 - 20\xi^5 r^2 + 4\xi^7 r^4)e^{-\xi^2 r^2}\right\} \tag{A7}$$
$$- \frac{3}{4}e_i e_j\left\{-\frac{3}{2}\frac{1}{r^3}\mathrm{erfc}(\xi r) + \frac{1}{\sqrt{\pi}}(-3\xi/r^2 - 2\xi^3 + 16\xi^5 r^2 - 4\xi^7 r^4)e^{-\xi^2 r^2}\right\}$$

$$M_{ij}^{(2)}(\mathbf{k}) = \frac{3\pi}{2}(\delta_{ij} - \hat{k}_i\hat{k}_j)(1 + \frac{1}{4}k^2/\xi^2 + \frac{1}{8}k^4/\xi^4)\exp(-\frac{1}{4}k^2/\xi^2), \tag{A8}$$

$$M_{ij}^{(2)}(\mathbf{r}=0) = \frac{10}{\sqrt{\pi}}\xi^3. \tag{A9}$$

(d) Translational velocity/stresslet, $U - S$, coupling:

$$M_{ijk}^{(1)}(\mathbf{r}) = \frac{3}{8}\left\{(x_4 + x_5)(e_k\delta_{ij} + e_j\delta_{ik}) + 2x_5(e_i\delta_{jk}) + 2x_6(e_i e_j e_k)\right.$$
$$\left. + \frac{4}{15}\left[(x_1 + x_2)(e_k\delta_{ij} + e_j\delta_{ik}) + 2x_2(e_i\delta_{jk}) + 2x_3(e_i e_j e_k)\right]\right\}, \tag{A10}$$

$$M_{ijk}^{(2)}(\mathbf{k}) = -3\pi(1 - \frac{4}{15}k^2)[\hat{k}_k(\delta_{ij} - \hat{k}_i\hat{k}_j) + \hat{k}_j(\delta_{ik} - \hat{k}_i\hat{k}_k)]$$
$$\mathrm{x}\ (1/k + \frac{1}{4}k/\xi^2 + \frac{1}{8}k^3/\xi^4)\exp(-\frac{1}{4}k^2/\xi^2), \tag{A11}$$

$$M_{ijk}^{(2)}(\mathbf{r}=0) = 0. \tag{A12}$$

where

$$x_1 = -6\frac{1}{r^4}\mathrm{erfc}(\xi r) + \frac{4}{\sqrt{\pi}}(-3\xi/r^3 - 2\xi^3/r - 68\xi^5 r + 56\xi^7 r^3 - 8\xi^9 r^5)e^{-\xi^2 r^2},$$
$$x_2 = 4\left[-\frac{3}{2}\frac{1}{r^4}\mathrm{erfc}(\xi r) + \frac{1}{\sqrt{\pi}}(-3\xi/r^3 - 2\xi^3/r + 16\xi^5 r - 4\xi^7 r^3)e^{-\xi^2 r^2}\right],$$

$$x_3 = 4\left[\frac{15}{2}\frac{1}{r^4}\mathrm{erfc}(\xi r) + \frac{1}{\sqrt{\pi}}(15\xi/r^3 + 10\xi^3/r + 4\xi^5 r - 40\xi^7 r^3 + 8\xi^9 r^5)e^{-\xi^2 r^2}\right],$$

$$x_4 = -\frac{1}{r^2}\mathrm{erfc}(\xi r) + \frac{2}{\sqrt{\pi}}\xi(-1/r + 10\xi^2 r - 4\xi^4 r^3)e^{-\xi^2 r^2},$$

$$x_5 = \frac{1}{r^2}\mathrm{erfc}(\xi r) + 2\sqrt{\pi}\xi(1/r - 2\xi^2 r)e^{-\xi^2 r^2}, \qquad (A13)$$

$$x_6 = -\frac{3}{r^2}\mathrm{erfc}(\xi r) + \frac{2}{\sqrt{\pi}}\xi(-3/r - 2\xi^2 r + 4\xi^4 r^3)e^{-\xi^2 r^2}.$$

(e) Rotational velocity/stresslet, $\Omega - S$, coupling:

$$M^{(1)}_{ijk}(\mathbf{r}) = -\frac{3}{16}(y_2 - y_1)[\hat{k}_k(\hat{k}_l\epsilon_{lik})], \qquad (A14)$$

$$M^{(2)}_{ijk}(\mathbf{k}) = -\frac{3\pi}{2}[\hat{k}_k(\hat{k}_l\epsilon_{lij}) + \hat{k}_j(\hat{k}_l\epsilon_{lik})](1 + \frac{1}{4}k^2/\xi^2 + \frac{1}{8}k^4/\xi^4)$$
$$\mathrm{x}\ \exp(-\frac{1}{4}k^2/\xi^2), \qquad (A15)$$

$$M^{(2)}_{ijk}(\mathbf{r} = 0) = 0, \qquad (A16)$$

where

$$y_1 = \frac{3}{r^3}\mathrm{erfc}(\xi r) + \frac{2}{\sqrt{\pi}}\xi(3/r^2 + 2\xi^2 - 28\xi^4 r^2 + 8\xi^6 r^4)e^{-\xi^2 r^2},$$

$$y_2 = -\frac{3}{r^3}\mathrm{erfc}(\xi r) + \frac{2}{\sqrt{\pi}}\xi(3/r^2 - 2\xi^2 - 4\xi^4 r^2)e^{-\xi^2 r^2}. \qquad (A17)$$

(f) Rate of strain/stresslet, $E - S$, coupling:

$$M^{(1)}_{iljk}(\mathbf{r}) = -\frac{3}{16}r^2 M^{(1A)}_{iljk}(\mathbf{r}) - \frac{3}{80}M^{(1B)}_{iljk}(\mathbf{r}), \qquad (A18)$$

$$M^{(2)}_{iljk}(\mathbf{k}) = \frac{3\pi}{2}(1 - \frac{1}{5}k^2)[\hat{k}_l\hat{k}_k(\delta_{ij} - \hat{k}_i\hat{k}_j) + \hat{k}_l\hat{k}_j(\delta_{ik} - \hat{k}_i\hat{k}_k)$$
$$+ \hat{k}_i\hat{k}_k(\delta_{lj} - \hat{k}_l\hat{k}_j) + \hat{k}_i\hat{k}_j(\delta_{lk} - \hat{k}_l\hat{k}_k)](1 + \frac{1}{4}k^2/\xi^2$$
$$+ \frac{1}{8}k^4/\xi^4)\exp(-\frac{1}{4}k^2/\xi^2), \qquad (A19)$$

$$M^{(2)}_{iljk}(\mathbf{r} = 0) = \frac{3}{\sqrt{\pi}}\left(2\xi^3 - \frac{126}{25}\xi^5\right)\left(\delta_{ij}\delta_{lk} + \delta_{ik}\delta_{lj} - \frac{2}{3}\delta_{il}\delta_{jk}\right), \qquad (A20)$$

where

$$M^{(1A)}_{iljk}(\mathbf{r}) = 2(z_3+z_1)(\delta_{lk}\delta_{ij}+\delta_{jl}\delta_{ik})+4z_3\delta_{jk}\delta_{il}$$
$$+(z_2+3z_4)(\delta_{ij}e_le_k+\delta_{jl}e_ie_k+\delta_{lk}e_ie_j+\delta_{ik}e_je_l) \qquad (A21)$$
$$+4z_4(\delta_{il}e_je_k+\delta_{jk}e_ie_l)+4z_5e_ie_je_ke_l,$$

$$M^{(1B)}_{iljk}(\mathbf{r}) = 2(D2z_1+2z_2+6z_4+D2z_3)(\delta_{jl}\delta_{ki}+\delta_{kl}\delta_{ij})$$
$$+4(D2z_3+4z_4)\delta_{jk}\delta_{il}+4(D2z_4+2z_5+4Dz_4)(\delta_{il}e_ke_j+\delta_{jk}e_ie_l)$$
$$+[3(D2z_4+2z_5+4Dz_4)+4Dz_2+D2z_2+2z_5](\delta_{ik}e_je_l$$
$$+\delta_{kl}e_ie_j+\delta_{jl}e_ie_k+\delta_{ij}e_ke_l)+4(8Dz_5+D2z_5)e_ie_je_ke_l, \qquad (A22)$$

and

$$z_1 = -1/r^5\mathrm{erfc}(\xi r)+\frac{2}{\sqrt{\pi}}\xi(-1/r^4+10\xi^2-4\xi^4)e^{-\xi^2r^2}$$
$$z_2 = 3/r^5\mathrm{erfc}(\xi r)+\frac{2}{\sqrt{\pi}}\xi(3/r^4-28\xi^4+2\xi^2+8\xi^6r^2)e^{-\xi^2r^2}$$
$$z_3 = 1/r^5\mathrm{erfc}(\xi r)+\frac{2}{\sqrt{\pi}}\xi(1/r^4-2\xi^2/r^2)e^{-\xi^2r^2}$$
$$z_4 = -3/r^5\mathrm{erfc}(\xi r)+\frac{2}{\sqrt{\pi}}\xi(-3/r^4-2\xi^2+4\xi^4)e^{-\xi^2r^2}$$
$$z_5 = 15/r^5\mathrm{erfc}(\xi r)+\frac{2}{\sqrt{\pi}}\xi(15/r^4+10\xi^2/r^2+4\xi^4-8\xi^6r^2)e^{-\xi^2r^2}$$
$$Dz_1 = 3/r^5\mathrm{erfc}(\xi r)+\frac{2}{\sqrt{\pi}}\xi(3/r^4-8\xi^4+2\xi^2/r^2-20\xi^4+8\xi^6r^2)e^{-\xi^2r^2}$$
$$Dz_2 = -15/r^5\mathrm{erfc}(\xi r)+\frac{2}{\sqrt{\pi}}\xi(-15/r^4-10\xi^2/r^2+72\xi^6r^2-4\xi^4-16\xi^8r^4)e^{-\xi^2r^2}$$
$$Dz_3 = -3/r^5\mathrm{erfc}(\xi r)+\frac{2}{\sqrt{\pi}}\xi(-3/r^4-2\xi^2/r^2+4\xi^4)e^{-\xi^2r^2}$$
$$Dz_4 = 15/r^5\mathrm{erfc}(\xi r)+\frac{2}{\sqrt{\pi}}\xi(15/r^4+10\xi^2/r^2+4\xi^4-8\xi^6r^z)e^{-\xi^2r^2}$$
$$Dz_5 = -105/r^5\mathrm{erfc}(\xi r)+\frac{2}{\sqrt{\pi}}\xi(-105/r^4-70\xi^z/r^2-28\xi^4-8\xi^6r^2+16\xi^8r^4)e^{-\xi^2r^2}$$
$$D2z_1 = -6/r^5\mathrm{erfc}(\xi r)+\frac{2}{\sqrt{\pi}}\xi(-6/r^4-88\xi^4-4\xi^2/r^2+96\xi^6r^2-16\xi^8r^4)e^{-\xi^2r^2}$$
$$D2z_2 = 60/r^5\mathrm{erfc}(\xi r)+\frac{2}{\sqrt{\pi}}\xi(60/r^4+40\xi^2/r^2+224\xi^6r^2+16\xi^4-224\xi^8r^4$$

$$+32\xi^{10}r^6)e^{-\xi^2r^2}$$

$$D2z_3 = 6/r^5\mathrm{erfc}(\xi r) + \frac{2}{\sqrt{\pi}}\xi(6/r^4 + 4\xi^2/r^2 + 16\xi^4 - 8\xi^6r^2)e^{-\xi^2r^2}$$

$$D2z_4 = -60/r^5\mathrm{erfc}(\xi r) + \frac{2}{\sqrt{\pi}}\xi(-60/r^4 - 40\xi^2/r^2 - 16\xi^4 - 32\xi^6r^2 + 16\xi^8r^4)e^{-\xi^2r^2}$$

$$D2z_5 = 630/r^5\mathrm{erfc}(\xi r) + \frac{2}{\sqrt{\pi}}\xi(630/r^4 + 420\xi^2/r^2 + 168\xi^4 + 48\xi^6r^2$$

$$+649^8r^4 - 32\xi^{10}r^6)e^{-\xi^2r^2}$$

APPENDIX B: SIMULATION RESULTS

This appendix contains the results of all the simulations discussed in Chapter 4. The appendix is divided into fifteen sections. Each section contains the results of one particular type of simulation; e.g., Appendix B1 contains the results of a sedimenting monolayer whose mobility interactions are approximated using the non-Ewald, FTS method. At the beginning of each section will be a description of the simulations within that section. This description will include the type of method used to approximate the mobility interactions, the number of spheres in the periodic cell, the areal fraction, the total time span, the time step, the frequency at which the mobility matrix is inverted, the convergence factors (in cases where the Ewald method is used), and any comments pertaining to the simulation or its results. (Unless noted, every type of simulation began with the same initial configuration of 25 spheres. This initial configuration is the result of a monolayer, Monte-Carlo simulation. All simulation use a fourth-order, Adams-Bashforth integrator to advance the sphere positions.)

After this description will appear a table listing important information for each simulation in that section. This includes the time units covered by each simulation, the computer the simulation was run on, how many CPU minutes were required, the average values of v_y, v_x, the v_y variance, the v_x variance, the v_{xy} variance, the long-time, self-diffusion coefficient in both directions, the time-averaged components of the short-time, self-diffusion tensor, and the values of the radial, pair-distribution function at $r = 2.0$, 3.5, and 4.0 radii. The time averages are over the time span of the individual simulation runs. The simulations are run on either a Sun 3/260 with a floating point accelerator or the Cray XMP at the San Diego Supercomputer Center. The numbers after the Cray designations are the priority that the simulation was run at. Dividing the CPU time by the priority gives the actual CPU time required on the Cray.

In each section, after this introductory material, there will be figures expressing the results of the simulation. In general, each section will contain: 1) the time trace of v_y; 2) the time trace of the v_y variance; 3) the time trace of the v_x variance; 4) the $(D^s_\infty)_{yy}$-defining curves; 5) the $(D^s_\infty)_{xx}$-defining curves; 6) the time trace of the components of the short-time, self-diffusion tensor; 7) the radial, pair-distribution function; 8) the full, pair-distribution function for spheres whose surfaces are separated by less than 0.05 radii; 8) any "snapshots" of the suspension microstructure taken from the simulation data.

Appendix B1: The FTSn simulation results

This suite of simulations uses a non-Ewald, FTS method to approximate the hydrodynamic interactions. Six separate simulation runs follow the evolution of a sedimenting system to a final time of 800 time units. There are 25 spheres within the periodic cell. The areal fraction is 0.453. There are no interparticle forces present. The time step is 0.001 time unit. The grand mobility matrix is inverted every 0.1 time unit. Position and velocity data is saved every 0.05 time unit. $\mathbf{D}_o^s$ is evaluated and reported at every time unit. The restart of run FTSn5 at $t = 380$ provides some idea of the effect that truncating the sphere position and velocity data at six decimal places (the computers normally carry sixteen decimal places). Attention is drawn to the time traces between $t = 380 - 400$.

	FTSn1	FTSn2	FTSn3	FTSn4	FTSn5	FTSn6
T	0-100	100-200	200-300	300-400	380-500	500-800
Cray/Sun	Sun	Sun	Sun	Sun	Cray 1.00	Sun
CPU(min)	1054	1023	1024	1029	52.33	3136
v_y	-6.33723	-6.32760	-6.33077	-6.32677	-6.26940	-6.25671
v_x	0.01474	-0.04167	-0.00318	0.01589	-0.00277	-0.02200
v_y variance	0.01438	0.02457	0.03918	0.02357	0.00582	0.00884
v_x variance	0.00797	0.00976	0.00766	0.00542	0.00251	0.00287
v_{xy} variance	-0.00261	-0.00181	-0.00041	0.00100	0.00033	-0.00066
$(D_\infty^s)_{yy}$				0.77	0.11	0.13
$(D_\infty^s)_{xx}$			0.035	0.030	0.030	0.024
$(D_o^s)_{yy}$	0.571	0.418	0.415	0.364	0.345	0.299
$(D_o^s)_{xx}$	0.561	0.417	0.413	0.372	0.355	0.315
$(D_o^s)_{xy}$	0.0006	0.0006	-0.0047	-0.0056	-0.0032	0.0042
$g(2)$					12.1	12.5
$g(3.5)$					5.38	10.8
$g(4)$					5.32	8.85

Table B1.1

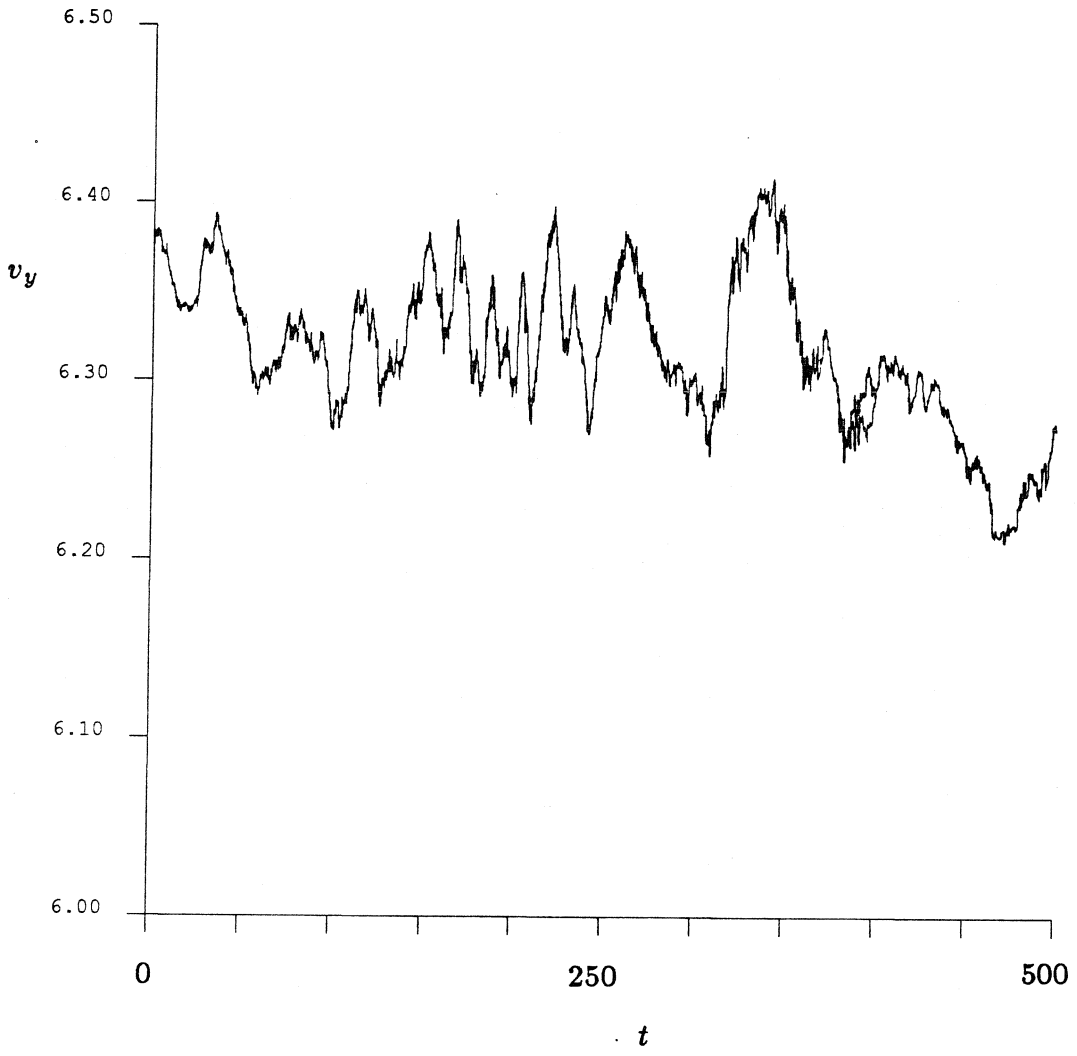

Figure B1.1 The time trace of v_y for the simulations FTSn1 through FTSn5. The double line from t=380 – 400 show the deviation that can occur when a restart of the simulation run is done.

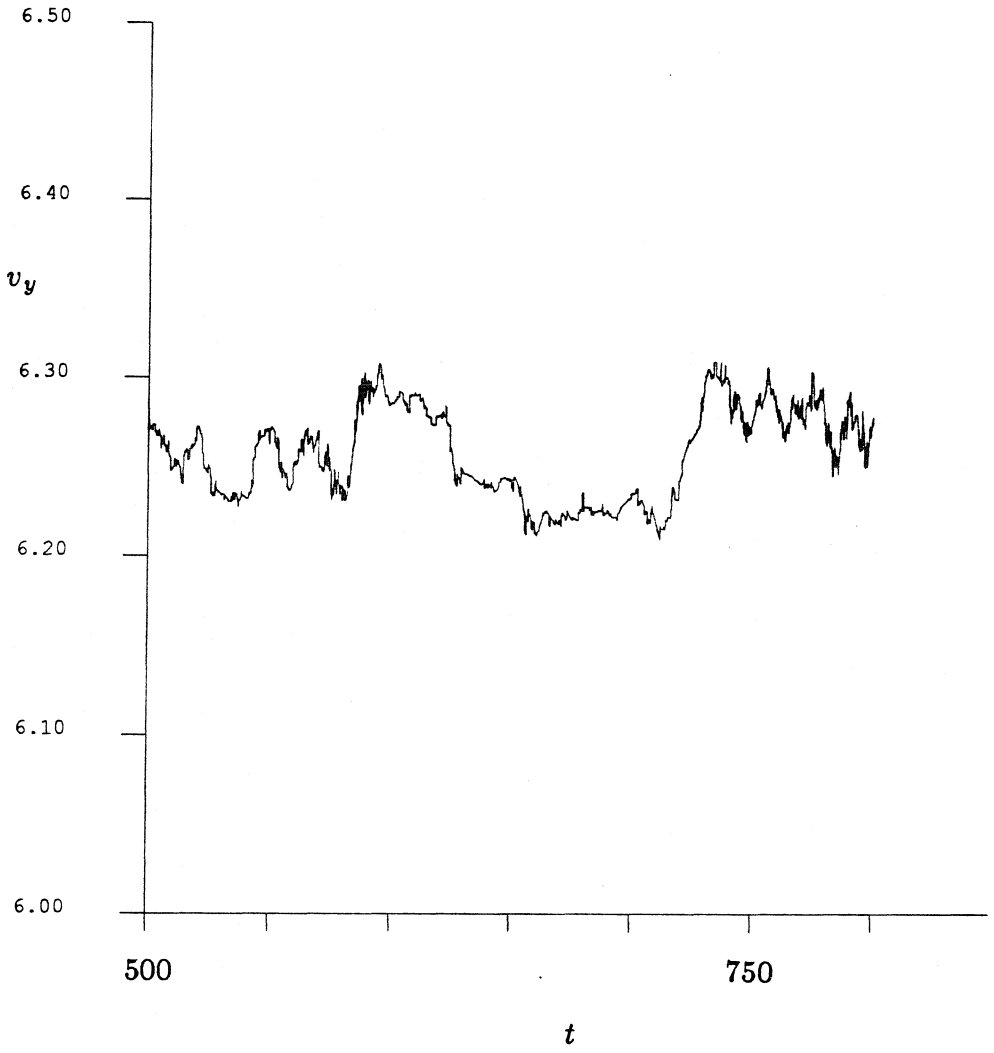

Figure B1.2 The time trace of v_y for the simulation FTSn6.

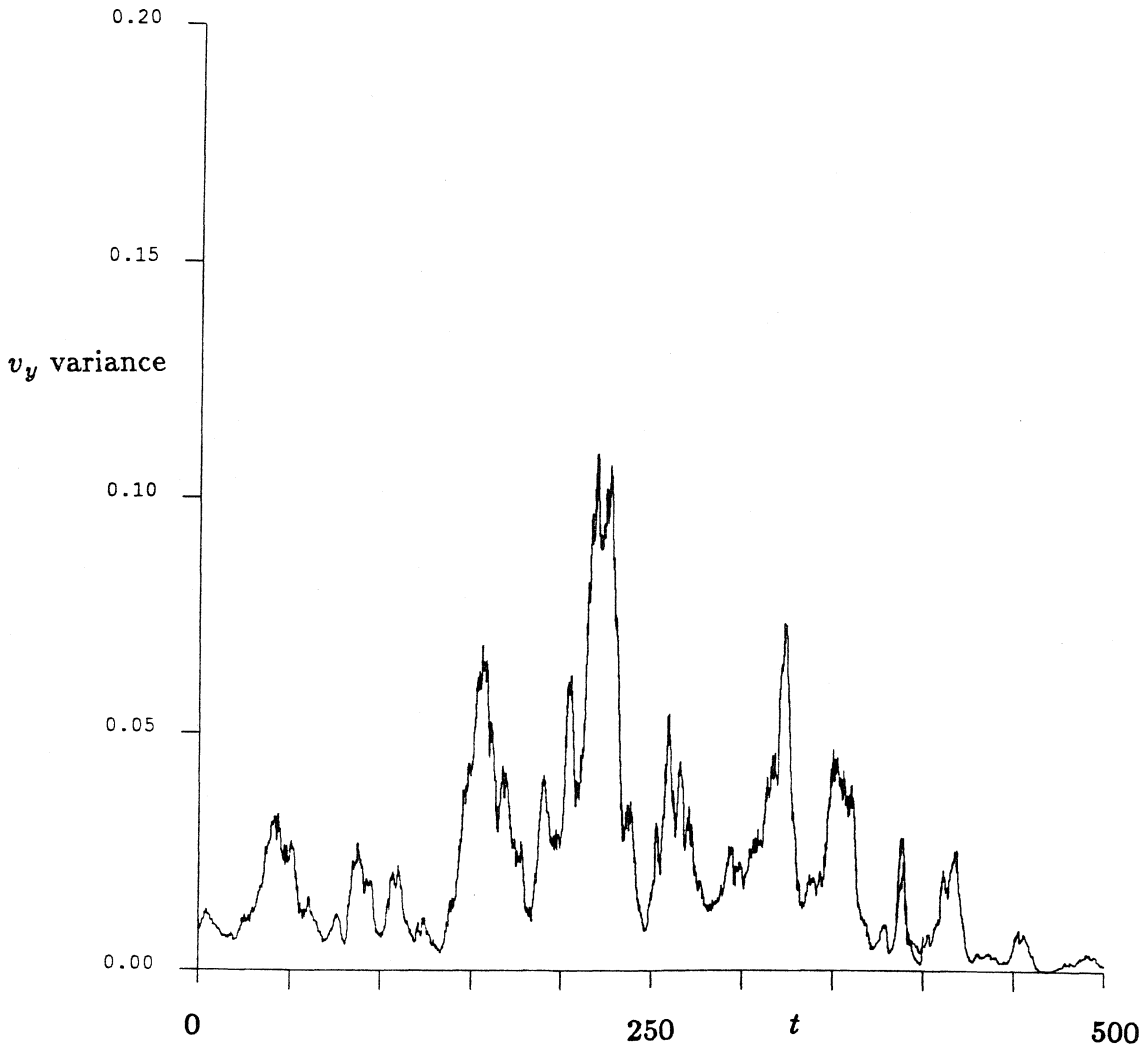

Figure B1.3 The time trace of the v_y variance for the simulations FTSn1 through FTSn5. The double line from t=380 – 400 show the deviation that can occur when a restart of the simulation run is done. This deviation is much smaller than seen in the v_y velocity trace.

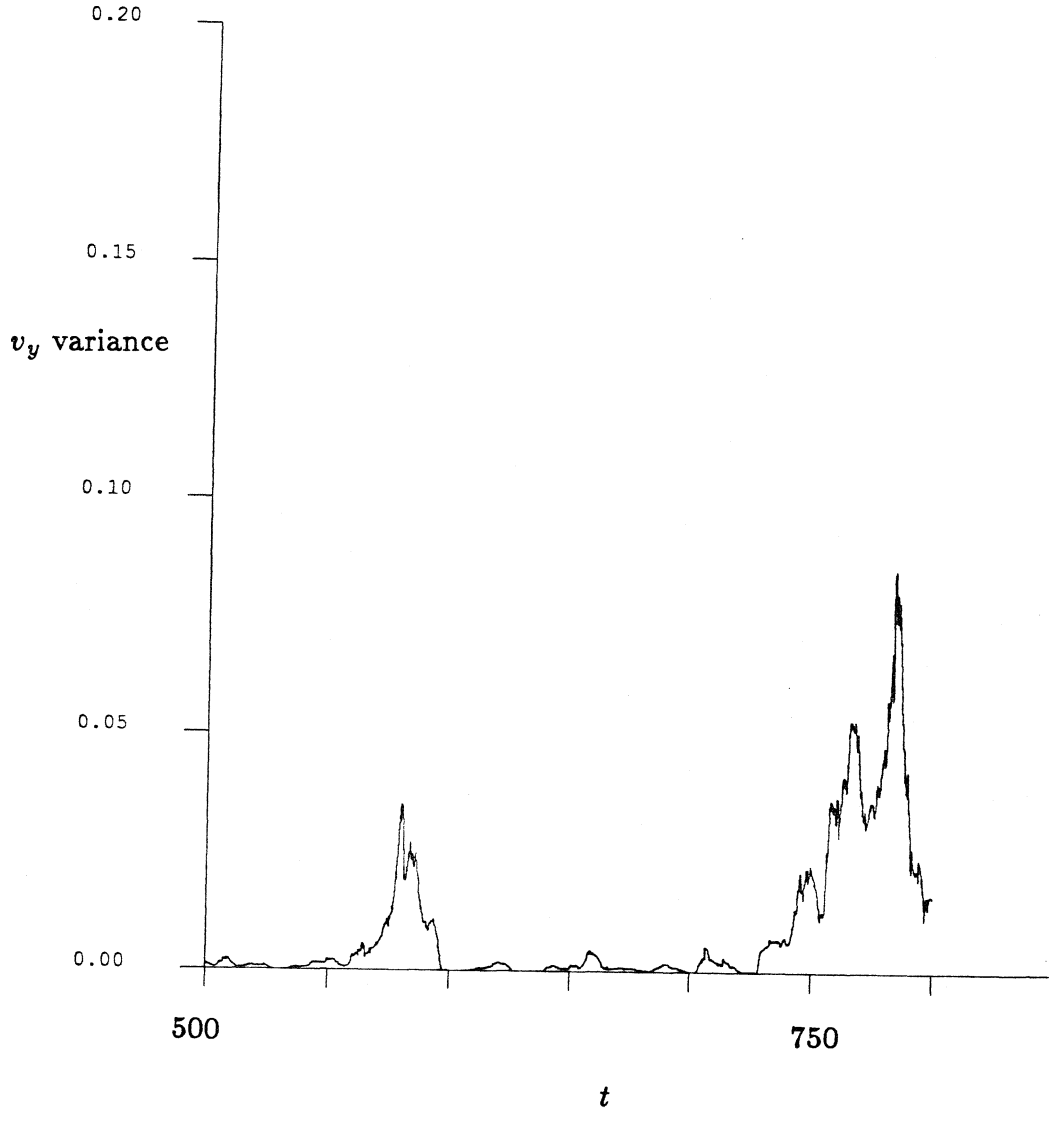

Figure B1.4 The time trace of the v_y variance for the simulation FTSn6. Note the long periods of near-zero variance.

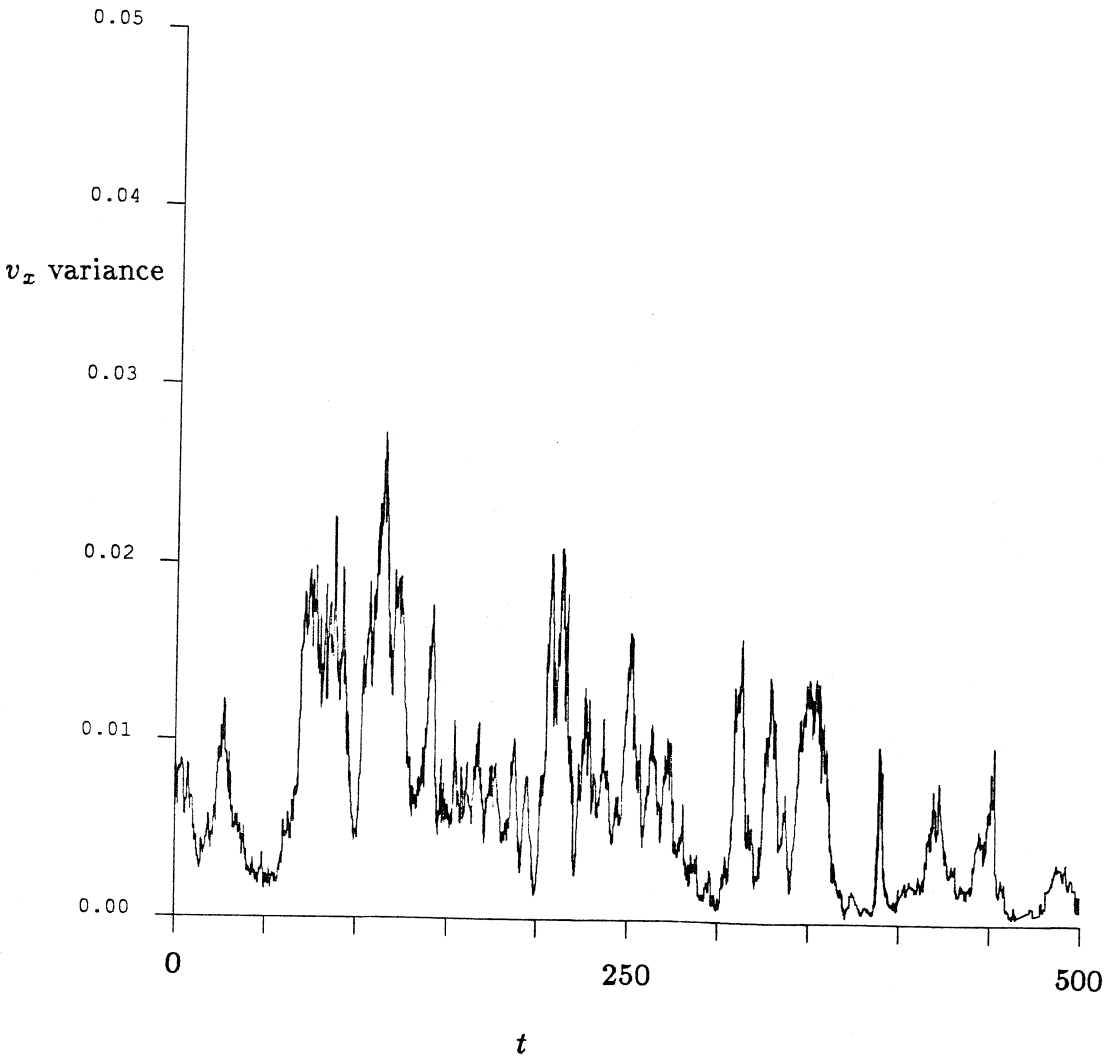

Figure B1.5 The time trace of the v_x variance for the simulations FTSn1 through FTSn5. The double line from t=380 – 400 show the deviation that can occur when a restart of the simulation run is done. Again, the deviation is very small.

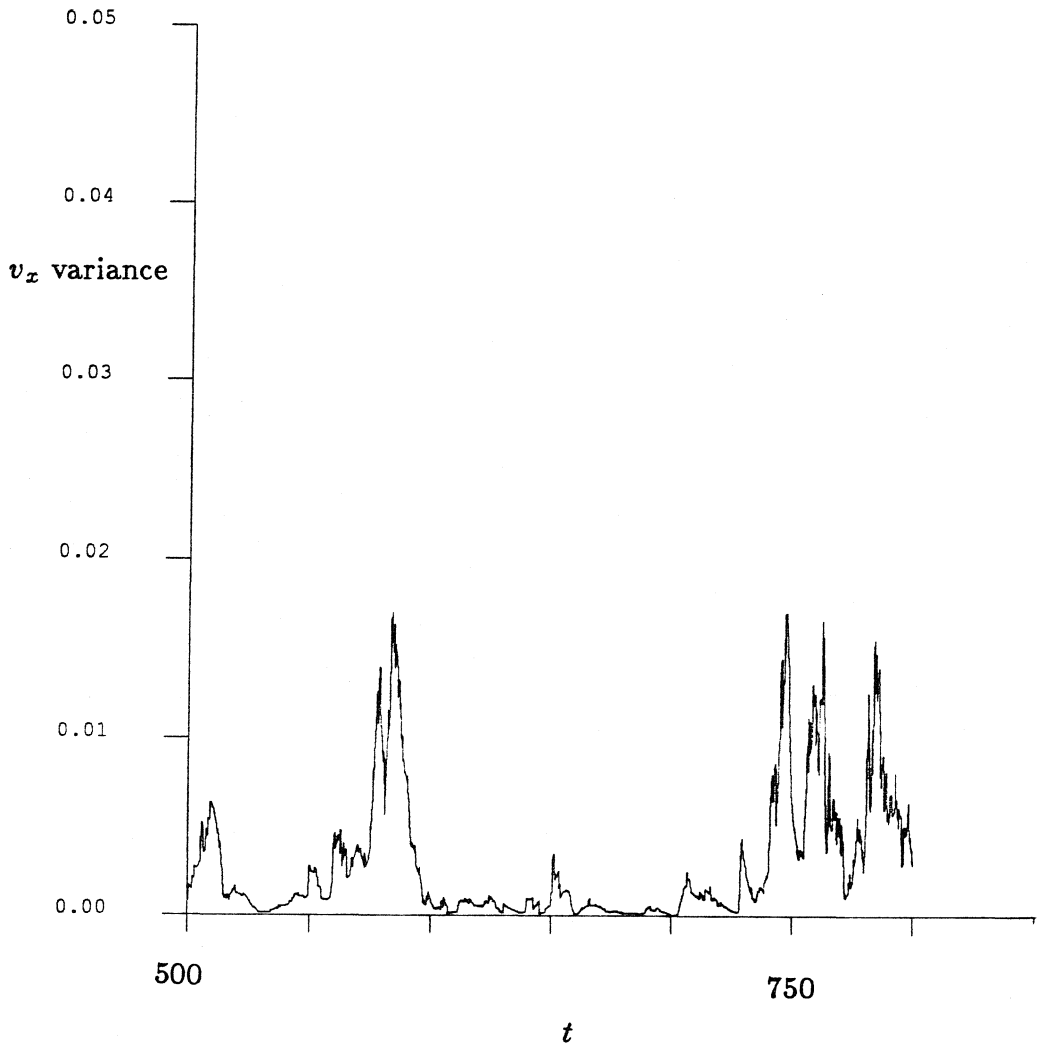

Figure B1.6 The time trace of the v_x variance for the simulation FTSn6. Note the long periods of near-zero variance.

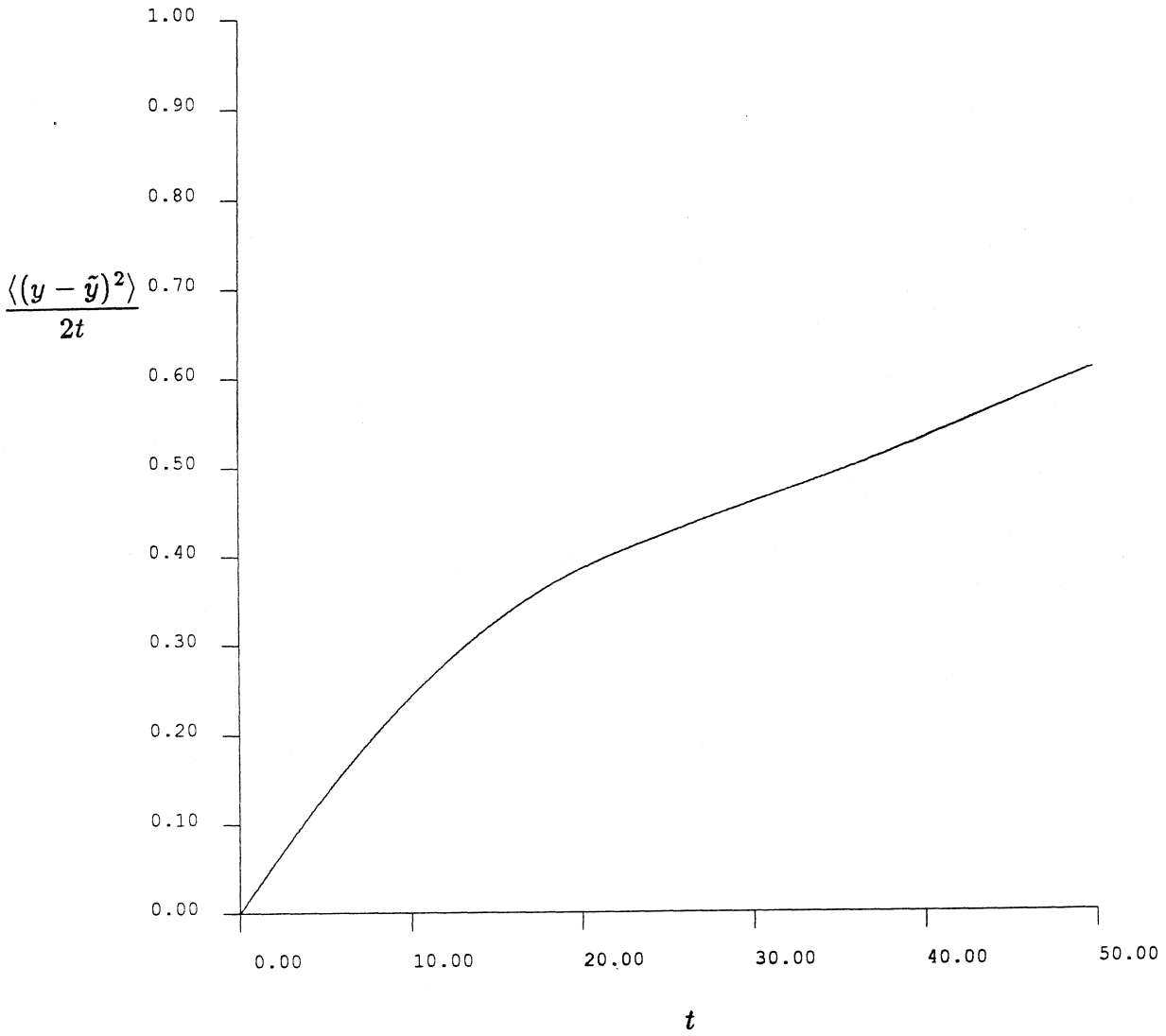

Figure B1.7 A $(D^s_\infty)_{yy}$-defining graph using displacement data from FTSn3 (t= 210 – 300). The graph interval is 50 time units, and the time between interval initial conditions is 0.01 time unit.

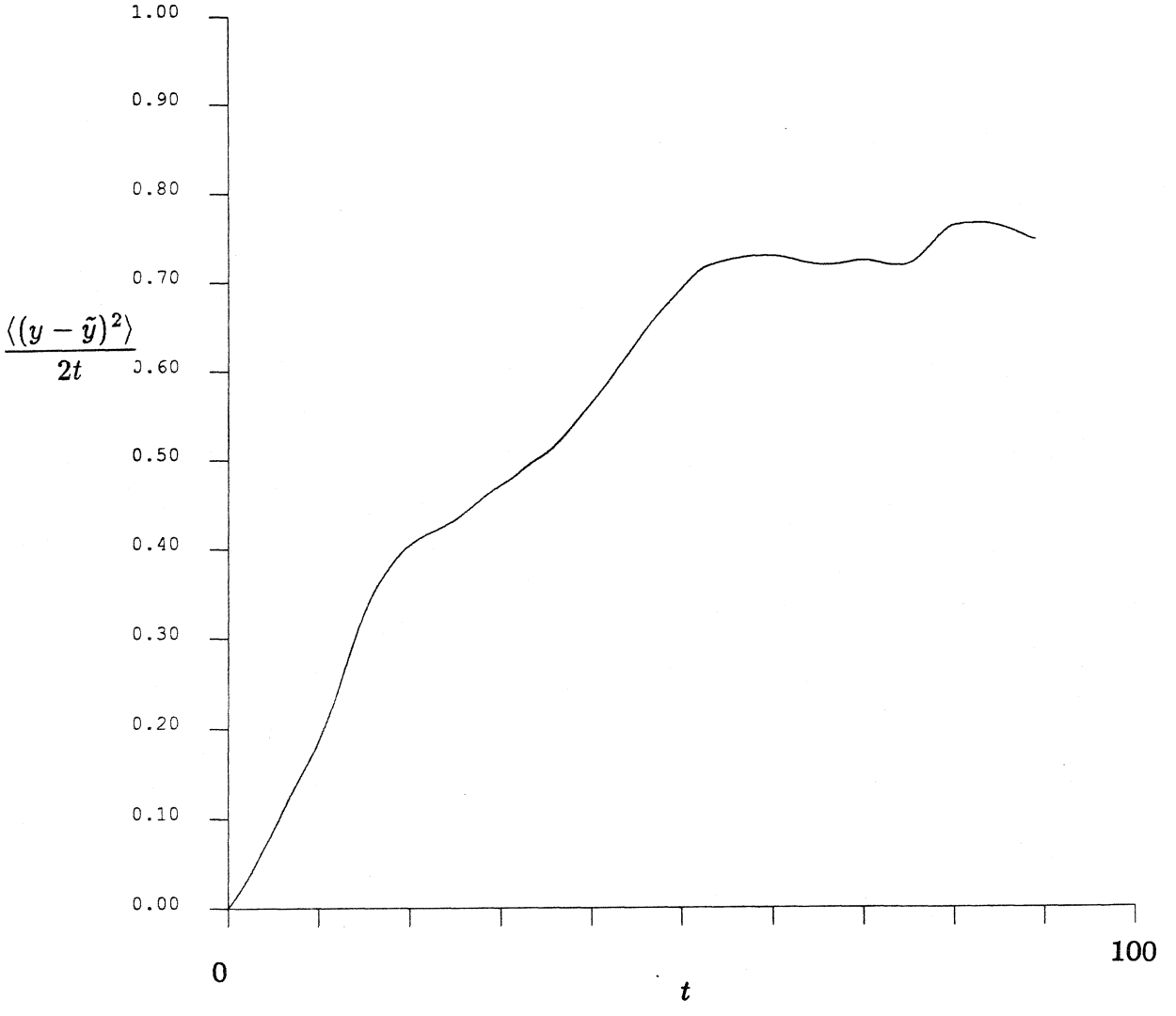

Figure B1.8 A $(D^s_\infty)_{yy}$-defining graph using displacement data from FTSn4 (t= 300 – 400). The graph interval is 90 time units, and the time between interval initial conditions is 0.01 time unit.

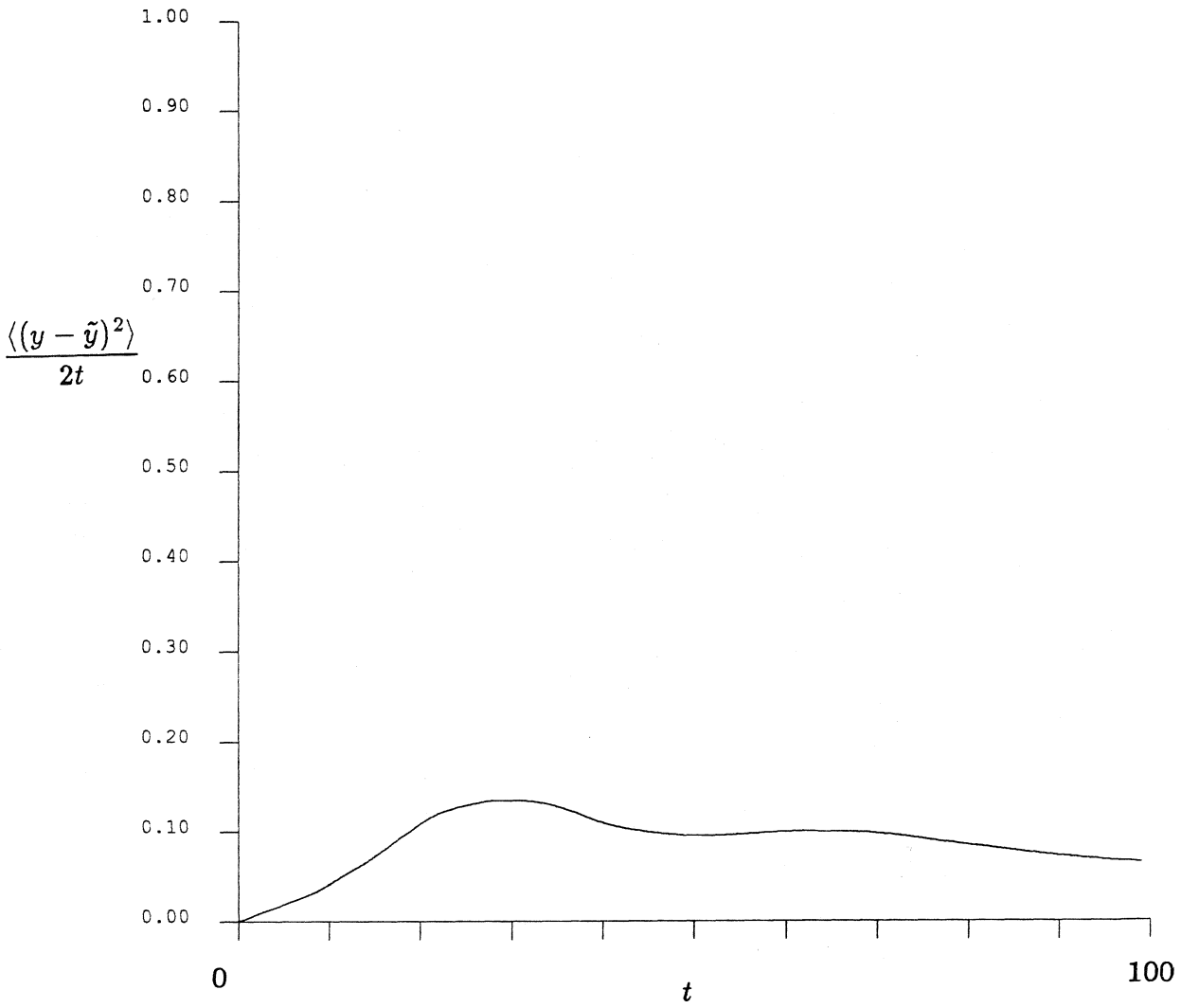

Figure B1.9 A $(D^s_\infty)_{yy}$-defining graph using displacement data from FTSn5 (t= 380 – 500). The graph interval is 99 time units, and the time between interval initial conditions is 0.01 time unit.

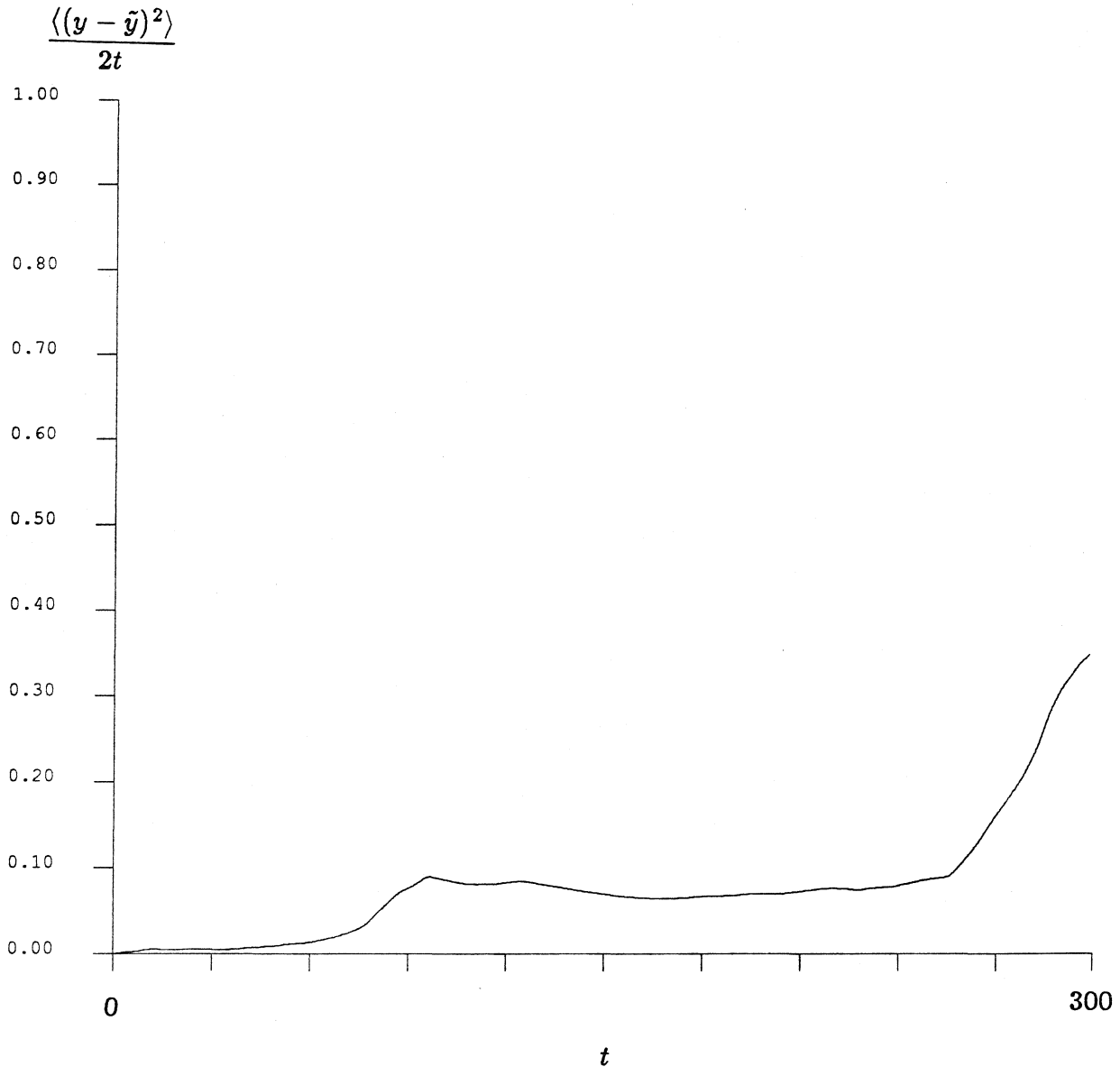

Figure B1.10 A $(D^s_\infty)_{yy}$-defining graph using displacement data from FTSn6 (t= 500 – 800). The graph interval is 300 time units, which means that no averaging over different initial conditions is done.

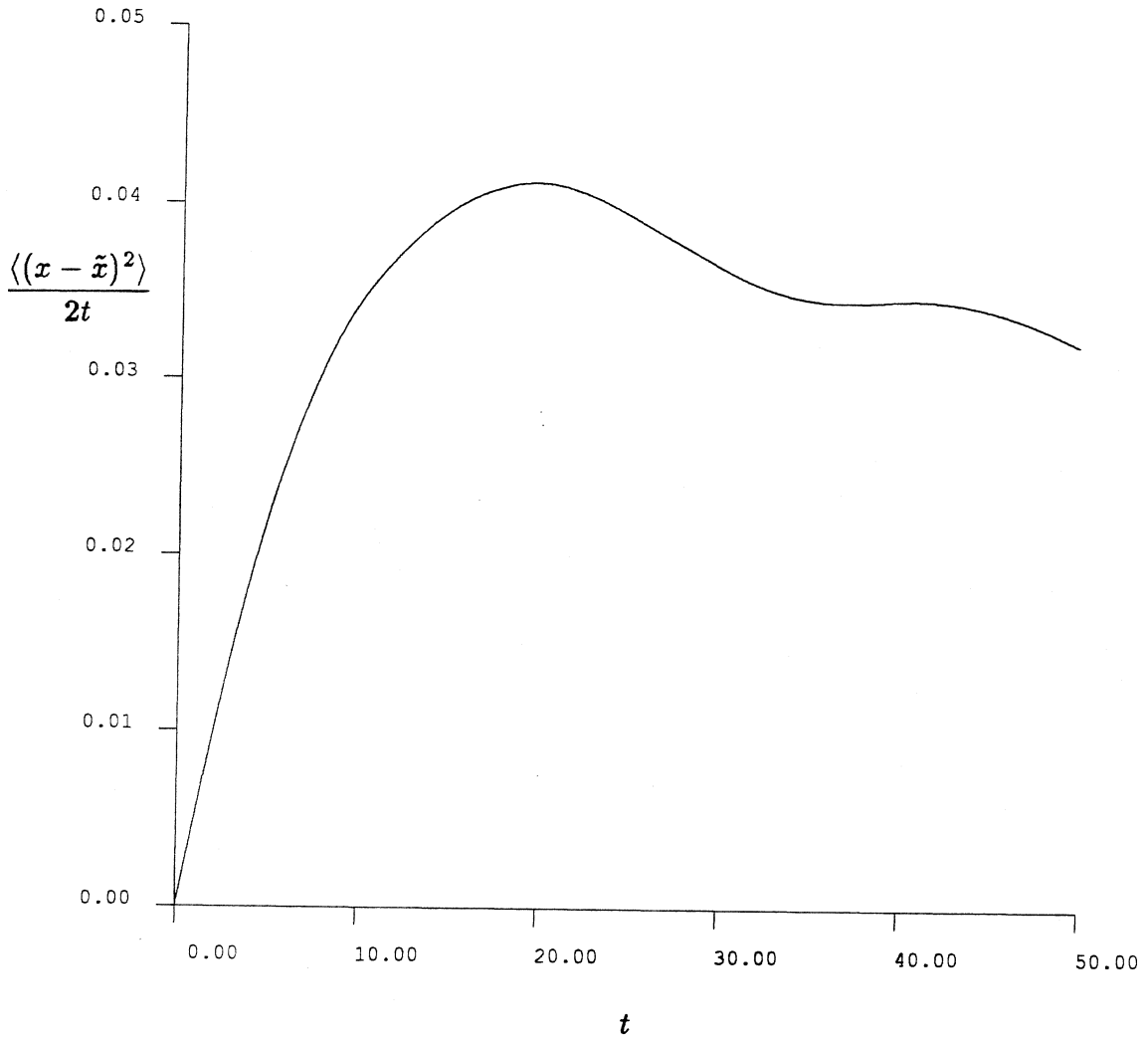

Figure B1.11 A $(D^s_\infty)_{xx}$-defining graph using displacement data from FTSn3 (t= 210 – 300). The graph interval is 50 time units, and the time between interval initial conditions is 0.01 time unit.

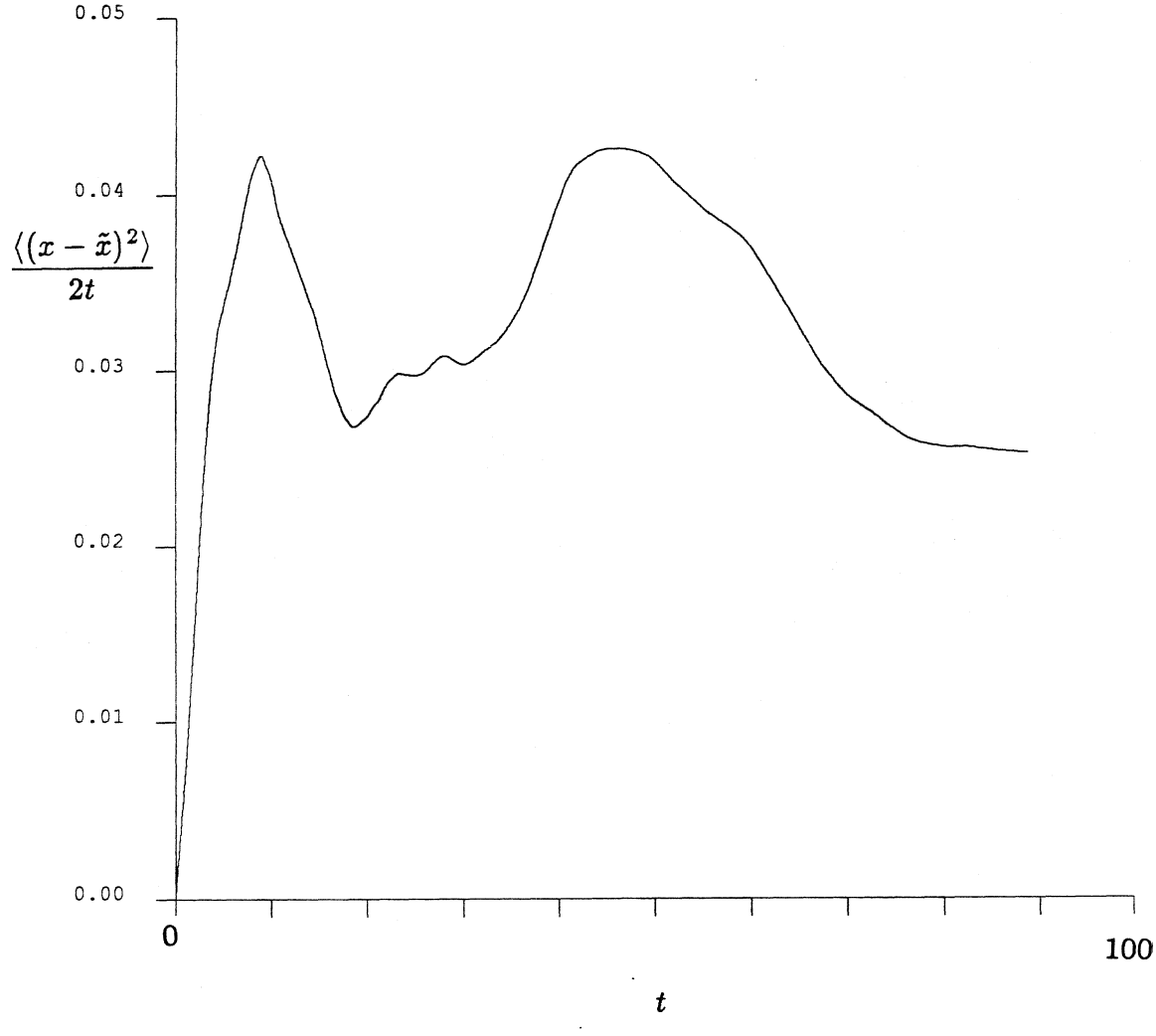

Figure B1.12 A $(D^s_\infty)_{xx}$-defining graph using displacement data from FTSn4 (t= 300 – 400). The graph interval is 90 time units, and the time between interval initial conditions is 0.01 time unit.

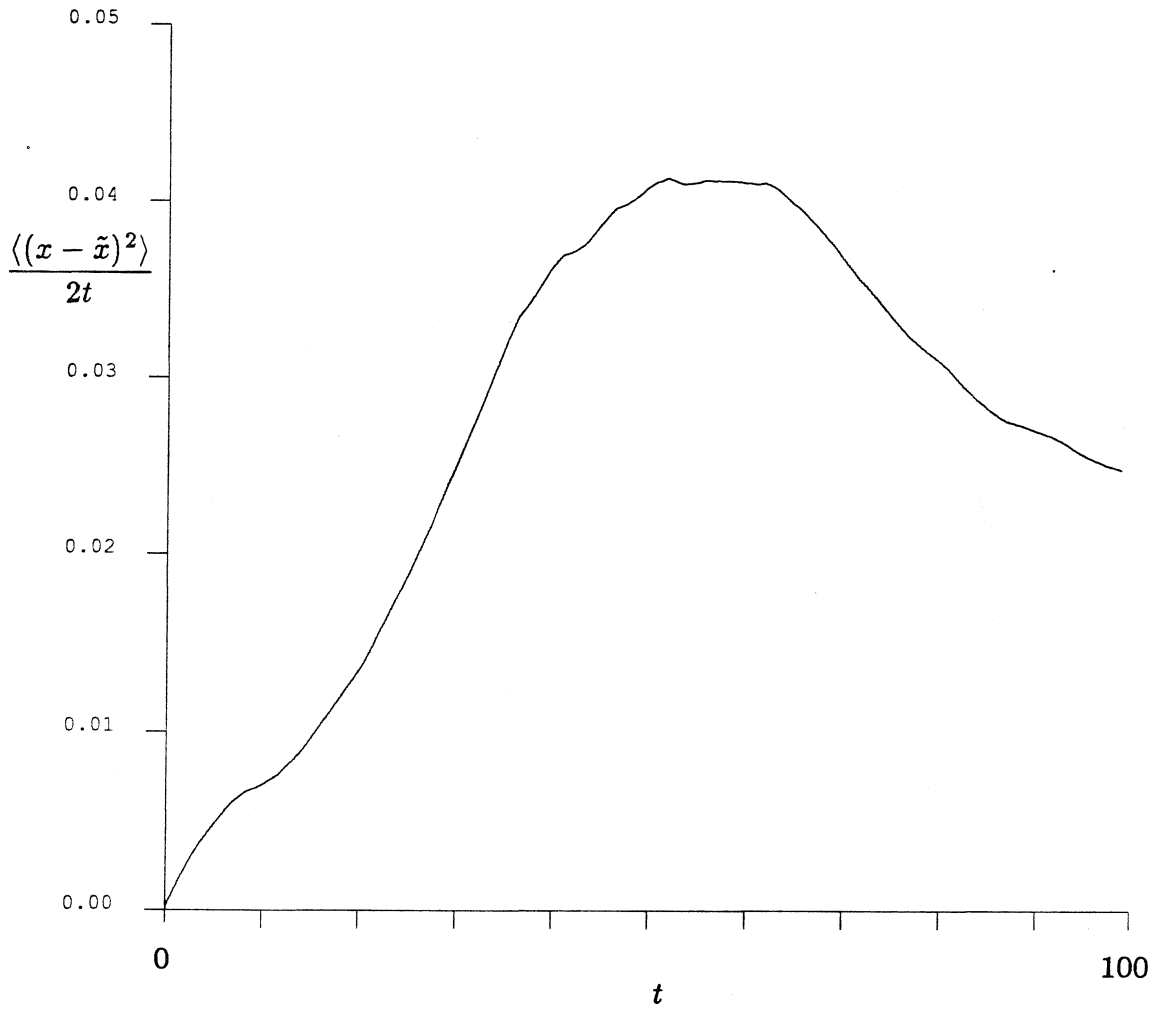

Figure B1.13 A $(D^s_\infty)_{xx}$-defining graph using displacement data from FTSn5 (t= 380 – 500). The graph interval is 99 time units, and the time between interval initial conditions is 0.01 time unit.

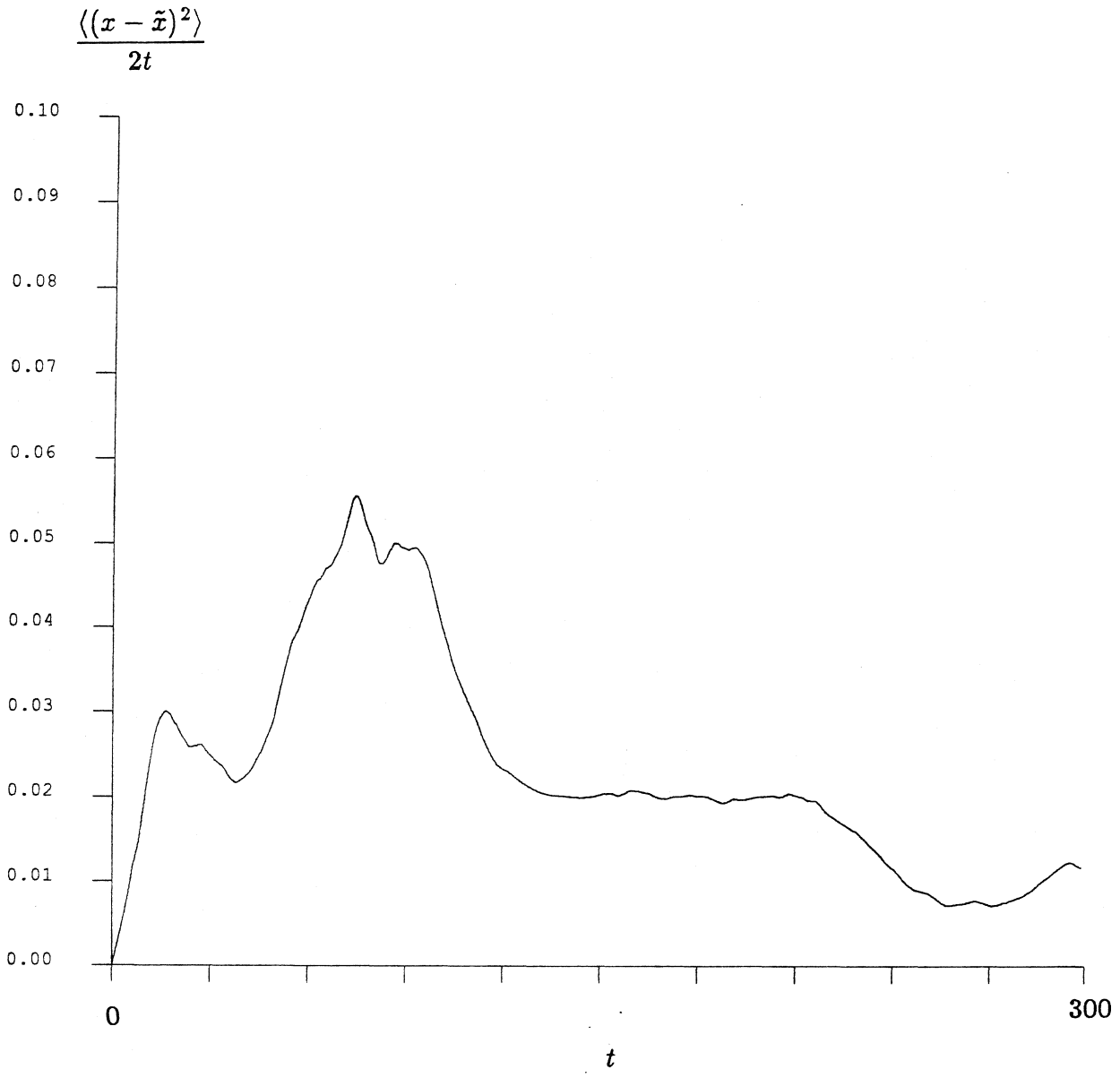

Figure B1.14 A $(D^s_\infty)_{xx}$-defining graph using displacement data from FTSn6 (t= 500 – 800). The graph interval is 300 time units, which means that no averaging over different initial conditions is done.

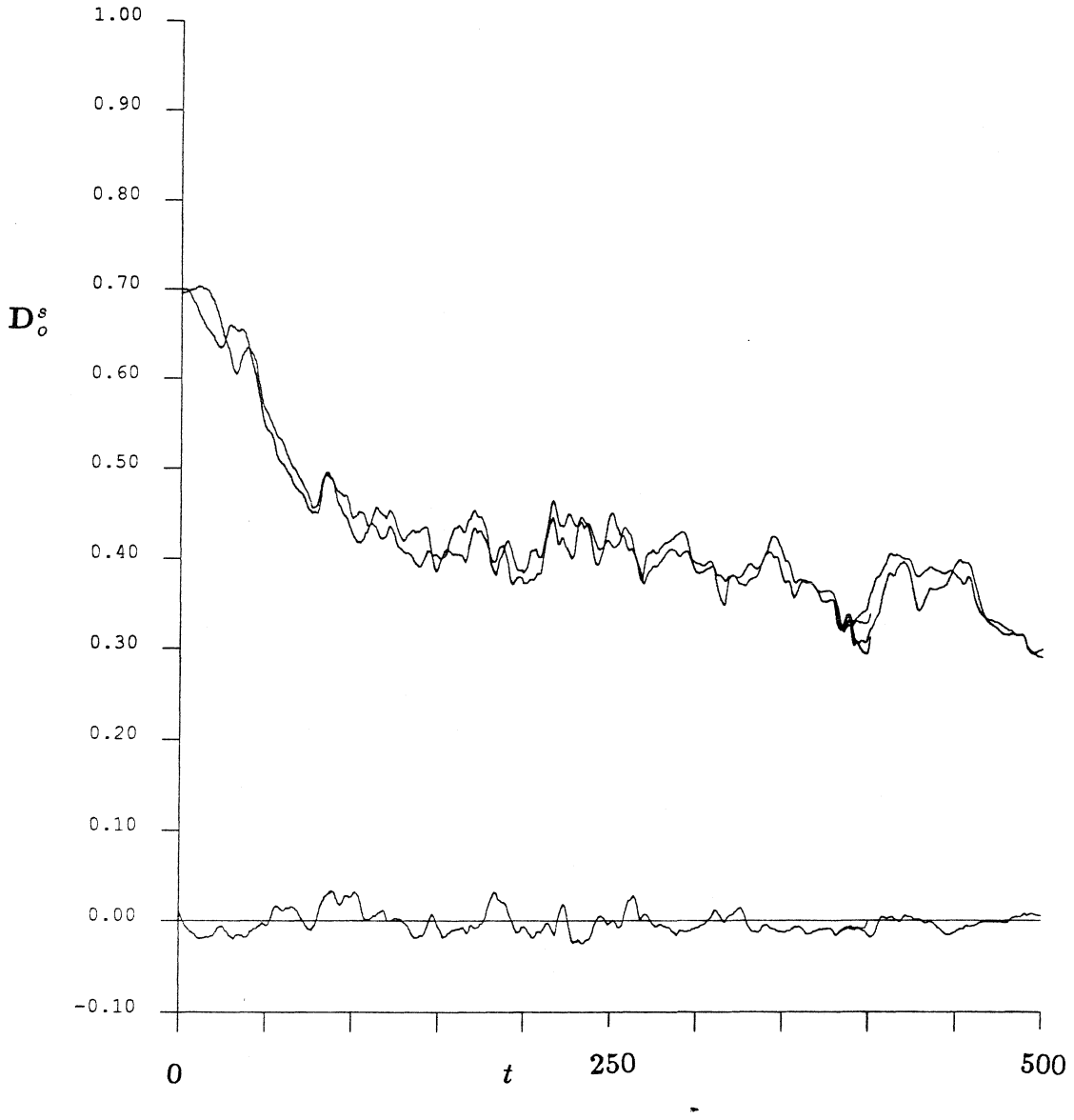

Figure B1.15 The time trace of $\mathbf{D}_o^s$ for the simulations FTSn1 through FTSn5. The upper two lines are the xx and yy components of this tensor. Of course, they should be equivalent for an infinite suspension – the slight variation occurs because of the finite number of spheres used in our simulation. The trace that fluctuates about the zero y-axis is the xy component of the short-time, self-diffusion tensor. Again, for an infinite number of spheres, this quantity would be exactly zero. The double lines from t=380 – 400 show the deviation that can occur when a restart of the simulation run is done.

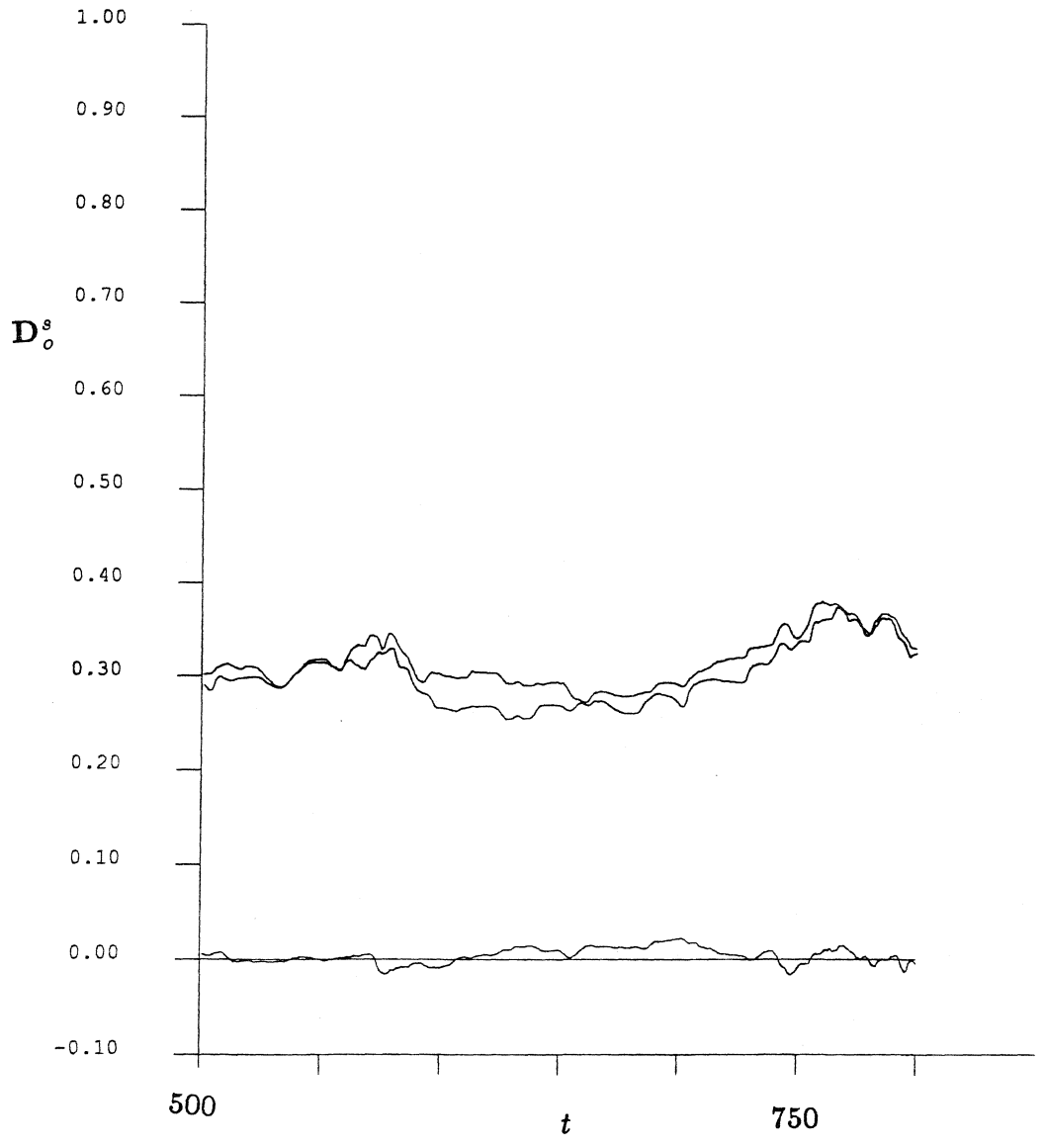

Figure B1.16 The time trace of $\mathbf{D}_o^s$ for the simulation FTSn6. The upper two lines are the xx and yy components of this tensor. Of course, they should be equivalent for an infinite suspension – the slight variation occurs because of the finite number of spheres used in our simulation. The trace that fluctuates about the zero y-axis is the xy component of the short-time, self-diffusion tensor. Again, for an infinite number of spheres, this quantity would be exactly zero.

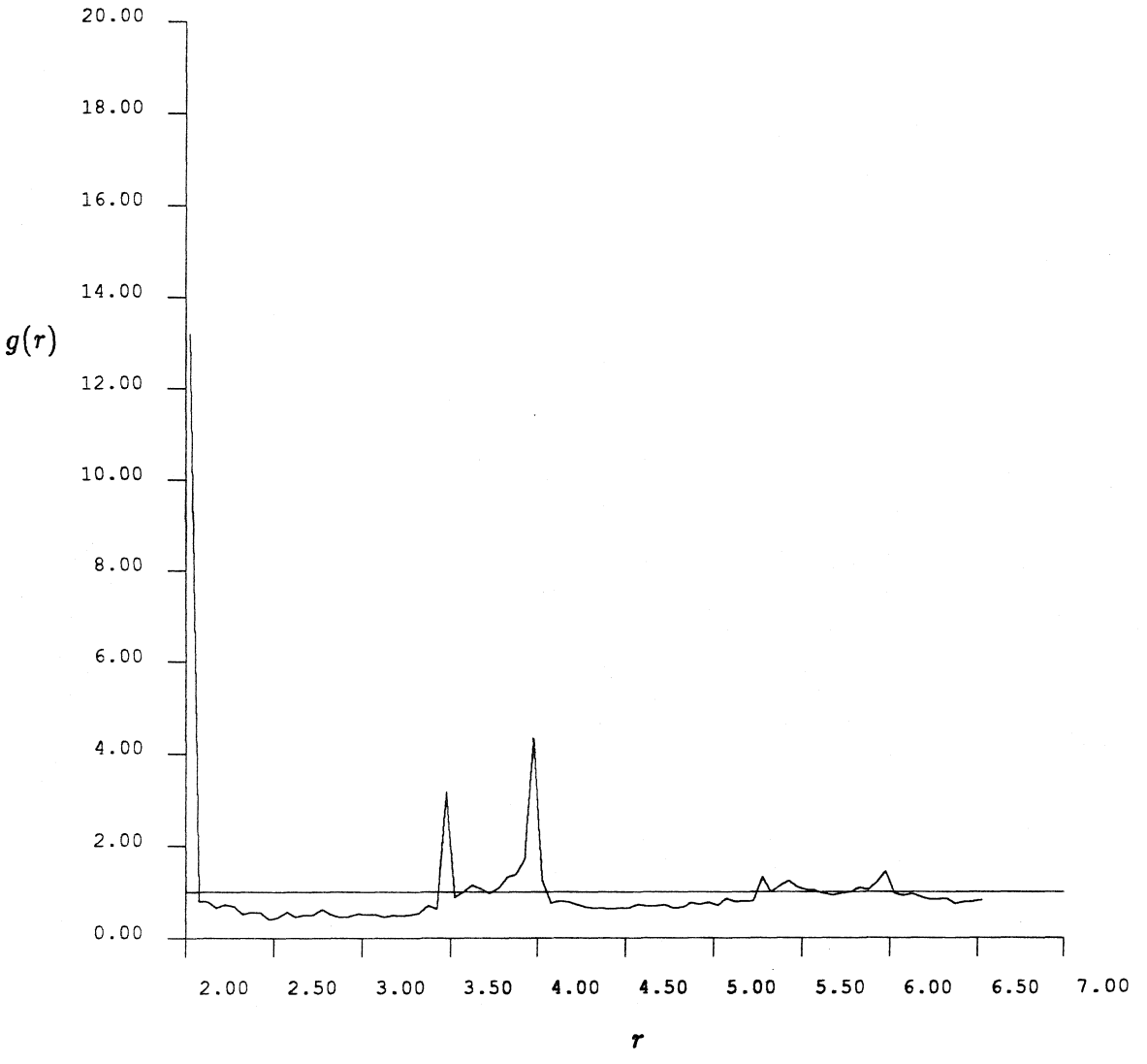

Figure B1.17 The radial pair-distribution function, $g(r)$, for the FTSn4 run ($t = 300 - 400$).

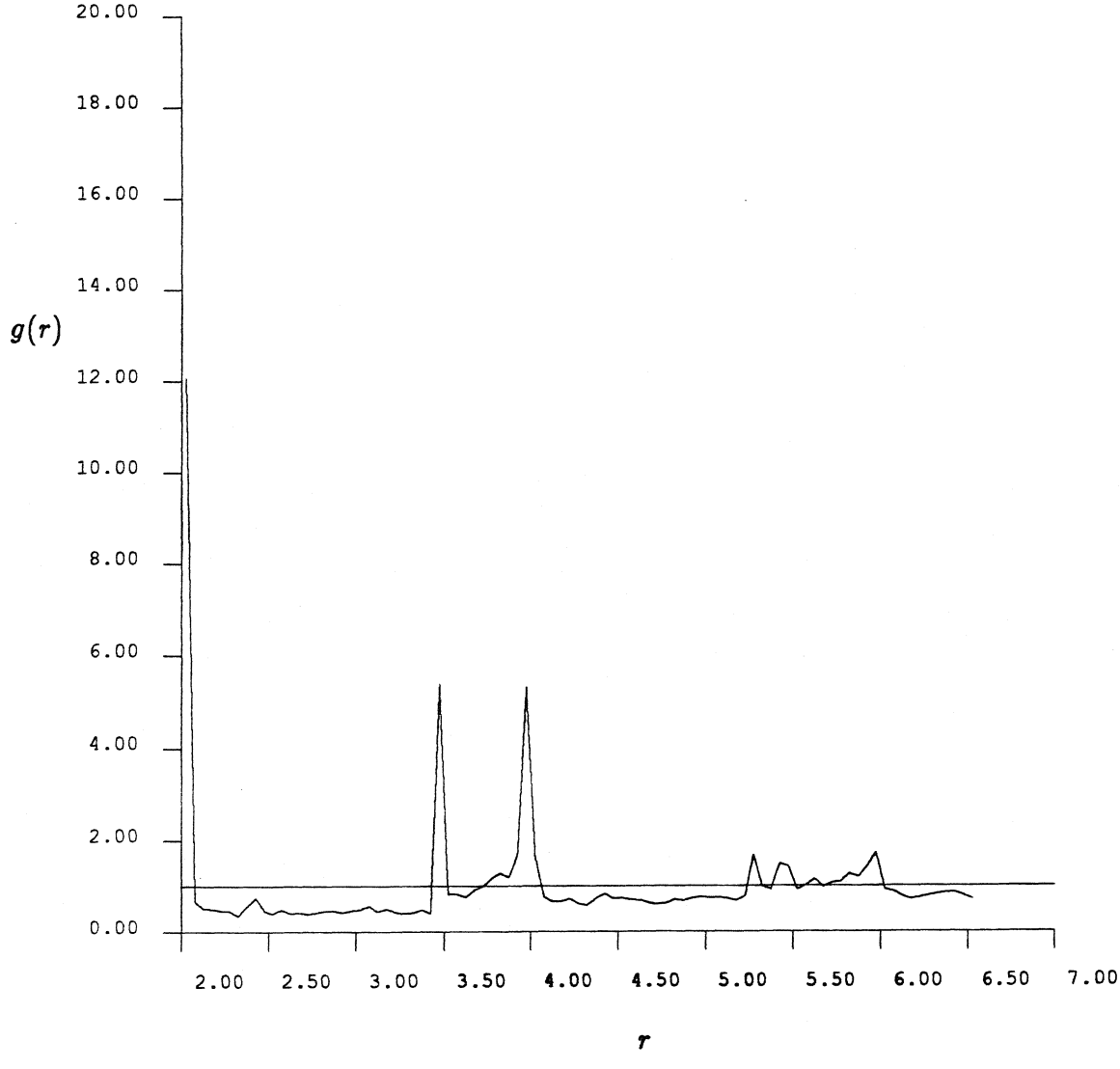

Figure B1.18 The radial pair-distribution function, $g(r)$, for the FTSn5 run ($t = 380 - 500$).

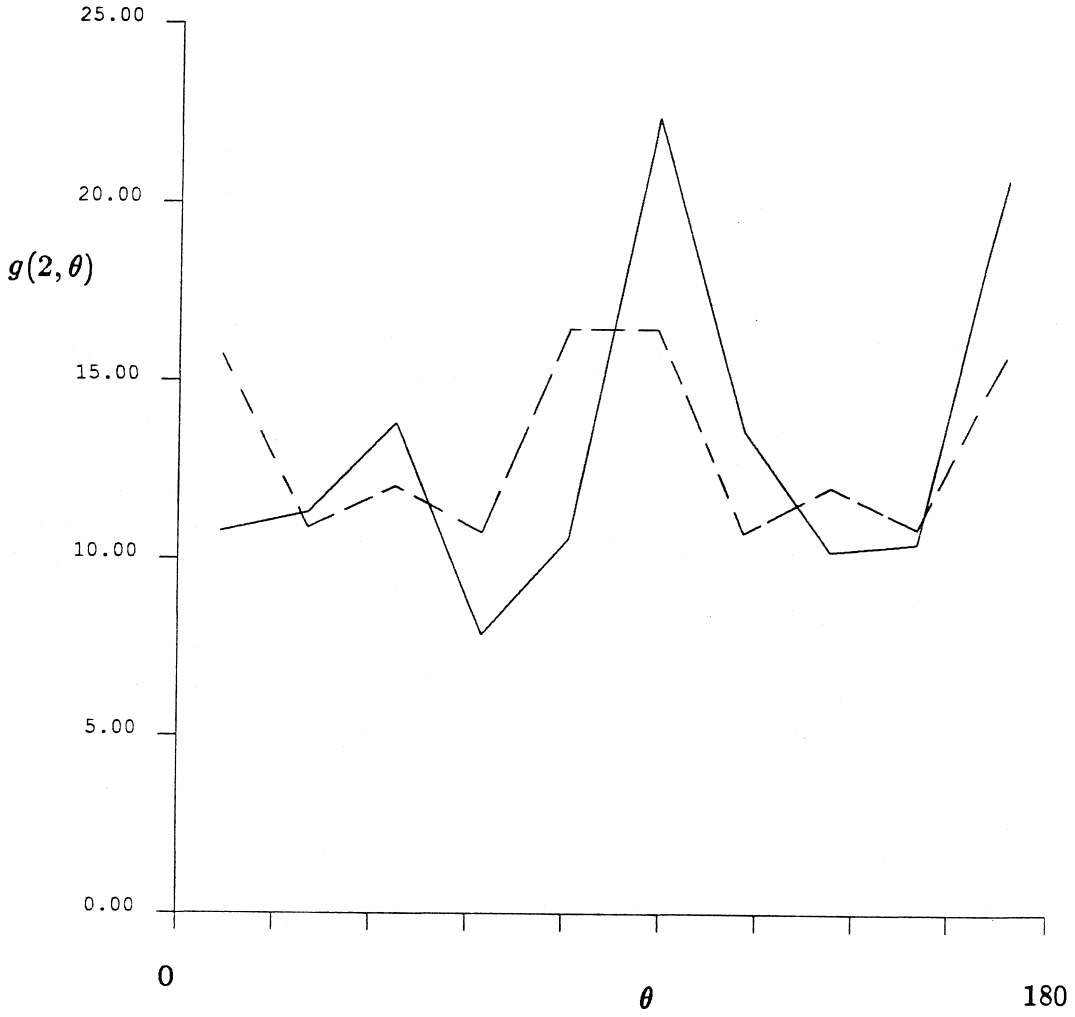

Figure B1.19 The full pair-distribution function for spheres whose surfaces are separated by less than 0.05 radii using data from the FTSn4 run (t = 300 – 400). The dashed curve represents this function when it is forced to be symmetric about $\theta = 90°$.

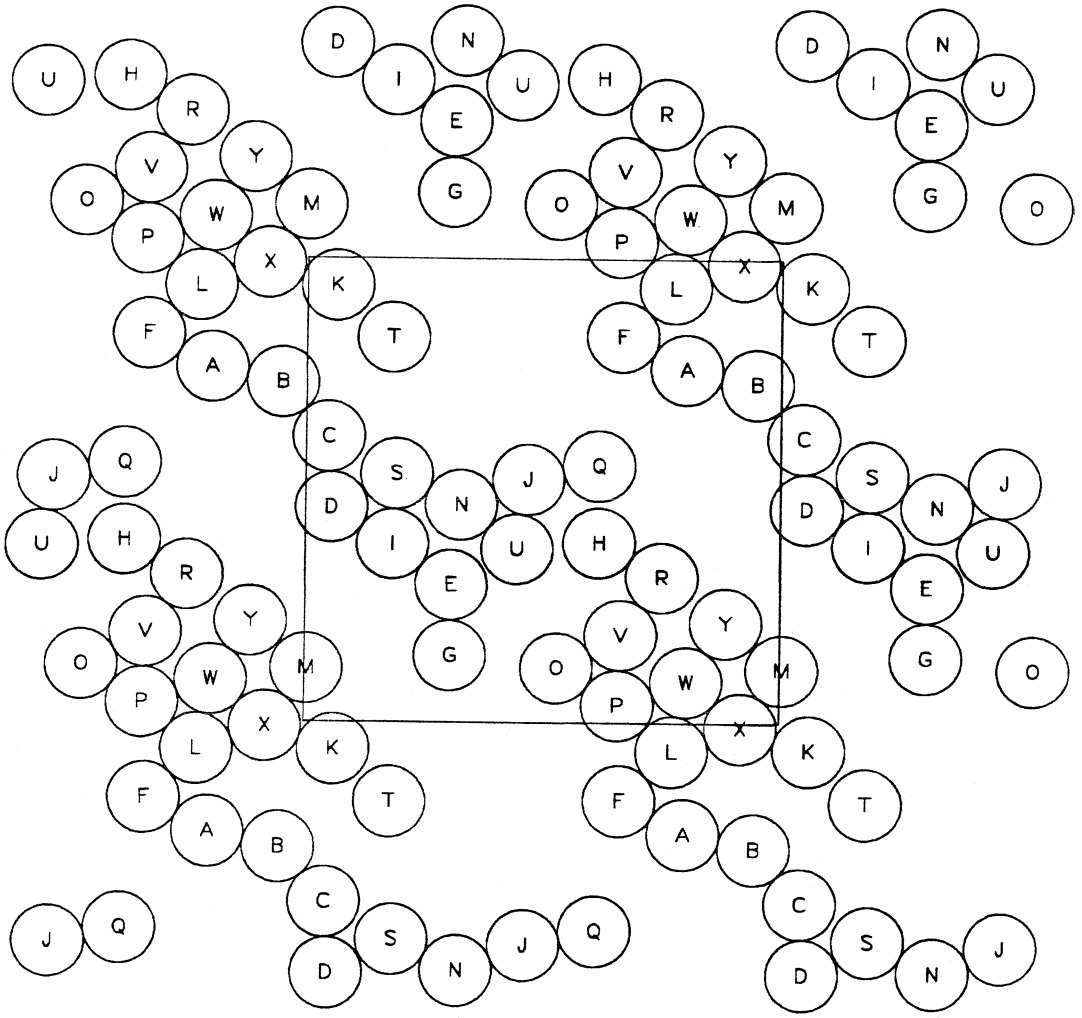

Figure B1.20 A "snapshot" of sphere positions. The square is the periodic cell. These are the sphere positions at $t = 100.05$ time units (FTSn2).

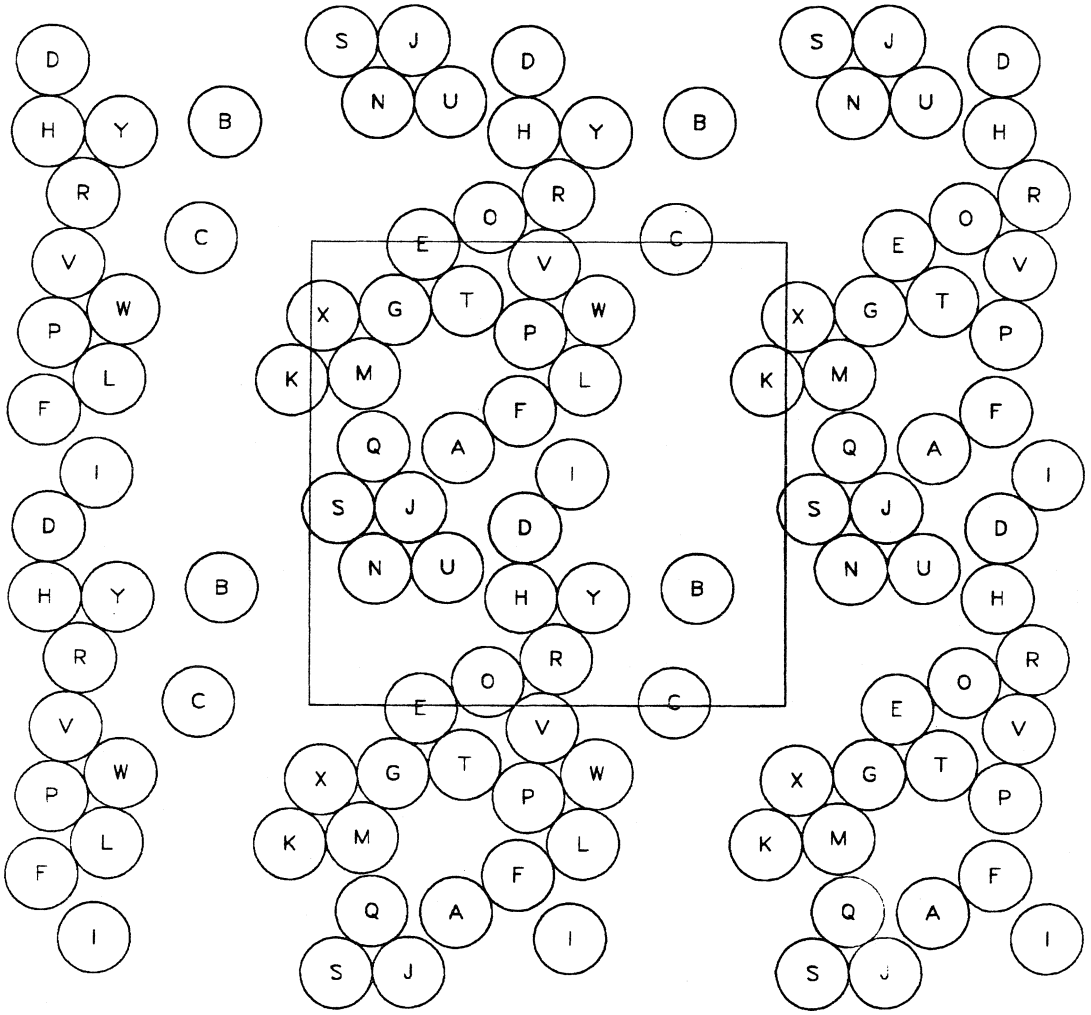

Figure B1.21 A "snapshot" of sphere positions. The square is the periodic cell. These are the sphere positions at $t = 154.40$ time units (FTSn2).

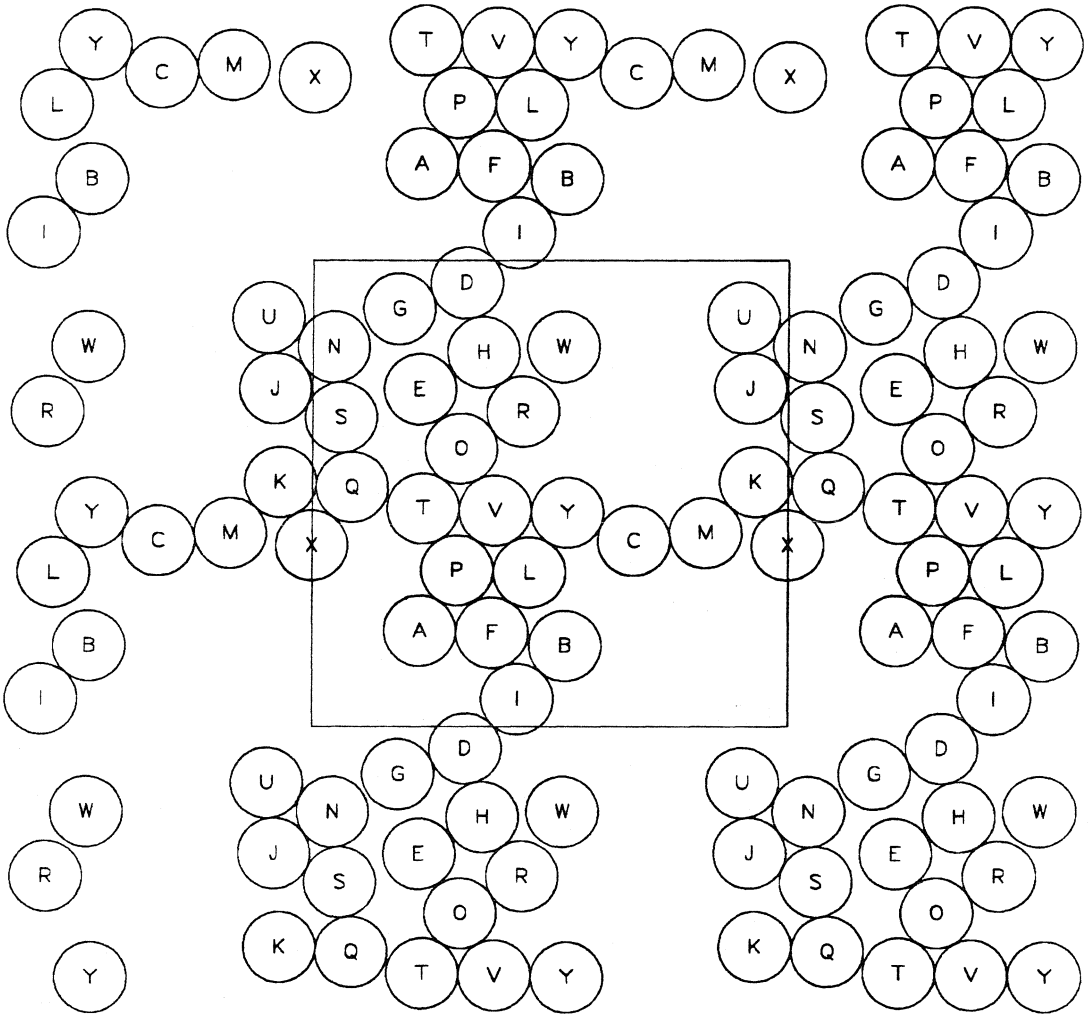

Figure B1.22 A "snapshot" of sphere positions. The square is the periodic cell. These are the sphere positions at $t = 200.05$ time units (FTSn3).

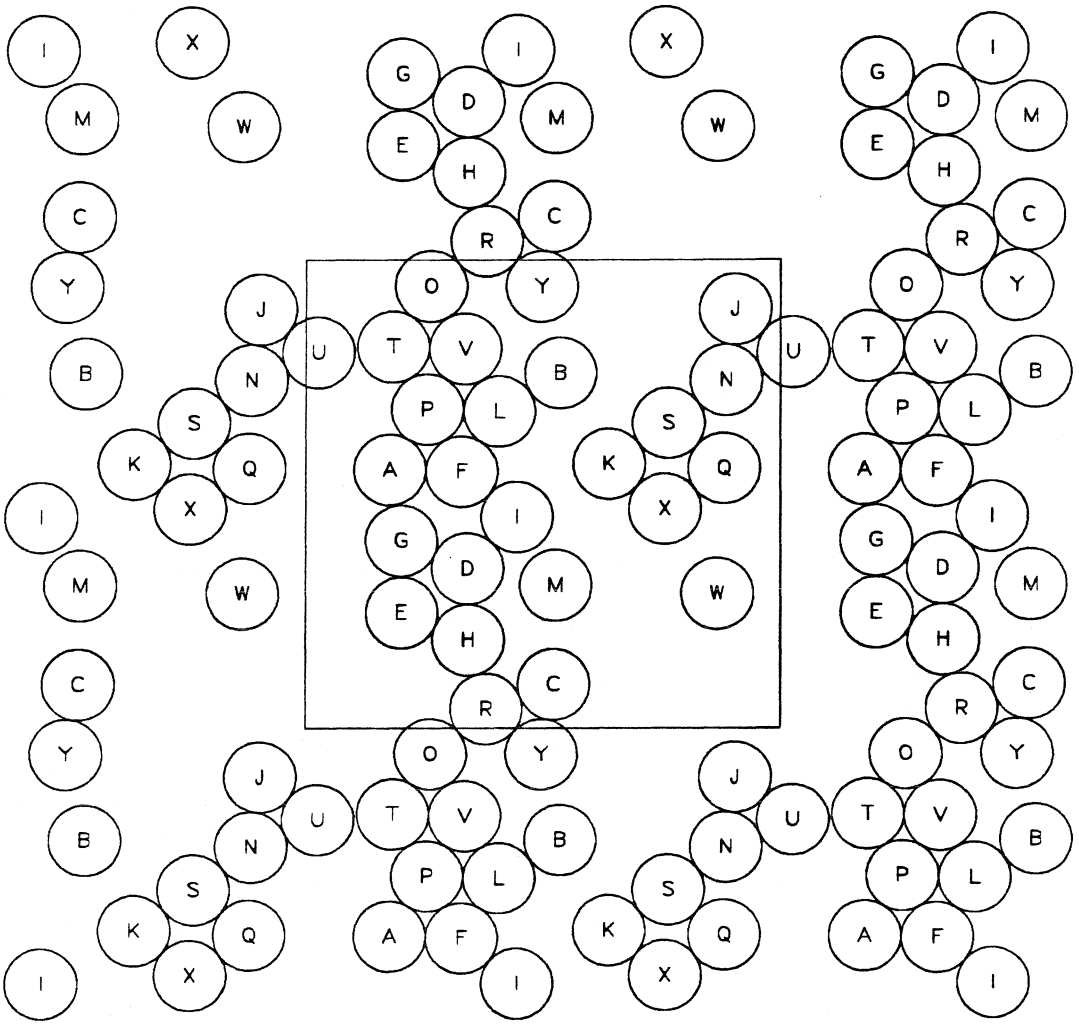

Figure B1.23 A "snapshot" of sphere positions. The square is the periodic cell. These are the sphere positions at $t = 219.50$ time units (FTSn3).

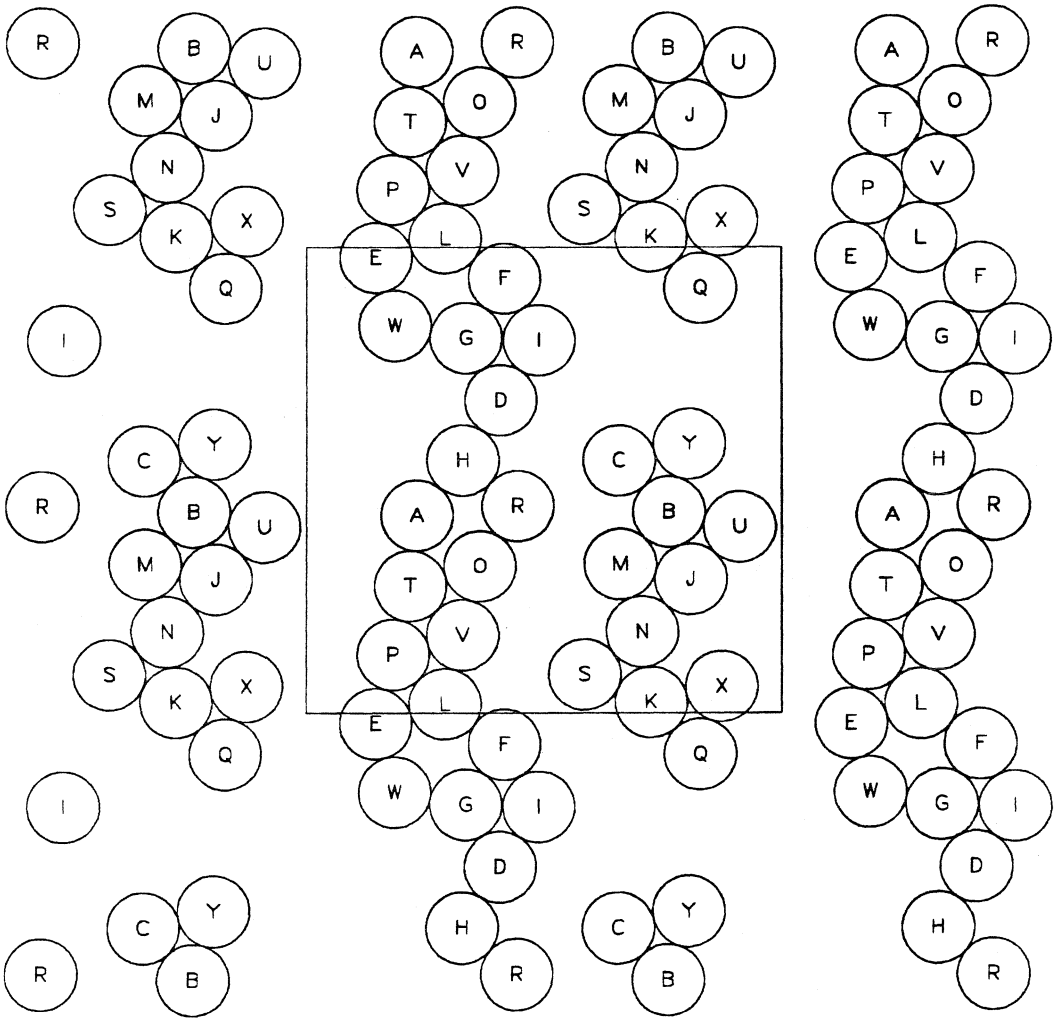

Figure B1.24 A "snapshot" of sphere positions. The square is the periodic cell. These are the sphere positions at $t = 300.05$ time units (FTSn4).

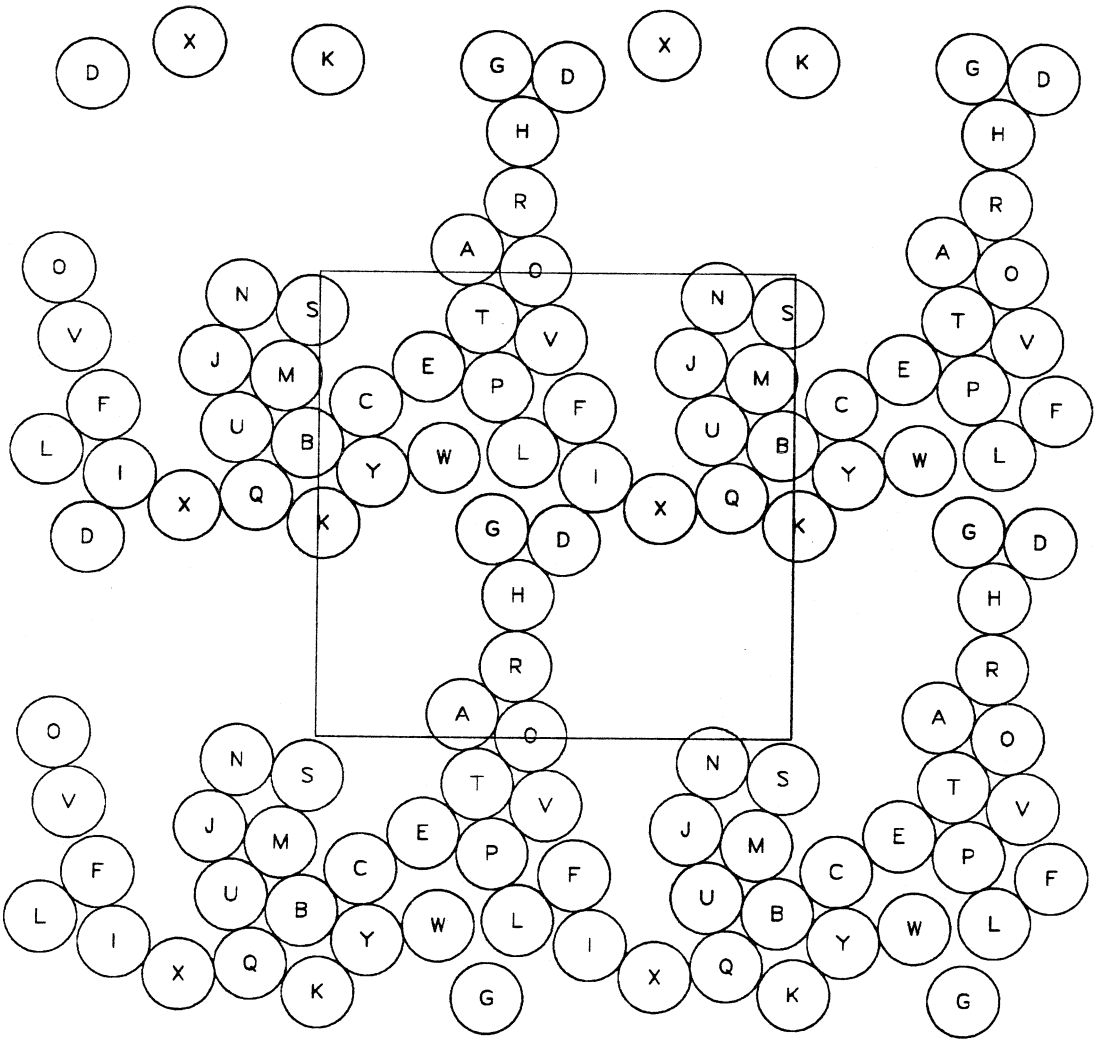

Figure B1.25 A "snapshot" of sphere positions. The square is the periodic cell. These are the sphere positions at $t = 380.05$ time units (FTSn5).

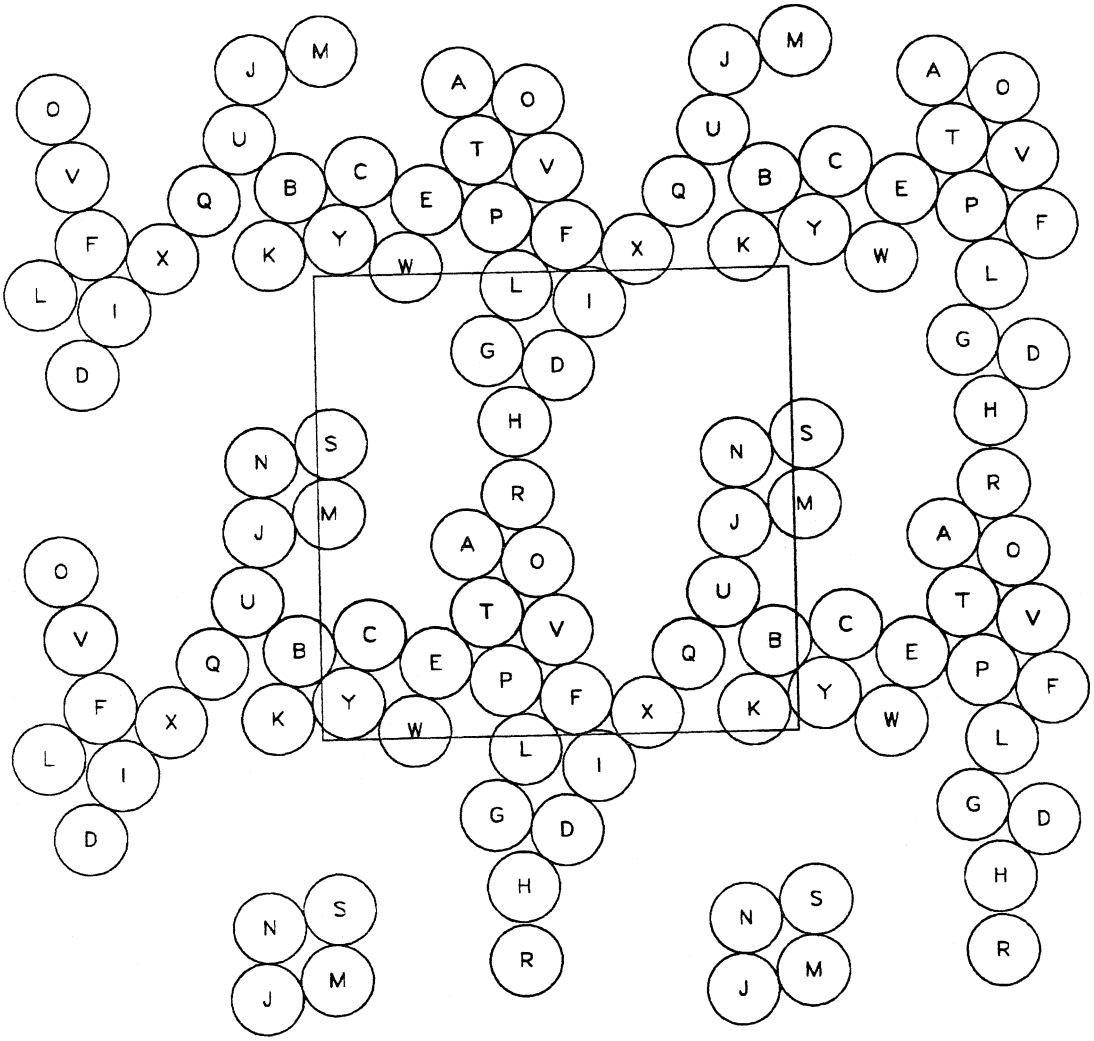

Figure B1.26 A "snapshot" of sphere positions. The square is the periodic cell. These are the sphere positions at $t = 400.00$ time units (FTSn5).

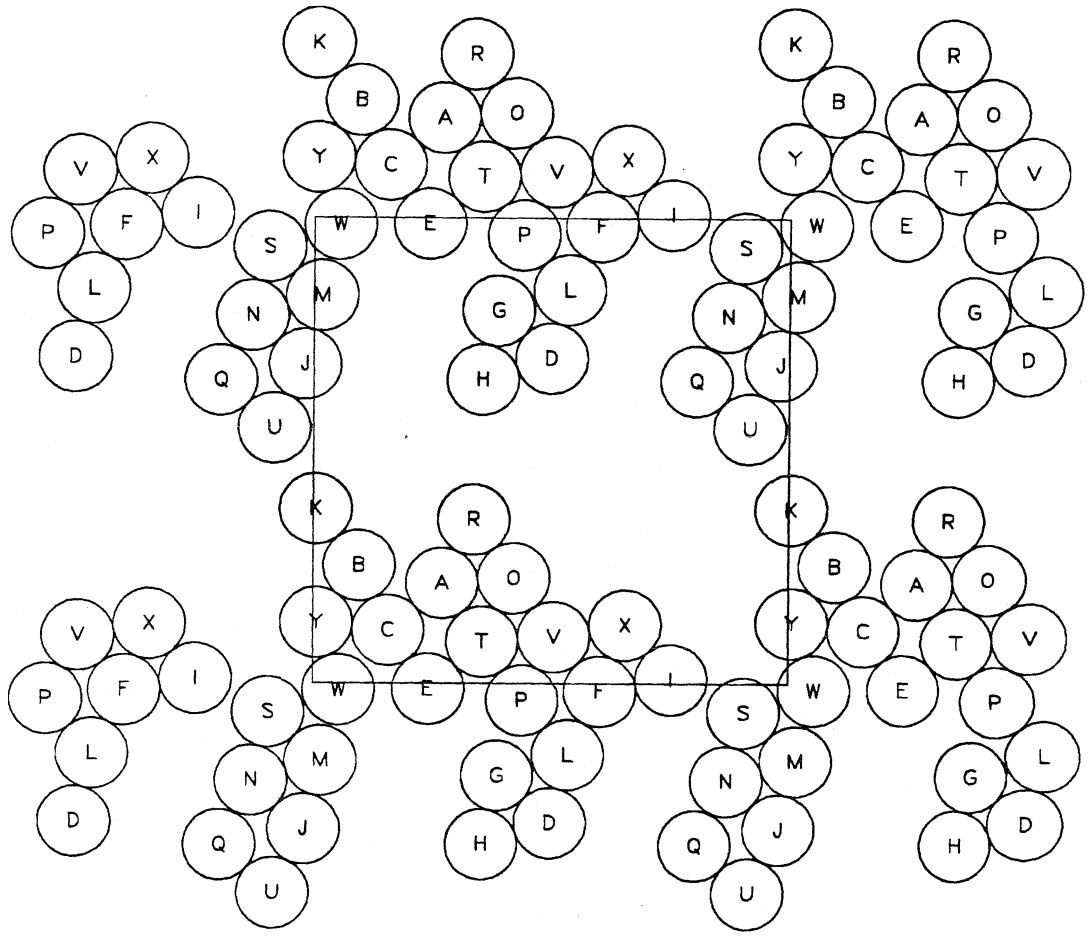

Figure B1.27 A "snapshot" of sphere positions. The square is the periodic cell. These are the sphere positions at $t = 425.00$ time units (FTSn5).

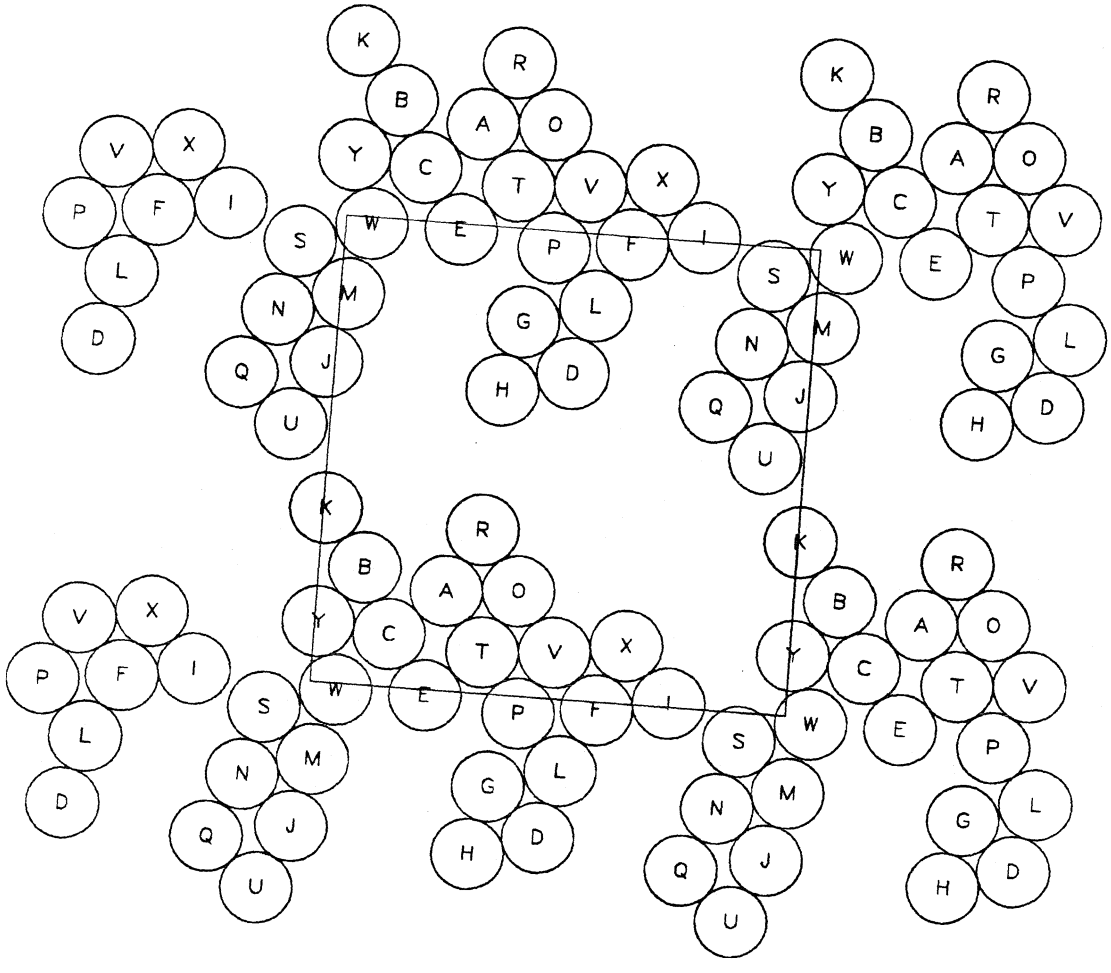

Figure B1.28 A "snapshot" of sphere positions. The square is the periodic cell. These are the sphere positions at $t = 450.00$ time units (FTSn5).

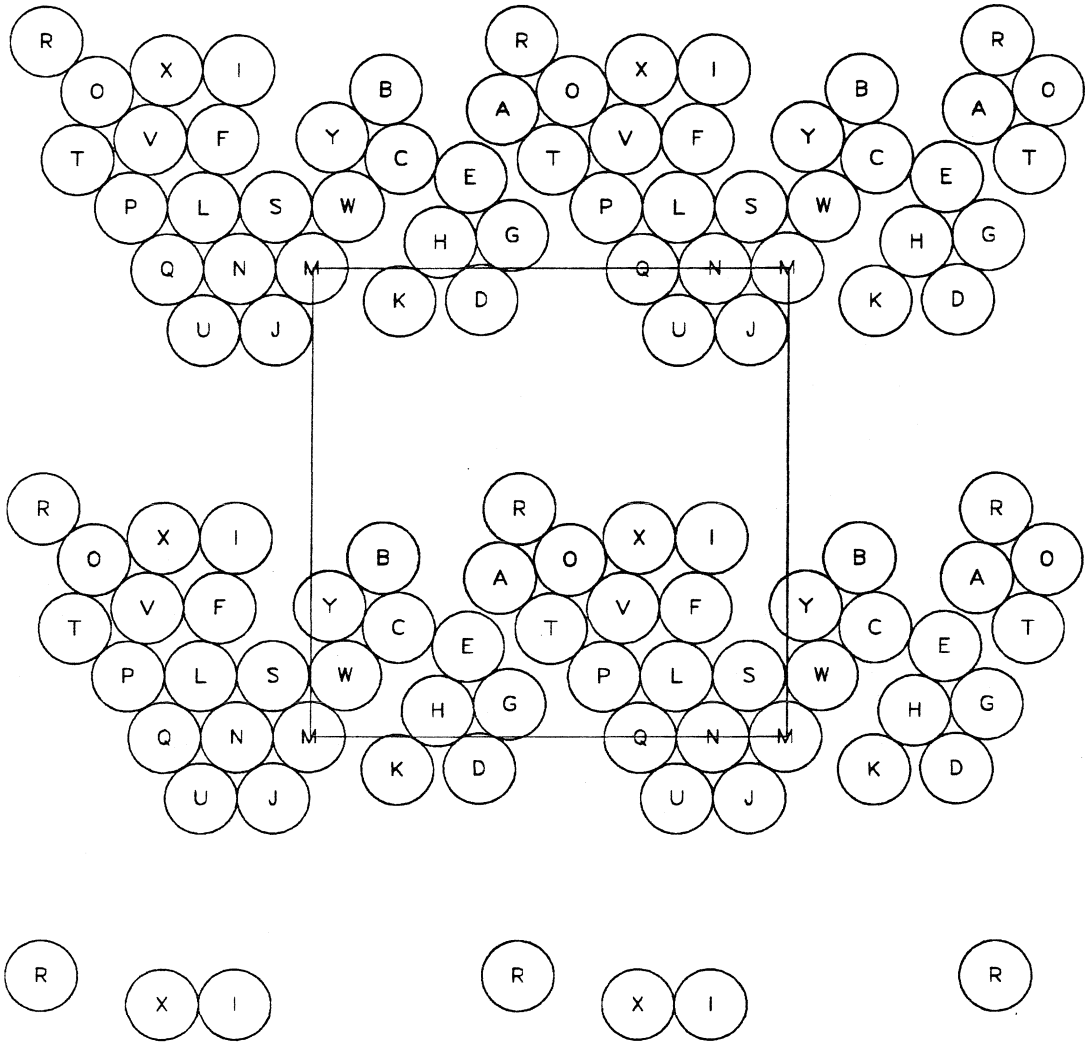

Figure B1.29 A "snapshot" of sphere positions. The square is the periodic cell. These are the sphere positions at $t = 475.00$ time units (FTSn6).

Appendix B2: The FTn simulation results

This suite of simulations uses a non-Ewald, FT method to approximate the hydrodynamic interactions. Two separate simulation runs follow the evolution of a sedimenting system to a final time of 1000 time units. The initial configuration is the same as in the FTSn simulations described in Appendix B1. There are 25 spheres within the periodic cell. The areal fraction is 0.453. There are no interparticle forces present. The time step is 0.001 time unit. The mobility matrix is inverted every 0.1 time unit. Position and velocity data is saved every 0.05 time unit. $\mathbf{D}_o^s$ is evaluated and reported at every time unit.

	FTn1	FTn2
T	0-500	500-1000
Cray/Sun	Sun	Sun
CPU(min)	4186	4185
v_y	-6.37155	-6.37076
v_x	0.00582	-0.00351
v_y variance	0.02616	0.03168
v_x variance	0.00809	0.00847
v_{xy} variance	-0.00036	0.00023
$(D_\infty^s)_{yy}$	0.46	
$(D_\infty^s)_{xx}$	0.048	0.030
$(D_o^s)_{yy}$	0.544	0.467
$(D_o^s)_{xx}$	0.546	0.478
$(D_o^s)_{xy}$	-0.0004	-0.0034
$g(2)$	16.2	15.2
$g(3.5)$	1.08	2.31
$g(4)$	2.74	3.06

Table B2.1

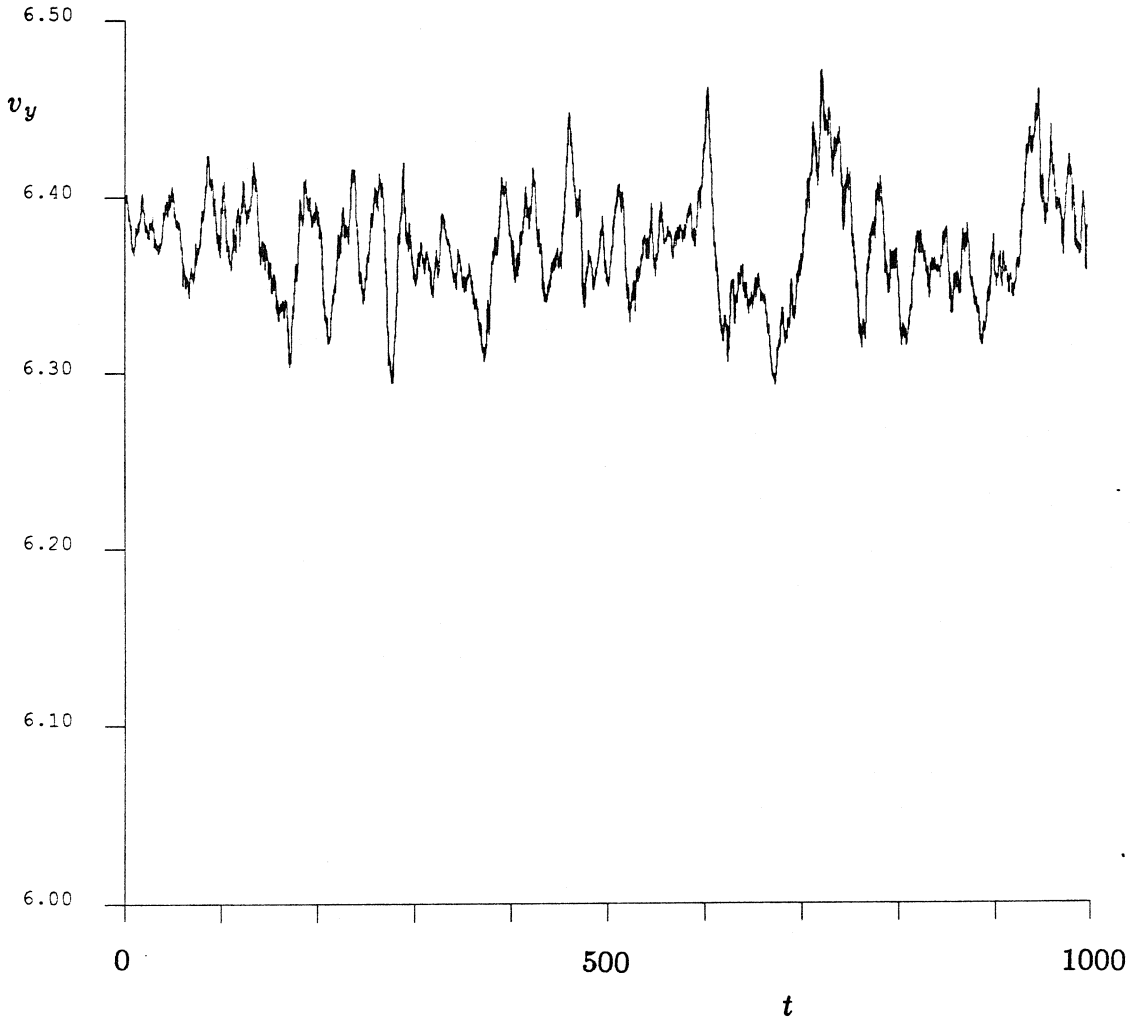

Figure B2.1 The time trace of v_y for the simulations FTn1 and FTn2.

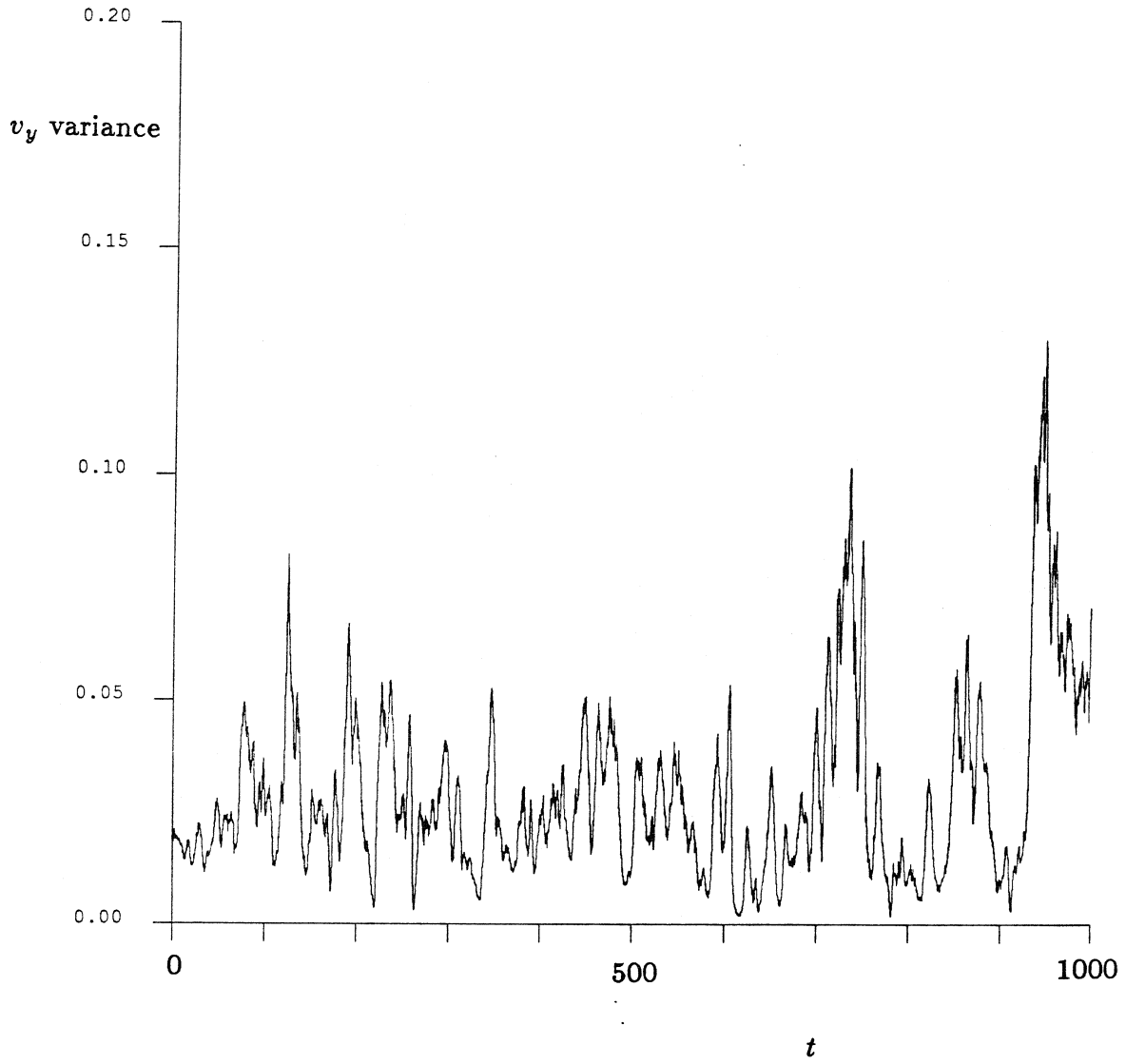

Figure B2.2 The time trace of the v_y variance for the simulations FTn1 and FTn2.

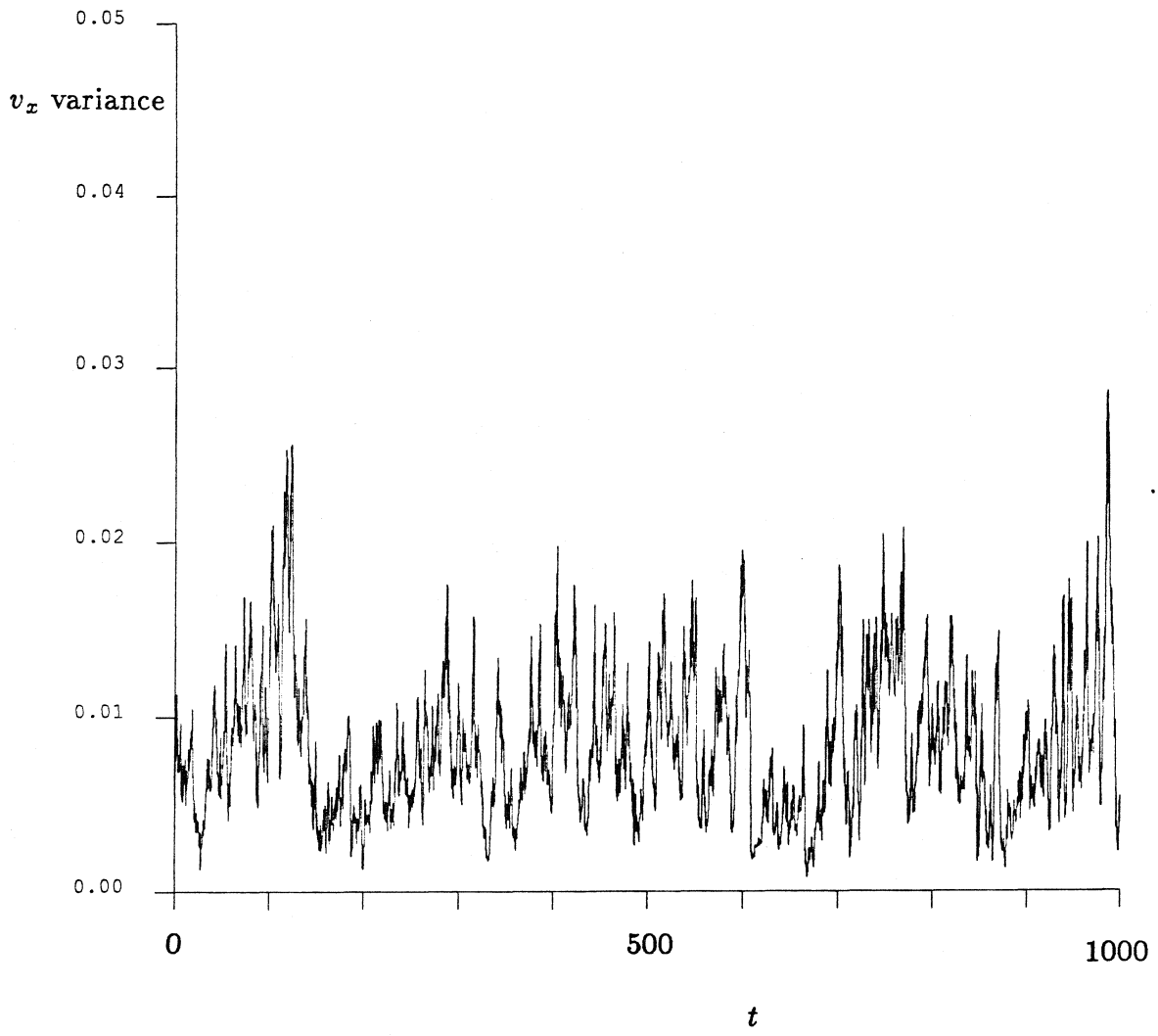

Figure B2.3 The time trace of the v_x variance for the simulations FTn1 and FTn2.

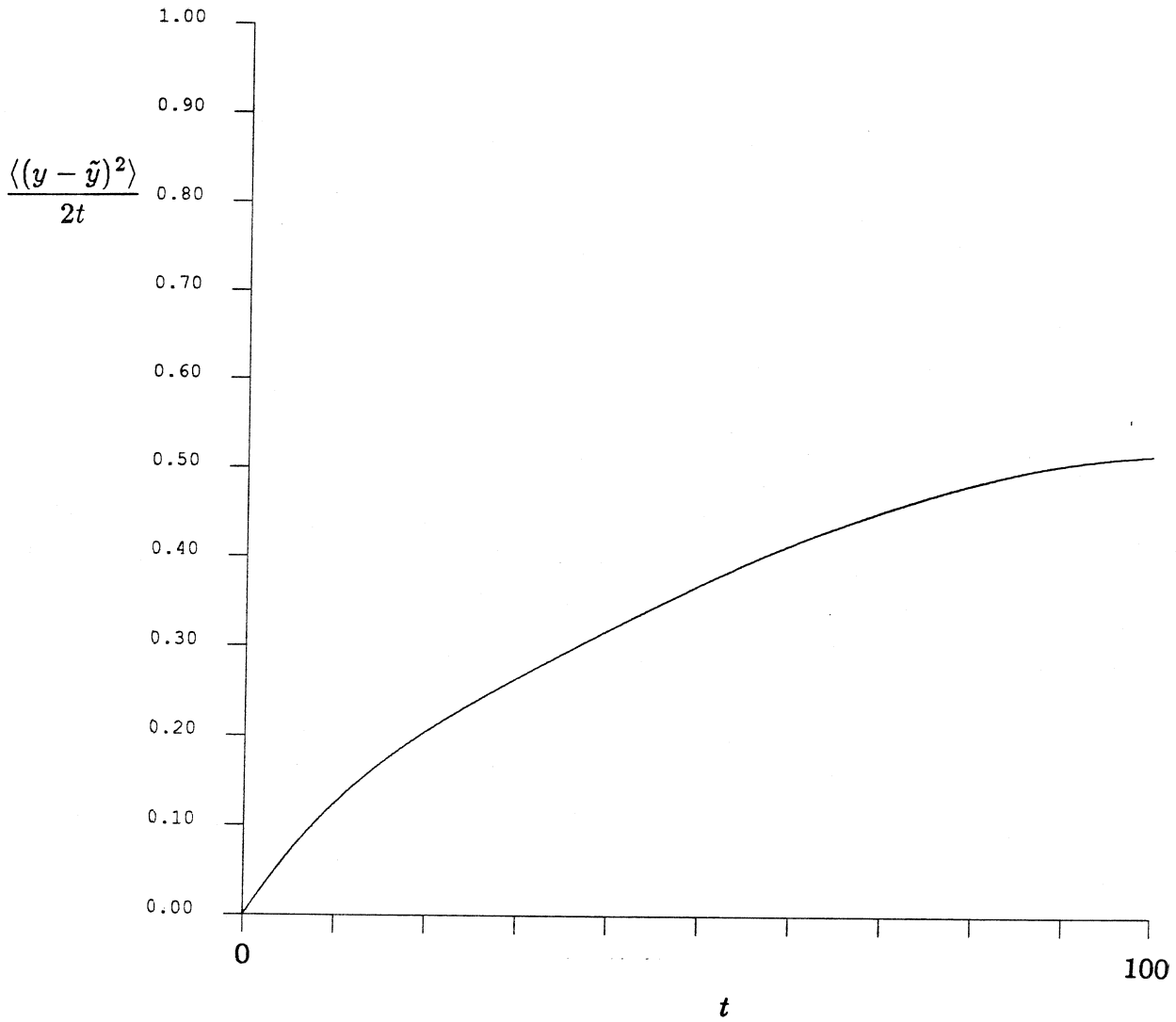

Figure B2.4 A $(D^s_\infty)_{yy}$-defining graph using displacement data from FTn1 (t= 150 – 400). The graph interval is 100 time units, and the time between interval initial conditions is 0.01 time unit.

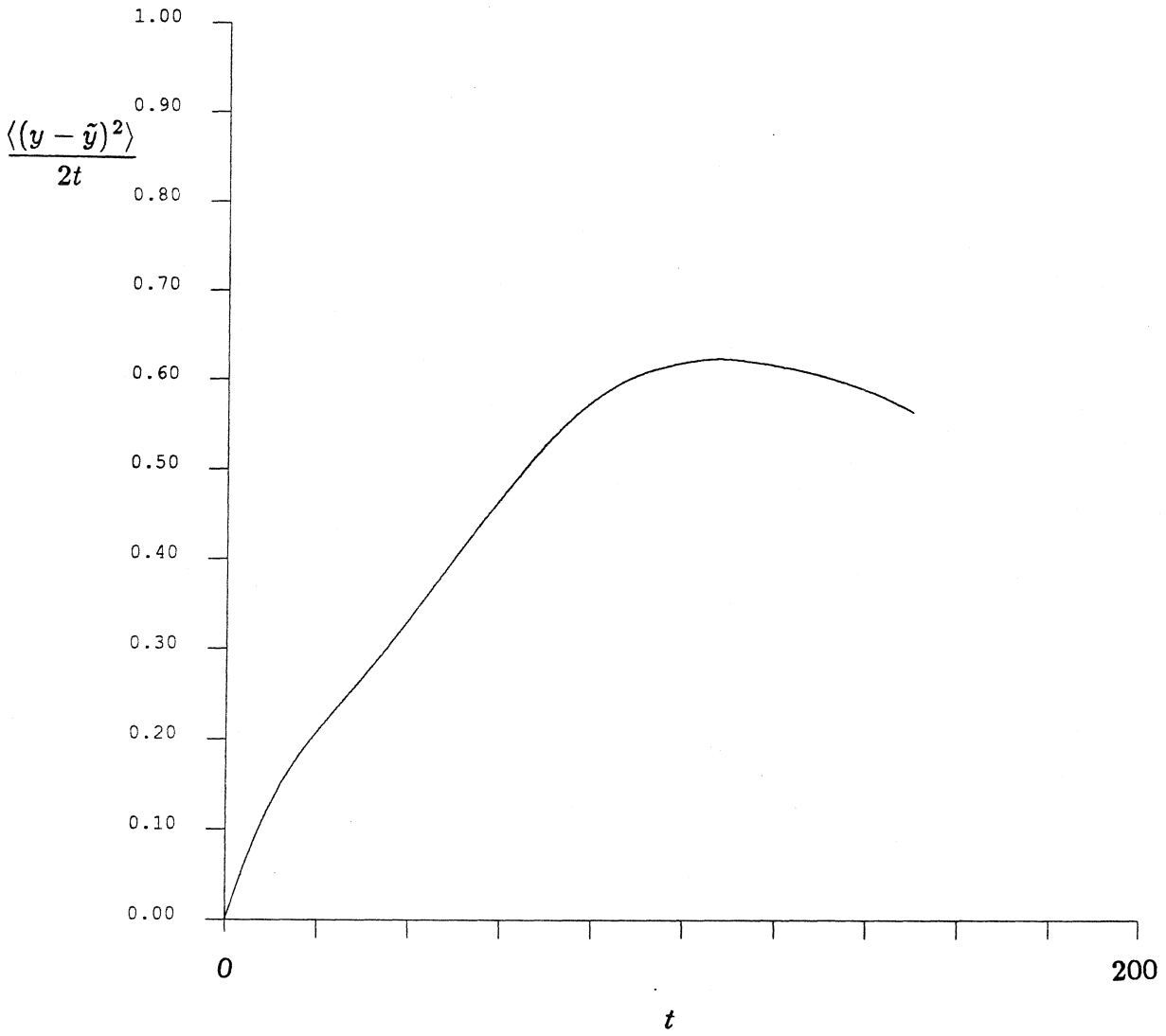

Figure B2.5 A $(D^s_\infty)_{yy}$-defining graph using displacement data from FTn1 (t= 150 – 400). The graph interval is 150 time units, and the time between interval initial conditions is 0.01 time unit.

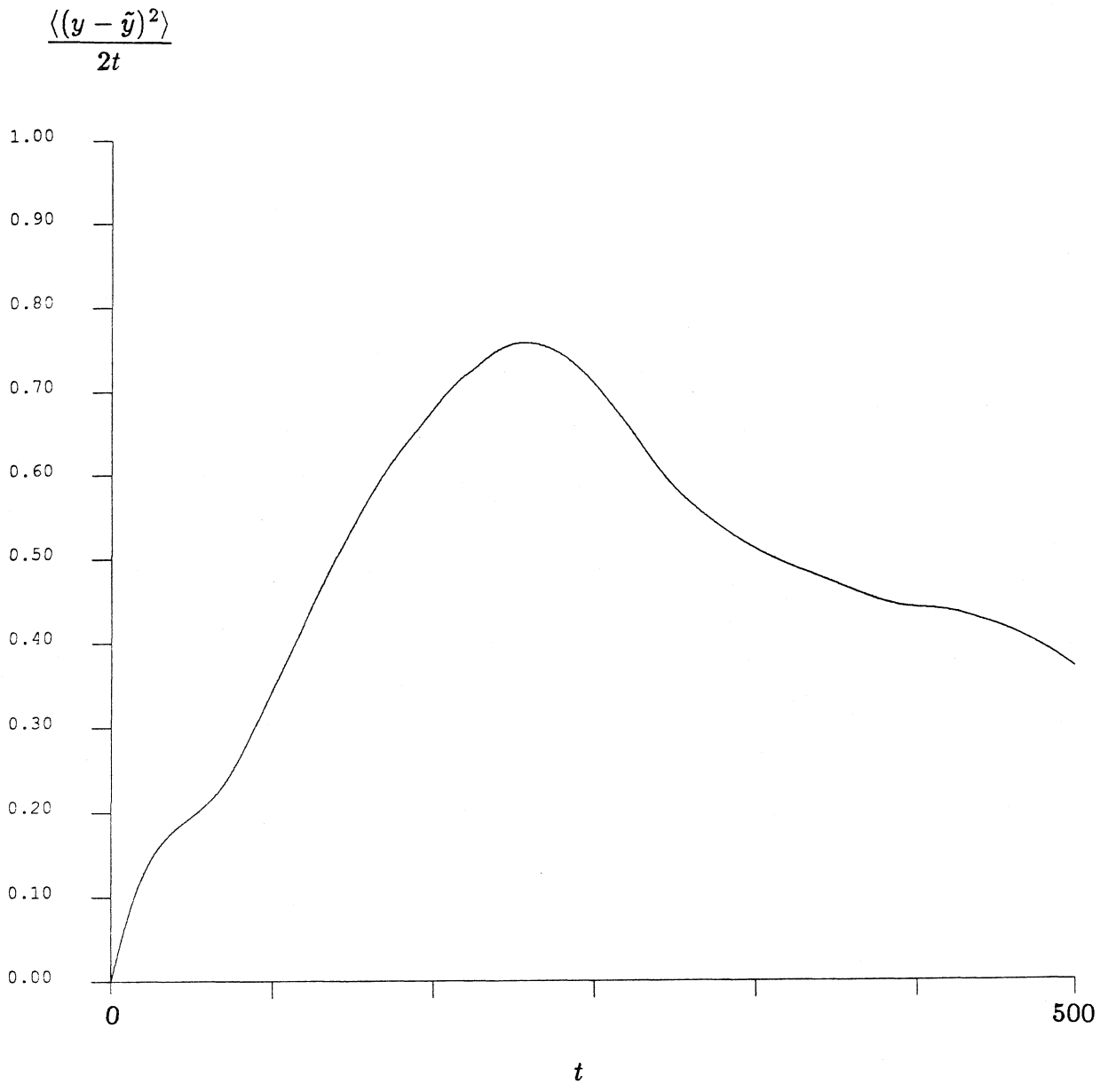

Figure B2.6 A $(D^s_\infty)_{yy}$-defining graph using displacement data from FTn1 (t= 0 – 500). The graph interval is 500 time units, which means that no averaging over different initial conditions is done.

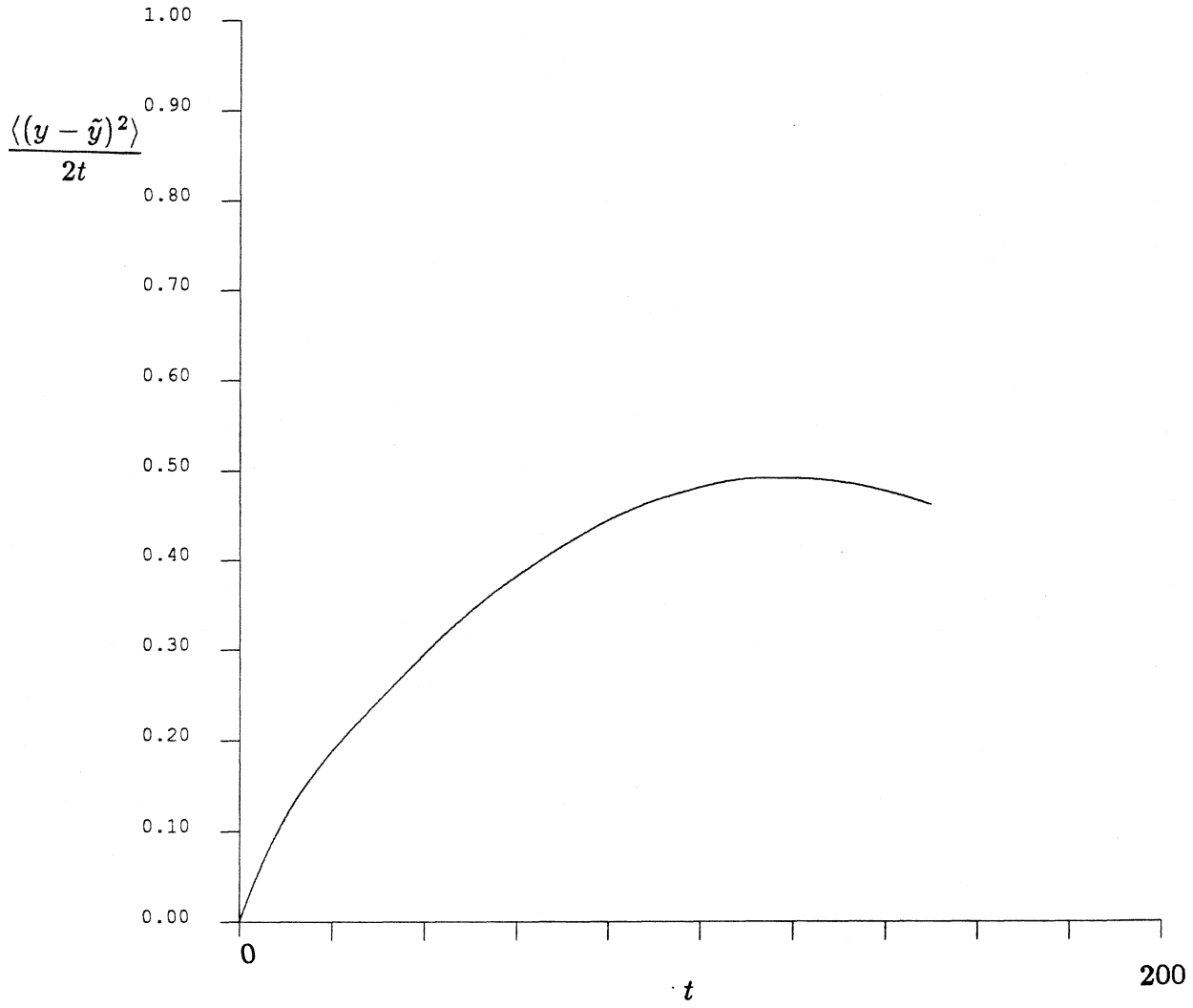

Figure B2.7 A $(D^s_\infty)_{yy}$-defining graph using displacement data from FTn1 (t= 150 – 500). The graph interval is 150 time units, and the time between interval initial conditions is 0.01 time unit.

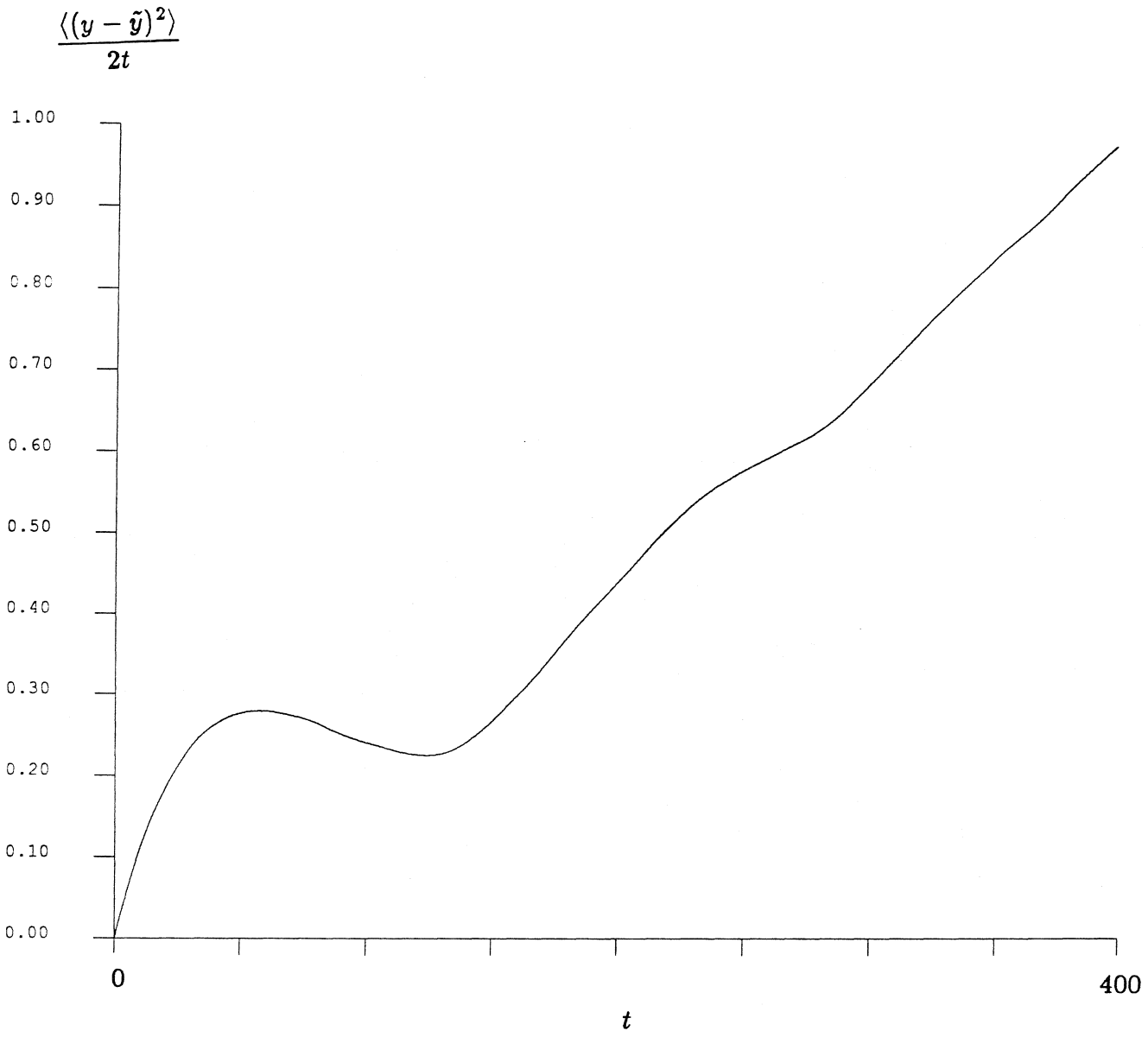

Figure B2.8 A $(D^s_\infty)_{yy}$-defining graph using displacement data from FTn2 (t= 500 – 1000). The graph interval is 400 time units, and the time between interval initial conditions is 0.01 time unit. Note that the graph indicates deterministic behavior for much of the this run.

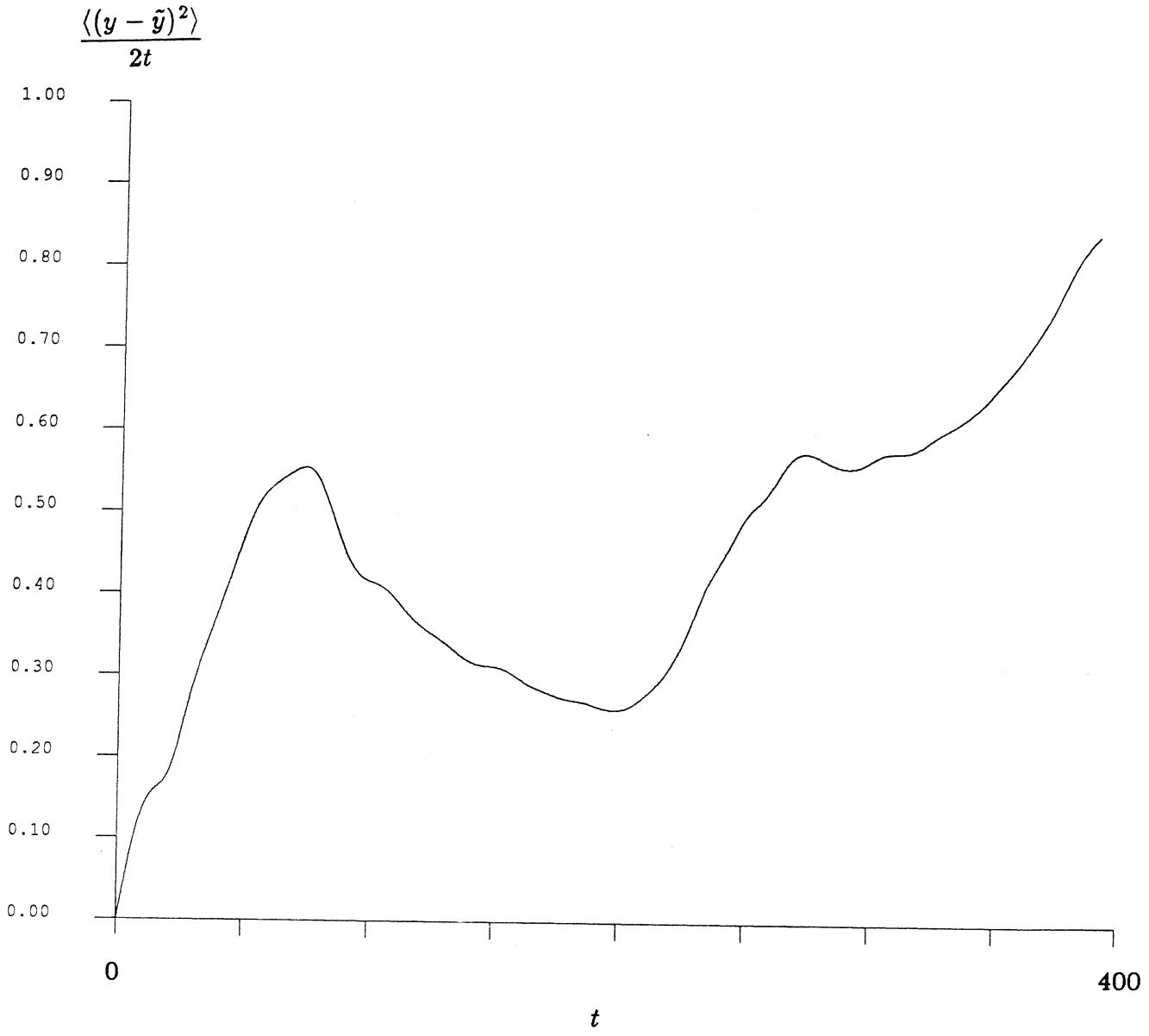

Figure B2.9 A $(D^e_\infty)_{yy}$-defining graph using displacement data from FTn2 (t= 500 – 900). The graph interval is 400 time units, which means that no averaging over different initial conditions is done.

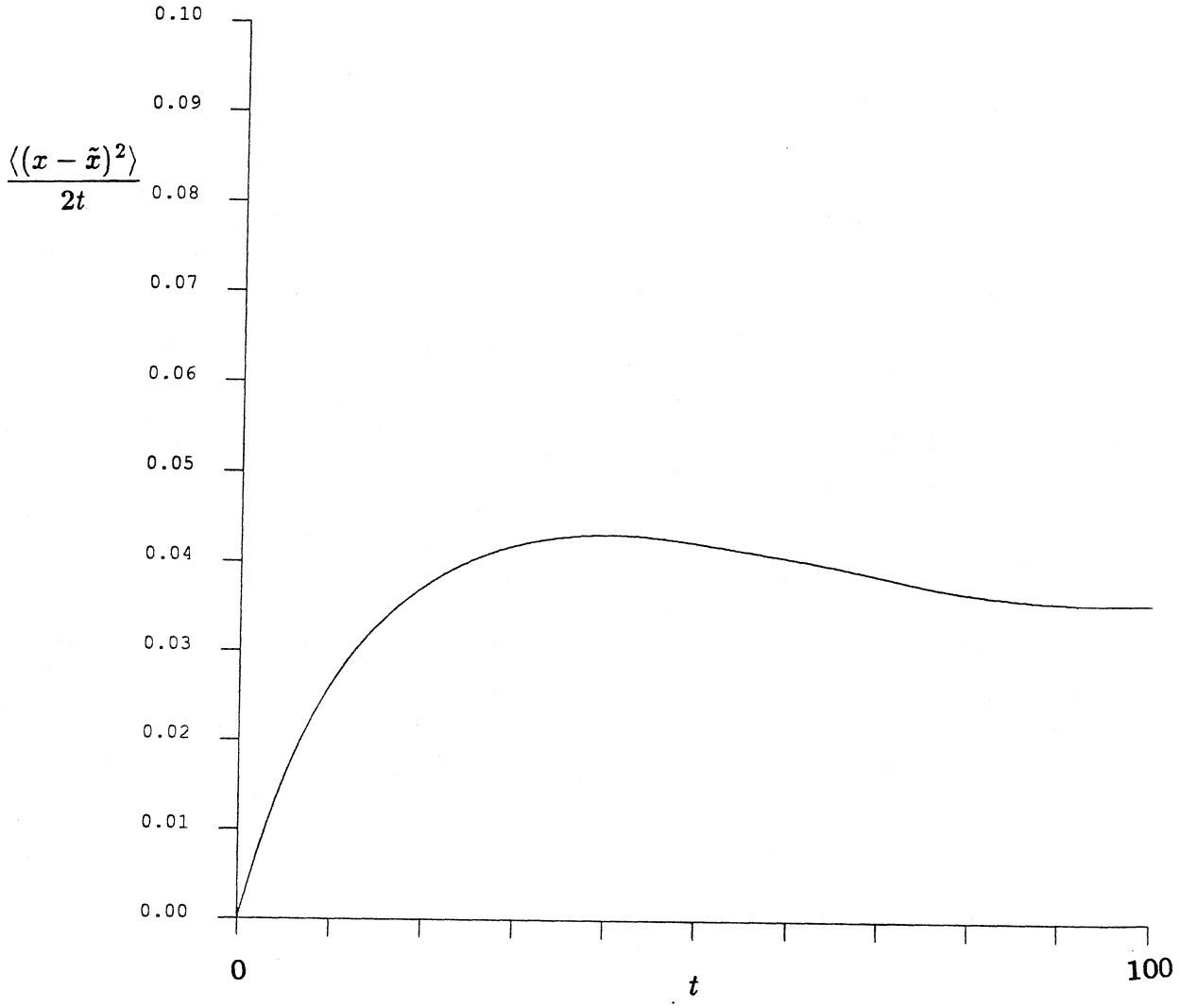

Figure B2.10 A $(D^s_\infty)_{xx}$-defining graph using displacement data from FTn1 (t= 150 – 400). The graph interval is 100 time units, and the time between interval initial conditions is 0.01 time unit.

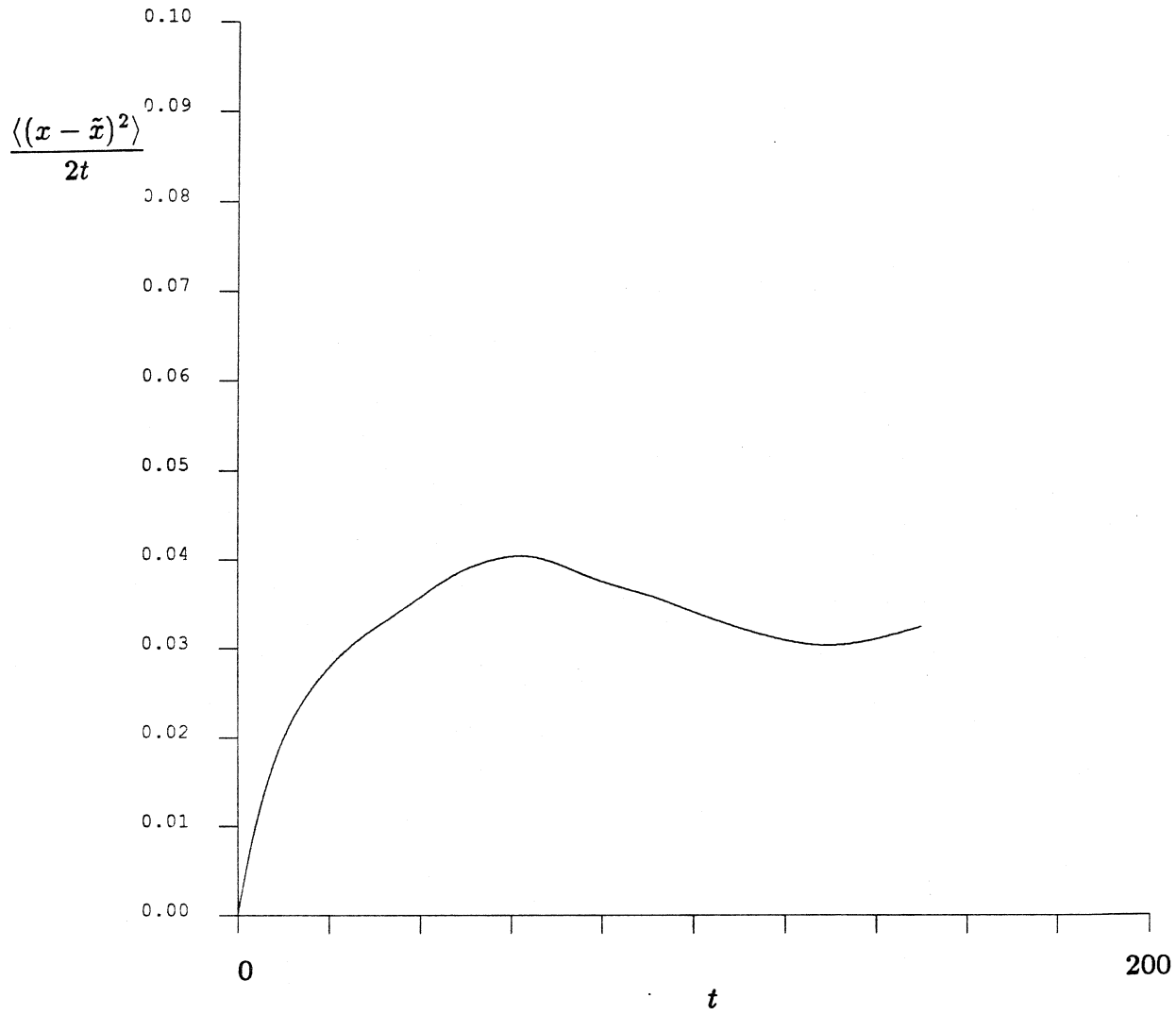

Figure B2.11 A $(D^s_\infty)_{xx}$-defining graph using displacement data from FTn1 (t= 150 – 400). The graph interval is 150 time units, and the time between interval initial conditions is 0.01 time unit.

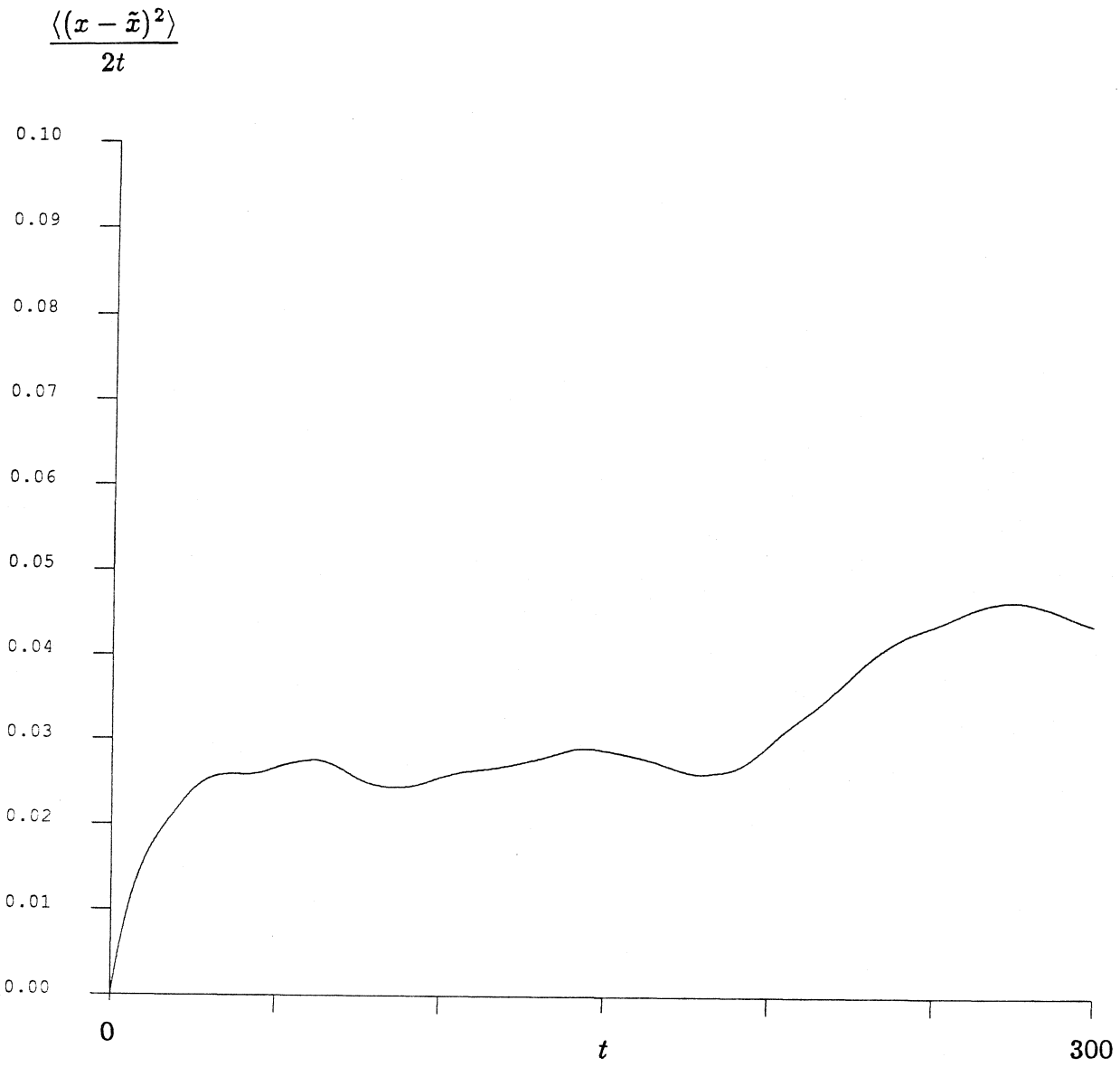

Figure B2.12 A $(D^s_\infty)_{xx}$-defining graph using displacement data from FTn1 (t= 200 – 500). The graph interval is 300 time units, which means that no averaging over different initial conditions is done.

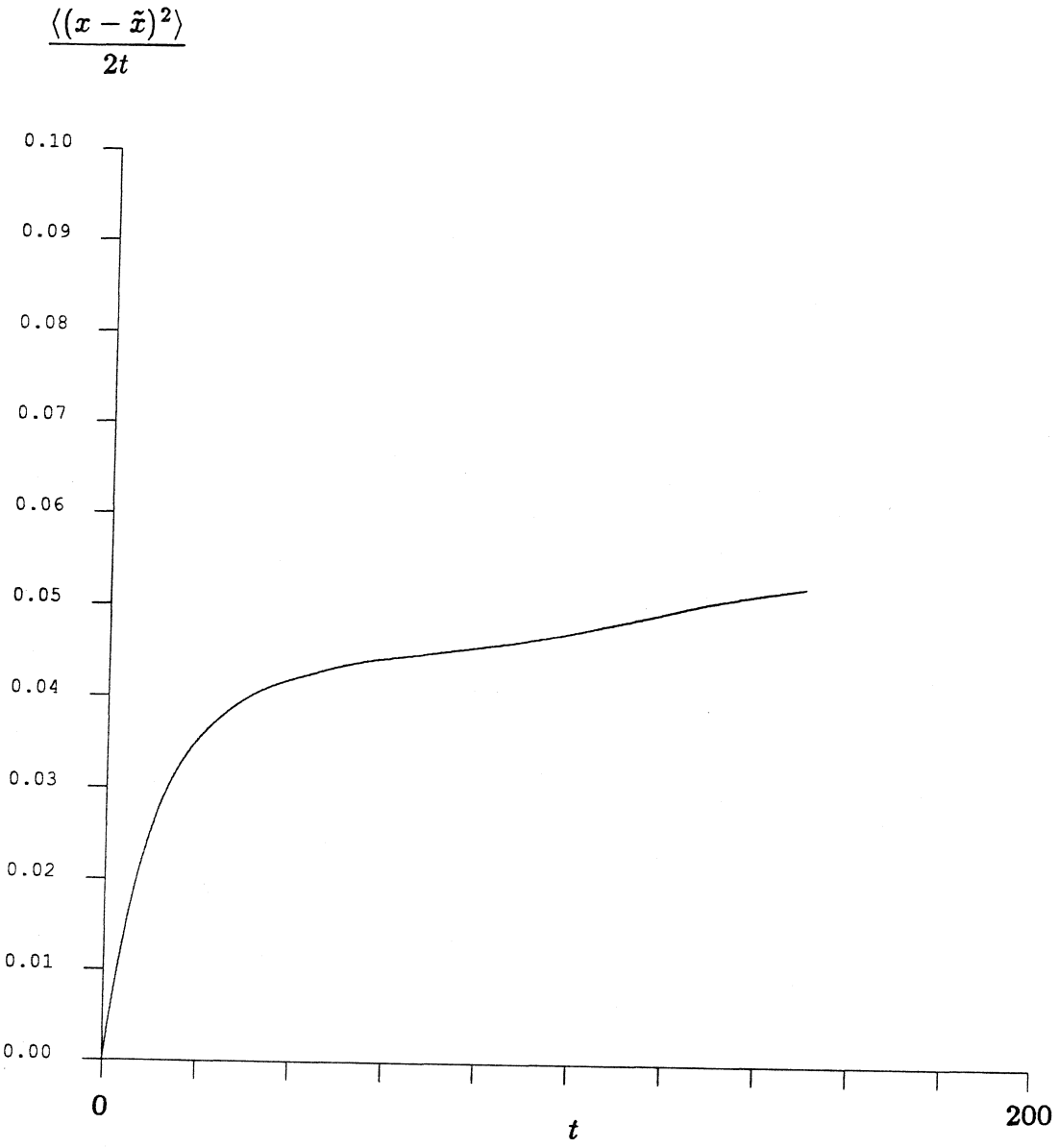

Figure B2.13 A $(D^s_\infty)_{xx}$-defining graph using displacement data from FTn1 (t= 150 – 500). The graph interval is 150 time units, and the time between interval initial conditions is 0.01 time unit.

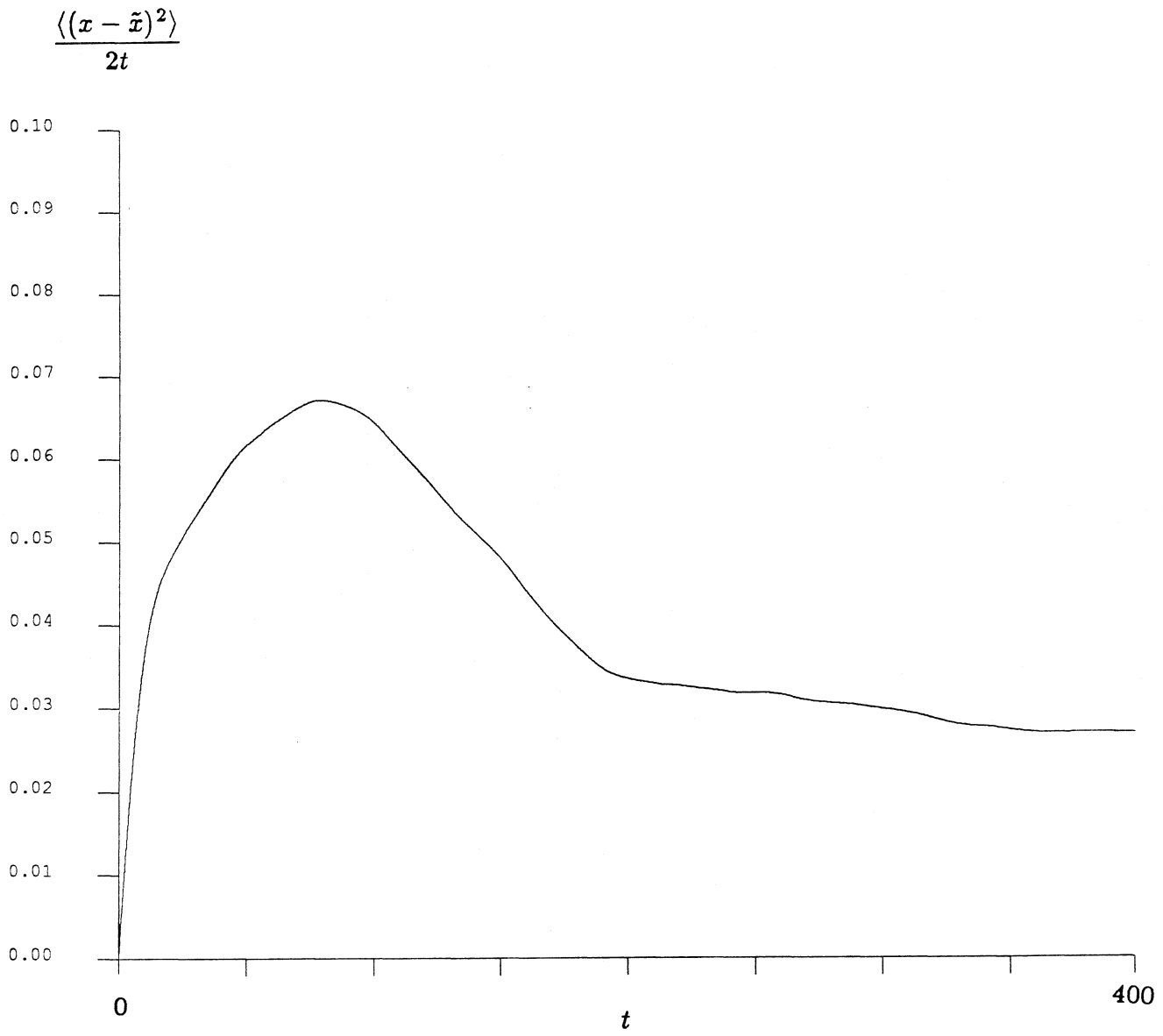

Figure B2.14 A $(D^s_\infty)_{xx}$-defining graph using displacement data from FTn2 (t= 500 – 1000). The graph interval is 400 time units, and the time between interval initial conditions is 0.01 time unit.

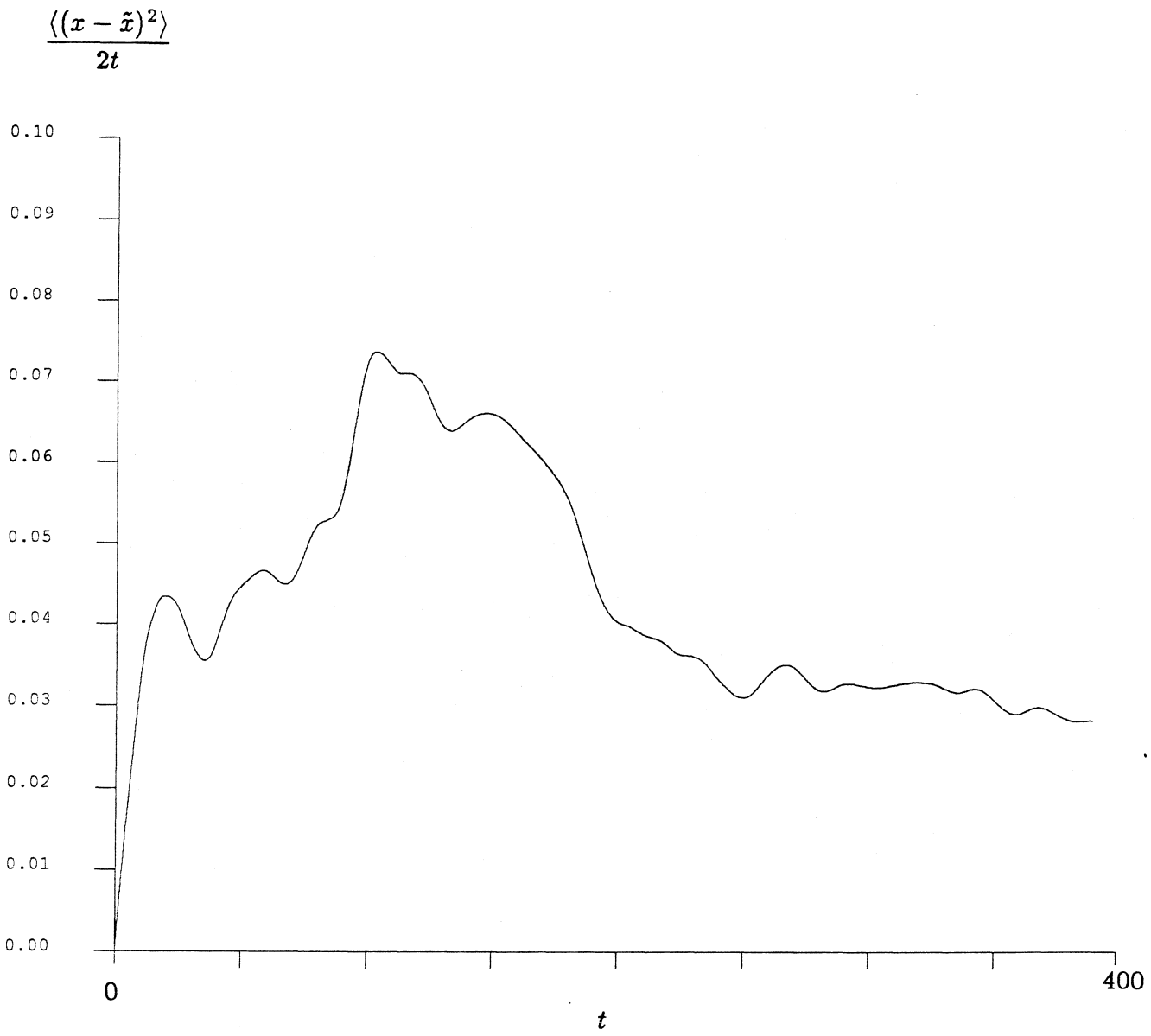

Figure B2.15 A $(D^s_\infty)_{xx}$-defining graph using displacement data from FTn2 (t= 500 – 900). The graph interval is 400 time units, which means that no averaging over different initial conditions is done.

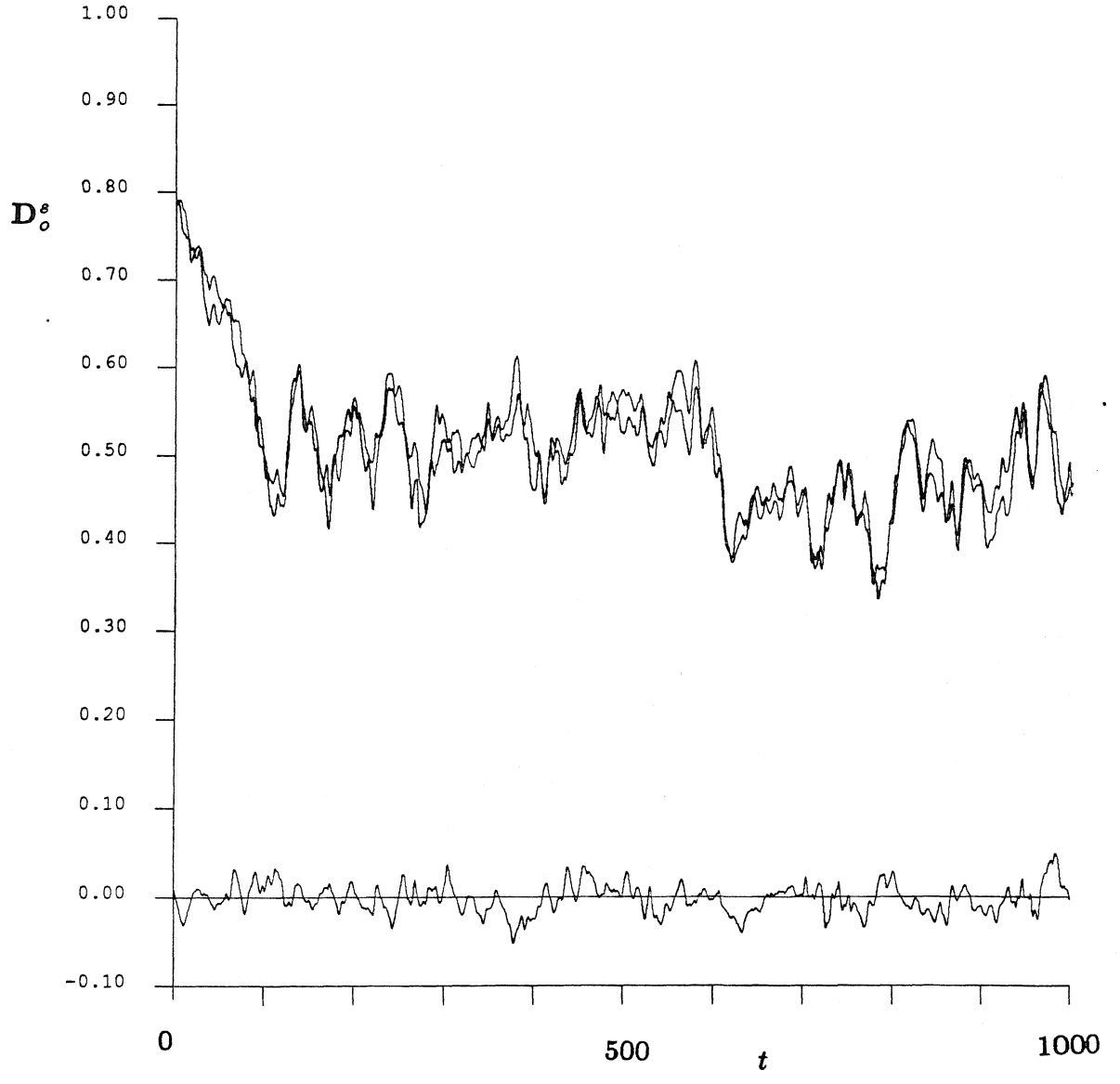

Figure B2.16 The time trace of $\mathbf{D}_o^s$ for the simulations FTn1 and FTn2. The upper two lines are the xx and yy components of this tensor. Of course, they should be equivalent for an infinite suspension – the slight variation occurs because of the finite number of spheres used in our simulation. The trace that fluctuates about the zero y-axis is the xy component of the short-time, self-diffusion tensor. Again, for an infinite number of spheres, this quantity would be exactly zero.

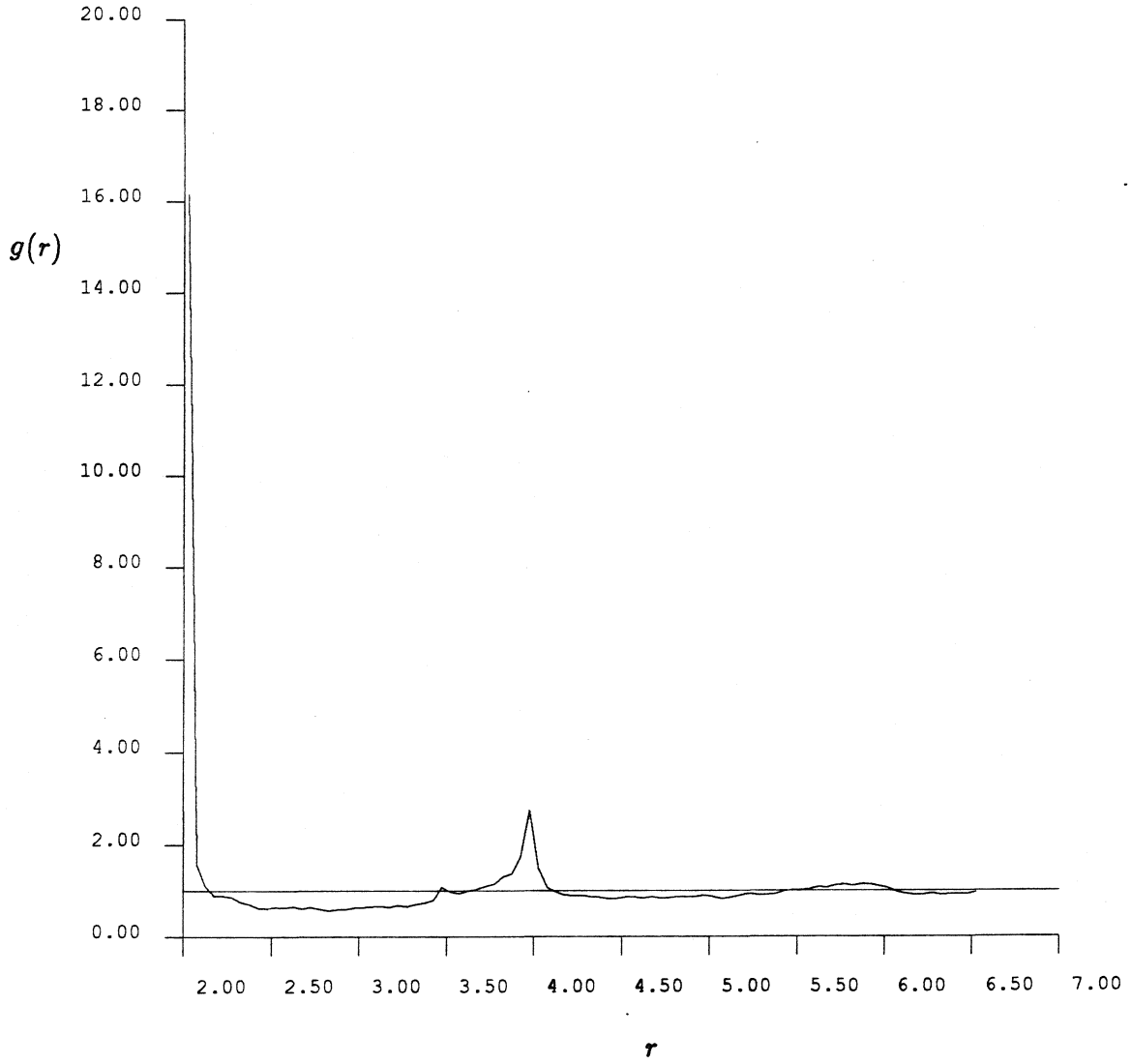

Figure B2.17 The radial pair-distribution function, $g(r)$, for the FTn1 run (t = 150 – 500).

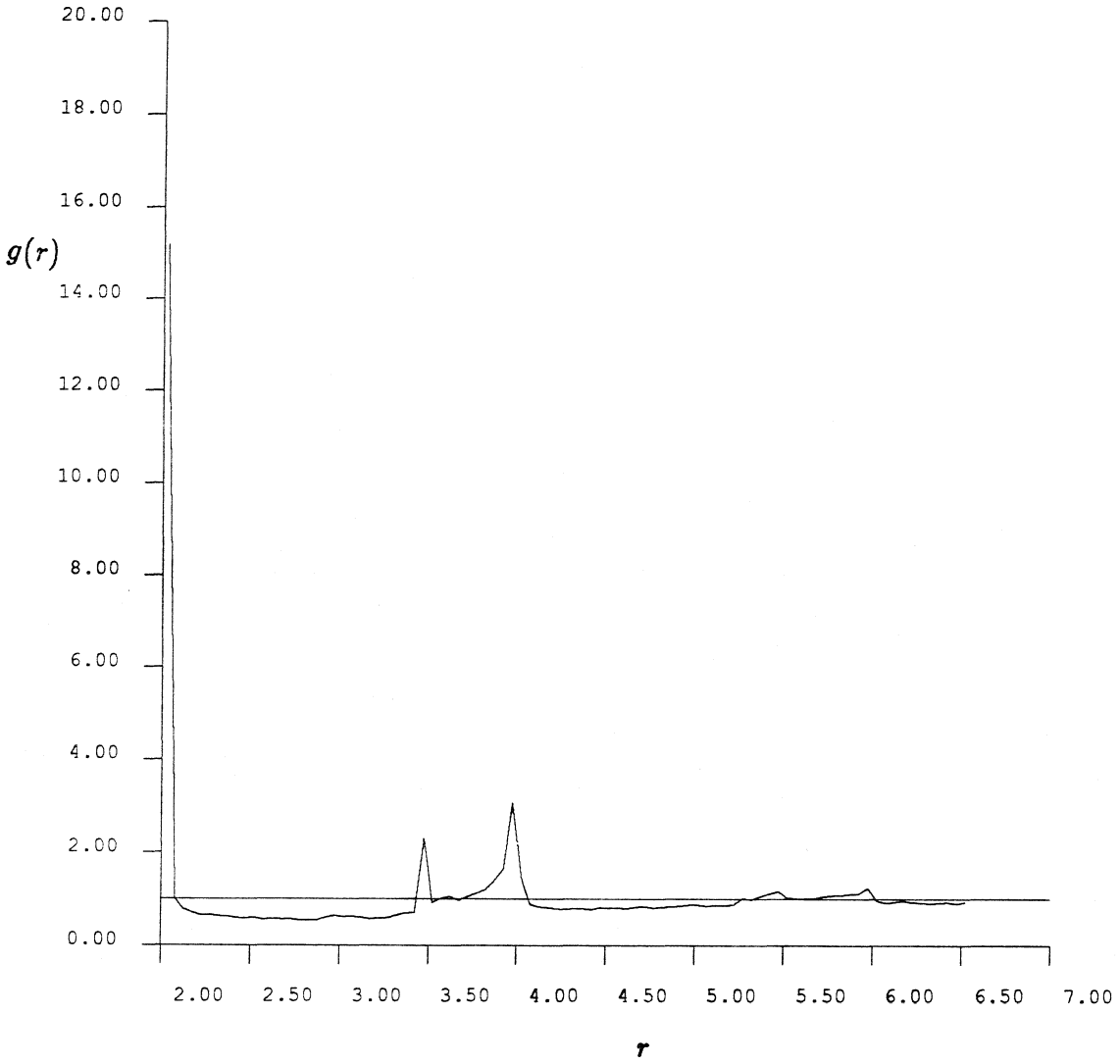

Figure B2.18 The radial pair-distribution function, $g(r)$, for the FTn2 run (t = 500 – 1000).

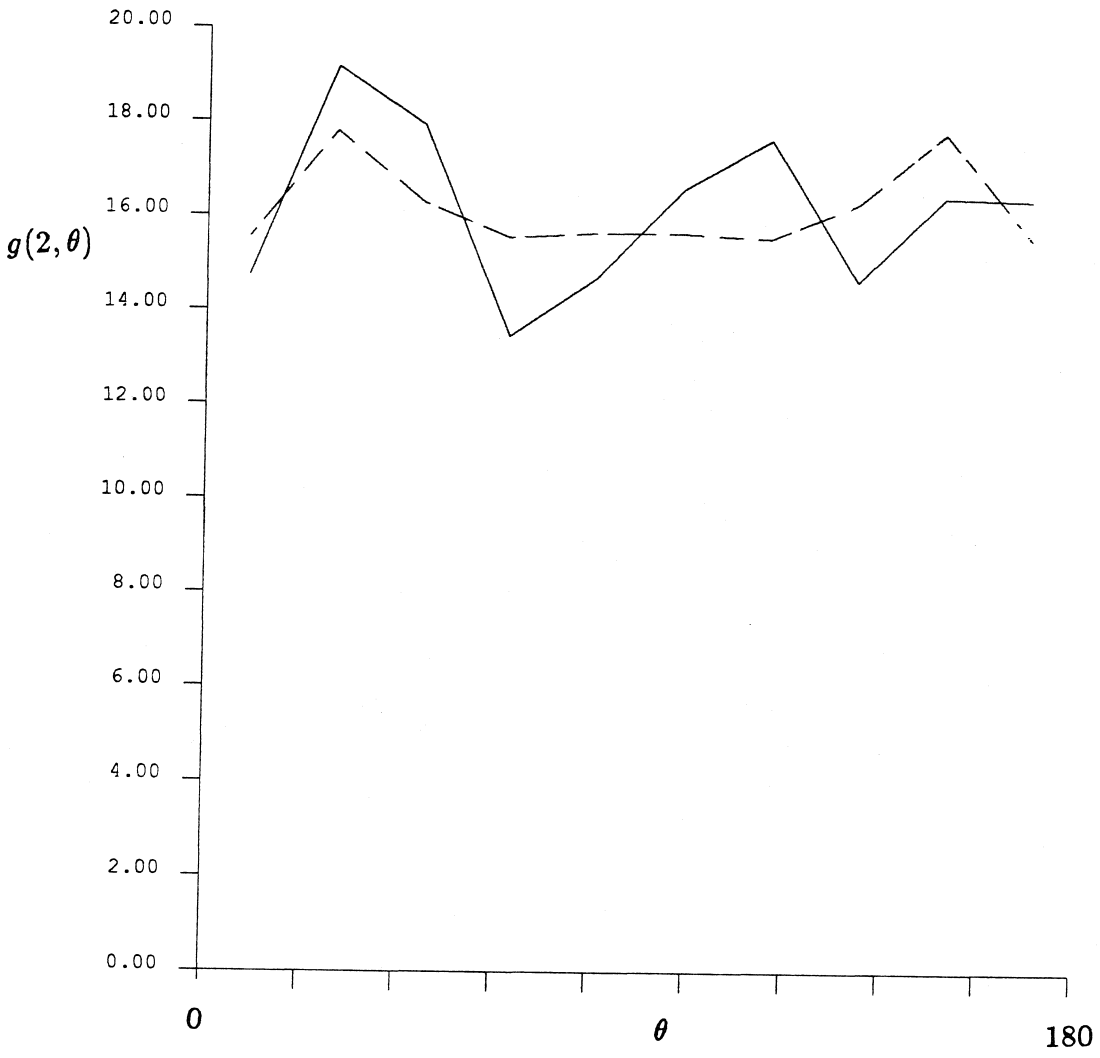

Figure B2.19 The full pair-distribution function for spheres whose surfaces are separated by less than 0.05 radii using data from the FTn1 run (t = 150 – 500). The dashed curve represents this function when it is forced to be symmetric about $\theta = 90°$.

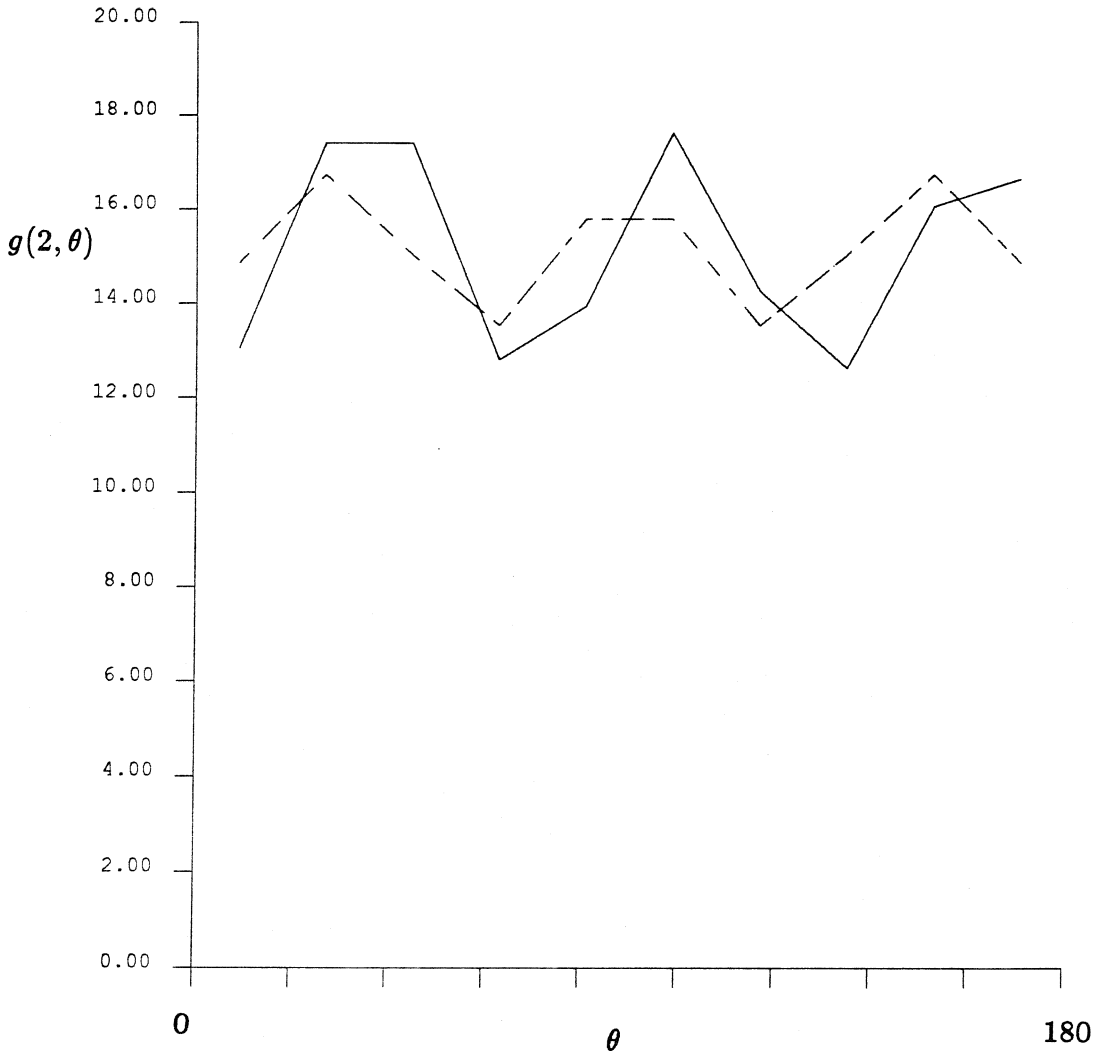

Figure B2.20 The full pair-distribution function for spheres whose surfaces are separated by less than 0.05 radii using data from the FTn2 run (t = 500 – 1000). The dashed curve represents this function when it is forced to be symmetric about $\theta = 90°$.

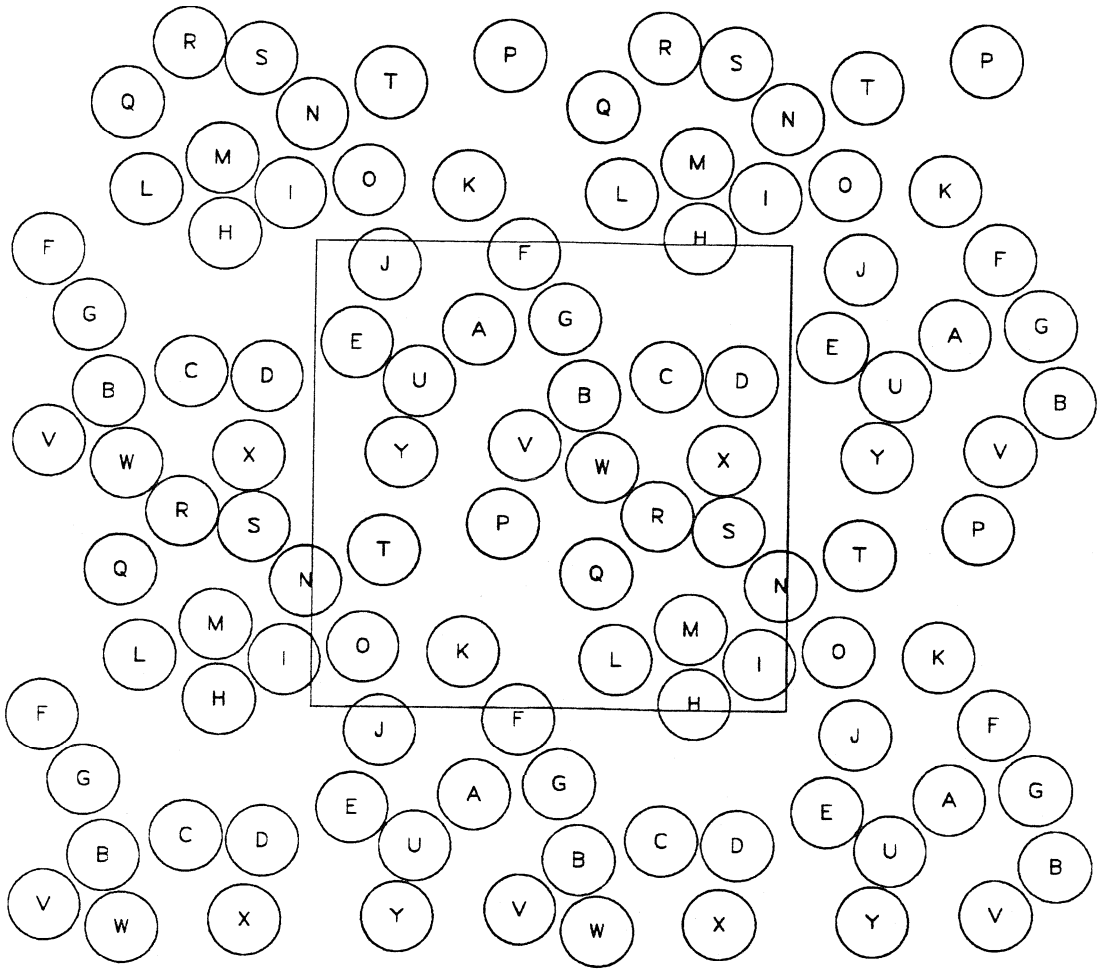

Figure B2.21 A "snapshot" of sphere positions. The square is the periodic cell. These are the sphere positions at $t = 0.05$ time units (FTn1). Note that this is the initial configuration for all simulations except for the n49 and FTa runs. It is generated from a Monte-Carlo simulation.

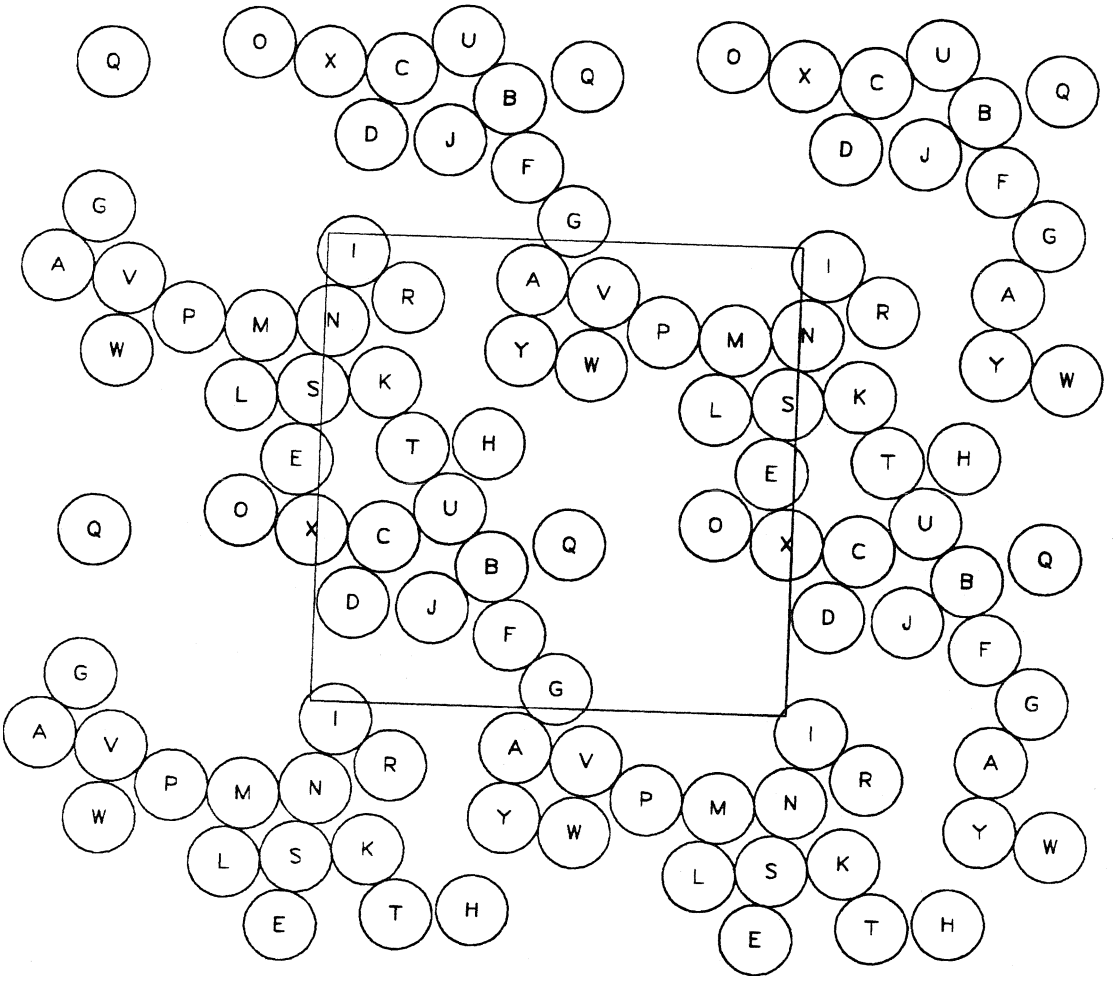

Figure B2.22 A "snapshot" of sphere positions. The square is the periodic cell. These are the sphere positions at $t = 100.00$ time units (FTn1).

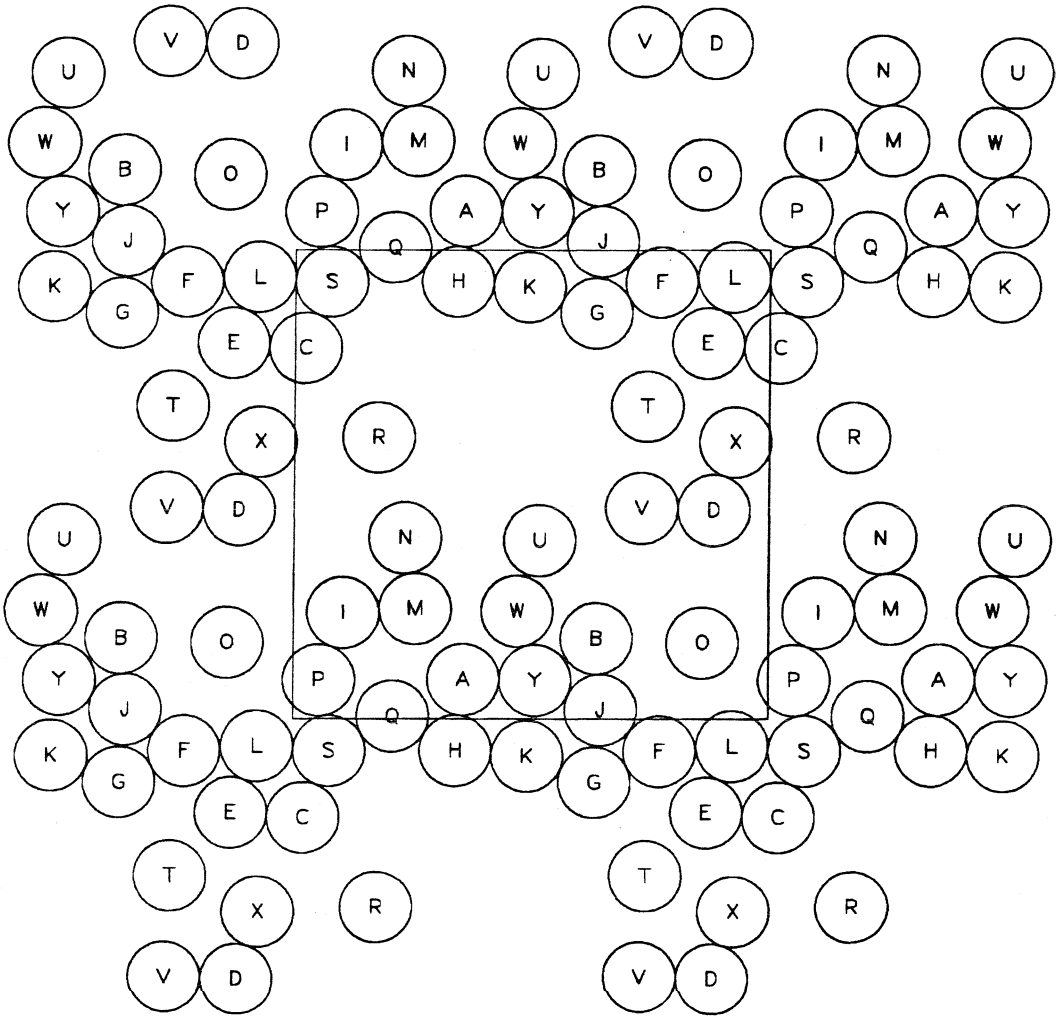

Figure B2.23 A "snapshot" of sphere positions. The square is the periodic cell. These are the sphere positions at $t = 150.00$ time units (FTn1).

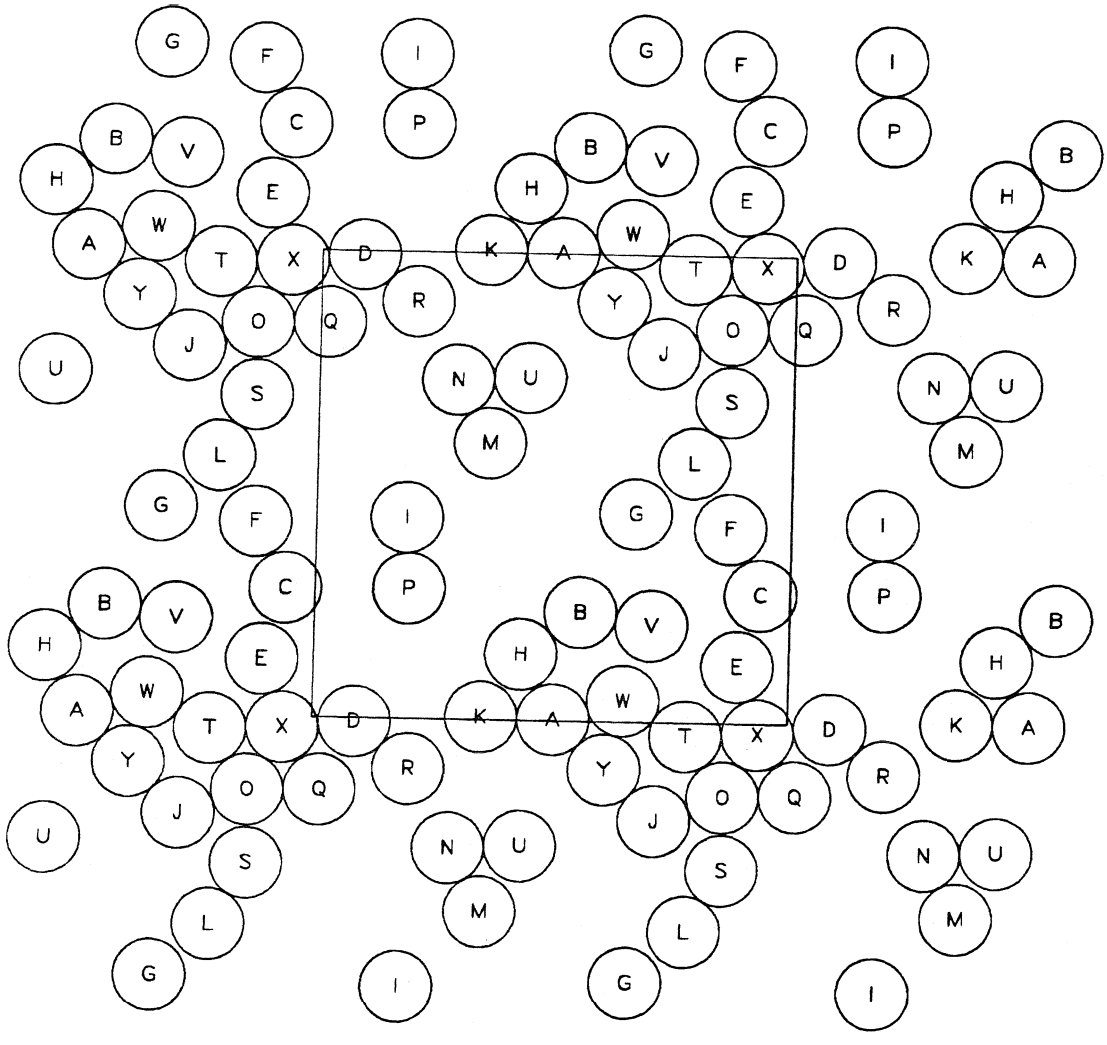

Figure B2.24 A "snapshot" of sphere positions. The square is the periodic cell. These are the sphere positions at $t = 200.00$ time units (FTn1).

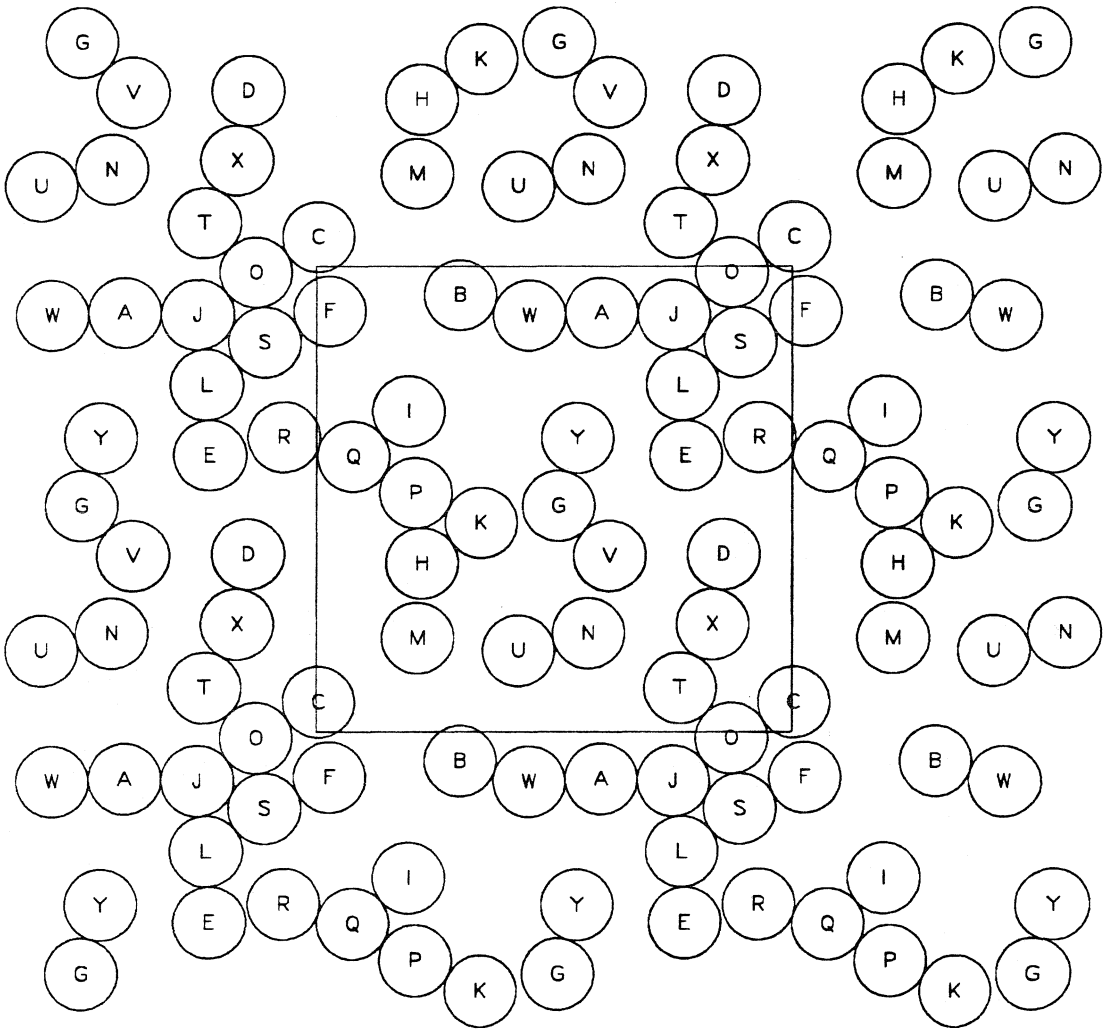

Figure B2.25 A "snapshot" of sphere positions. The square is the periodic cell. These are the sphere positions at $t = 250.00$ time units (FTn1).

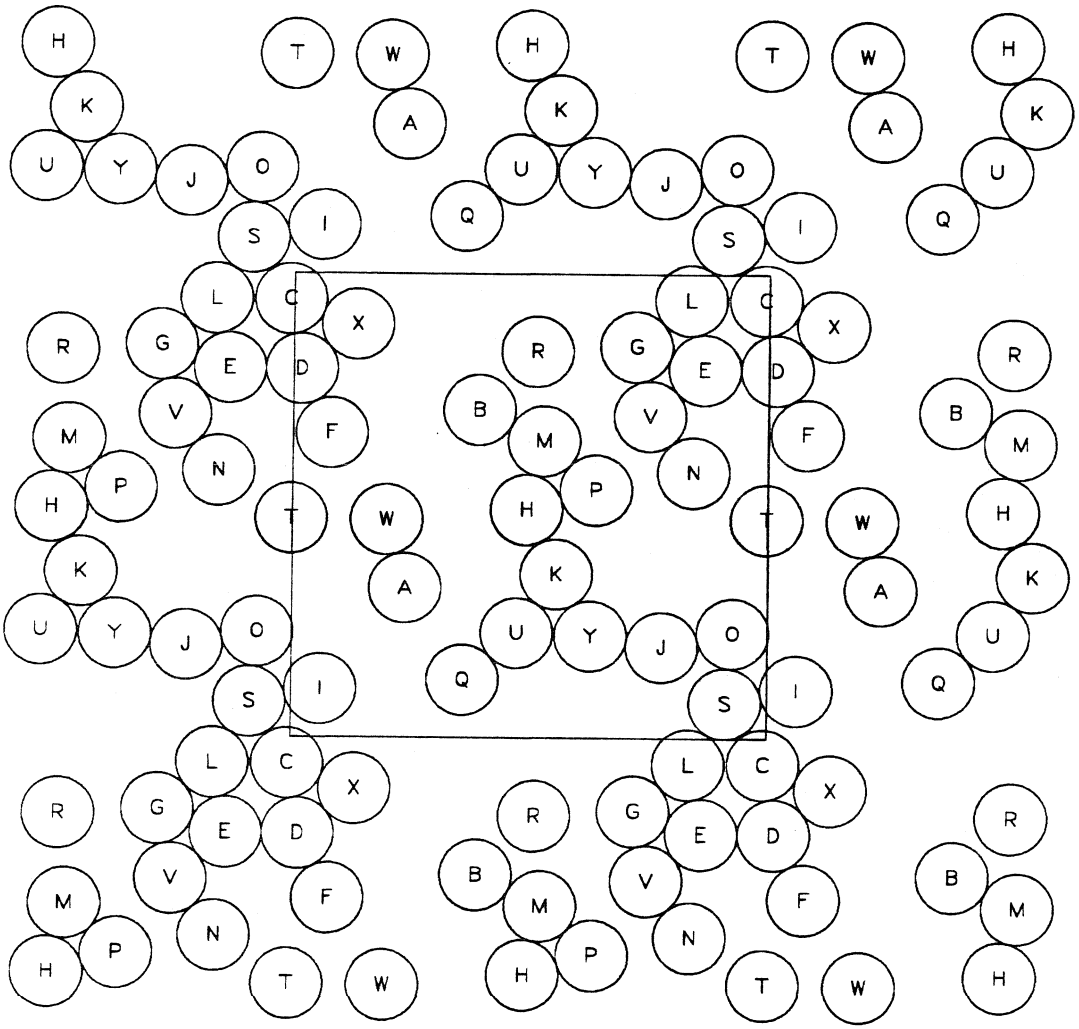

Figure B2.26 A "snapshot" of sphere positions. The square is the periodic cell. These are the sphere positions at $t = 300.00$ time units (FTn1).

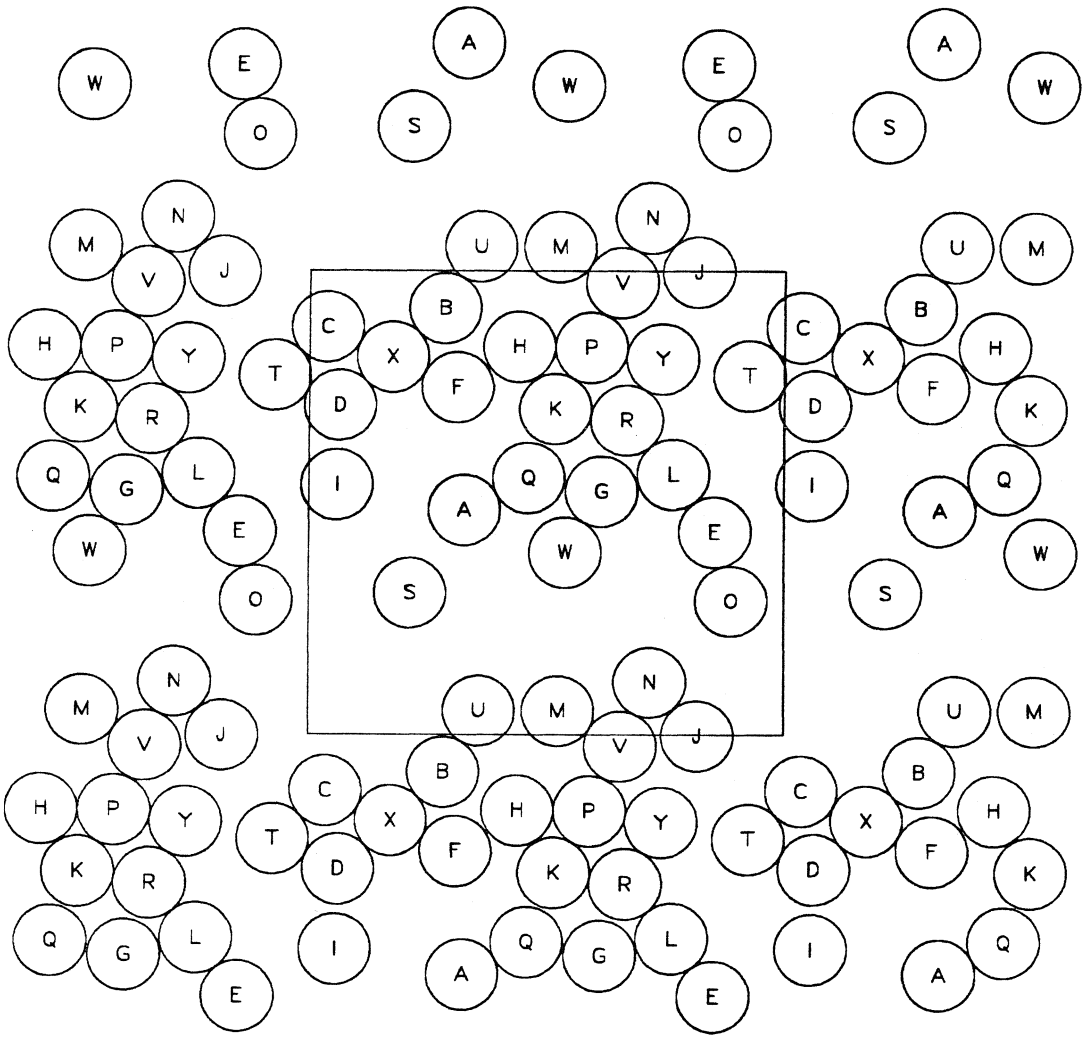

Figure B2.27 A "snapshot" of sphere positions. The square is the periodic cell. These are the sphere positions at $t = 350.00$ time units (FTn1).

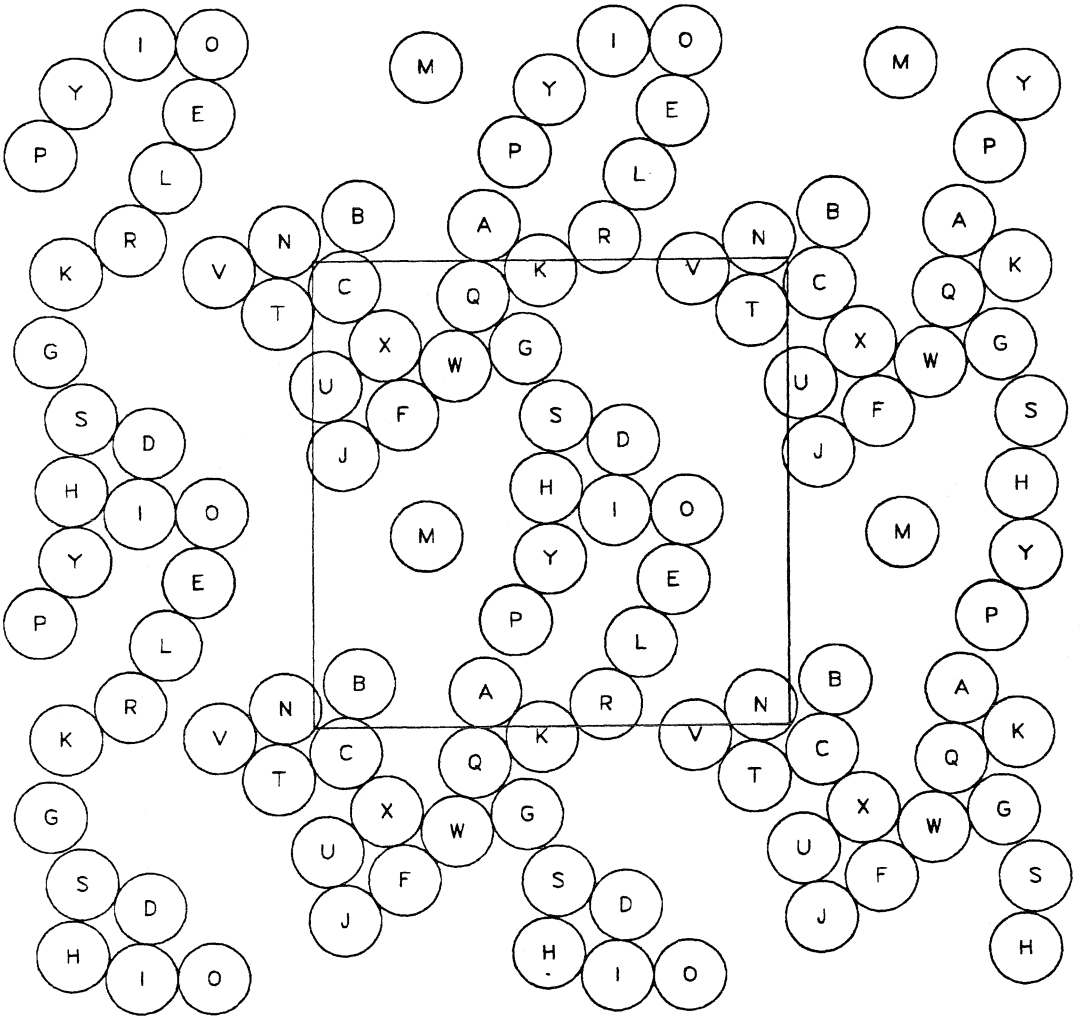

Figure B2.28 A "snapshot" of sphere positions. The square is the periodic cell. These are the sphere positions at $t = 400.00$ time units (FTn1).

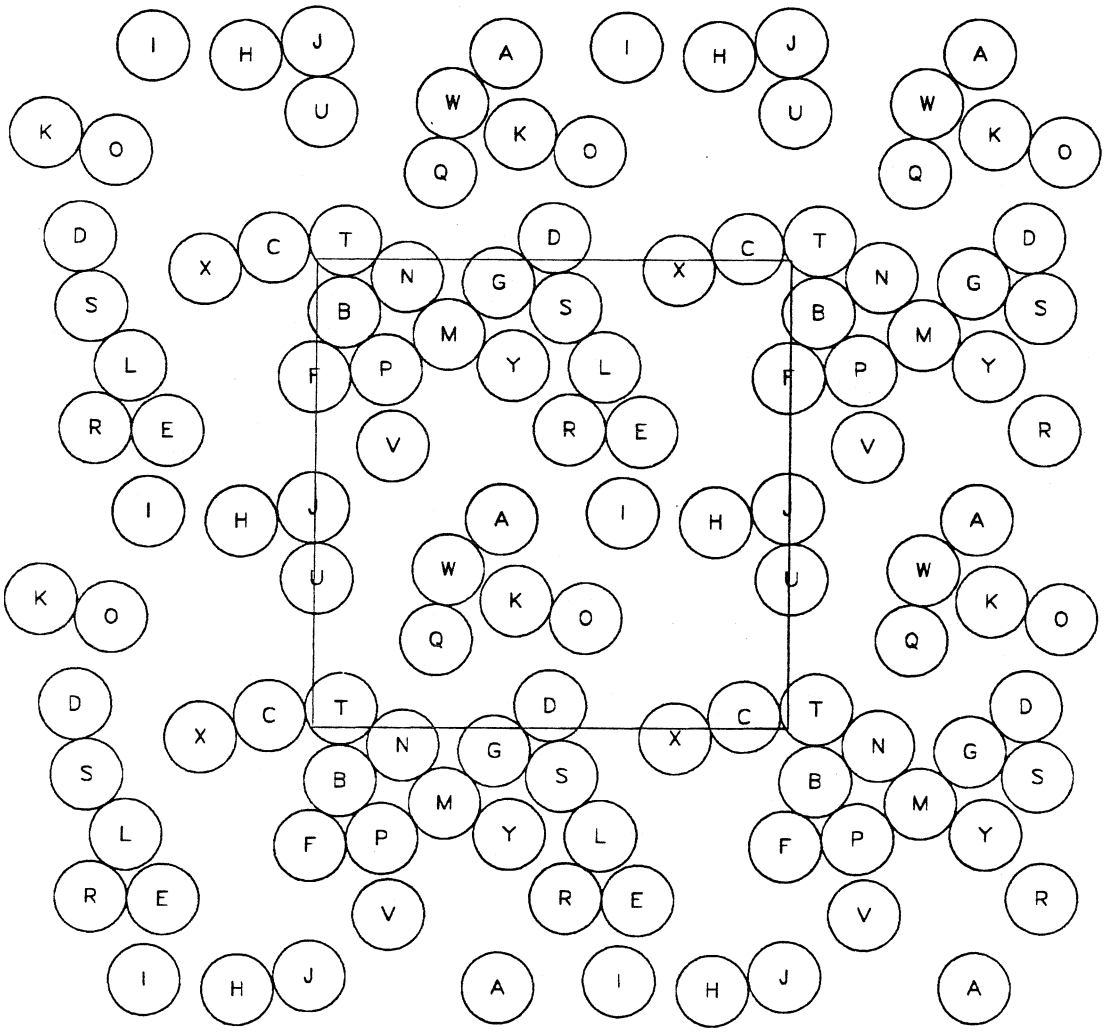

Figure B2.29 A "snapshot" of sphere positions. The square is the periodic cell. These are the sphere positions at $t = 450.00$ time units (FTn1).

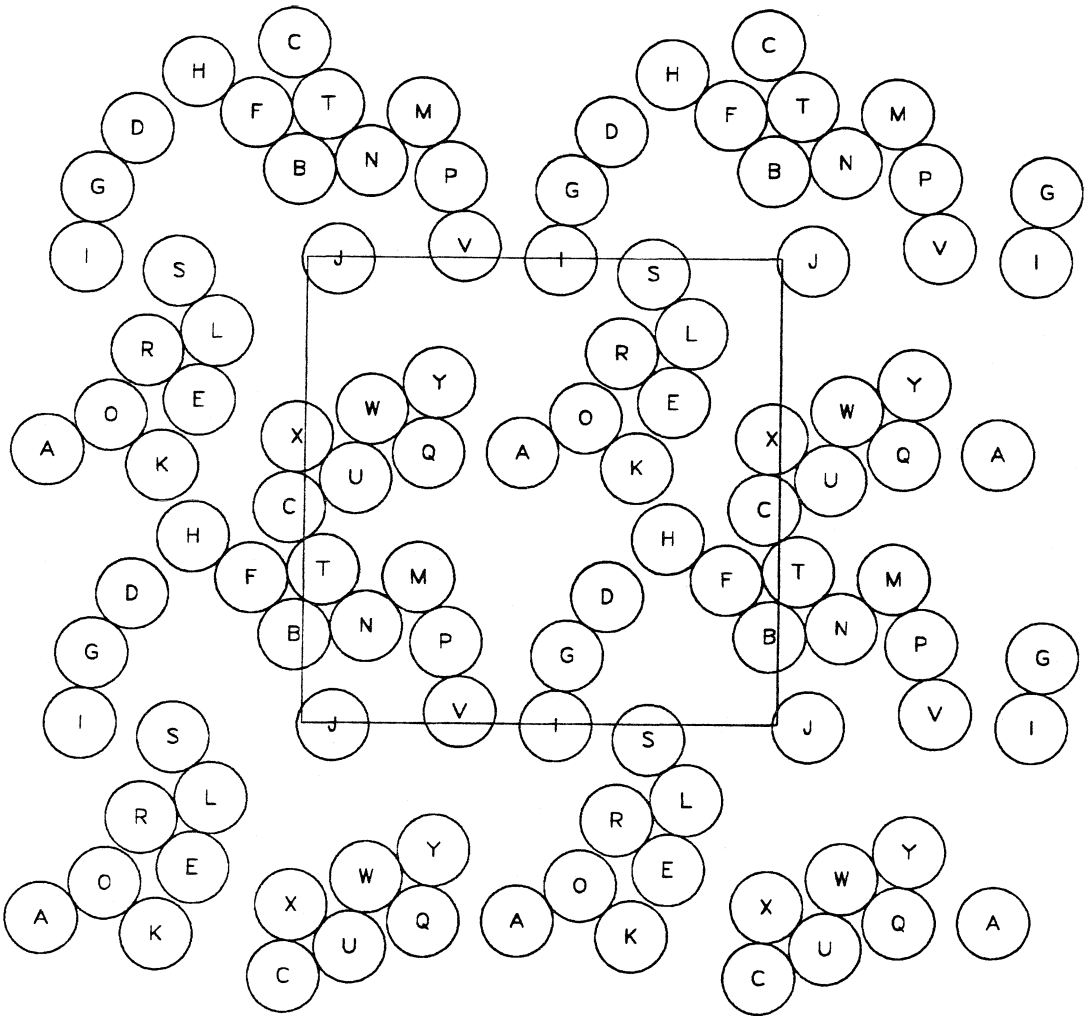

Figure B2.30 A "snapshot" of sphere positions. The square is the periodic cell. These are the sphere positions at $t = 500.00$ time units (FTn1).

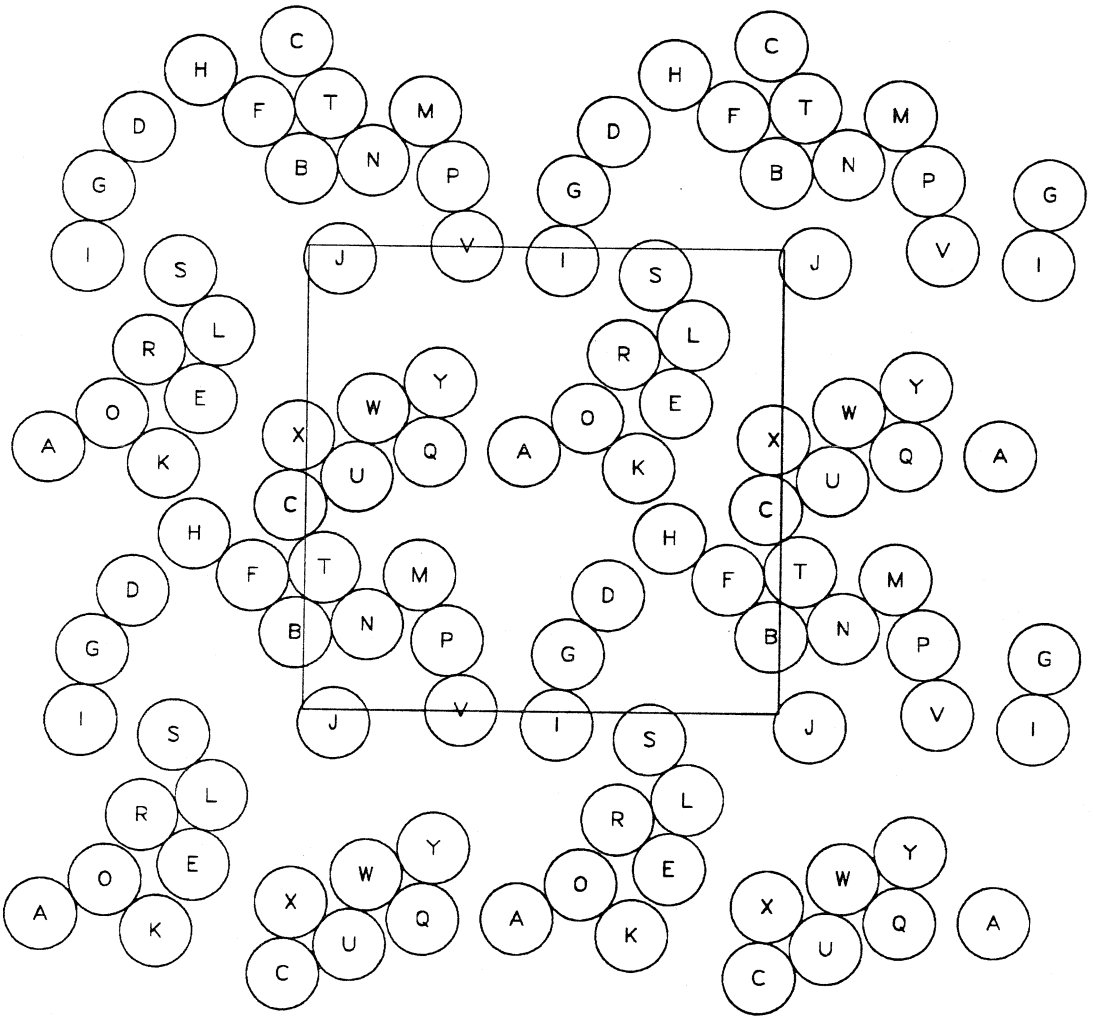

Figure B2.31 A "snapshot" of sphere positions. The square is the periodic cell. These are the sphere positions at $t = 500.05$ time units (FTn2).

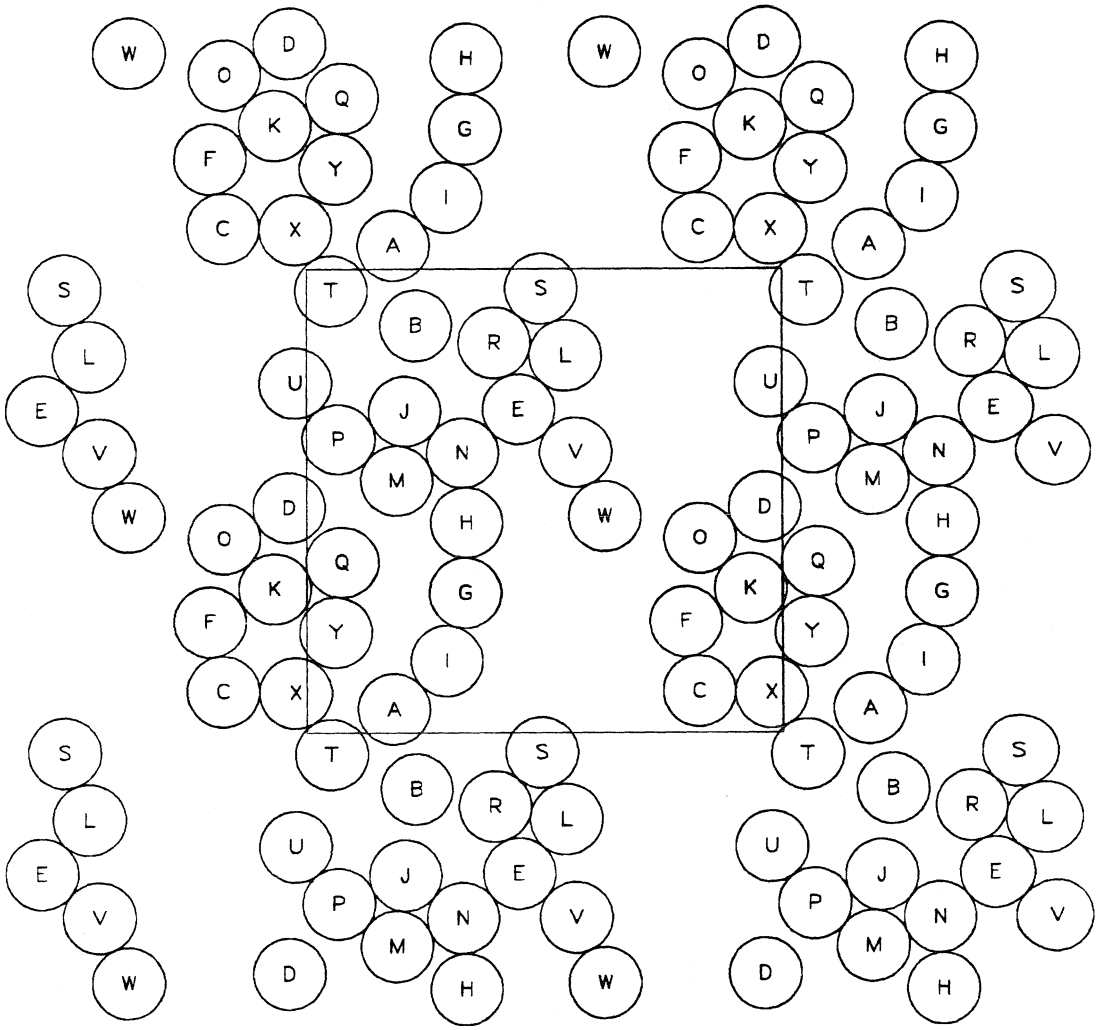

Figure B2.32 A "snapshot" of sphere positions. The square is the periodic cell. These are the sphere positions at $t = 600.00$ time units (FTn2).

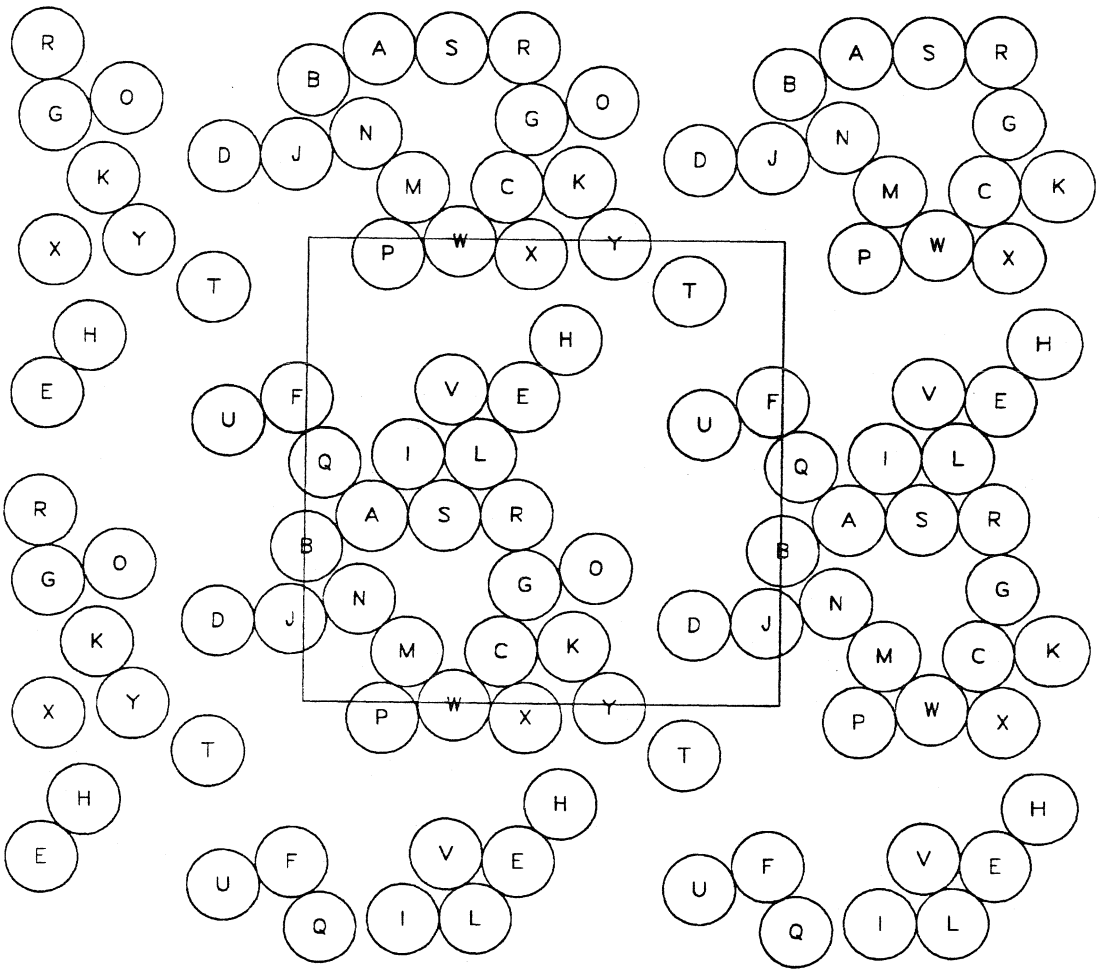

Figure B2.33 A "snapshot" of sphere positions. The square is the periodic cell. These are the sphere positions at $t = 700.00$ time units (FTn2).

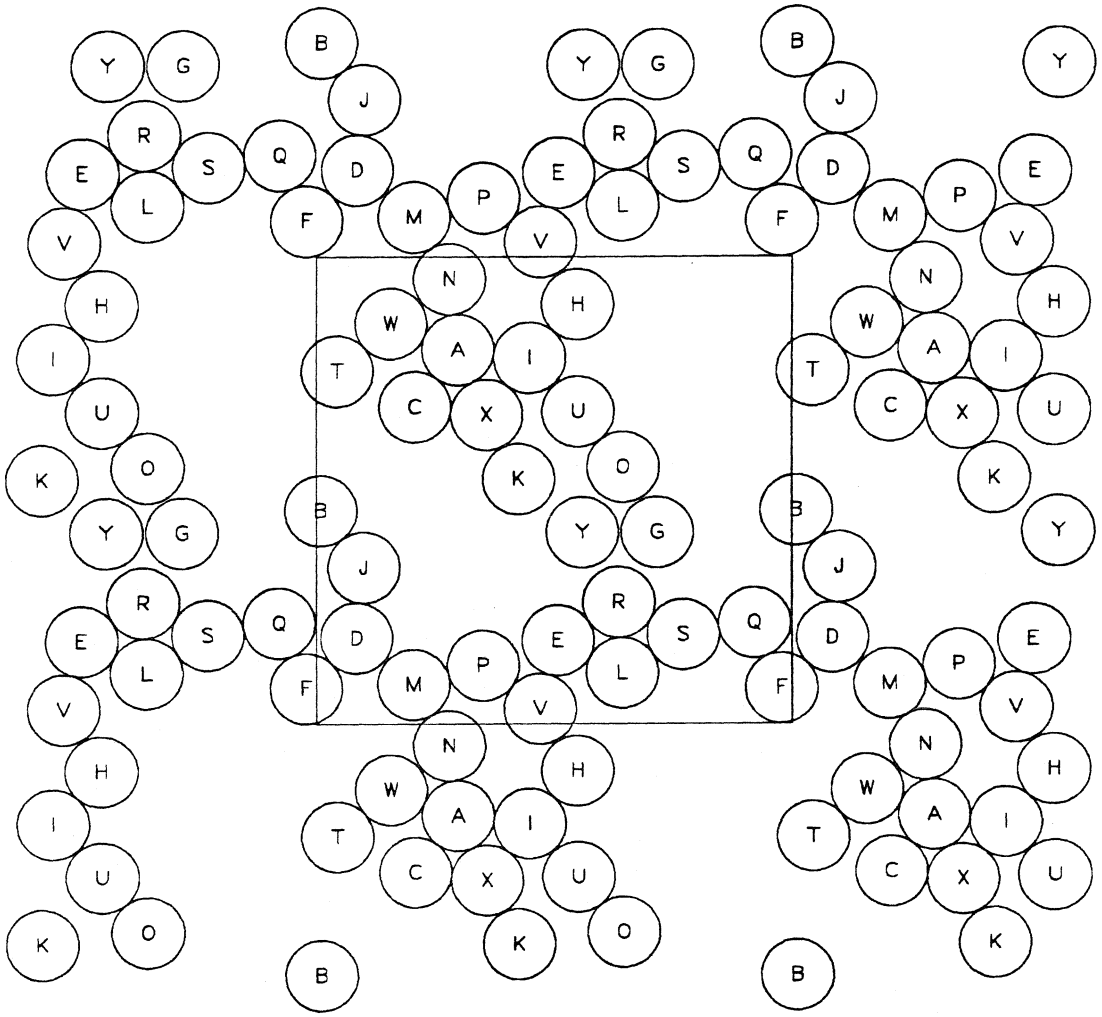

Figure B2.34 A "snapshot" of sphere positions. The square is the periodic cell. These are the sphere positions at $t = 800.00$ time units (FTn2).

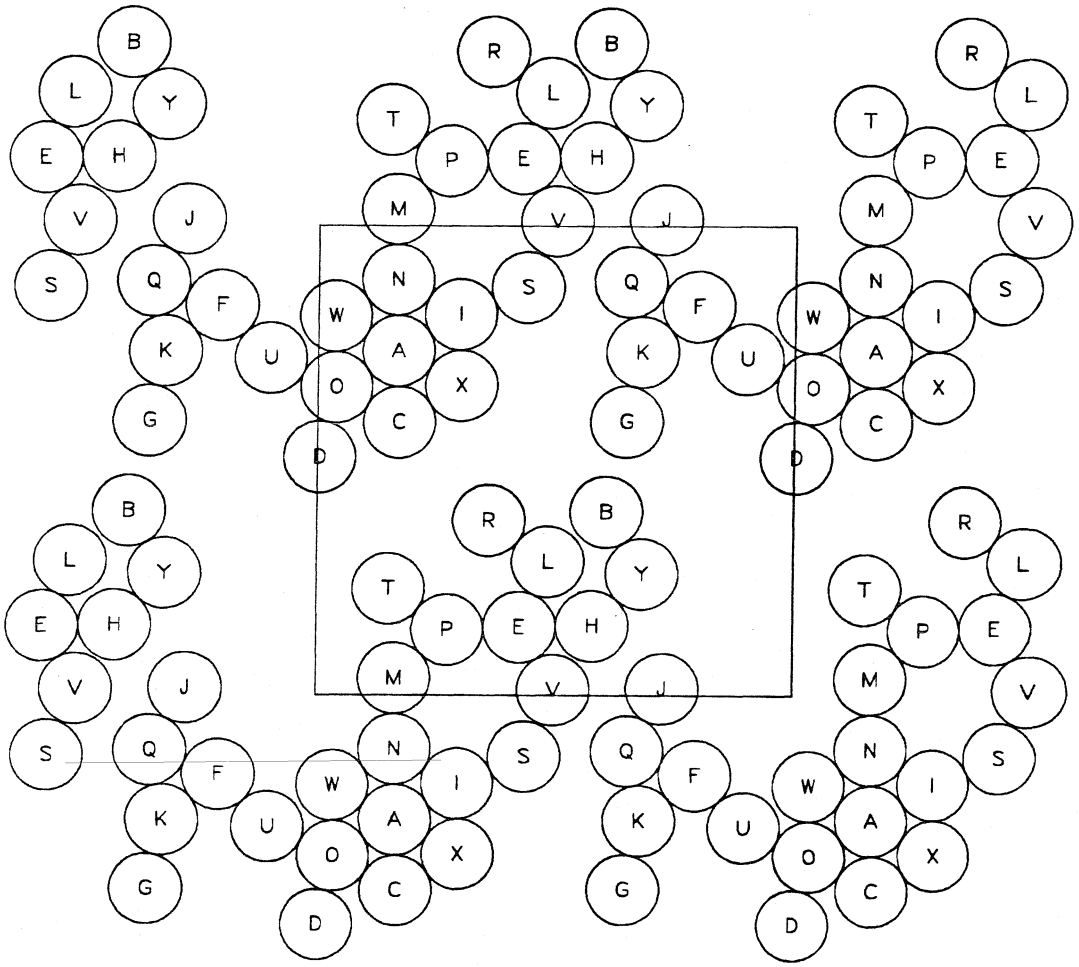

Figure B2.35 A "snapshot" of sphere positions. The square is the periodic cell. These are the sphere positions at $t = 900.00$ time units (FTn2).

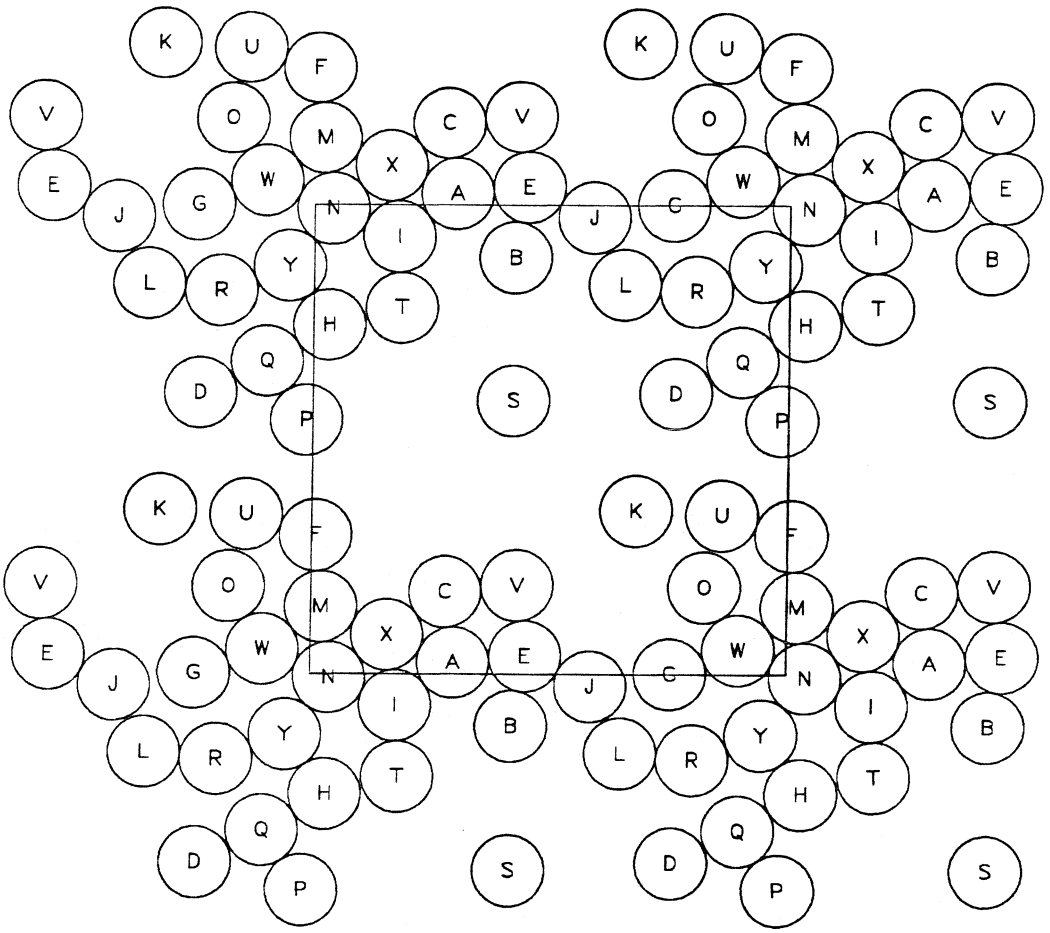

Figure B2.36 A "snapshot" of sphere positions. The square is the periodic cell. These are the sphere positions at $t = 1000.00$ time units (FTn2).

Appendix B3: The FTa simulation results

This suite of simulations uses a non-Ewald, FT method to approximate the hydrodynamic interactions. All simulation conditions are the same as in the FTn simulation described in Appendix B2, except that this suite begins with a different initial configuration of spheres. This configuration is also the result of a Monte-Carlo simulation. Two separate simulation runs follow the evolution of a sedimenting system to a final time of 1000 time units. There are 25 spheres within the periodic cell. The areal fraction is 0.453. There are no interparticle forces present. The time step is 0.001 time unit. The mobility matrix is inverted every 0.1 time unit. Position and velocity data is saved every 0.05 time unit. $\mathbf{D}_o^s$ is evaluated and reported at every time unit.

	FTa1	FTa2
T Cray/Sun CPU(min)	0-500 Sun	500-1000 Sun
v_y	-6.37422	-6.35890
v_x	0.00393	-0.00268
v_y variance	0.02569	0.01533
v_x variance	0.00893	0.00704
v_{xy} variance	0.00022	-0.00004
$(D_\infty^s)_{yy}$		0.34
$(D_\infty^s)_{xx}$		0.023
$(D_o^s)_{yy}$	0.540	0.402
$(D_o^s)_{xx}$	0.544	0.421
$(D_o^s)_{xy}$	0.0038	-0.0019
$g(2)$		15.8
$g(3.5)$		2.44
$g(4)$		4.03

Table B3.1

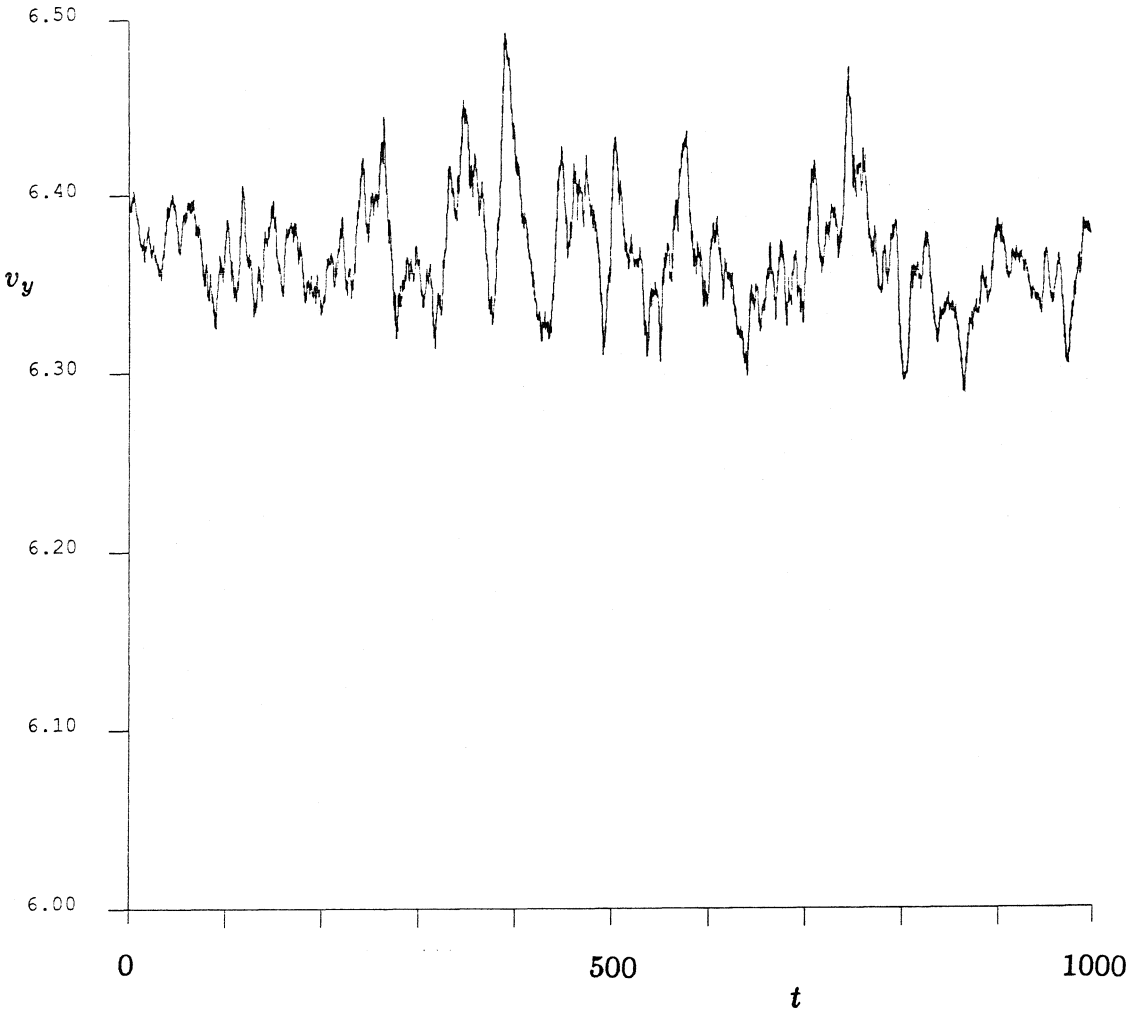

Figure B3.1 The time trace of v_y for the simulations FTa1 and FTa2.

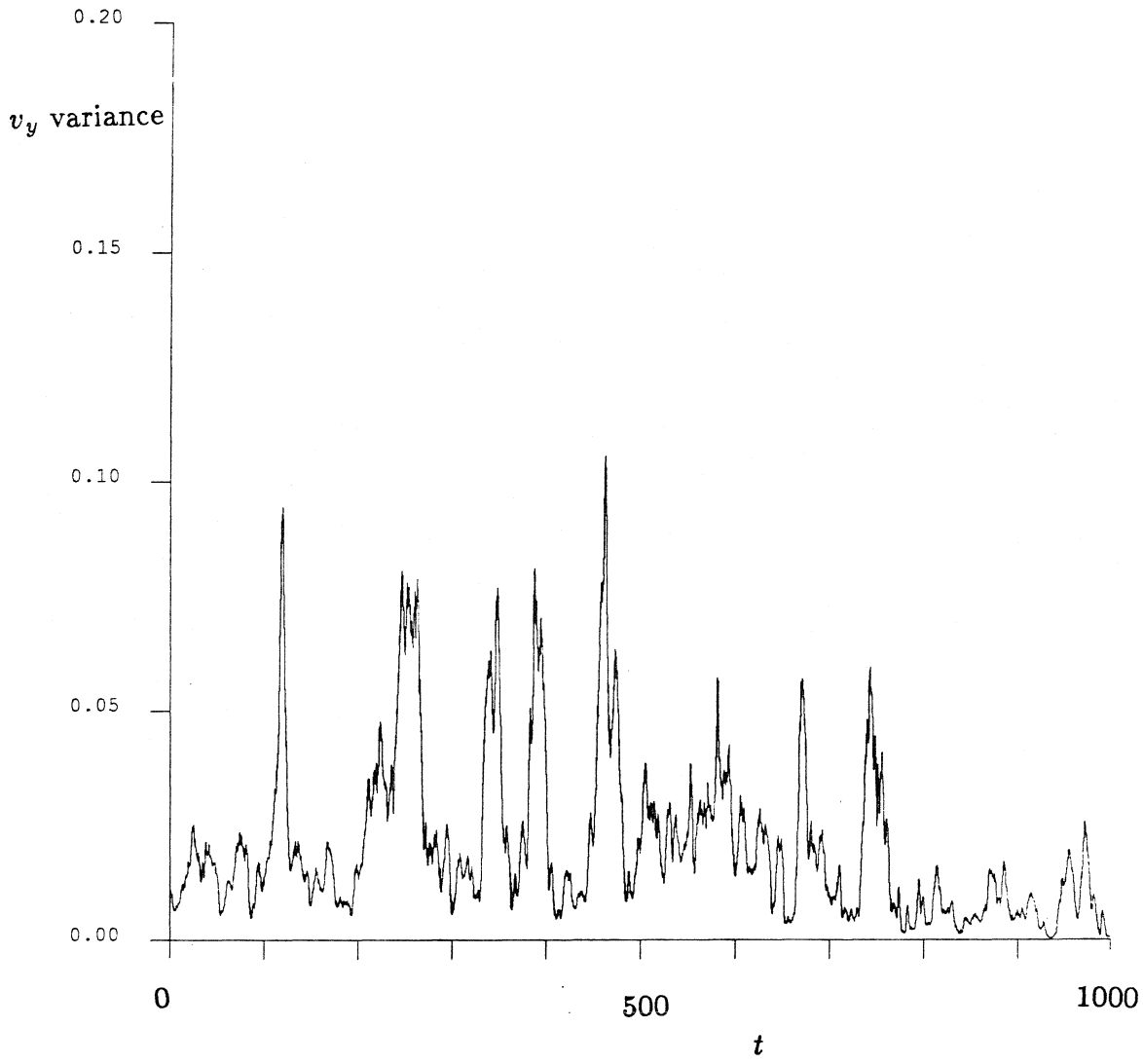

Figure B3.2 The time trace of the v_y variance for the simulations FTa1 and FTa2.

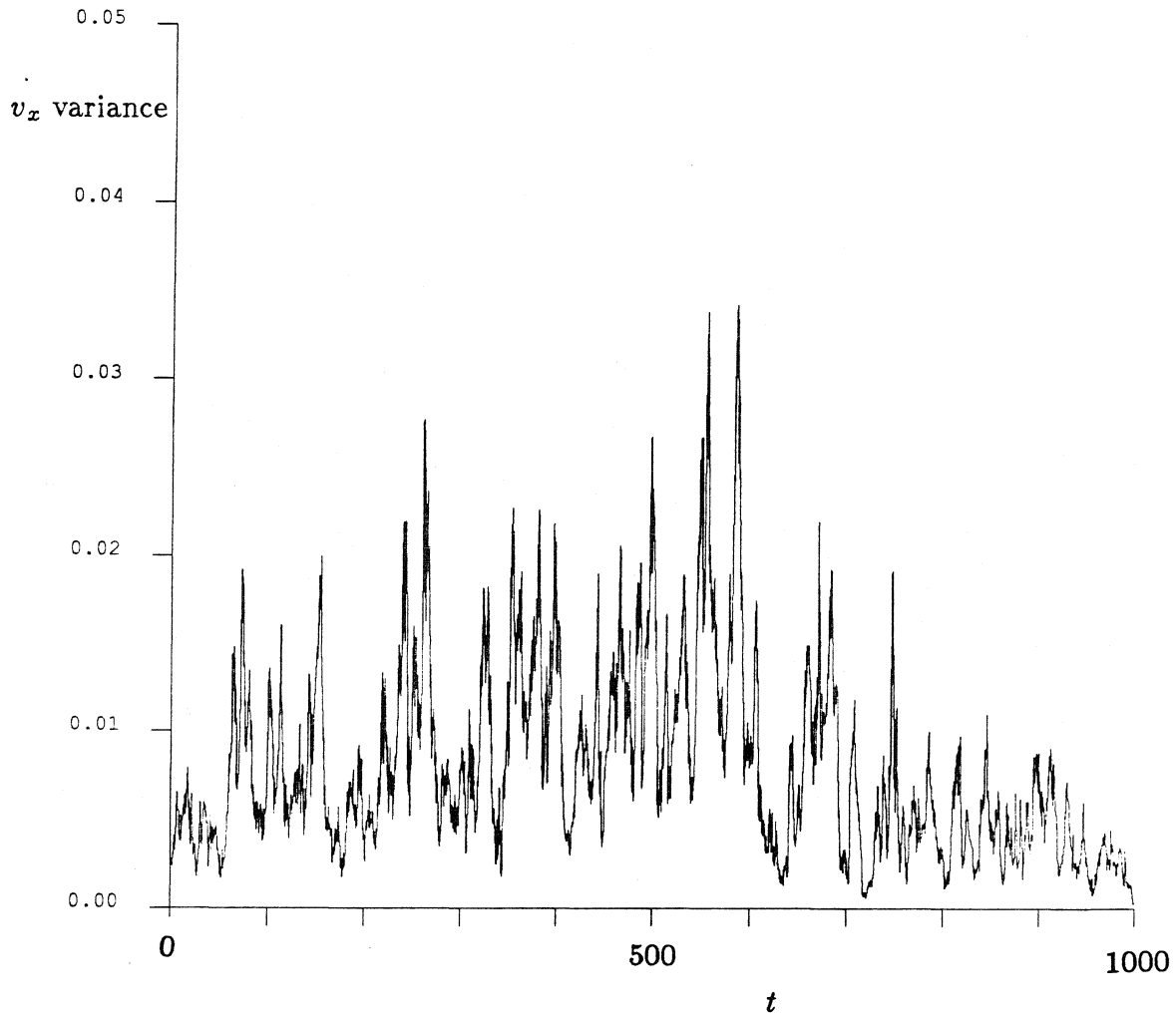

Figure B3.3 The time trace of the v_x variance for the simulations FTa1 and FTa2.

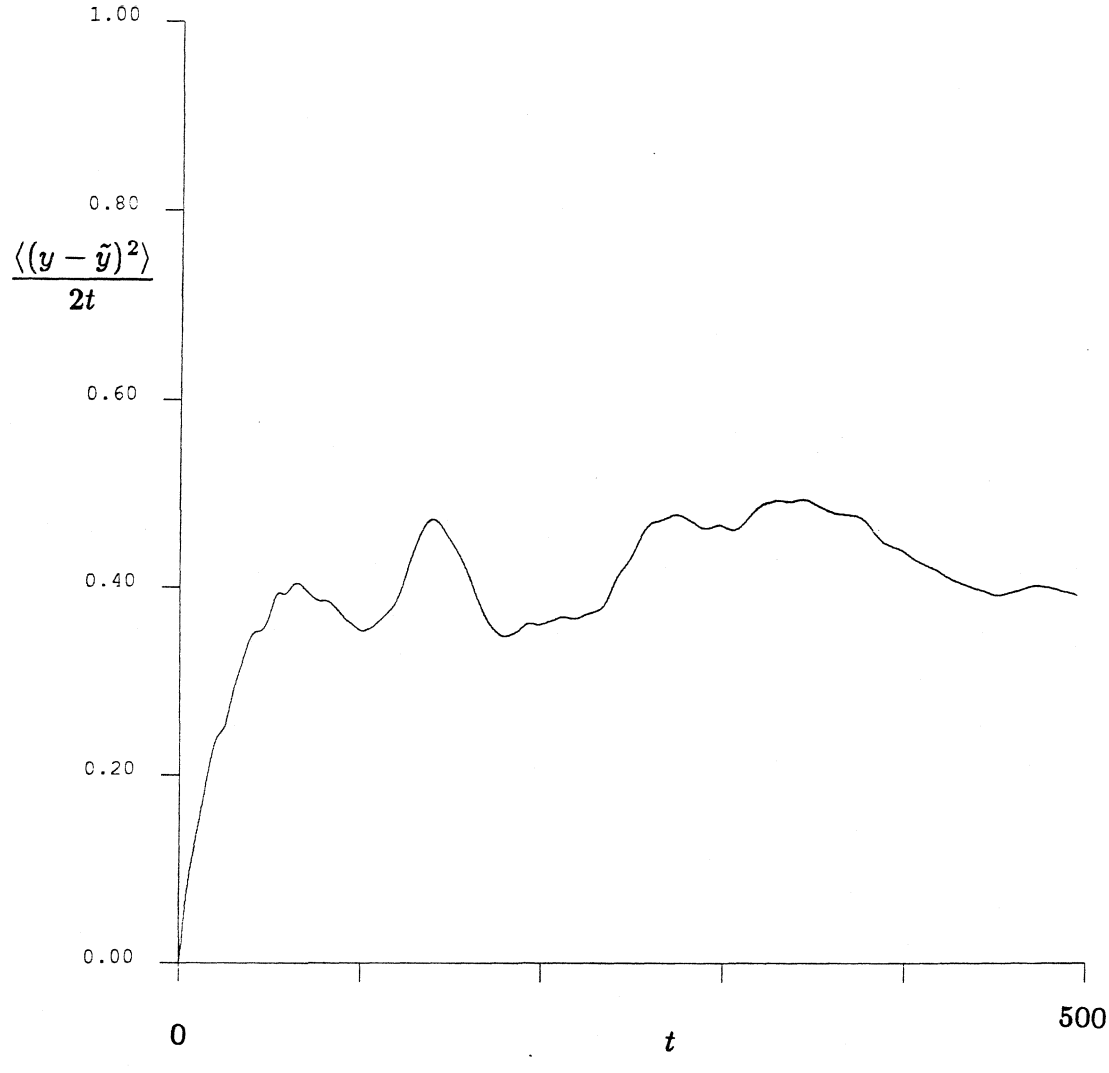

Figure B3.4 A $(D^s_\infty)_{yy}$-defining graph using displacement data from FTa2 (t=500 – 1000). The graph interval is 500 time units, which means that no averaging over different initial conditions is done.

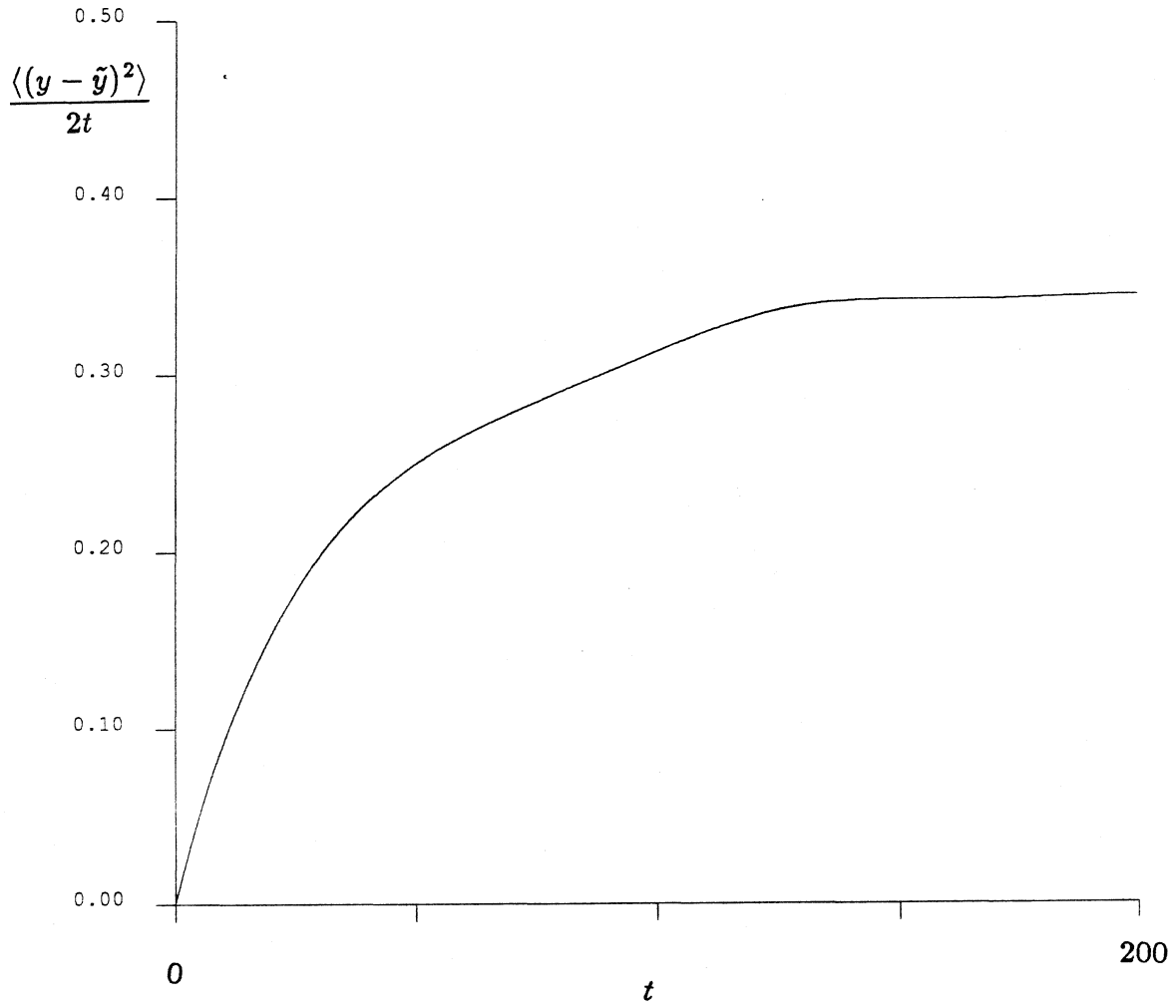

Figure B3.5 A $(D^s_\infty)_{yy}$-defining graph using displacement data from FTa2 (t= 500 – 1000). The graph interval is 200 time units, and the time between interval initial conditions is 0.01 time unit.

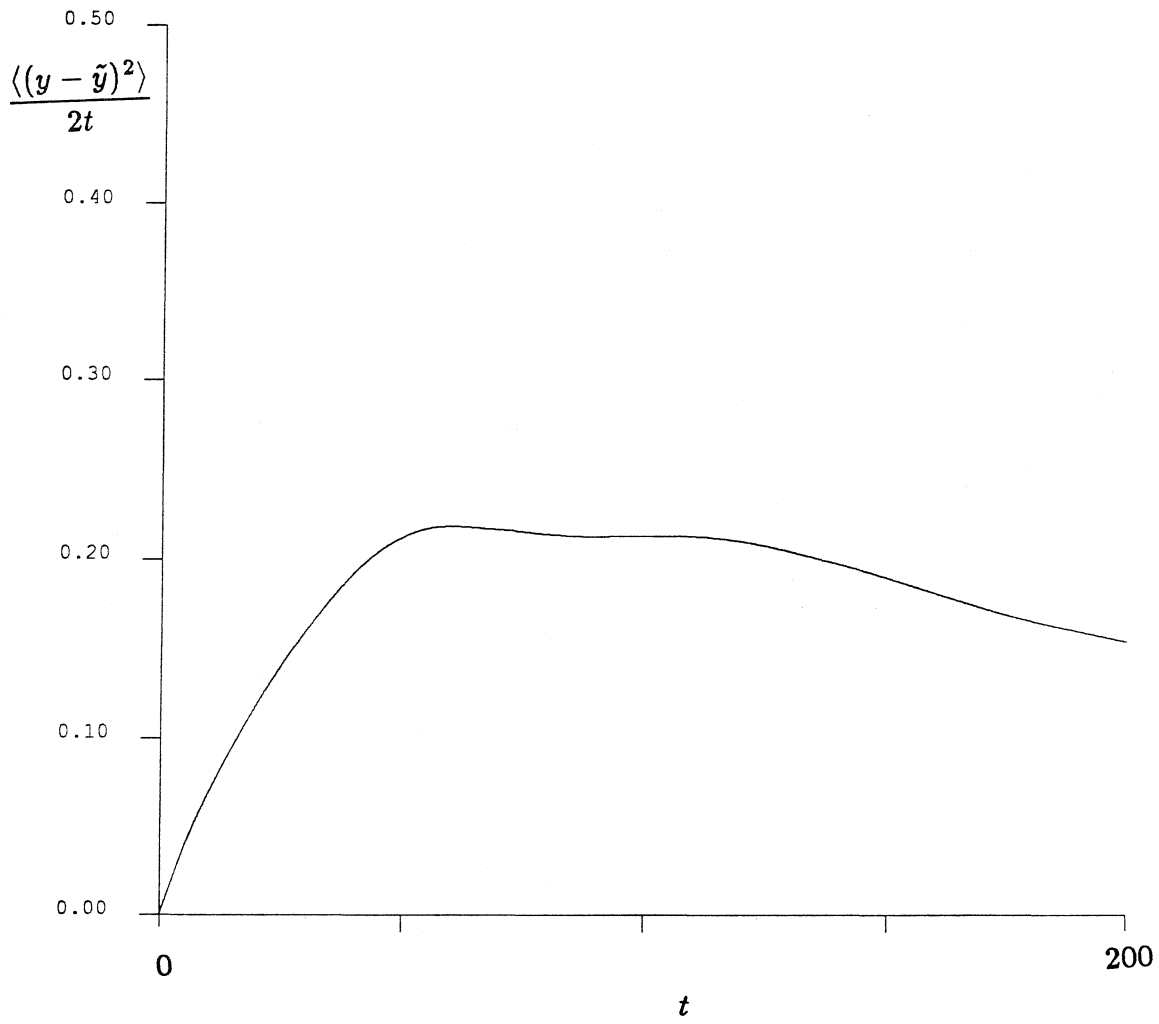

Figure B3.6 A $(D^s_\infty)_{yy}$-defining graph using displacement data from FTa2 (t= 700 – 1000). The graph interval is 200 time units, and the time between interval initial conditions is 0.01 time unit.

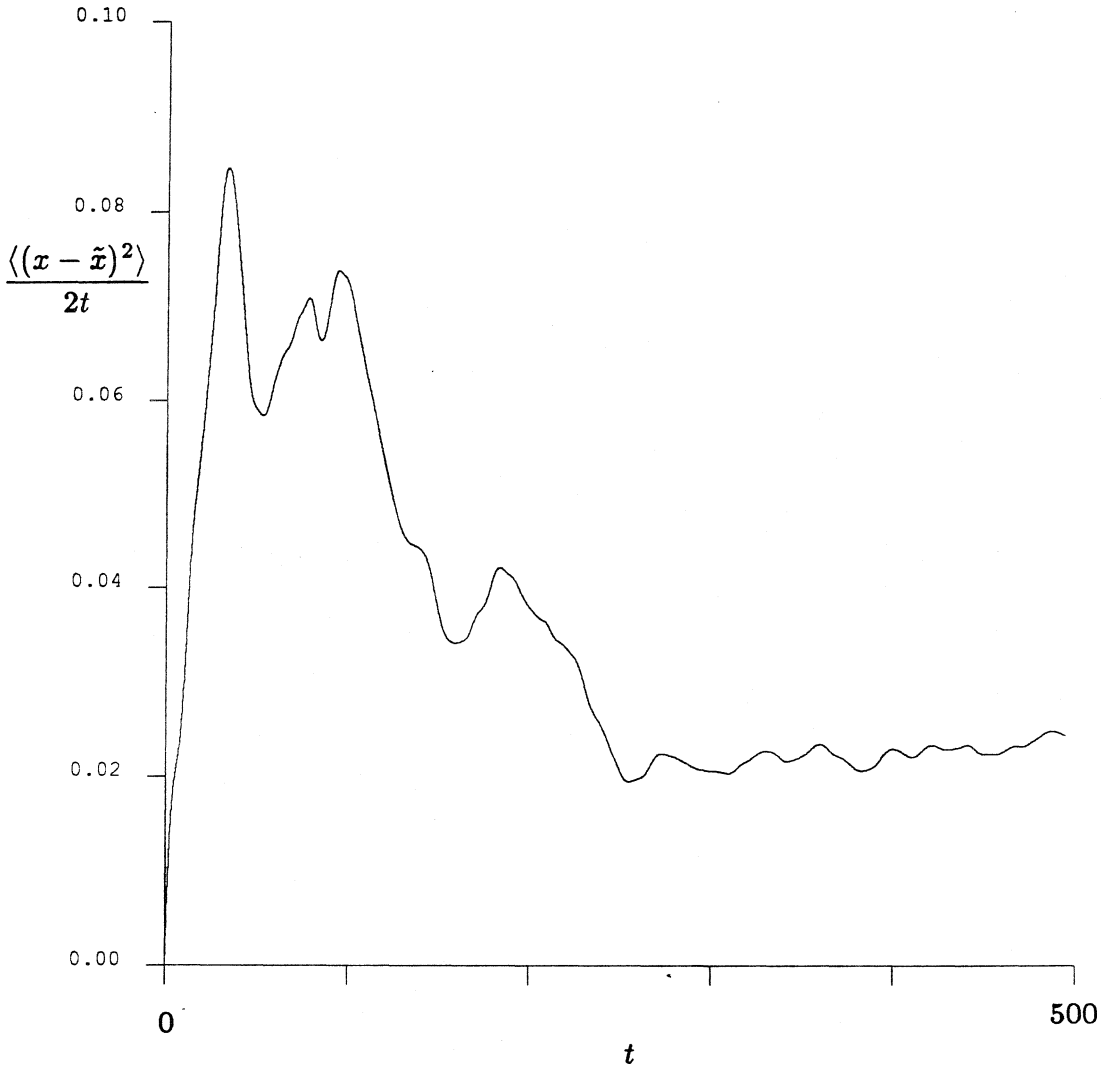

Figure B3.7 A $(D^s_\infty)_{xx}$-defining graph using displacement data from FTa2 (t= 500 – 1000). The graph interval is 500 time units, which means that no averaging over different initial conditions is done.

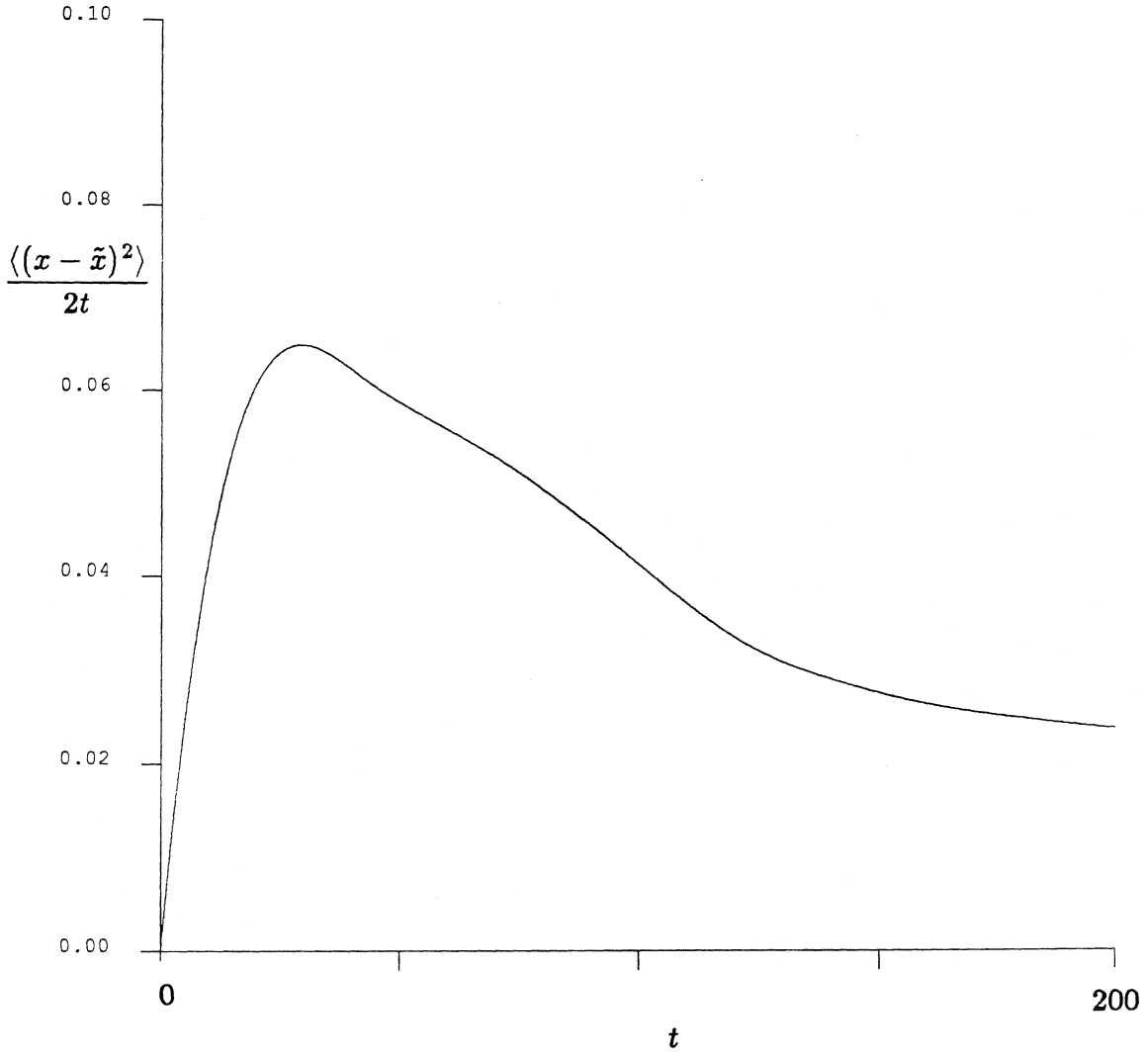

Figure B3.8 A $(D^s_\infty)_{xx}$-defining graph using displacement data from FTa2 (t= 500 – 1000). The graph interval is 200 time units, and the time between interval initial conditions is 0.01 time unit.

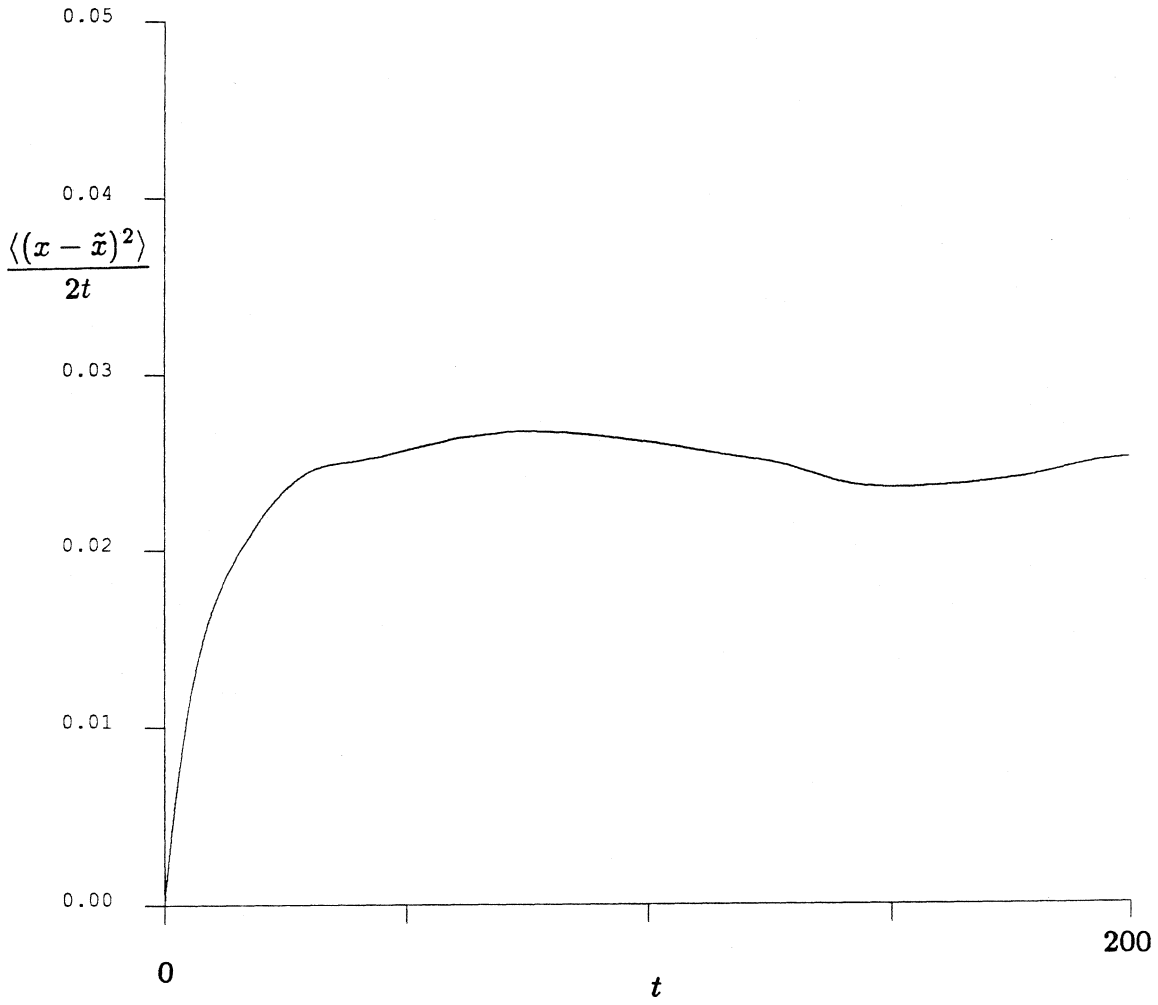

Figure B3.9 A $(D^s_\infty)_{xx}$-defining graph using displacement data from FTa2 (t= 700 – 1000). The graph interval is 200 time units, and the time between interval initial conditions is 0.01 time unit.

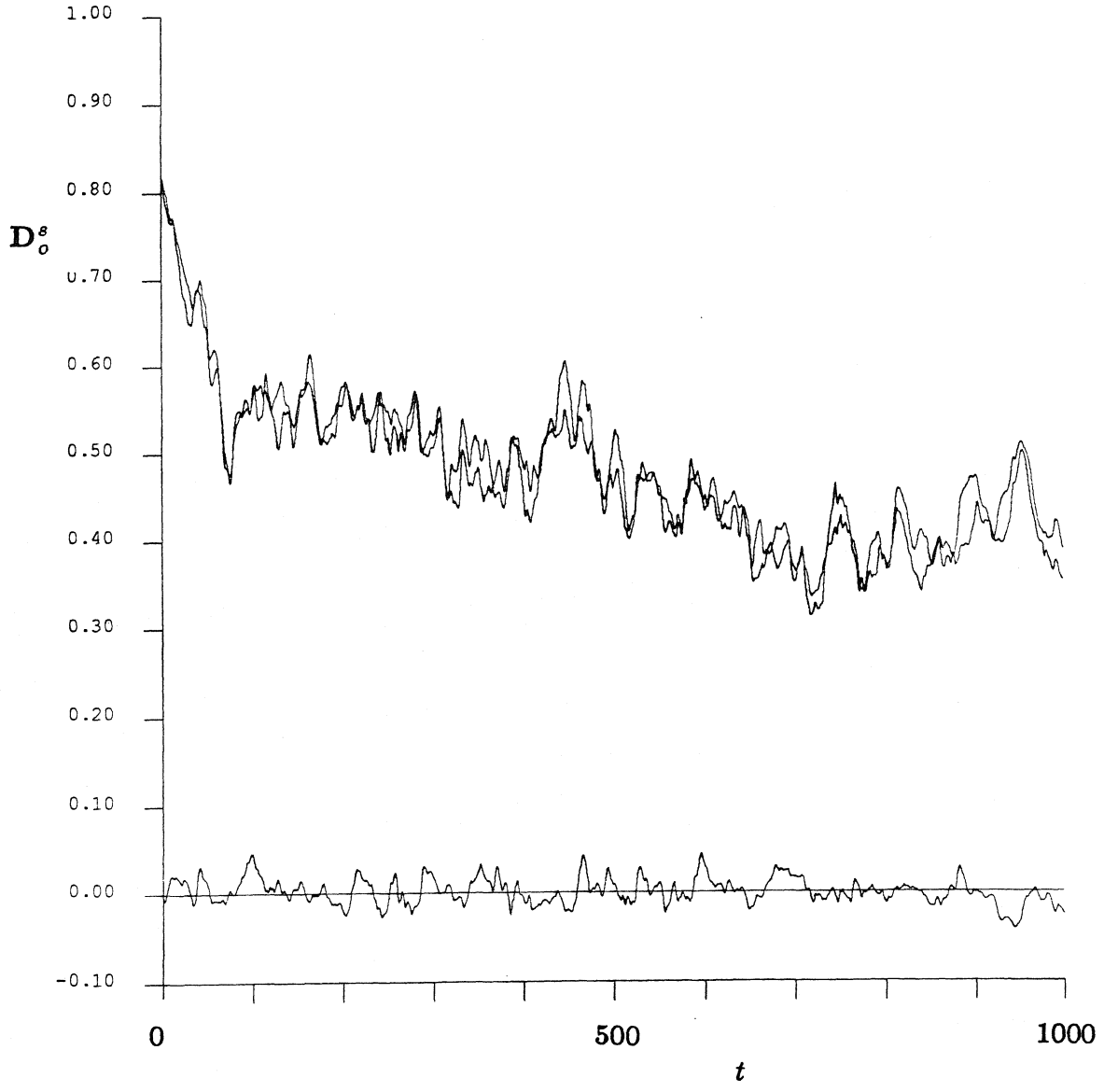

Figure B3.10 The time trace of $\mathbf{D}_o^s$ for the simulations FTa1 and FTa2. The upper two lines are the xx and yy components of this tensor. Of course, they should be equivalent for an infinite suspension – the slight variation occurs because of the finite number of spheres used in our simulation. The trace that fluctuates about the zero y-axis is the xy component of the short-time, self-diffusion tensor. Again, for an infinite number of spheres, this quantity would be exactly zero.

Figure B3.11 There is no Figure *B3.11.*

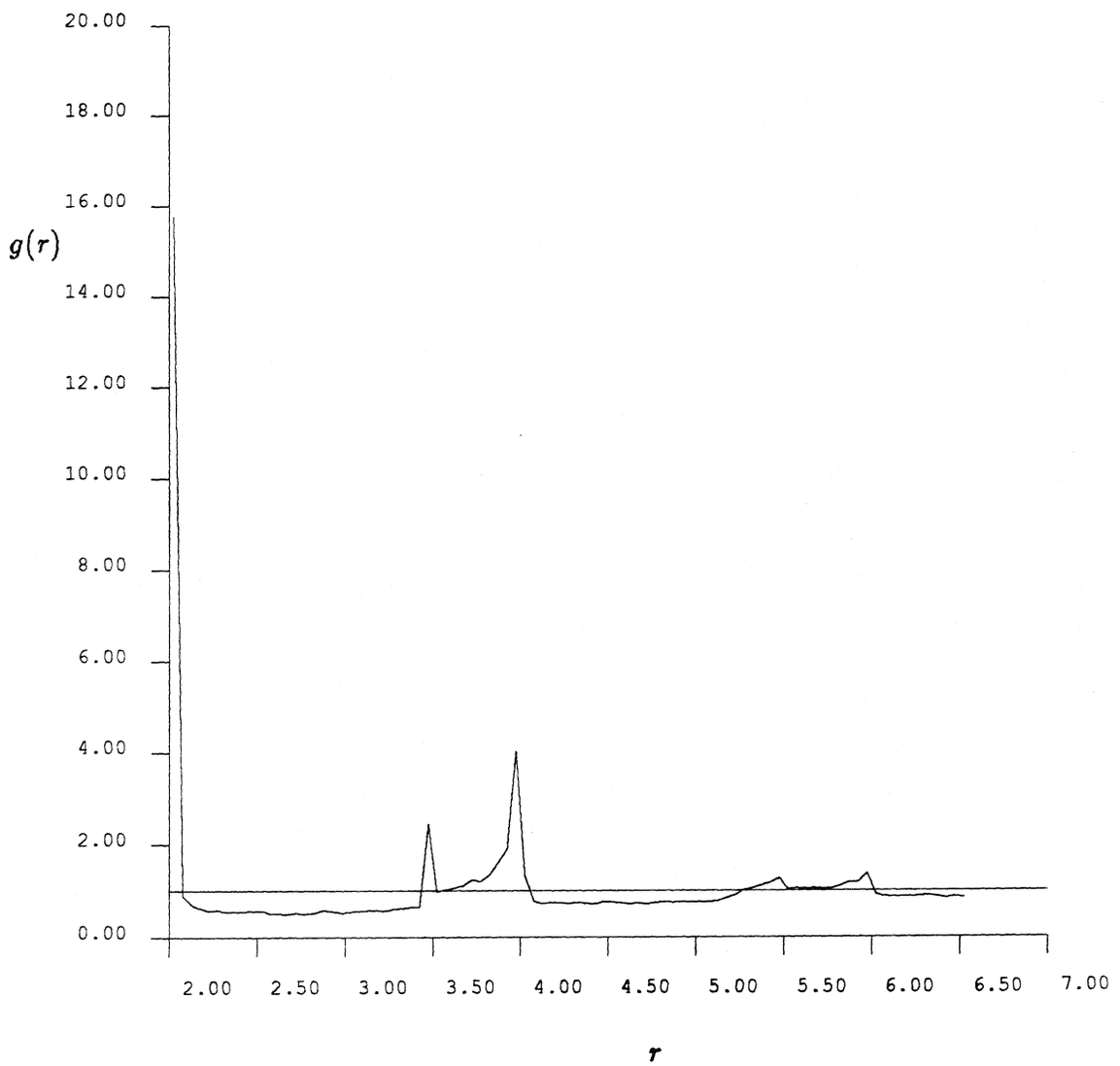

Figure B3.12 The radial pair-distribution function, $g(r)$, for the FTa2 run (t = 500 – 1000).

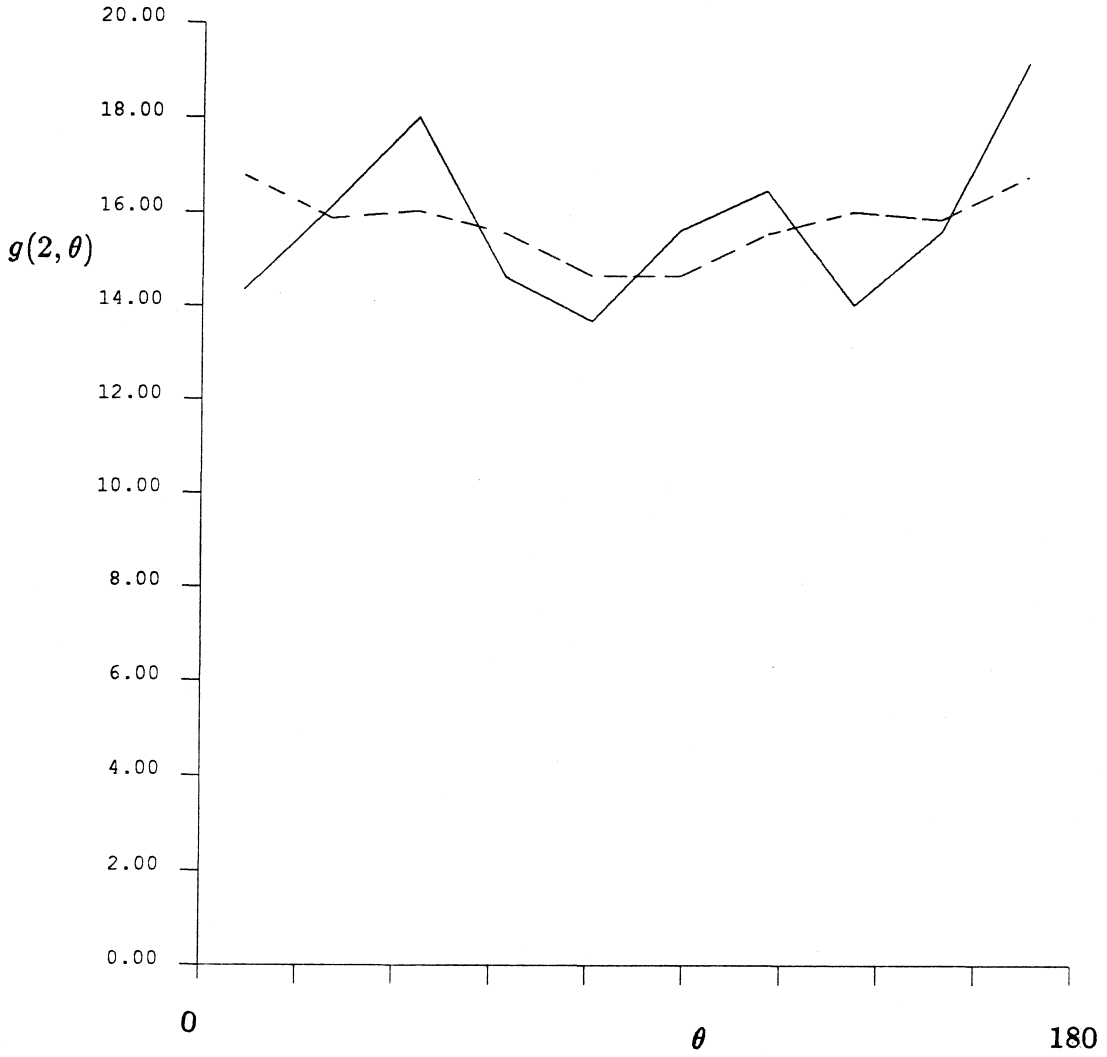

Figure B3.13 The full pair-distribution function for spheres whose surfaces are separated by less than 0.05 radii using data from the FTa2 run (t = 500 – 1000). The dashed curve represents this function when it is forced to be symmetric about $\theta = 90°$.

Appendix B4: The Fn simulation results

This suite of simulations uses a non-Ewald, F method to approximate Three separate simulation runs follow the evolution of a sedimenting system to a final time of 1000 time units. The initial configuration is the same as in the FTSn simulations described in Appendix B1. There are 25 spheres within the periodic cell. The areal fraction is 0.453. There are no interparticle forces present. The time step is 0.001 time unit. The mobility matrix is inverted every 0.1 time unit. Position and velocity data is saved every 0.05 time unit. $\mathbf{D}_o^s$ is evaluated and reported at every time unit. The * in the table denotes that the simulation data in the Fn2–3 runs are a compilation of data from the Fn2 and Fn3 simulations. The reason behind this is that the data after 700 time units for the Fn2 simulation was destroyed by the computer as it was copying the data from one disk to another. For that reason, we can report the time-averaged statistics for the full Fn2 run, but cannot report the time traces of the velocity-related properties, the diffusion coefficients, or the distribution function. Instead, we began run Fn3 at $t = 700$ time units and concatenated the data from this run with the preserved data from the Fn2 run.

	Fn1	Fn2	Fn3	Fn2-3 (*)
T	0-500	500-1000	700-1000	500-1000 (*)
Cray/Sun	Sun	Sun	Sun	Sun
CPU(min)	1503	1515		
v_y	-6.36365	-6.35657		-6.35547
v_x	-0.00883	-0.00719		0.00542
v_y variance	0.01477	0.00678		0.01156
v_x variance	0.00483	0.00319		0.00336
v_{xy} variance	-0.00037			0.00043
$(D_\infty^s)_{yy}$	0.18			0.20
$(D_\infty^s)_{xx}$	0.029			0.021
$(D_o^s)_{yy}$	0.453	0.355	0.364	
$(D_o^s)_{xx}$	0.452	0.356	0.364	
$(D_o^s)_{xy}$	-0.0025	0.0034	0.0003	
$g(2)$	15.9			13.3
$g(3.5)$	1.43			3.36
$g(4)$	3.03			4.19

Table B4.1

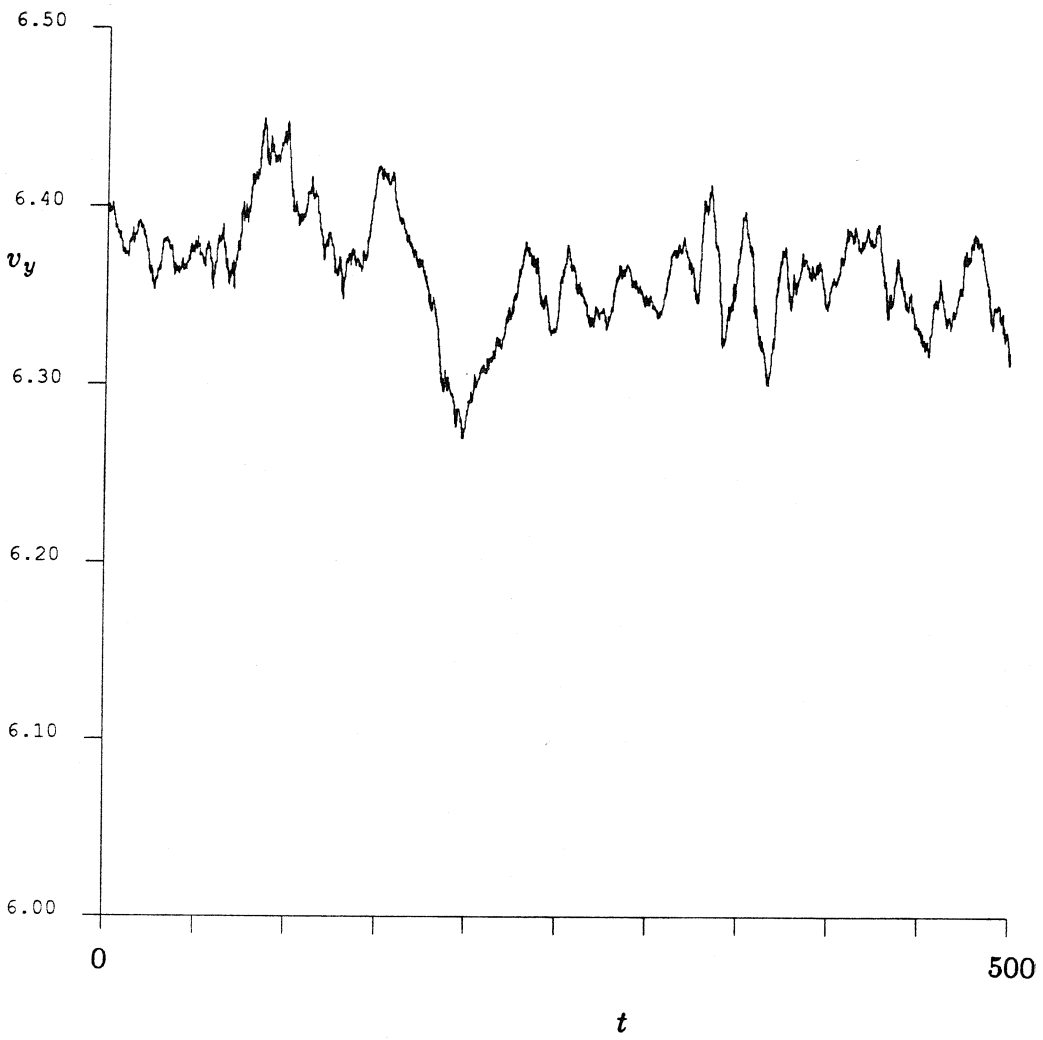

Figure B4.1 The time trace of v_y for the simulation Fn1.

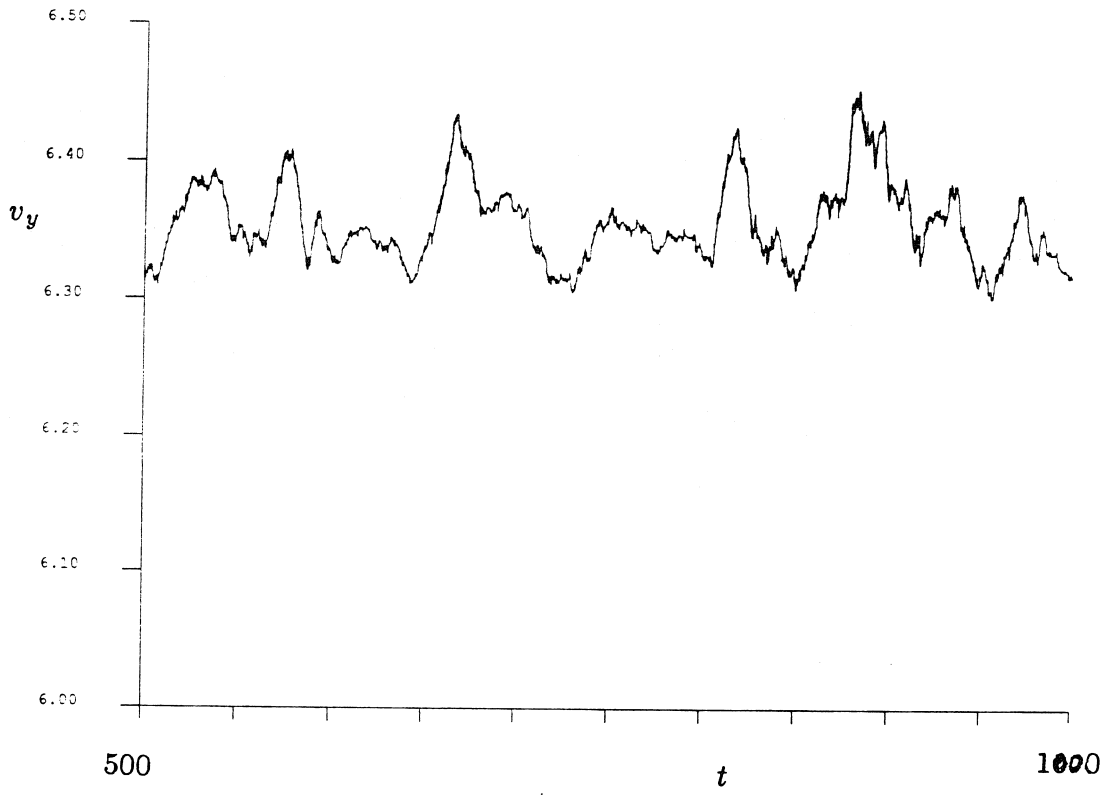

Figure B4.2 The time trace of v_y for the simulation Fn2–3.

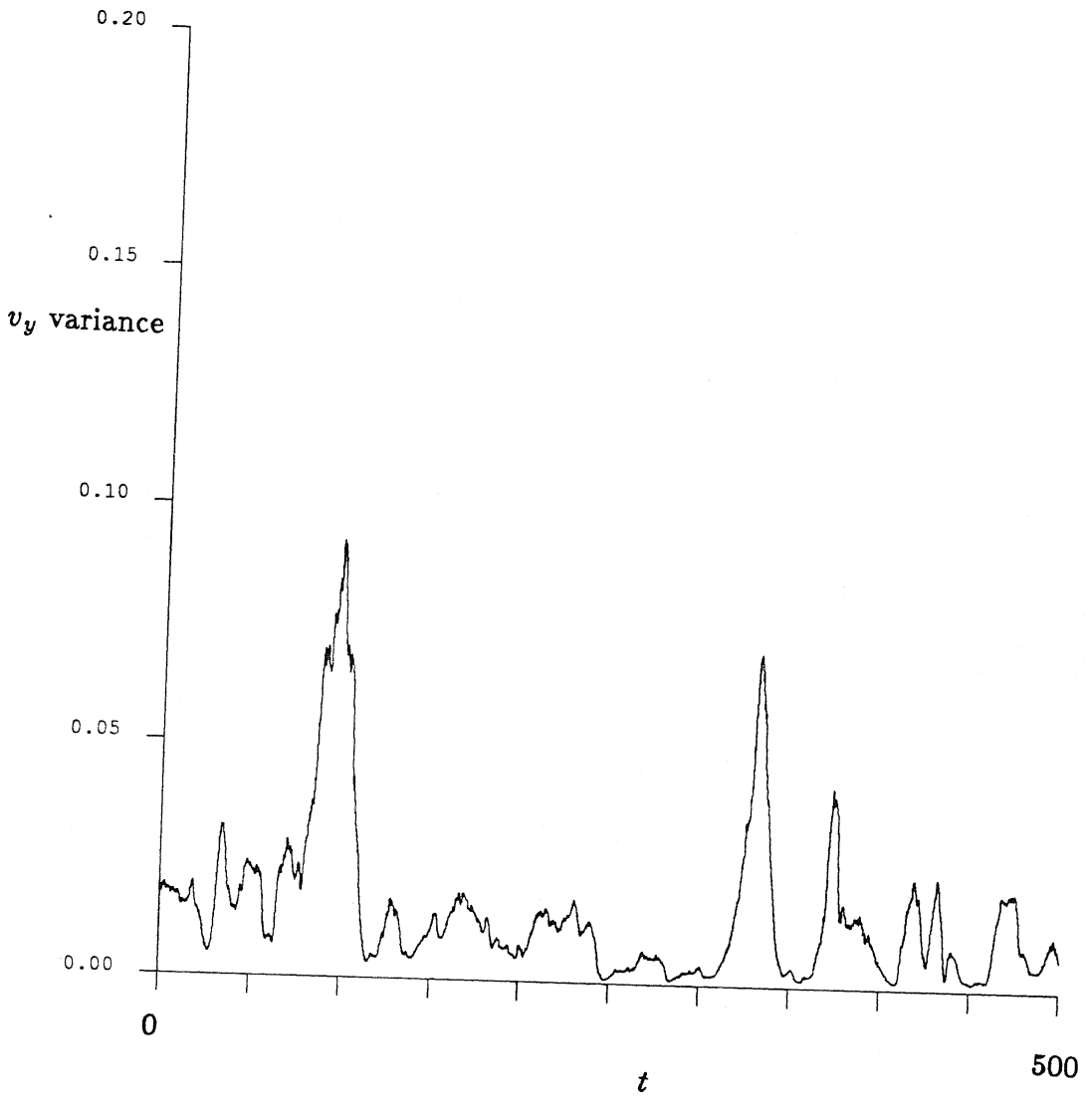

Figure B4.3 The time trace of the v_y variance for the simulation Fn1.

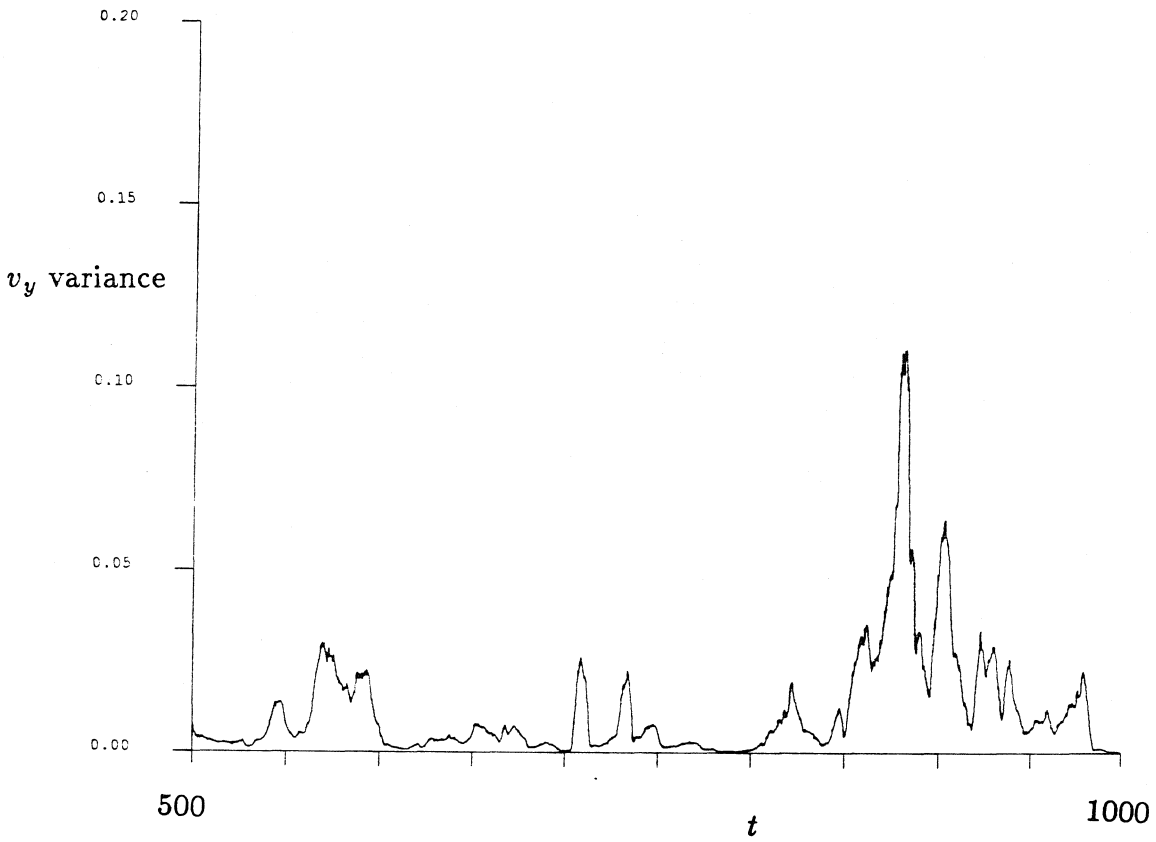

Figure B4.4 The time trace of the v_y variance for the simulation Fn2–3. Note the long periods of near-zero variance.

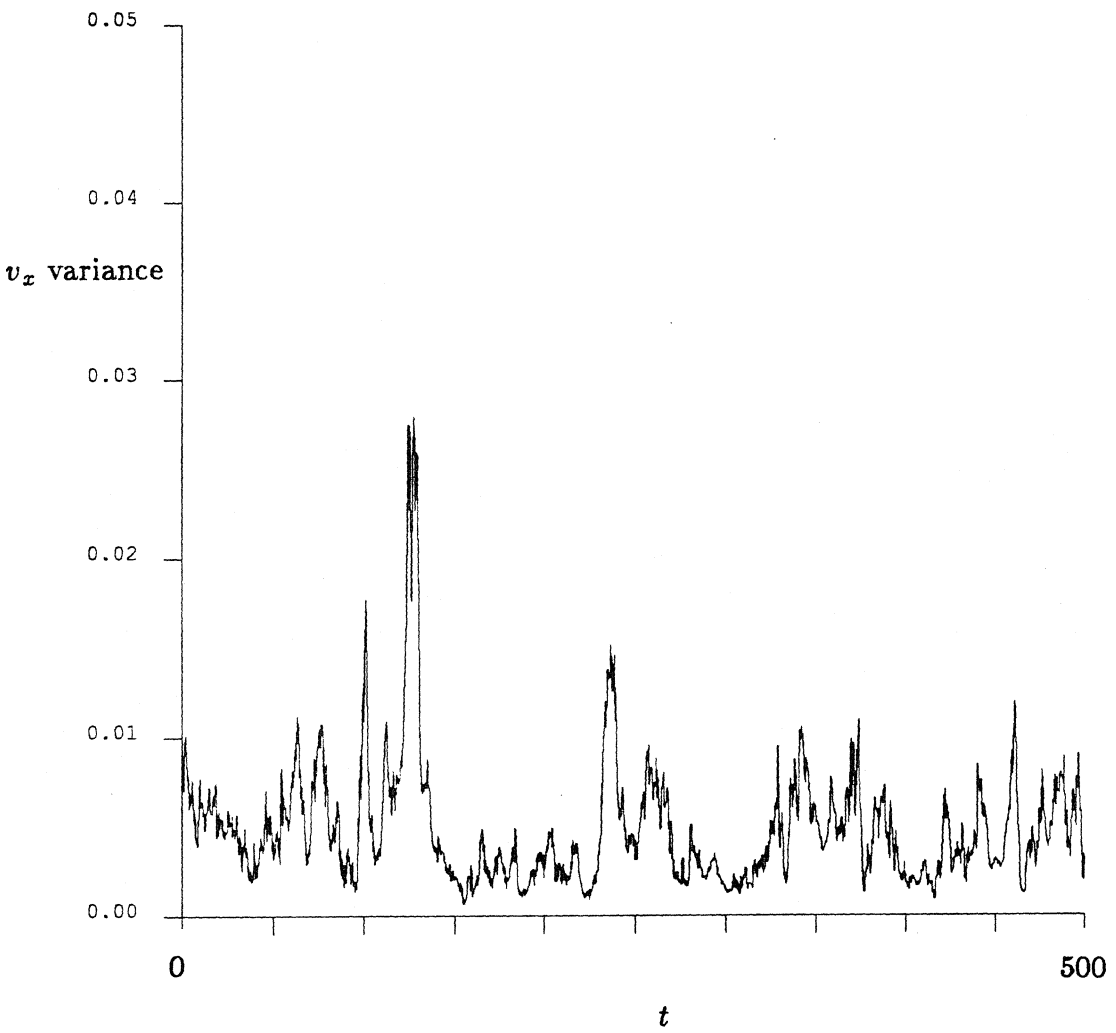

Figure B4.5 The time trace of the v_x variance for the simulation Fn1.

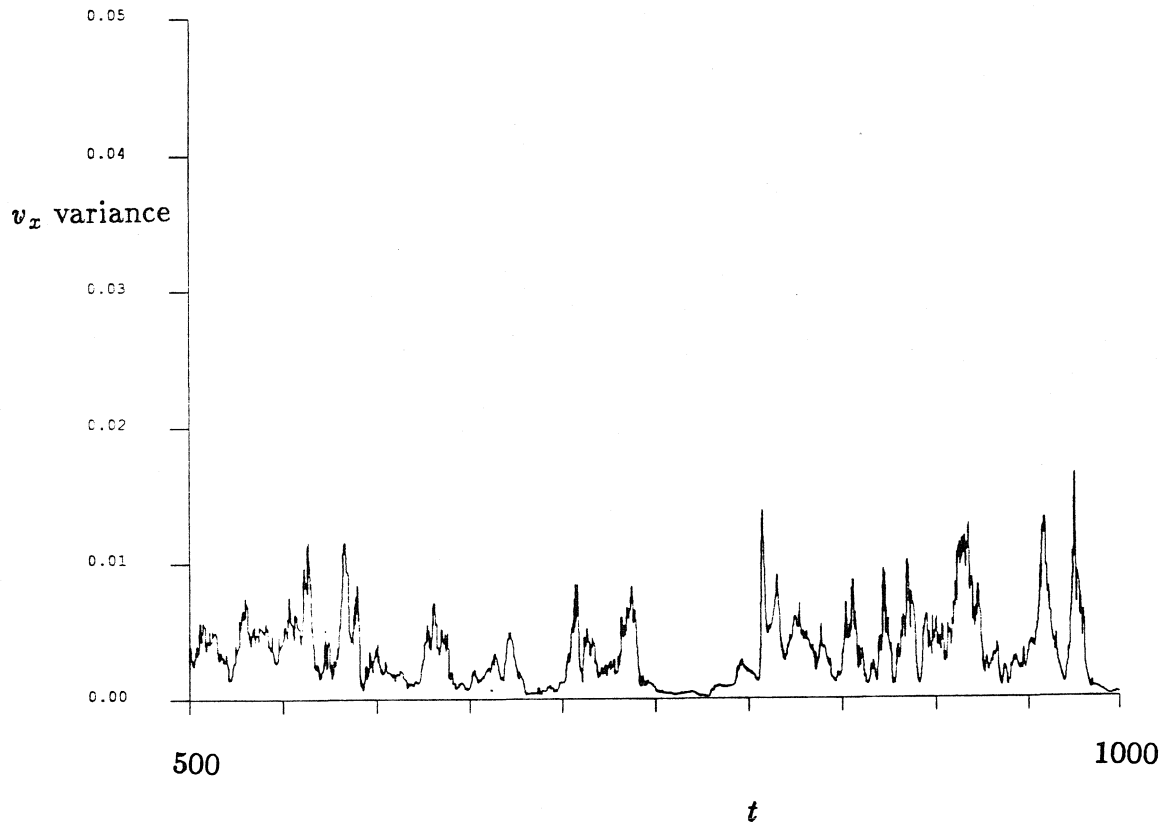

Figure B4.6 The time trace of the v_x variance for the simulation Fn2–3.

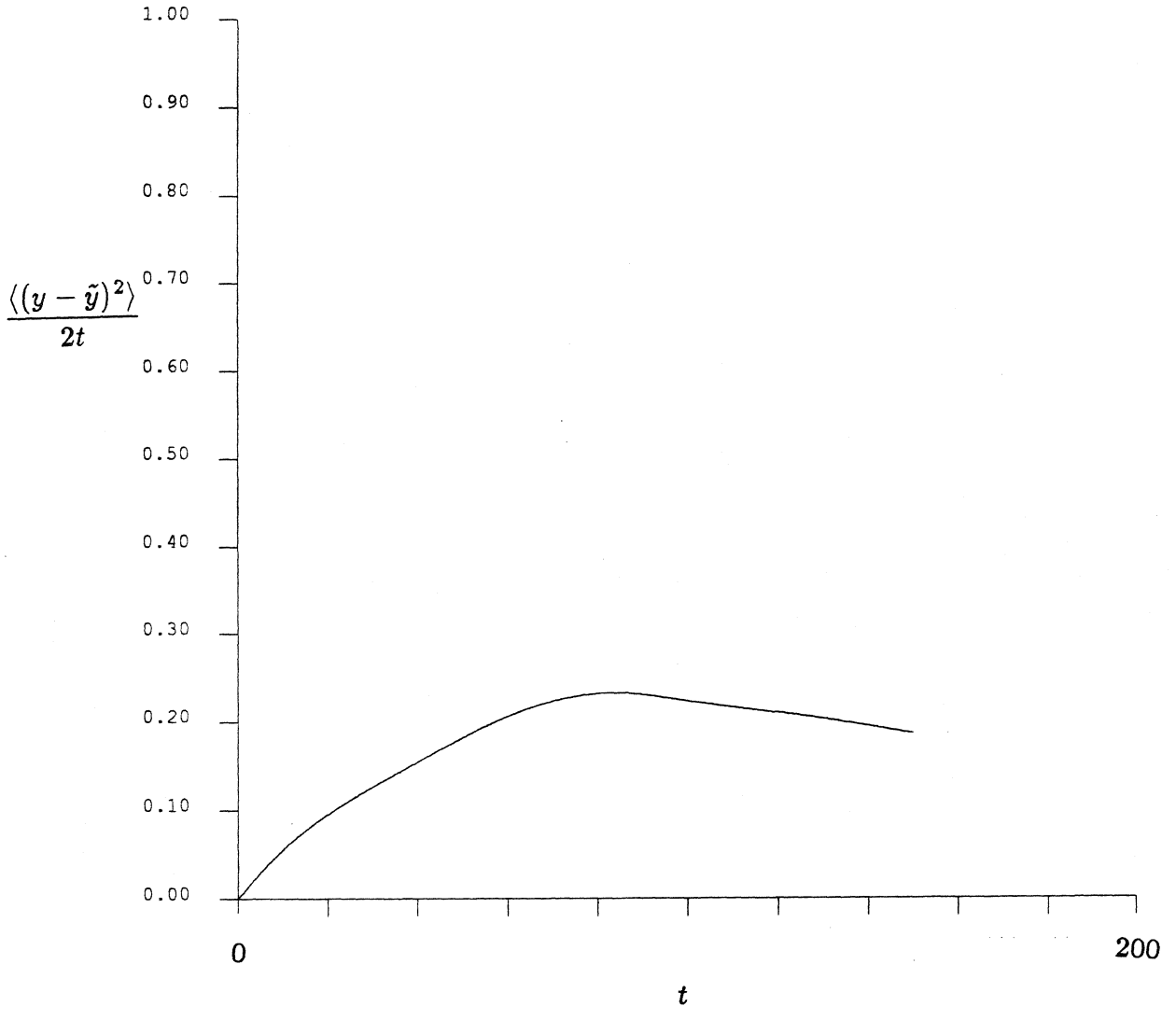

Figure B4.7 A $(D^s_\infty)_{yy}$-defining graph using displacement data from Fn1 (t= 300 – 500). The graph interval is 150 time units, and the time between interval initial conditions is 0.01 time unit.

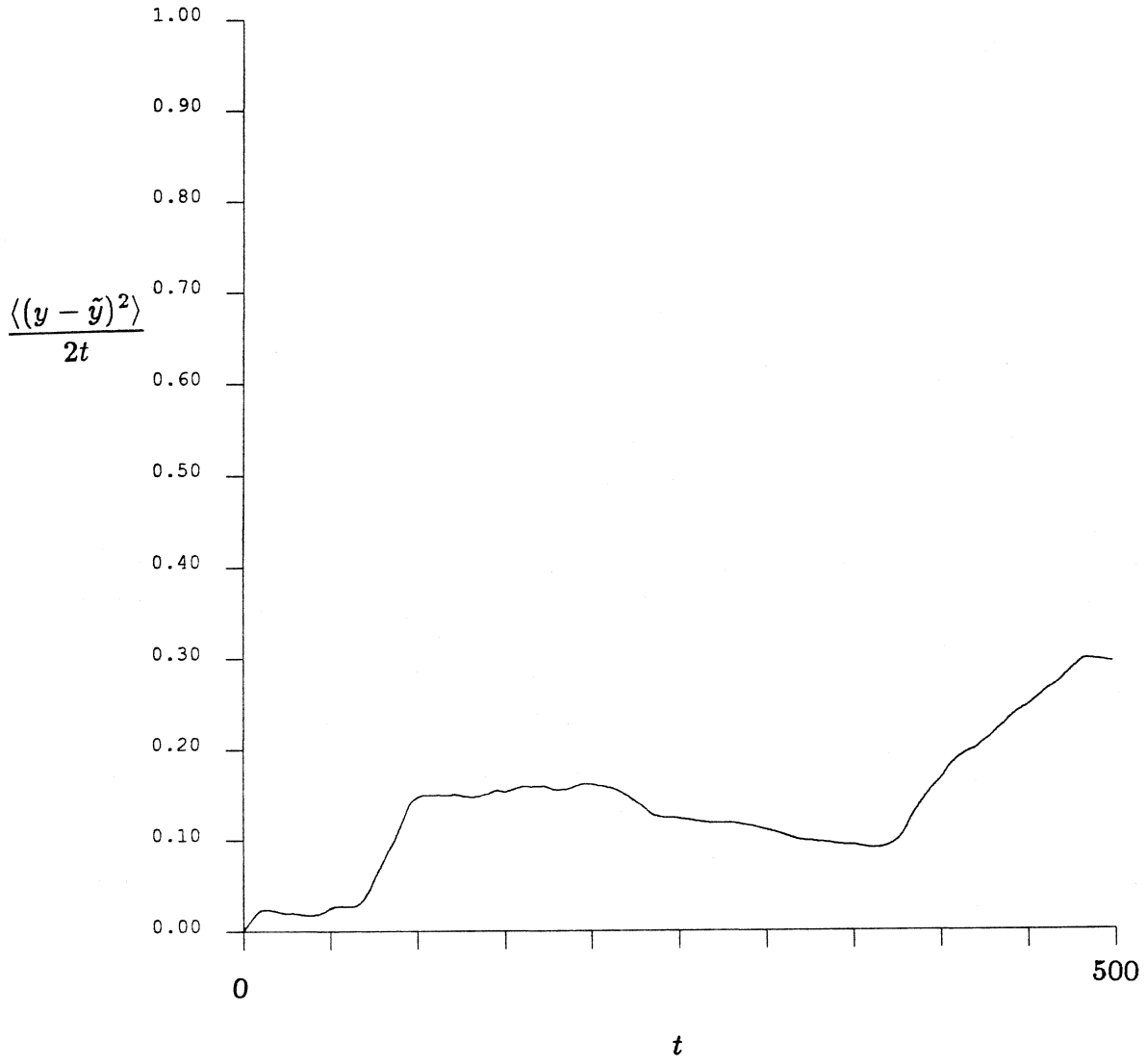

Figure B4.8 A $(D^s_\infty)_{yy}$-defining graph using displacement data from Fn2–3 (t= 500 – 1000). The graph interval is 500 time units, which means that no averaging over different initial conditions is done.

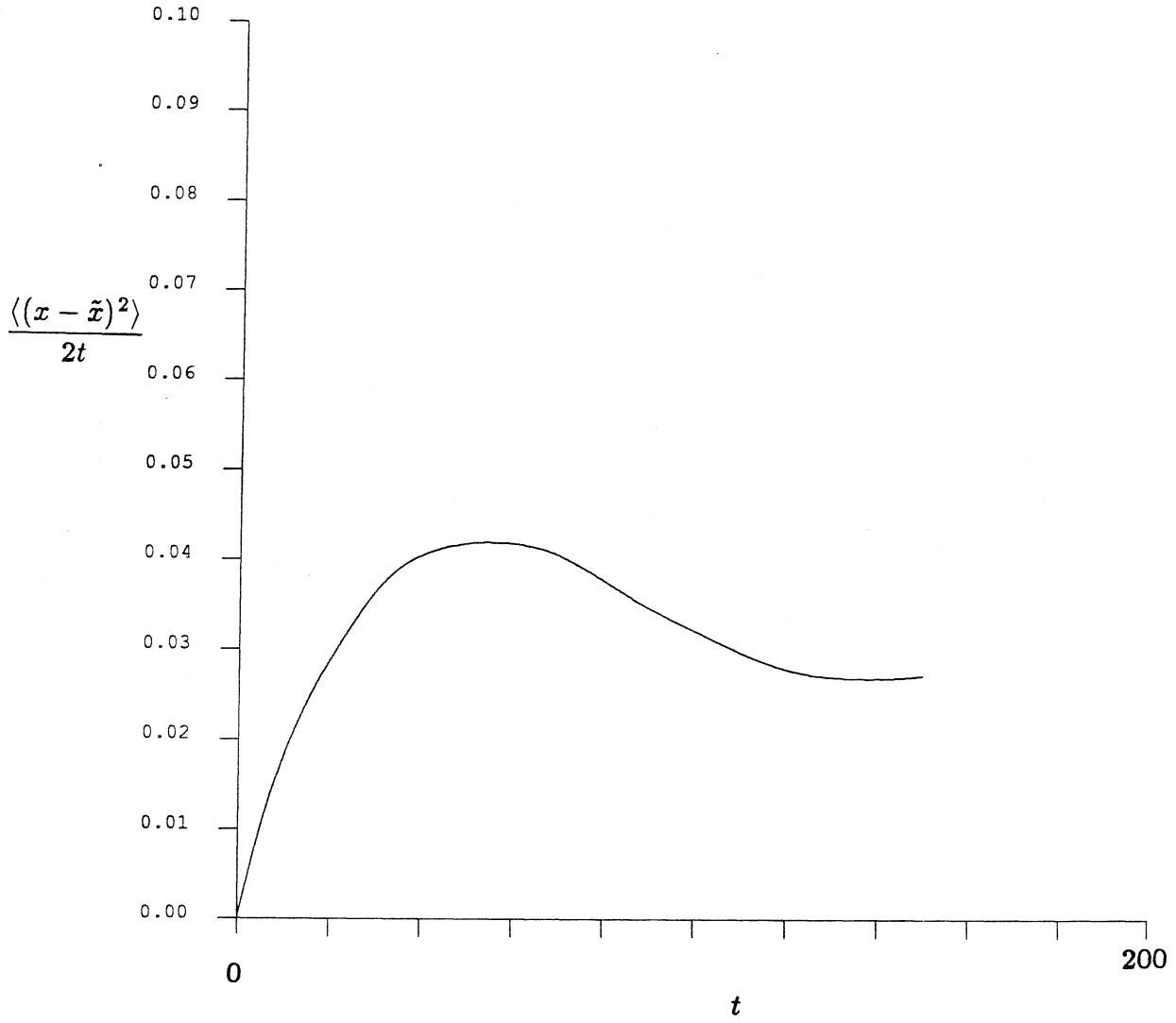

Figure B4.9 A $(D^e_\infty)_{xx}$-defining graph using displacement data from Fn1 (t= 300 – 500). The graph interval is 150 time units, and the time between interval initial conditions is 0.01 time unit.

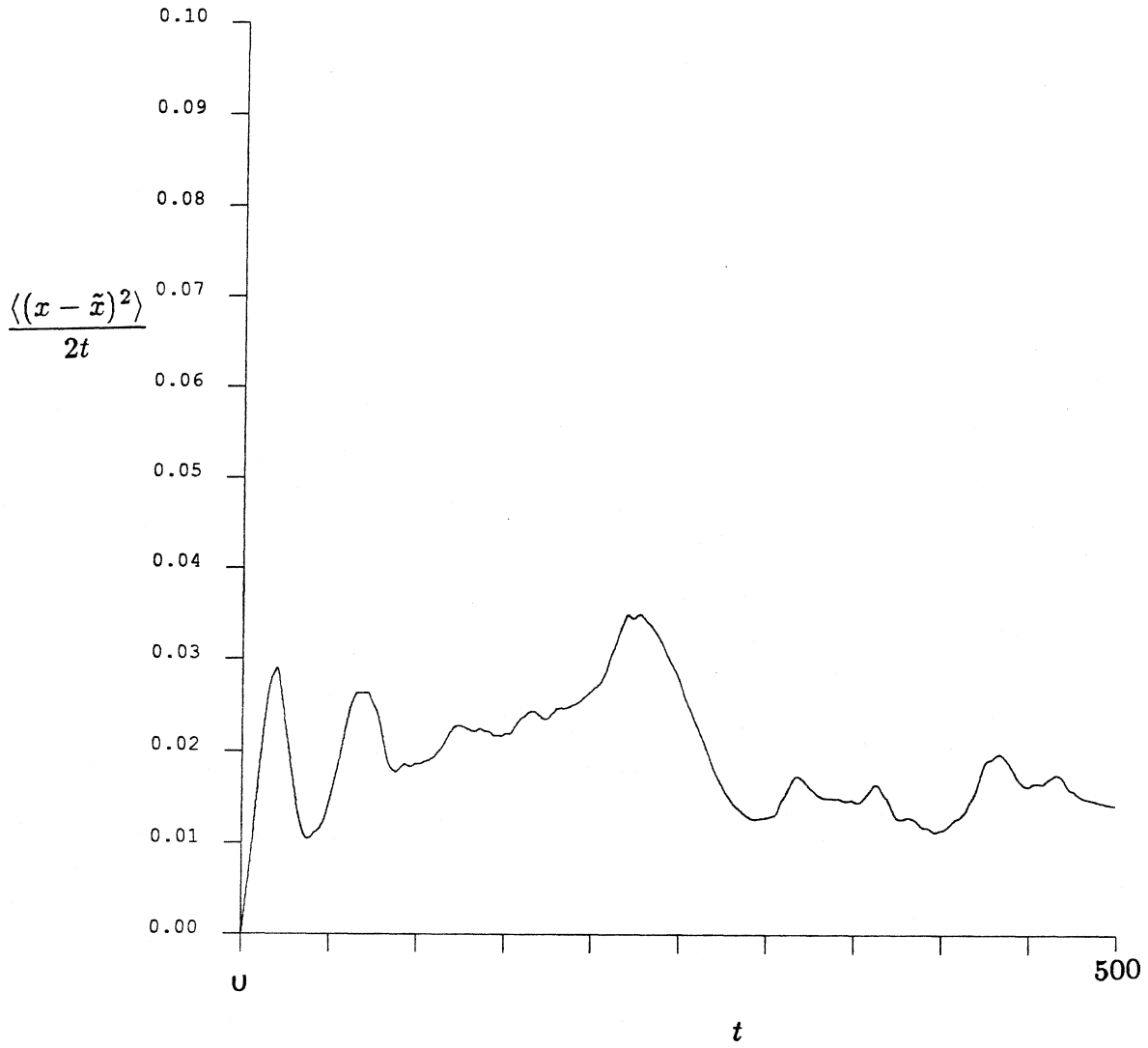

Figure B4.10 A $(D^e_\infty)_{xx}$-defining graph using displacement data from Fn2–3 (t= 500 – 1000). The graph interval is 500 time units, which means that no averaging over different initial conditions is done.

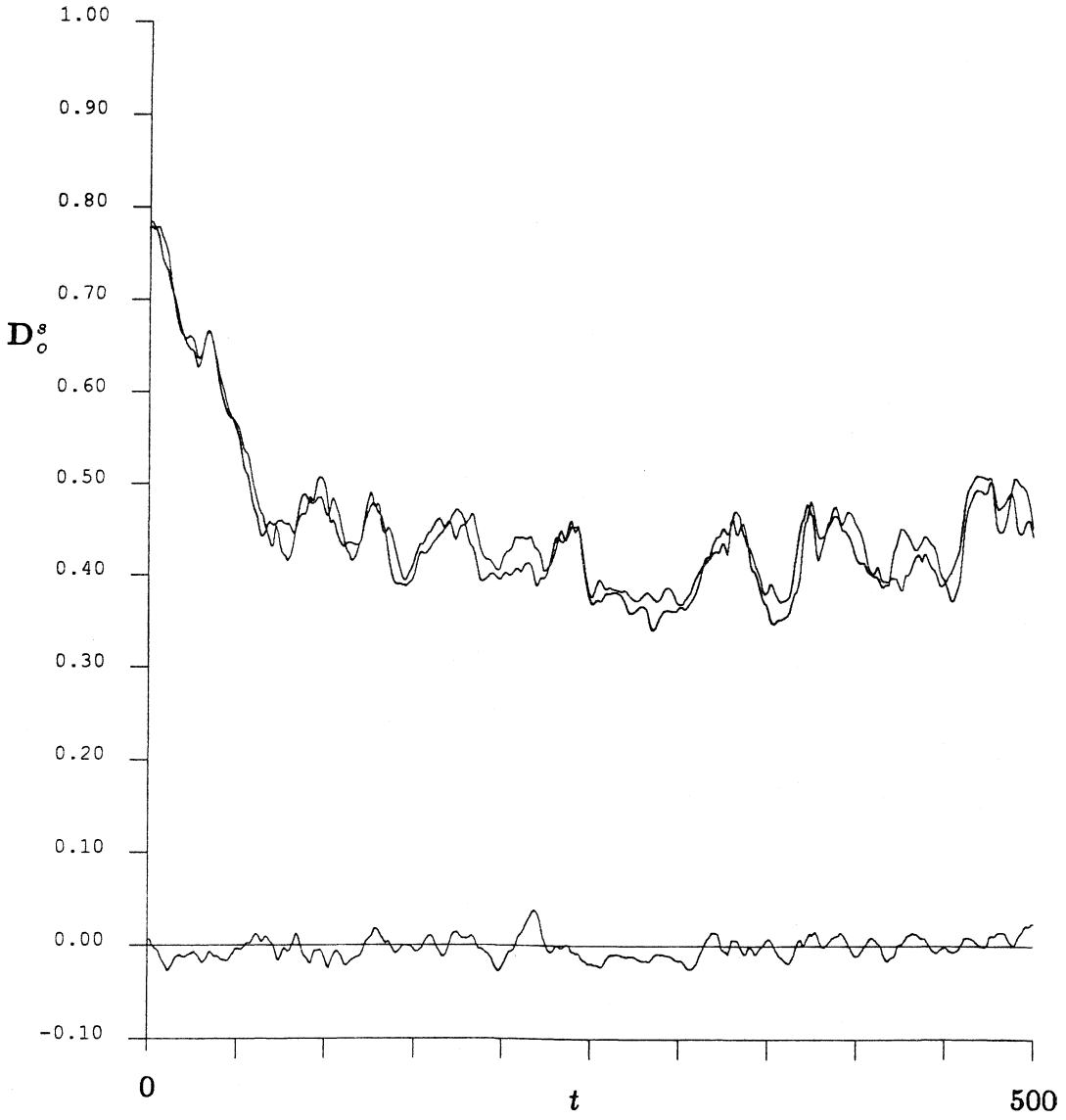

Figure B4.11 The time trace of $\mathbf{D}_o^s$ for the simulation Fn1. The upper two lines are the xx and yy components of this tensor. Of course, they should be equivalent for an infinite suspension – the slight variation occurs because of the finite number of spheres used in our simulation. The trace that fluctuates about the zero y-axis is the xy component of the short-time, self-diffusion tensor. Again, for an infinite number of spheres, this quantity would be exactly zero.

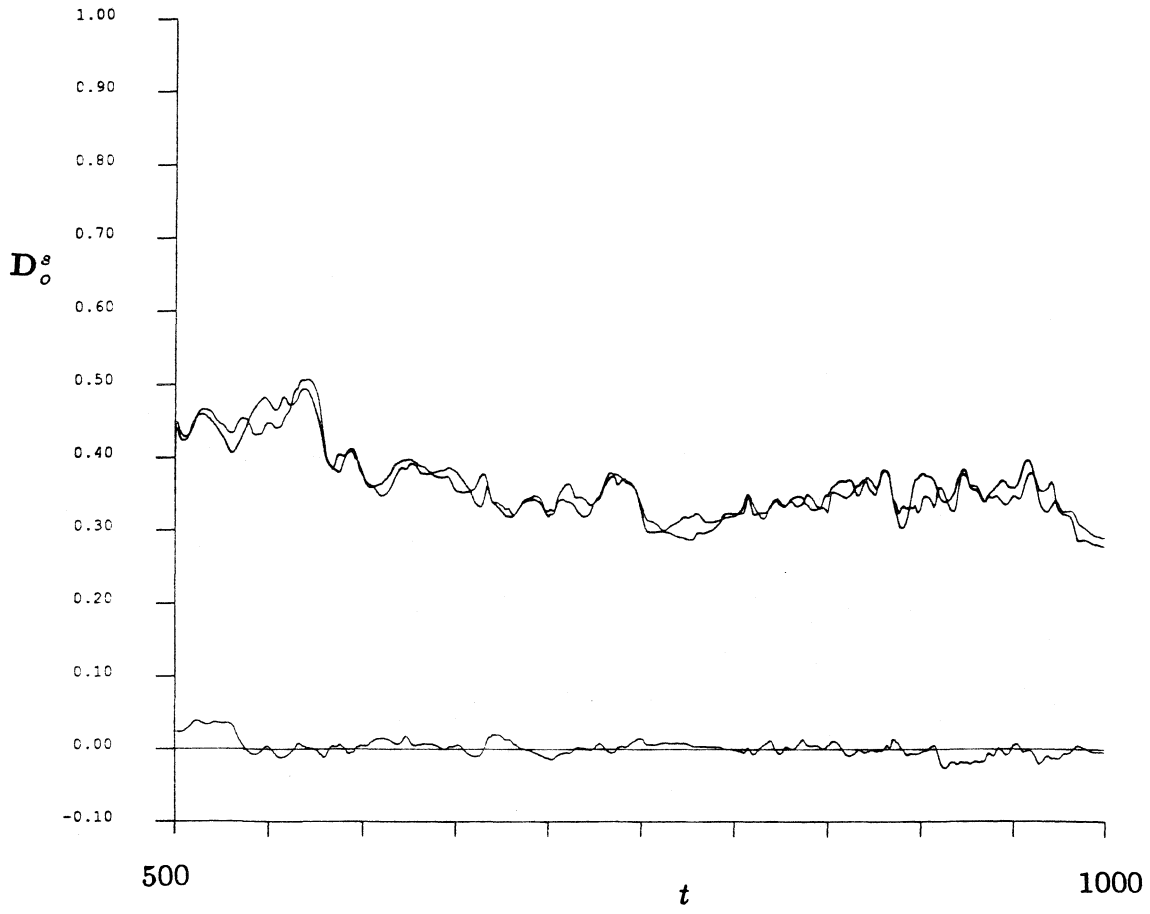

Figure B4.12 The time trace of $\mathbf{D}_o^s$ for the simulation Fn2–3. The upper two lines are the xx and yy components of this tensor. Of course, they should be equivalent for an infinite suspension – the slight variation occurs because of the finite number of spheres used in our simulation. The trace that fluctuates about the zero y-axis is the xy component of the short-time, self-diffusion tensor. Again, for an infinite number of spheres, this quantity would be exactly zero.

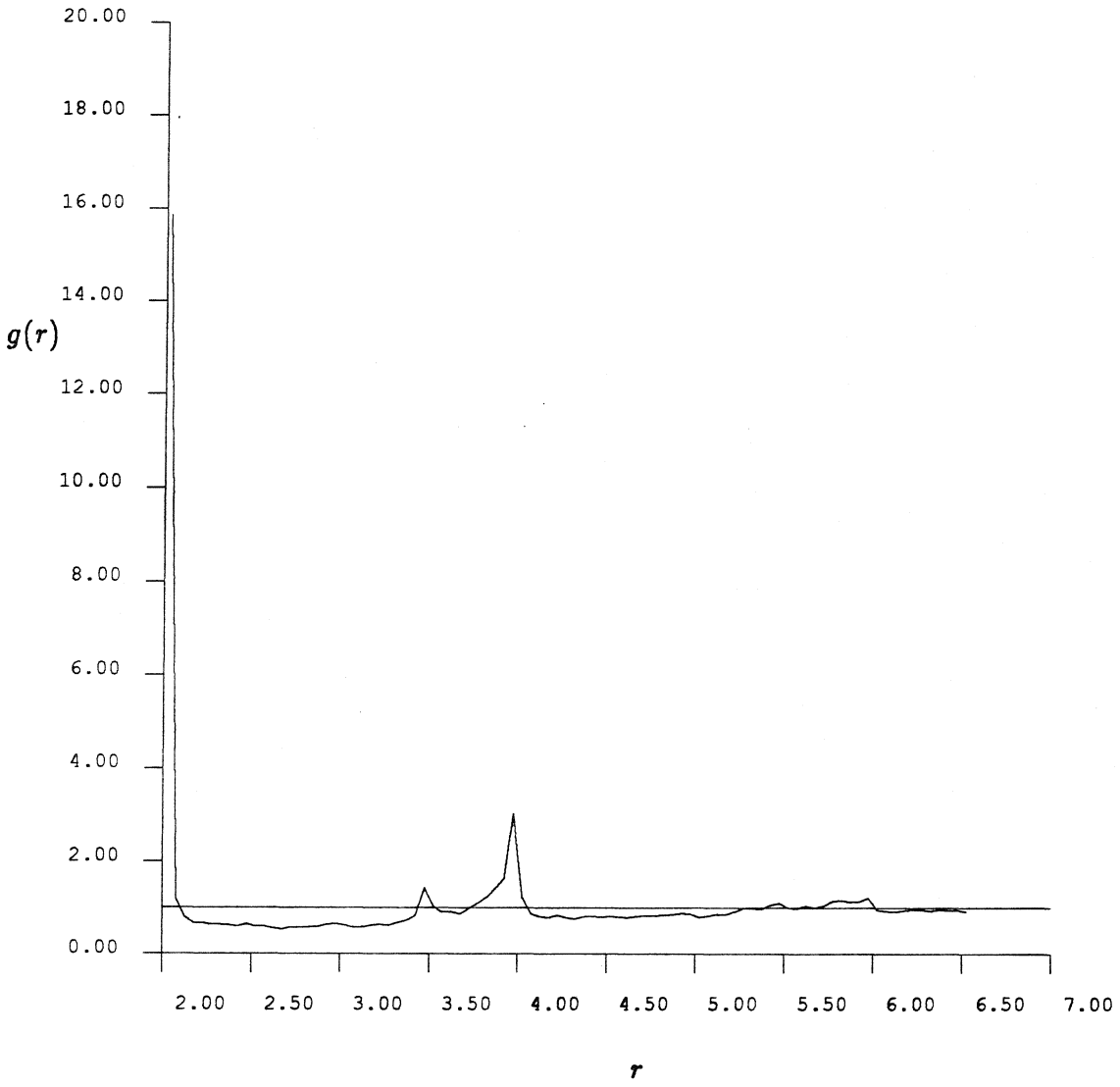

Figure B4.13 The radial pair-distribution function, $g(r)$, for the Fn1 run ($t = 100 - 400$).

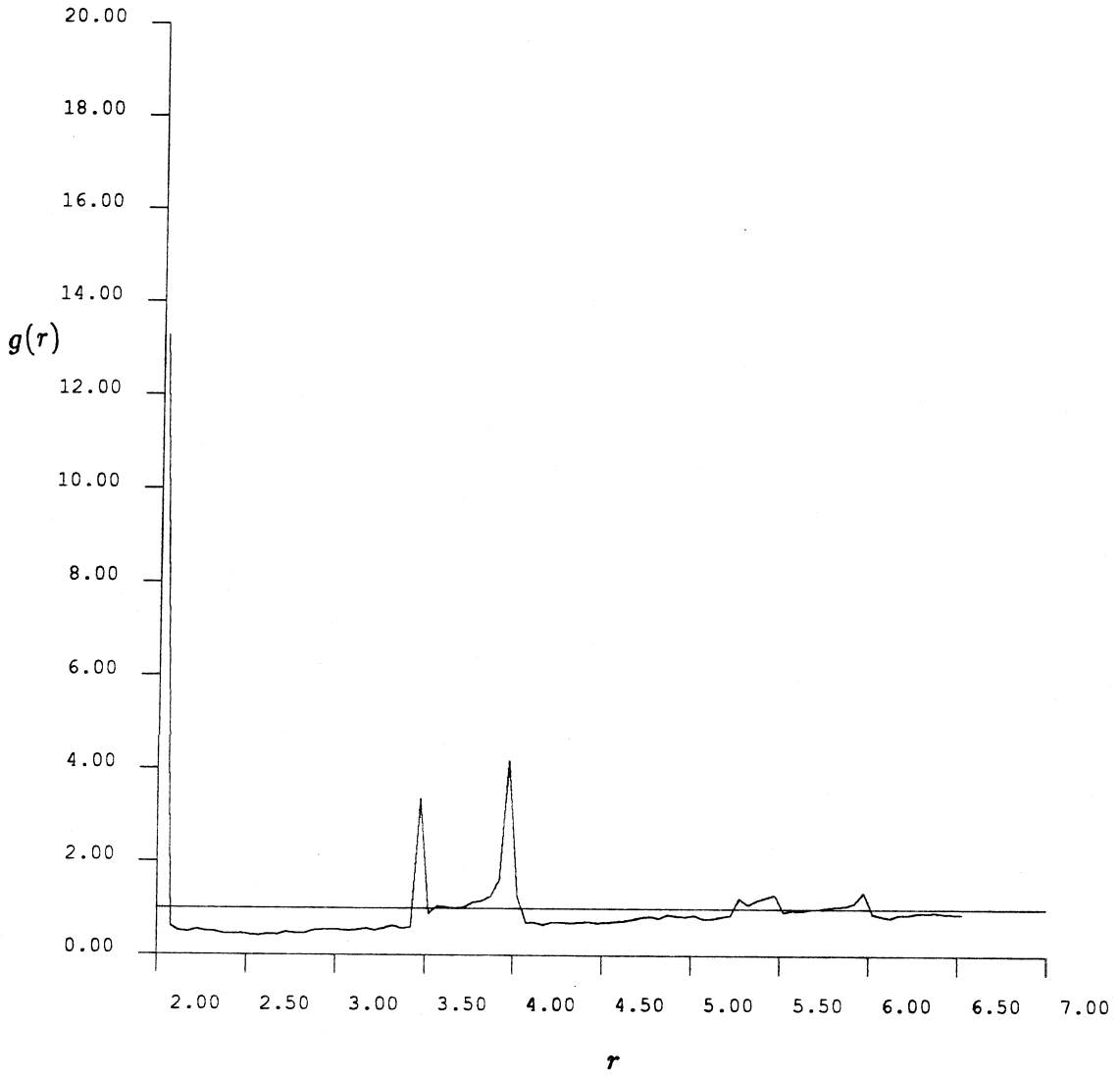

Figure B4.14 The radial pair-distribution function, $g(r)$, for the Fn2–3 run (t = 500 – 1000).

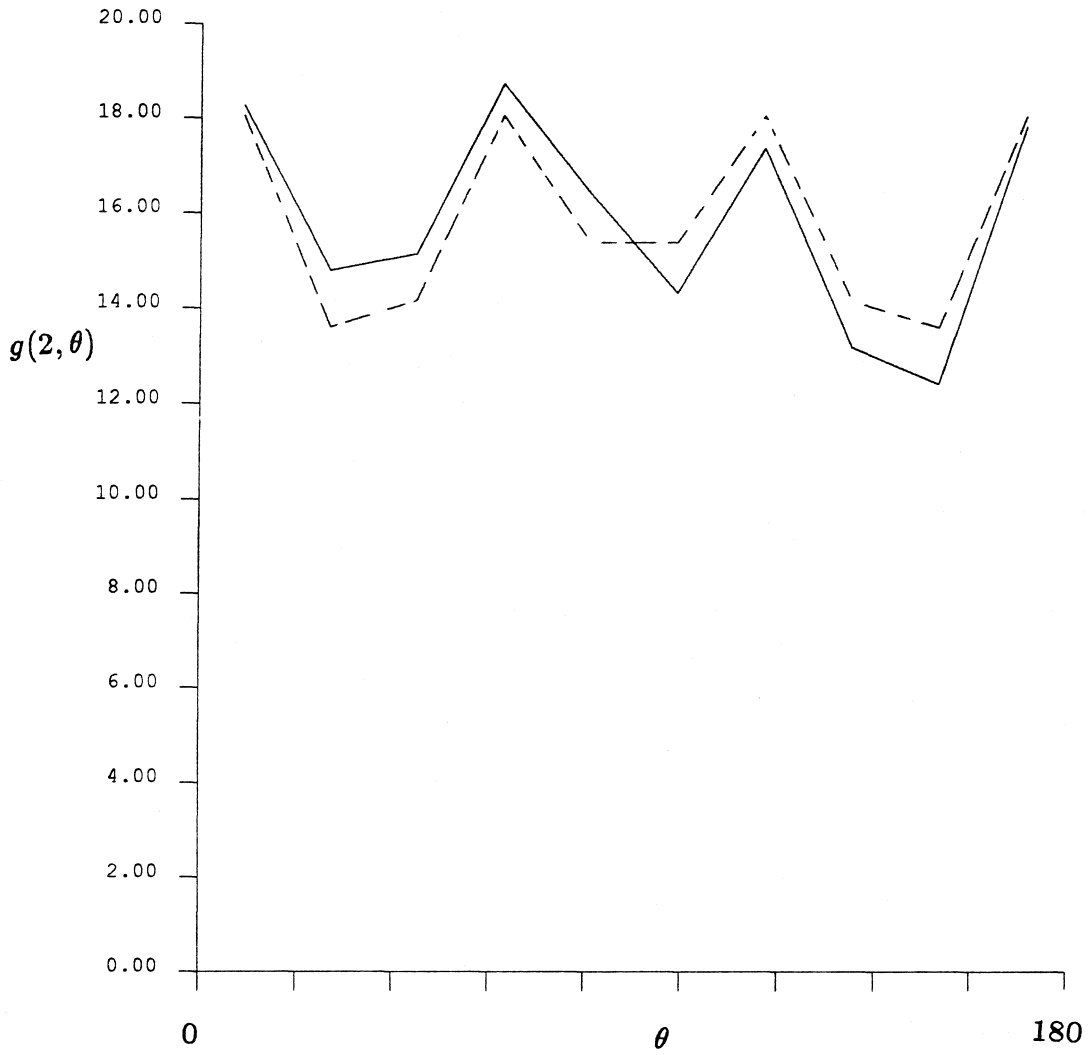

Figure B4.15 The full pair-distribution function for spheres whose surfaces are separated by less than 0.05 radii using data from the Fn1 run (t = 100 – 500). The dashed curve represents this function when it is forced to be symmetric about $\theta = 90°$.

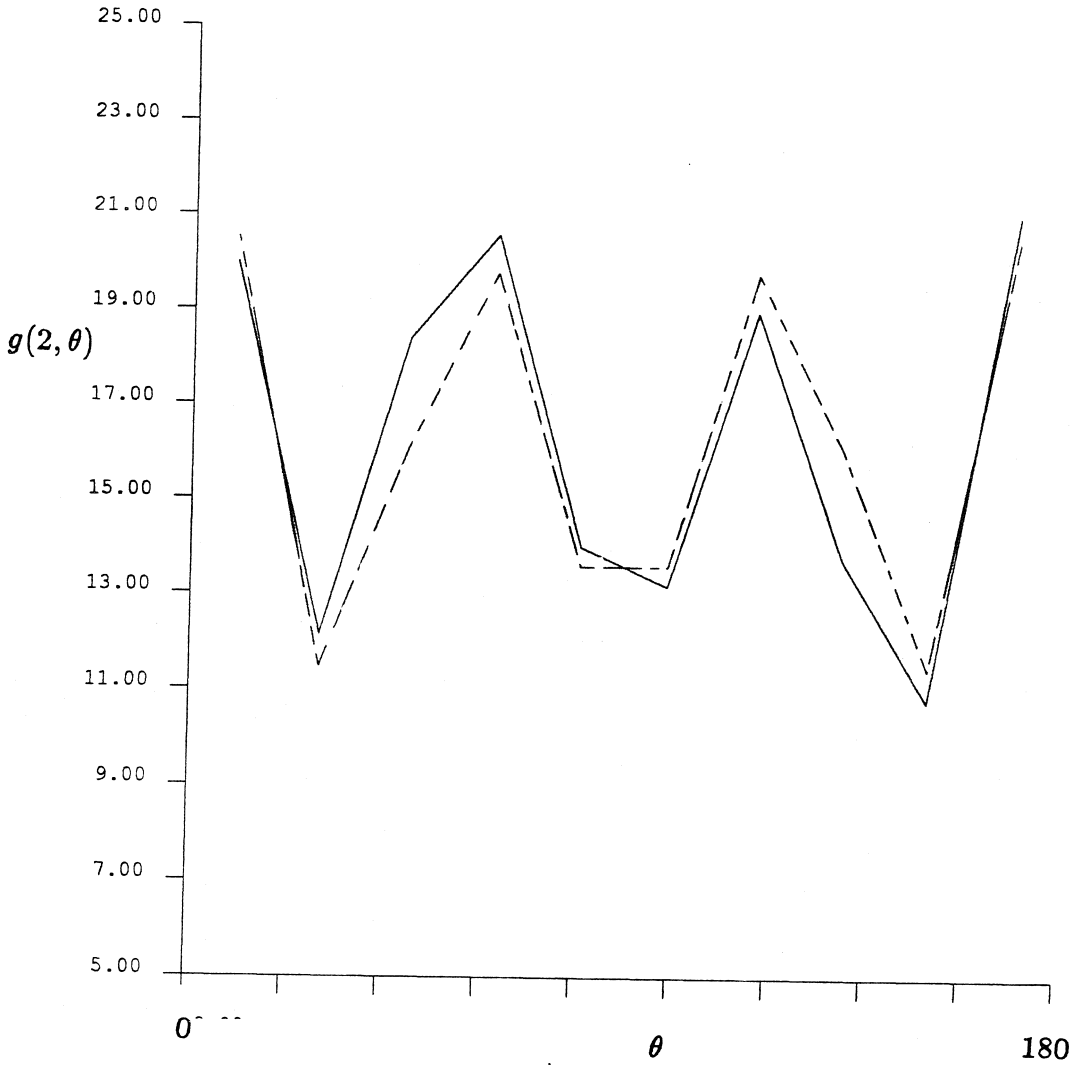

Figure B4.16 The full pair-distribution function for spheres whose surfaces are separated by less than 0.05 radii using data from the Fn1 run (t = 250 – 500). The dashed curve represents this function when it is forced to be symmetric about $\theta = 90°$.

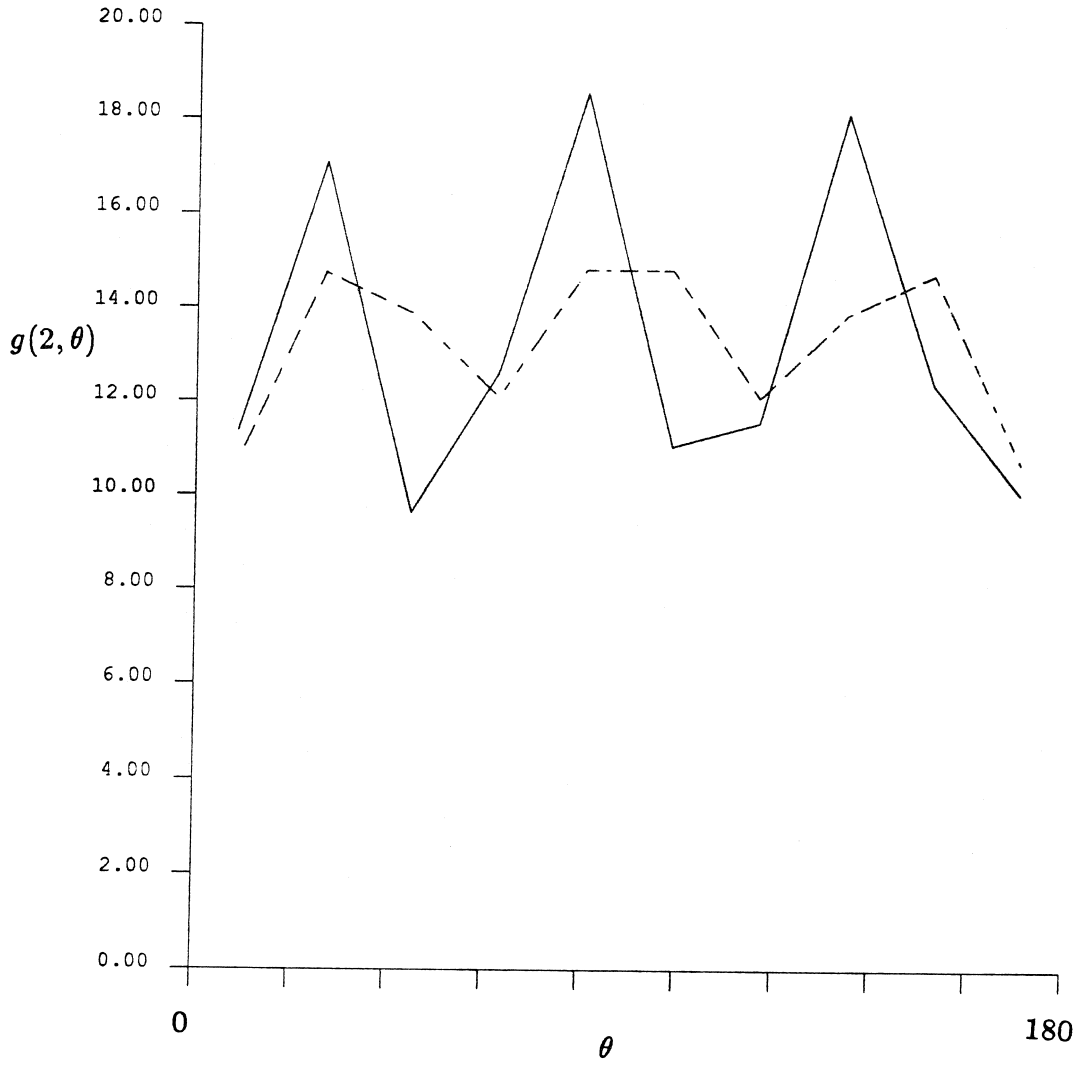

Figure B4.17 The full pair-distribution function for spheres whose surfaces are separated by less than 0.05 radii using data from the Fn2–3 run (t = 500 – 1000). The dashed curve represents this function when it is forced to be symmetric about $\theta = 90°$.

Figure B4.18 There is no Figure *B4.18*.

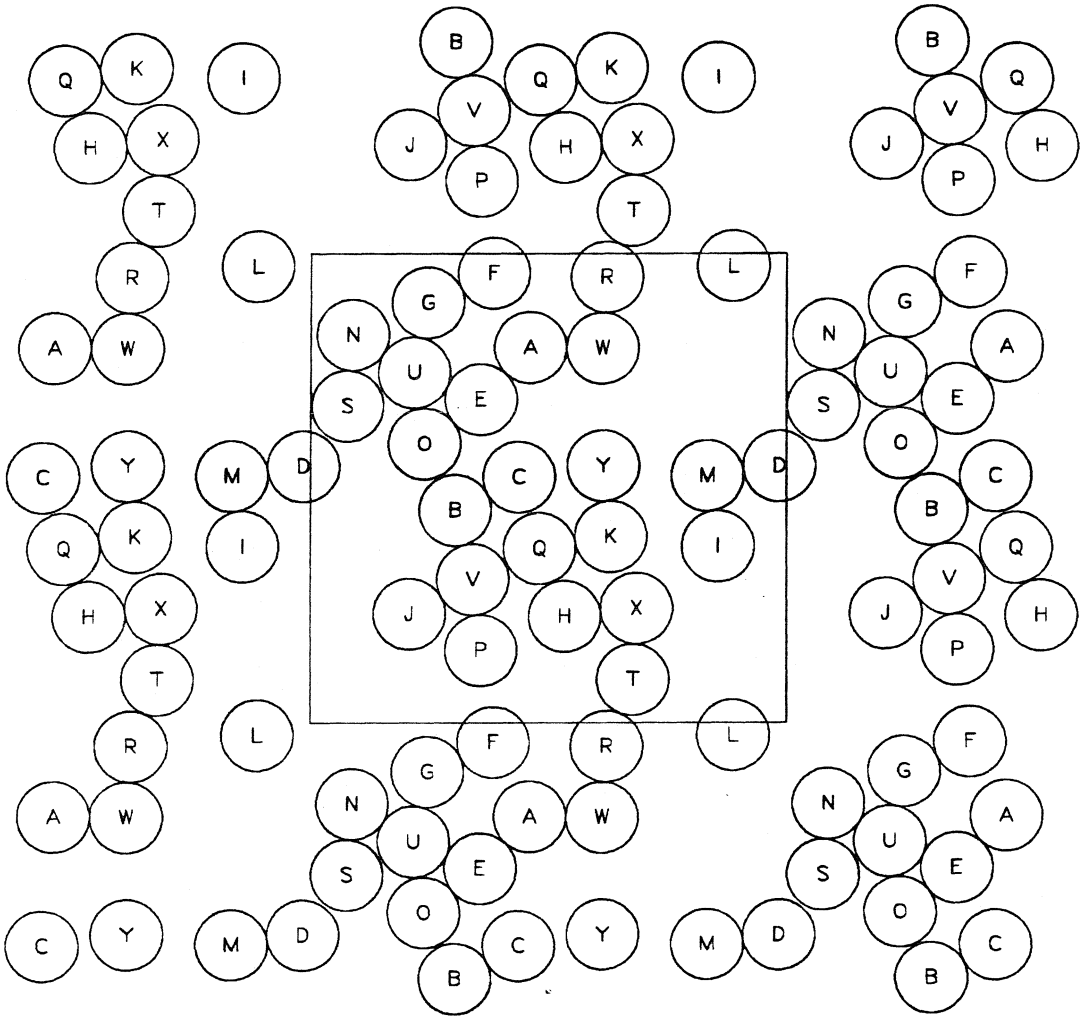

Figure B4.19 A "snapshot" of sphere positions. The square is the periodic cell. These are the sphere positions at $t = 100.05$ time units (Fn1).

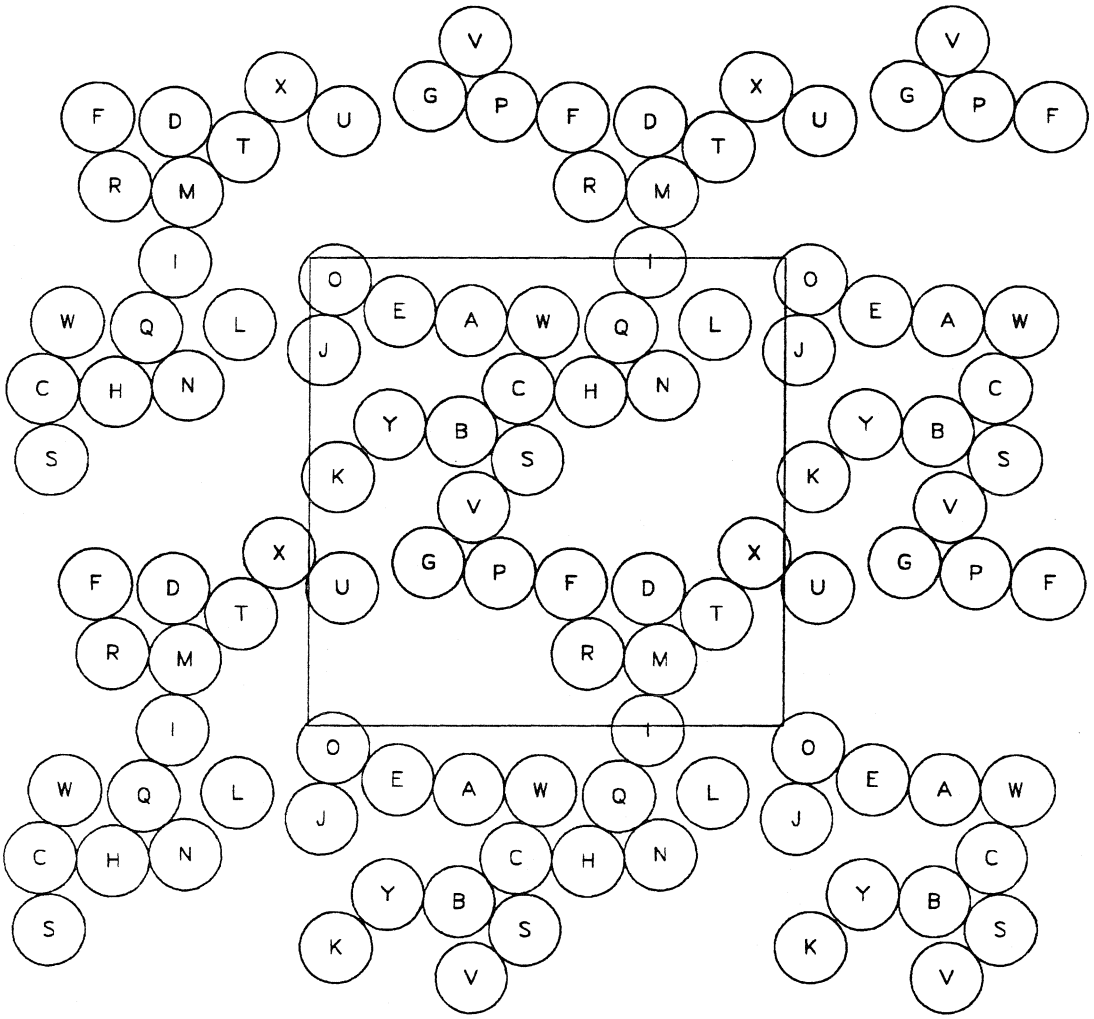

Figure B4.20 A "snapshot" of sphere positions. The square is the periodic cell. These are the sphere positions at $t = 200.00$ time units (Fn1).

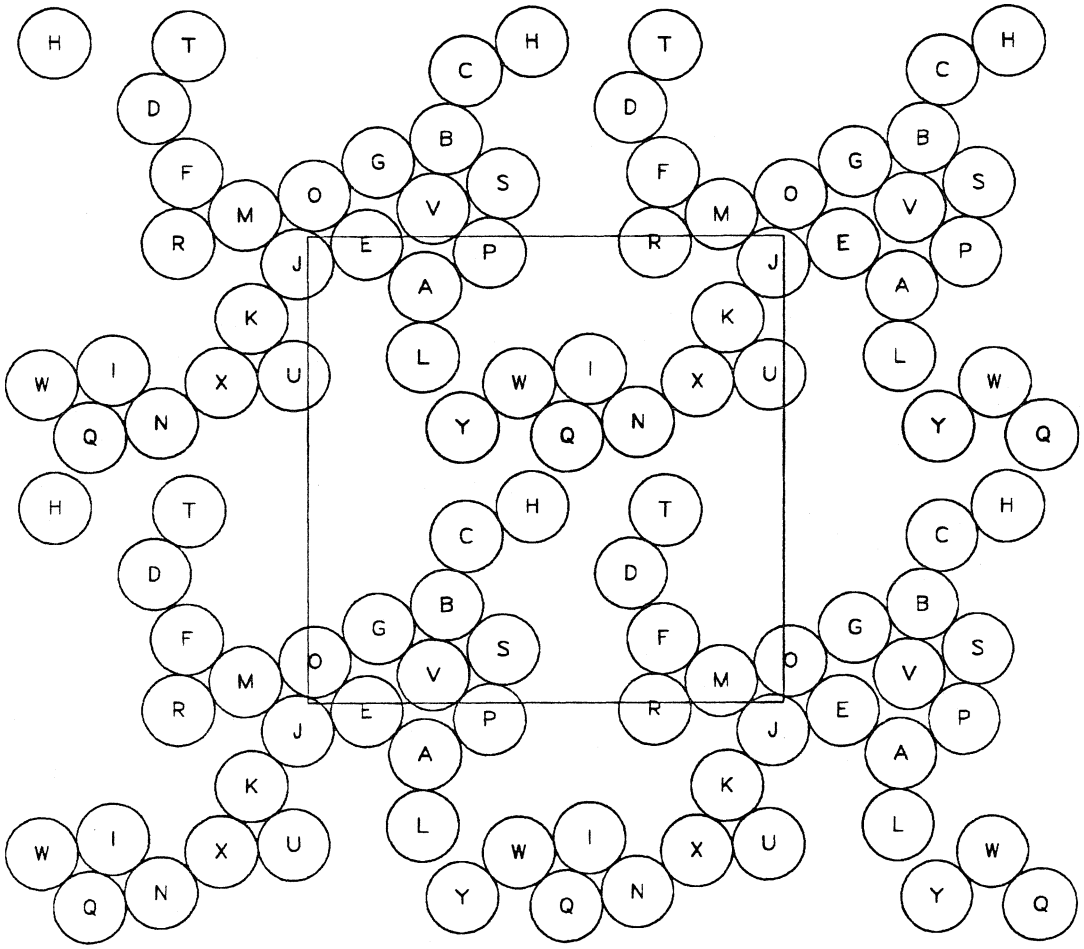

Figure B4.21 A "snapshot" of sphere positions. The square is the periodic cell. These are the sphere positions at $t = 250.00$ time units (Fn1).

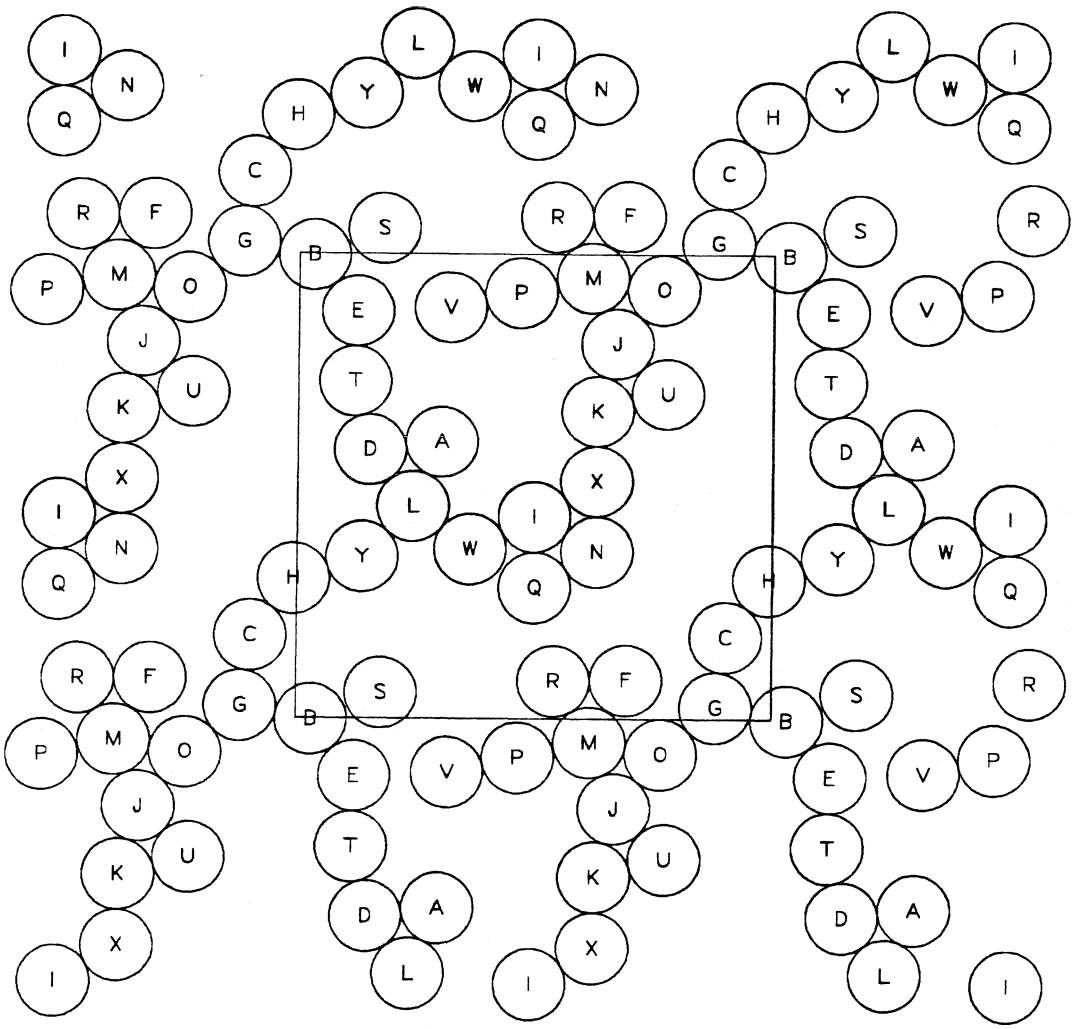

Figure B4.22 A "snapshot" of sphere positions. The square is the periodic cell. These are the sphere positions at $t = 300.00$ time units (Fn1).

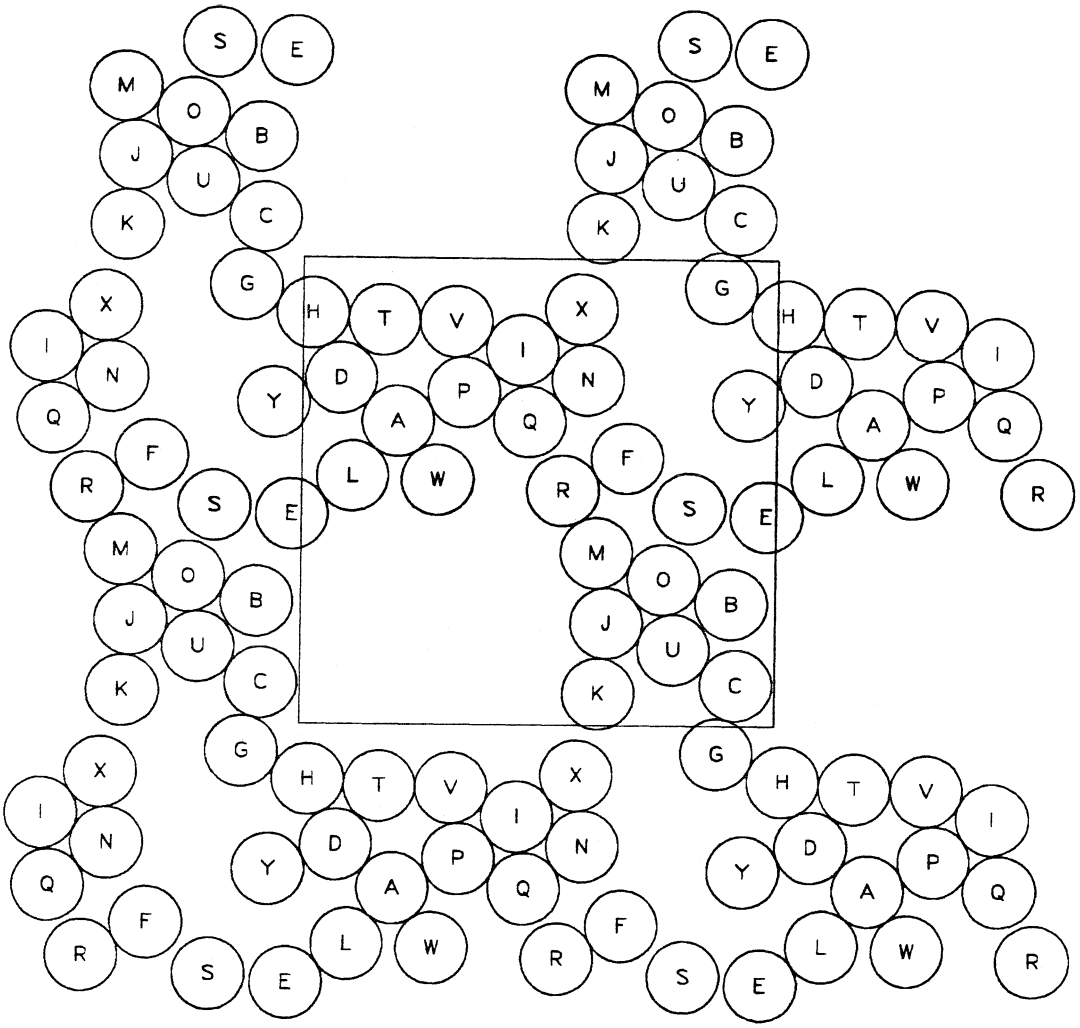

Figure B4.23 A "snapshot" of sphere positions. The square is the periodic cell. These are the sphere positions at $t = 350.00$ time units (Fn1).

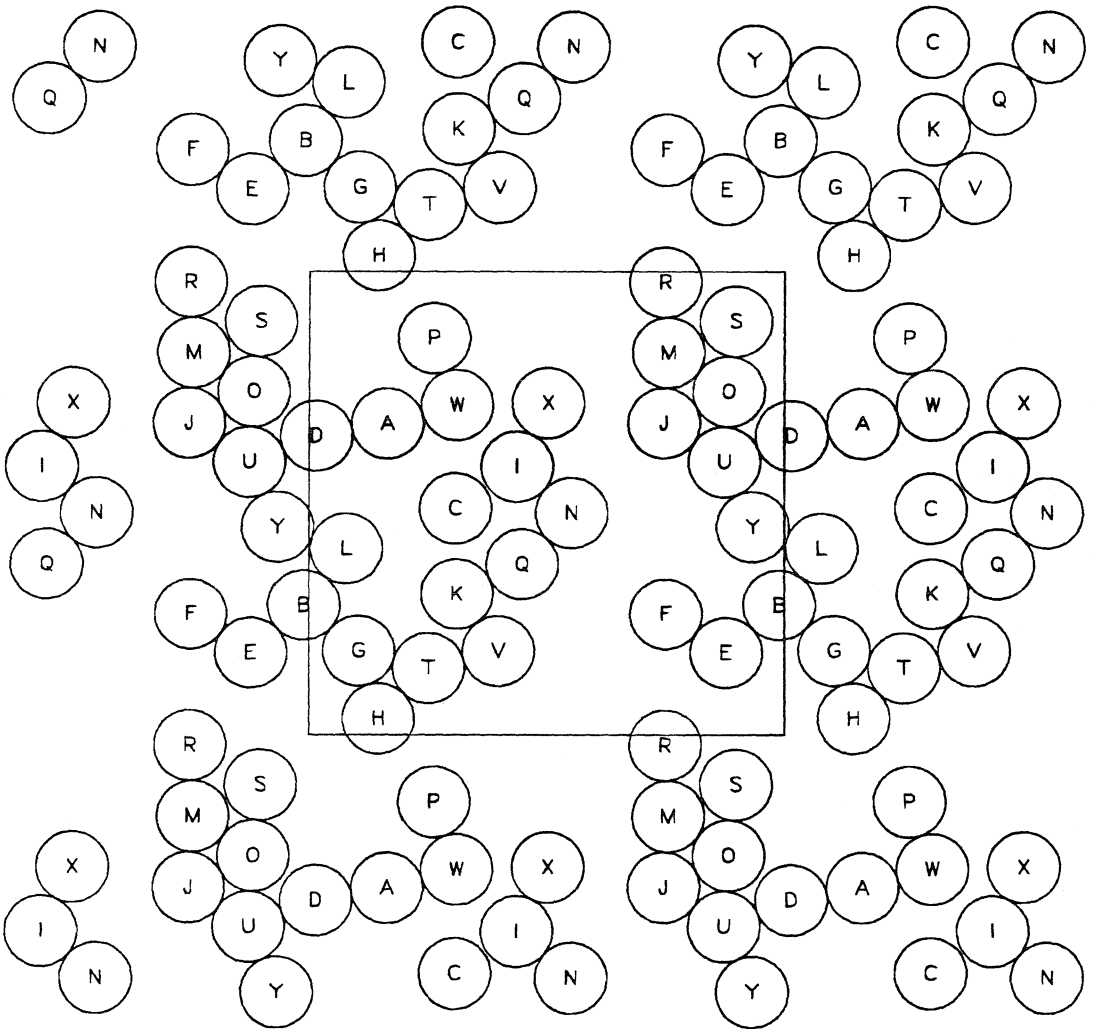

Figure B4.24 A "snapshot" of sphere positions. The square is the periodic cell. These are the sphere positions at $t = 400.00$ time units (Fn1).

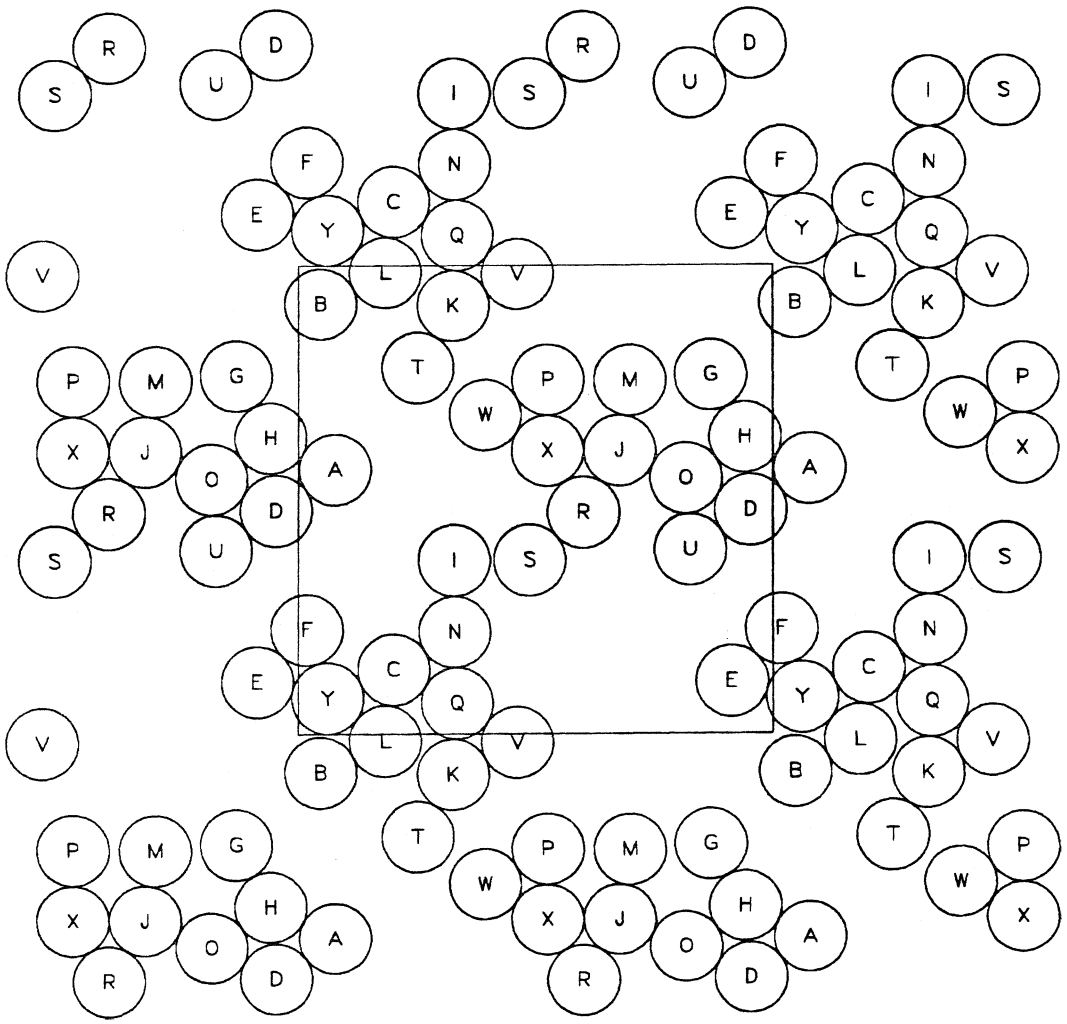

Figure B4.25 A "snapshot" of sphere positions. The square is the periodic cell. These are the sphere positions at $t = 450.00$ time units (Fn1).

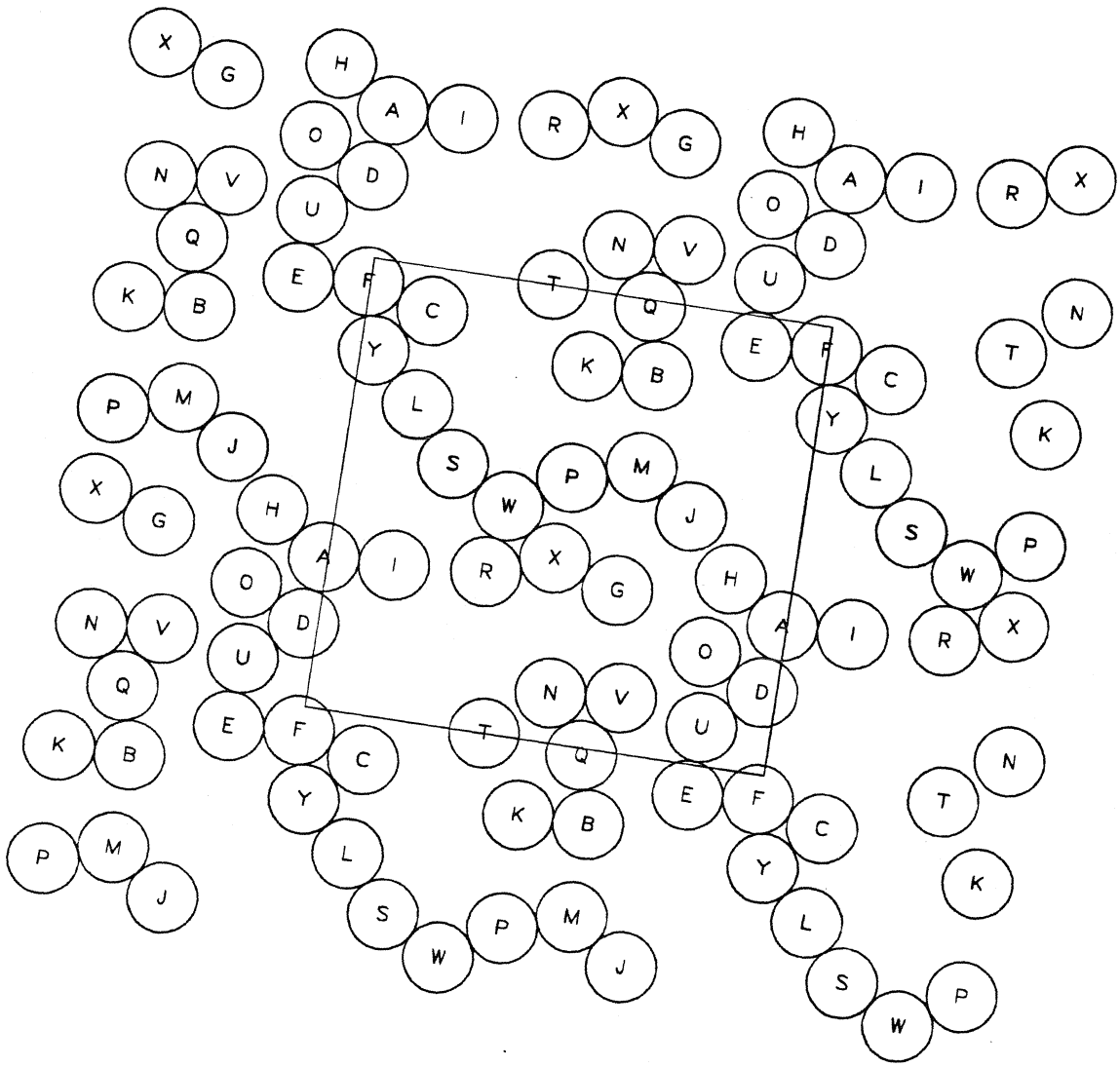

Figure B4.26 A "snapshot" of sphere positions. The square is the periodic cell. These are the sphere positions at $t = 500.00$ time units (Fn1).

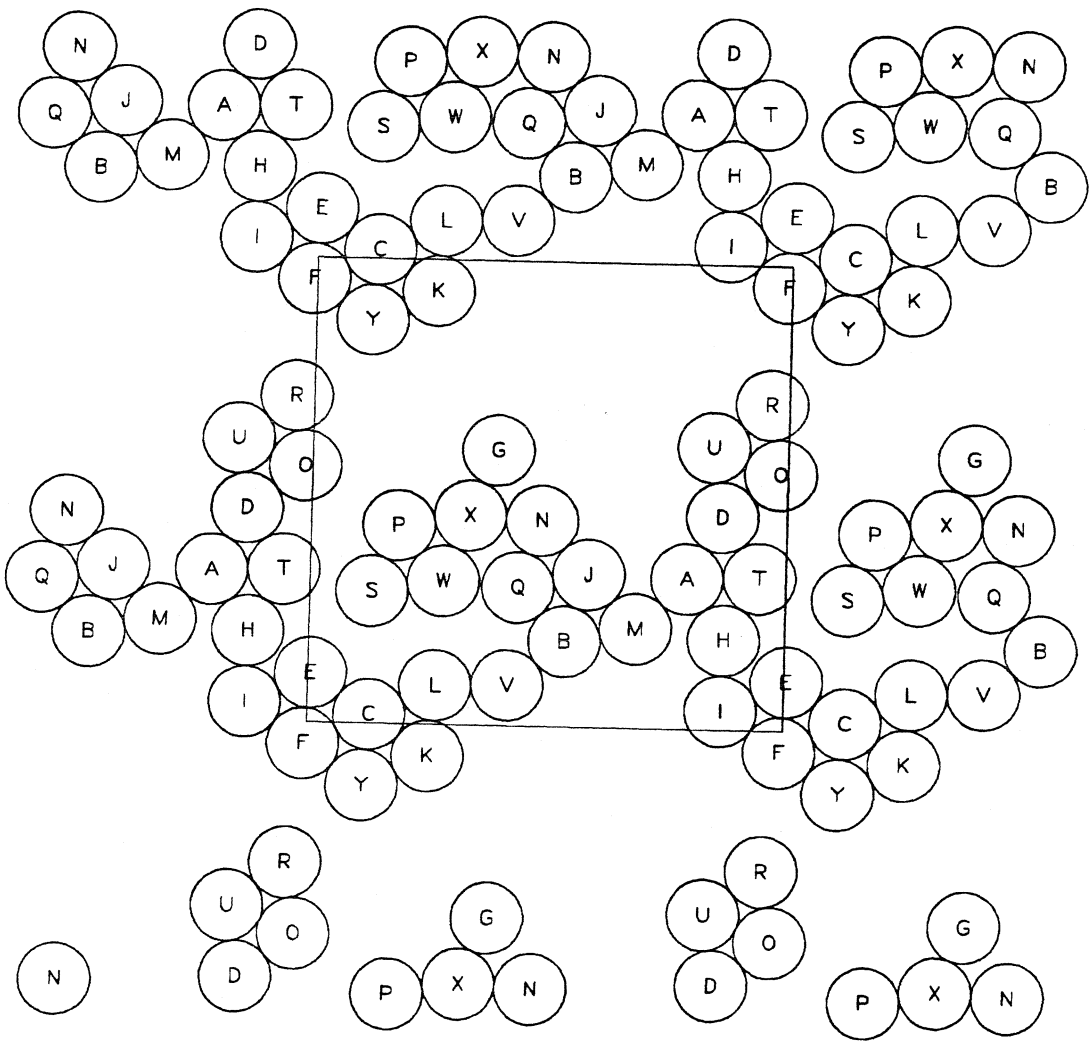

Figure B4.27 A "snapshot" of sphere positions. The square is the periodic cell. These are the sphere positions at $t = 700.05$ time units (Fn3).

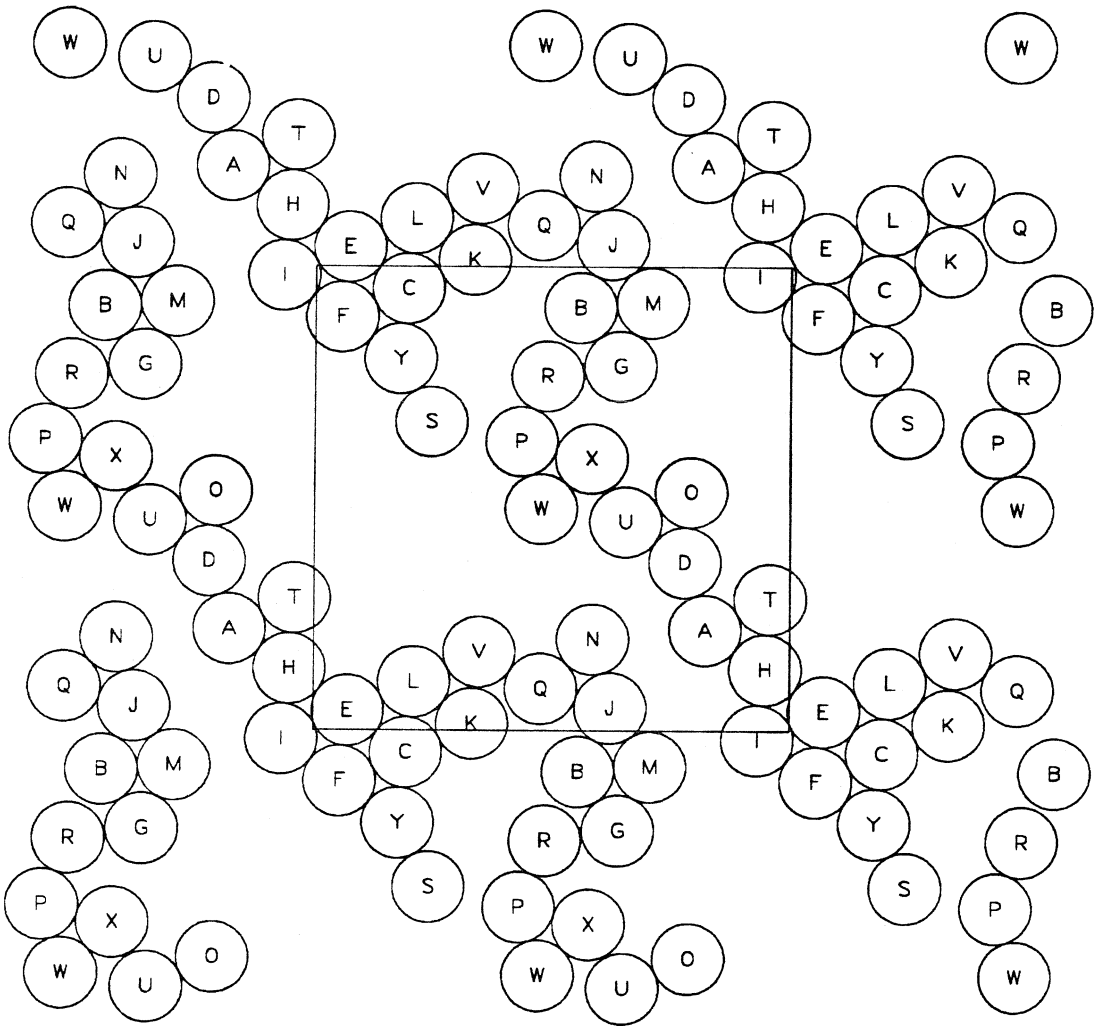

Figure B4.28 A "snapshot" of sphere positions. The square is the periodic cell. These are the sphere positions at $t = 750.00$ time units (Fn3).

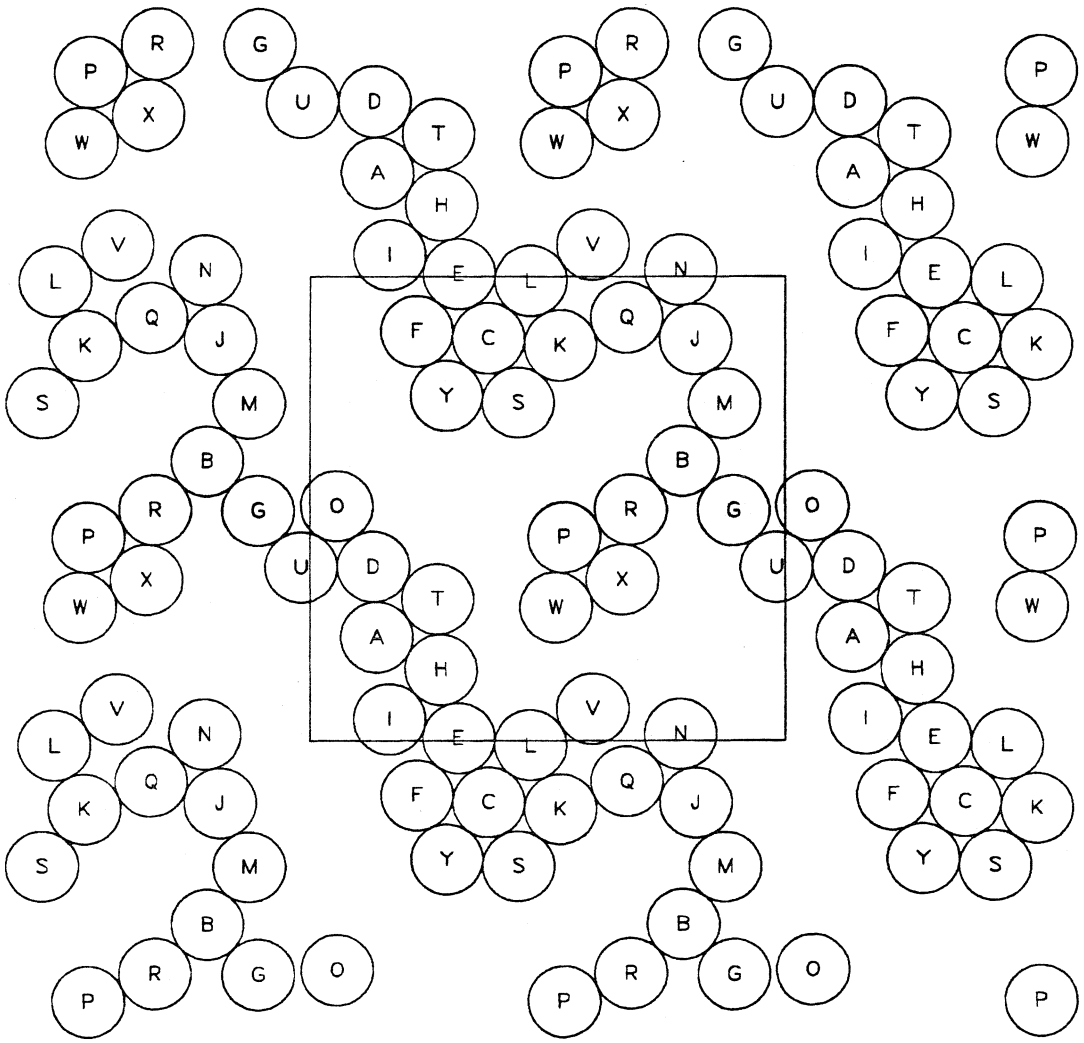

Figure B4.29 A "snapshot" of sphere positions. The square is the periodic cell. These are the sphere positions at $t = 800.00$ time units (Fn3).

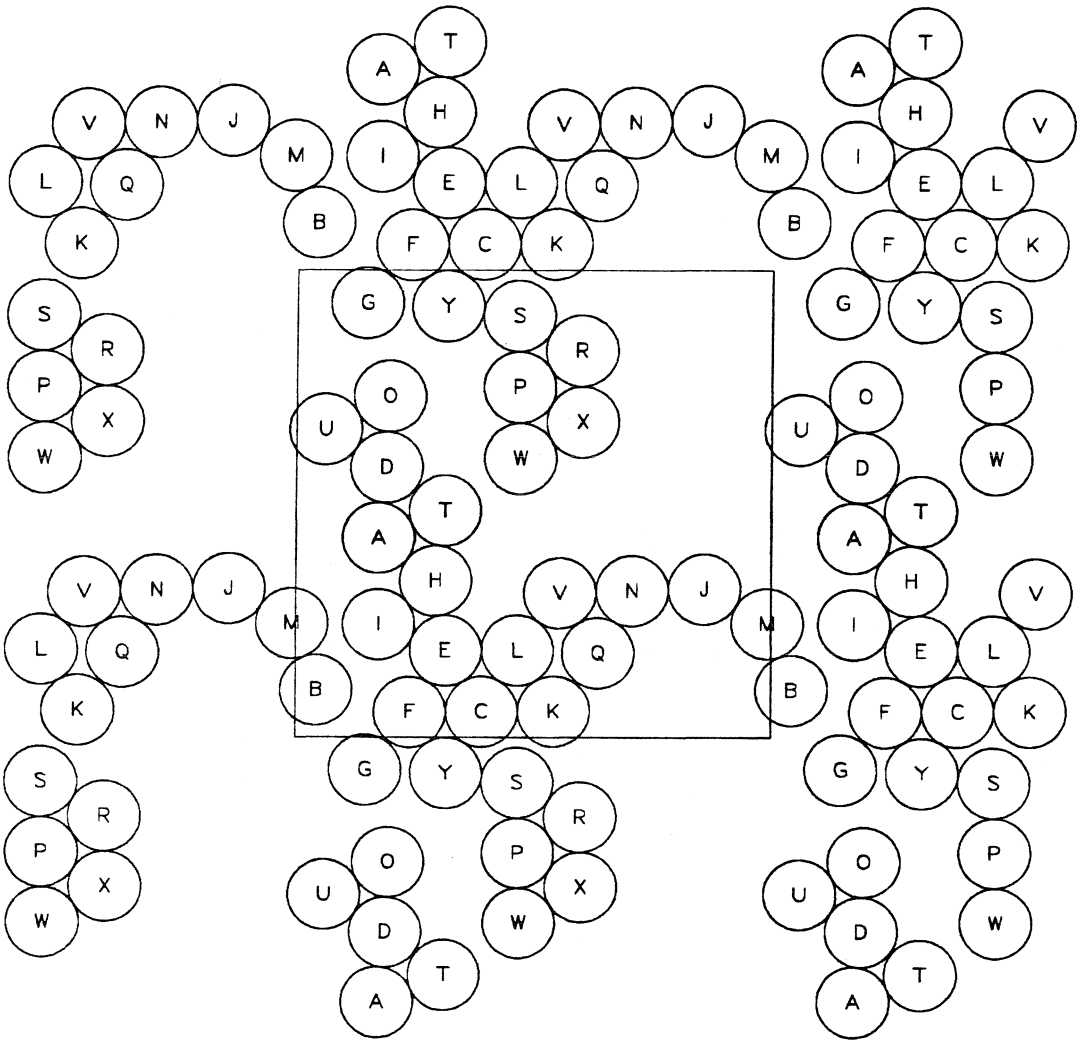

Figure B4.30 A "snapshot" of sphere positions. The square is the periodic cell. These are the sphere positions at $t = 822.15$ time units (Fn3).

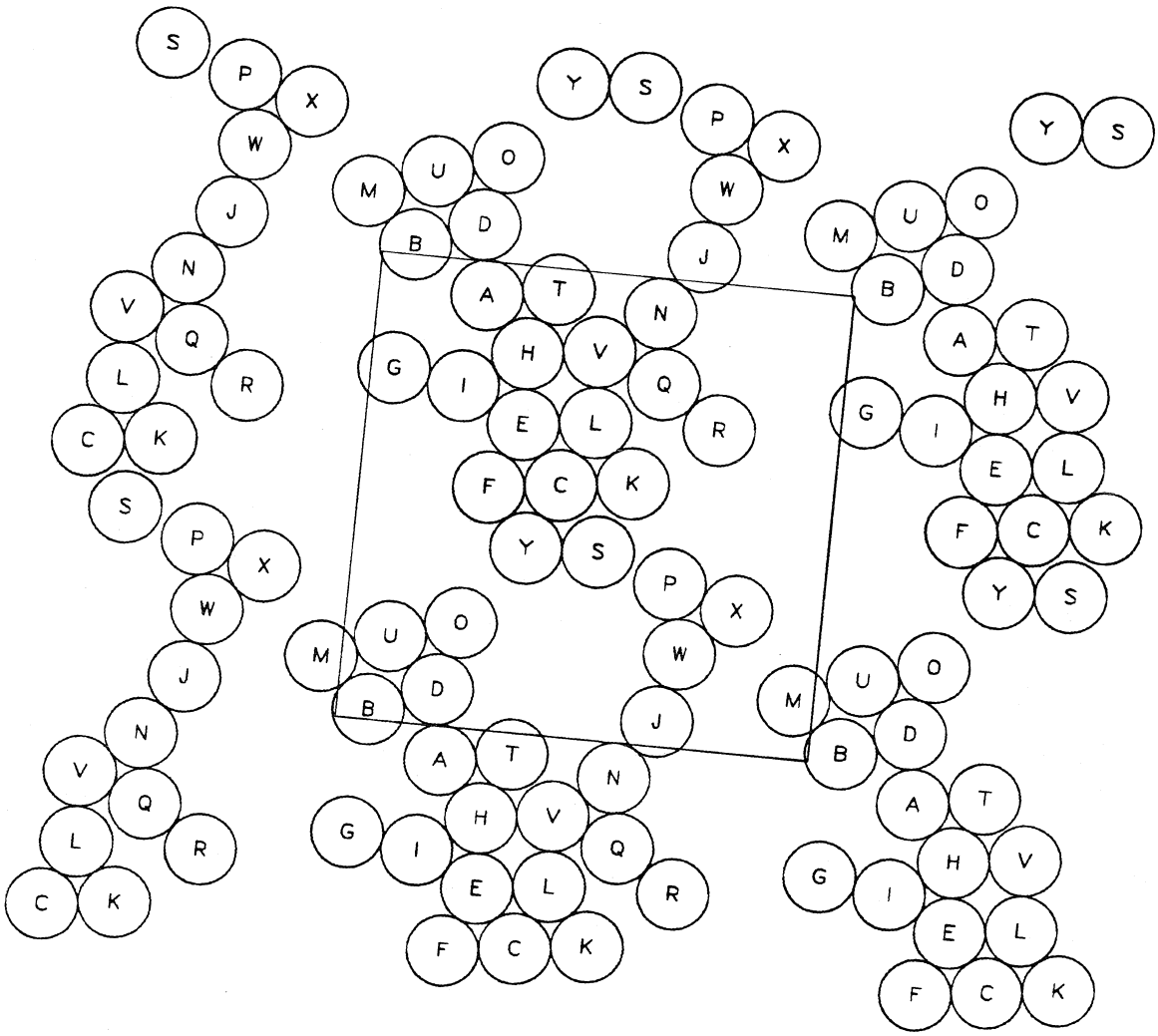

Figure B4.31 A "snapshot" of sphere positions. The square is the periodic cell. These are the sphere positions at $t = 850.00$ time units (Fn3).

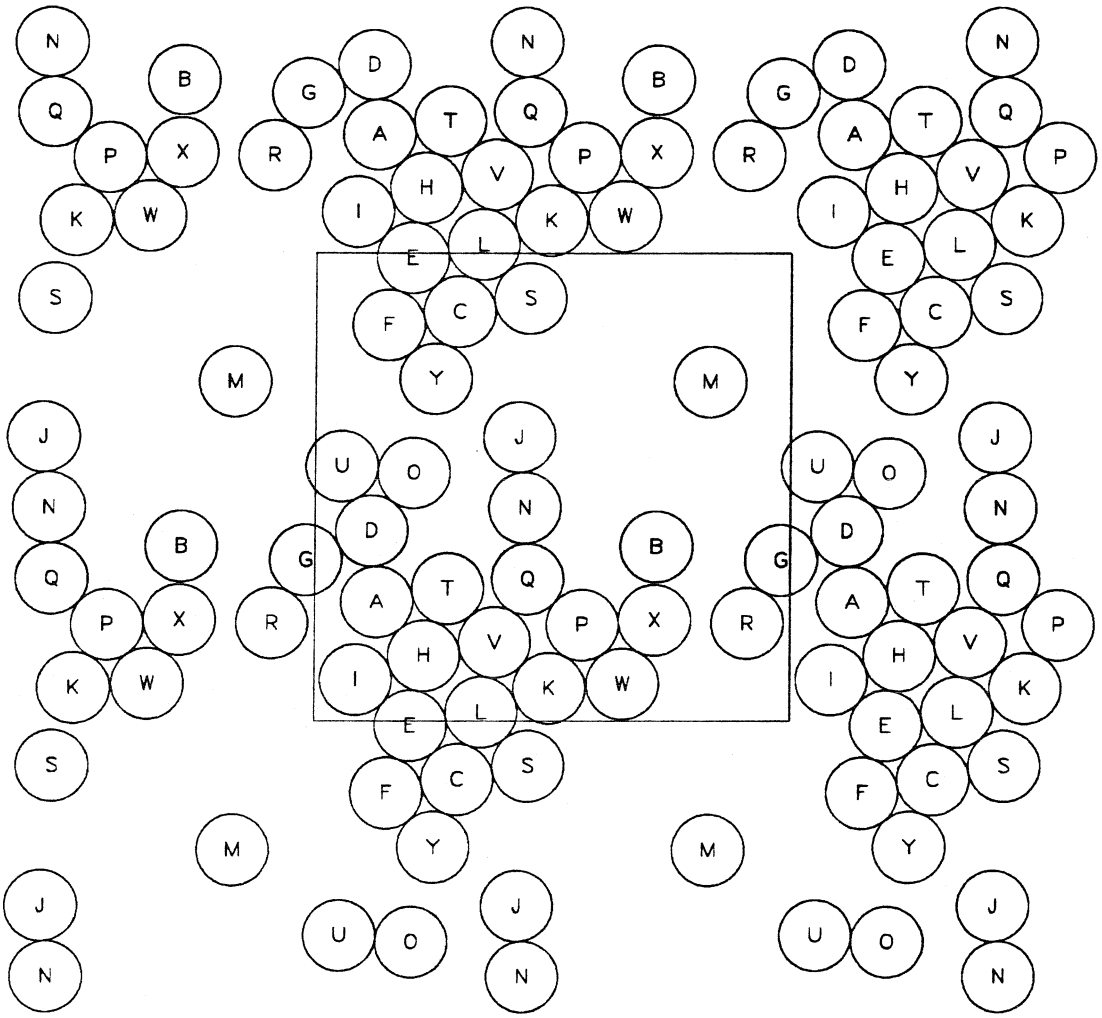

Figure B4.32 A "snapshot" of sphere positions. The square is the periodic cell. These are the sphere positions at $t = 900.00$ time units (Fn3).

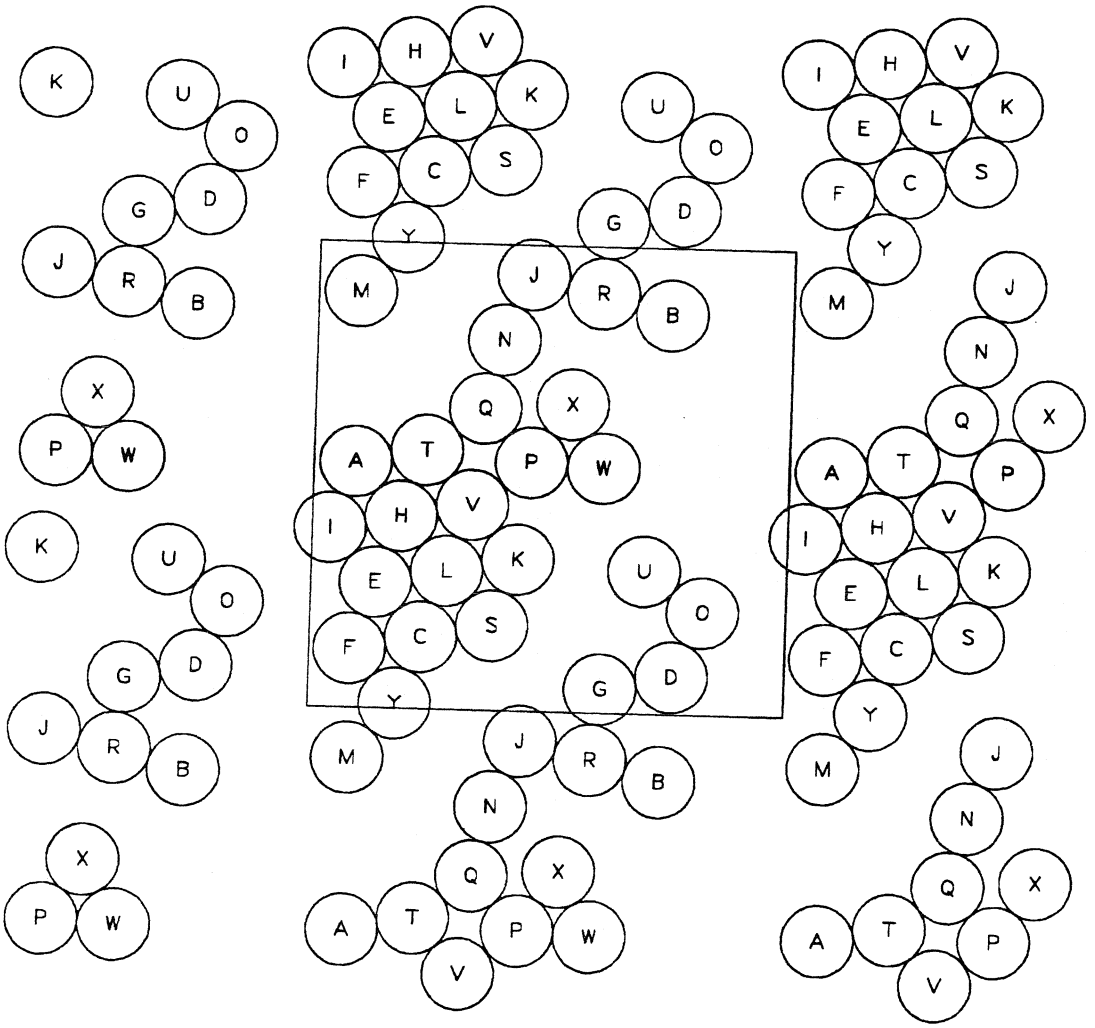

Figure B4.33 A "snapshot" of sphere positions. The square is the periodic cell. These are the sphere positions at $t = 928.00$ time units (Fn3).

Appendix B5: The ef simulation results

This suite of simulations uses an Ewald, F method to approximate the hydrodynamic interactions. The separation factor, z_l, is 2. 126 image cells are used to insure the convergence of the mobility interactions. Four separate simulation runs follow the evolution of a sedimenting system to a final time of 1000 time units. The initial configuration is the same as in the FTSn simulations described in Appendix B1. There are 25 spheres within the periodic cell. The areal fraction is 0.453. There are no interparticle forces present. The time step is 0.001 time unit. The mobility matrix is inverted every 0.1 time unit. Position and velocity data is saved every 0.05 time unit. $\mathbf{D}_o^s$ is evaluated and reported at every time unit.

	ef1	ef2	ef3	ef4
T	0-250	250-500	500-750	750-1000
Cray/Sun	Cray 0.80	Cray 0.70	Cray 0.70	Sun
CPU(min)	108	72		1723
v_y	-5.01027	-5.06561	-5.08465	-5.10151
v_x	0.00057	0.00016	-0.01051	0.00074
v_y variance	0.01008	0.01137	0.00854	0.02544
v_x variance	0.00266	0.00256	0.00196	0.00224
v_{xy} variance	0.00019	-0.00039	0.00008	-0.00042
$(D_\infty^s)_{yy}$	0.08	0.12	0.27	
$(D_\infty^s)_{xx}$	0.032		0.023	0.011
$(D_o^s)_{yy}$	0.549	0.353	0.294	0.280
$(D_o^s)_{xx}$	0.555	0.356	0.300	0.279
$(D_o^s)_{xy}$	-0.0052	-0.0067	0.0043	-0.0006
$g(2)$		15.7	15.4	15.3
$g(3.5)$		1.61	2.28	4.83
$g(4)$		3.18	4.34	6.04

Table B5.1

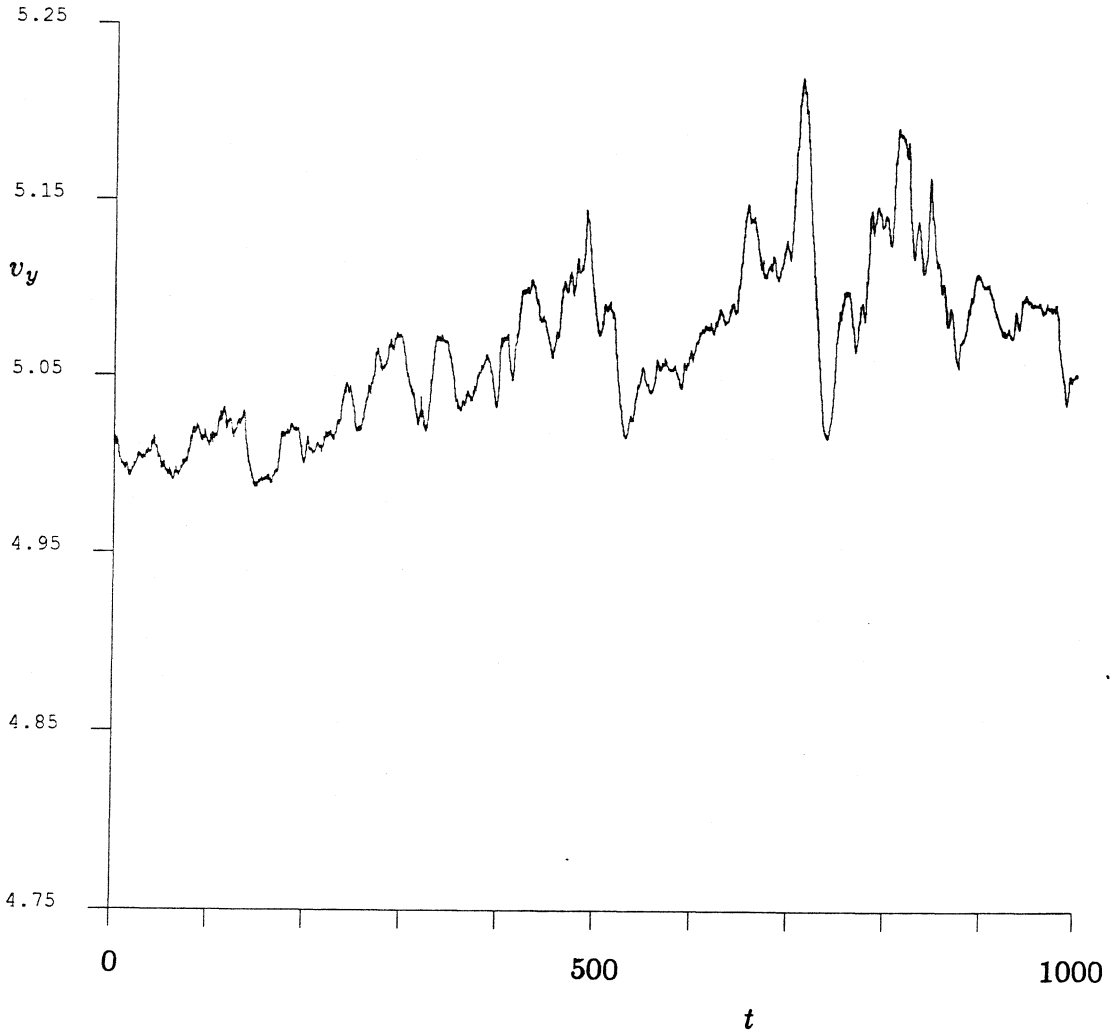

Figure B5.1 The time trace of v_y for the simulations ef1 through ef4.

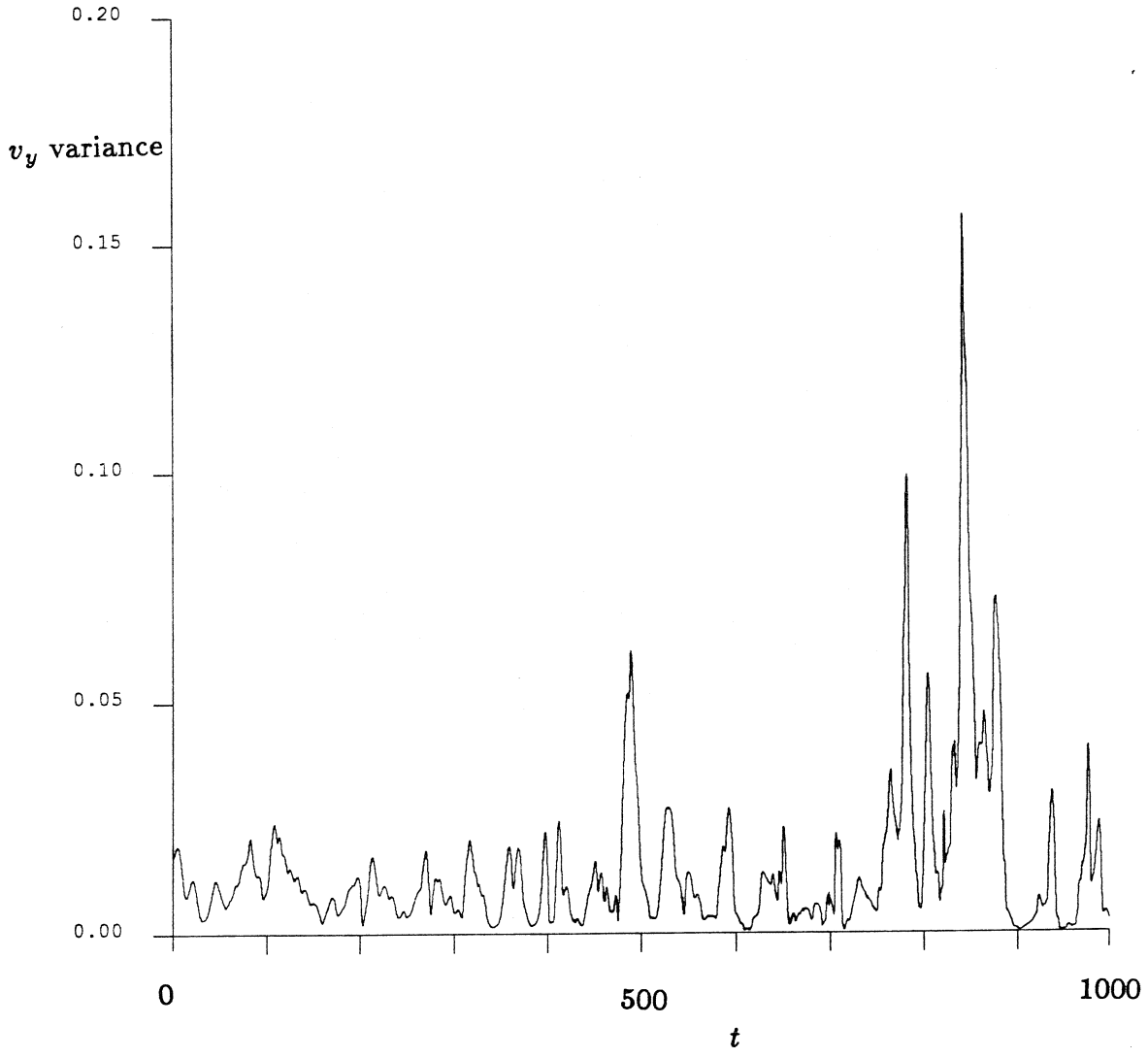

Figure B5.2 The time trace of the v_y variance for the simulations ef1 through efr4.

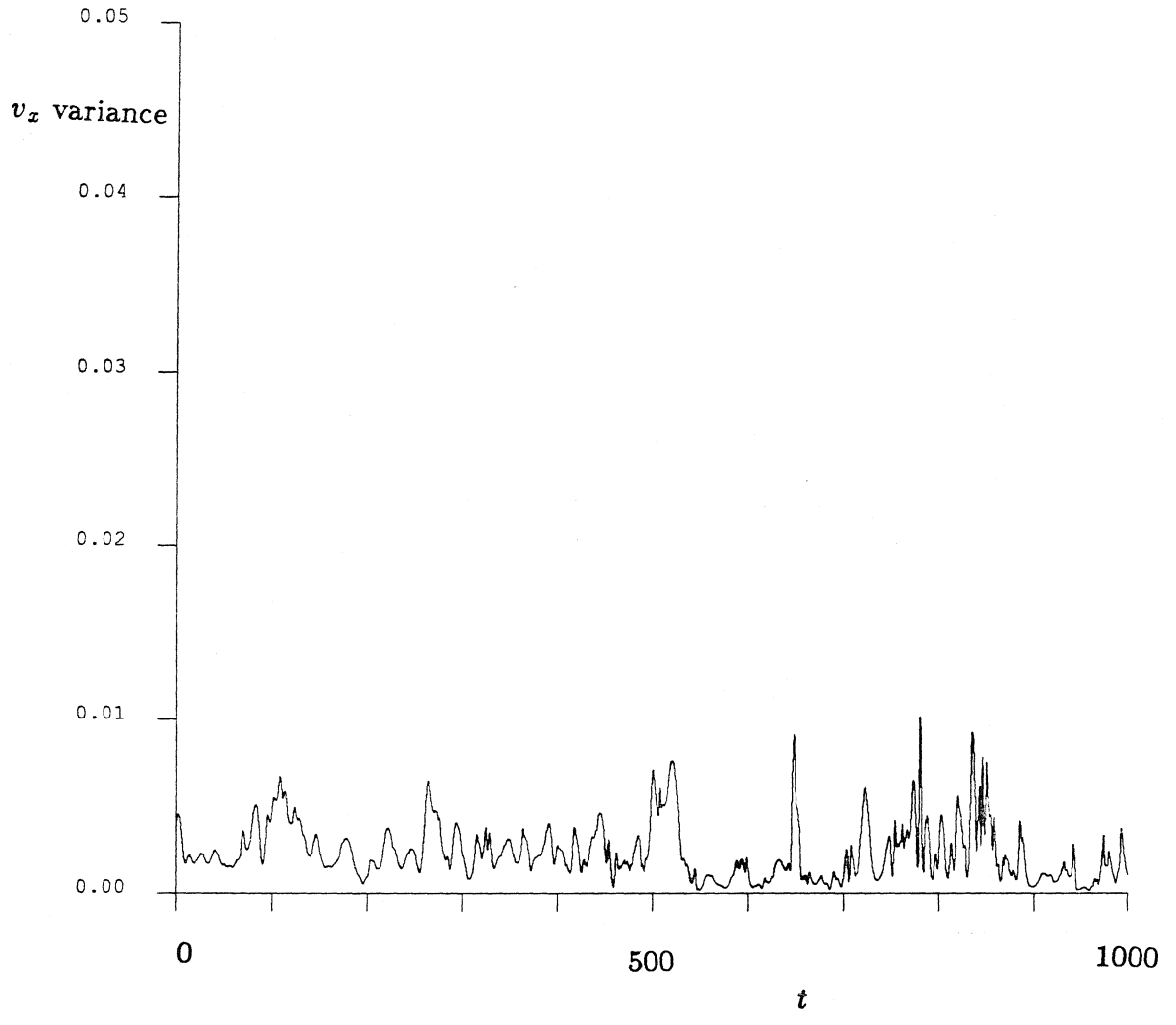

Figure B5.3 The time trace of the v_x variance for the simulations ef1 through ef4.

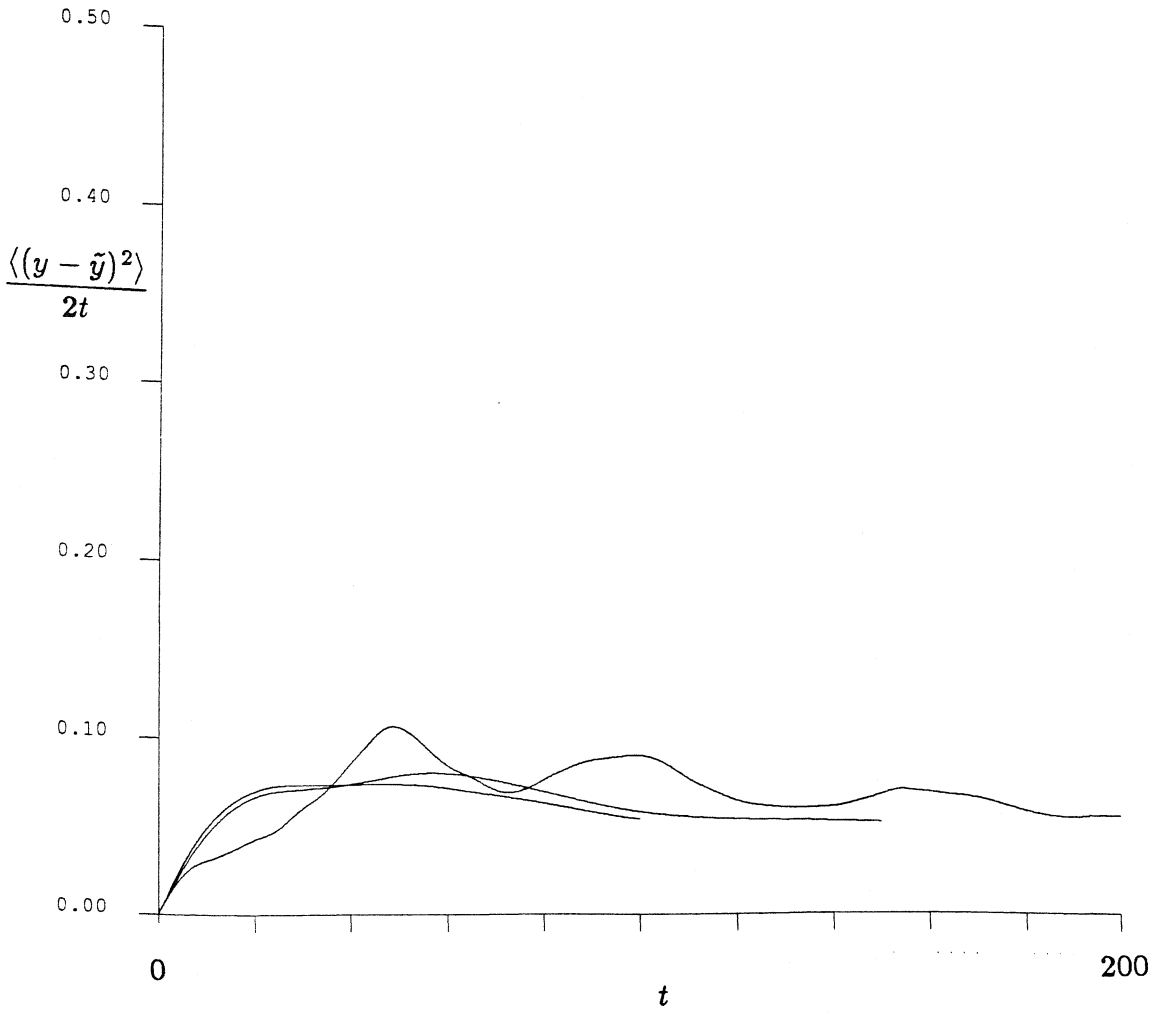

Figure B5.4 A $(D^s_\infty)_{yy}$-defining graph using displacement data from ef1 (t= 50 – 250). The graph interval is 100, 150 and 200 time units. The time between interval initial conditions is 0.01 time unit, except for the 200 time units curve where no averaging over initial conditions is performed.

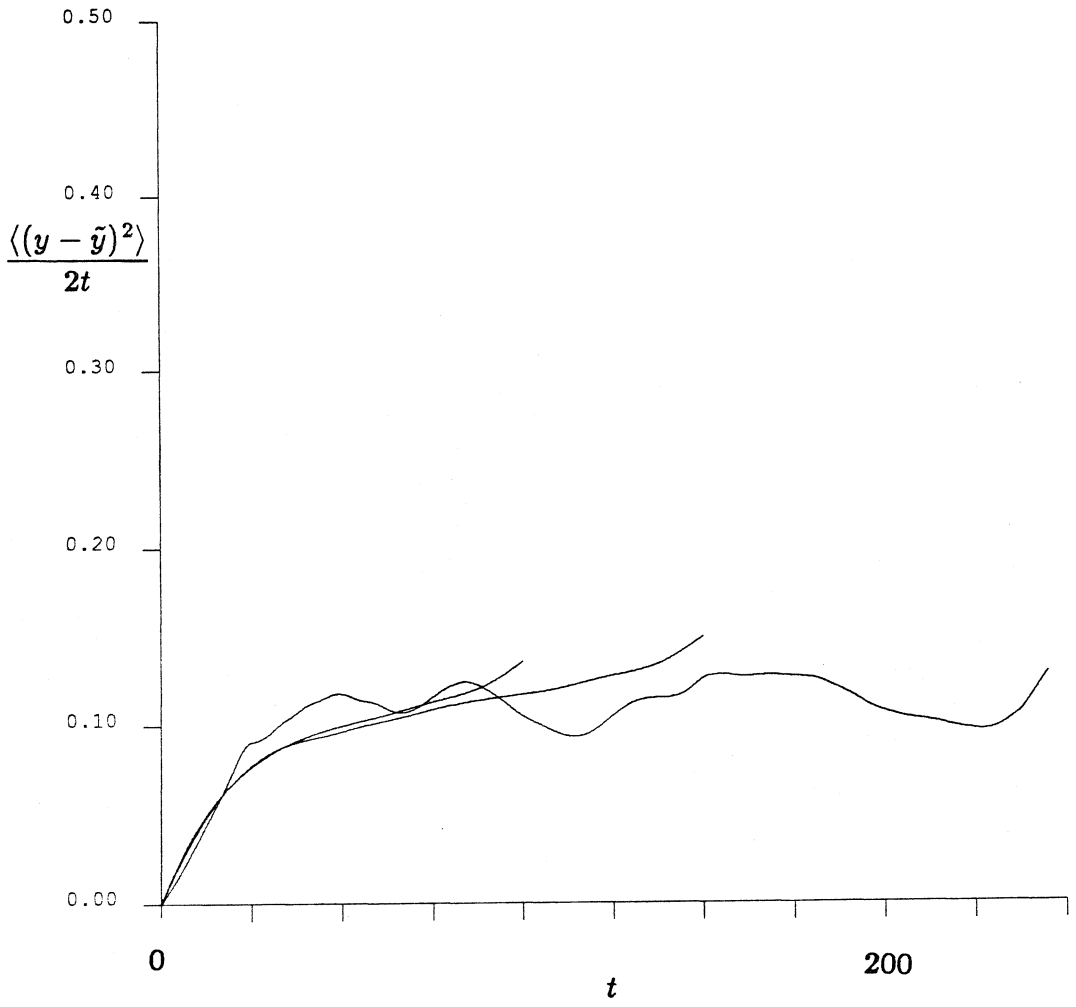

Figure B5.5 A $(D^s_\infty)_{yy}$-defining graph using displacement data from ef2 (t= 250 – 500). The graph interval is 100, 150 and 250 time units. The time between interval initial conditions is 0.01 time unit, except for the 250 time units curve where no averaging over initial conditions is performed.

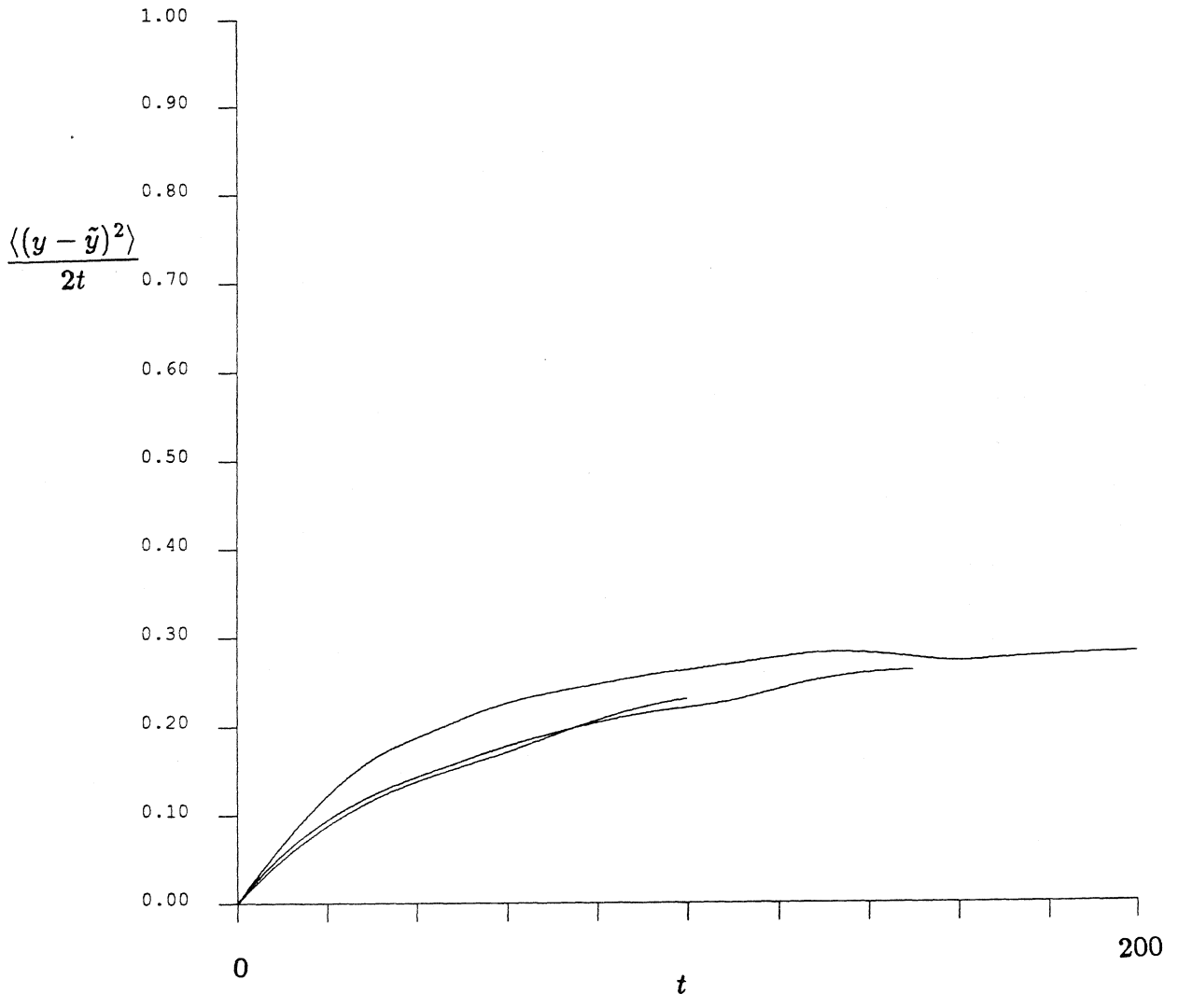

Figure B5.6 A $(D^e_\infty)_{yy}$-defining graph using displacement data from ef3 (t= 500 – 750). The graph interval is 100, 150 and 200 time units. The time between interval initial conditions is 0.01 time unit.

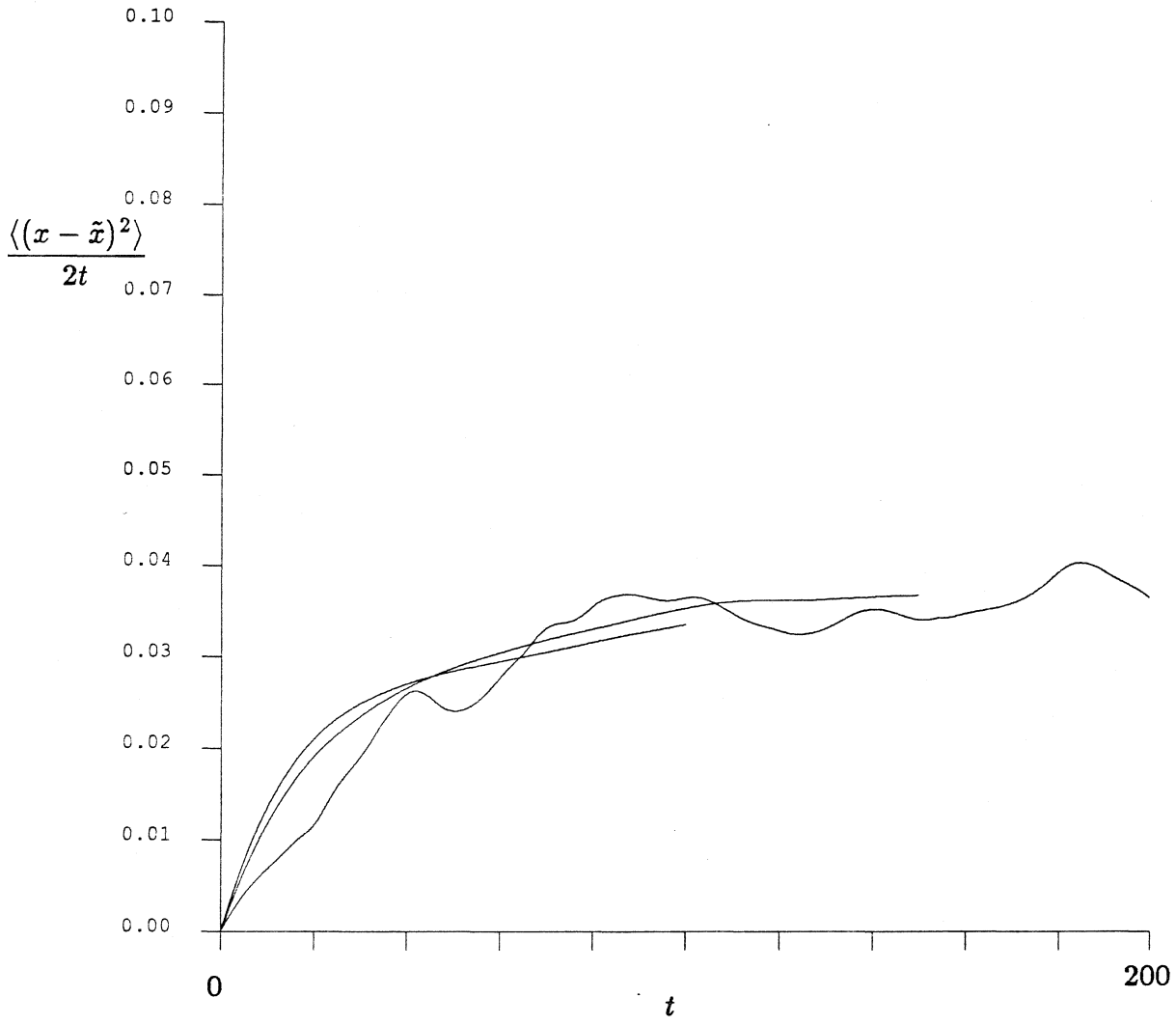

Figure B5.7 A $(D^s_\infty)_{xx}$-defining graph using displacement data from ef1 (t= 50 – 250). The graph interval is 100, 150 and 200 time units. The time between interval initial conditions is 0.01 time unit, except for the 200 time units curve where no averaging over initial conditions is performed.

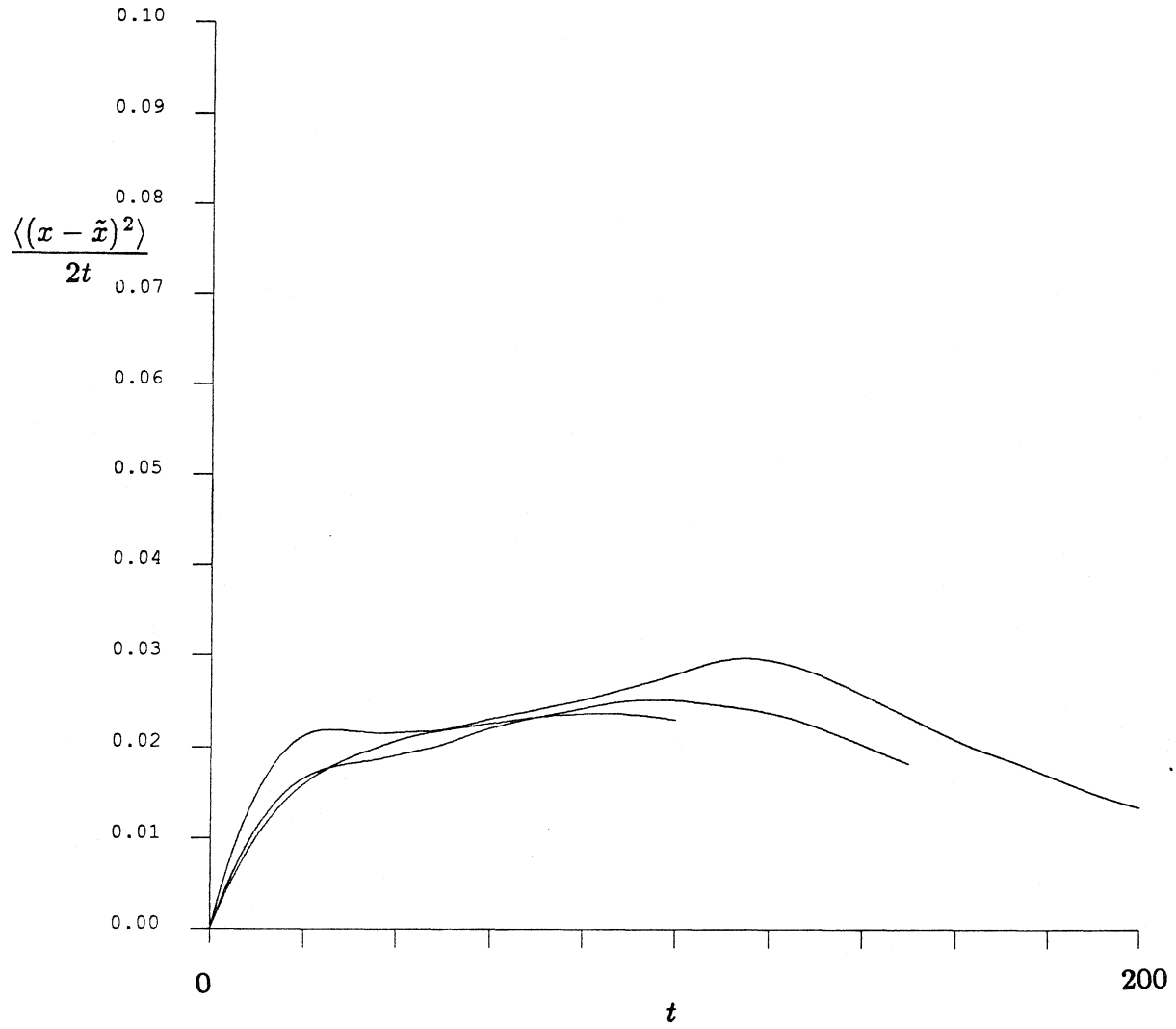

Figure B5.8 A $(D^e_\infty)_{xx}$-defining graph using displacement data from ef3 (t= 500 – 750). The graph interval is 100, 150 and 200 time units. The time between interval initial conditions is 0.01 time unit.

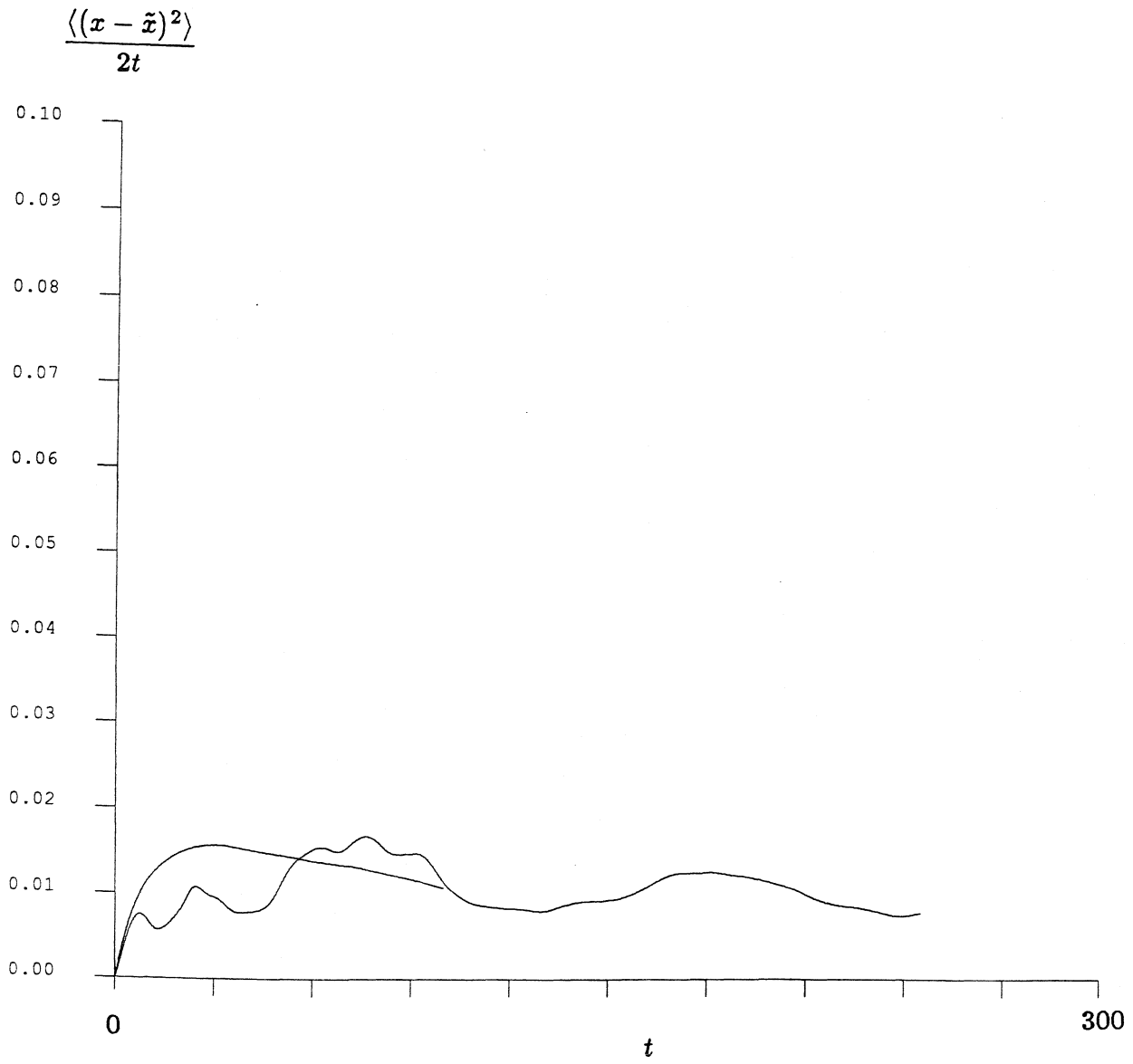

Figure B5.9 A $(D^s_\infty)_{xx}$-defining graph using displacement data from ef4 (t= 750 – 1000). The graph interval is 100 and 250 time units. The time between interval initial conditions is 0.01 time unit, except for the 250 time units curve where no averaging over initial conditions is performed.

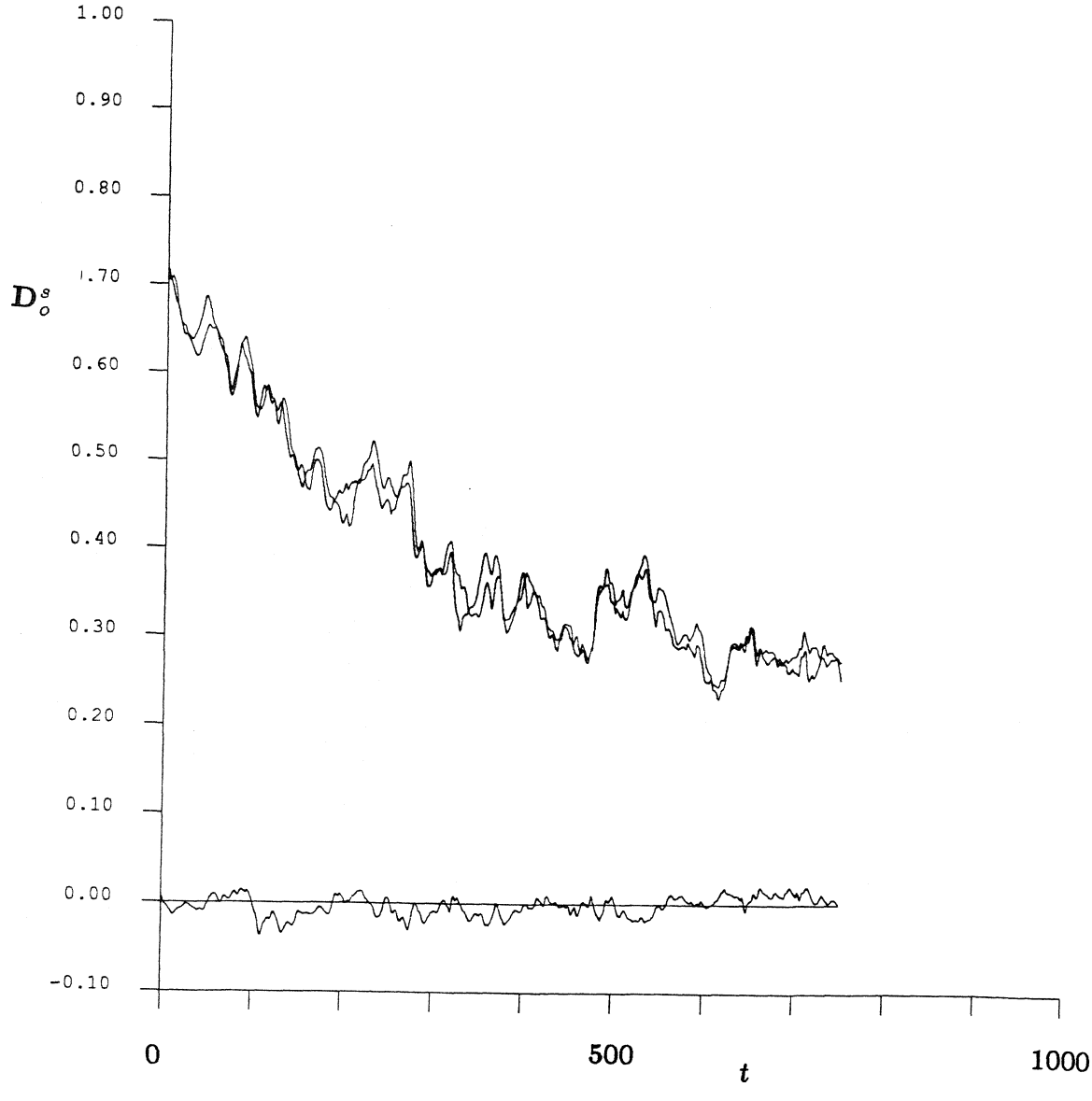

Figure B5.10 The time trace of $\mathbf{D}_o^s$ for the simulations ef1 through ef3. The upper two lines are the xx and yy components of this tensor. Of course, they should be equivalent for an infinite suspension – the slight variation occurs because of the finite number of spheres used in our simulation. The trace that fluctuates about the zero y-axis is the xy component of the short-time, self-diffusion tensor. Again, for an infinite number of spheres, this quantity would be exactly zero.

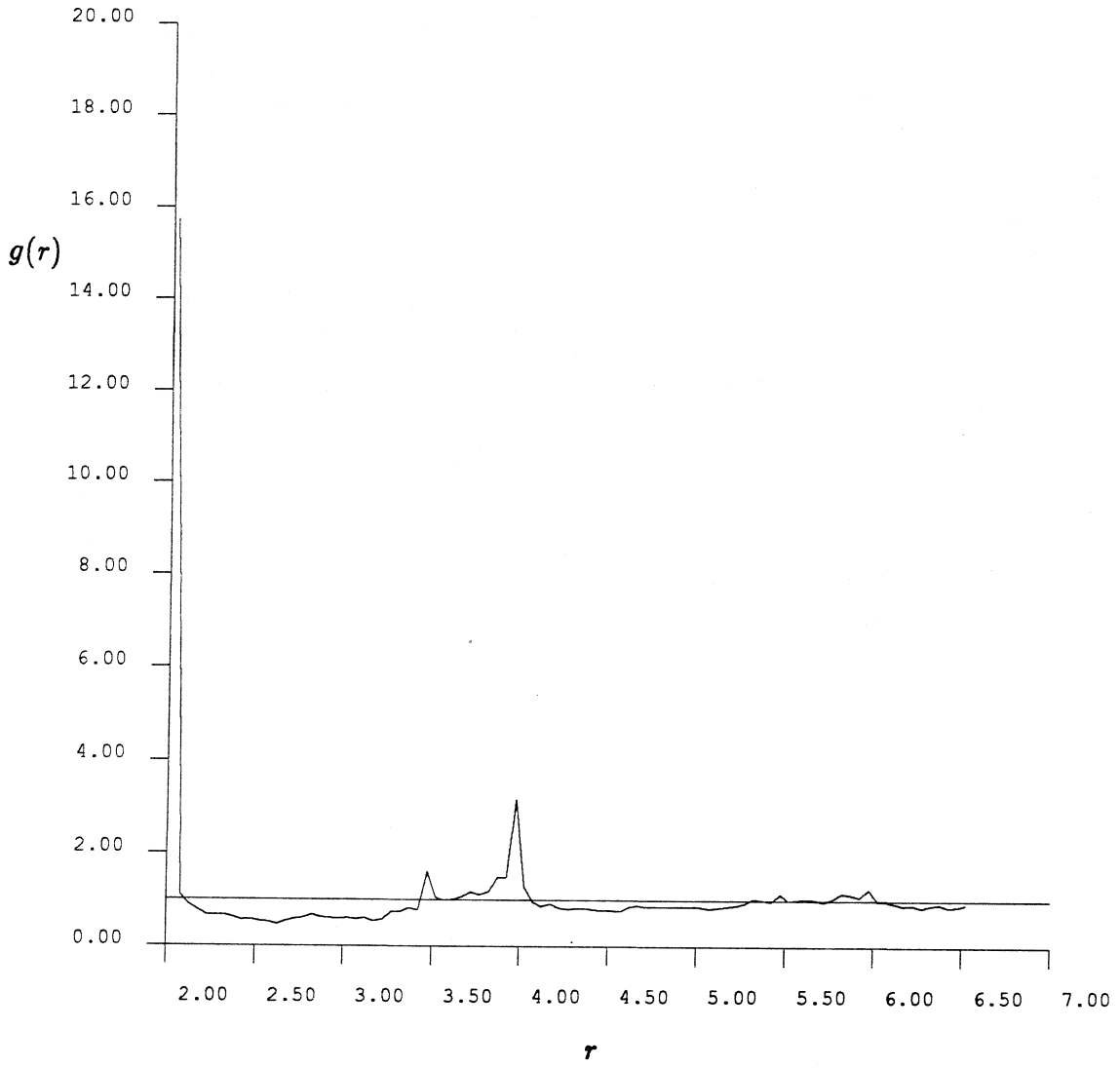

Figure B5.11 The radial pair-distribution function, $g(r)$, for the ef2 run ($t = 250 - 500$).

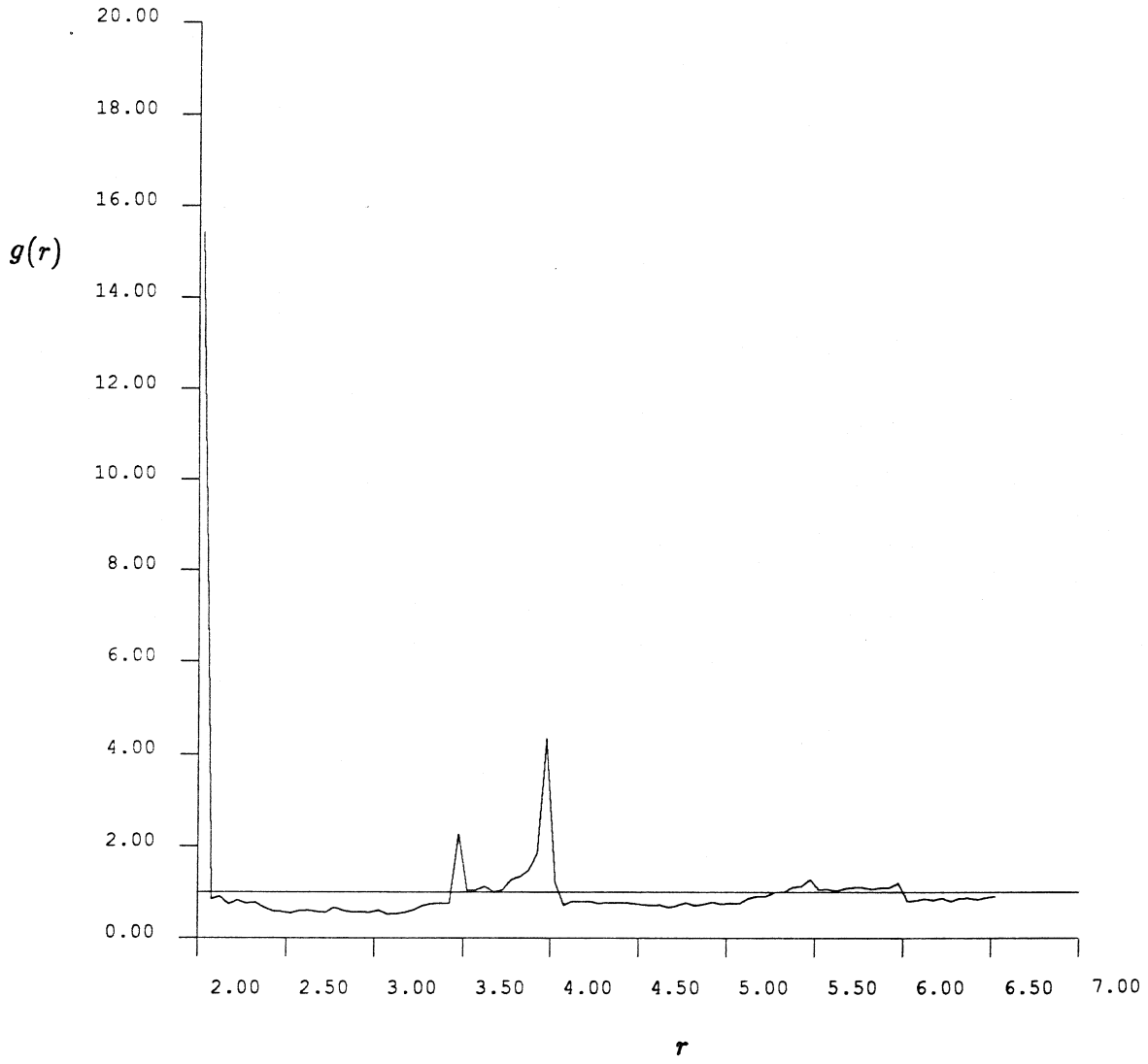

Figure B5.12 The radial pair-distribution function, $g(r)$, for the ef3 run (t = 500 – 750).

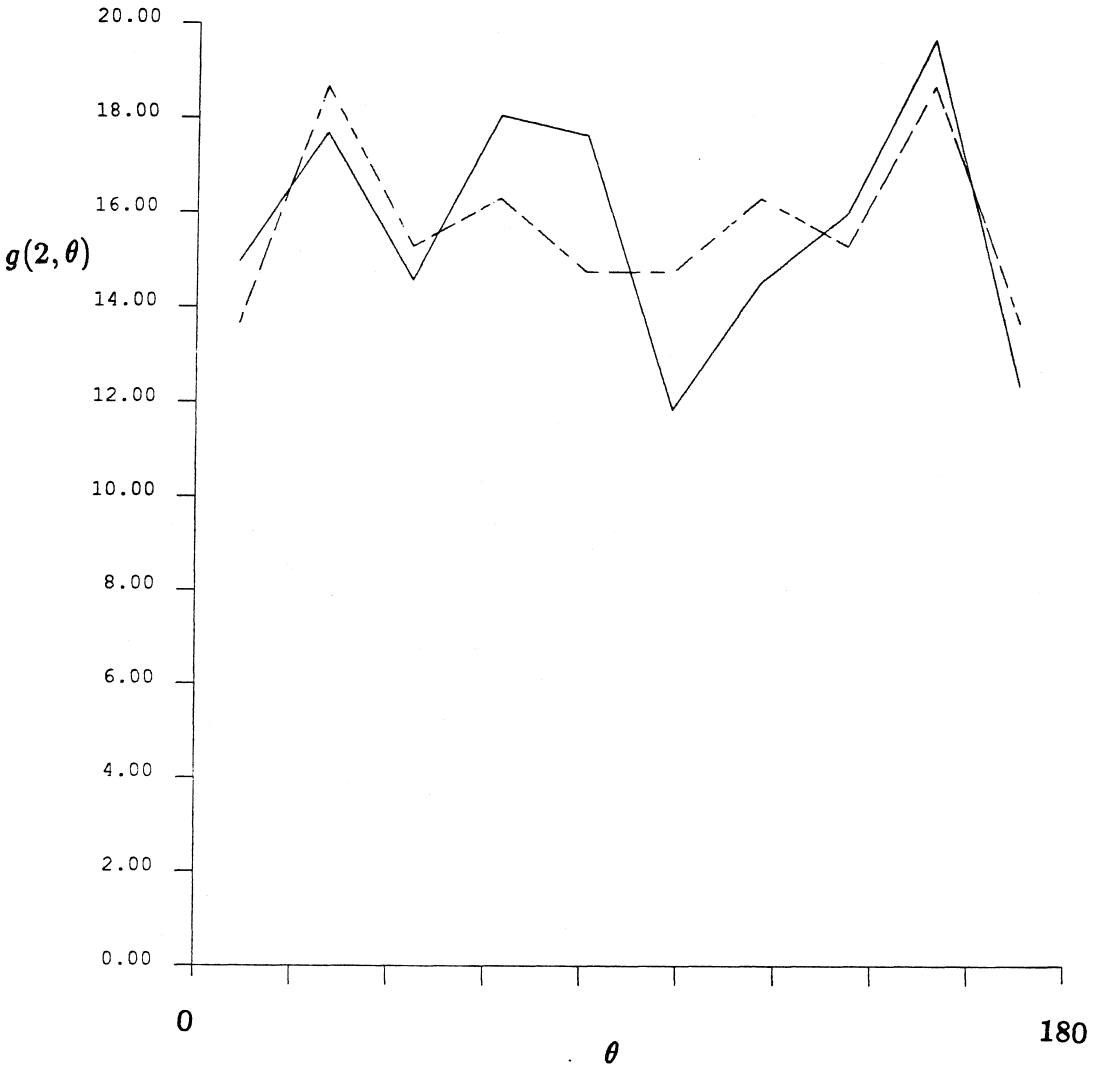

Figure B5.13 The full pair-distribution function for spheres whose surfaces are separated by less than 0.05 radii using data from the ef2 run (t = 250 – 500). The dashed curve represents this function when it is forced to be symmetric about $\theta = 90°$.

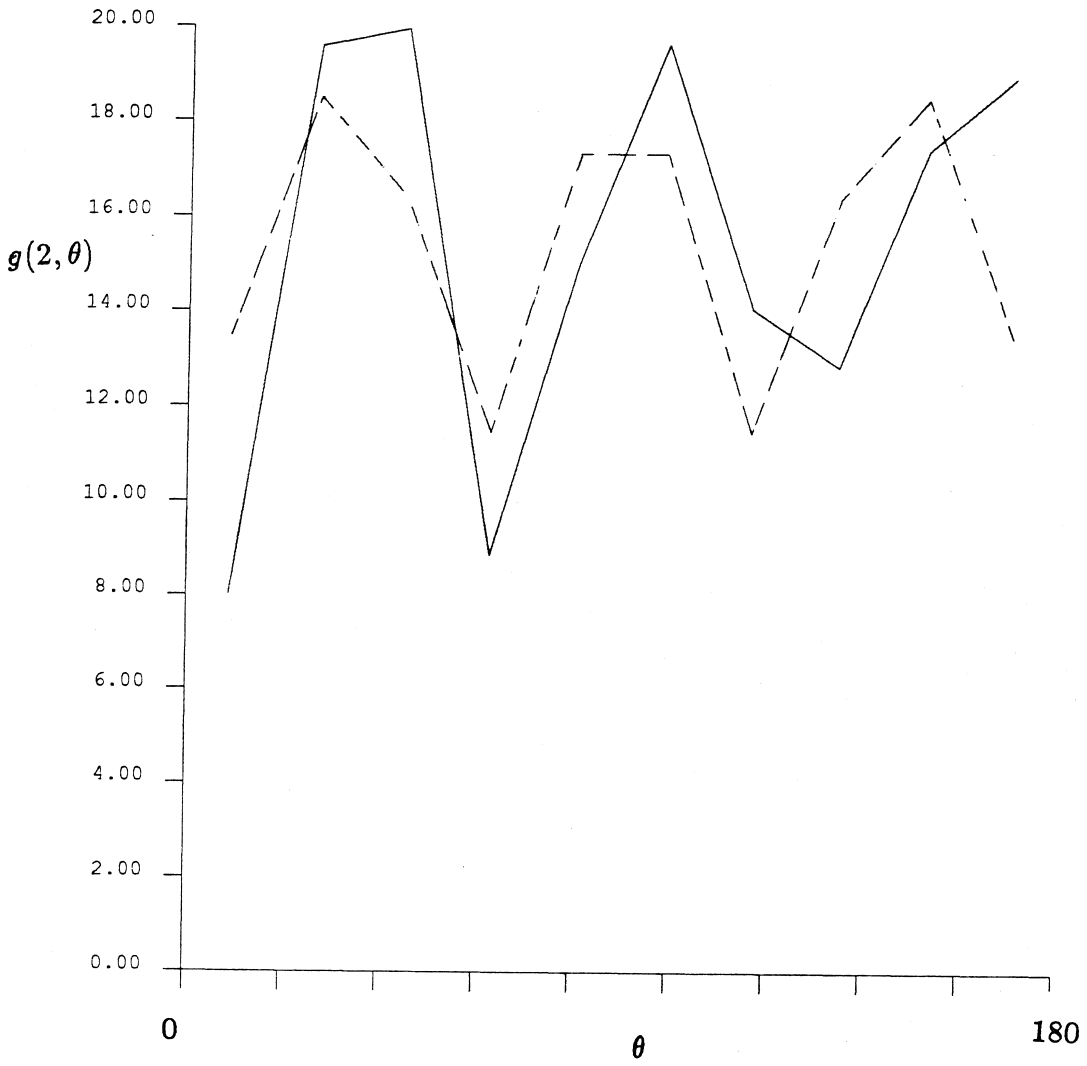

Figure B5.14 The full pair-distribution function for spheres whose surfaces are separated by less than 0.05 radii using data from the ef3 run (t = 500 – 750). The dashed curve represents this function when it is forced to be symmetric about $\theta = 90°$.

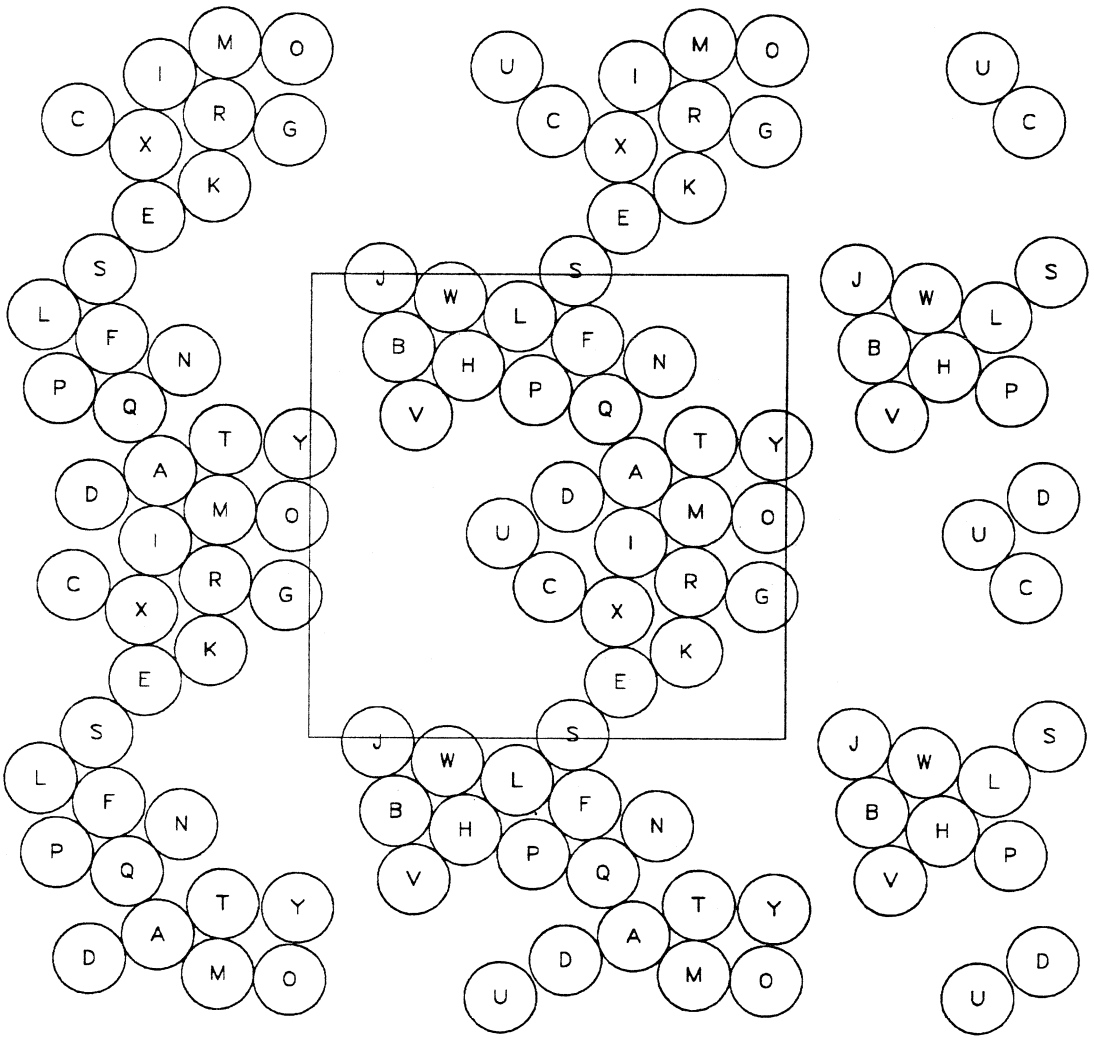

Figure B5.15 A "snapshot" of sphere positions. The square is the periodic cell. These are the sphere positions at $t = 750.05$ time units (ef4).

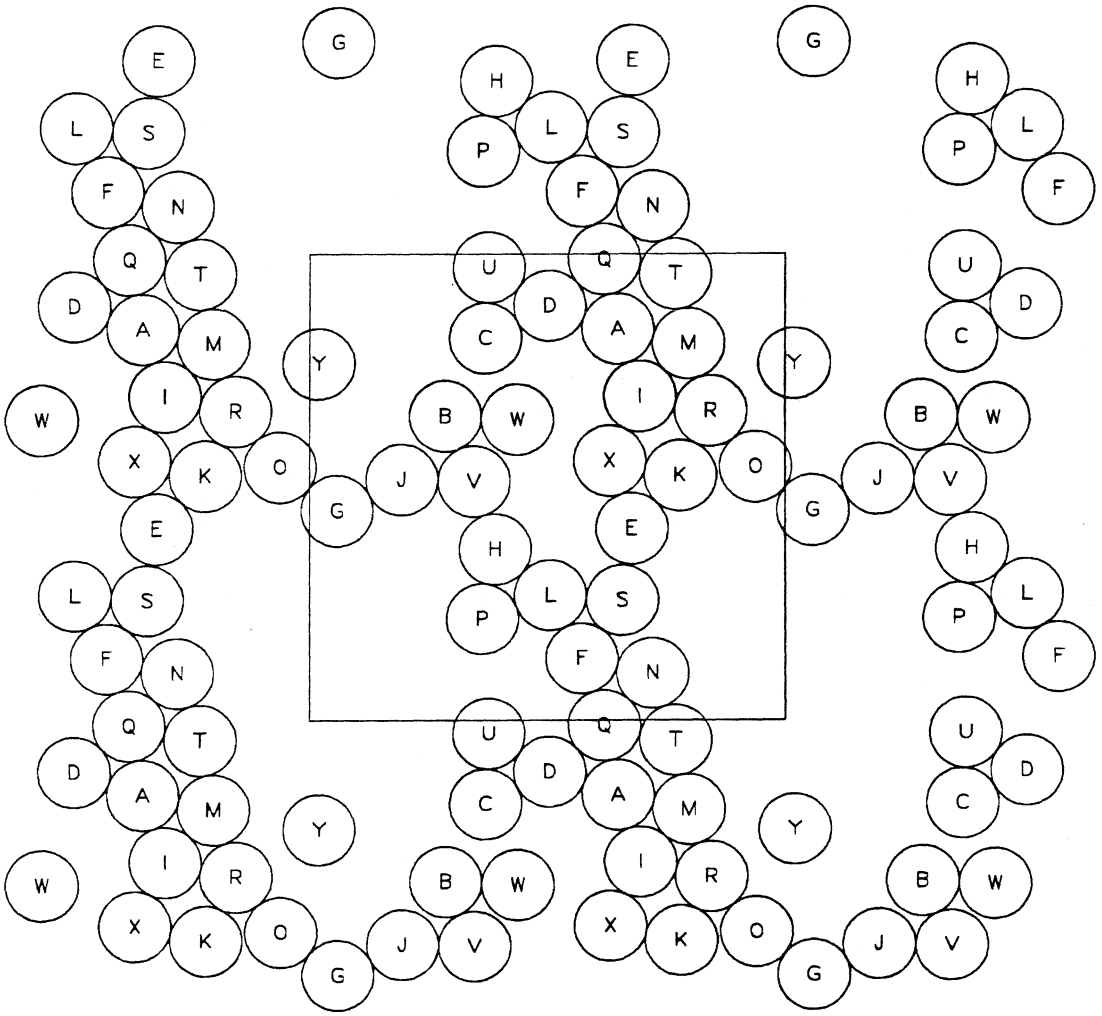

Figure B5.16 A "snapshot" of sphere positions. The square is the periodic cell. These are the sphere positions at $t = 800.00$ time units (ef4).

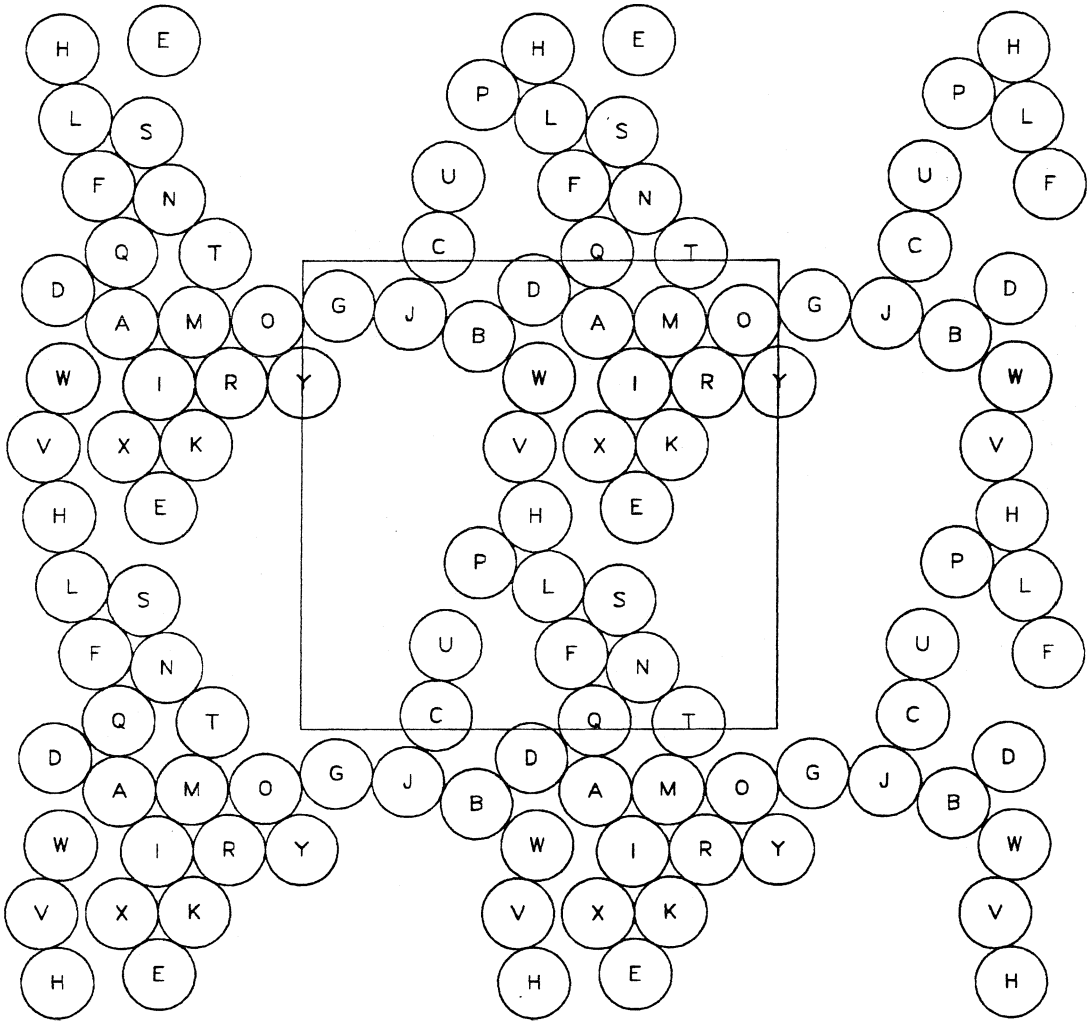

Figure B5.17 A "snapshot" of sphere positions. The square is the periodic cell. These are the sphere positions at $t = 820.00$ time units (ef4).

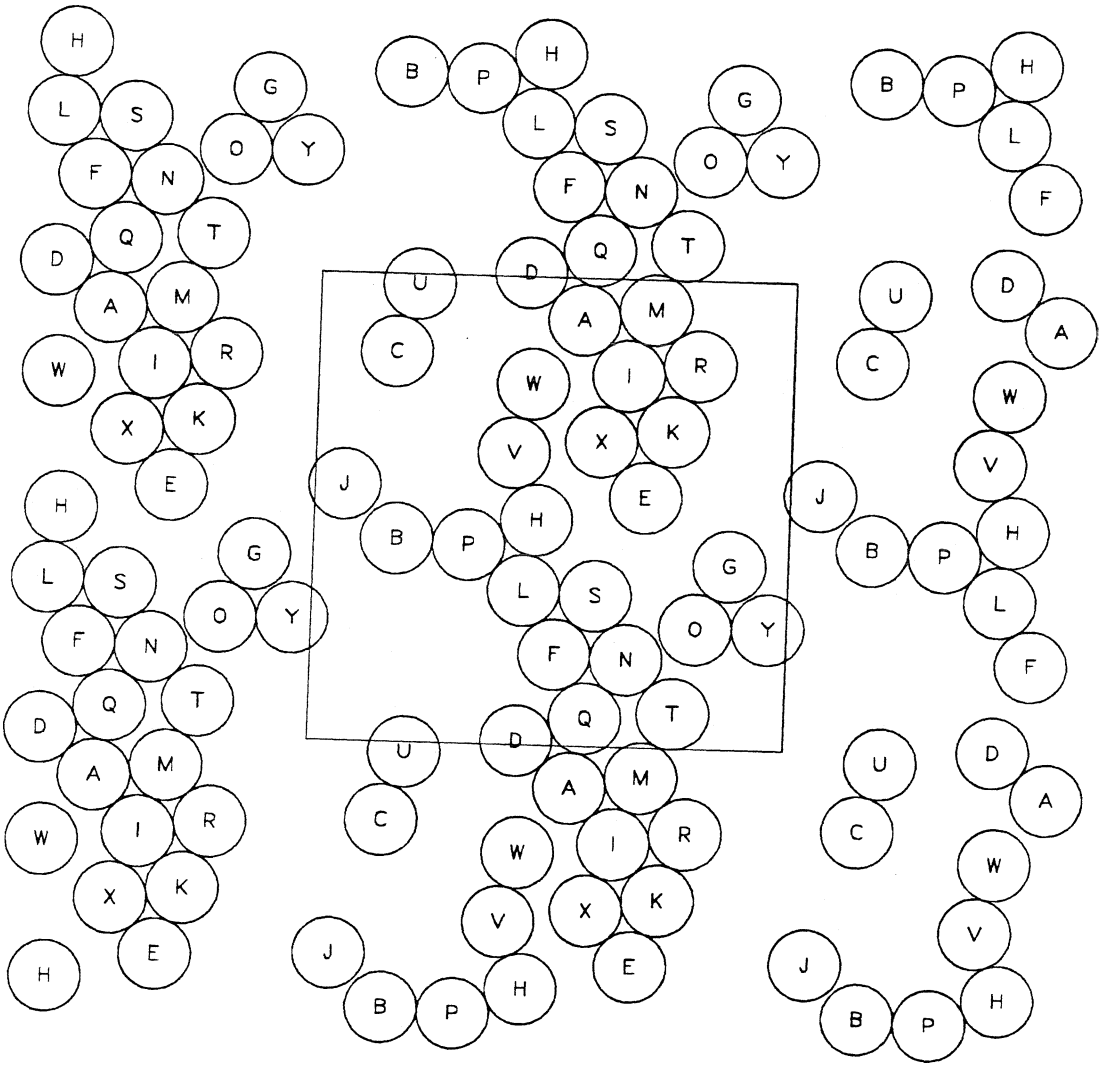

Figure B5.18 A "snapshot" of sphere positions. The square is the periodic cell. These are the sphere positions at $t = 840.00$ time units (ef4).

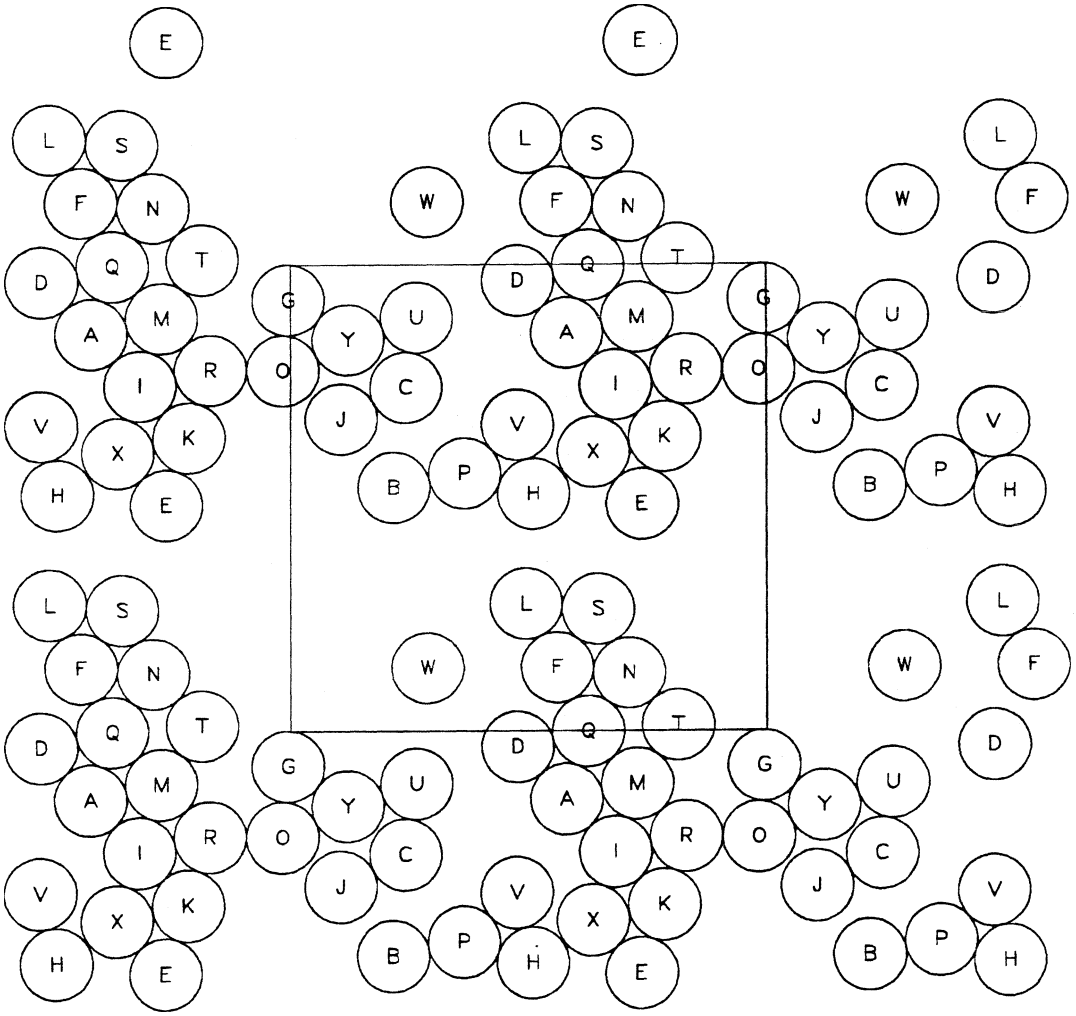

Figure B5.19 A "snapshot" of sphere positions. The square is the periodic cell. These are the sphere positions at $t = 860.00$ time units (ef4).

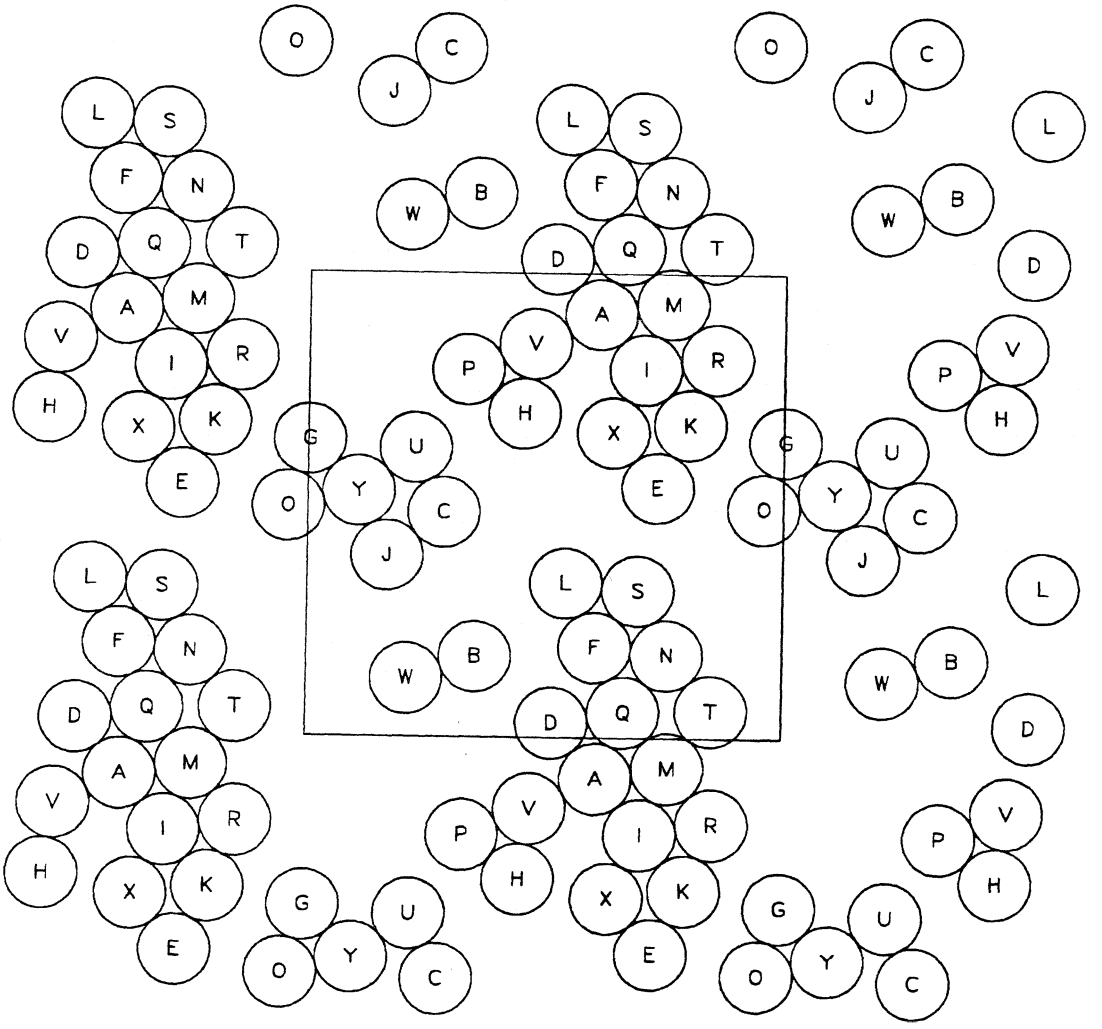

Figure B5.20 A "snapshot" of sphere positions. The square is the periodic cell. These are the sphere positions at $t = 880.00$ time units (ef4).

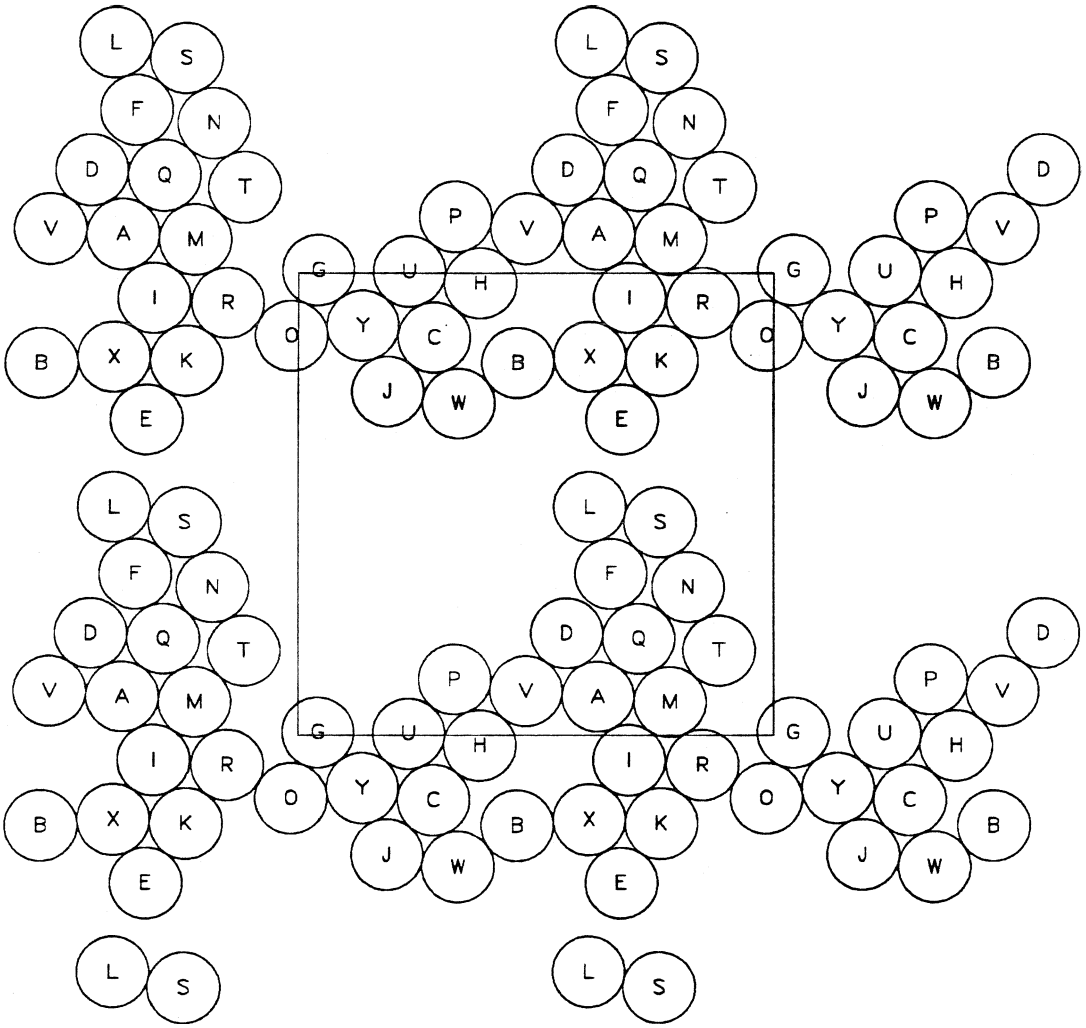

Figure B5.21 A "snapshot" of sphere positions. The square is the periodic cell. These are the sphere positions at $t = 900.00$ time units (ef4).

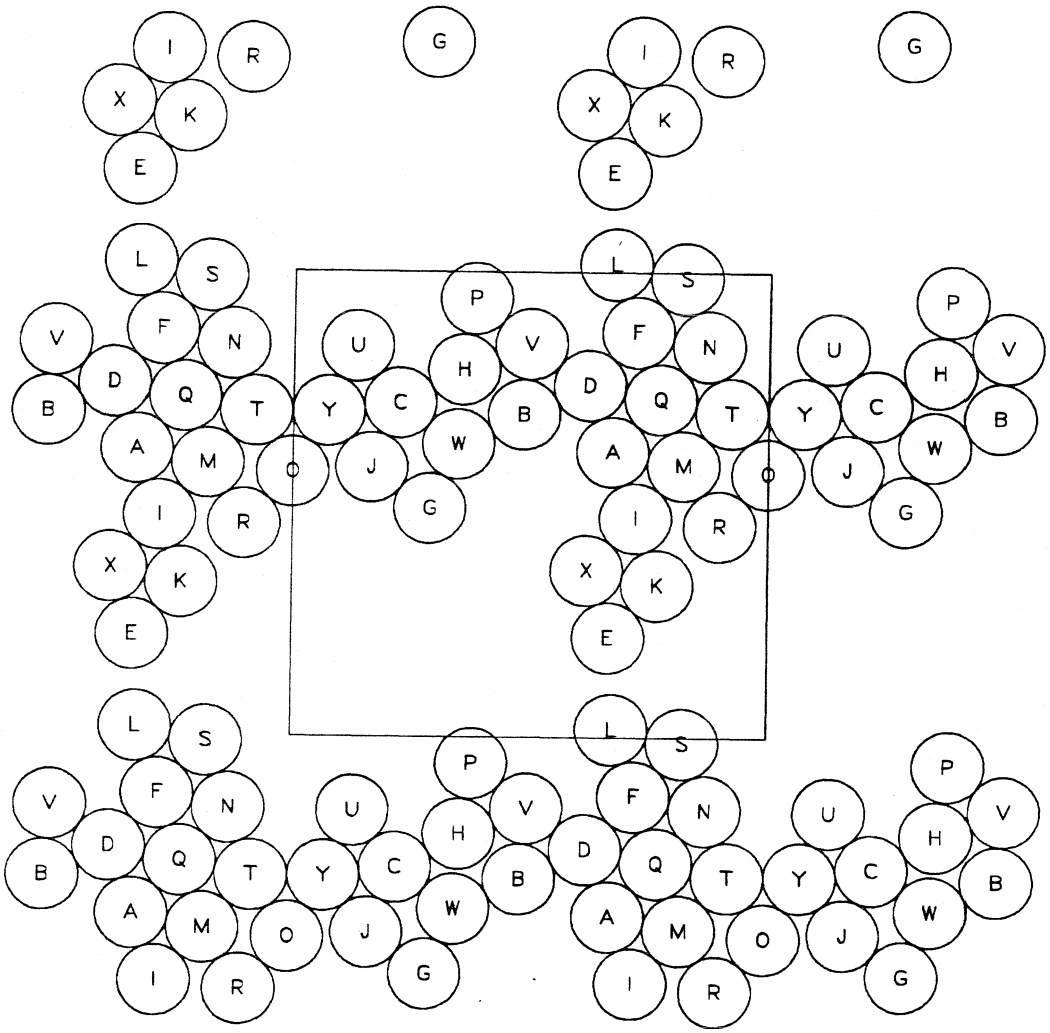

Figure B5.22 A "snapshot" of sphere positions. The square is the periodic cell. These are the sphere positions at $t = 950.00$ time units (ef4).

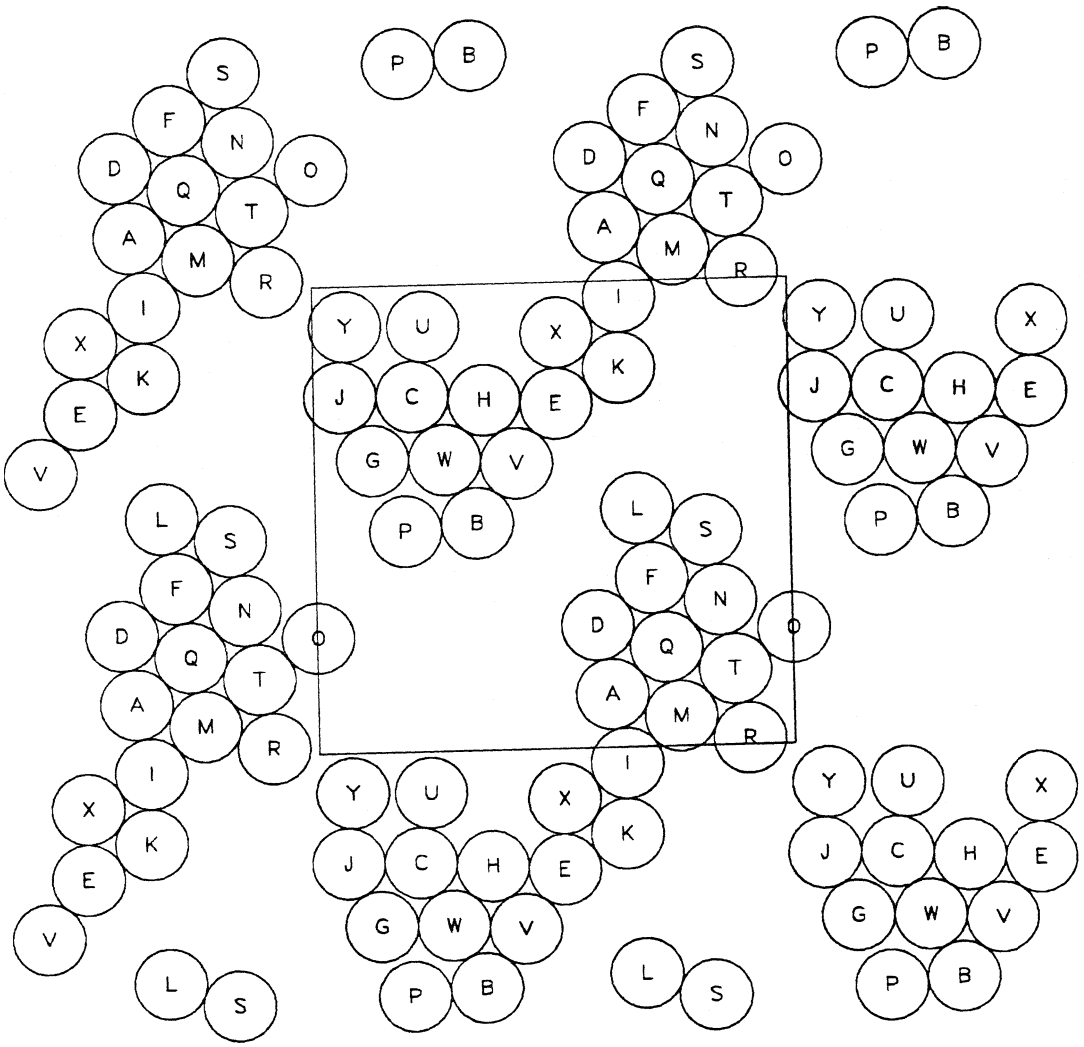

Figure B5.23 A "snapshot" of sphere positions. The square is the periodic cell. These are the sphere positions at $t = 1000.00$ time units (ef4).

Appendix B6: The nfr1 simulation results

This simulation uses a non-Ewald, F method to approximate the hydrodynamic interactions. The final time is 500 time units. The initial configuration is the same as in the FTSn simulations described in Appendix B1. There are 25 spheres within the periodic cell. The areal fraction is 0.453. There are interparticle forces present ($\tau = 10^3$). The time step is 0.001 time unit. The mobility matrix is inverted every 0.1 time unit. Position and velocity data is saved every 0.05 time unit. $\mathbf{D}_o^s$ is evaluated and reported at every time unit.

	nfr1
T	0-500
Cray/Sun	Cray 0.70
CPU(min)	69
v_y	-6.38492
v_x	-0.00388
v_y variance	0.01990
v_x variance	0.00781
v_{xy} variance	-0.00082
$(D_\infty^s)_{yy}$	0.17
$(D_\infty^s)_{xx}$	0.065
$(D_o^s)_{yy}$	0.694
$(D_o^s)_{xx}$	0.690
$(D_o^s)_{xy}$	-0.0045
$g(2)$	11.5
$g(3.5)$	0.92
$g(4)$	1.44

Table B6.1

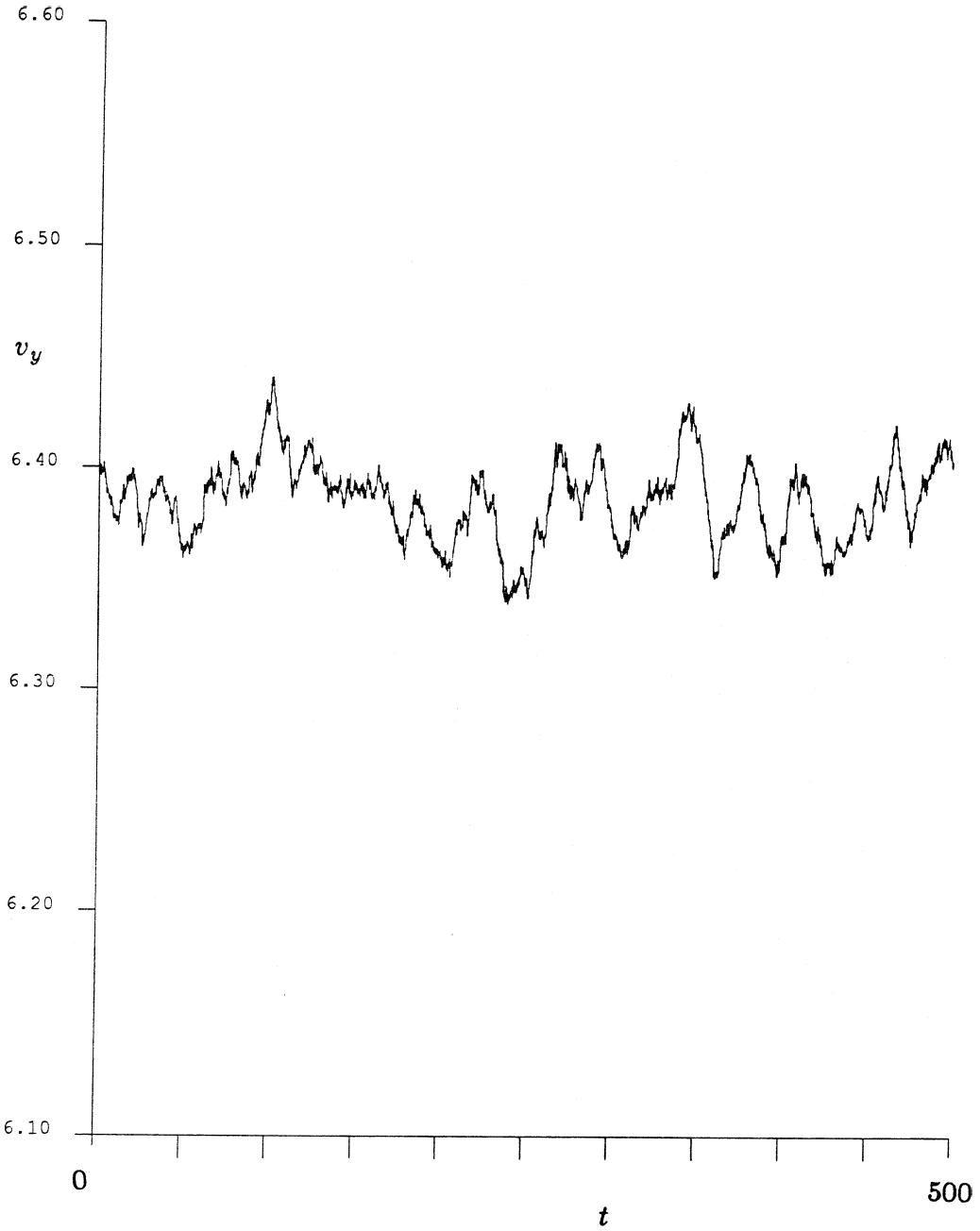

Figure B6.1 The time trace of v_y for the simulation nfr1.

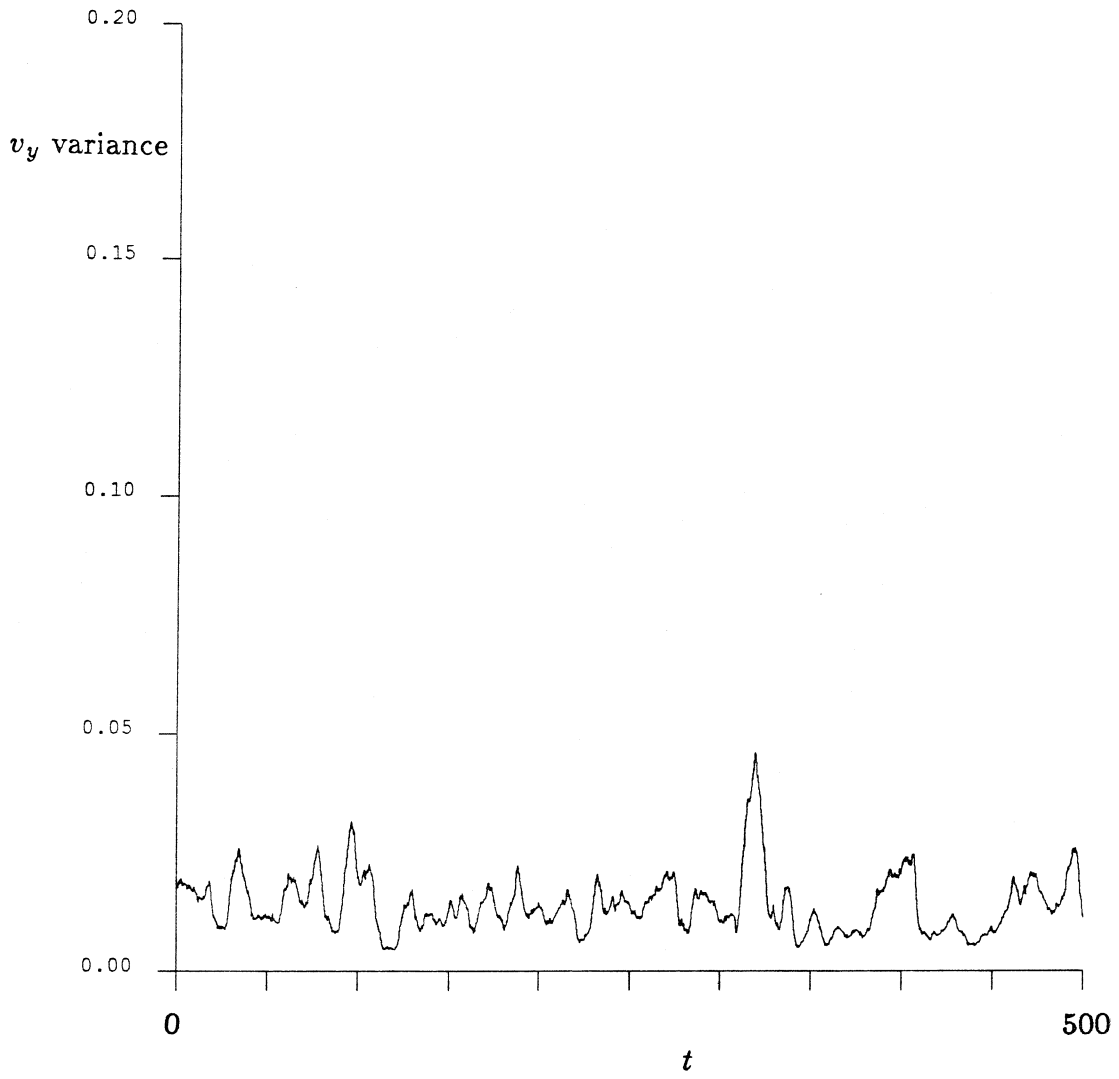

Figure B6.2 The time trace of the v_y variance for the simulation nfr1.

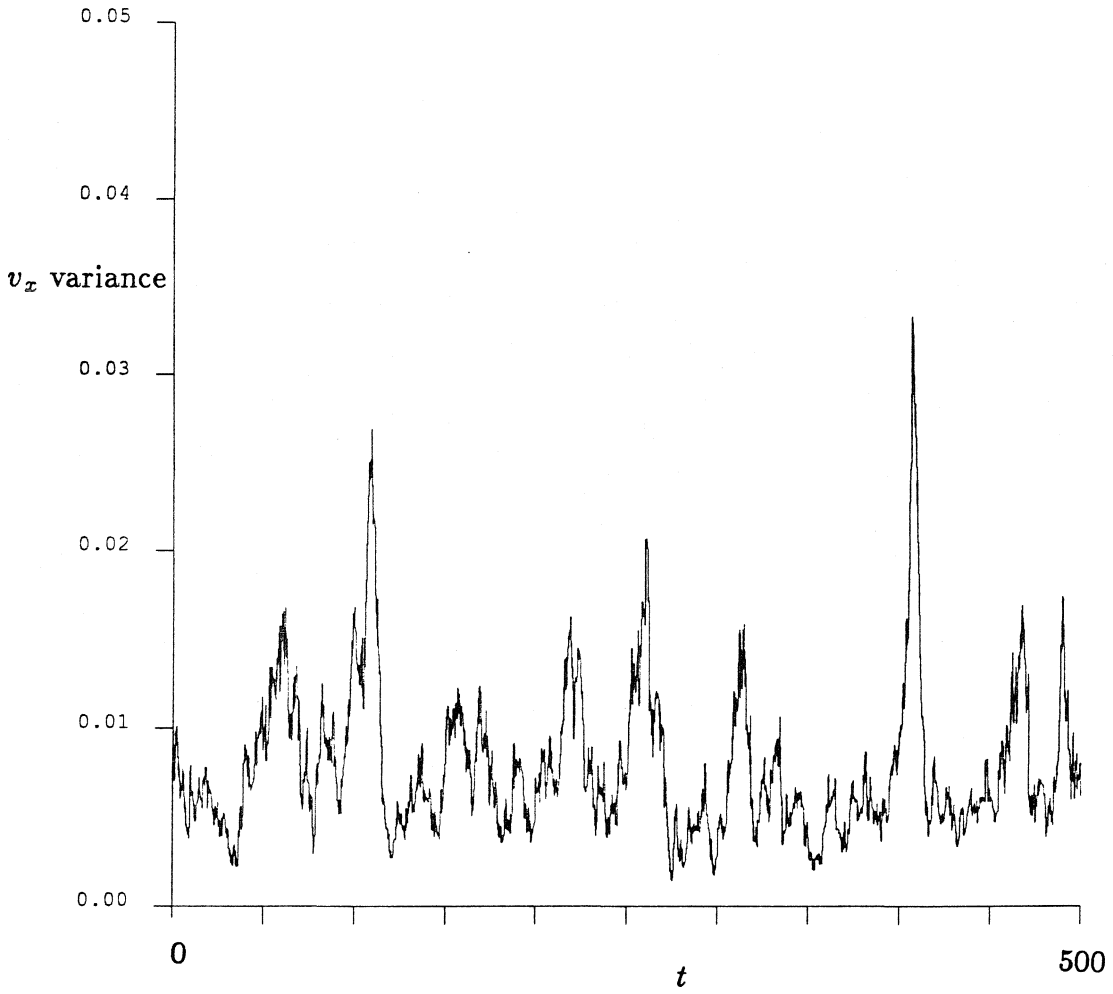

Figure B6.3 The time trace of the v_x variance for the simulation nfr1.

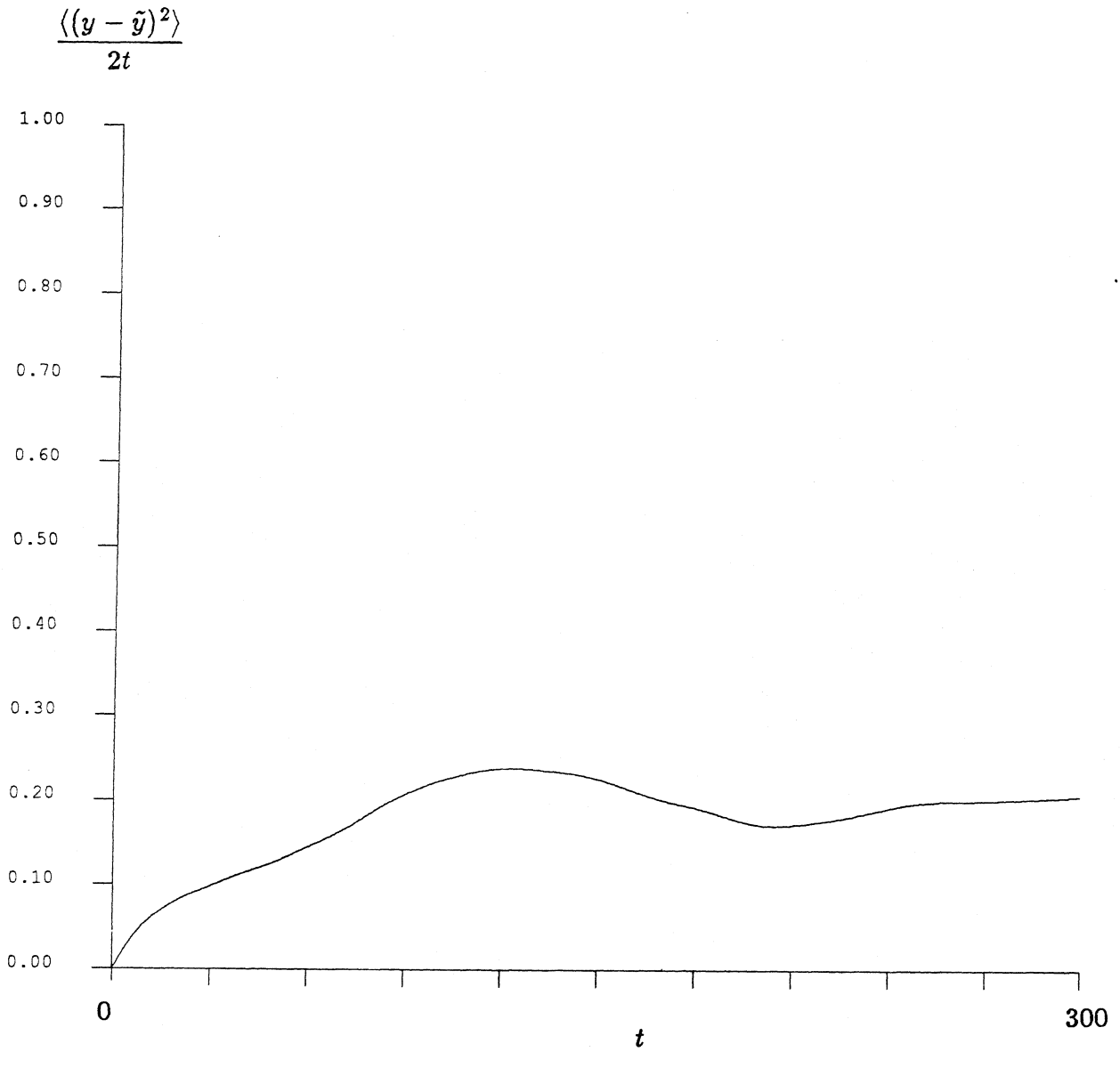

Figure B6.4 A $(D^s_\infty)_{yy}$-defining graph using displacement data from nfr1 (t= 150 – 500). The graph interval is 300 time units, and the time between interval initial conditions is 0.01 time unit.

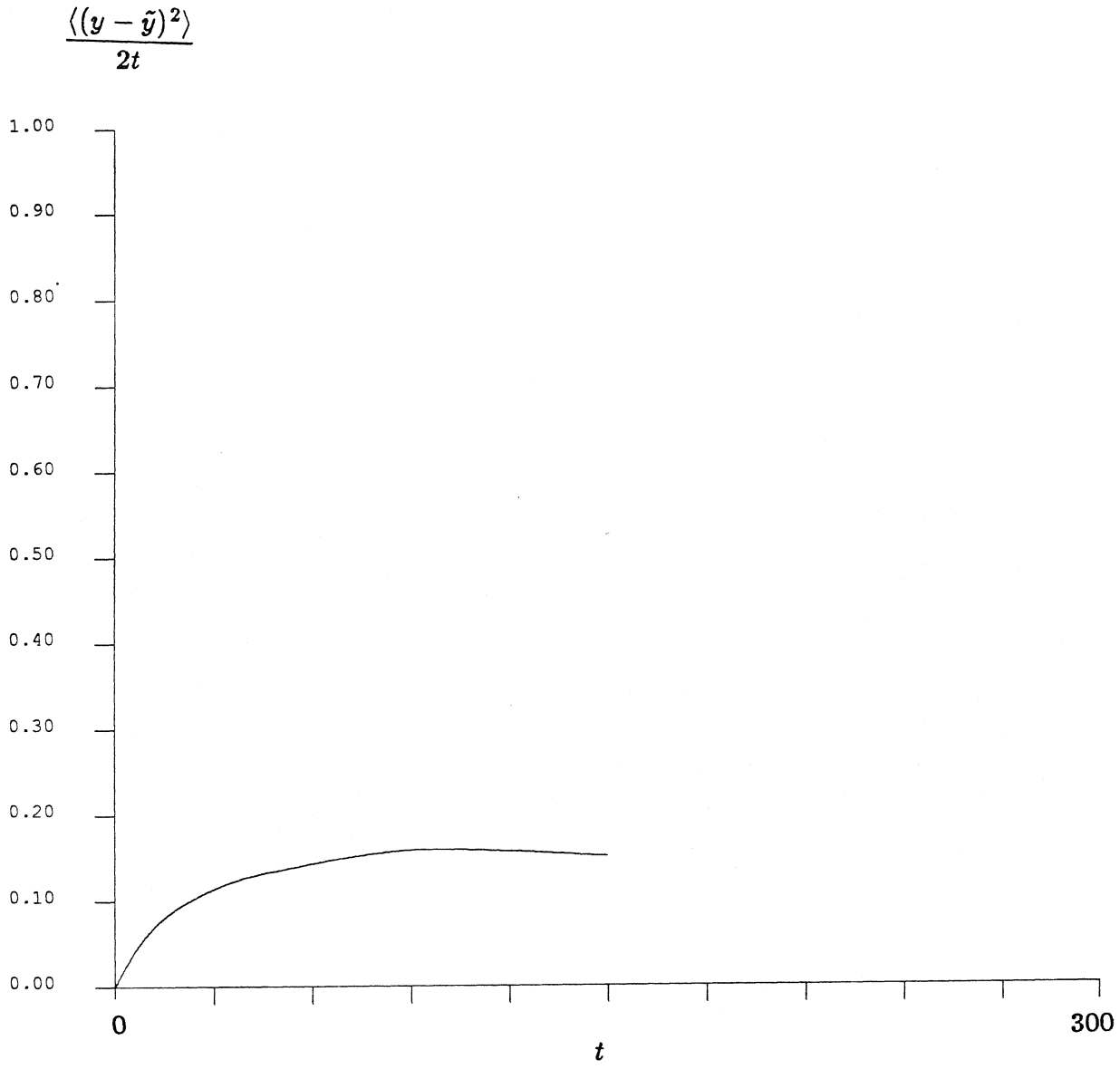

Figure B6.5 A $(D^s_\infty)_{yy}$-defining graph using displacement data from nfr1 (t= 150 – 500). The graph interval is 150 time units, and the time between interval initial conditions is 0.01 time unit.

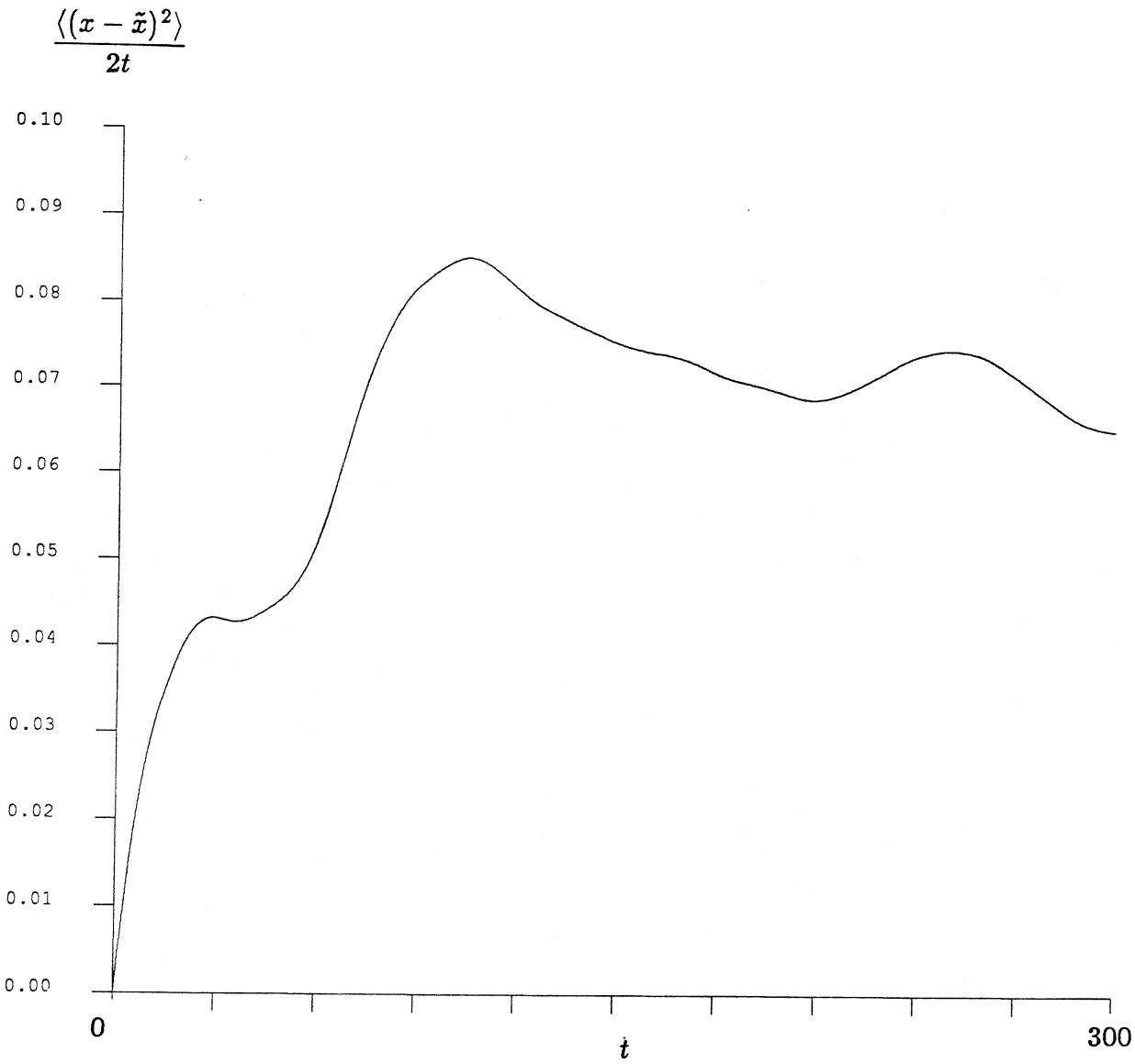

Figure B6.6 A $(D^s_\infty)_{xx}$-defining graph using displacement data from nfr1 (t= 150 – 500). The graph interval is 300 time units, and the time between interval initial conditions is 0.01 time unit.

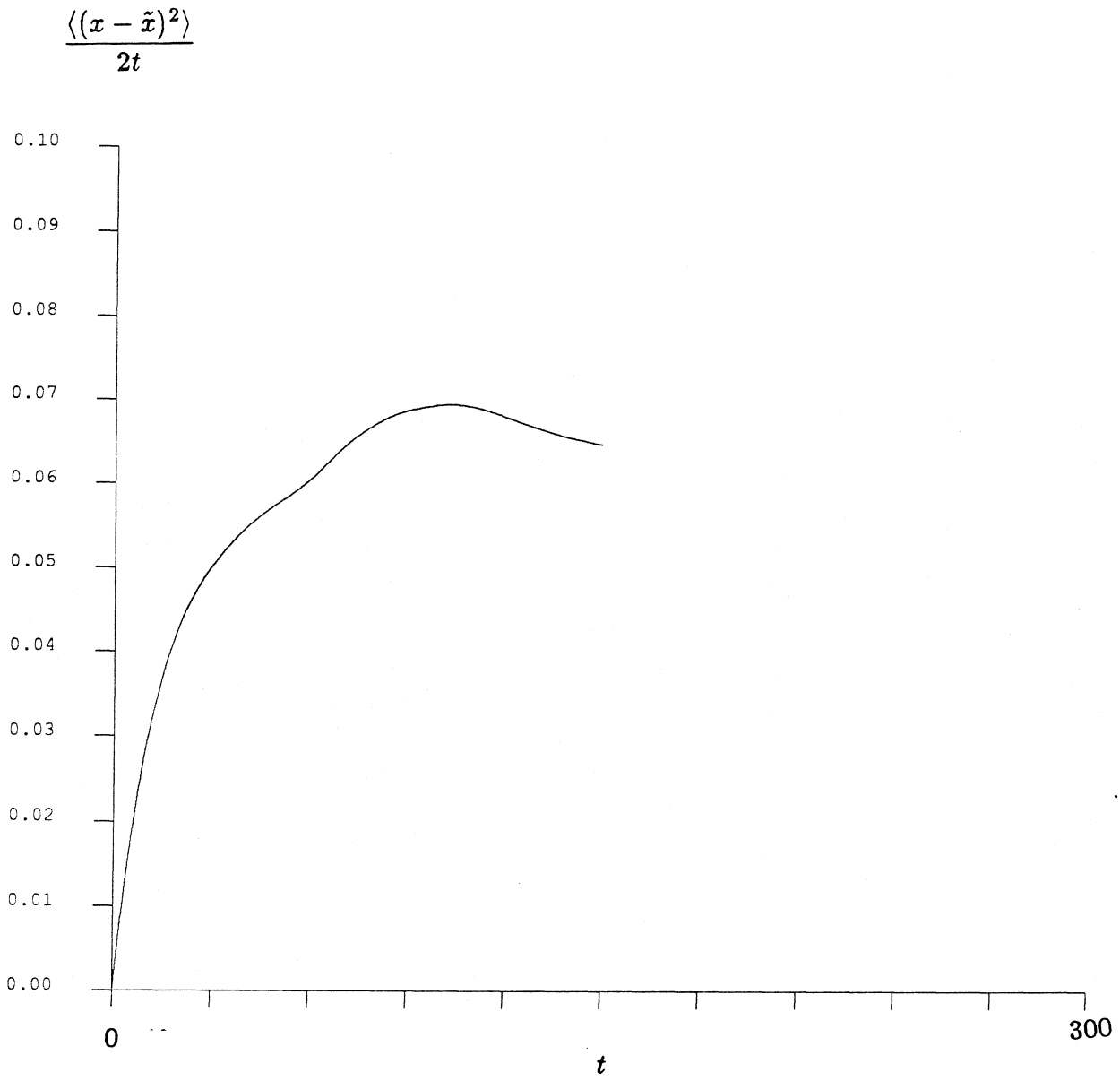

Figure B6.7 A $(D^s_\infty)_{xx}$-defining graph using displacement data from nfr1 (t= 150 – 500). The graph interval is 150 time units, and the time between interval initial conditions is 0.01 time unit.

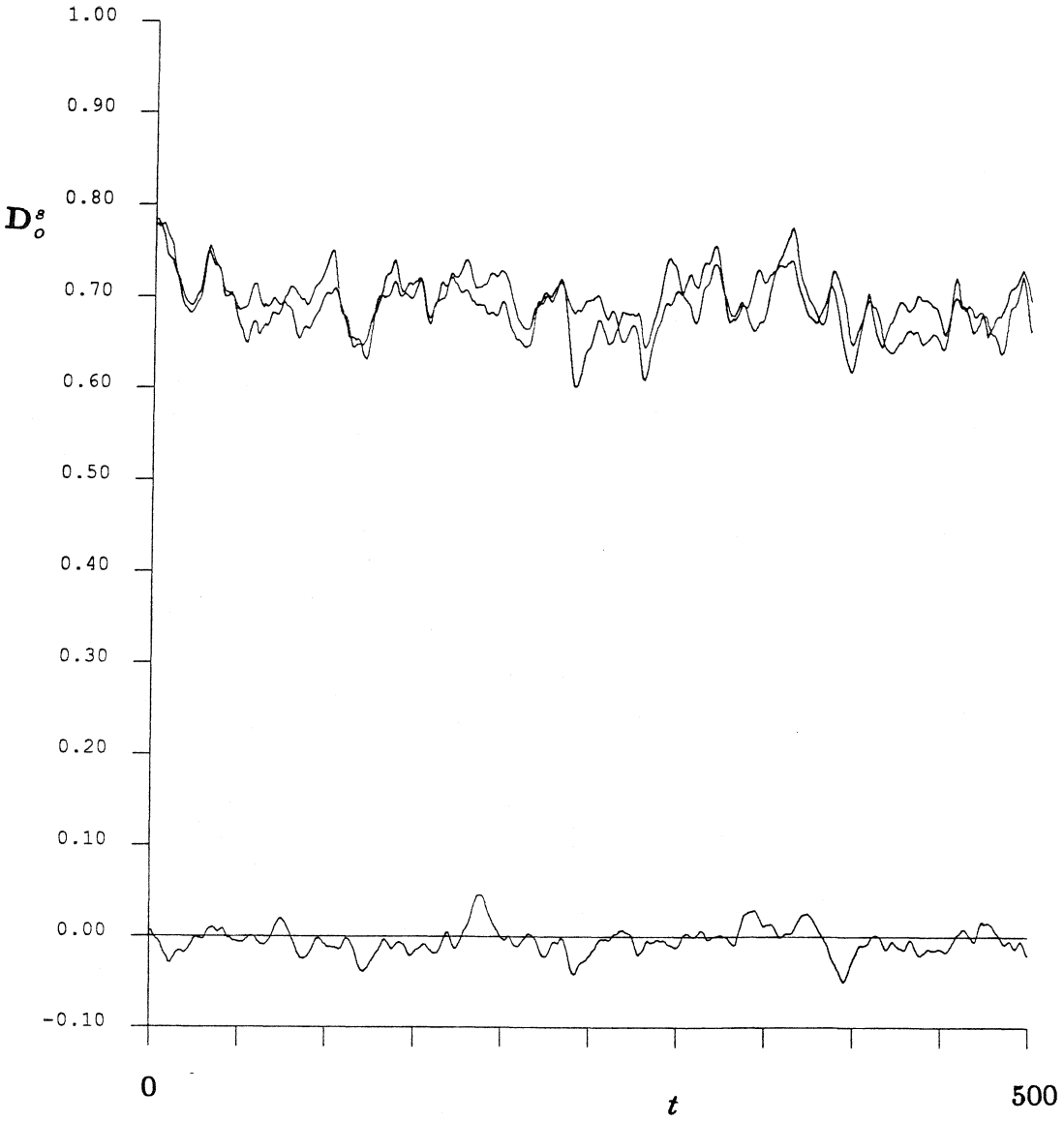

Figure B6.8 The time trace of $\mathbf{D}_o^s$ for the simulation nfr1. The upper two lines are the xx and yy components of this tensor. Of course, they should be equivalent for an infinite suspension – the slight variation occurs because of the finite number of spheres used in our simulation. The trace that fluctuates about the zero y-axis is the xy component of the short-time, self-diffusion tensor. Again, for an infinite number of spheres, this quantity would be exactly zero.

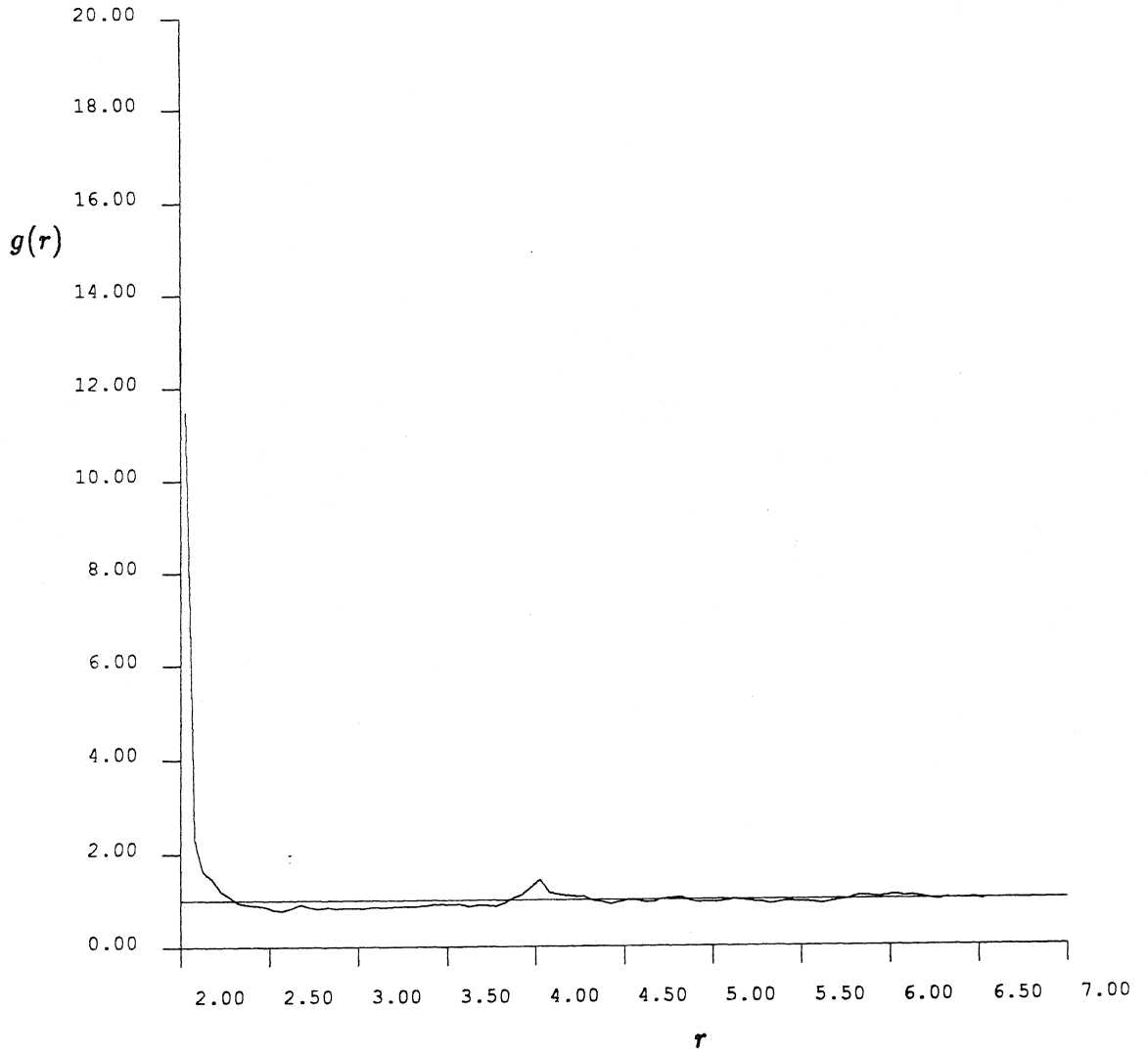

Figure B6.9 The radial pair-distribution function, $g(r)$, for the nfr1 run ($t = 150 - 500$). Note the absence of the $g(3.5)$ peak present in all the preceeding simulation results. This indicates an absence of hexagonal packing.

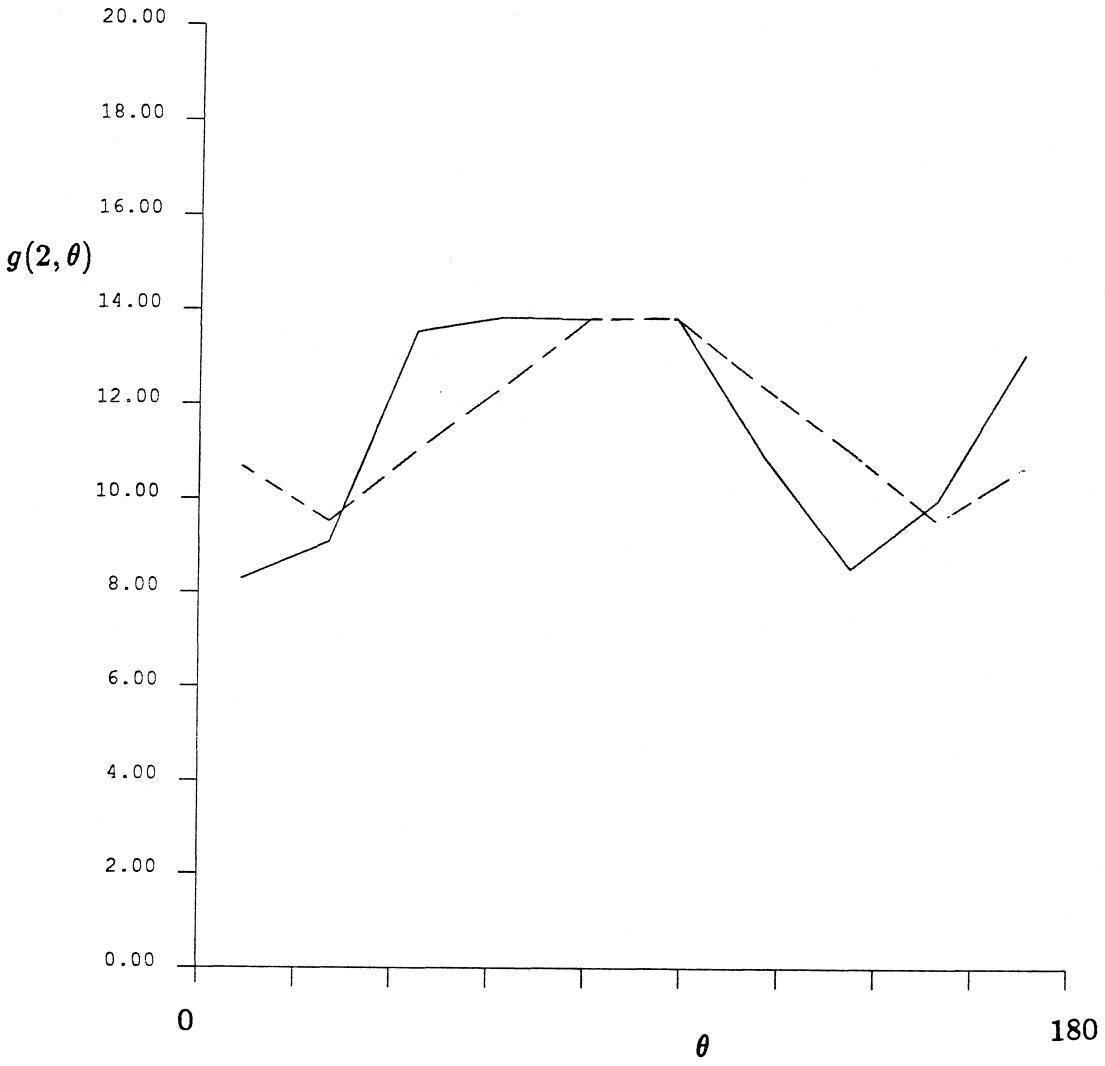

Figure B6.10 The full pair-distribution function for spheres whose surfaces are separated by less than 0.05 radii using data from the nfr1 run (t = 150 – 500). The dashed curve represents this function when it is forced to be symmetric about $\theta = 90°$.

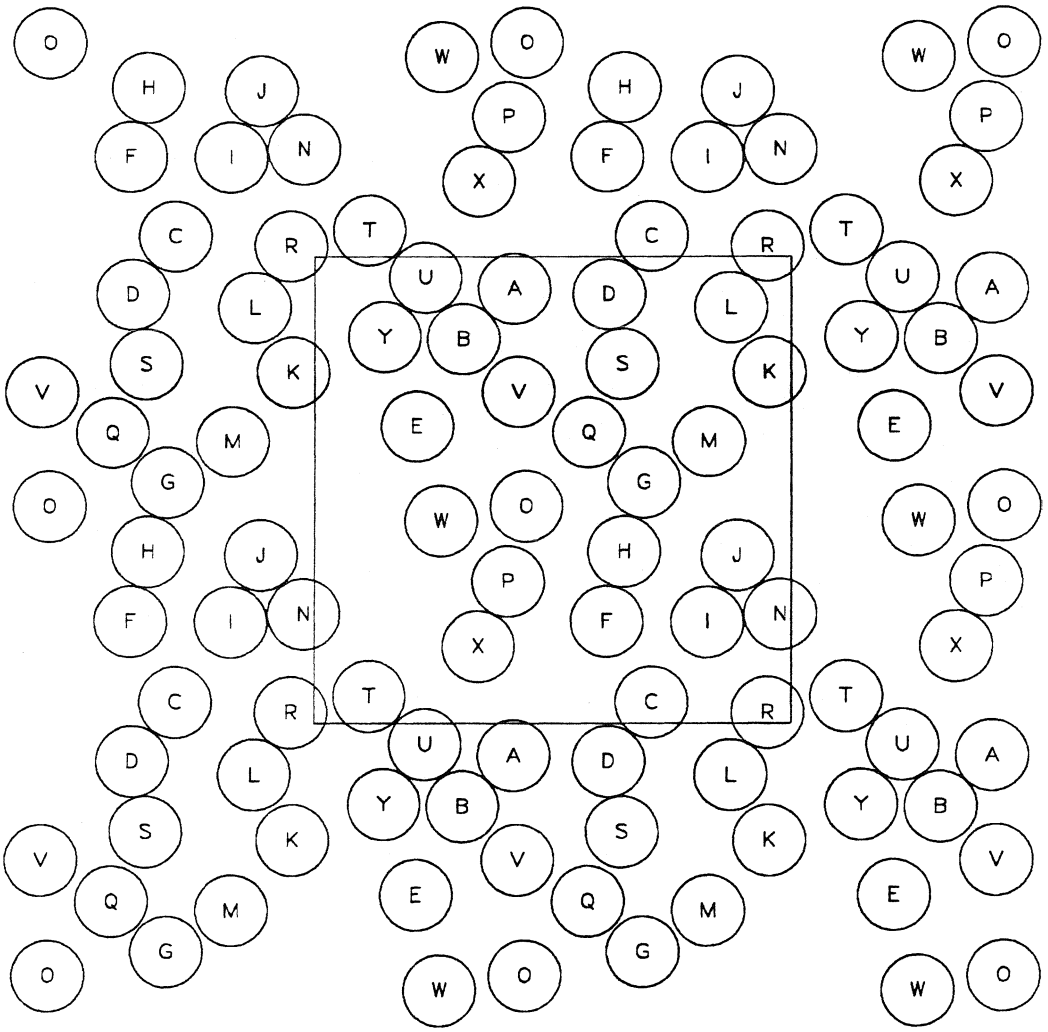

Figure B6.11 A "snapshot" of sphere positions. The square is the periodic cell. These are the sphere positions at $t = 100.00$ time units (nfr1). Notice the absence of hexagonal packing in this and subsequent "snapshots".

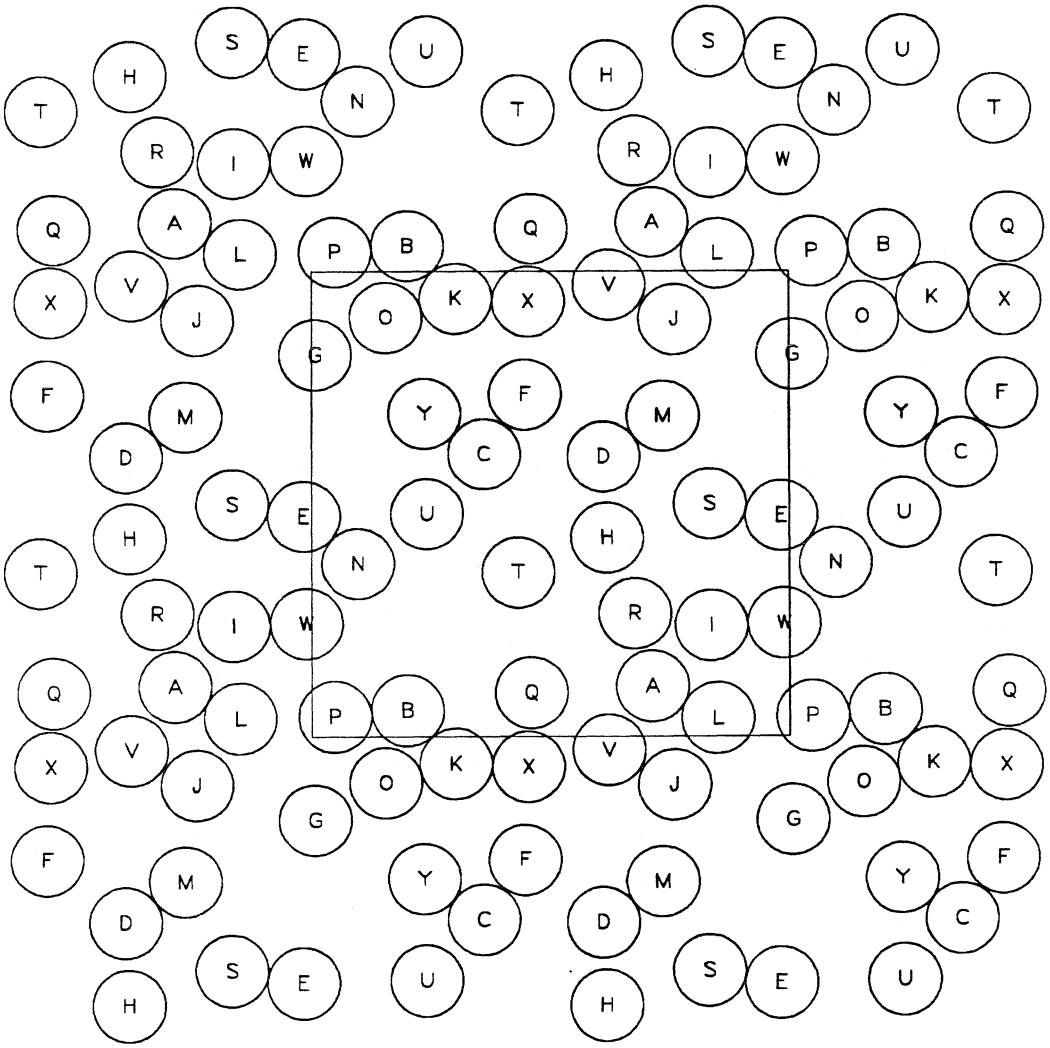

Figure B6.12 A "snapshot" of sphere positions. The square is the periodic cell. These are the sphere positions at $t = 200.00$ time units (nfr1).

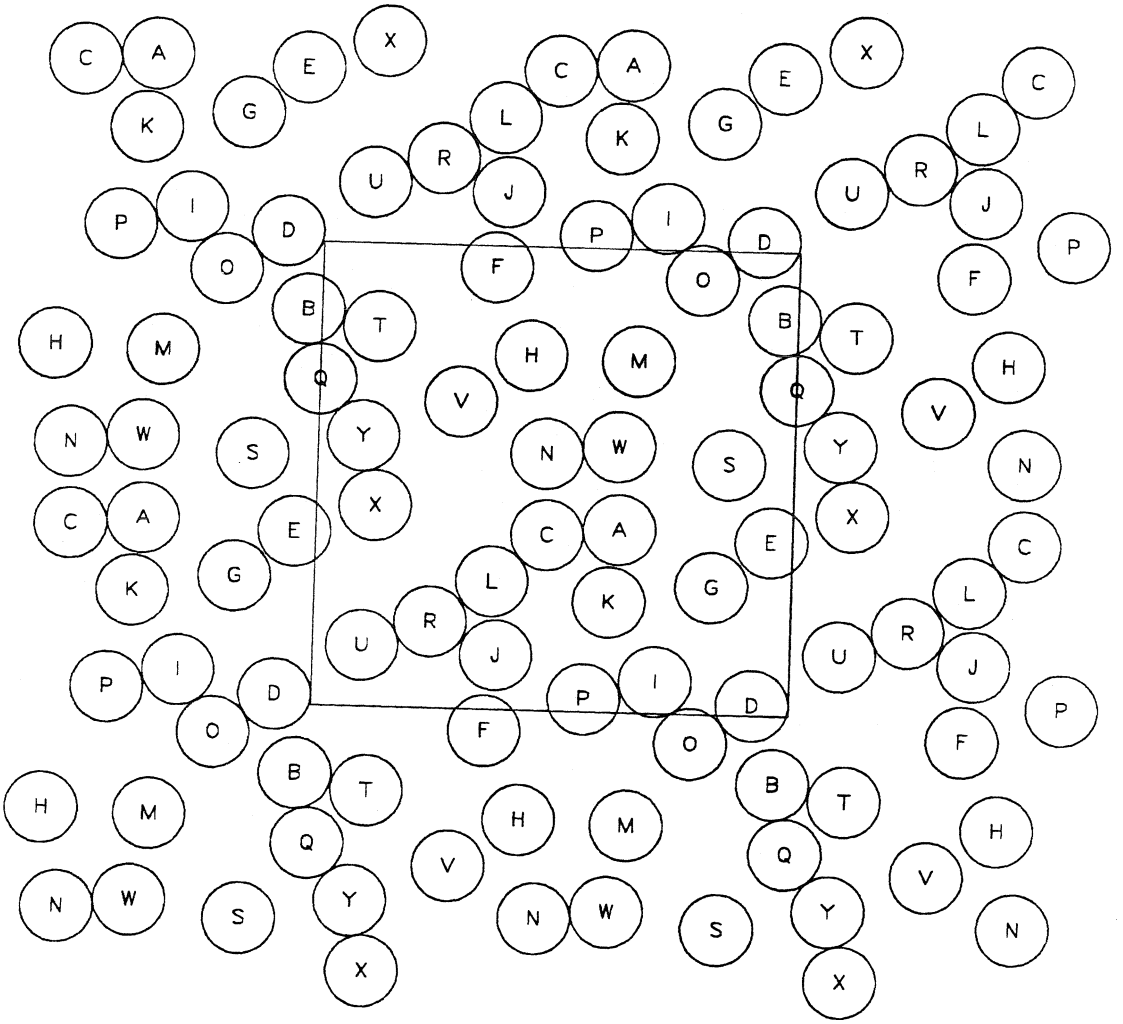

Figure 6.13 A "snapshot" of sphere positions. The square is the periodic cell. These are the sphere positions at $t = 300.00$ time units (nfr1).

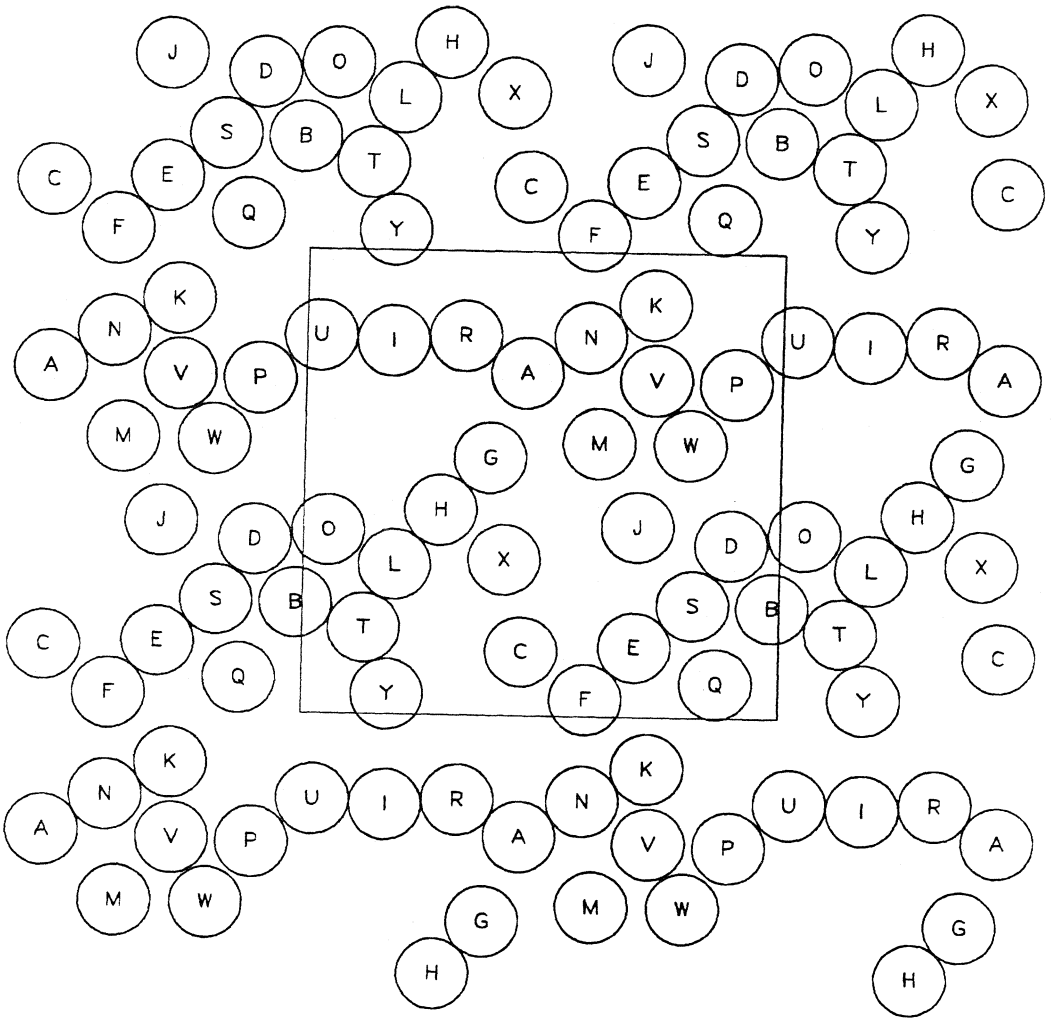

Figure B6.14 A "snapshot" of sphere positions. The square is the periodic cell. These are the sphere positions at $t = 400.00$ time units (nfr1).

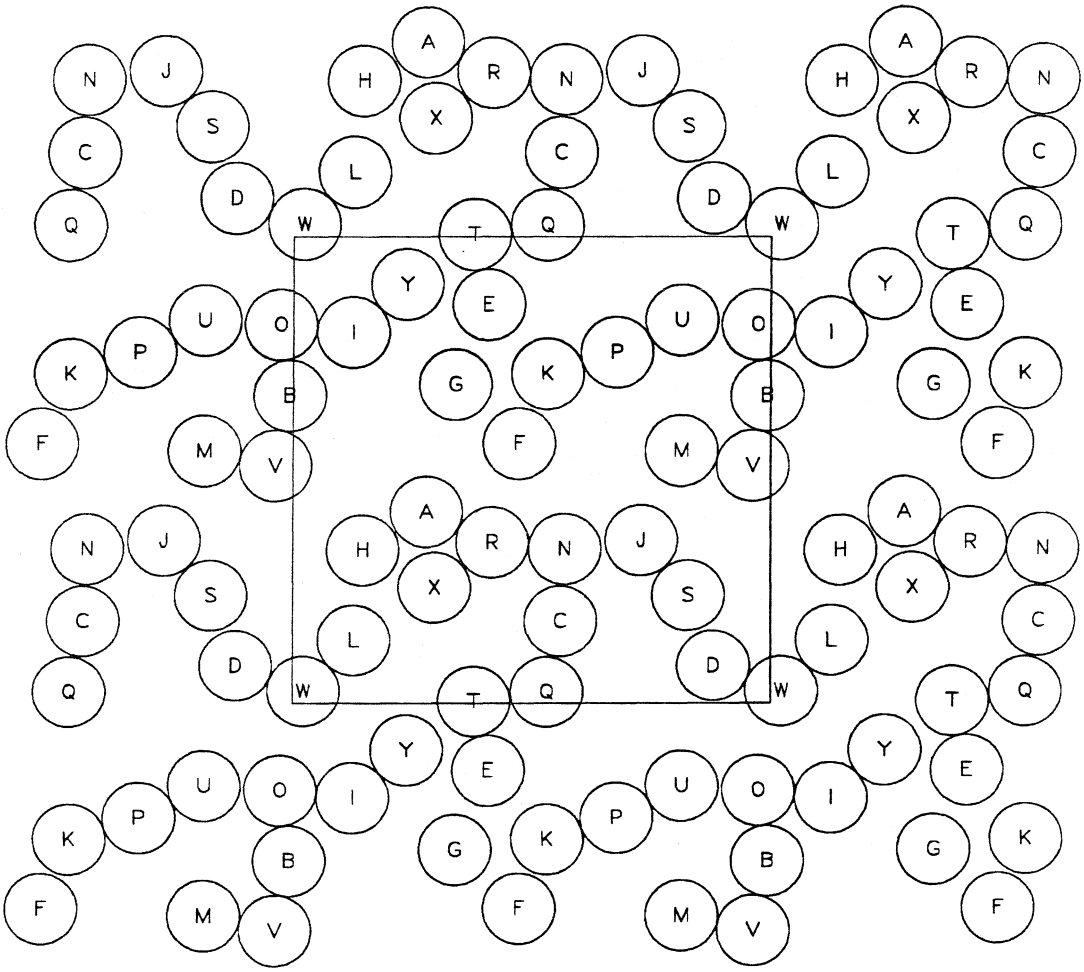

Figure B6.15 A "snapshot" of sphere positions. The square is the periodic cell. These are the sphere positions at $t = 450.00$ time units (nfr1).

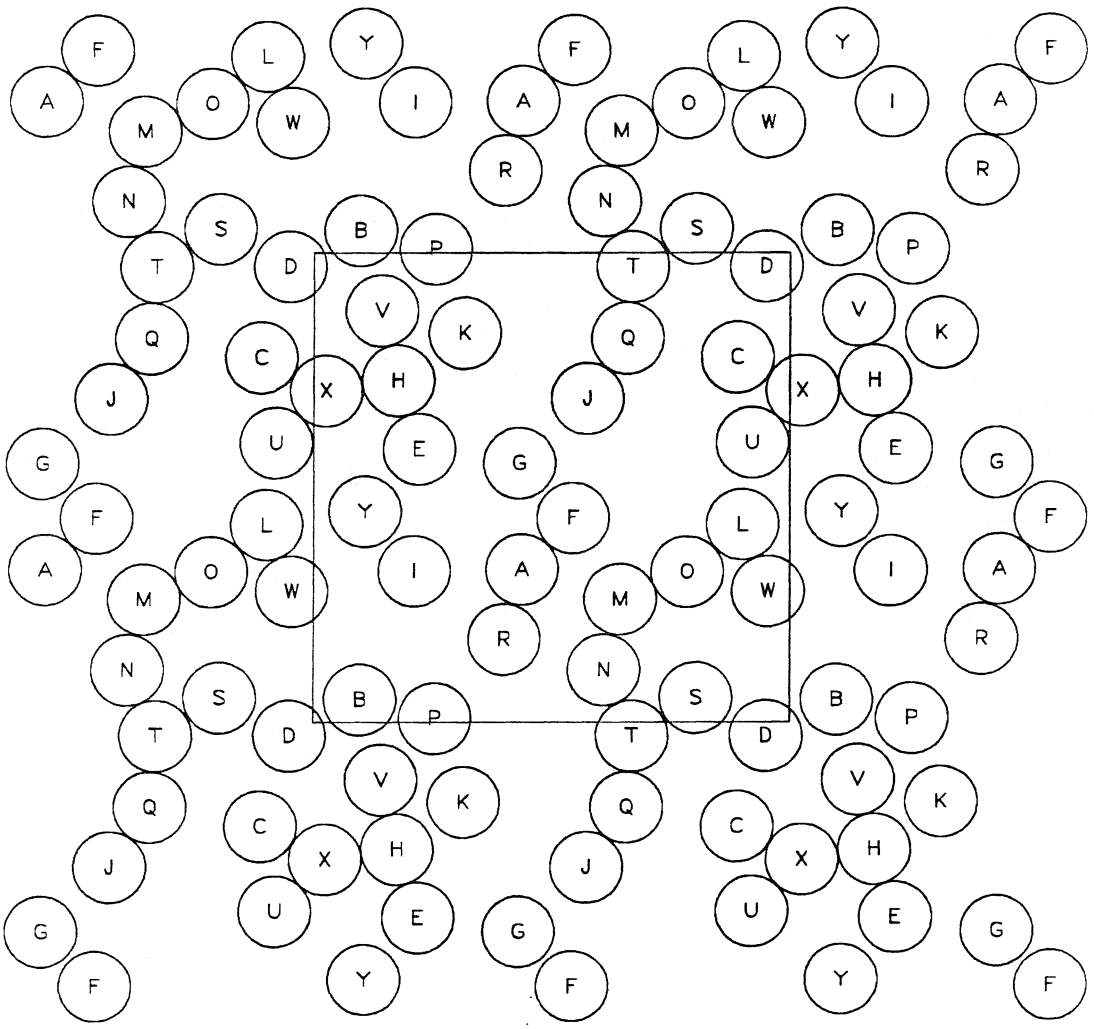

Figure B6.16 A "snapshot" of sphere positions. The square is the periodic cell. These are the sphere positions at $t = 500.00$ time units (nfr1).

Appendix B7: The n49 simulation results

This suite of simulations uses a non-Ewald, FT method to approximate the hydrodynamic interactions. All simulation conditions are the same as in the nfr1 simulation described in Appendix B6, except that the number of spheres in the periodic cell is 49. This initial configuration is the result of a Monte-Carlo simulation. Two separate simulation runs follow the evolution of a sedimenting system to a final time of 1000 time units. The areal fraction is 0.453. There are interparticle forces present ($\tau = 10^3$). The time step is 0.001 time unit. The mobility matrix is inverted every 0.1 time unit. Position and velocity data is saved every 0.05 time unit. $\mathbf{D}_o^s$ is evaluated and reported at every time unit.

	49a	49b
T	0-500	500-1000
Cray/Sun	Sun	Sun
CPU(min)	9215	9218
v_y	-8.90357	-8.90844
v_x	-0.00188	-0.00216
v_y variance	0.02358	0.02087
v_x variance	0.00622	0.00655
v_{xy} variance	-0.00047	-0.00025
$(D_\infty^s)_{yy}$		0.21
$(D_\infty^s)_{xx}$		0.068
$(D_o^s)_{yy}$	0.682	0.693
$(D_o^s)_{xx}$	0.672	0.687
$(D_o^s)_{xy}$	-0.0012	-0.0030
$g(2)$		10.5
$g(3.5)$		0.89
$g(4)$		1.38

Table B7.1

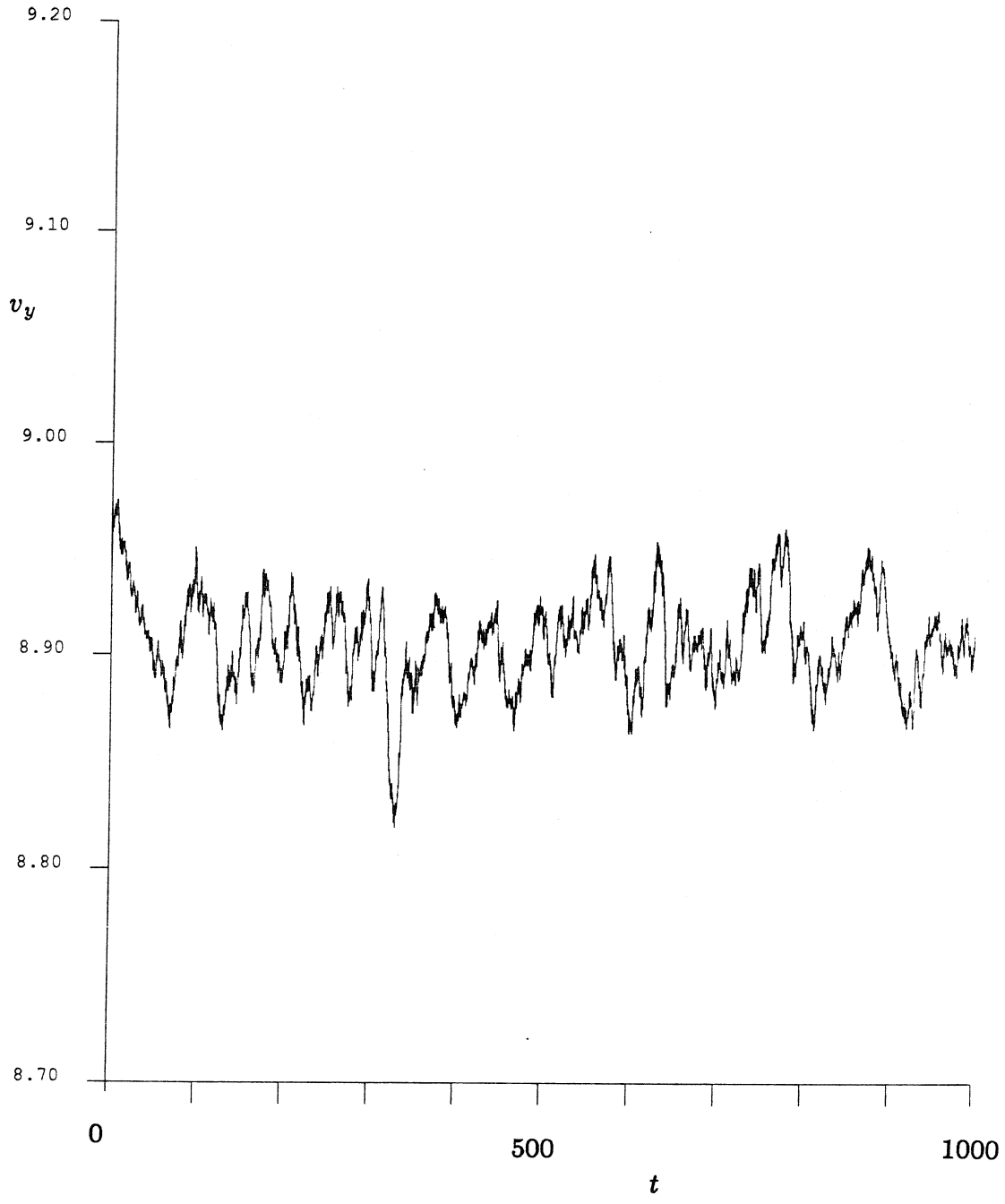

Figure B7.1 The time trace of v_y for the simulations n49a and n49b.

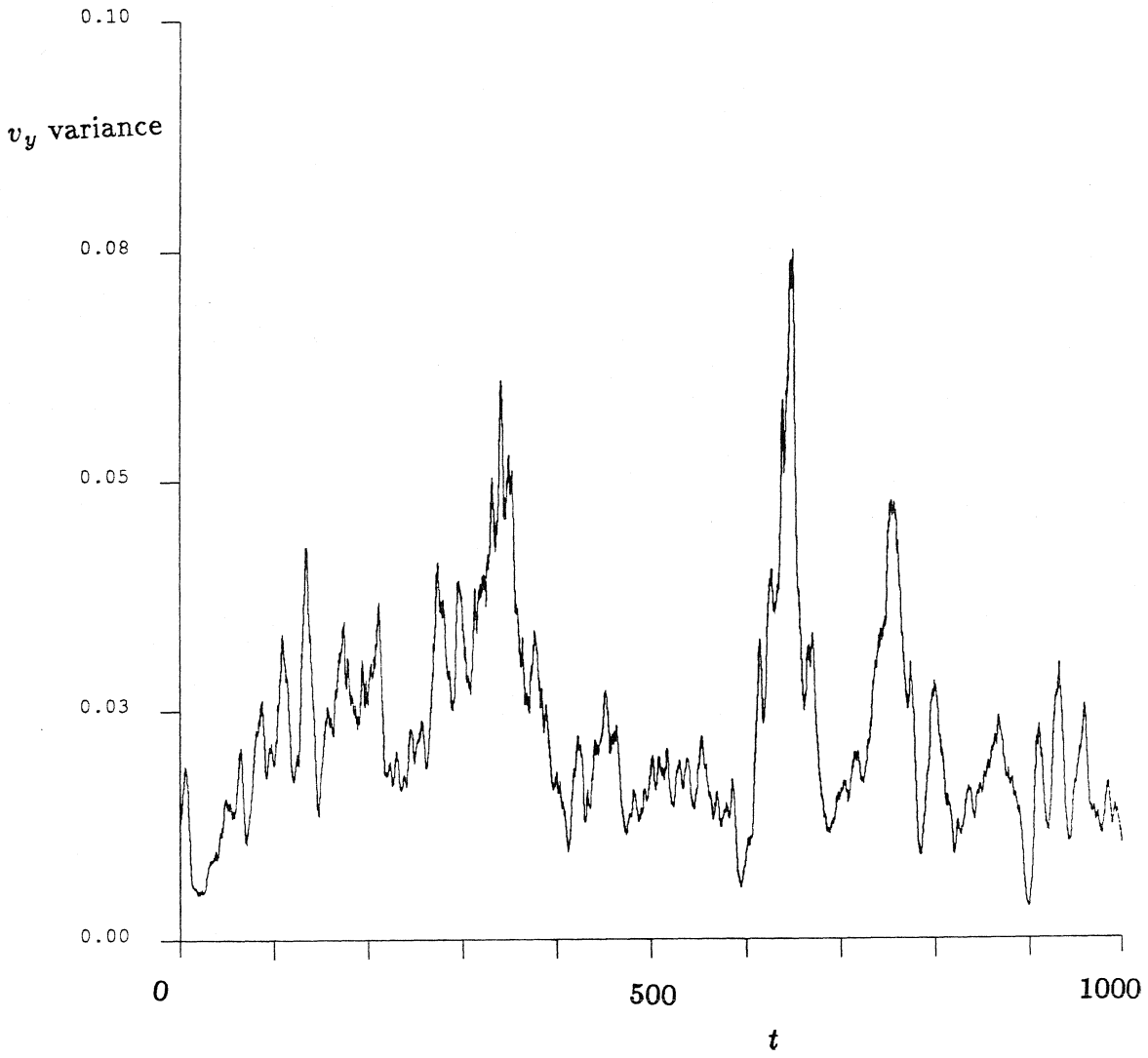

Figure B7.2 The time trace of the v_y variance for the simulations n49a and n49b.

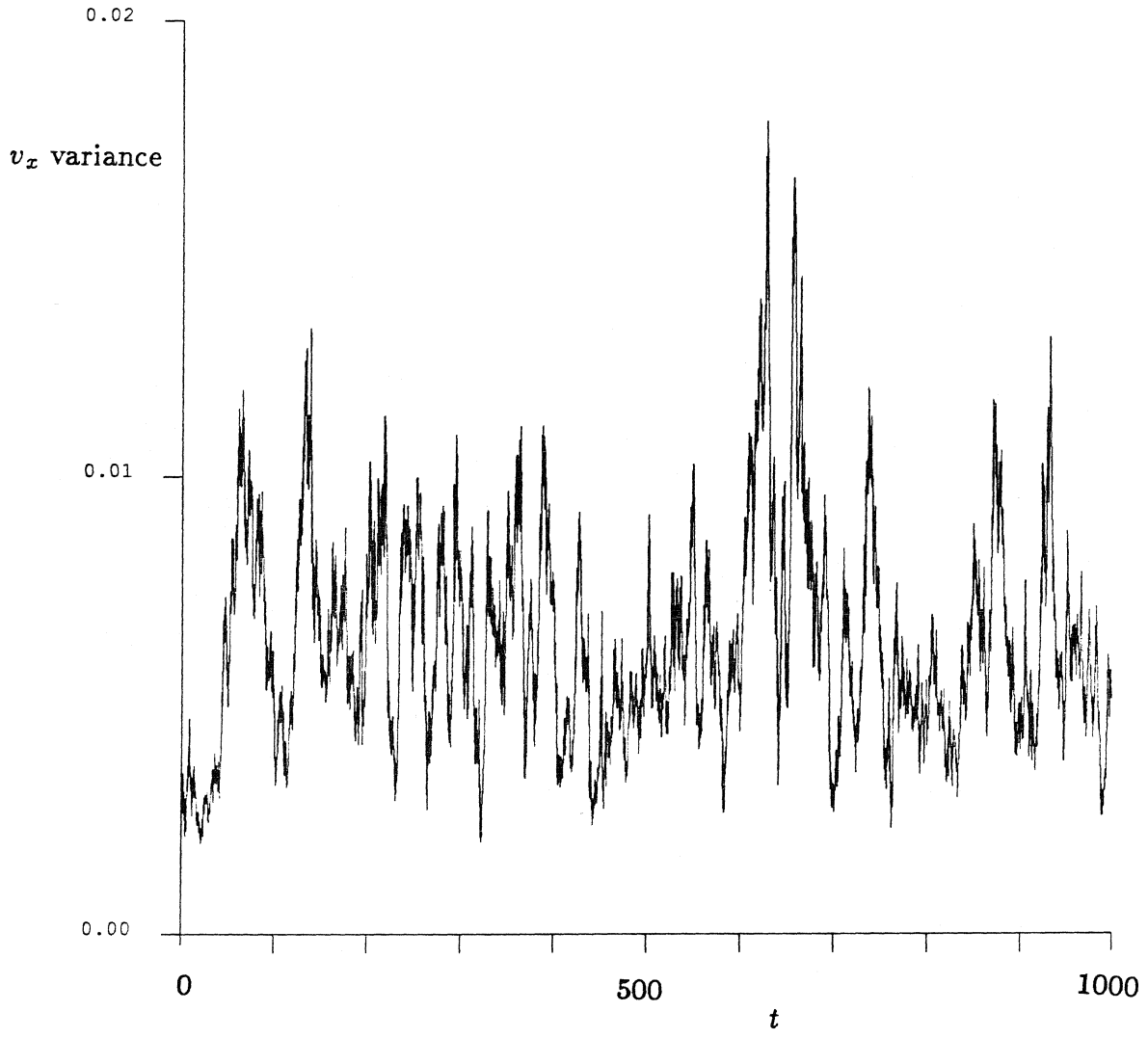

Figure B7.3 The time trace of the v_x variance for the simulations m49a and n49b.

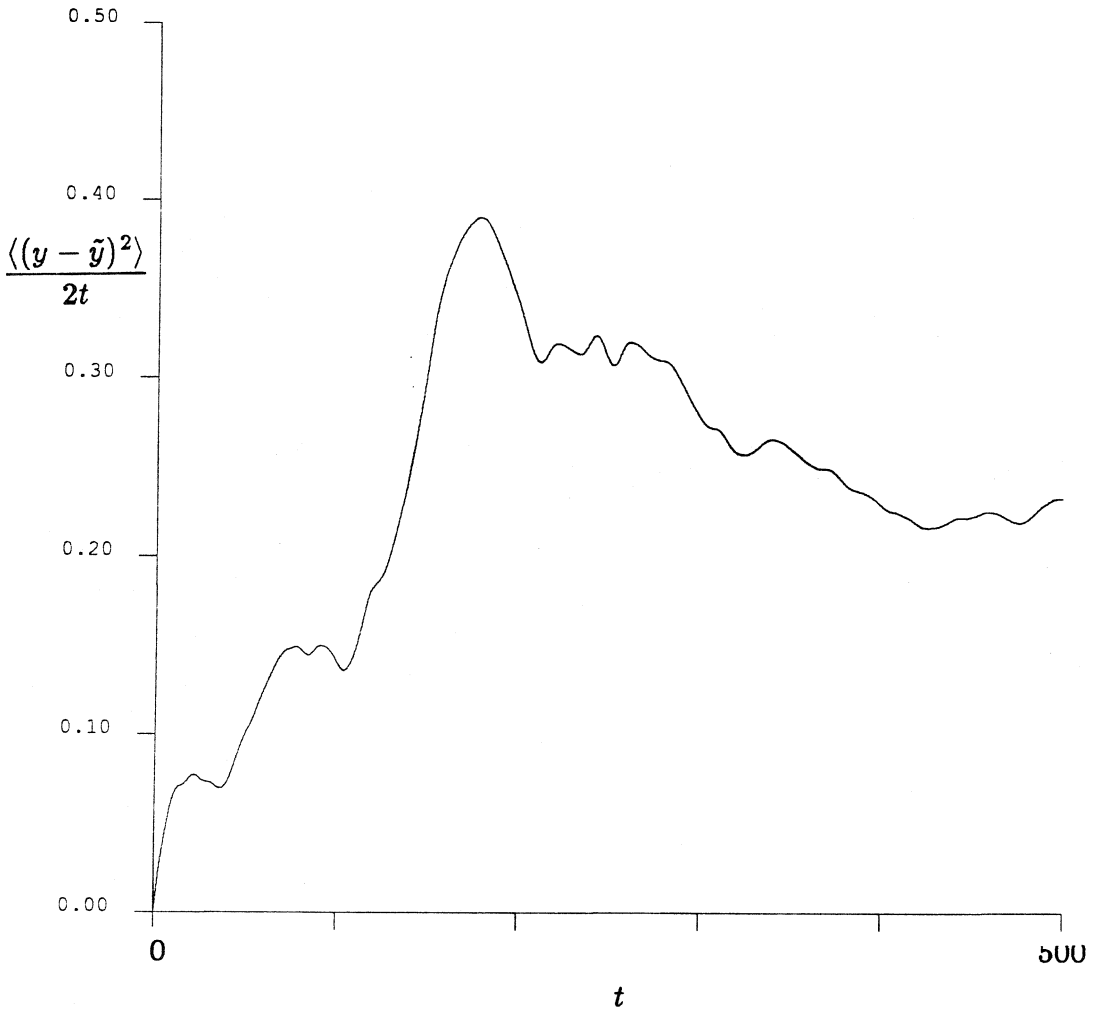

Figure B7.4 A $(D^s_\infty)_{yy}$-defining graph using displacement data from n49b (t= 500 – 1000). The graph interval is 500 time units, which means that no averaging over different initial conditions is done.

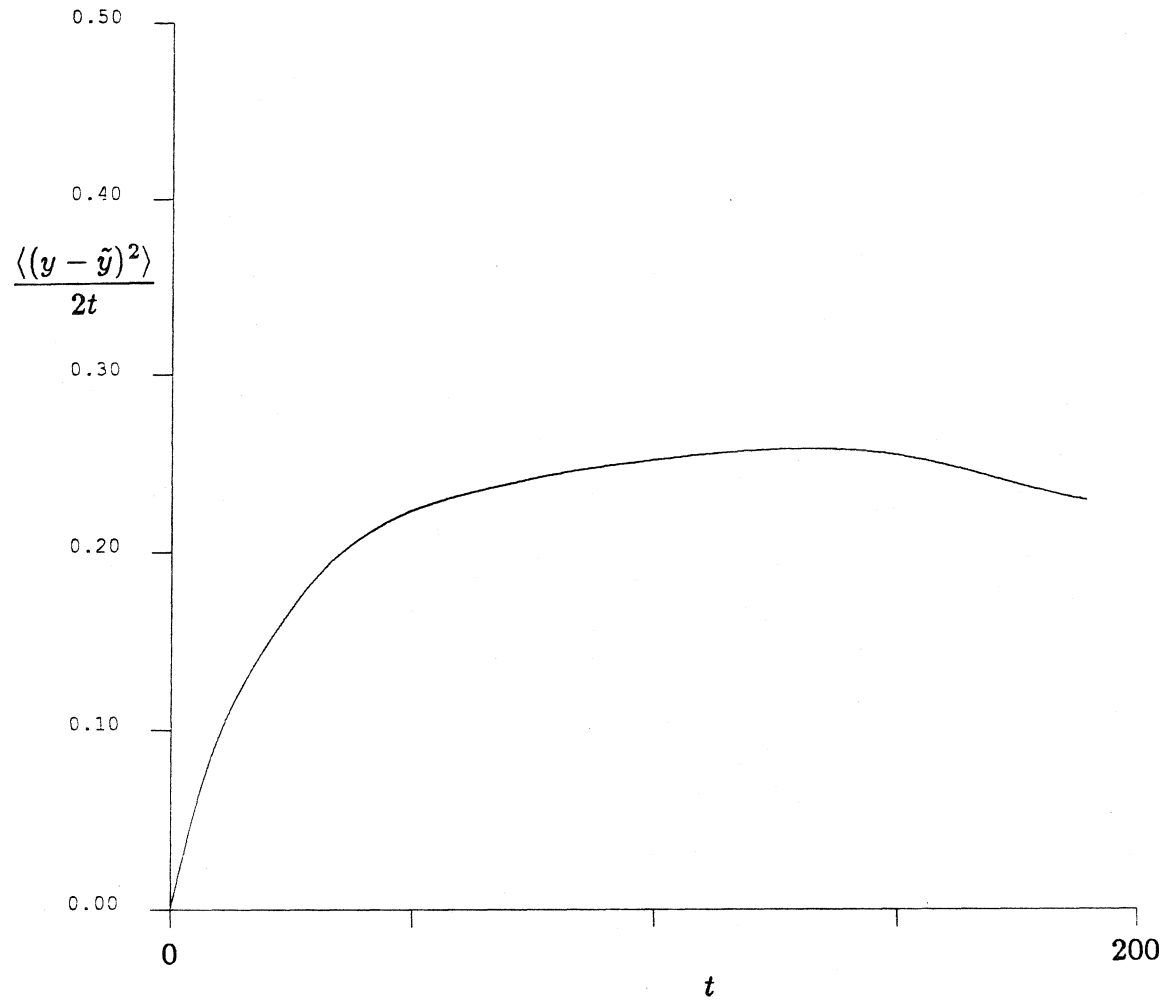

Figure B7.5 A $(D^s_\infty)_{yy}$-defining graph using displacement data from n49b (t= 500 – 1000). The graph interval is 200 time units, and the time between interval initial conditions is 0.01 time unit.

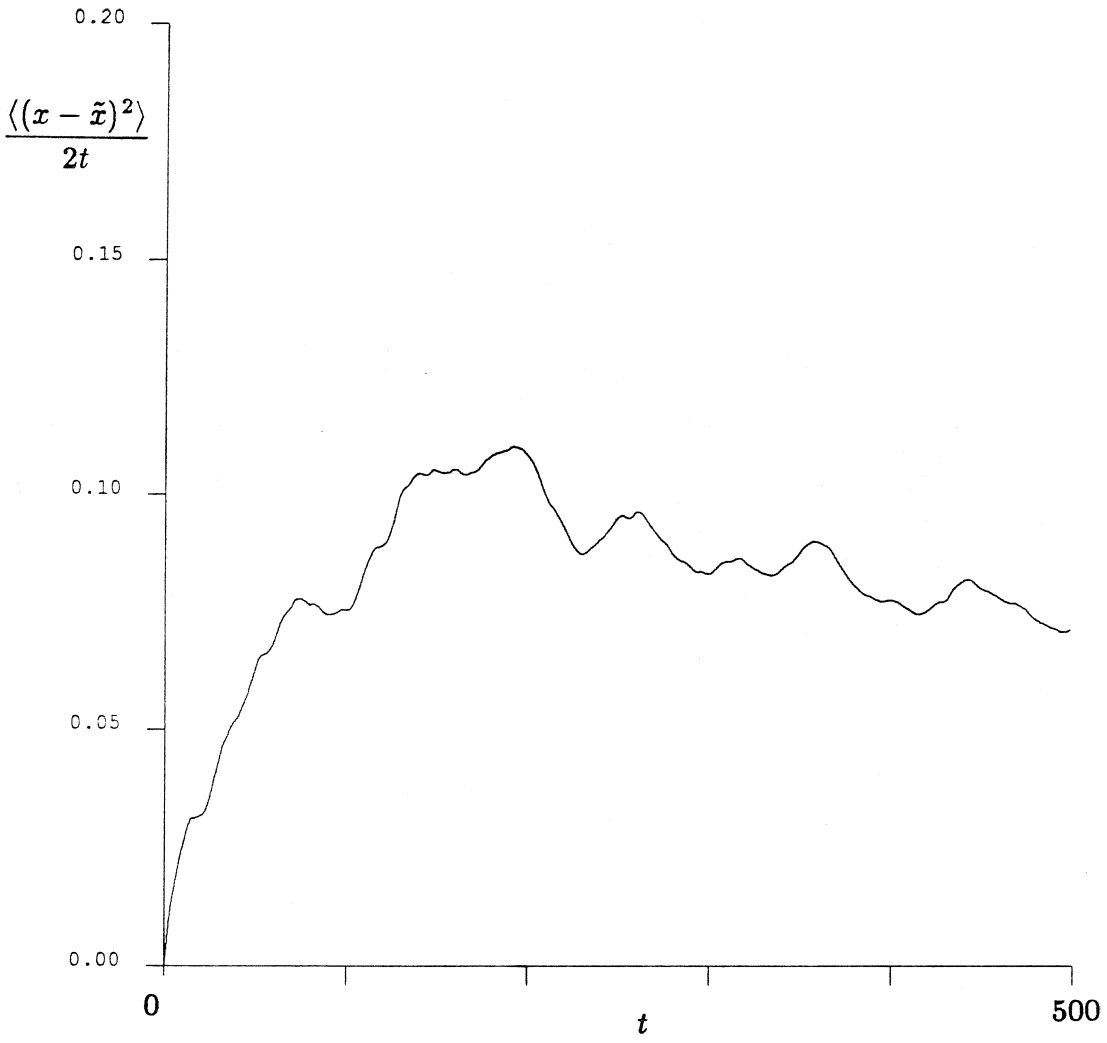

Figure B7.6 A $(D^s_\infty)_{xx}$-defining graph using displacement data from n49b (t= 500 – 1000). The graph interval is 500 time units, which means that no averaging over different initial conditions is done.

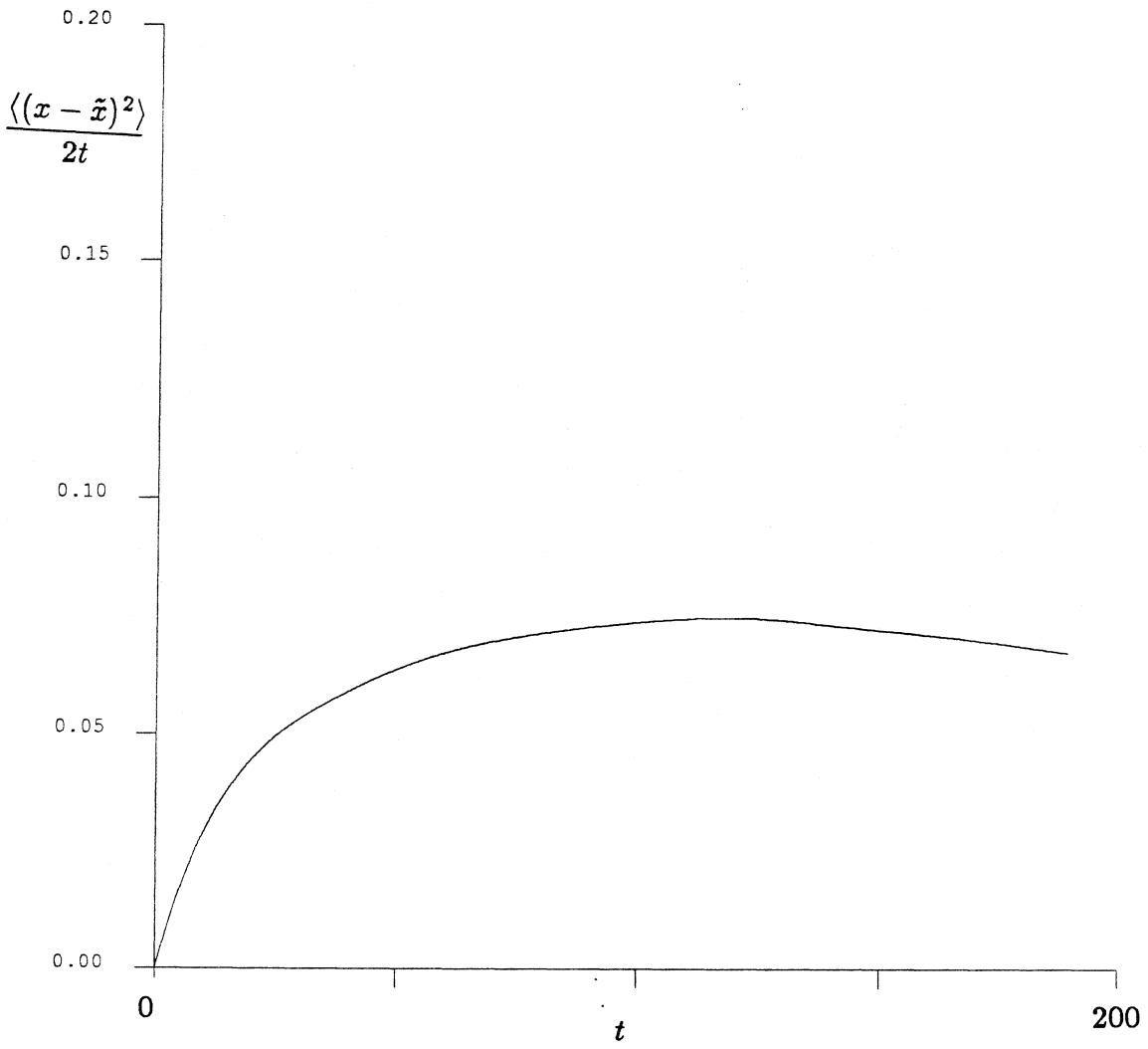

Figure B7.7 A $(D^s_\infty)_{xx}$-defining graph using displacement data from n49b (t= 500 – 1000). The graph interval is 200 time units, and the time between interval initial conditions is 0.01 time unit.

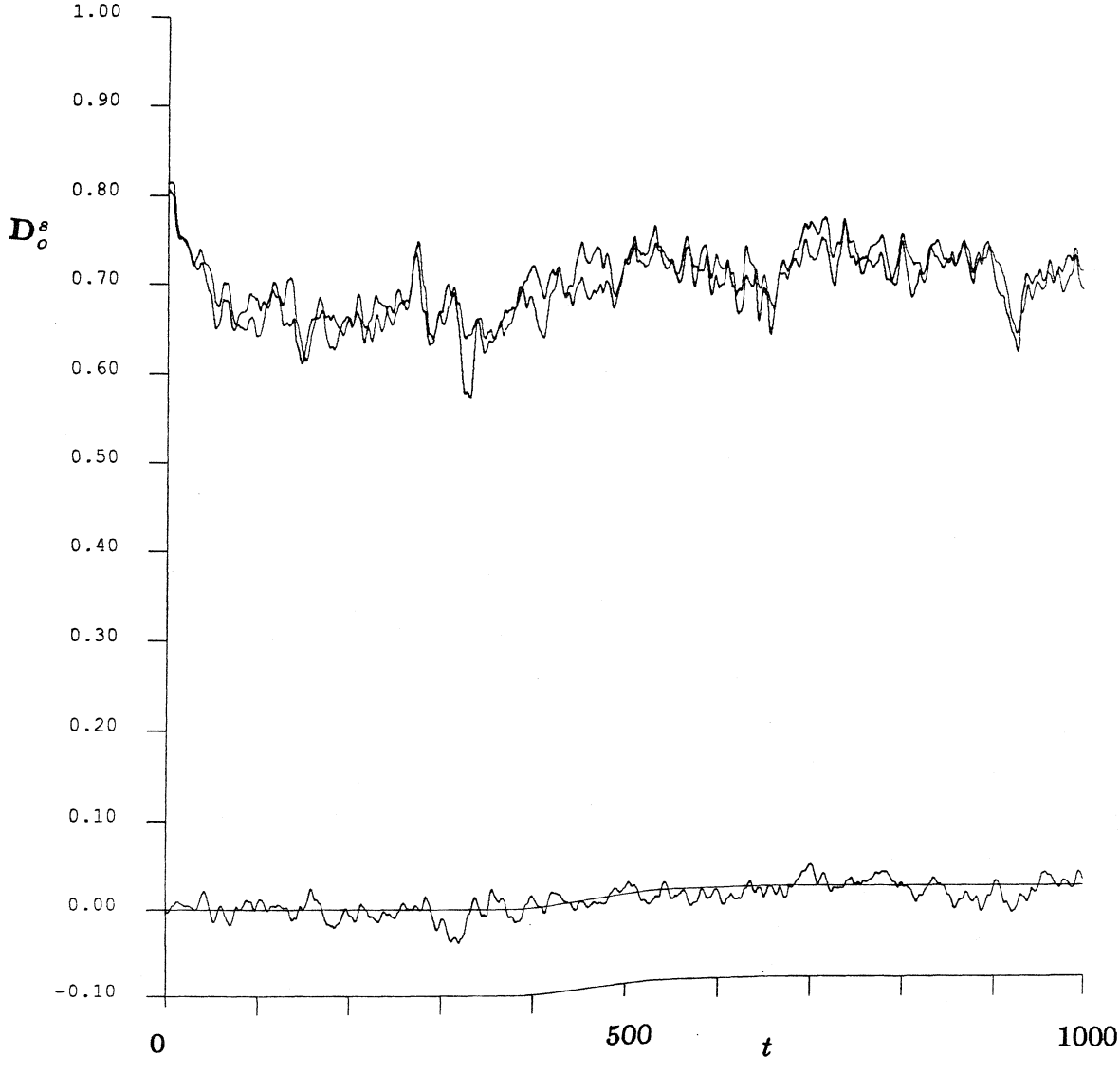

Figure B7.8 The time trace of $\mathbf{D}_o^s$ for the simulations n49a and n49b. The upper two lines are the xx and yy components of this tensor. Of course, they should be equivalent for an infinite suspension – the slight variation occurs because of the finite number of spheres used in our simulation. The trace that fluctuates about the zero y-axis is the xy component of the short-time, self-diffusion tensor. Again, for an infinite number of spheres, this quantity would be exactly zero.

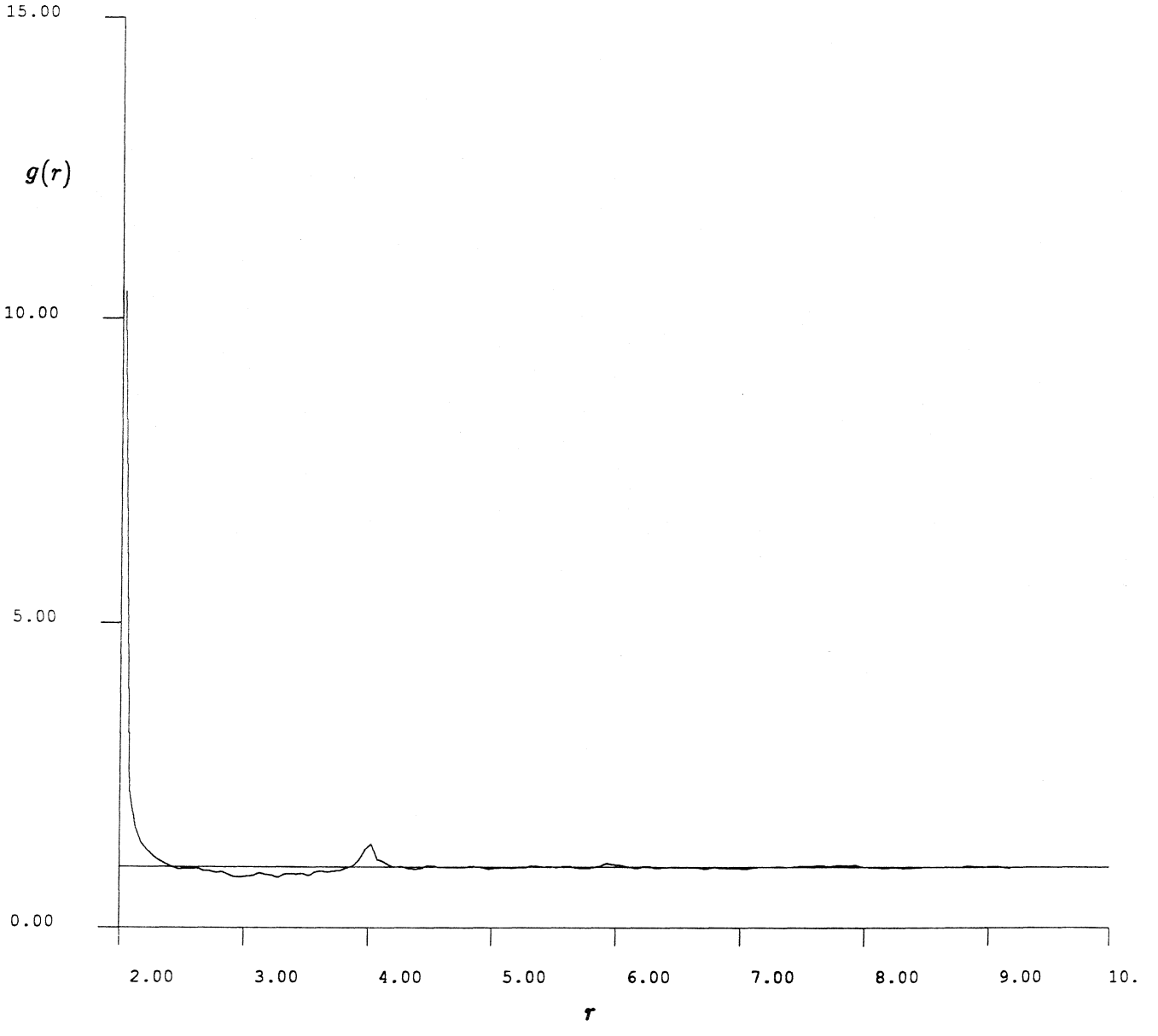

Figure B7.9 The radial pair-distribution function, $g(r)$, for the n49b run (t = 500 – 1000).

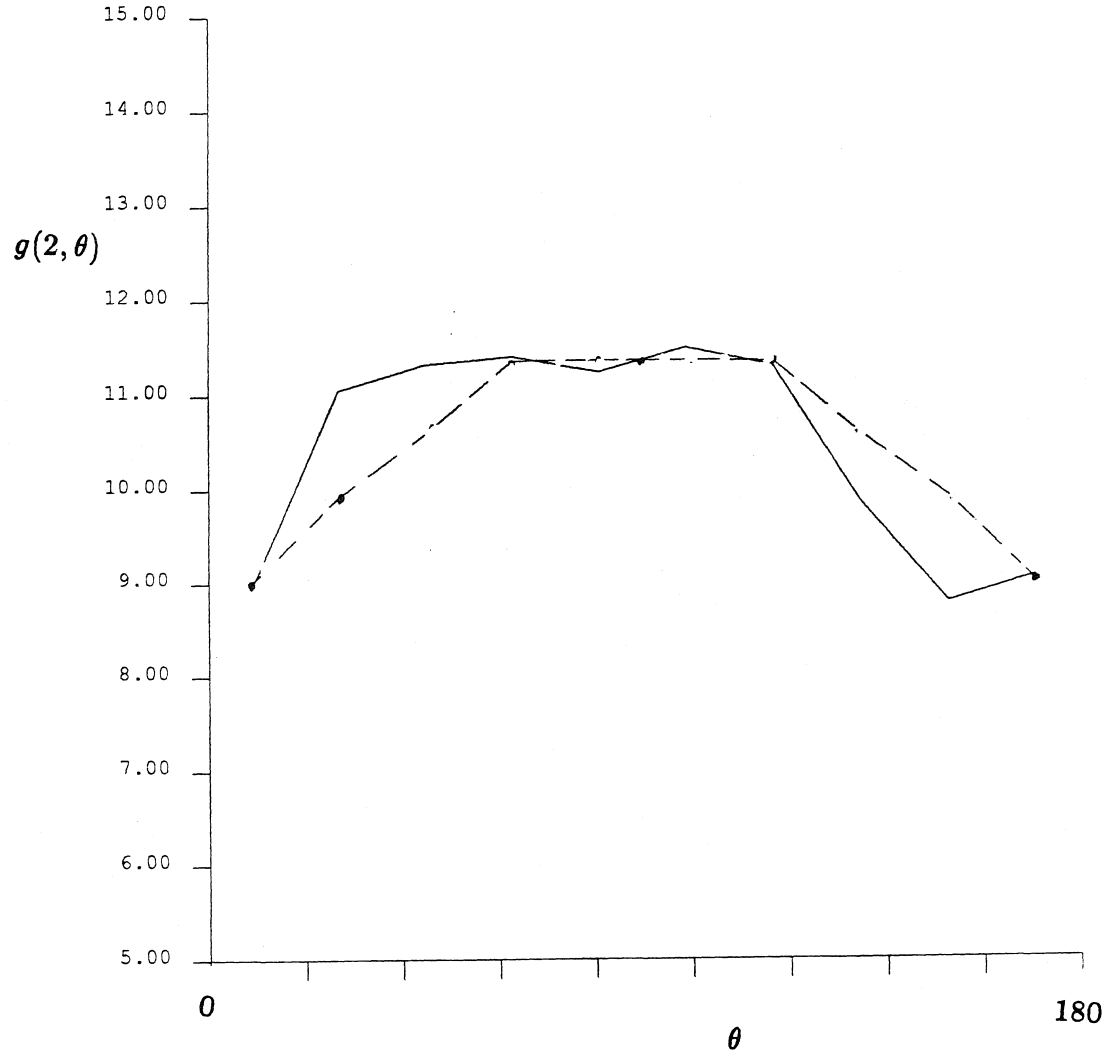

Figure B7.10 The full pair-distribution function for spheres whose surfaces are separated by less than 0.05 radii using data from the n49b run (t = 500 – 1000). The dashed curve represents this function when it is forced to be symmetric about $\theta = 90°$.

Appendix B8: The nfr2 simulation results

This simulation uses a non-Ewald, F method to approximate the hydrodynamic interactions. The simulation conditions are identical to the nfr1 simulation described in Appendix B6, except that the interparticle variable, τ, is 10^5, instead of 10^3. The final time is 500 time units. The initial configuration is the same as in the FTSn simulations described in Appendix B1. There are 25 spheres within the periodic cell. The areal fraction is 0.453. There are interparticle forces present ($\tau = 10^5$). The time step is 0.001 time unit. The mobility matrix is inverted every 0.1 time unit. Position and velocity data is saved every 0.05 time unit. $\mathbf{D}_o^s$ is evaluated and reported at every time unit.

	nfr2
T Cray/Sun CPU(min)	0-500 Cray 0.50
v_y	-6.38132
v_x	0.00886
v_y variance	0.01785
v_x variance	0.00677
v_{xy} variance	-0.00014
$(D_\infty^s)_{yy}$	0.21
$(D_\infty^s)_{xx}$	0.090
$(D_o^s)_{yy}$	0.611
$(D_o^s)_{xx}$	0.615
$(D_o^s)_{xy}$	0.0076
$g(2)$	15.8
$g(3.5)$	0.83
$g(4)$	1.45

Table B8.1

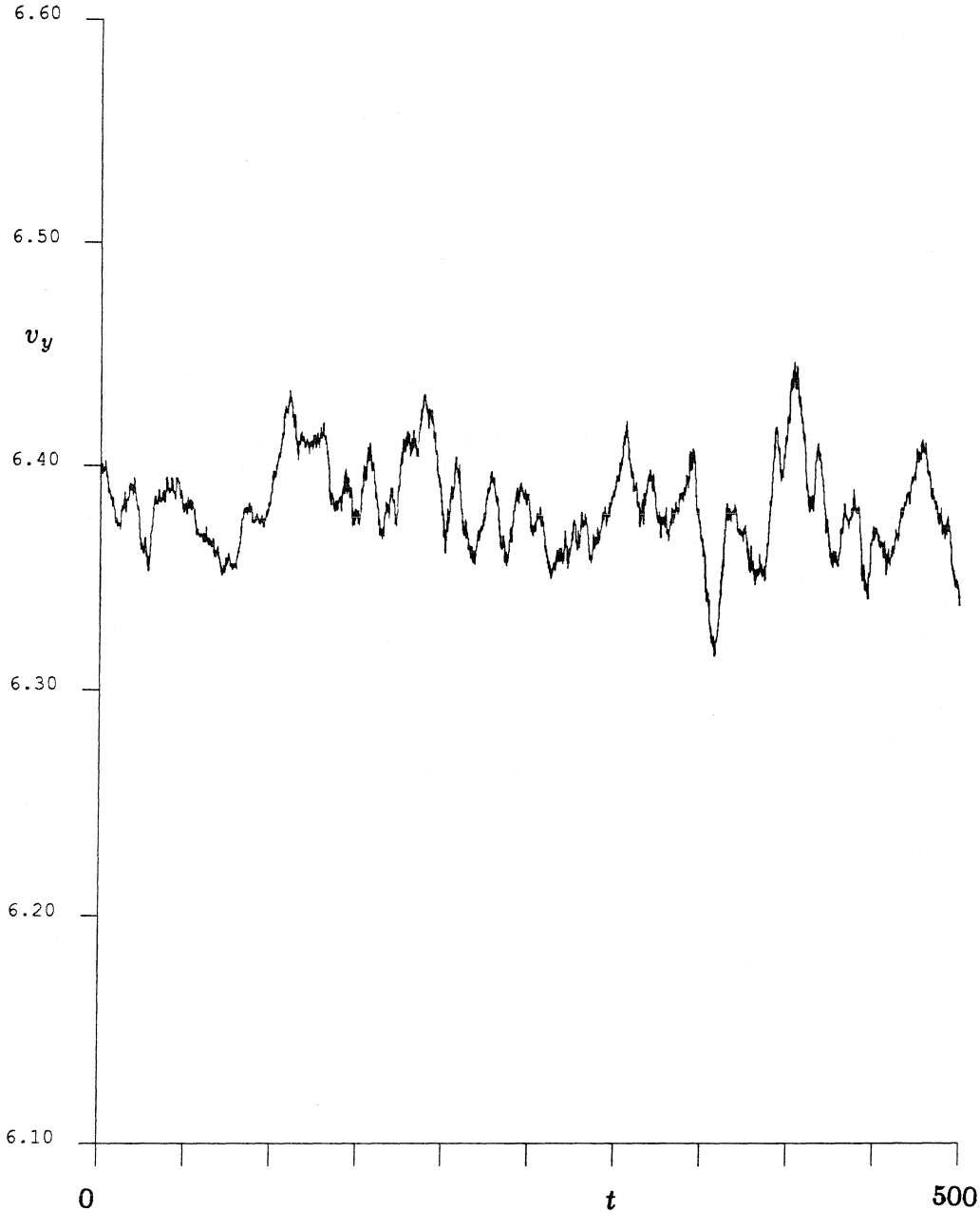

Figure B8.1 The time trace of v_y for the simulation nfr2.

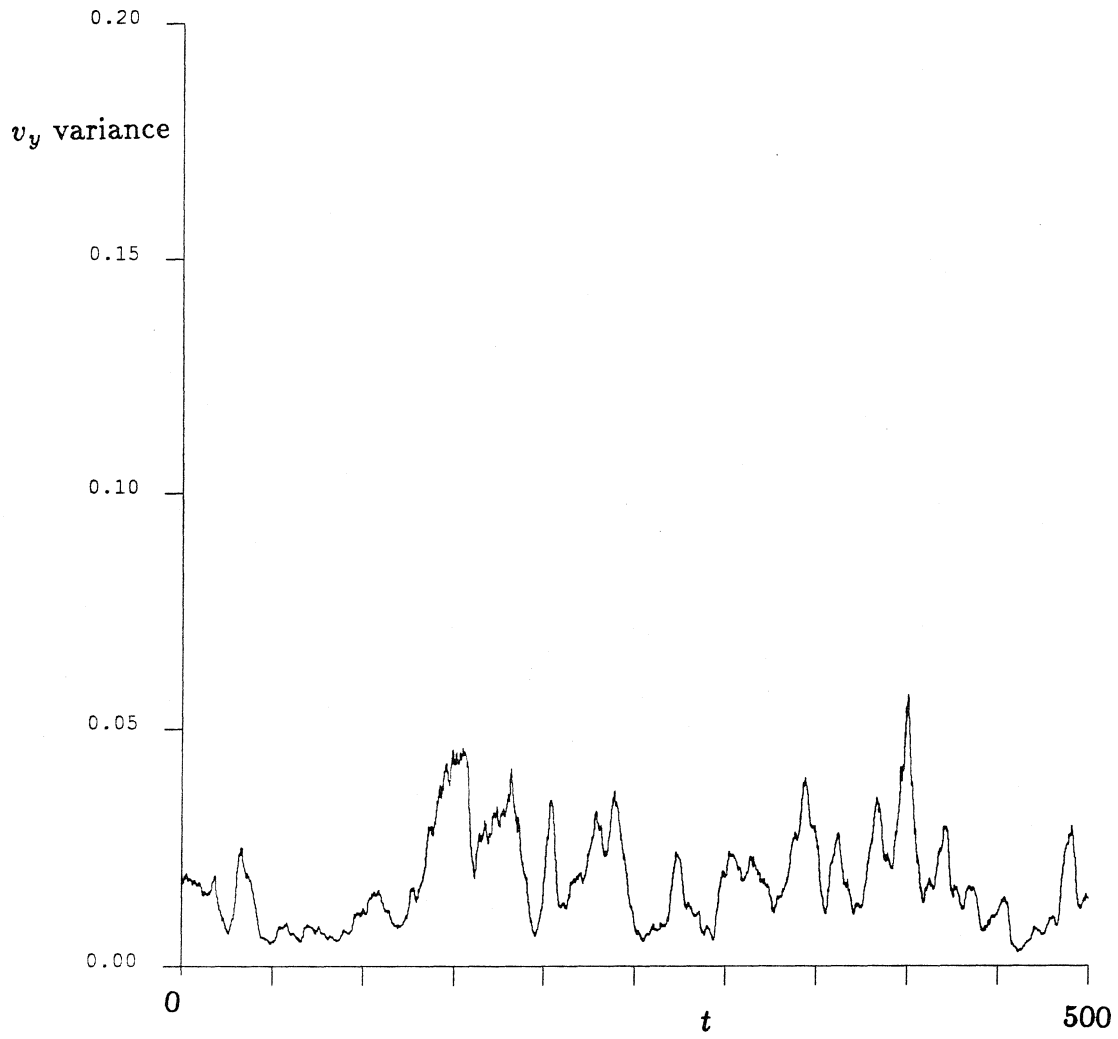

Figure B8.2 The time trace of the v_y variance for the simulation nfr2.

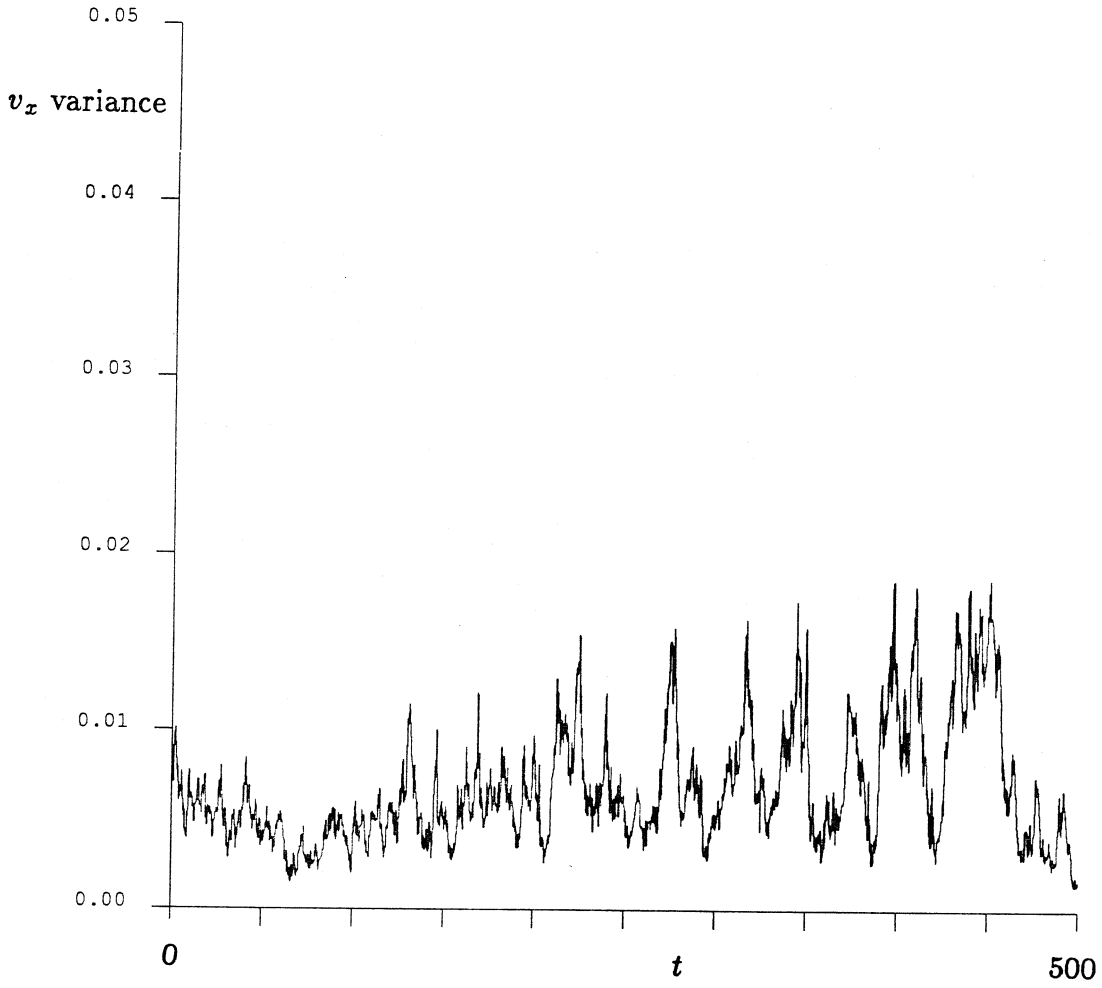

Figure B8.3 The time trace of the v_x variance for the simulation nfr2.

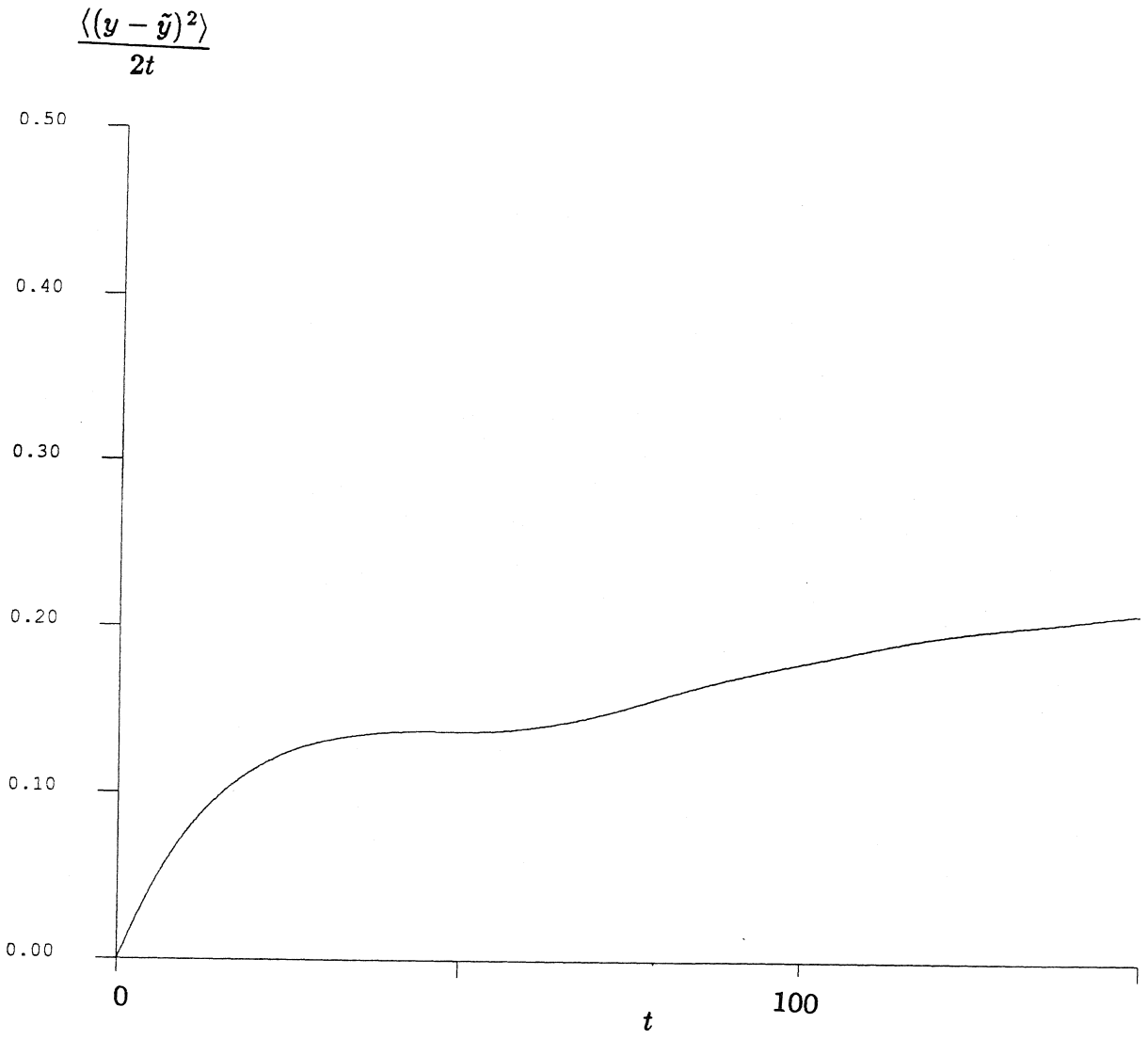

Figure B8.4 A $(D^{\varepsilon}_{\infty})_{yy}$-defining graph using displacement data from nfr2 (t= 200 – 500). The graph interval is 150 time units, and the time between interval initial conditions is 0.01 time unit.

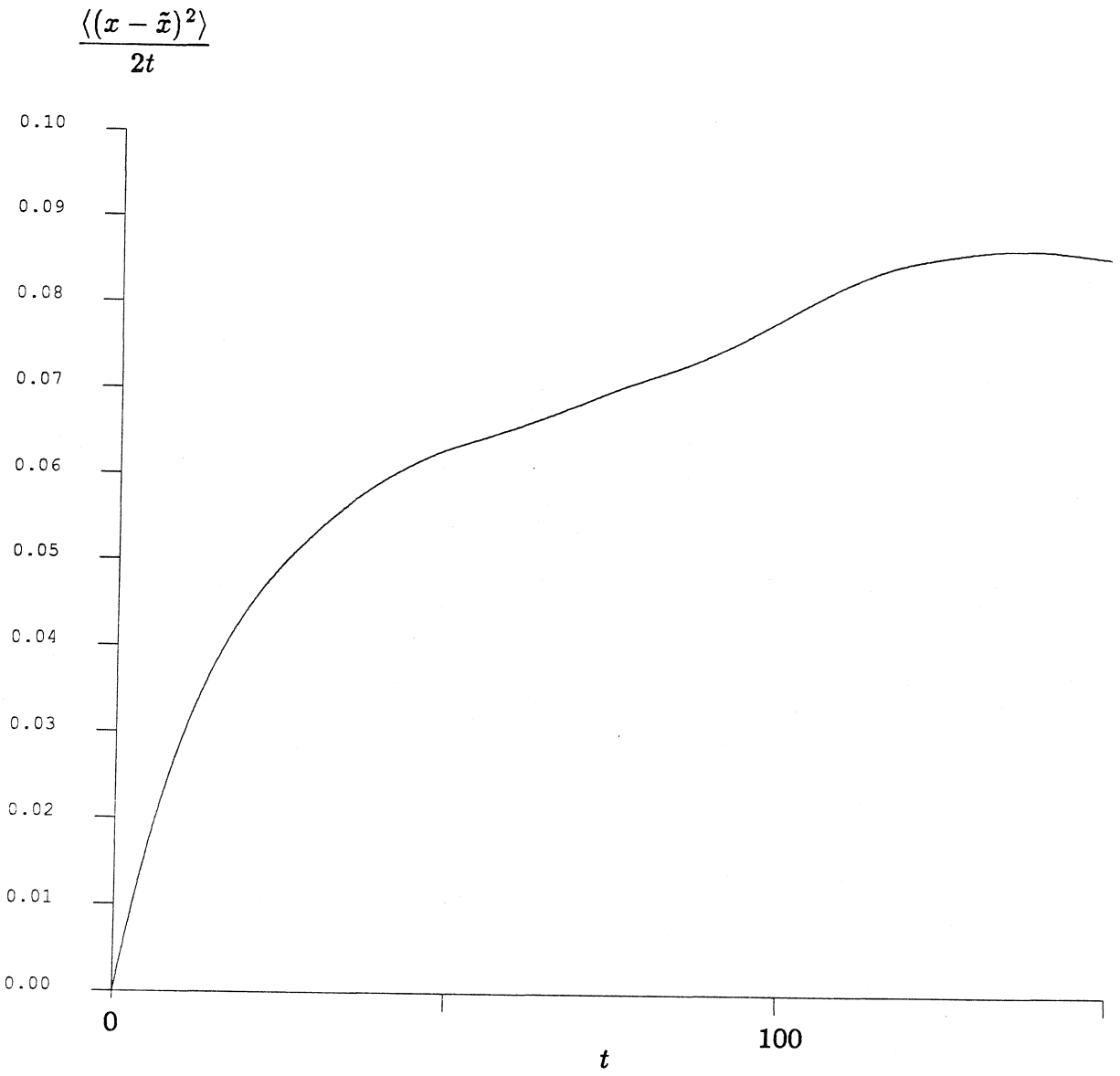

Figure B8.5 A $(D^s_\infty)_{xx}$-defining graph using displacement data from nfr2 (t= 200 – 500). The graph interval is 150 time units, and the time between interval initial conditions is 0.01 time unit.

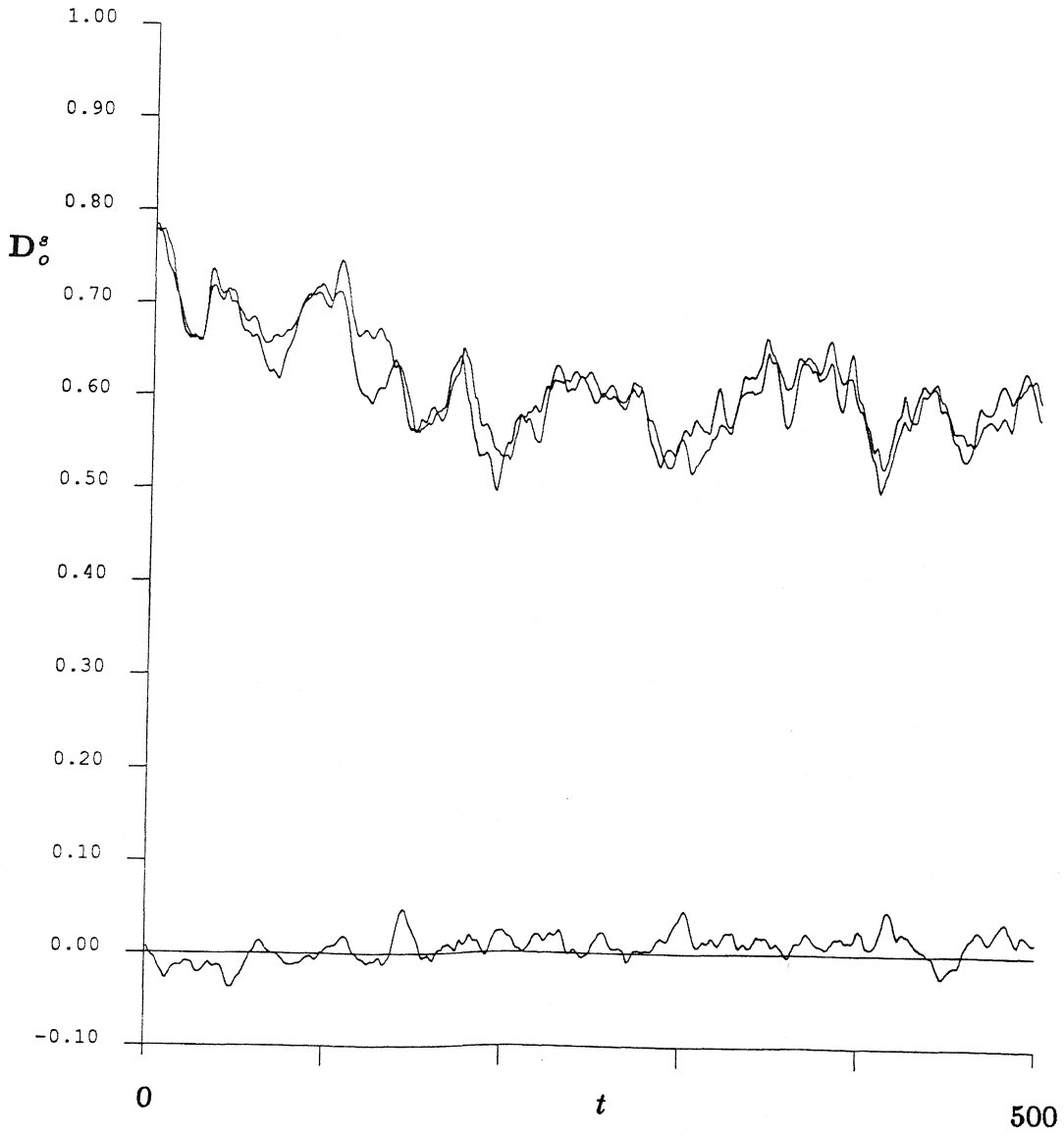

Figure B8.6 The time trace of $\mathbf{D}_o^s$ for the simulation nfr2. The upper two lines are the xx and yy components of this tensor. Of course, they should be equivalent for an infinite suspension – the slight variation occurs because of the finite number of spheres used in our simulation. The trace that fluctuates about the zero y-axis is the xy component of the short-time, self-diffusion tensor. Again, for an infinite number of spheres, this quantity would be exactly zero.

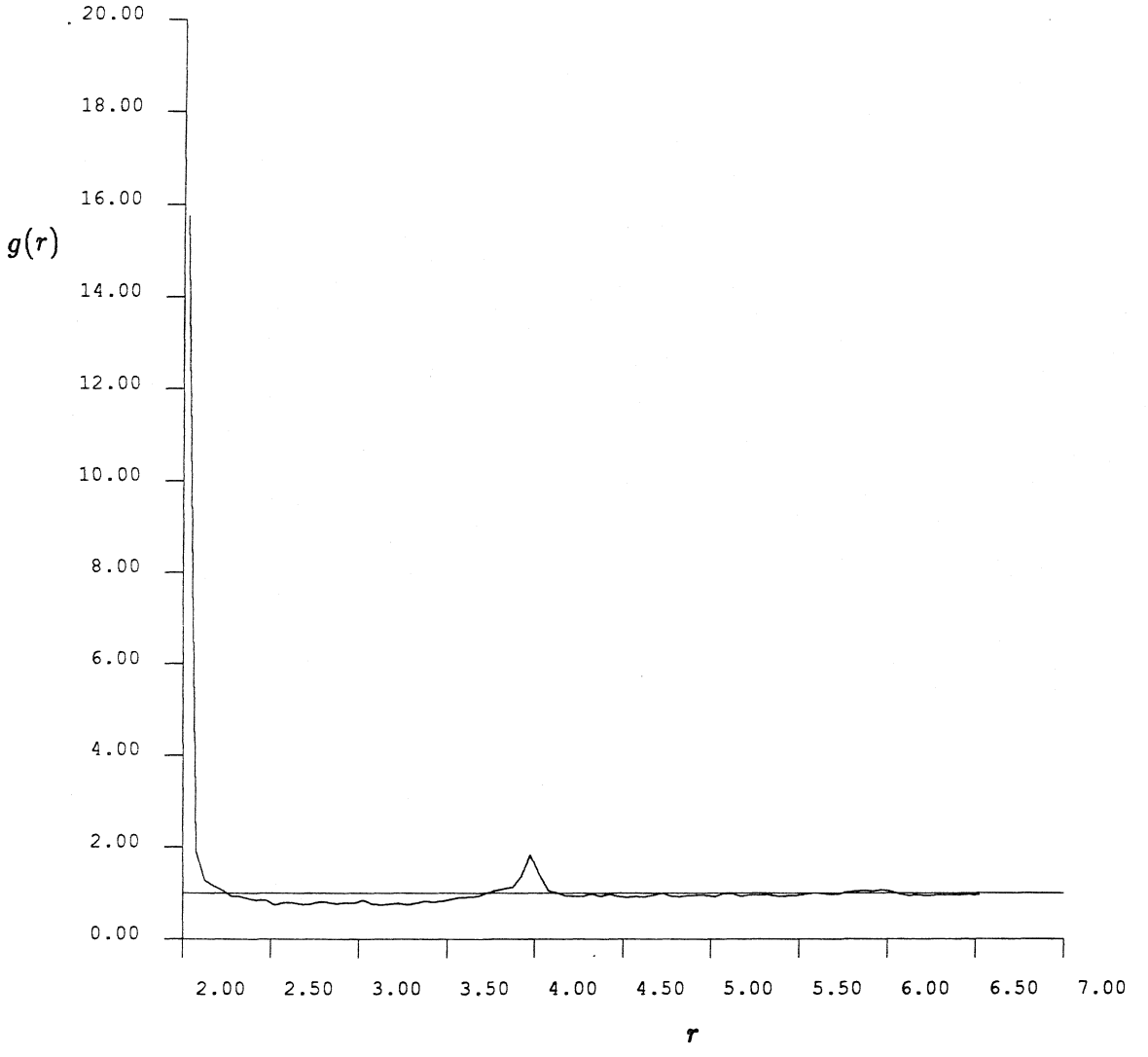

Figure B8.7 The radial pair-distribution function, $g(r)$, for the nfr2 run ($t = 200 - 500$).

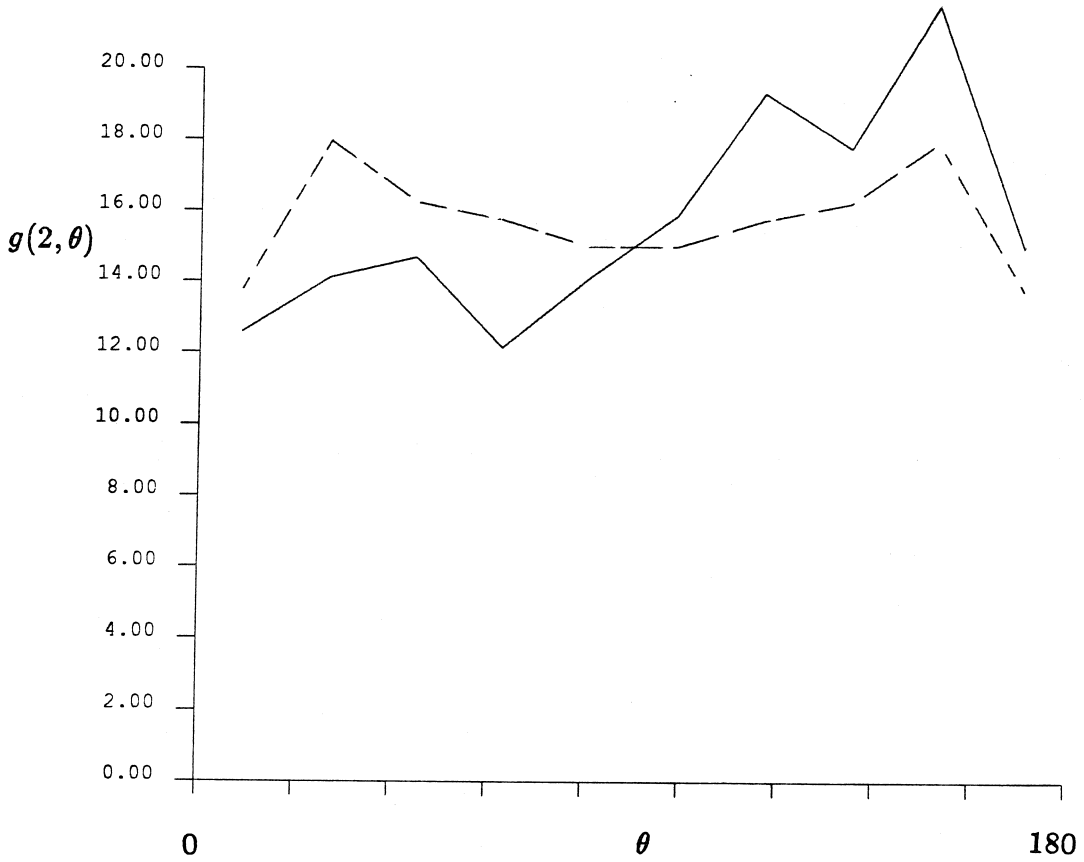

Figure B8.8 The full pair-distribution function for spheres whose surfaces are separated by less than 0.05 radii using data from the nfr2 run (t = 200 – 500). The dashed curve represents this function when it is forced to be symmetric about $\theta = 90°$.

Appendix B9: The nfr3 simulation results

This simulation uses a non-Ewald, F method to approximate the hydrodynamic interactions. The simulation conditions are identical to the nfr2 simulation described in Appendix B8, except that the time step is 0.005, instead of 0.001. The simulation terminated at 270.685 time units because the mobility matrix lost positive definiteness. The initial configuration is the same as in the FTSn simulations described in Appendix B1. There are 25 spheres within the periodic cell. The areal fraction is 0.453. There are interparticle forces present ($\tau = 10^5$). The time step is 0.005 time unit. The mobility matrix is still inverted every 0.1 time unit. Position and velocity data is saved every 0.05 time unit. $\mathbf{D}_o^s$ is evaluated and reported at every time unit.

	nfr3
T	0-270.685
Cray/Sun	Cray 0.70
CPU(min)	8
v_y	-6.38039
v_x	-0.01161
v_y variance	0.01344
v_x variance	0.00543
v_{xy} variance	-0.00028
$(D_\infty^s)_{yy}$	
$(D_\infty^s)_{xx}$	
$(D_o^s)_{yy}$	
$(D_o^s)_{xx}$	
$(D_o^s)_{xy}$	
$g(2)$	
$g(3.5)$	
$g(4)$	

Table B9.1

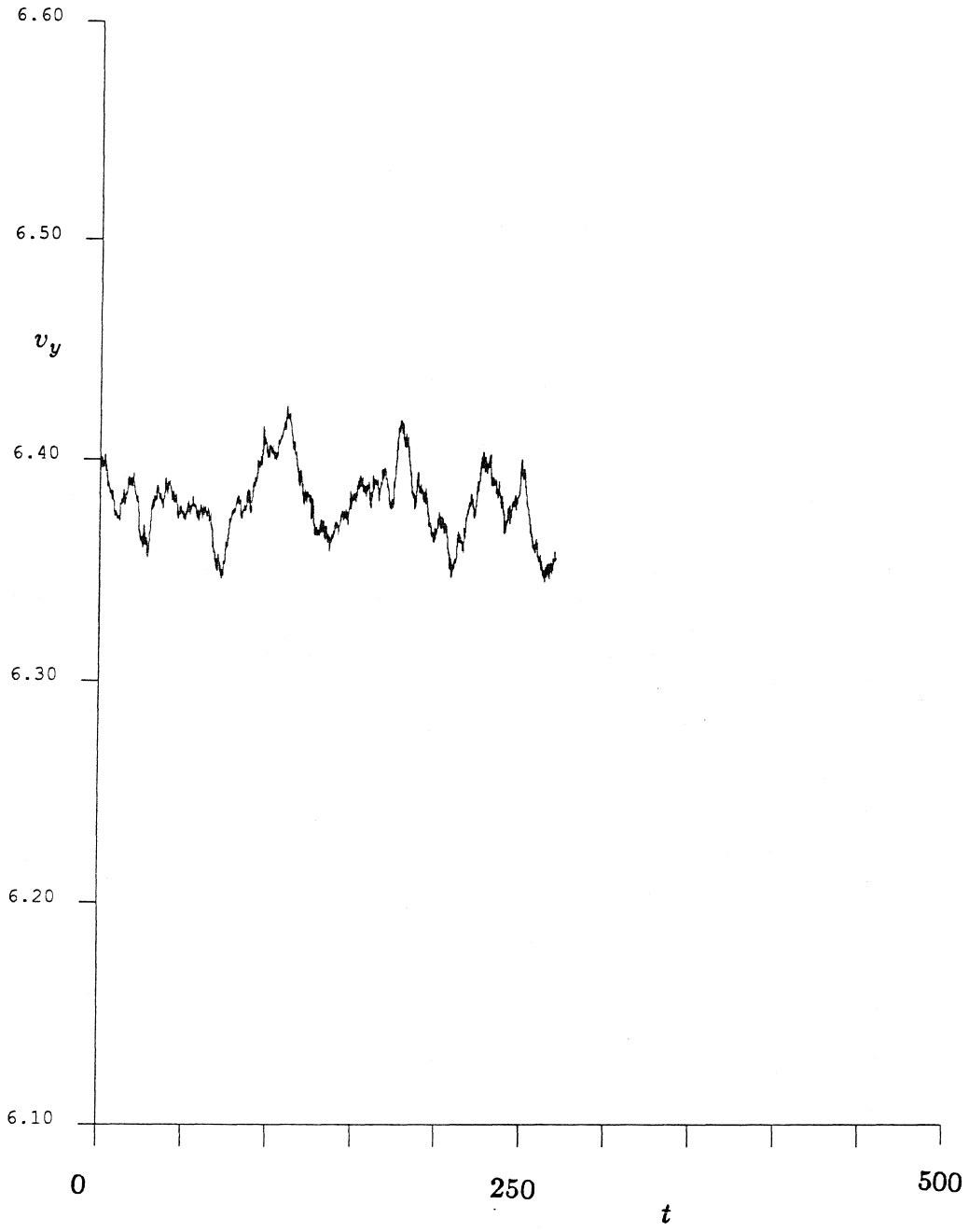

Figure B9.1 The time trace of v_y for the simulation nfr3.

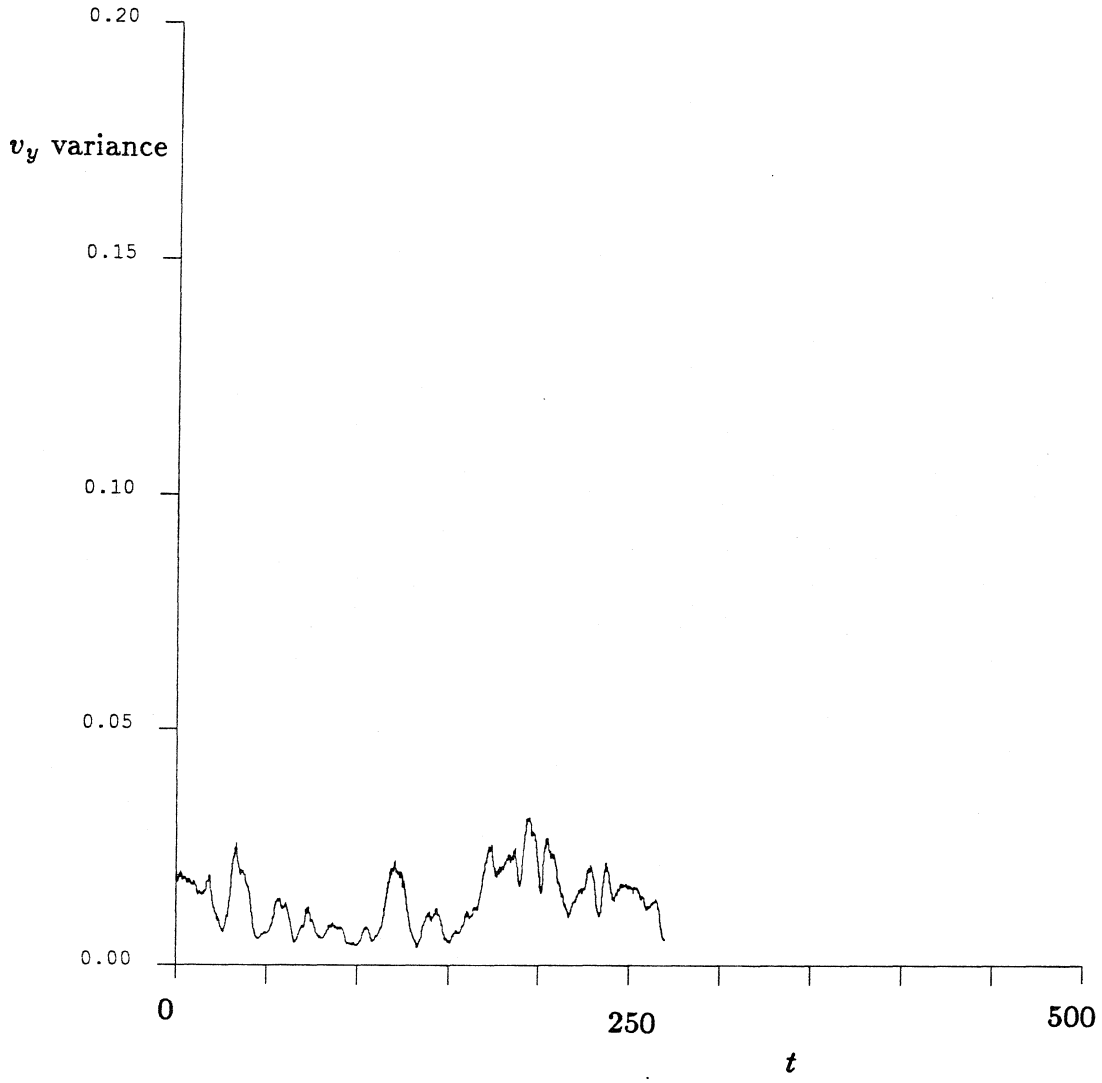

Figure B9.2 The time trace of the v_y variance for the simulation nfr3.

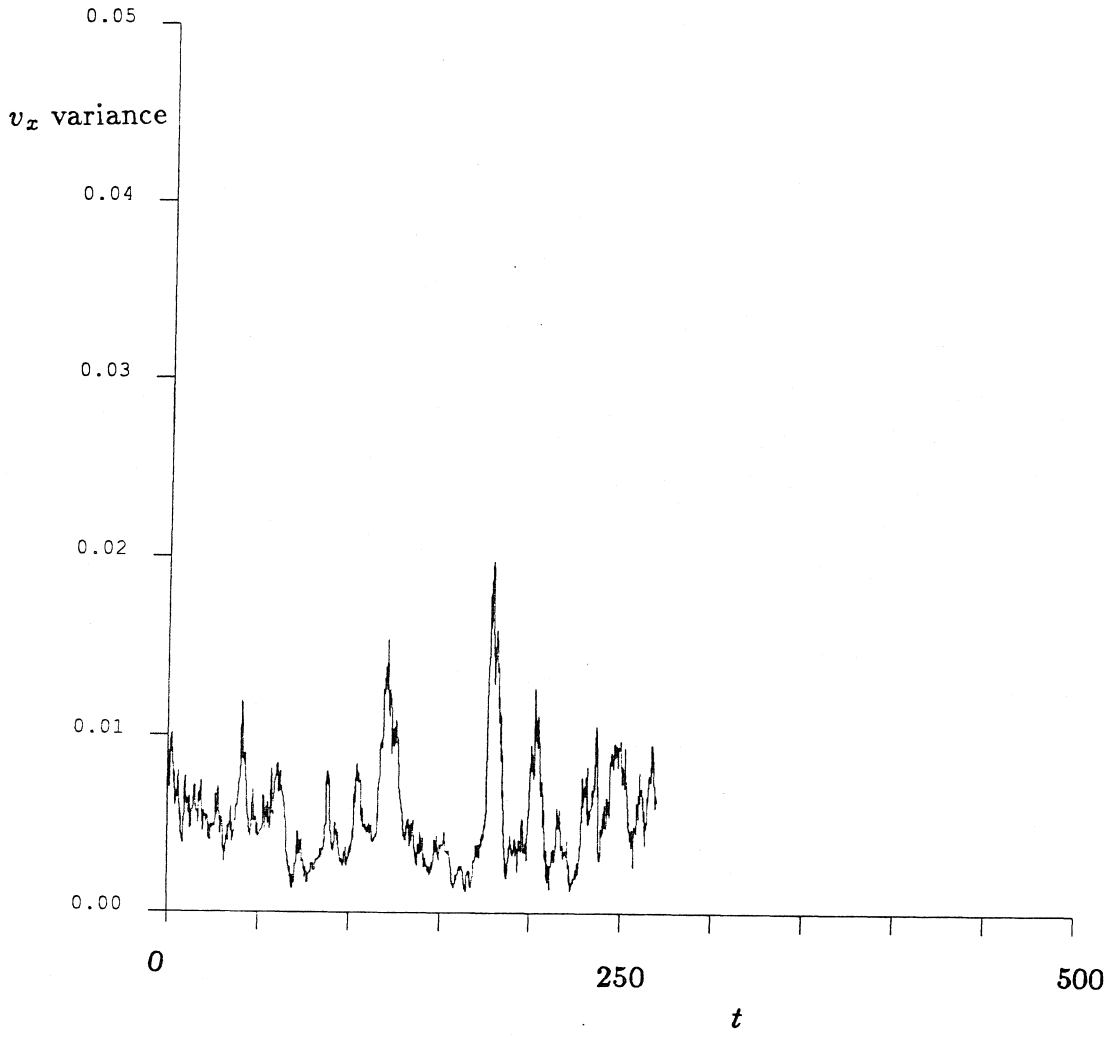

Figure B9.3 The time trace of the v_x variance for the simulation nfr3.

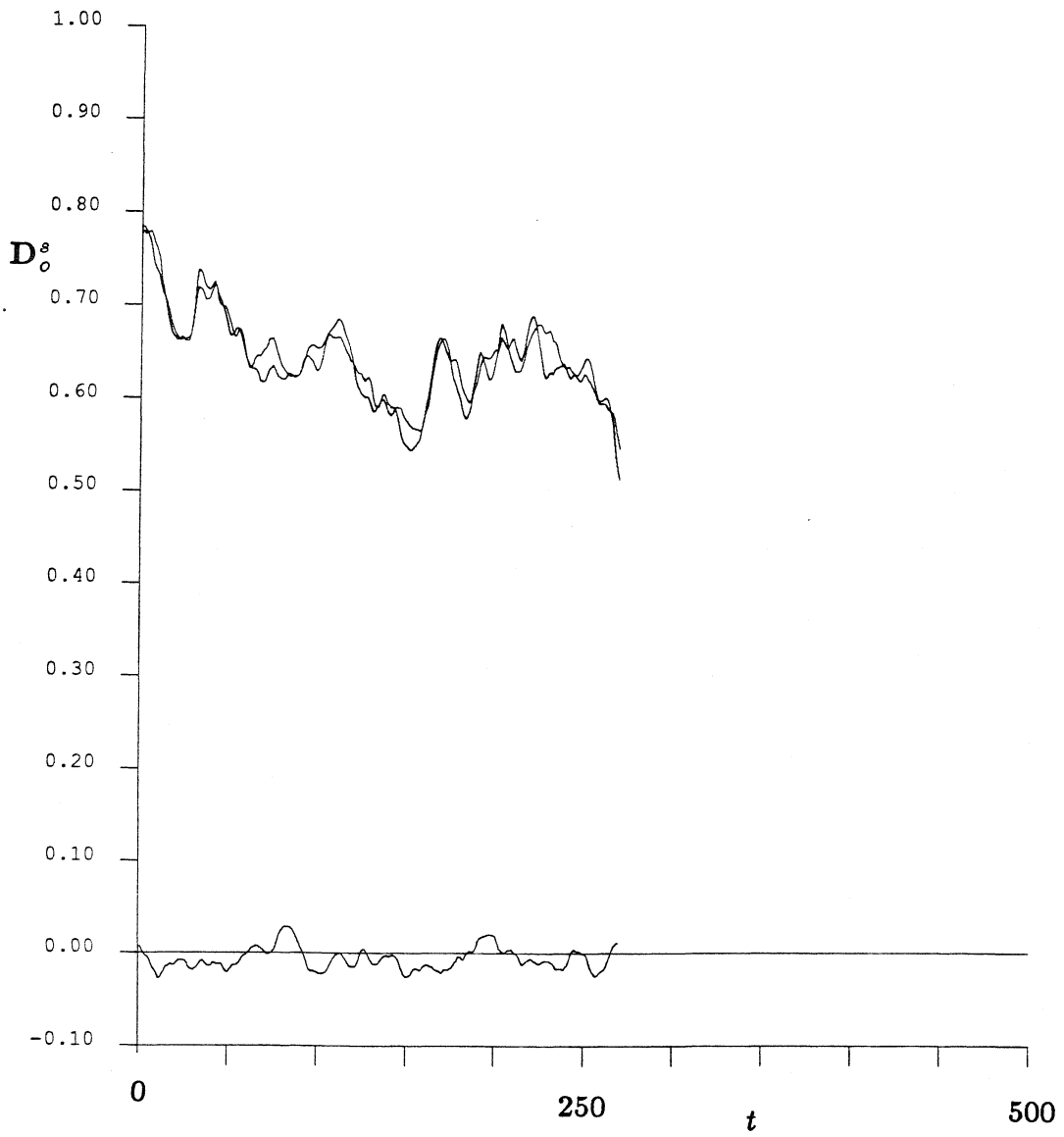

Figure B9.4 The time trace of $\mathbf{D}_o^s$ for the simulation nfr3. The upper two lines are the xx and yy components of this tensor. Of course, they should be equivalent for an infinite suspension – the slight variation occurs because of the finite number of spheres used in our simulation. The trace that fluctuates about the zero y-axis is the xy component of the short-time, self-diffusion tensor. Again, for an infinite number of spheres, this quantity would be exactly zero.

Appendix B10: The nfr4 simulation results

This simulation uses a non-Ewald, F method to approximate the hydrodynamic interactions. The simulation conditions are identical to the nfr2 simulation described in Appendix B8, except that the time step is 0.0025, instead of 0.001. The simulation terminated at 202 time units because of excessive sphere overlap. Excessive sphere overlap is defined as less than 1.99 radii separating any two sphere centers. The initial configuration is the same as in the FTSn simulations described in Appendix B1. There are 25 spheres within the periodic cell. The areal fraction is 0.453. There are interparticle forces present ($\tau = 10^5$). The time step is 0.0025 time unit. The mobility matrix is still inverted every 0.1 time unit. Position and velocity data is saved every 0.05 time unit. $\mathbf{D}_o^s$ is evaluated and reported at every time unit.

	nfr4
T	0-202
Cray/Sun	Cray 0.50
CPU(min)	8.6
v_y	-6.38150
v_x	-0.00496
v_y variance	0.01426
v_x variance	0.00684
v_{xy} variance	0.00002
$(D_\infty^s)_{yy}$	
$(D_\infty^s)_{xx}$	
$(D_o^s)_{yy}$	0.616
$(D_o^s)_{xx}$	0.622
$(D_o^s)_{xy}$	-0.0036
$g(2)$	
$g(3.5)$	
$g(4)$	

Table B10.1

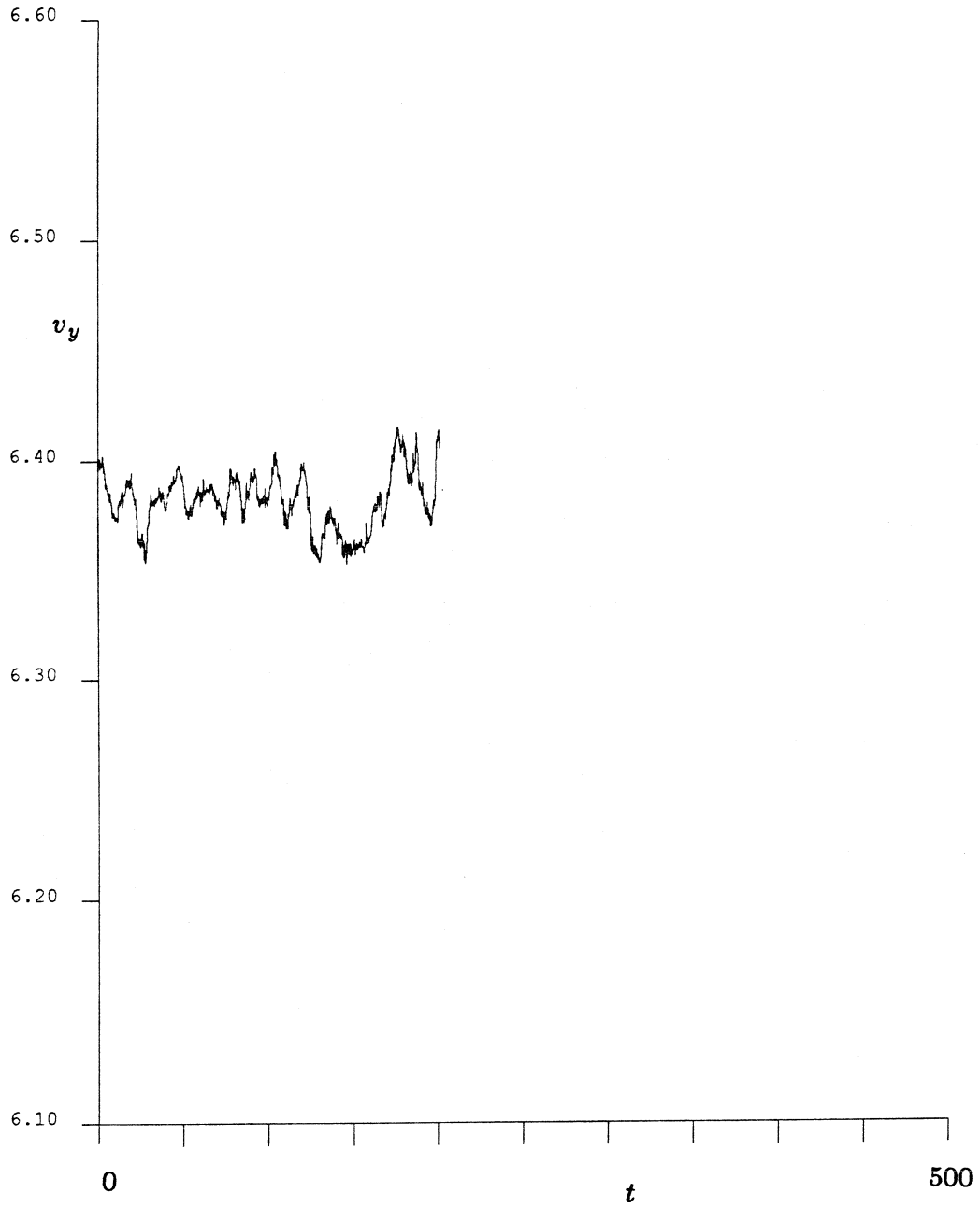

Figure B10.1 The time trace of v_y for the simulation nfr4.

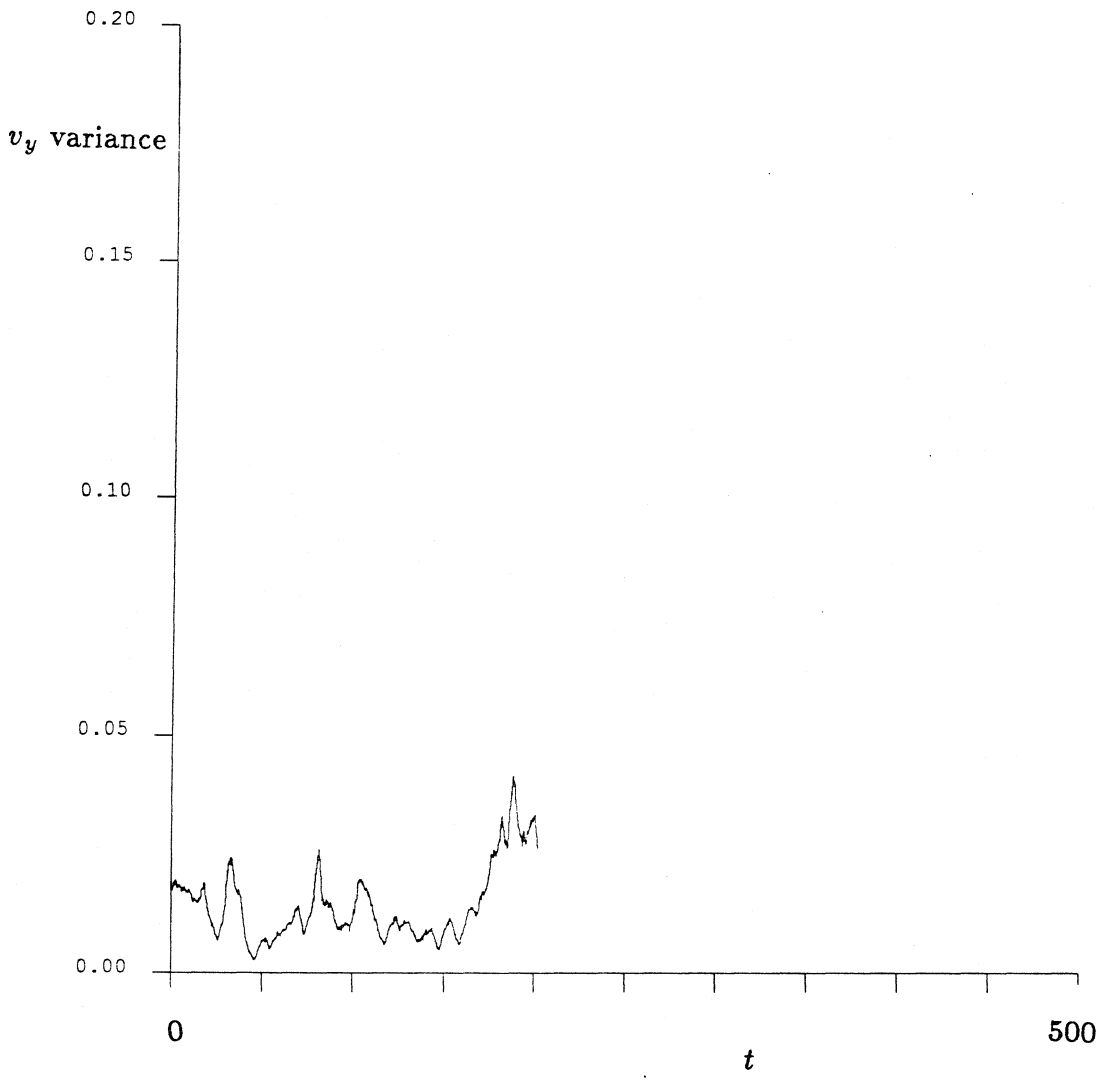

Figure B10.2 The time trace of the v_y variance for the simulation nfr4.

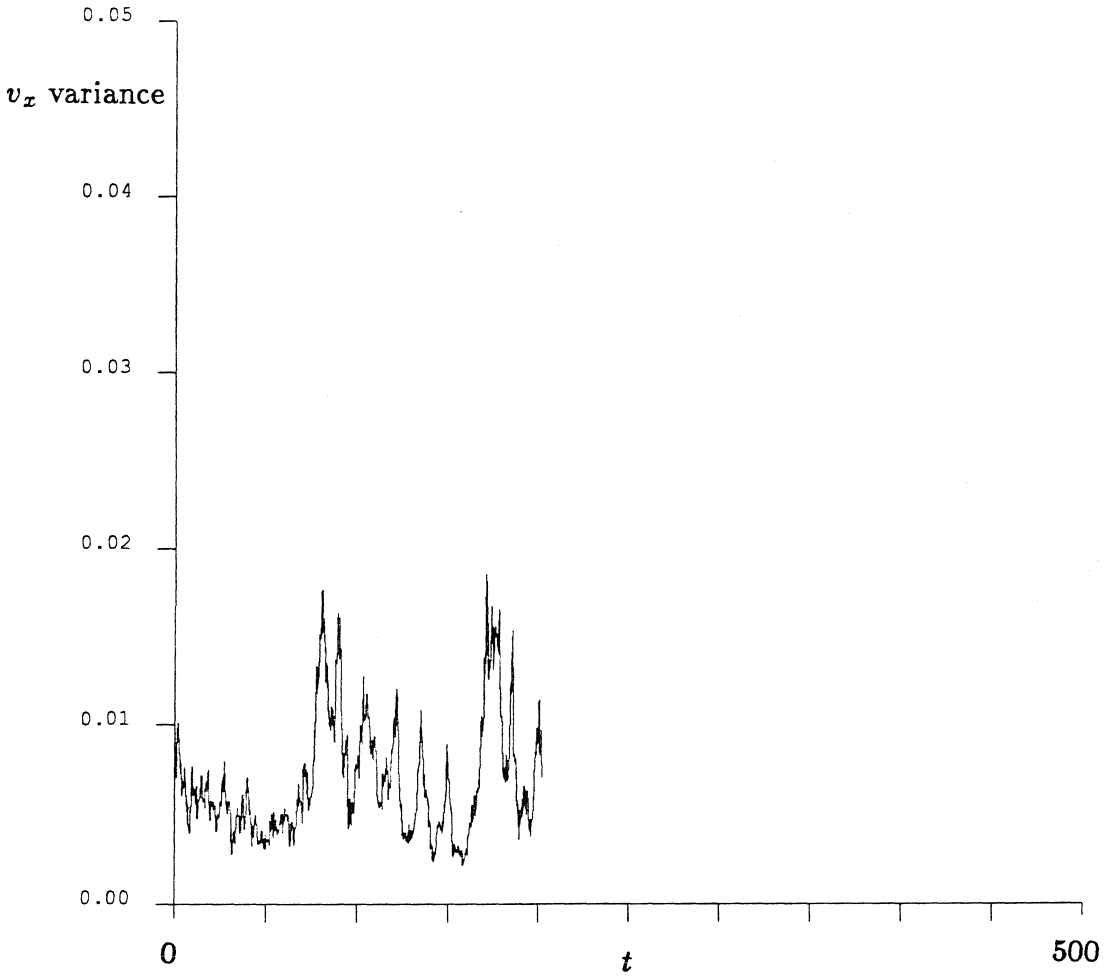

Figure B10.3 The time trace of the v_x variance for the simulation nfr4.

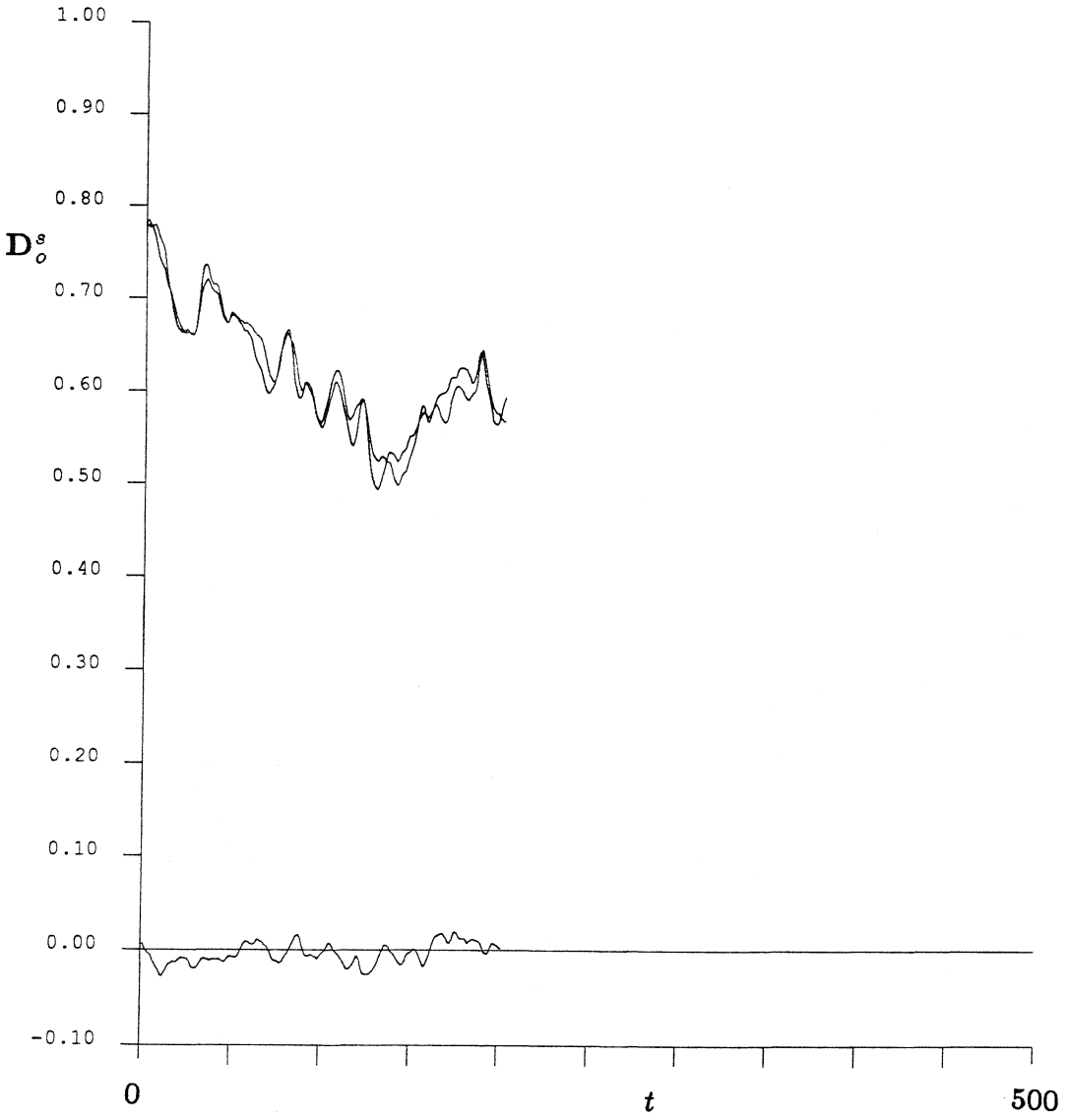

Figure B10.4 The time trace of $\mathbf{D}_o^s$ for the simulation nfr4. The upper two lines are the xx and yy components of this tensor. Of course, they should be equivalent for an infinite suspension – the slight variation occurs because of the finite number of spheres used in our simulation. The trace that fluctuates about the zero y-axis is the xy component of the short-time, self-diffusion tensor. Again, for an infinite number of spheres, this quantity would be exactly zero.

Appendix B11a: The efr1 simulation results

This simulation uses an Ewald, F method to approximate the hydrodynamic interactions. The separation factor, z_l, is 2. 126 image cells are used to insure the convergence of the mobility interactions. The simulation terminated at 88 time units because of excessive sphere overlap. Excessive sphere overlap is defined as less than 1.99 radii separating any two sphere centers. The initial configuration is the same as in the FTSn simulations described in Appendix B1. There are 25 spheres within the periodic cell. The areal fraction is 0.453. There are interparticle forces present ($\tau = 10^5$). The time step is 0.005 time unit. The mobility matrix is inverted every 0.1 time unit. Position and velocity data is saved every 0.05 time unit. $\mathbf{D}_o^s$ is evaluated and reported at every time unit.

	efr1
T	0-88
Cray/Sun	Cray 0.50
CPU(min)	15.2
v_y	-5.00200
v_x	-0.00405
v_y variance	0.00895
v_x variance	0.00246
v_{xy} variance	-0.00048
$(D_\infty^s)_{yy}$	
$(D_\infty^s)_{xx}$	
$(D_o^s)_{yy}$	0.643
$(D_o^s)_{xx}$	0.648
$(D_o^s)_{xy}$	-0.0041
$g(2)$	
$g(3.5)$	
$g(4)$	

Table B11a.1

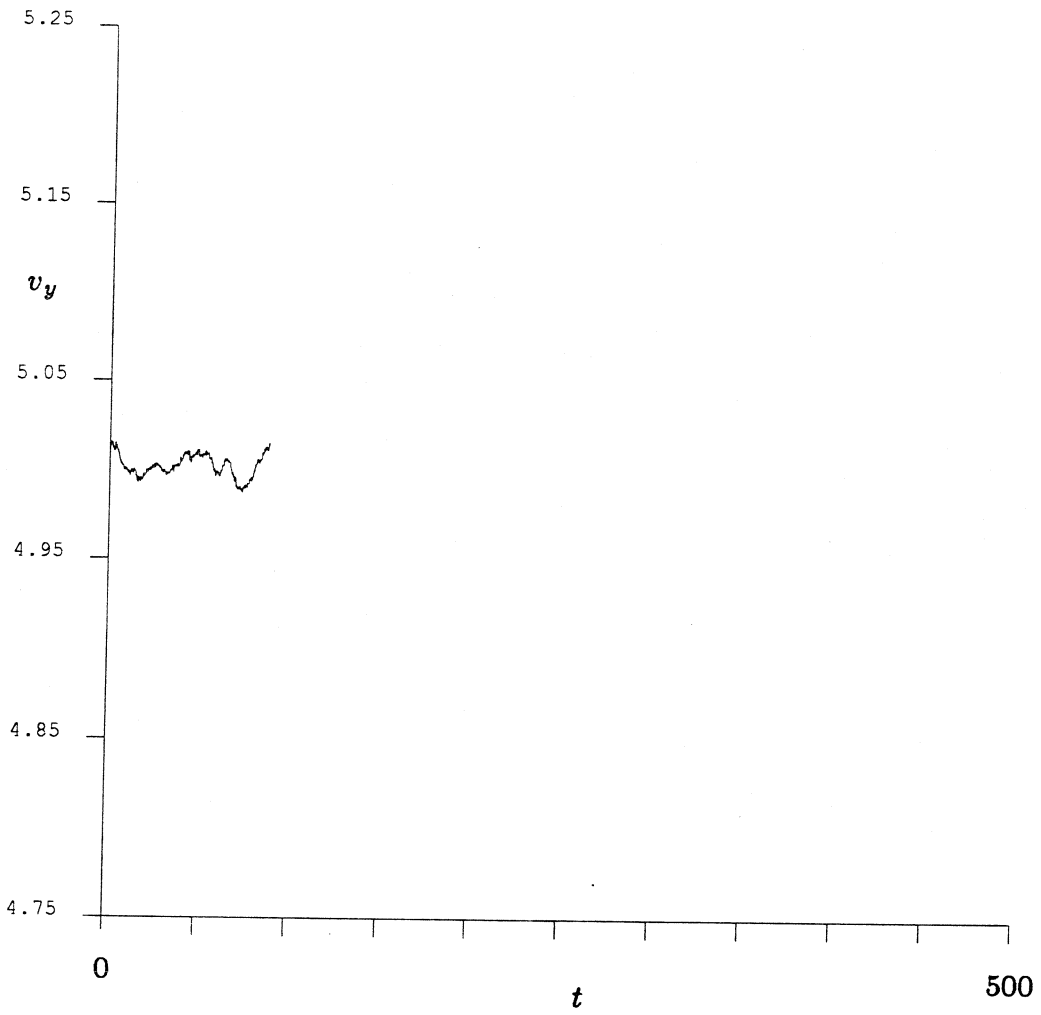

Figure B11a.1 The time trace of v_y for the simulation efr1.

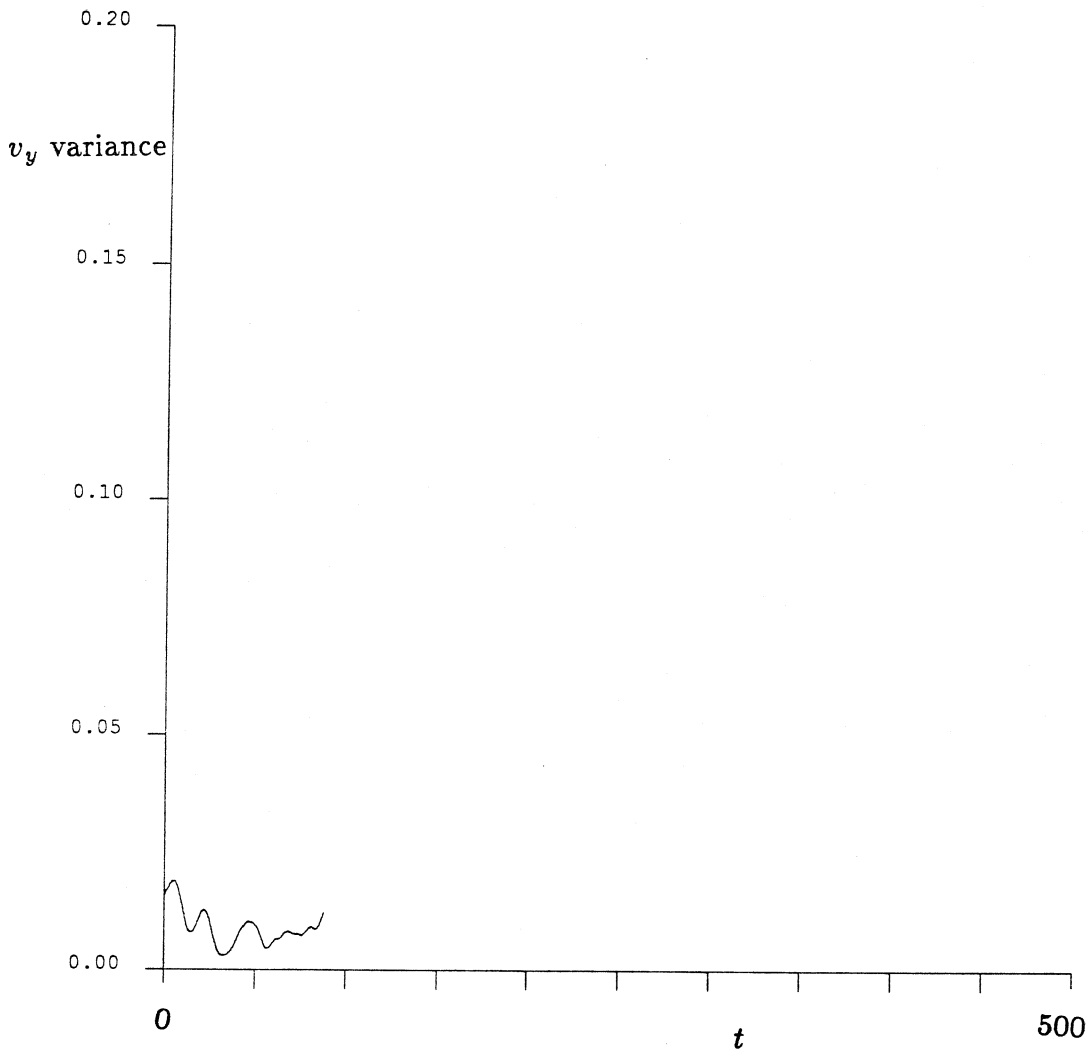

Figure B11a.2 The time trace of the v_y variance for the simulation efr1.

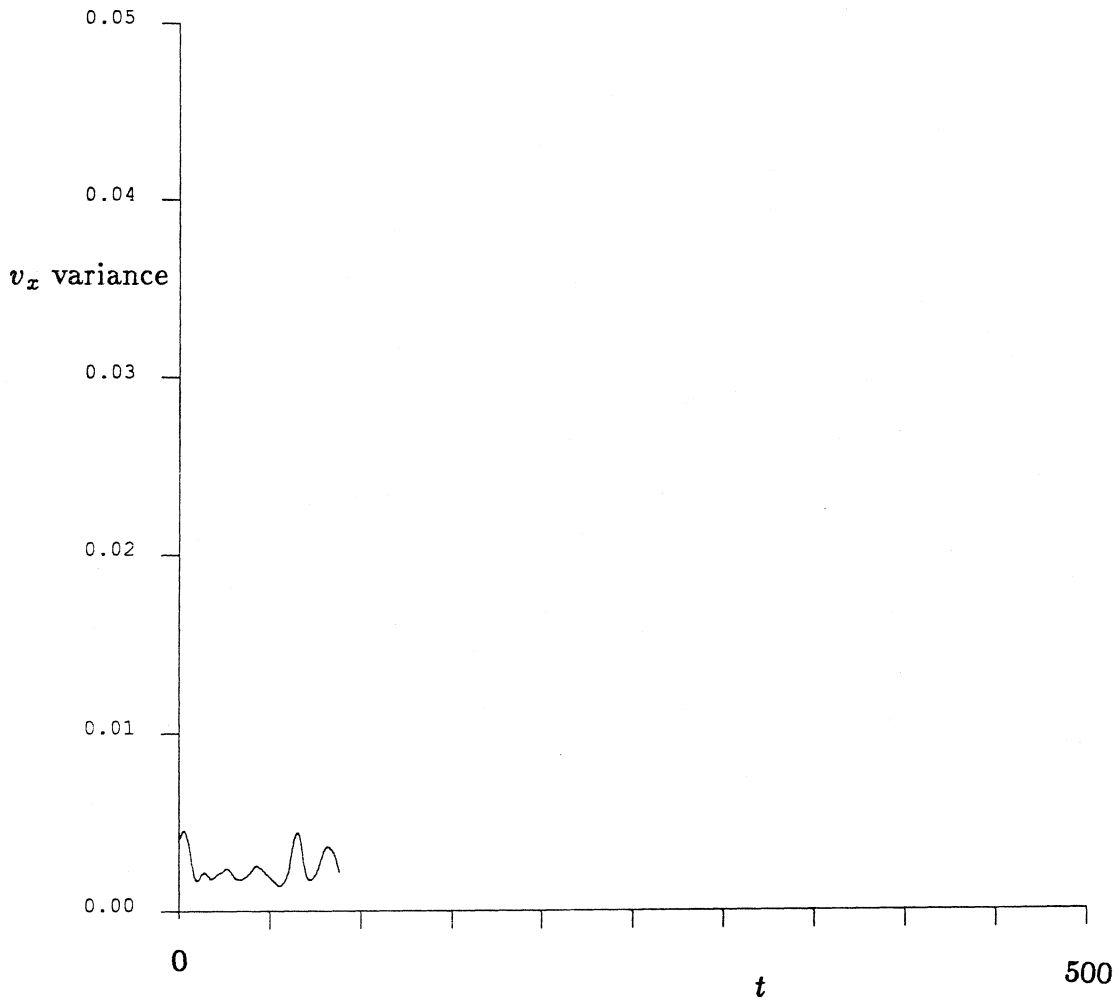

Figure B11a.3 The time trace of the v_x variance for the simulation efr1.

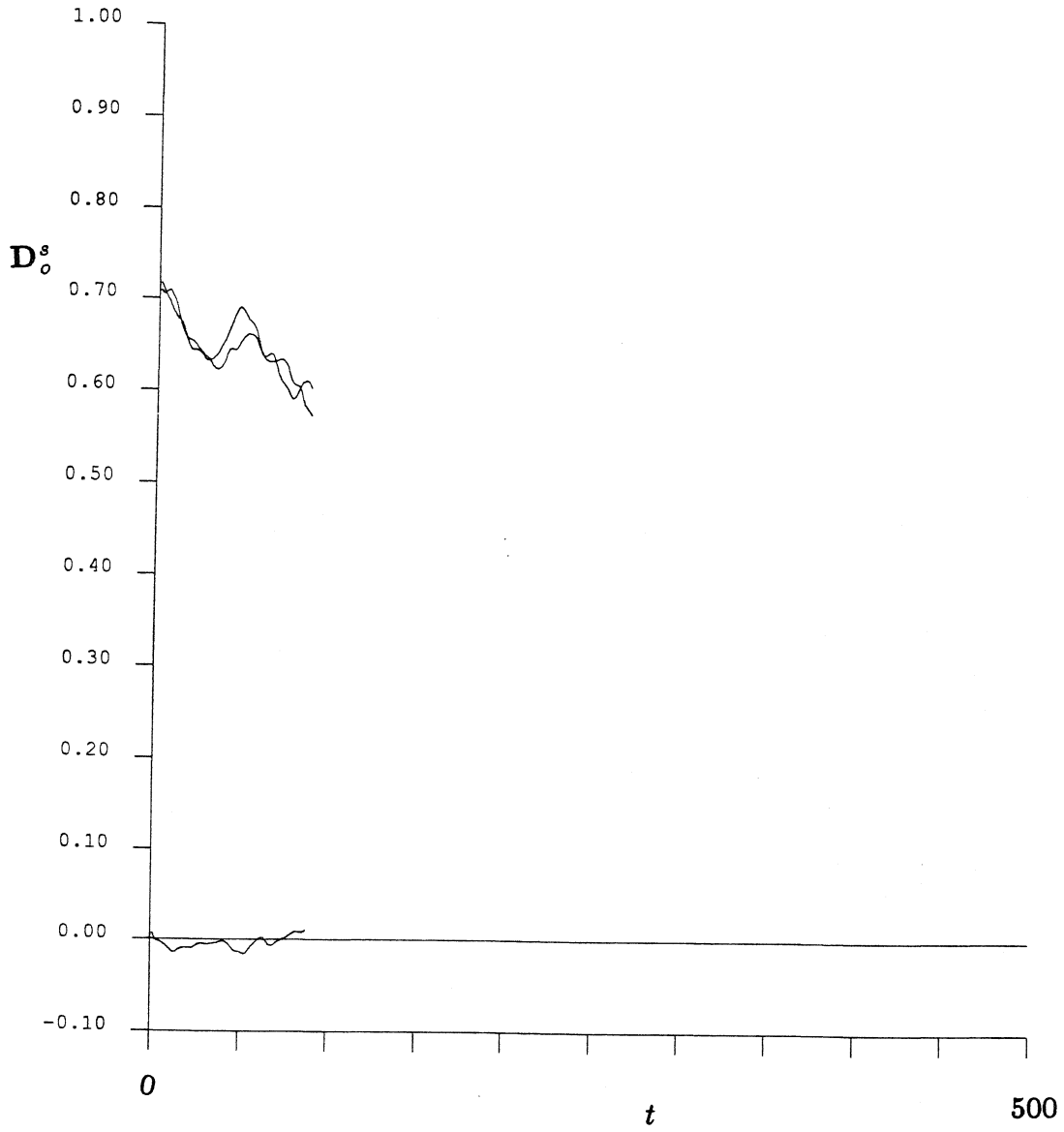

Figure B11a.4 The time trace of $\mathbf{D}_o^s$ for the simulation efr1. The upper two lines are the xx and yy components of this tensor. Of course, they should be equivalent for an infinite suspension – the slight variation occurs because of the finite number of spheres used in our simulation. The trace that fluctuates about the zero y-axis is the xy component of the short-time, self-diffusion tensor. Again, for an infinite number of spheres, this quantity would be exactly zero.

Appendix B11b: The efr2 simulation results

This simulation uses an Ewald, F method to approximate the hydrodynamic interactions. The separation factor, z_l, is 2. 126 image cells are used to insure the convergence of the mobility interactions. The simulation conditions are identical to those in the efr1 simulations described in Appendix B11a, except that the time step is 0.0025 time unit. The final time is 500 time units. The initial configuration is the same as in the FTSn simulations described in Appendix B1. There are 25 spheres within the periodic cell. The areal fraction is 0.453. There are interparticle forces present ($\tau = 10^5$). The time step is 0.0025 time unit. The mobility matrix is inverted every 0.1 time unit. Position and velocity data is saved every 0.05 time unit. $\mathbf{D}_o^s$ is evaluated and reported at every time unit.

	efr2
T	0-500
Cray/Sun	Cray 0.50
CPU(min)	95
v_y	-5.00617
v_x	0.00289
v_y variance	0.01318
v_x variance	0.00274
v_{xy} variance	-0.00008
$(D_\infty^s)_{yy}$	0.22
$(D_\infty^s)_{xx}$	0.027
$(D_o^s)_{yy}$	0.603
$(D_o^s)_{xx}$	0.601
$(D_o^s)_{xy}$	0.0035
$g(2)$	12.1
$g(3.5)$	0.86
$g(4)$	1.45

Table B11b.1

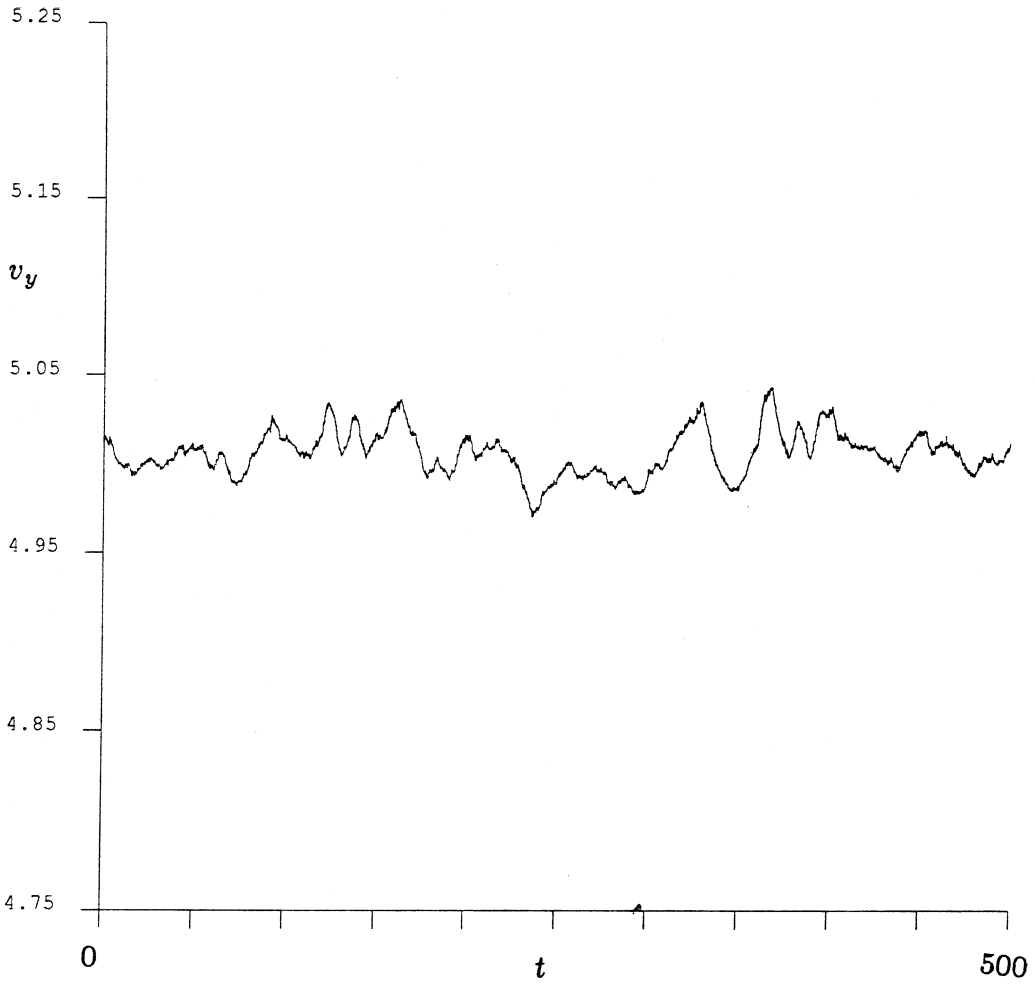

Figure B11b.1 The time trace of v_y for the simulation efr2.

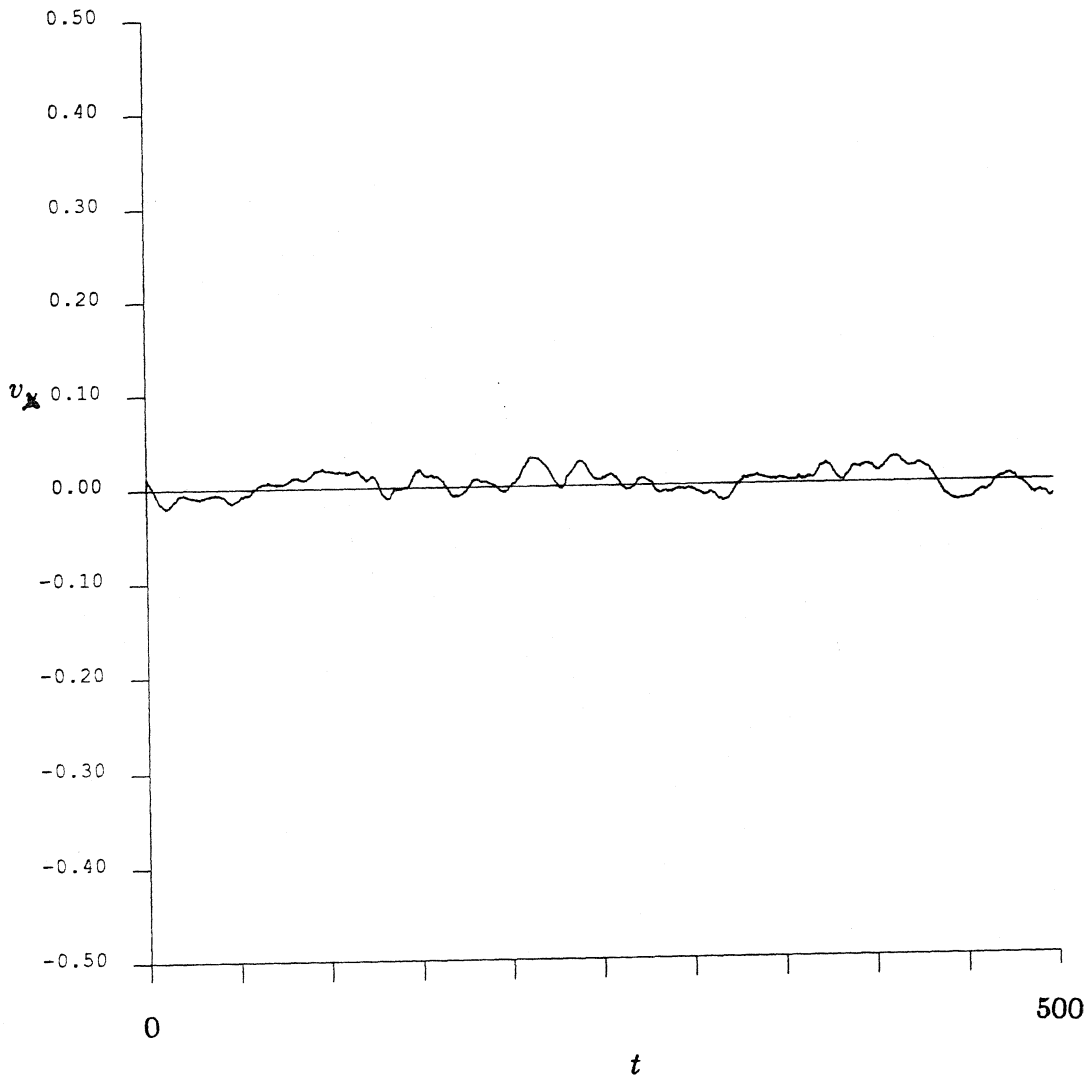

Figure B11b.2 The time trace of v_x for the simulation efr2.

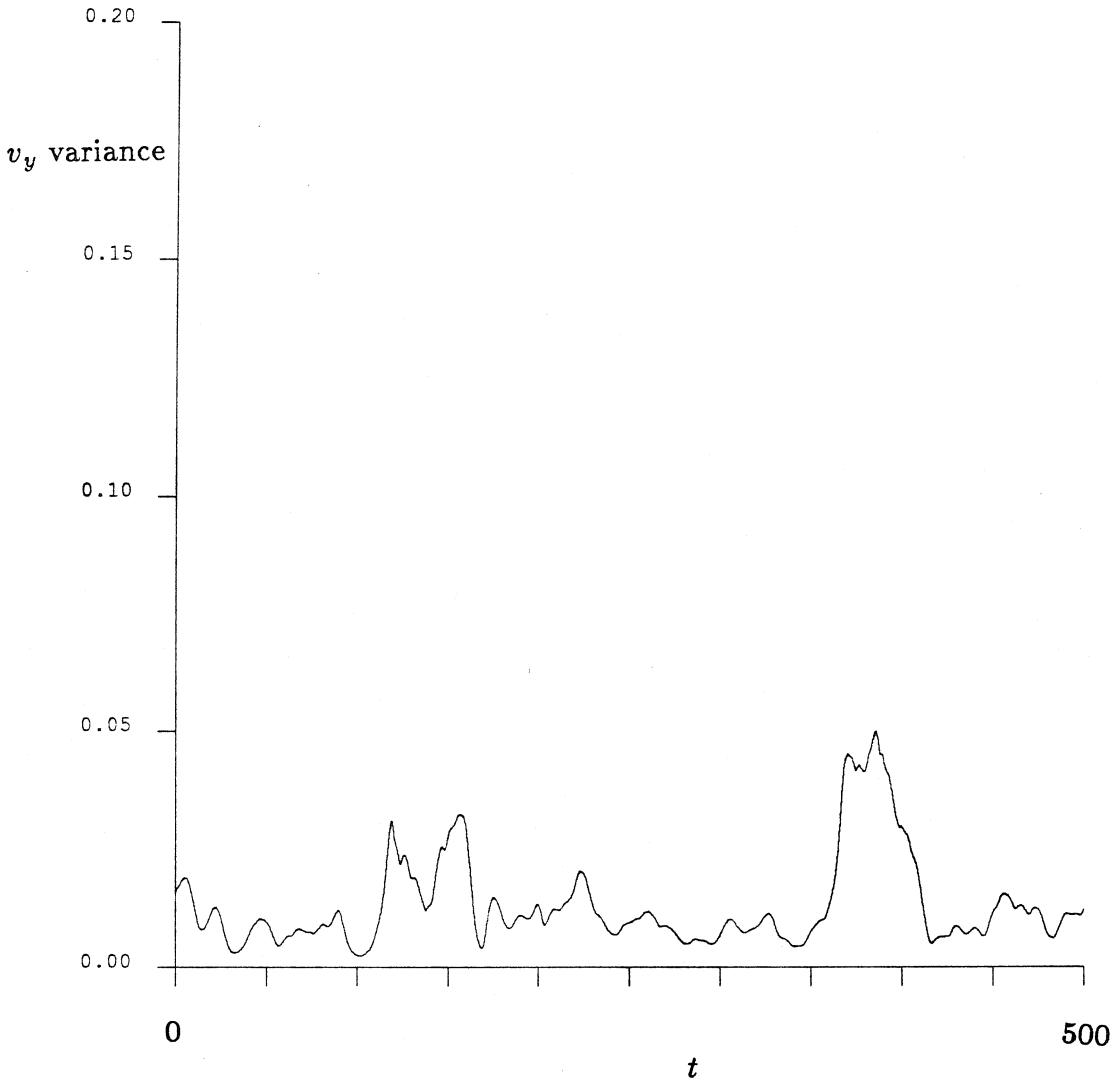

Figure B11b.3 The time trace of the v_y variance for the simulation efr2.

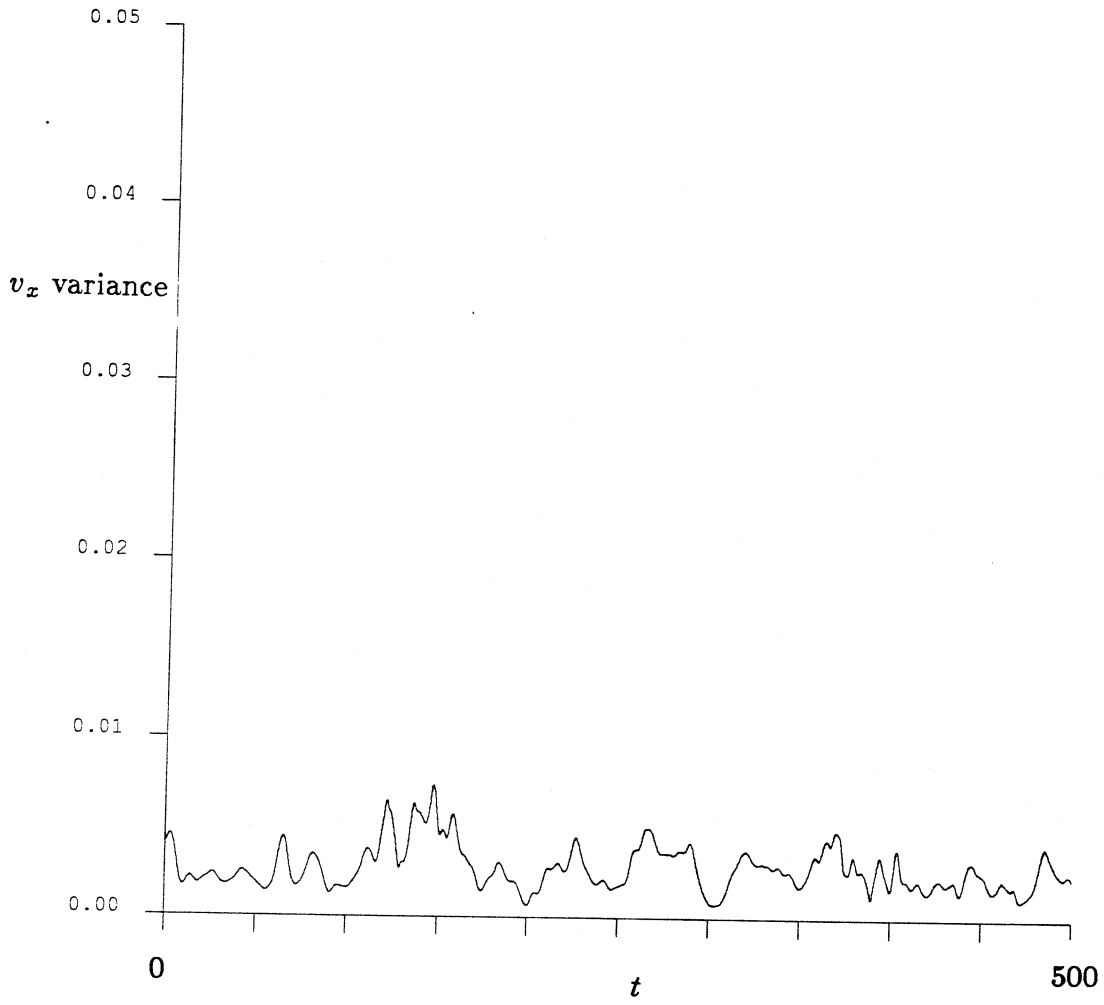

Figure B11b.4 The time trace of the v_x variance for the simulation efr2.

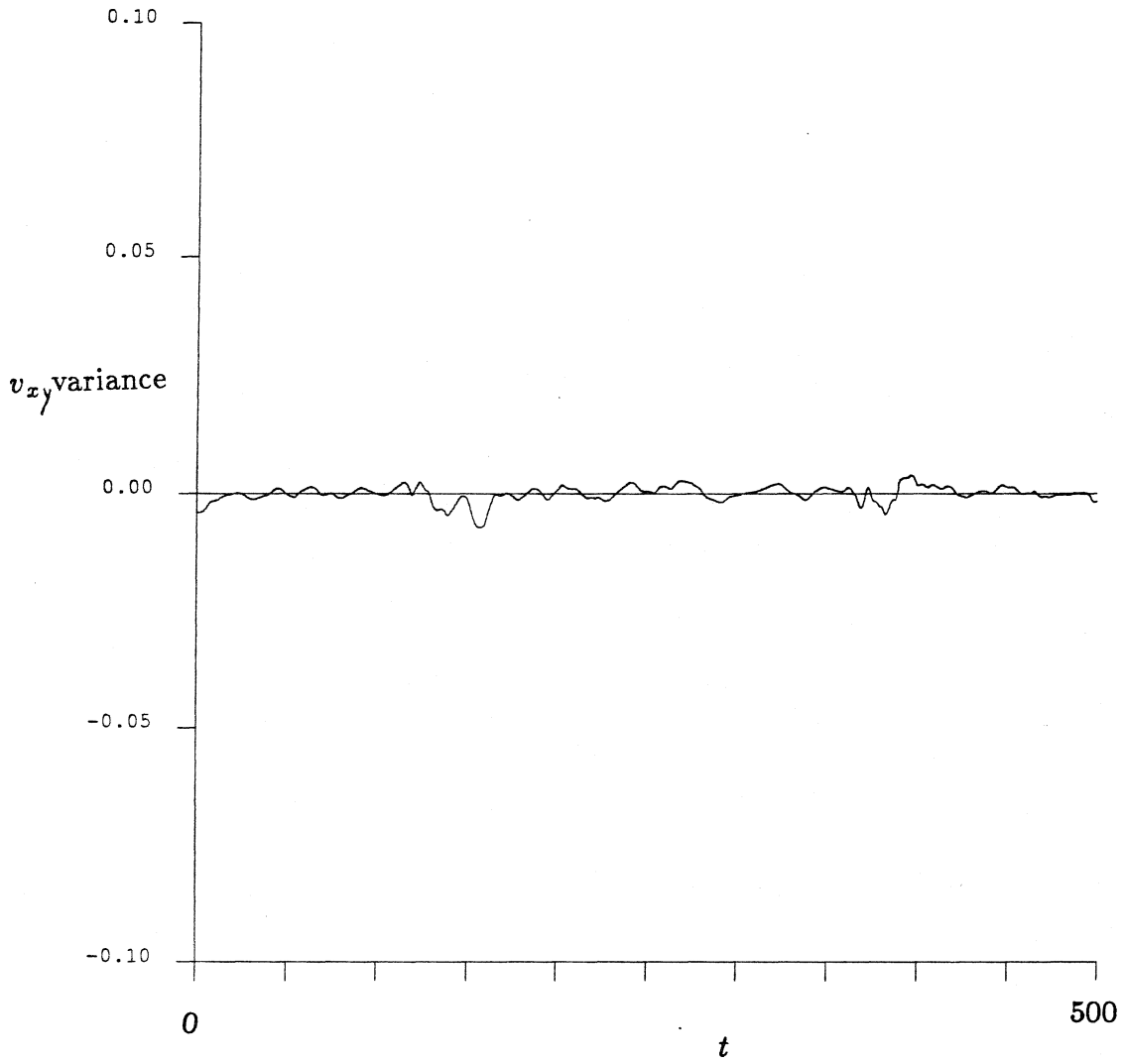

Figure B11b.5 The time trace of the v_{xy} variance for the simulation efr2.

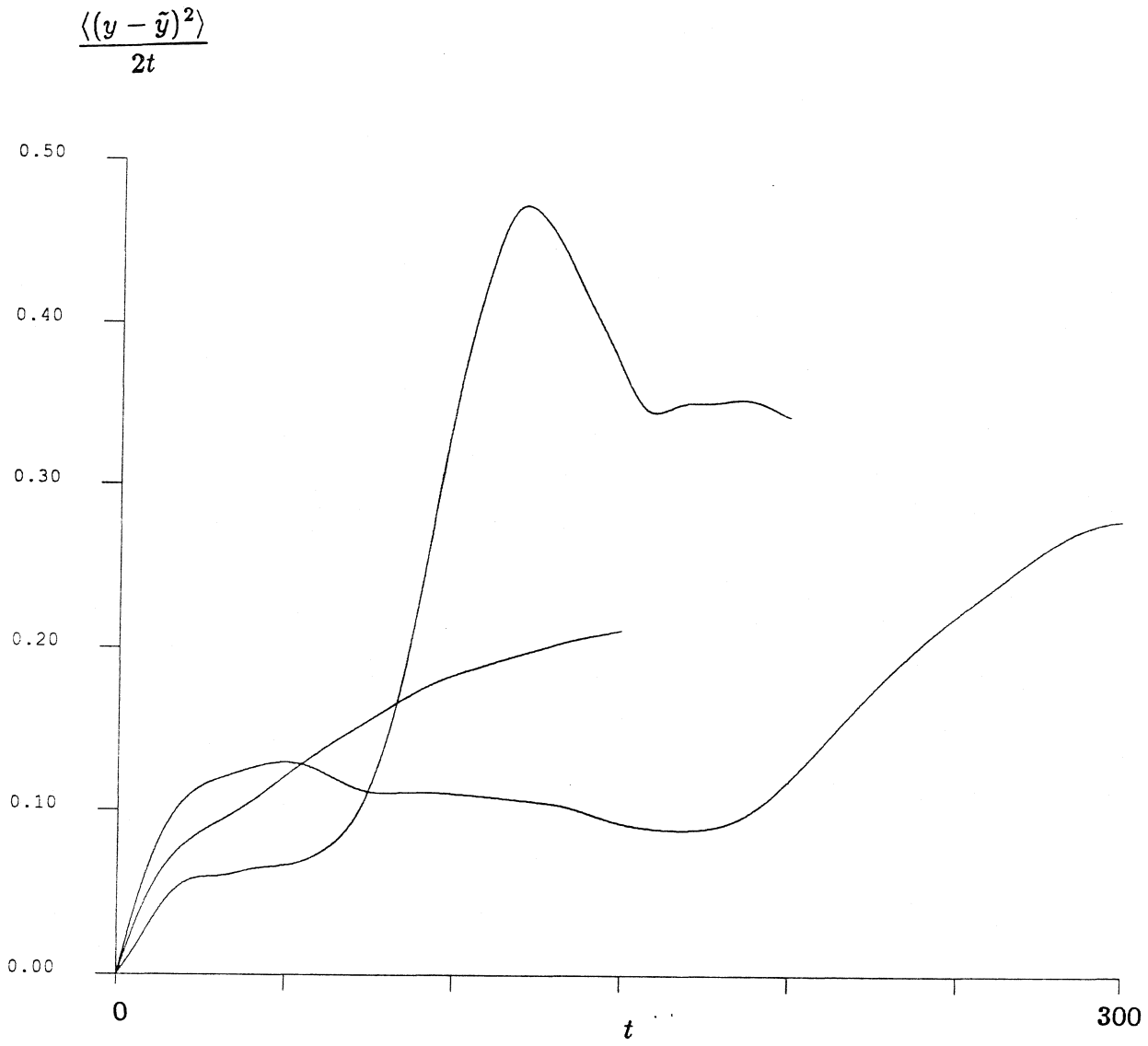

Figure B11b.6 A $(D^s_\infty)_{yy}$-defining graph using displacement data from efr2 (t= 100 – 500). The graph interval is 150, 200, and 300 time units, and the time between interval initial conditions is 0.01 time unit.

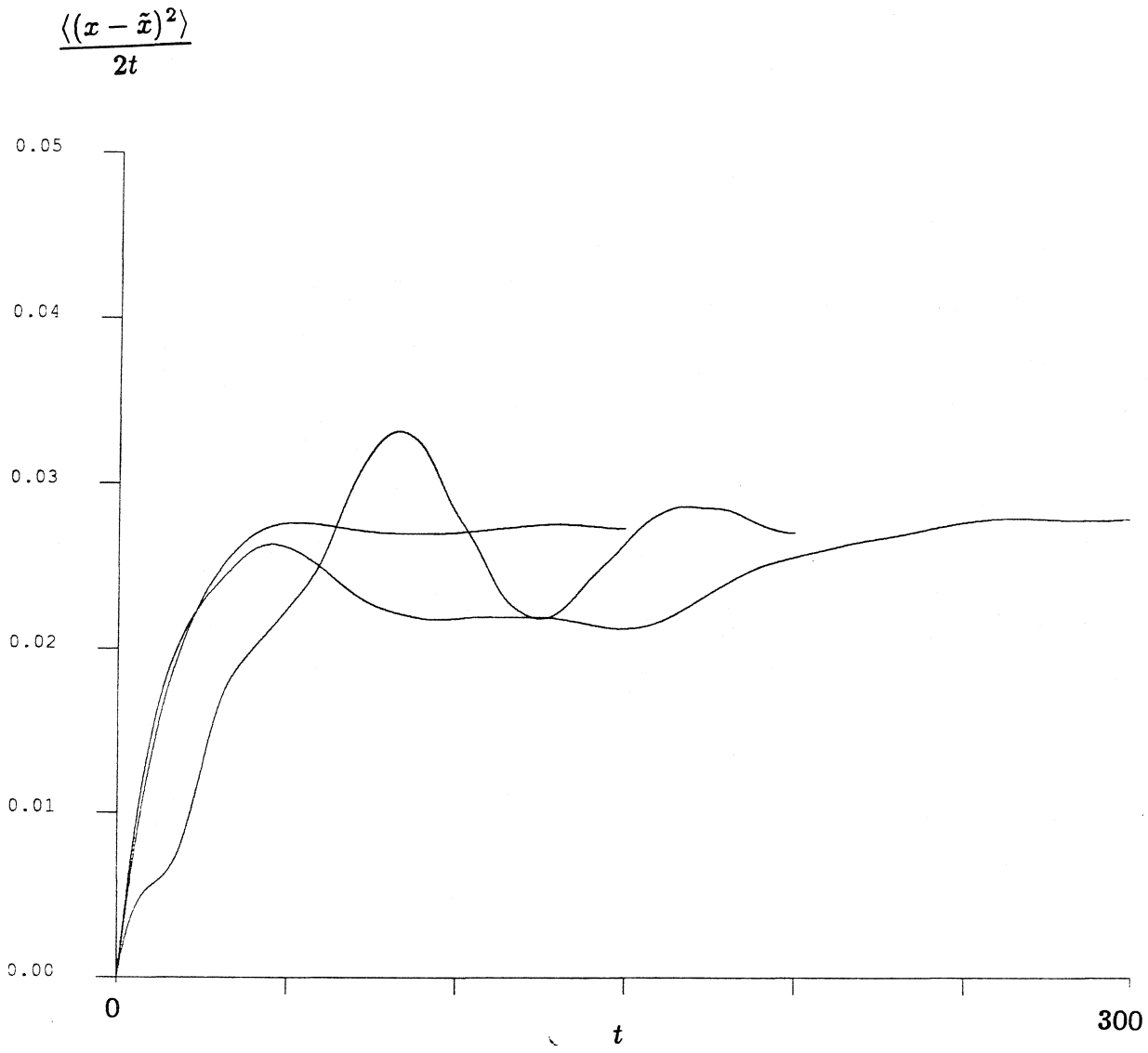

Figure B11b.7 A $(D^s_\infty)_{xx}$-defining graph using displacement data from efr2 (t= 100 – 500). The graph interval is 150, 200, and 300 time units, and the time between interval initial conditions is 0.01 time unit.

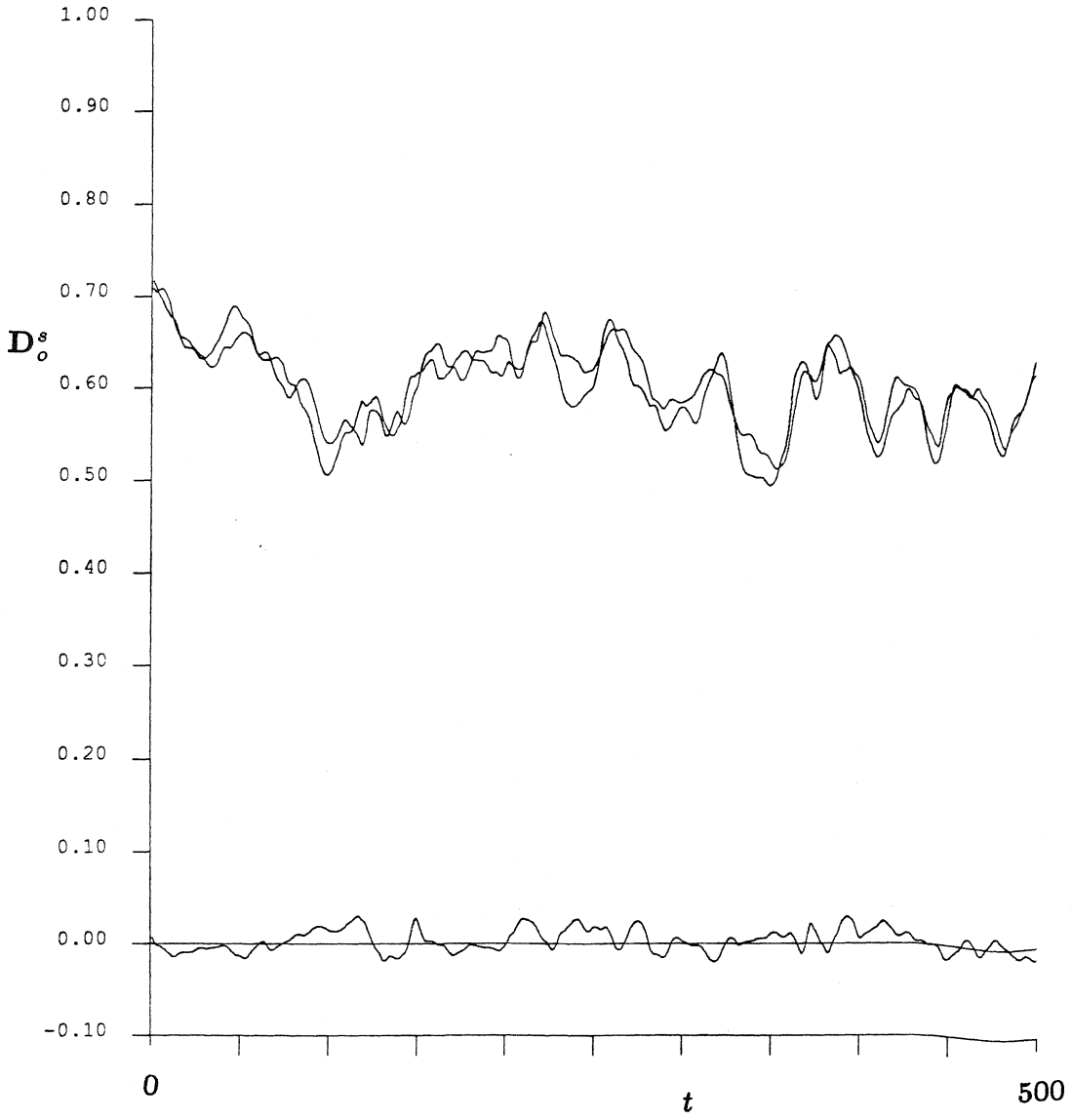

Figure B11b.8 The time trace of $\mathbf{D}_o^s$ for the simulation efr2. The upper two lines are the xx and yy components of this tensor. Of course, they should be equivalent for an infinite suspension – the slight variation occurs because of the finite number of spheres used in our simulation. The trace that fluctuates about the zero y-axis is the xy component of the short-time, self-diffusion tensor. Again, for an infinite number of spheres, this quantity would be exactly zero.

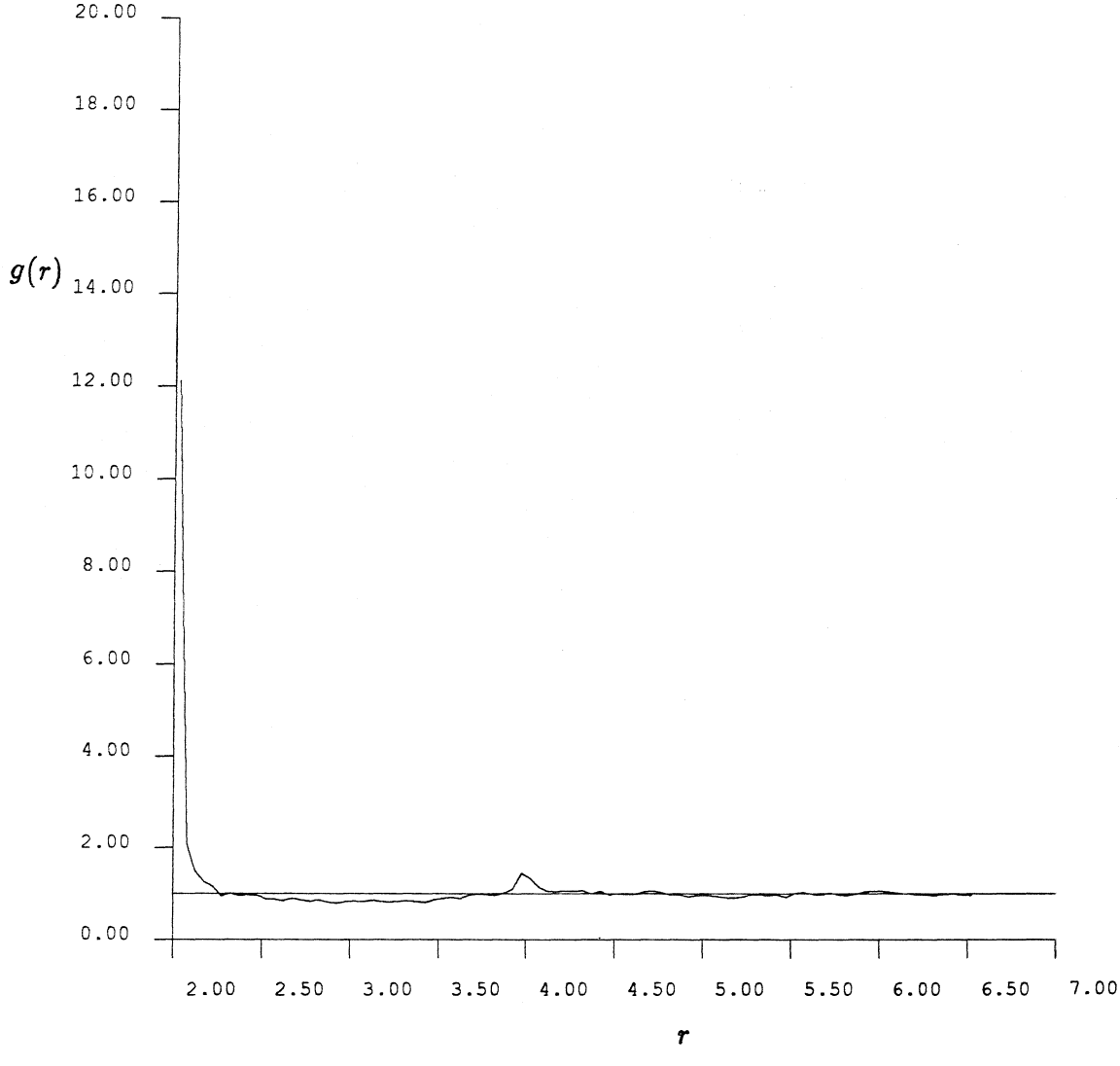

Figure B11b.9 The radial pair-distribution function, $g(r)$, for the efr2 run ($t = 100 - 500$).

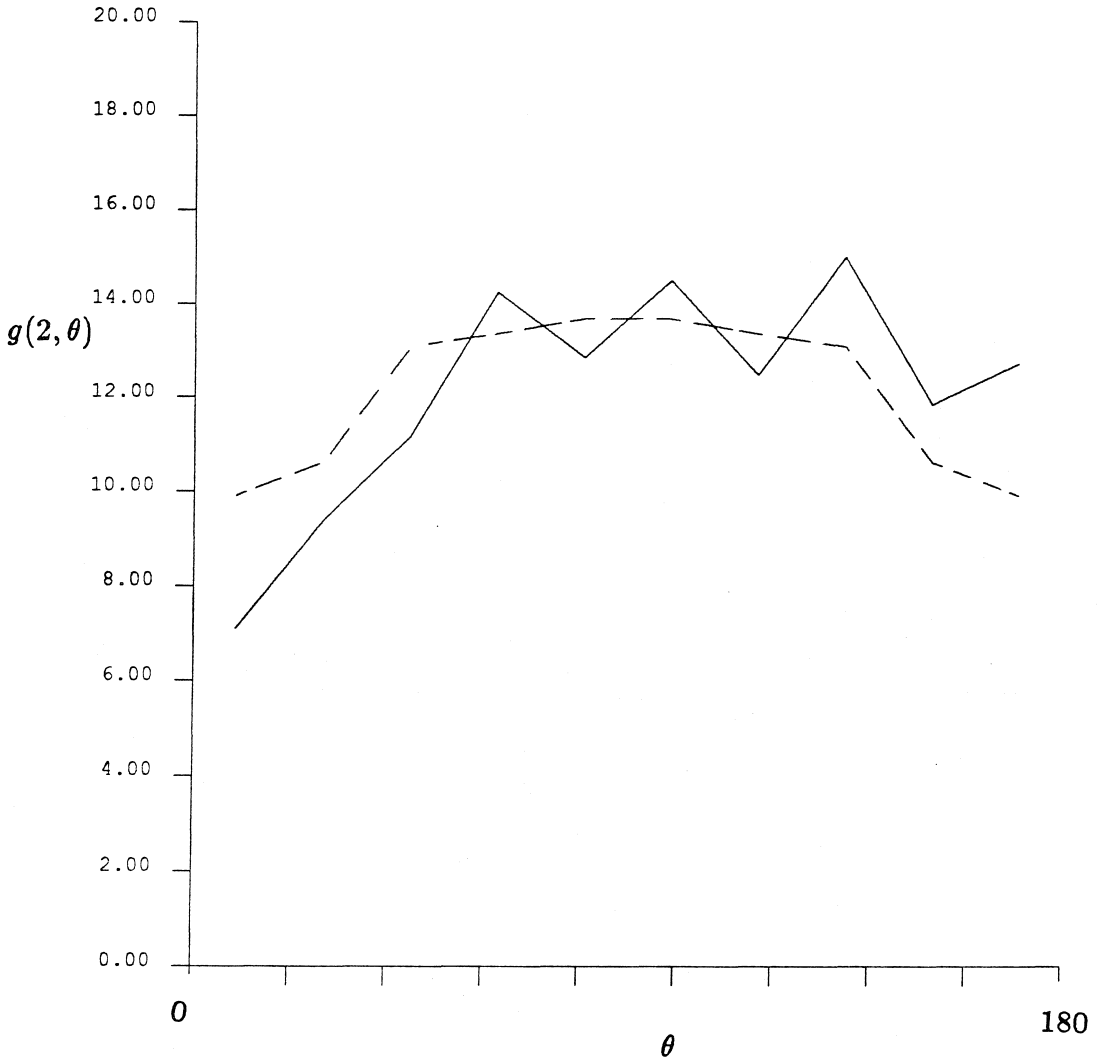

Figure B11b.10 The full pair-distribution function for spheres whose surfaces are separated by less than 0.05 radii using data from the efr2 run (t = 100 – 500). The dashed curve represents this function when it is forced to be symmetric about $\theta = 90°$.

Appendix B12: The phi1efr simulation results

This suite of simulations uses an Ewald, F method to approximate the hydrodynamic interactions. The separation factor, z_l, is 2. 126 image cells are used to insure the convergence of the mobility interactions. Two separate simulation runs follow the evolution of a sedimenting system to a final time of 1000 time units. There are 25 spheres in the periodic cell. The areal fraction is 0.1. There are interparticle forces present ($\tau = 10^5$). The initial configuration is taken from a Monte-Carlo simulation. The time step is 0.005 time unit. The mobility matrix is inverted every 0.1 time unit. Position and velocity data is saved every 0.05 time unit. $\mathbf{D}_o^s$ is evaluated and reported at every time unit.

	phi1efr1	phi1ef2
T	0-500	500-1000
Cray/Sun	Cray 0.50	Cray 0.50
CPU(min)	84.7	85.0
v_y	-3.29081	-3.30232
v_x	0.00104	0.00250
v_y variance	0.09987	0.11198
v_x variance	0.01011	0.01158
v_{xy} variance	-0.00201	0.00075
$(D_\infty^s)_{yy}$	3.8	4.77
$(D_\infty^s)_{xx}$		0.11
$(D_o^s)_{yy}$	0.894	0.894
$(D_o^s)_{xx}$	0.896	0.897
$(D_o^s)_{xy}$	-0.0014	0.0006
$g(2)$		13.0
$g(3.5)$		0.80
$g(4)$		1.07

Table B12.1

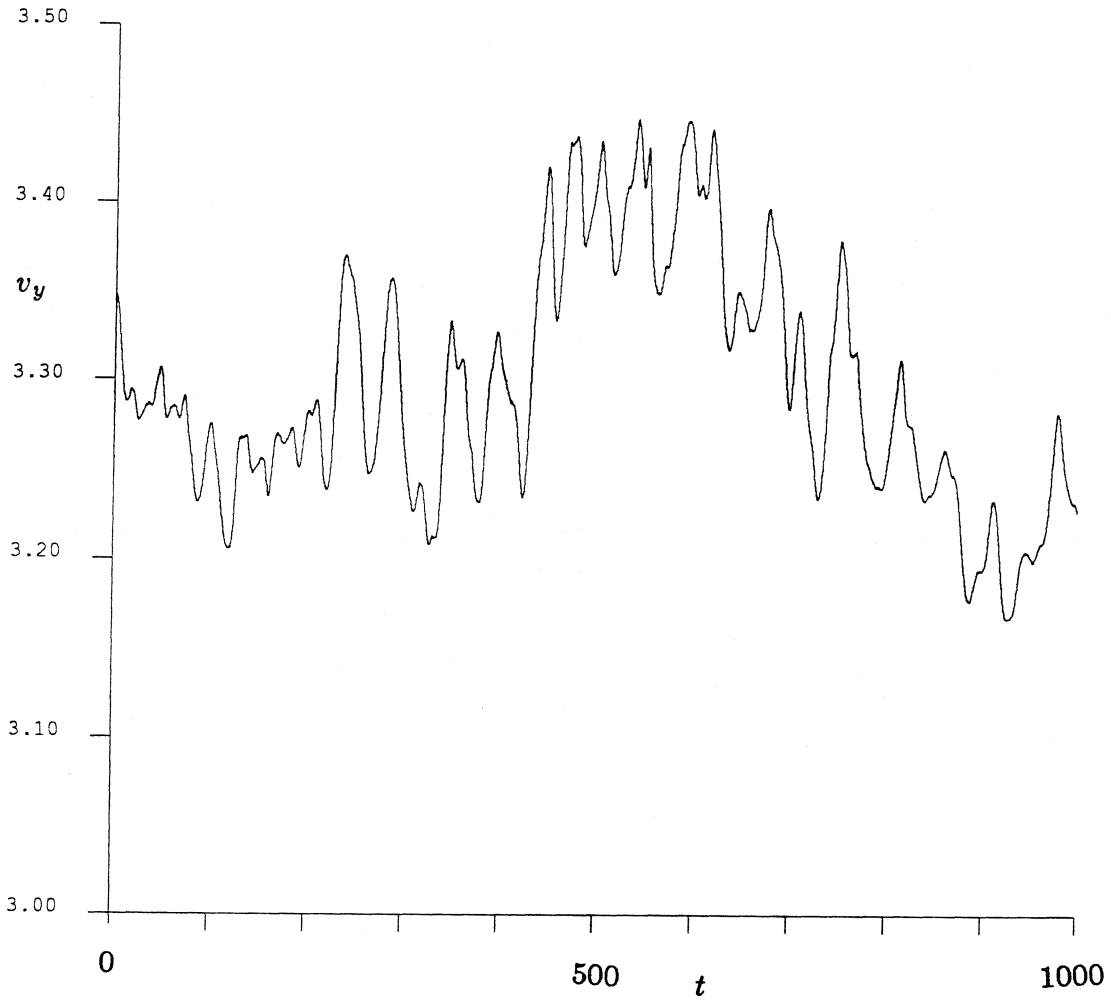

Figure B12.1 The time trace of v_y for the simulations phi1efr1 and phi1efr2.

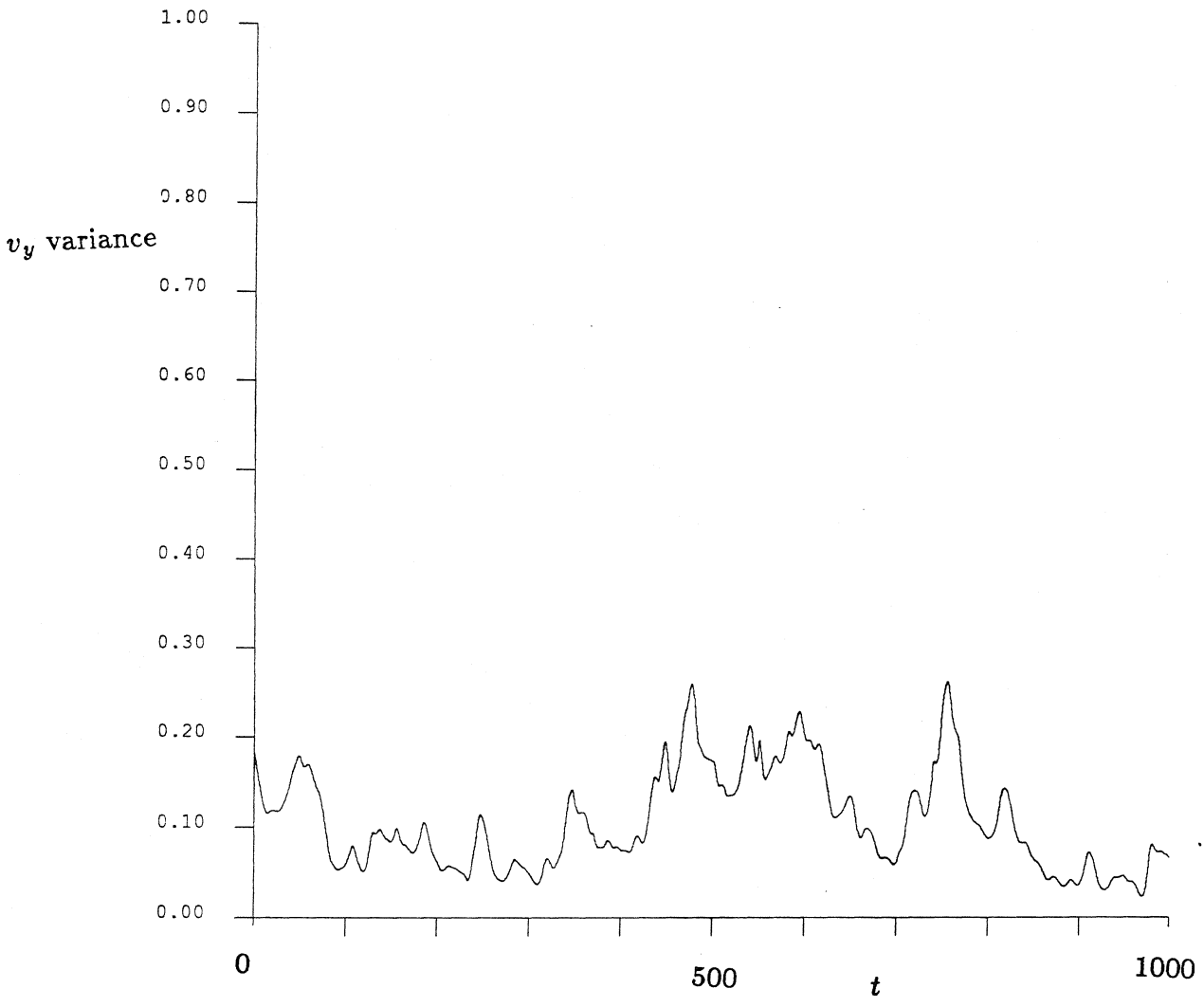

Figure B12.2 The time trace of the v_y variance for the simulations phi1efr1 and phi1efr2.

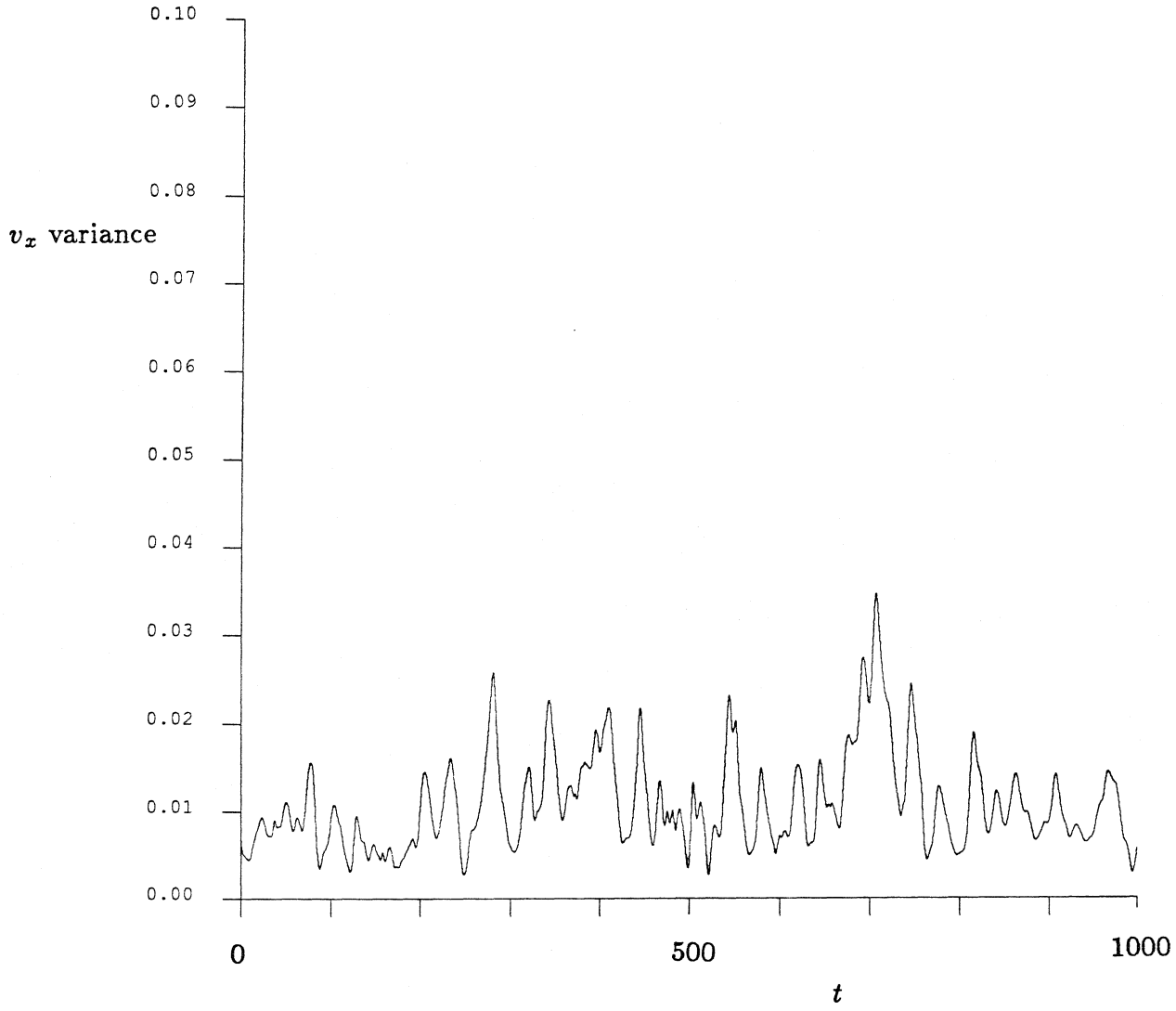

Figure B12.3 The time trace of the v_x variance for the simulations phi1efr1 and phi1efr2.

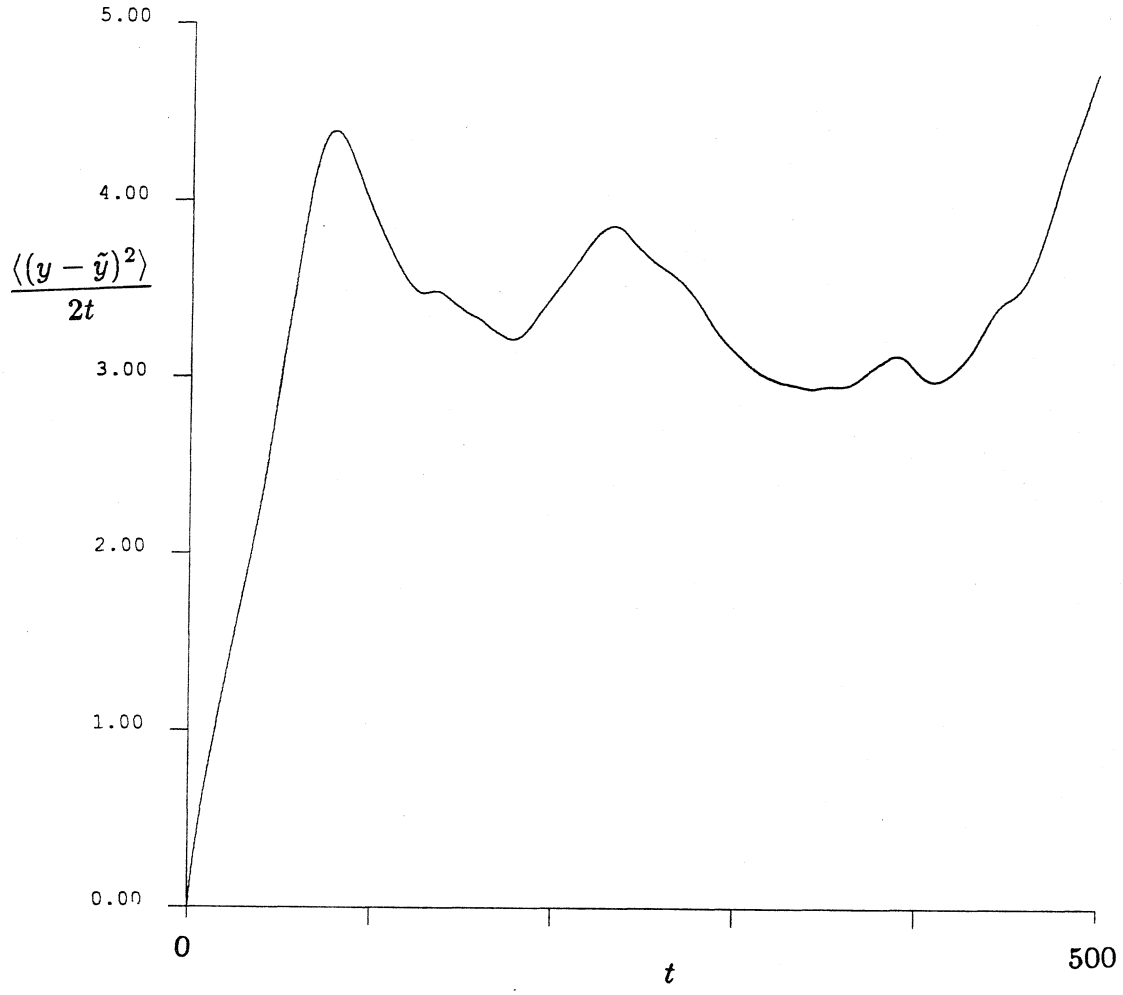

Figure B12.4 A $(D^s_\infty)_{yy}$-defining graph using displacement data from phi1efr1 (t= 0 – 500). The graph interval is 500 time units, which means that no averaging over different initial conditions is done.

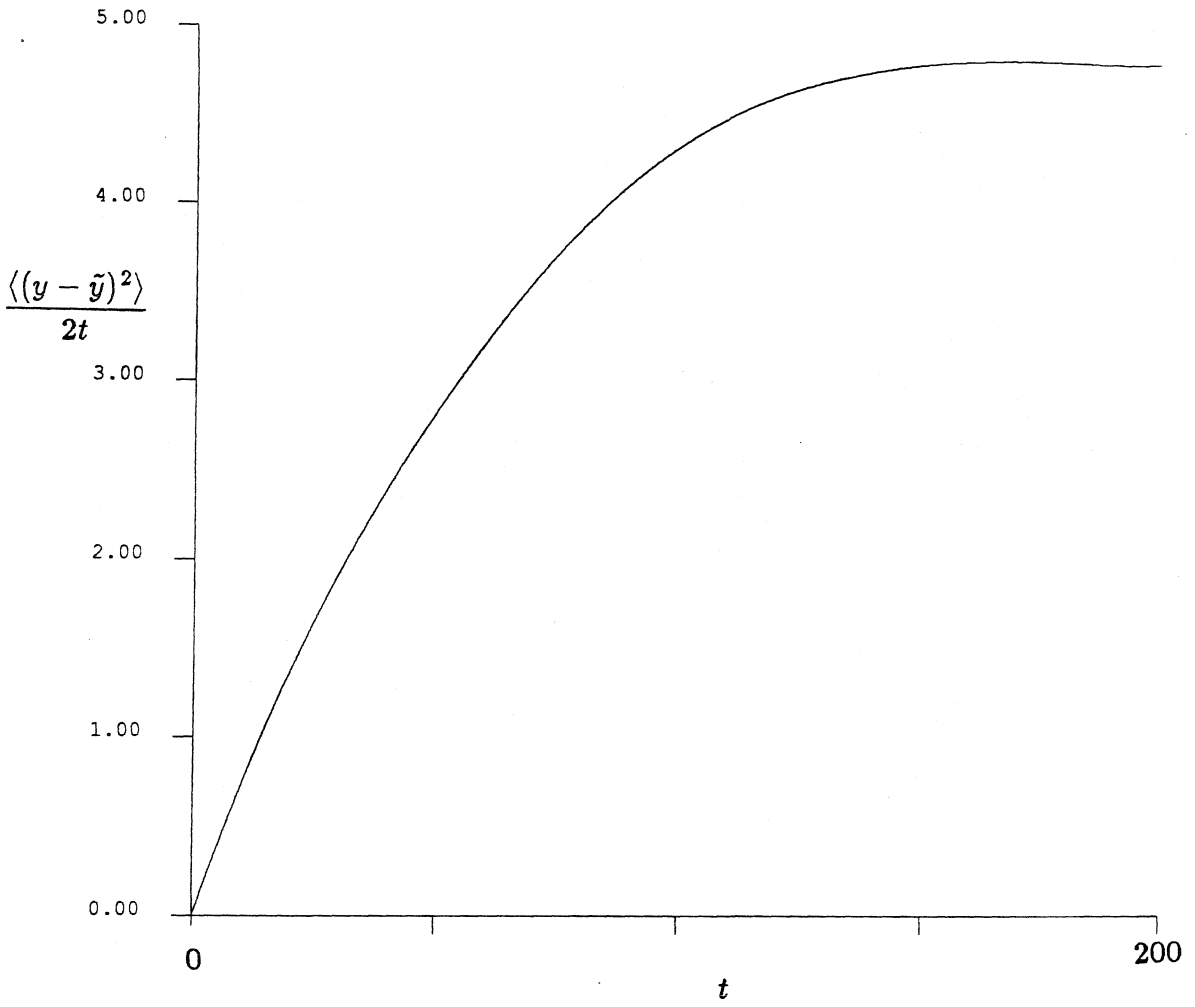

Figure B12.5 A $(D^s_\infty)_{yy}$-defining graph using displacement data from phi1efr2 (t= 500 – 1000). The graph interval is 200 time units, and the time between interval initial conditions is 0.01 time unit.

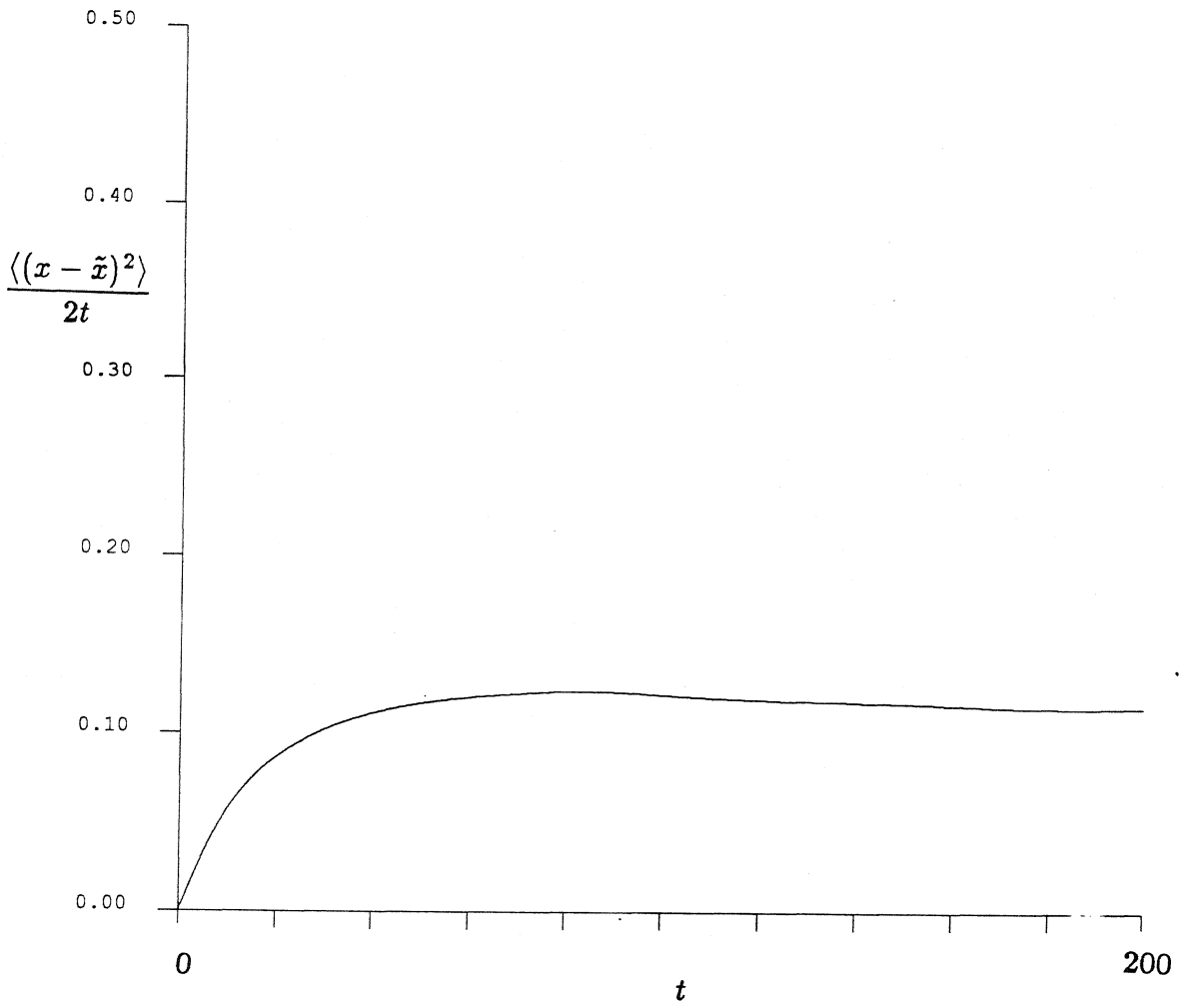

Figure B12.6 A $(D^s_\infty)_{xx}$-defining graph using displacement data from phi1efr2 (t= 500 – 1000). The graph interval is 200 time units, and the time between interval initial conditions is 0.01 time unit.

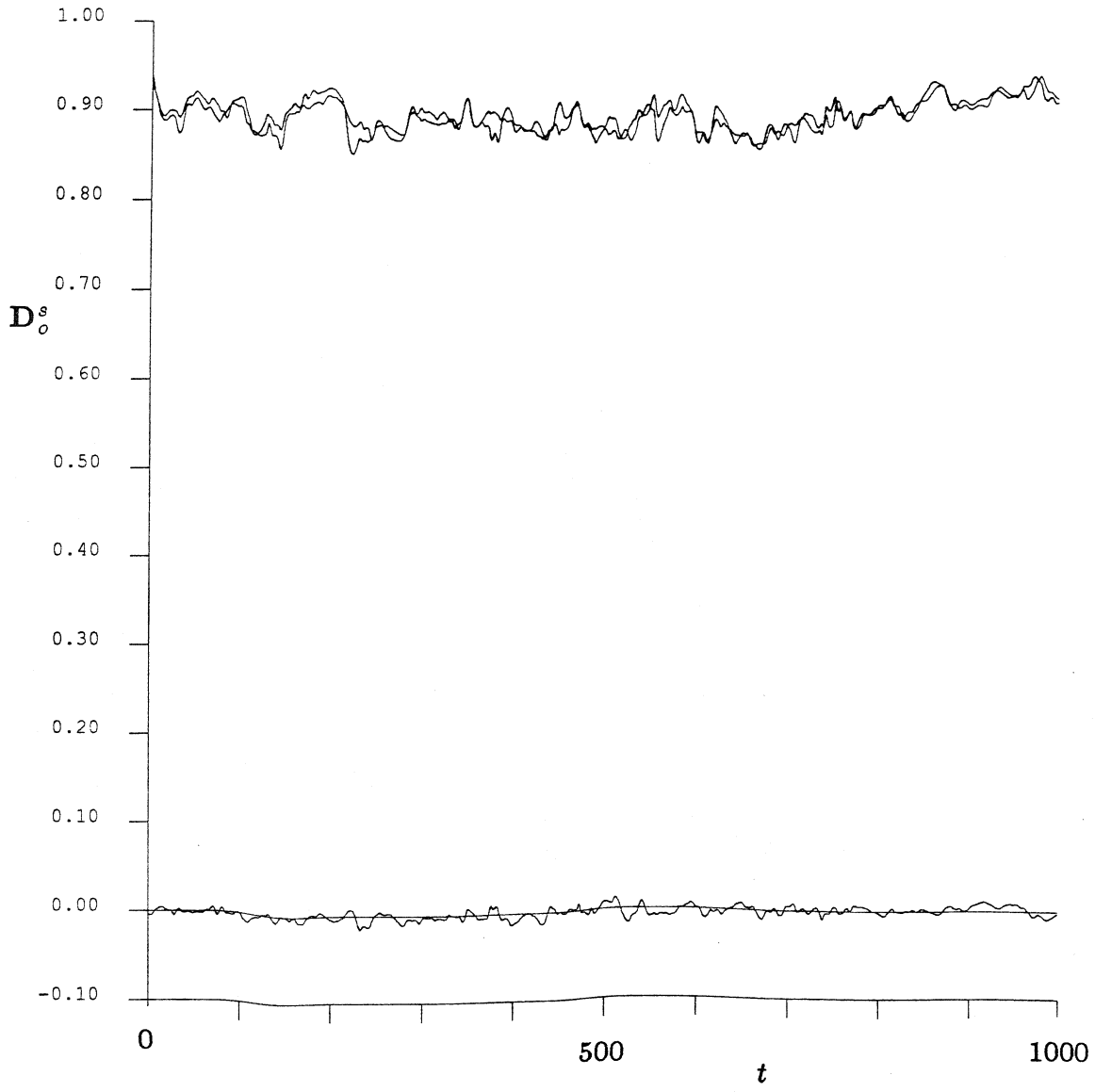

Figure B12.7 The time trace of $\mathbf{D}_o^s$ for the simulations phi1efr1 and phi1efr2. The upper two lines are the xx and yy components of this tensor. Of course, they should be equivalent for an infinite suspension – the slight variation occurs because of the finite number of spheres used in our simulation. The trace that fluctuates about the zero y-axis is the xy component of the short-time, self-diffusion tensor. Again, for an infinite number of spheres, this quantity would be exactly zero.

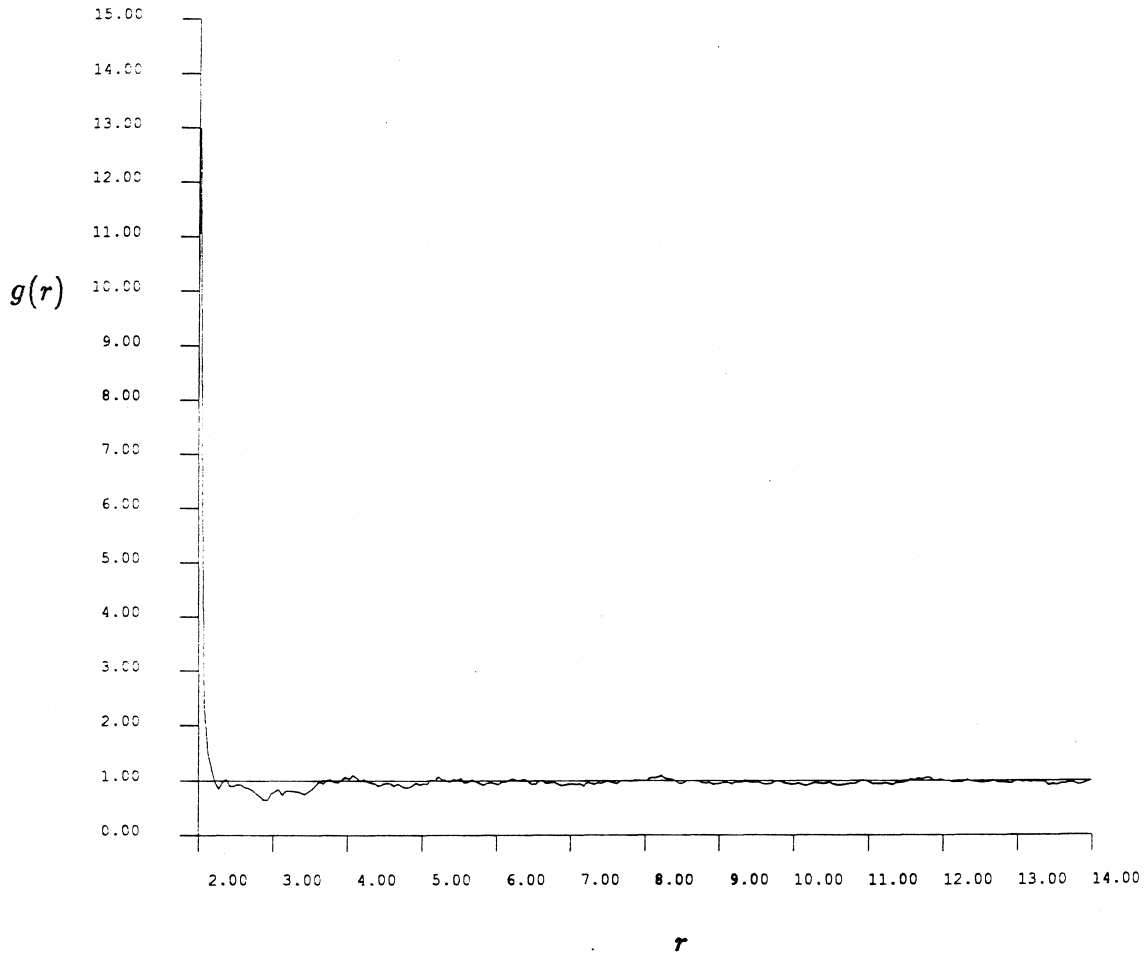

Figure B12.8 The radial pair-distribution function, $g(r)$, for the ph1efr2 run (t = 500 – 1000).

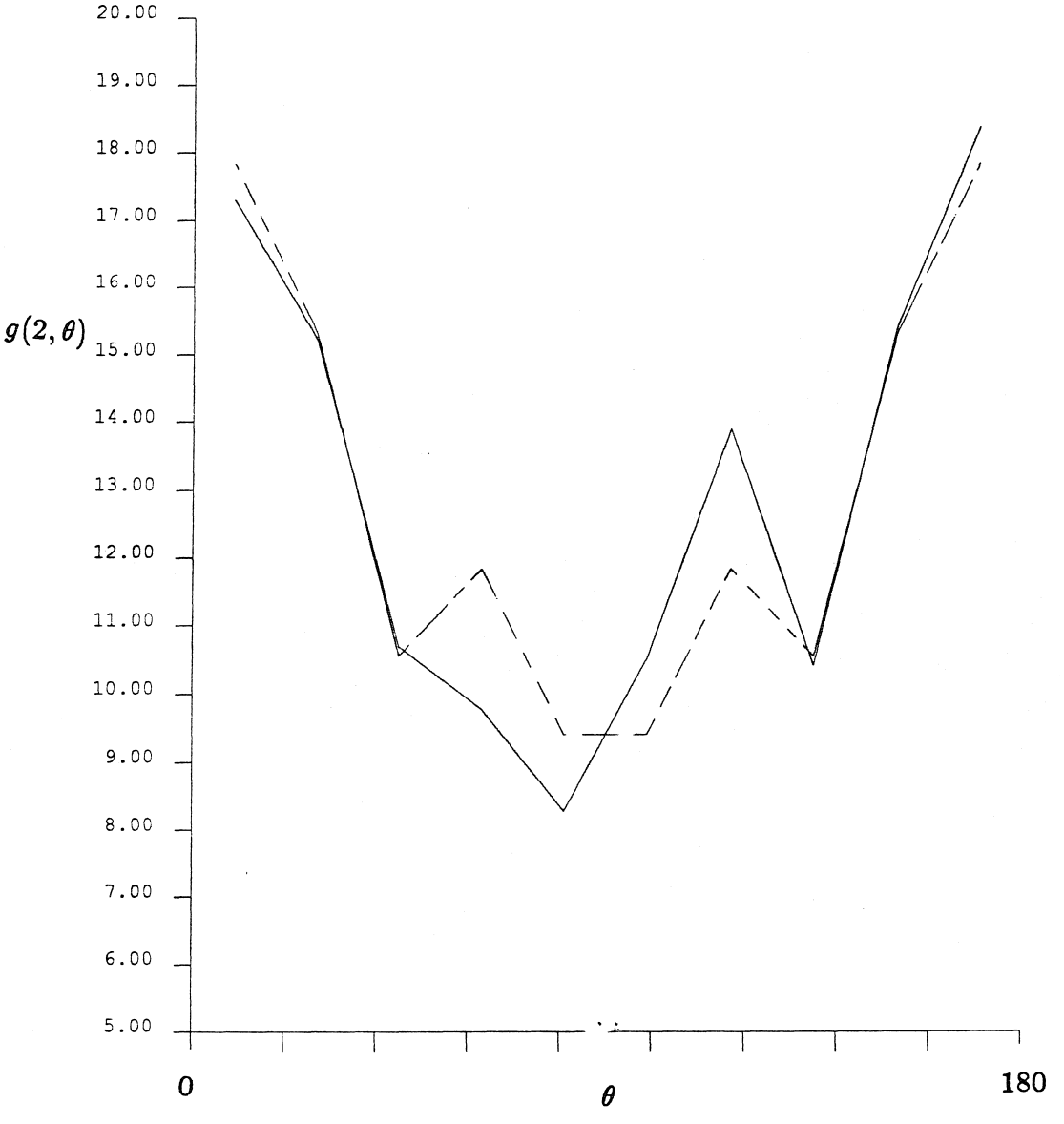

Figure B12.9 The full pair-distribution function for spheres whose surfaces are separated by less than 0.05 radii using data from the phi1efr2 run (t = 500 – 1000). The dashed curve represents this function when it is forced to be symmetric about $\theta = 90°$.

Appendix B13: The .1n simulation results

This suite of simulations uses a non-Ewald, F method to approximate the hydrodynamic interactions. Two separate simulation runs follow the evolution of a sedimenting system to a final time of 1000 time units. There are 25 particles in the periodic cell. The areal fraction is 0.1. There are no interparticle forces present. The initial configuration is not the same as in the phi1efr simulations described in Appendix B12. The time step is 0.001 time unit. The mobility matrix is inverted every 0.1 time unit. Position and velocity data is saved every 0.05 time unit. $\mathbf{D}_o^s$ is evaluated and reported at every time unit. Note that the simulation never achieves a steady sedimentation velocity. This made finding the long-time, self-diffusion coefficient in the direction of gravity impossible.

	.1n1	.1n2
T	0-500	500-1000
Cray/Sun	Sun	Sun
CPU(min)	1375	
v_y	-4.08586	-4.29924
v_x	0.00249	0.00822
v_y variance	0.15725	0.43943
v_x variance	0.01714	0.02284
v_{xy} variance	-0.00342	-0.00491
$(D_\infty^s)_{yy}$		
$(D_\infty^s)_{xx}$		
$(D_o^s)_{yy}$	0.904	0.782
$(D_o^s)_{xx}$	0.904	0.781
$(D_o^s)_{xy}$	0.0001	0.0008
$g(2)$		26.4
$g(3.5)$		3.70
$g(4)$		3.98

Table B13.1

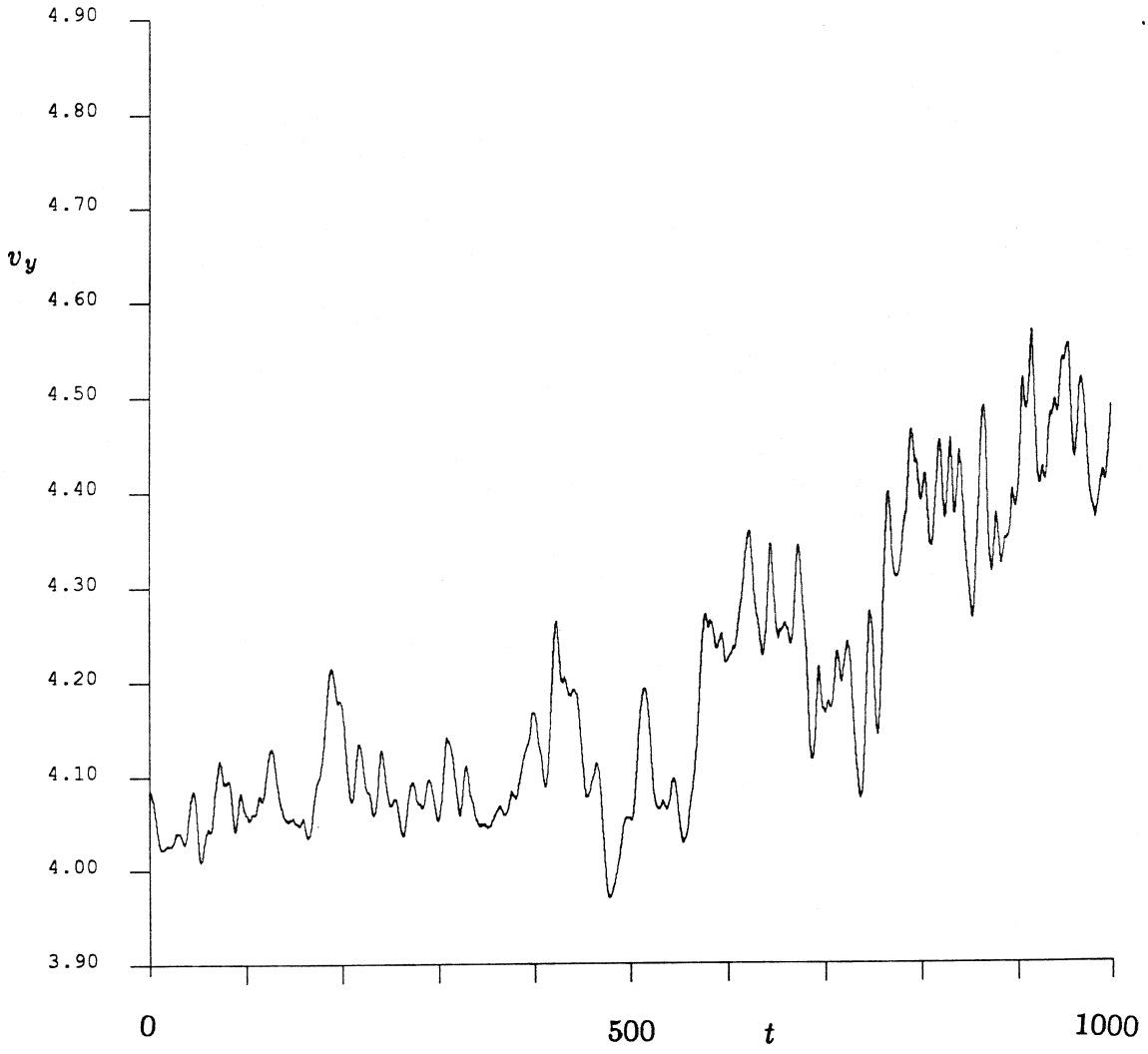

Figure B13.1 The time trace of v_y for the simulations .1n1 and .1n2.

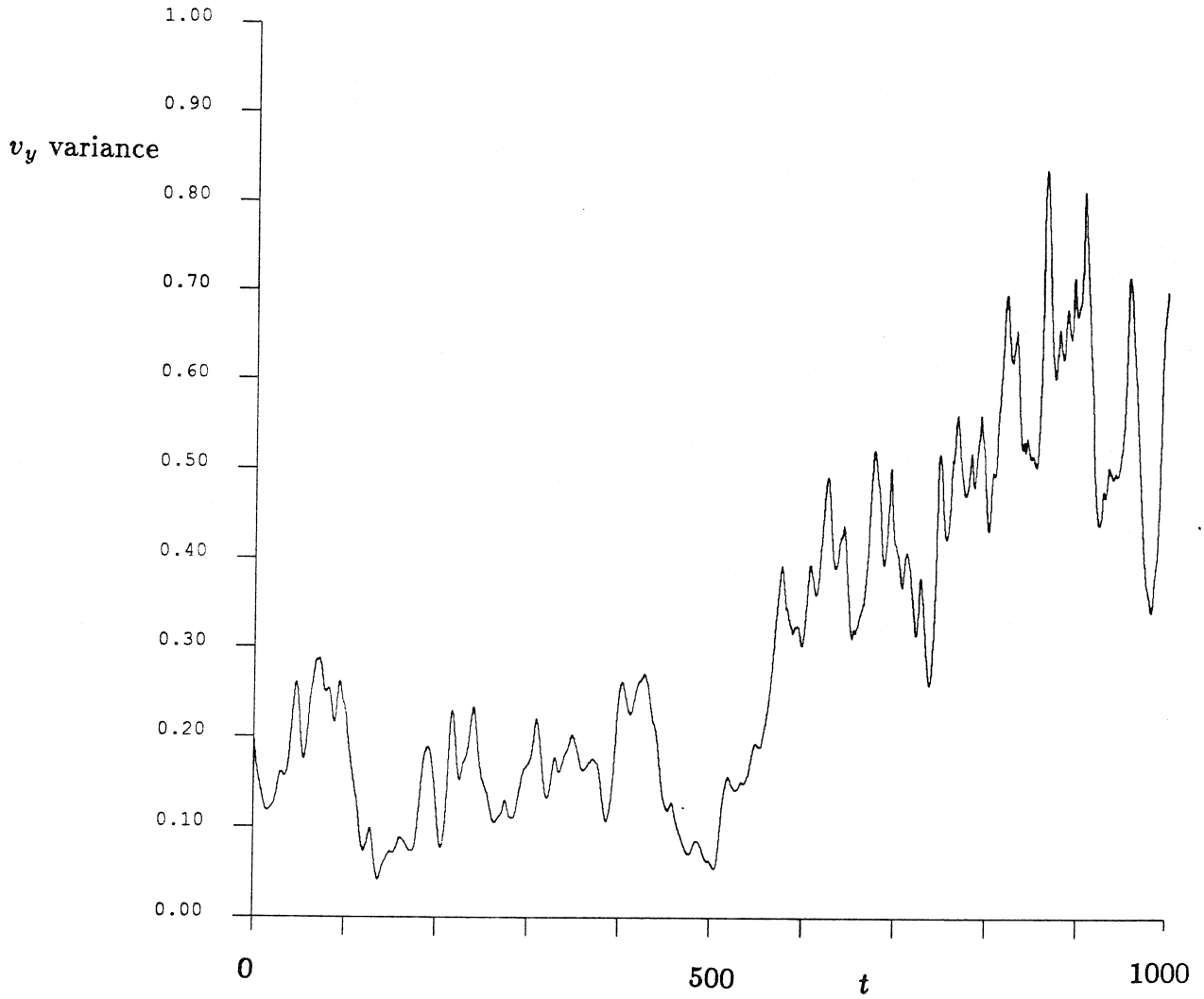

Figure B13.2 The time trace of the v_y variance for the simulations .1n1 and .1n2.

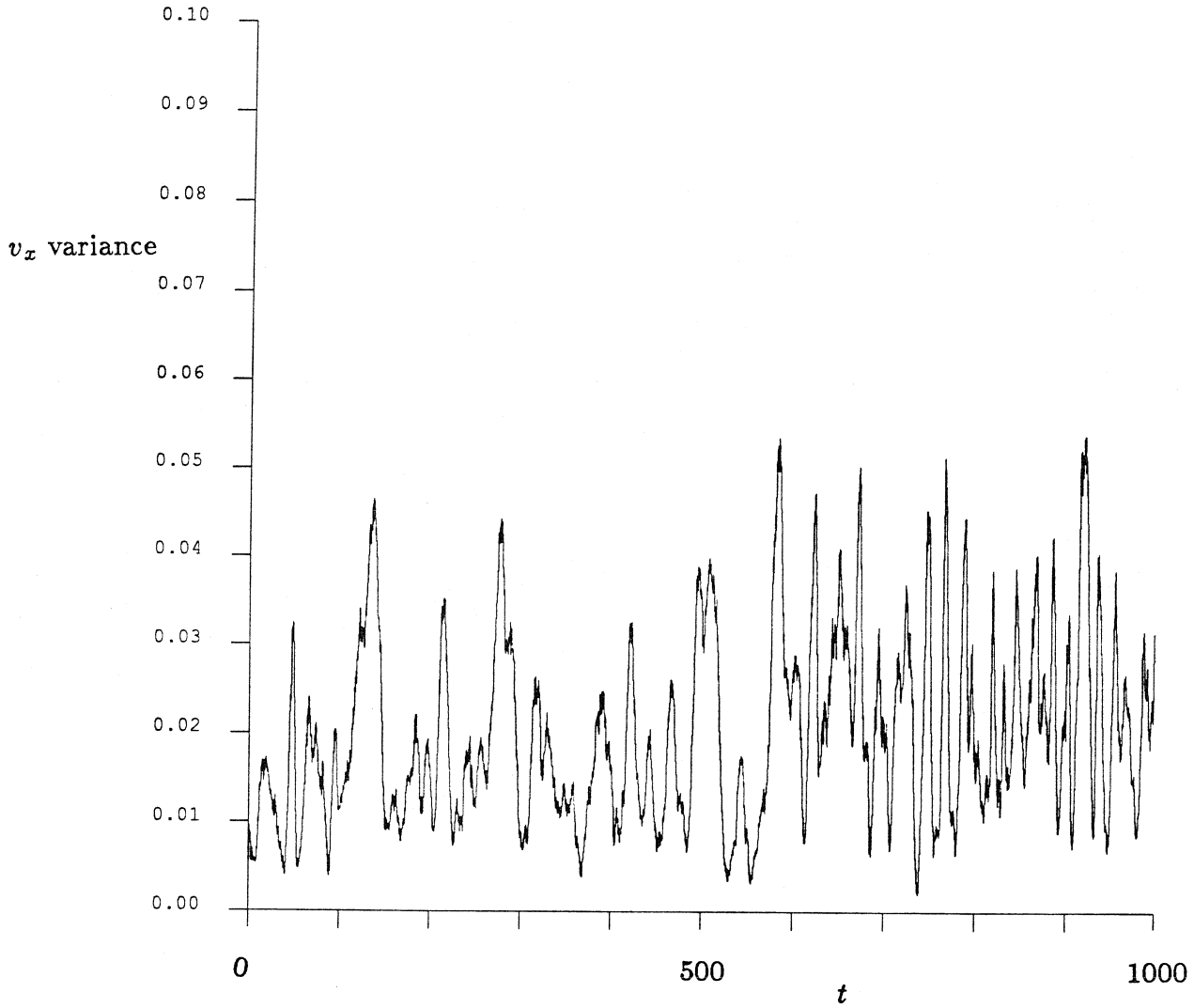

Figure B13.3 The time trace of the v_x variance for the simulations .1n1 and .1n2.

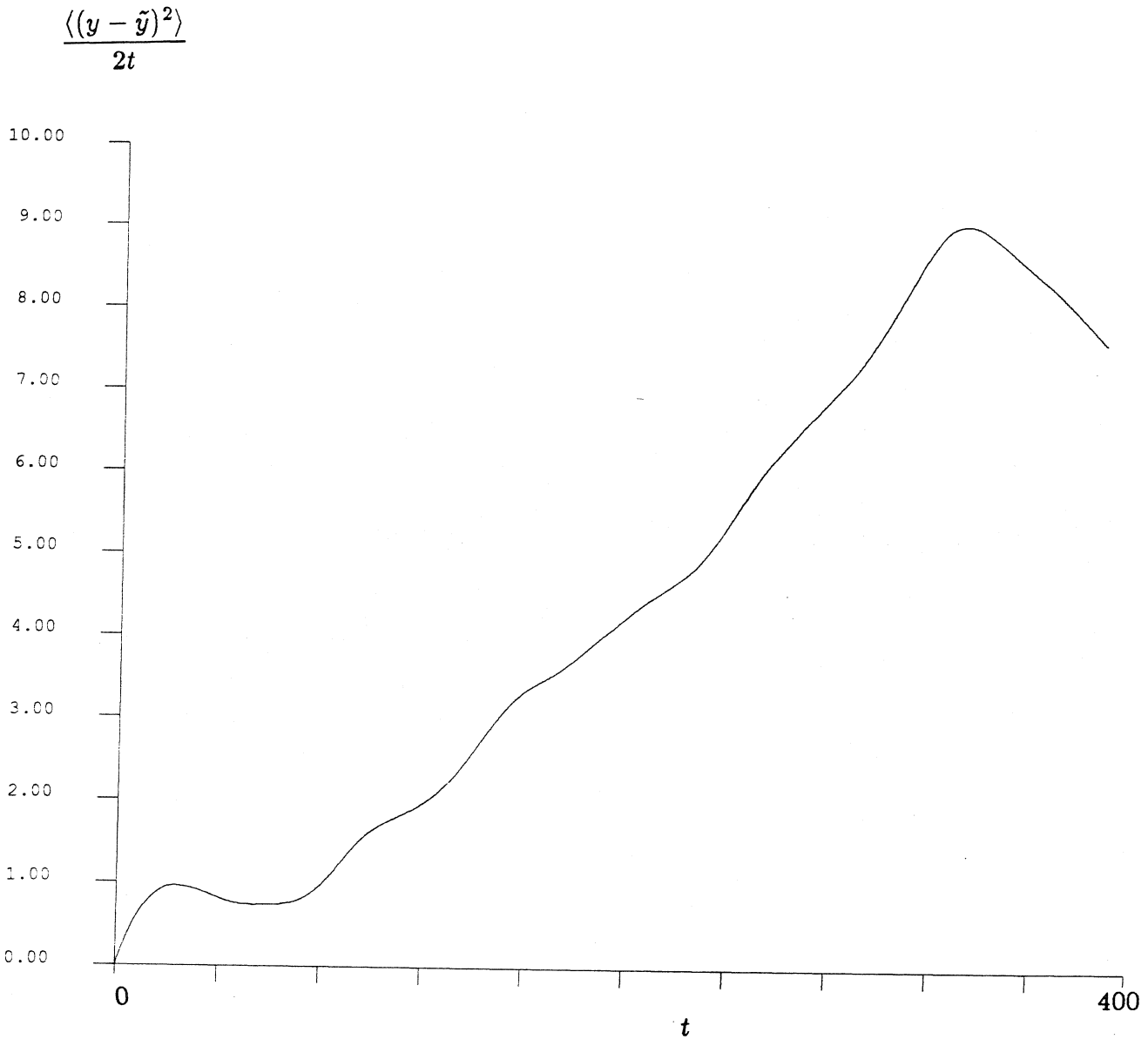

Figure B13.4 A $(D^s_\infty)_{yy}$-defining graph using displacement data from .1n1 (t= 100 – 500). The graph interval is 400 time units, which means that no averaging over different initial conditions is done.

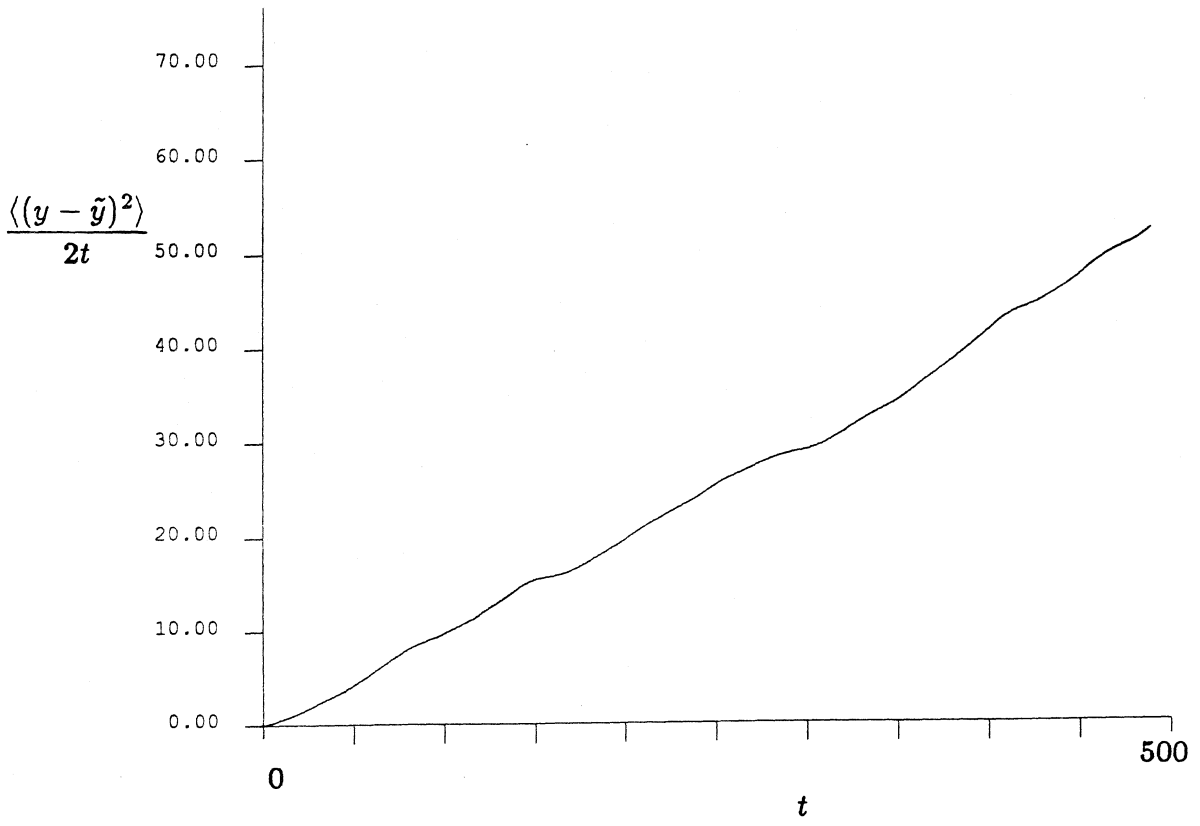

Figure B13.5 A $(D^s_\infty)_{yy}$-defining graph using displacement data from .1n2 (t= 500 – 1000). The graph interval is 500 time units, which means that no averaging over different initial conditions is done. Clearly, the motion is deterministic in this case – the sedimentation velocity is not constant over this time.

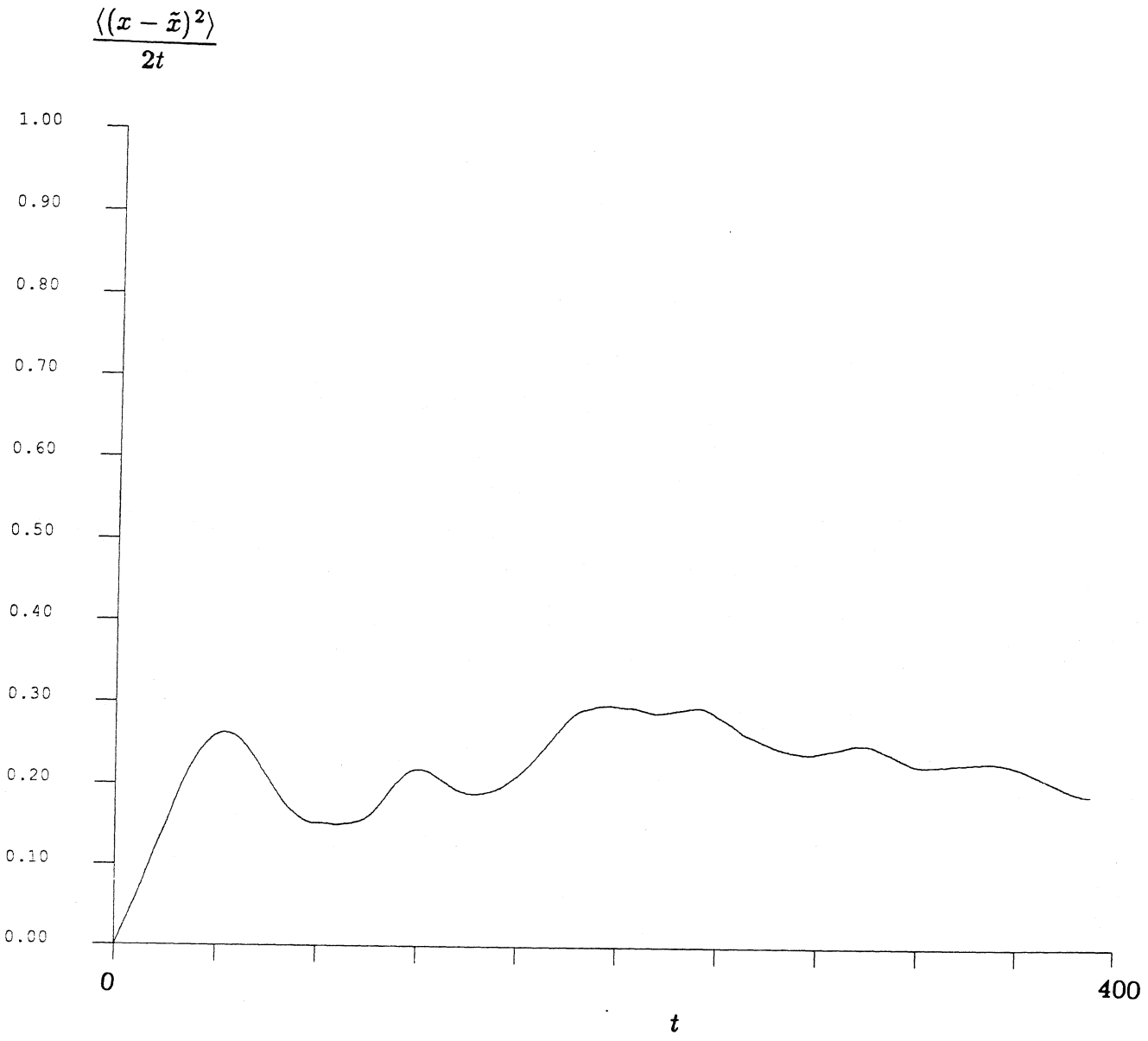

Figure B13.6 A $(D^s_\infty)_{xx}$-defining graph using displacement data from .1n1 (t= 100 – 500). The graph interval is 400 time units, which means that no averaging over different initial conditions is done.

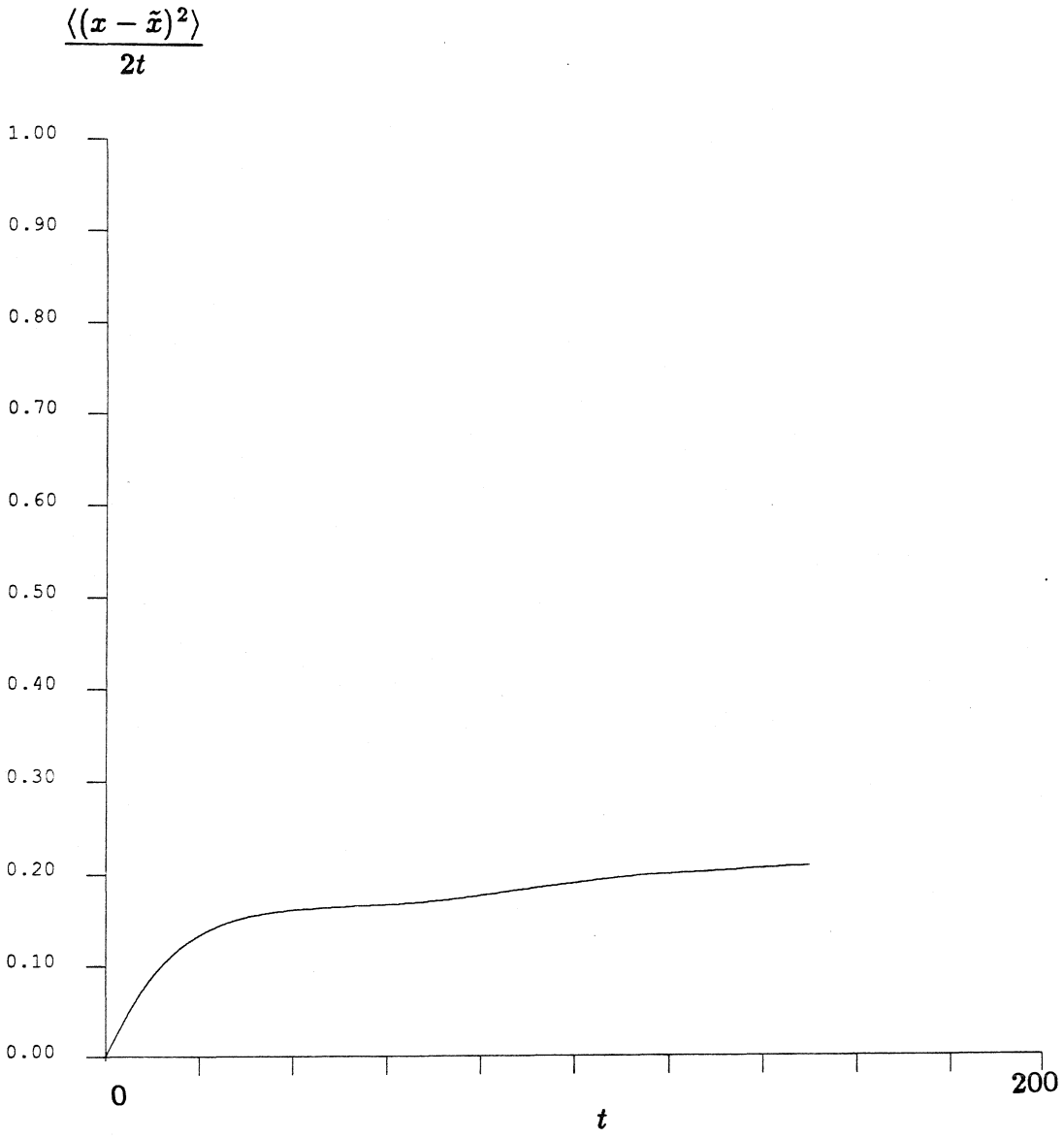

Figure B13.7 A $(D^s_\infty)_{xx}$-defining graph using displacement data from .1n1 (t= 100 – 500). The graph interval is 150 time units, and the time between interval initial conditions is 0.01 time unit.

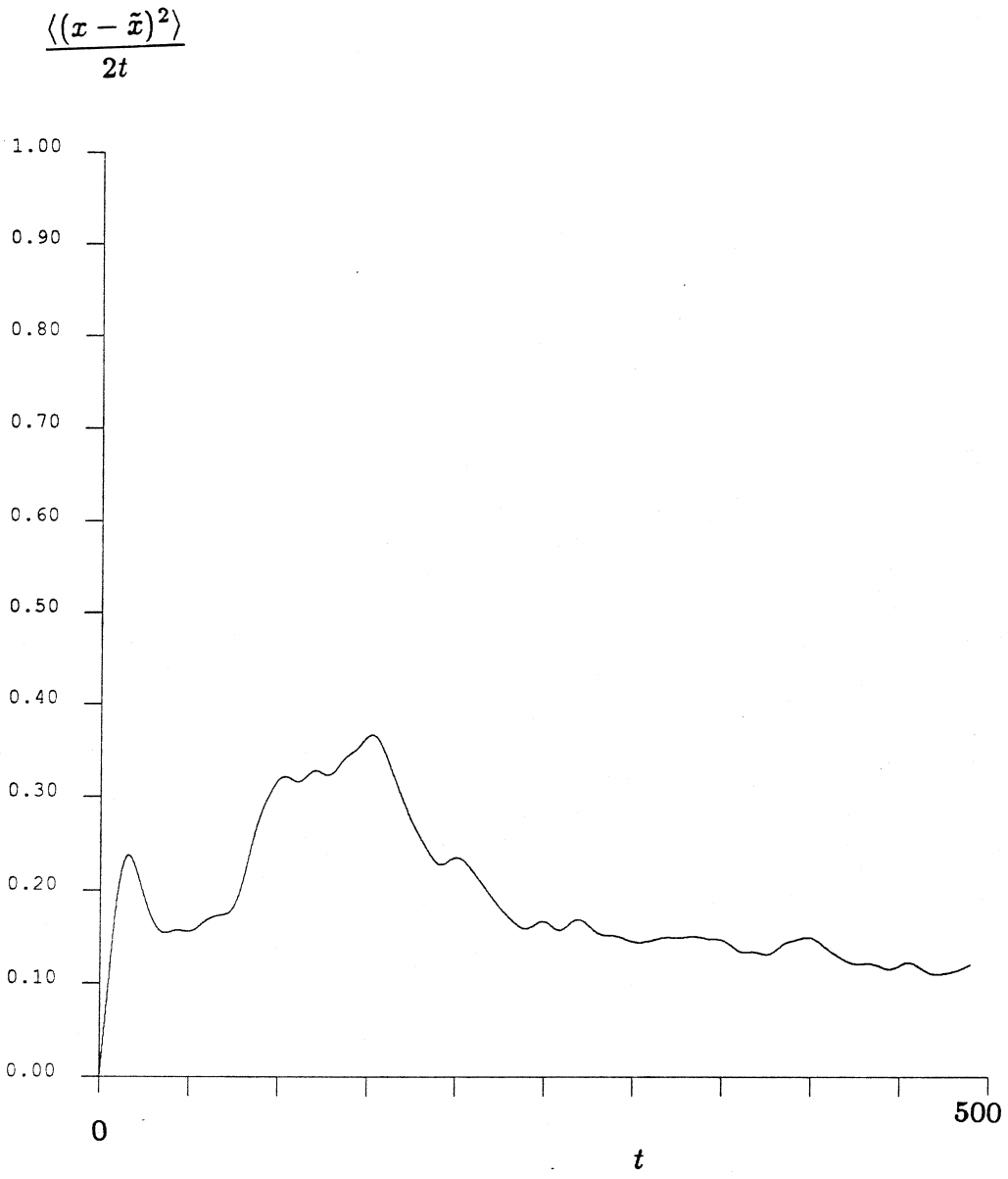

Figure B13.8 A $(D^s_\infty)_{xx}$-defining graph using displacement data from .1n2 (t= 500 – 1000). The graph interval is 500 time units, which means that no averaging over different initial conditions is done.

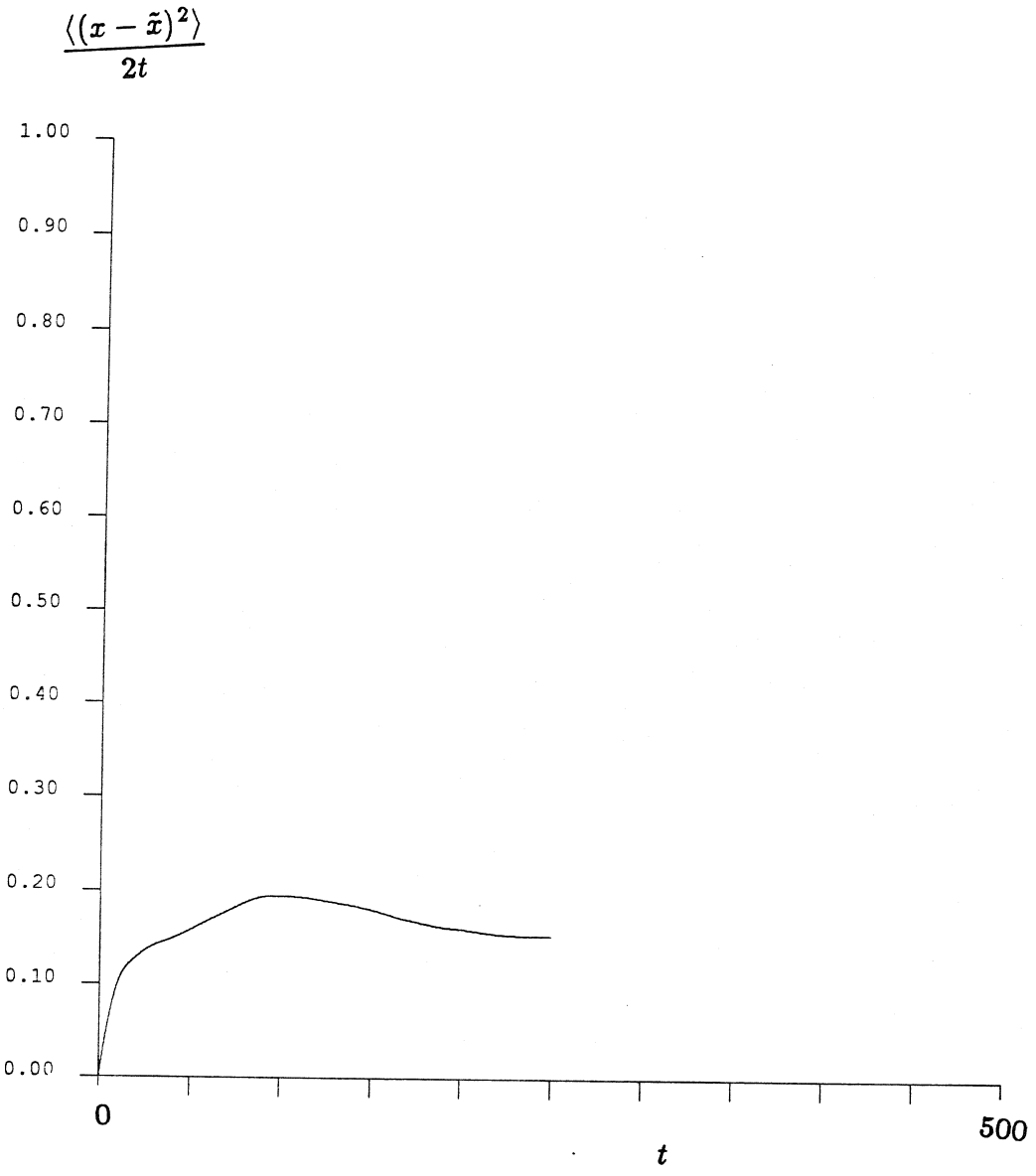

Figure B13.9 A $(D^{s}_{\infty})_{xx}$-defining graph using displacement data from .1n2 (t= 100 – 500). The graph interval is 250 time units, and the time between interval initial conditions is 0.01 time unit.

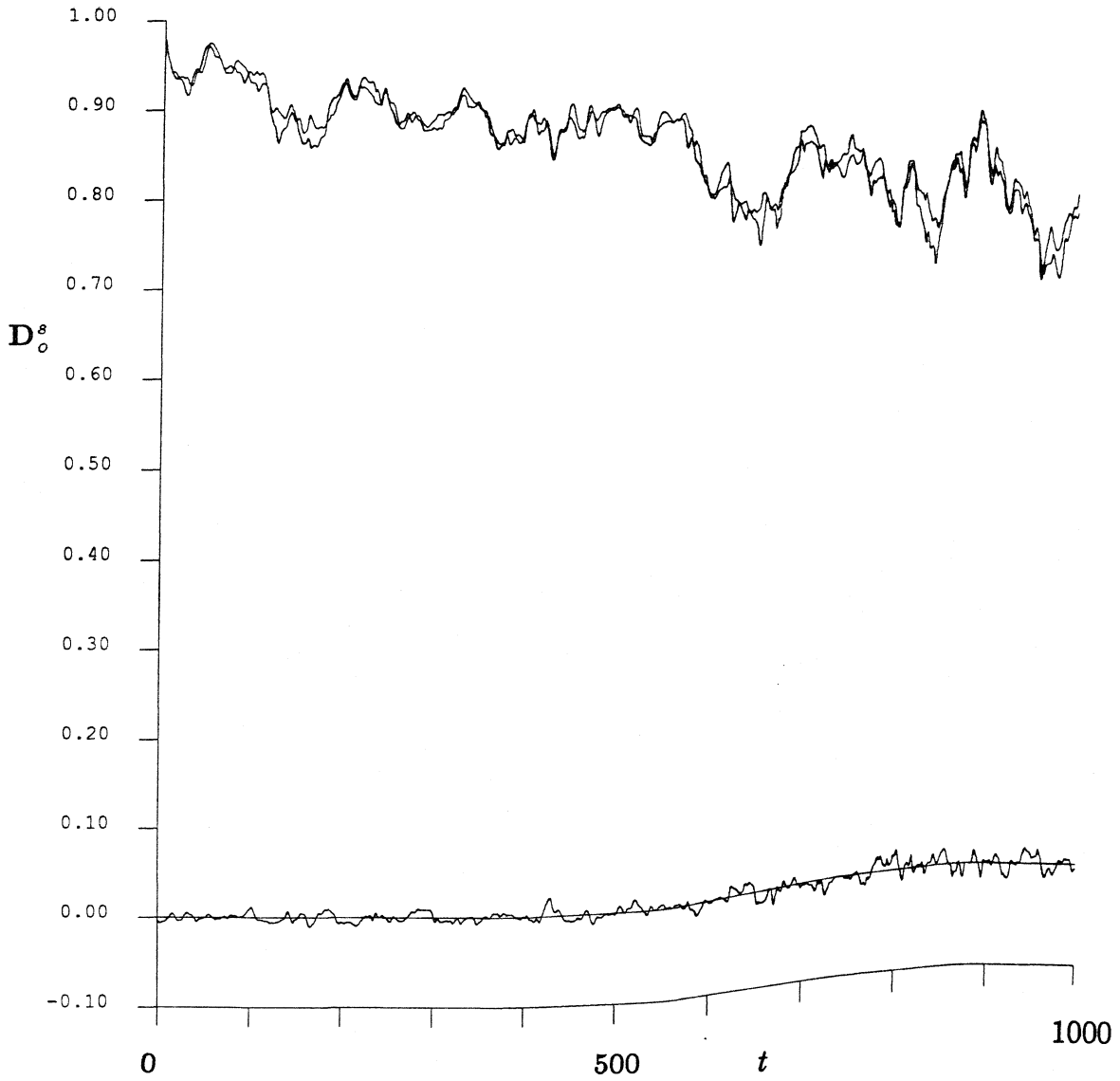

Figure B13.10 The time trace of $\mathbf{D}_o^s$ for the simulations .1n1 and .1n2. The upper two lines are the xx and yy components of this tensor. Of course, they should be equivalent for an infinite suspension – the slight variation occurs because of the finite number of spheres used in our simulation. The trace that fluctuates about the zero y-axis is the xy component of the short-time, self-diffusion tensor. Again, for an infinite number of spheres, this quantity would be exactly zero.

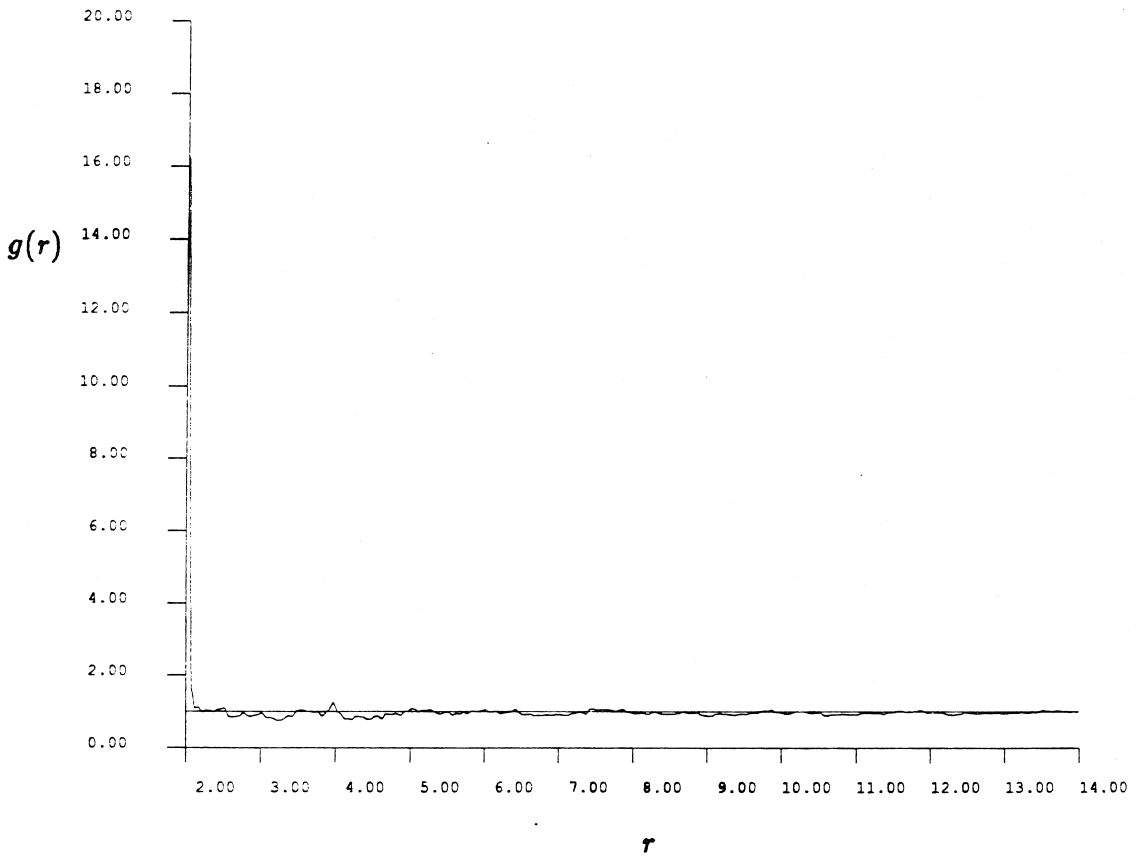

Figure B13.11 The radial pair-distribution function, $g(r)$, for the .1n1 run ($t = 100 - 500$).

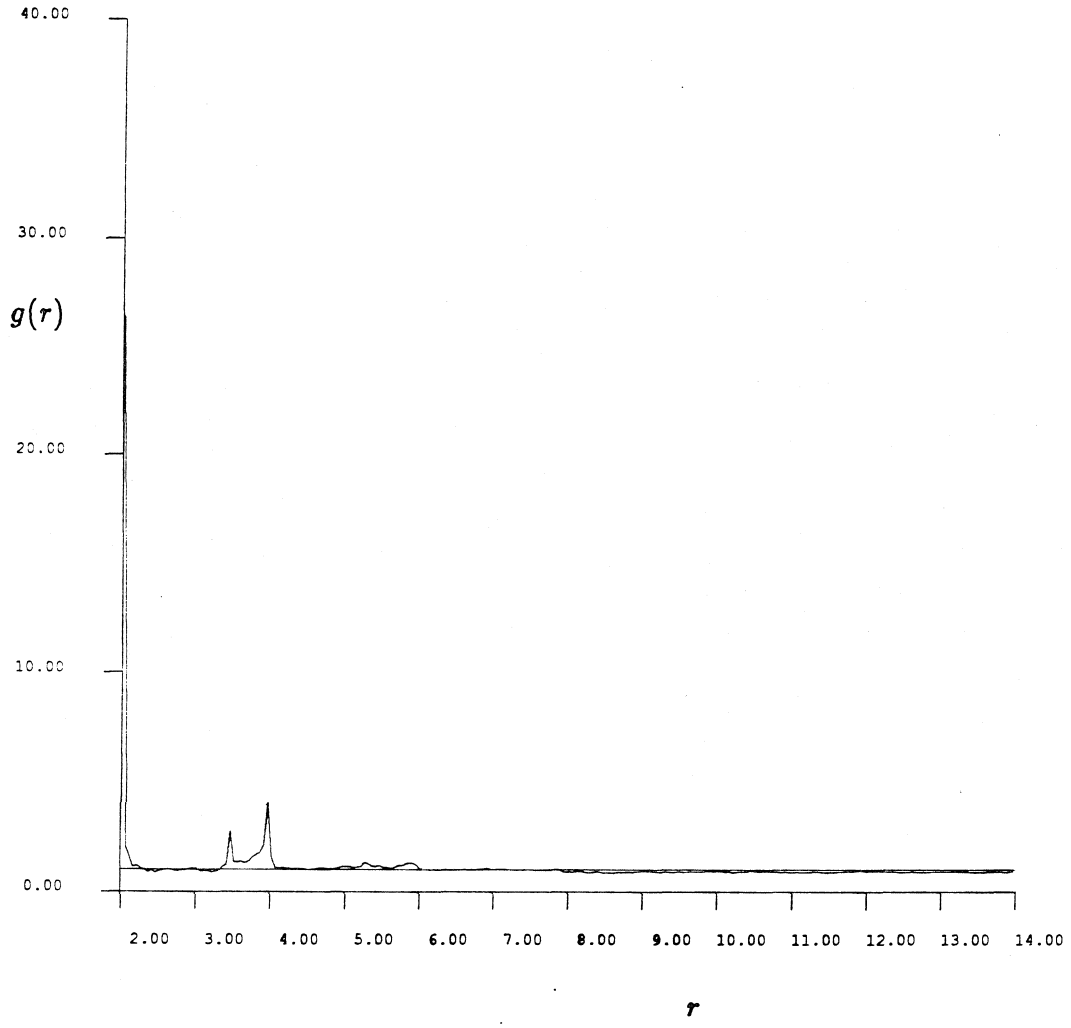

Figure B13.12 The radial pair-distribution function, $g(r)$, for the .1n2 run ($t = 500 - 1000$).

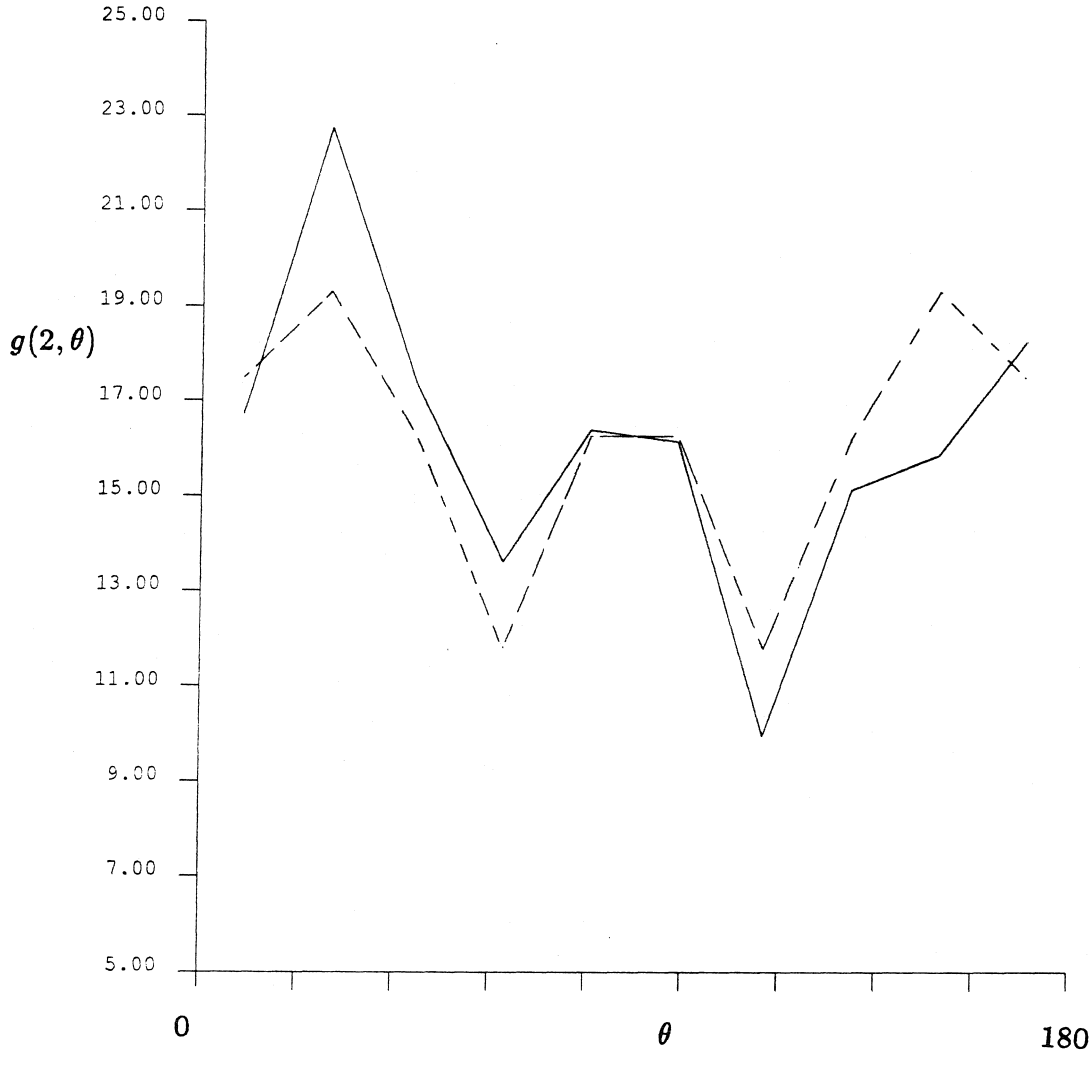

Figure B13.13 The full pair-distribution function for spheres whose surfaces are separated by less than 0.05 radii using data from the .1n1 run (t = 100 – 500). The dashed curve represents this function when it is forced to be symmetric about $\theta = 90°$.

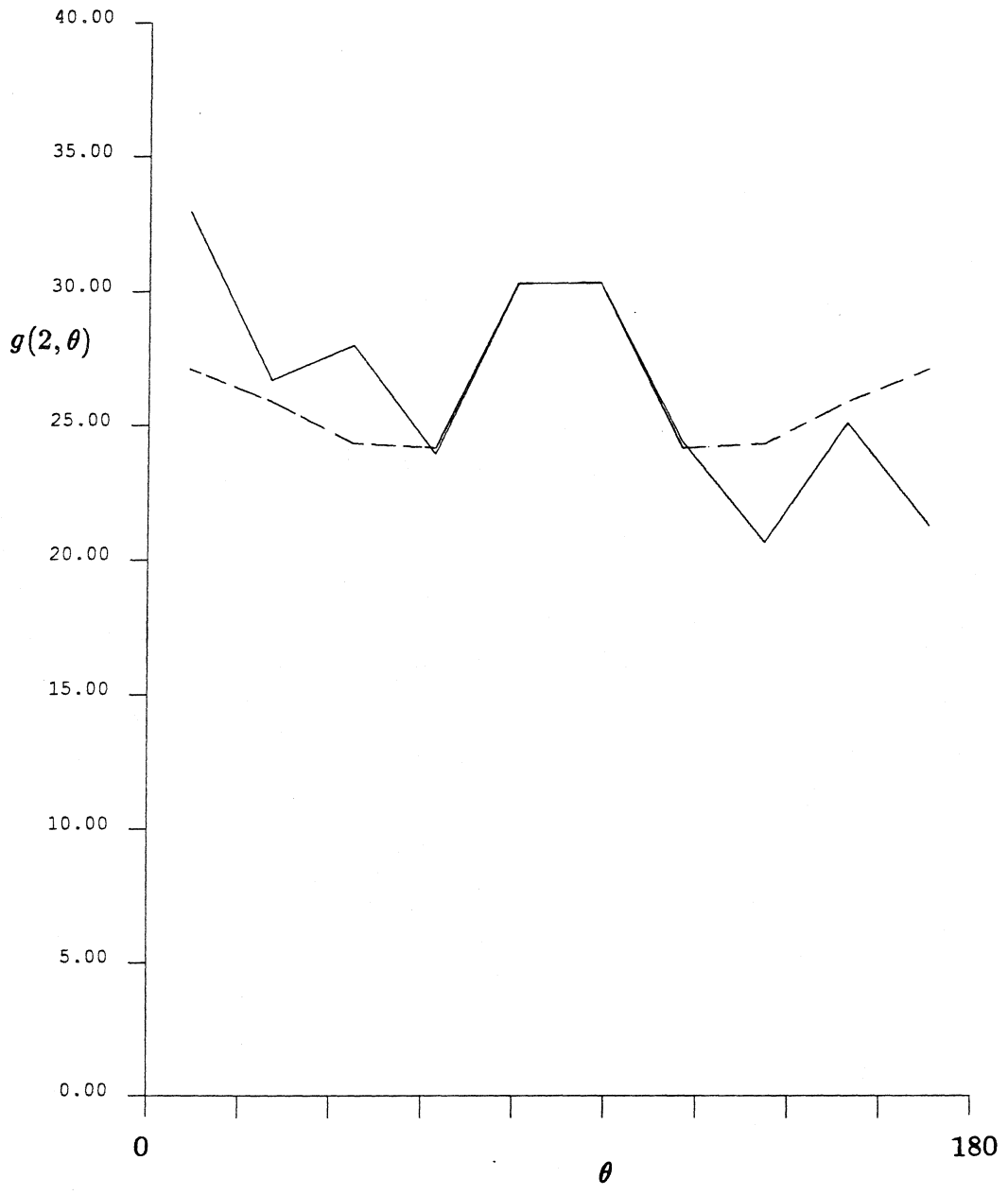

Figure B13.14 The full pair-distribution function for spheres whose surfaces are separated by less than 0.05 radii using data from the .1n2 run ($t = 500 - 1000$). The dashed curve represents this function when it is forced to be symmetric about $\theta = 90°$.

Appendix B14: The phi25efr simulation results

This suite of simulations uses an Ewald, F method to approximate the hydrodynamic interactions. The separation factor, z_l, is 2. 126 image cells are used to insure the convergence of the mobility interactions. Two separate simulation runs follow the evolution of a sedimenting system to a final time of 1000 time units. There are 25 particles in the periodic cell. The areal fraction is 0.25. There are interparticle forces present ($\tau = 10^5$). The initial configuration is taken from a Monte-Carlo simulation. The time step is 0.005 time unit. The mobility matrix is inverted every 0.1 time unit. Position and velocity data is saved every 0.05 time unit. $\mathbf{D}_o^s$ is evaluated and reported at every time unit.

	phi25efr1	phi25efr2
T	0-500	500-1000
Cray/Sun	Cray 0.80	Cray 0.50
CPU(min)	136	85
v_y	-4.25520	-4.26502
v_x	0.00752	-0.00187
v_y variance	0.04535	0.05193
v_x variance	0.00894	0.00998
v_{xy} variance	0.00024	0.00091
$(D_\infty^s)_{yy}$		1.05
$(D_\infty^s)_{xx}$		0.10
$(D_o^s)_{yy}$	0.787	0.773
$(D_o^s)_{xx}$	0.789	0.775
$(D_o^s)_{xy}$	0.0044	-0.0021
$g(2)$		12.1
$g(3.5)$		0.81
$g(4)$		1.11

Table B14.1

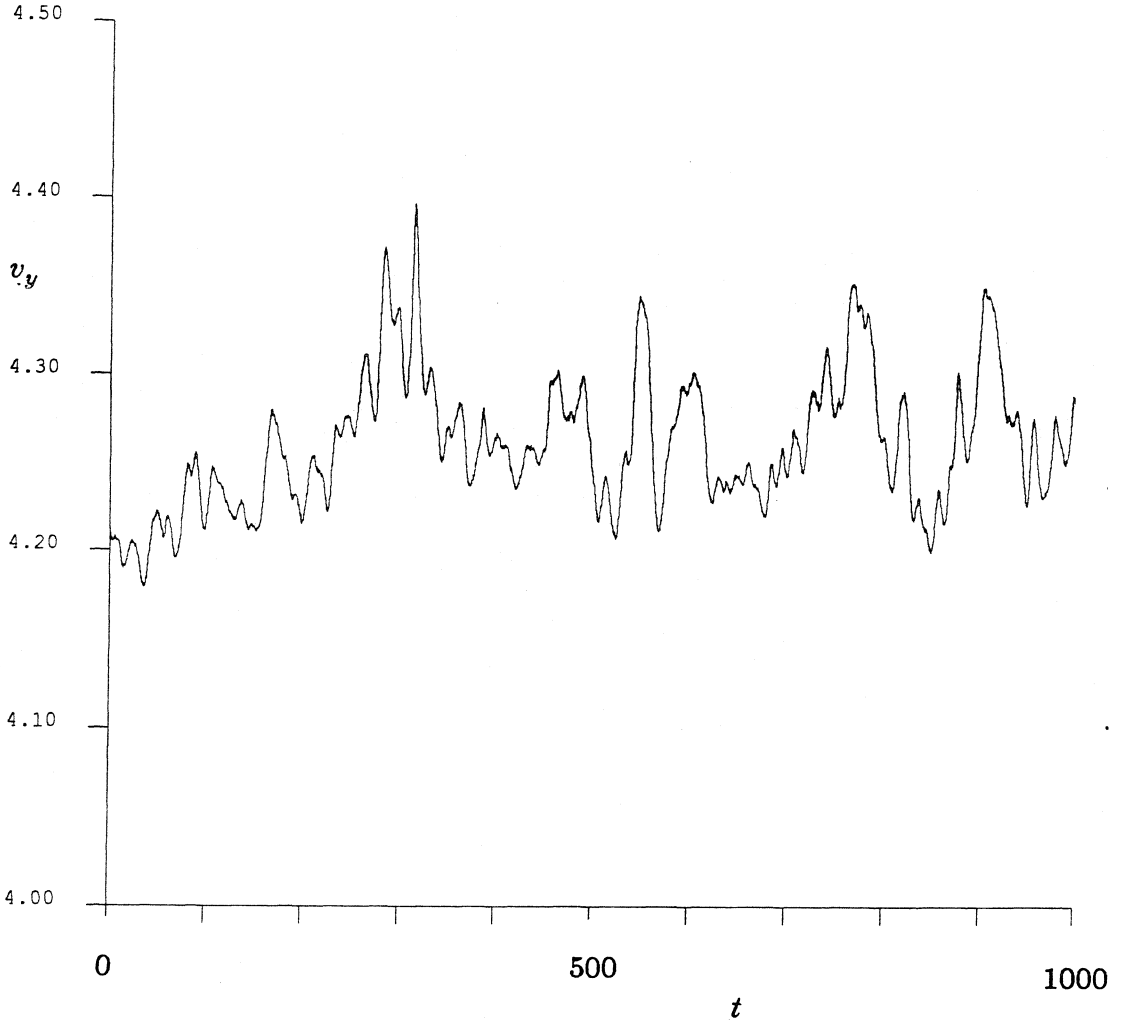

Figure B14.1 The time trace of v_y for the simulations phi25efr1 and phi25efr2.

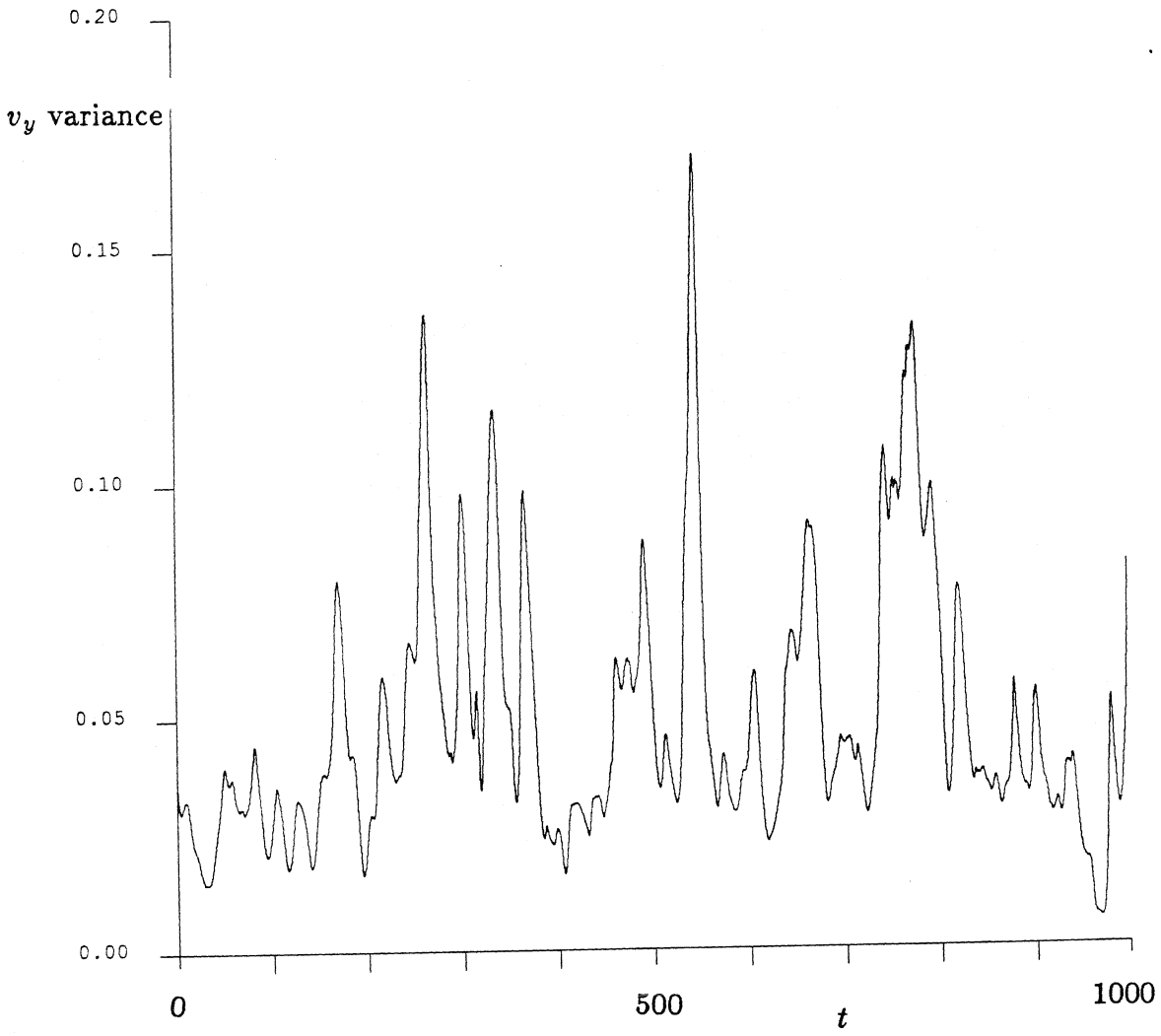

Figure B14.2 The time trace of the v_y variance for the simulations phi25efr1 and phi25efr2.

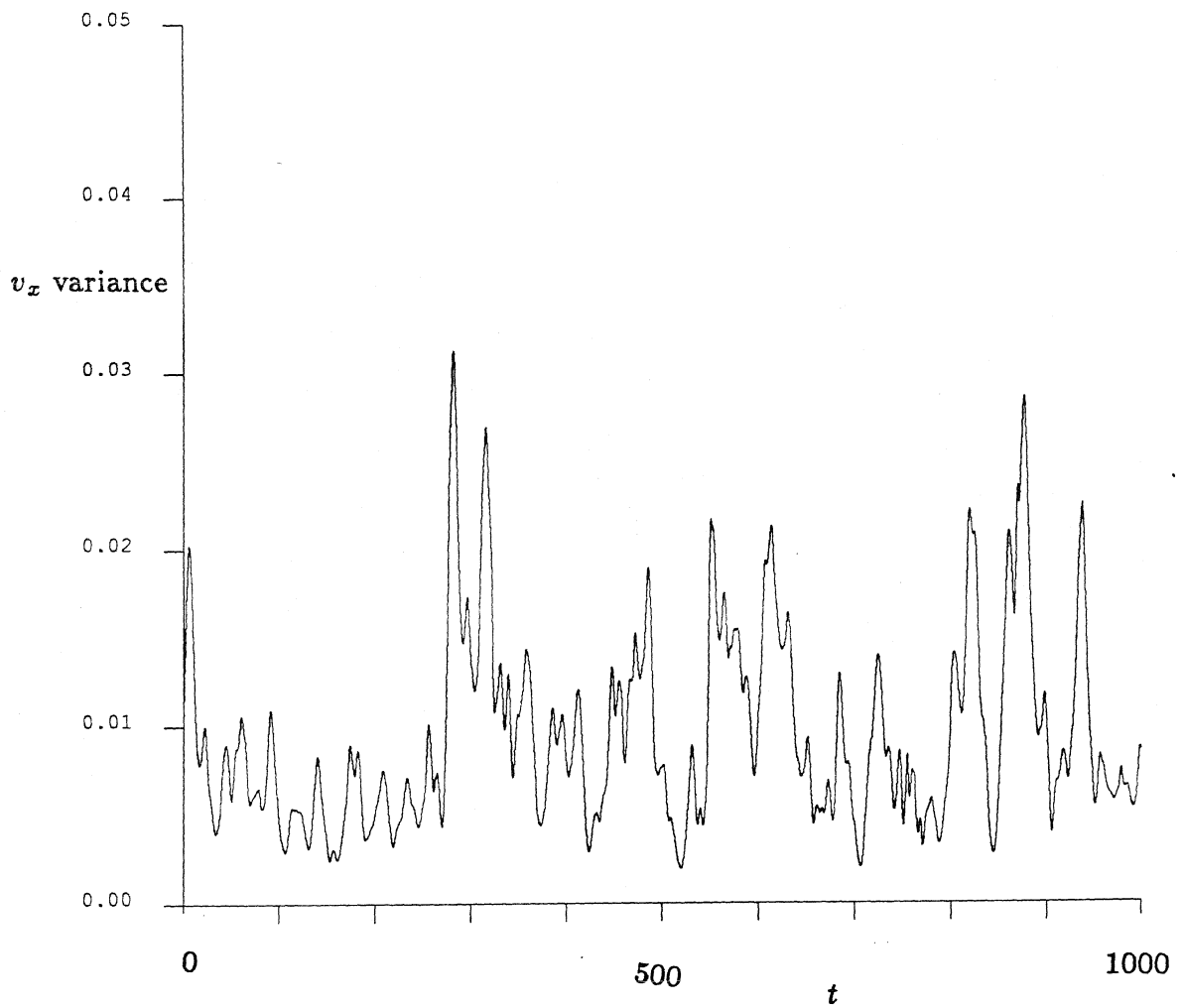

Figure B14.3 The time trace of the v_x variance for the simulations phi25efr1 and phi25efr2.

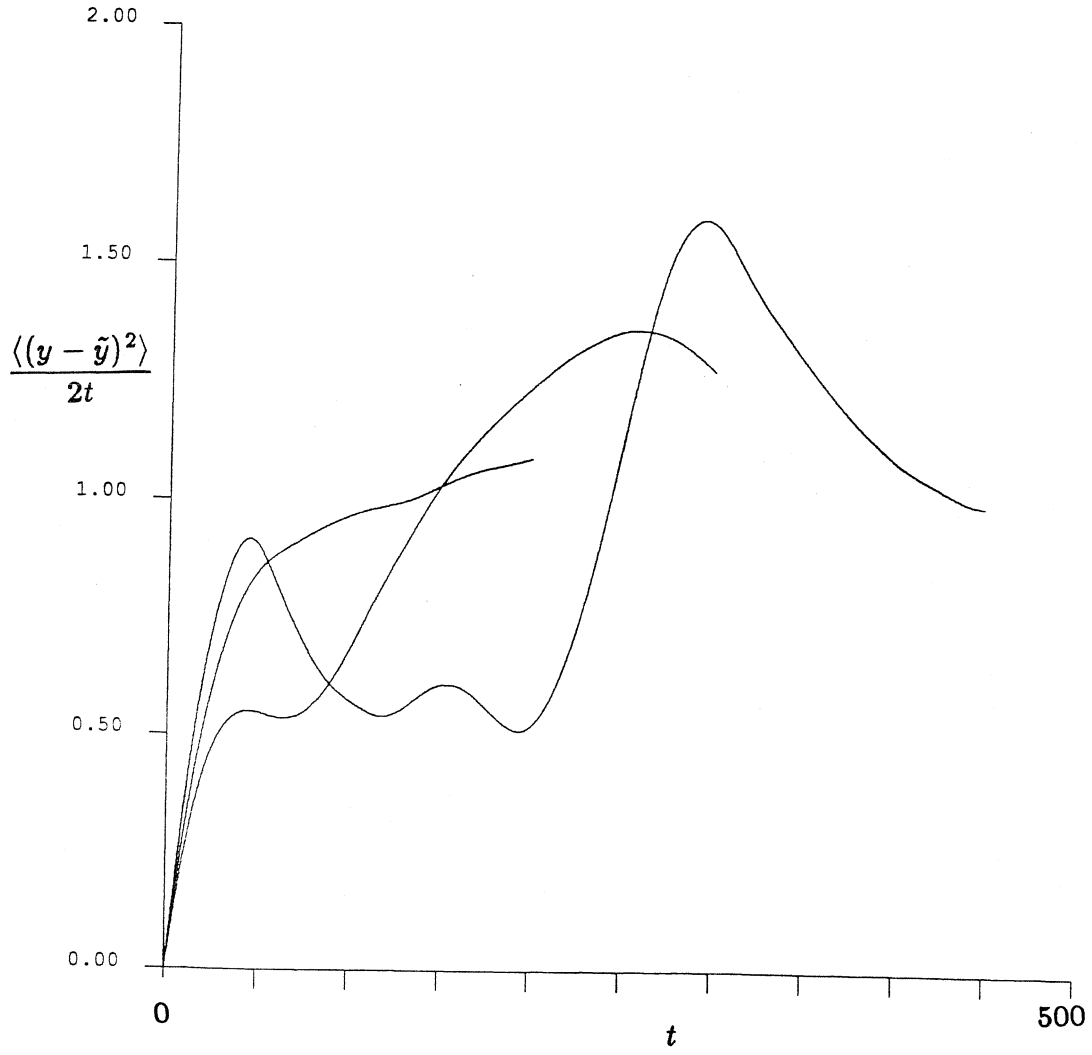

Figure B14.4 A $(D^s_\infty)_{yy}$-defining graph using displacement data from phi25efr2 (t= 500 – 1000). The graph interval is 200, 300 and 450 time units, and the time between interval initial conditions is 0.01 time unit.

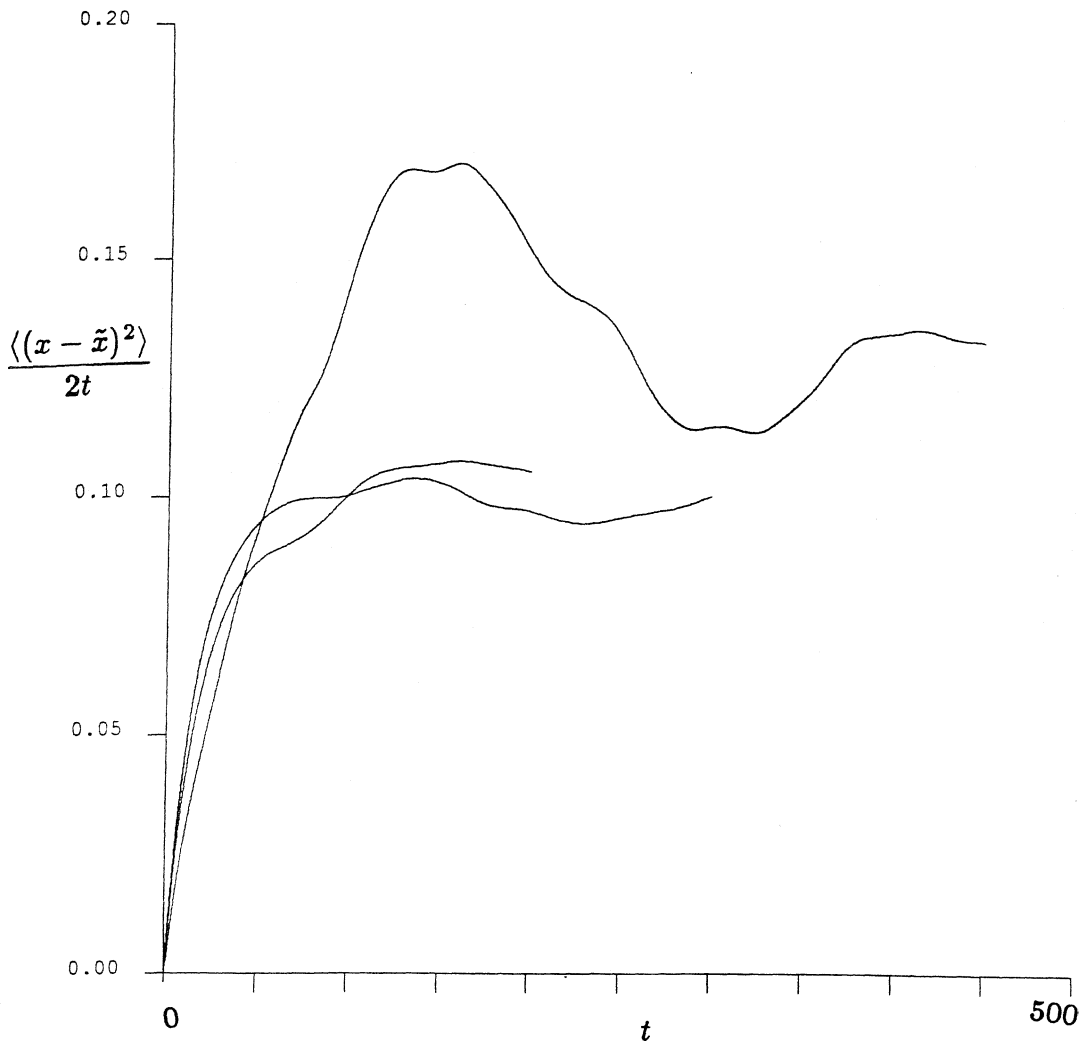

Figure B14.5 A $(D^s_\infty)_{xx}$-defining graph using displacement data from phi25efr2 (t= 500 – 1000). The graph interval is 200, 300 and 450 time units, and the time between interval initial conditions is 0.01 time unit.

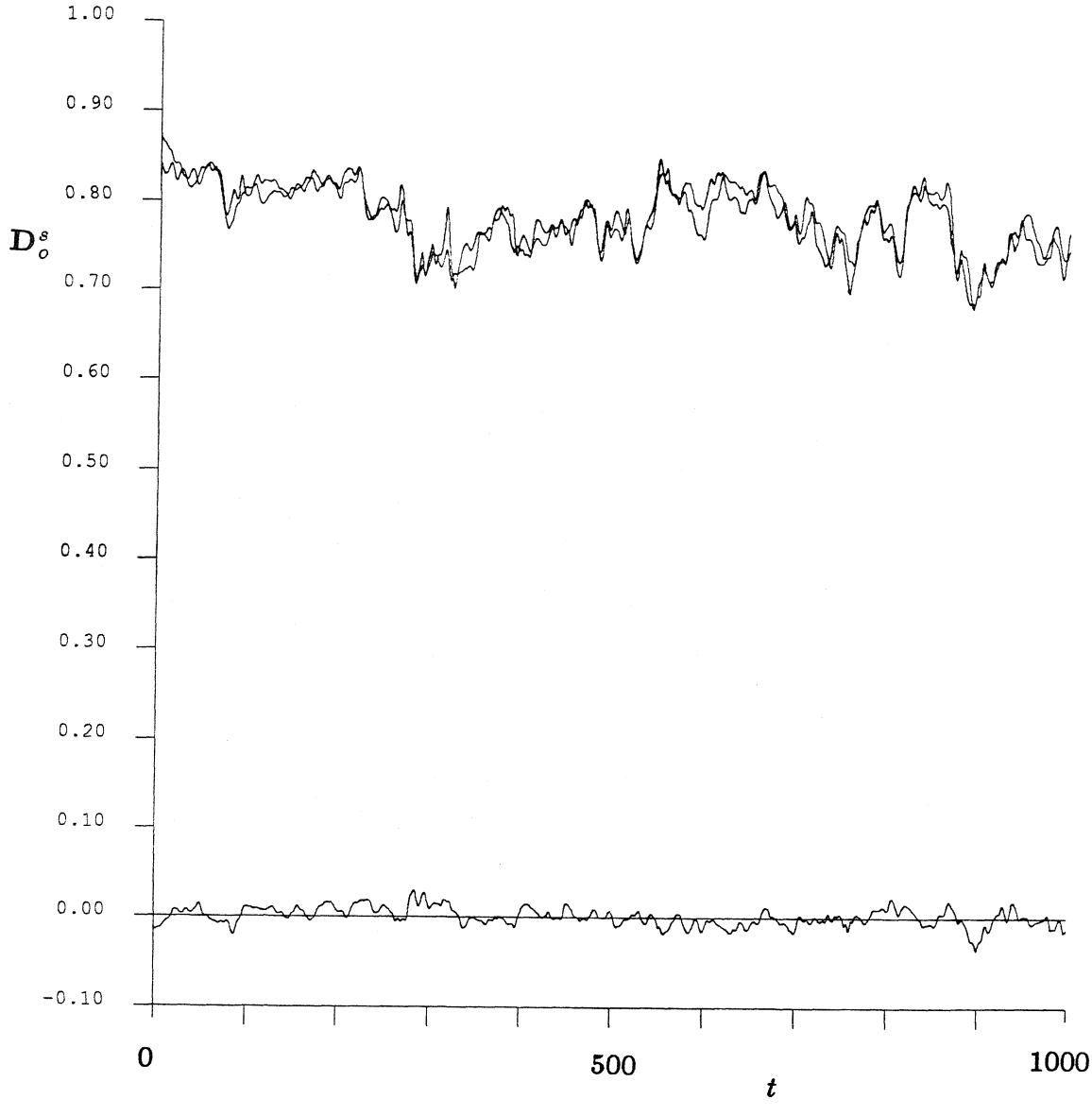

Figure B14.6 The time trace of $\mathbf{D}_o^s$ for the simulations phi25efr1 and phi25efr2. The upper two lines are the xx and yy components of this tensor. Of course, they should be equivalent for an infinite suspension – the slight variation occurs because of the finite number of spheres used in our simulation. The trace that fluctuates about the zero y-axis is the xy component of the short-time, self-diffusion tensor. Again, for an infinite number of spheres, this quantity would be exactly zero.

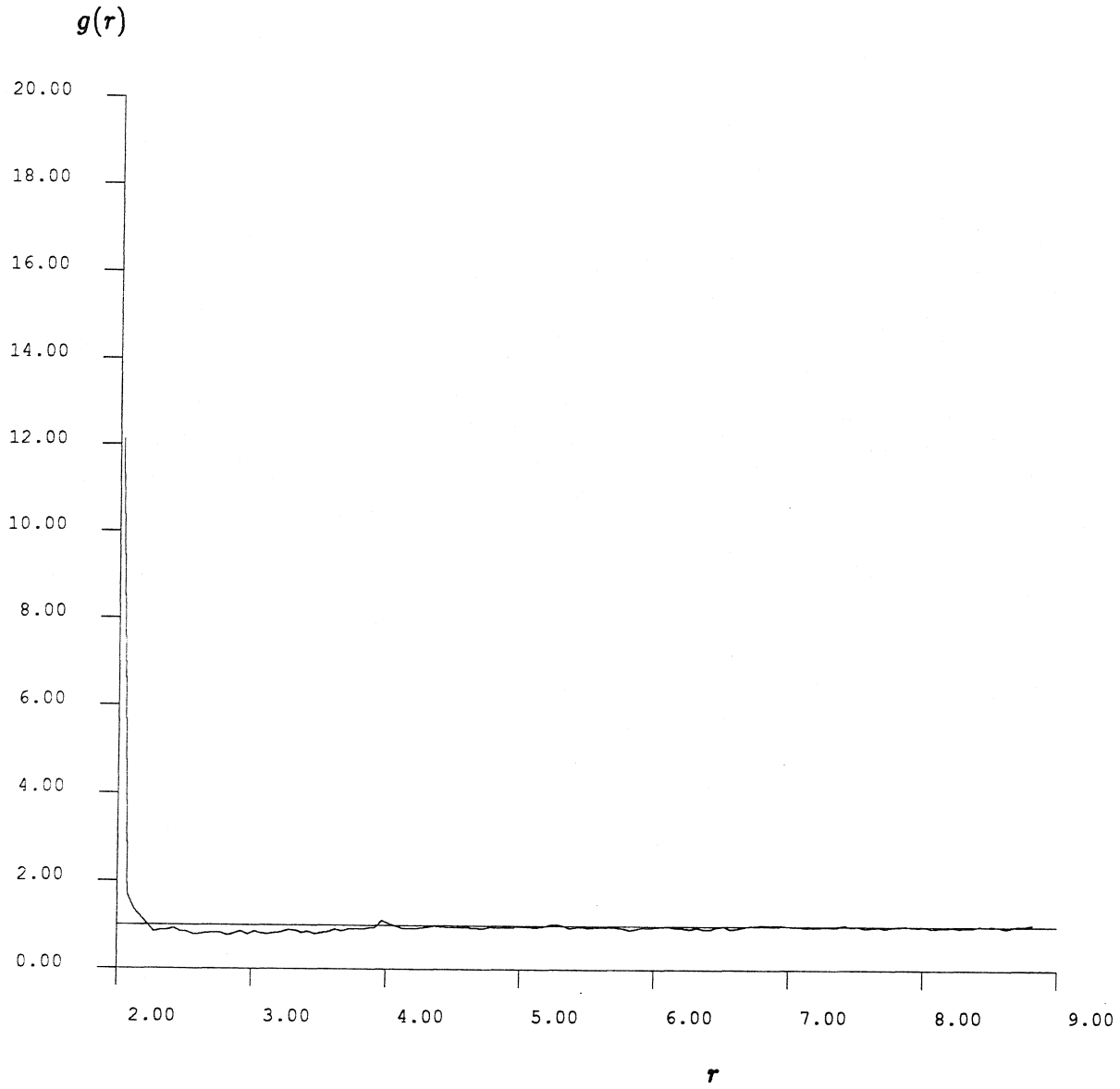

Figure B14.7 The radial pair-distribution function, $g(r)$, for the phi25efr2 run (t = 500 – 1000).

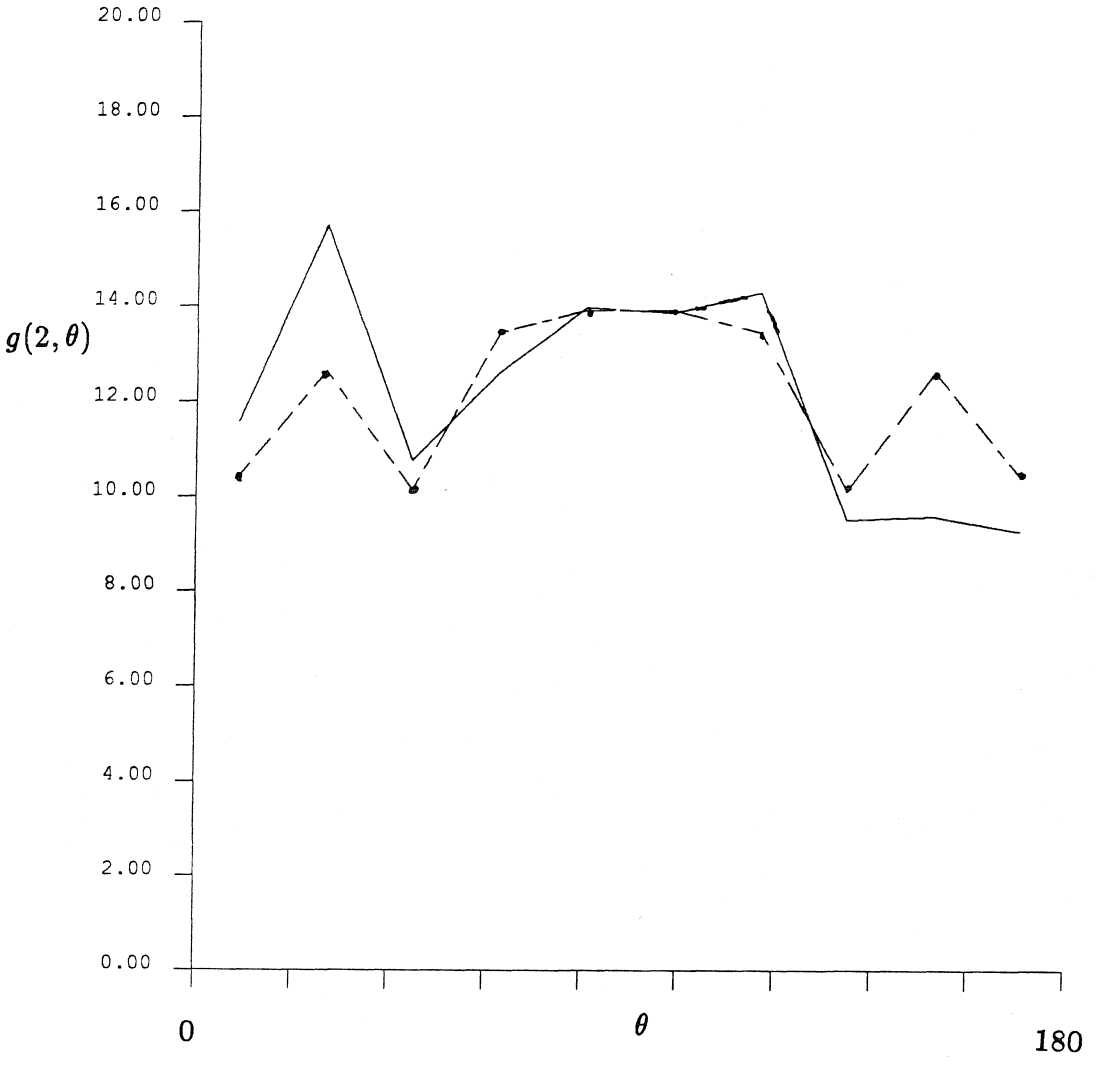

Figure B14.8 The full pair-distribution function for spheres whose surfaces are separated by less than 0.05 radii using data from the phi25efr2 run ($t = 500 - 1000$). The dashed curve represents this function when it is forced to be symmetric about $\theta = 90°$.

Appendix B15: The phi6efr simulation results

This suite of simulations uses an Ewald, F method to approximate the hydrodynamic interactions. The separation factor, z_l, is 2. 126 image cells are used to insure the convergence of the mobility interactions. Three separate simulation runs follow the evolution of a sedimenting system to a final time of 500 time units. The areal fraction is 0.25. There are interparticle forces present ($\tau = 10^5$). The time step is 0.0025 time unit for the phi6efr1 simulation run. The time step is 0.001 time unit for the phi6efr2 and phi6efr3 simulation runs. The mobility matrix is inverted every 0.1 time unit for all runs. Position and velocity data is saved every 0.05 time unit. $\mathbf{D}_o^s$ is evaluated and reported at every time unit.

	phi6efr1	phi6efr2	phi6efr3
T Cray/Sun CPU(min)	0-126.6 Cray ?	120-250 Cray 0.50 33	250-500 Cray 0.50 62
v_y	-5.36140	-5.34074	-5.34862
v_x	-0.00637	-0.00173	0.00217
v_y variance	0.00330	0.00251	0.00213
v_x variance	0.00062	0.00043	0.00062
v_{xy} variance	0.00007	0.00004	0.00001
$(D_\infty^s)_{yy}$			0.012
$(D_\infty^s)_{xx}$			0.0075
$(D_o^s)_{yy}$	0.469	0.414	0.427
$(D_o^s)_{xx}$	0.480	0.401	0.416
$(D_o^s)_{xy}$	-0.0093	0.0018	0.0006
$g(2)$			15.7
$g(3.5)$			0.78
$g(4)$			2.10

Table B15.1

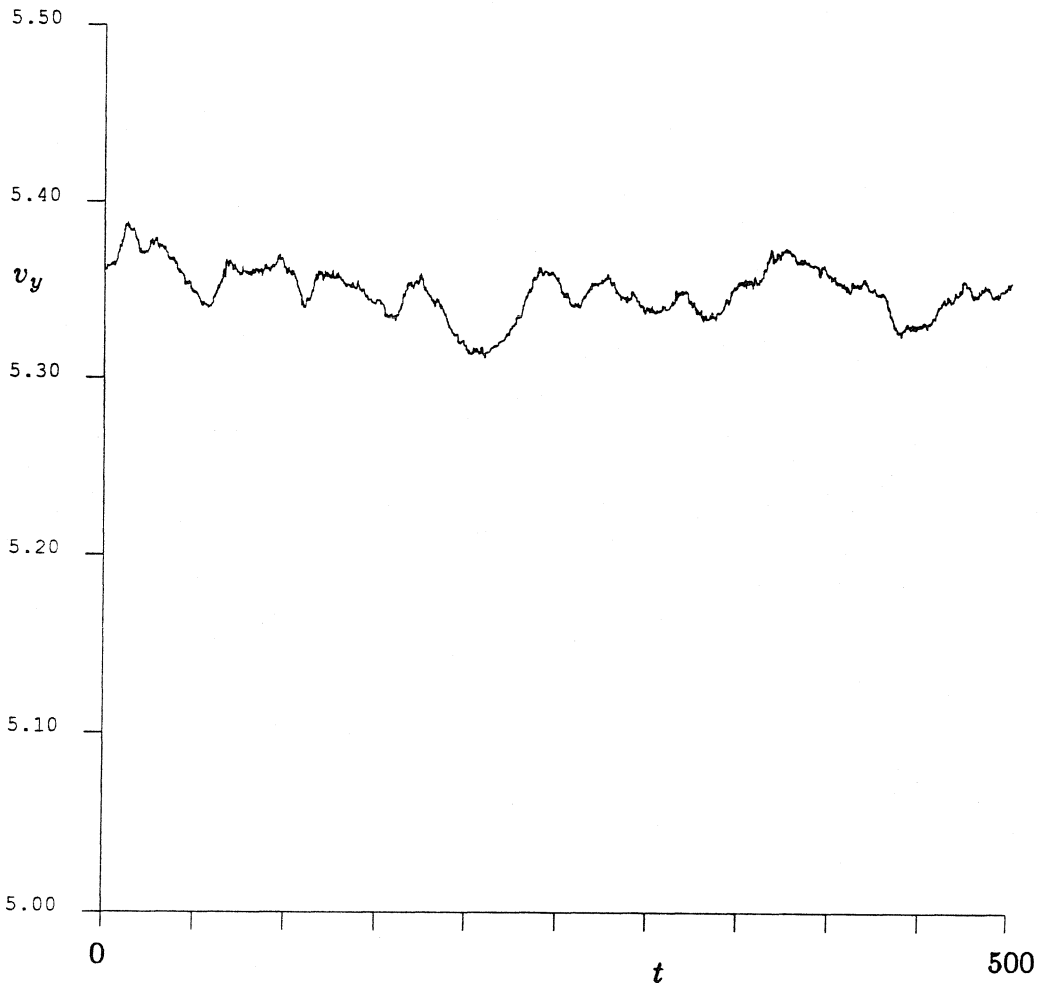

Figure B15.1 The time trace of v_y for the simulations phi6efr1 through phi6efr3.

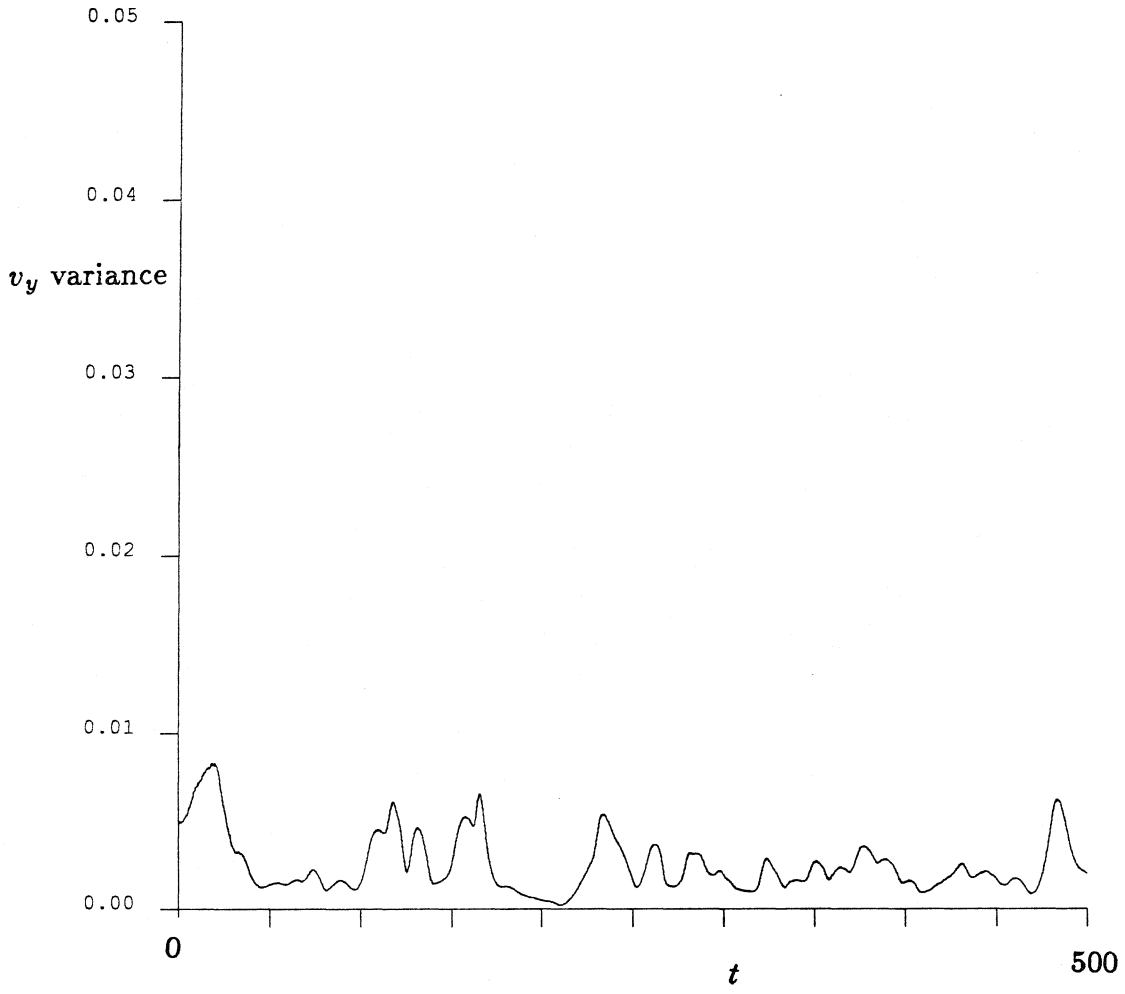

Figure B15.2 The time trace of the v_y variance for the simulations phi6efr1 through phi6efr3.

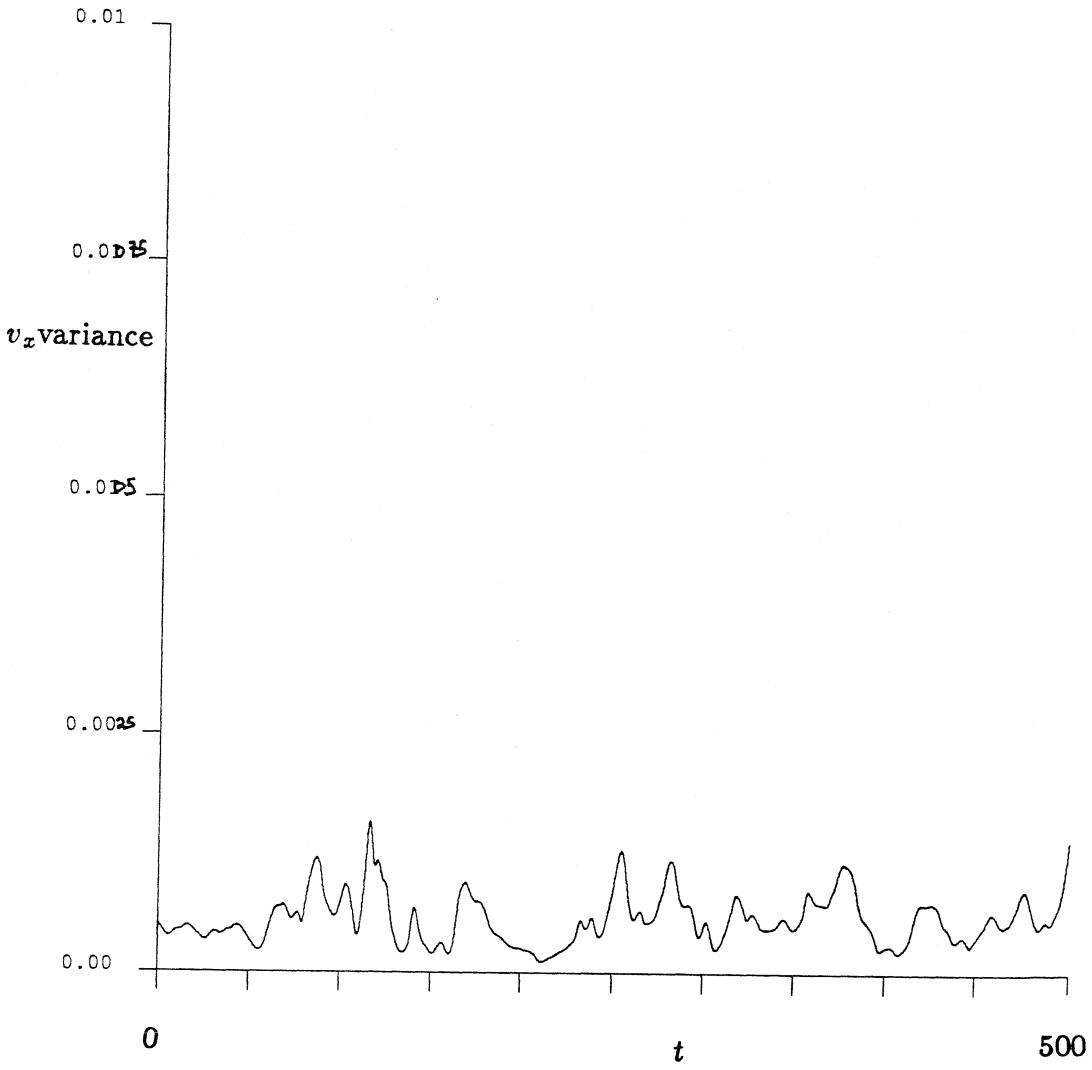

Figure B15.3 The time trace of the v_x variance for the simulations phi6efr1 through phi6efr3.

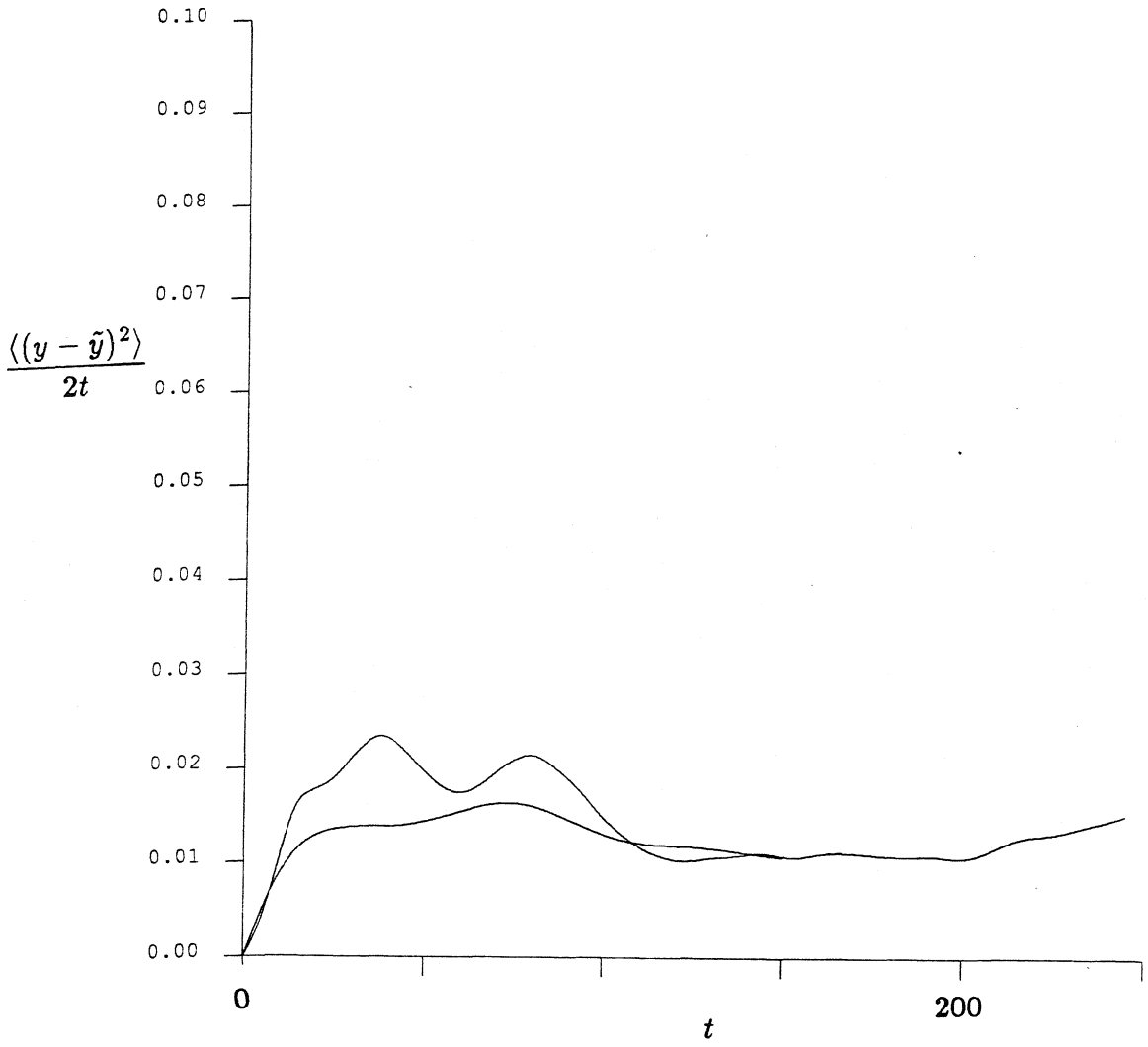

Figure B15.4 A $(D^s_\infty)_{yy}$-defining graph using displacement data from phi6efr3 (t= 250 – 500). The graph interval is 150 and 250 time units. The time between interval initial conditions is 0.01 time unit, except for the 250 time units curve where no averaging over initial conditions is done.

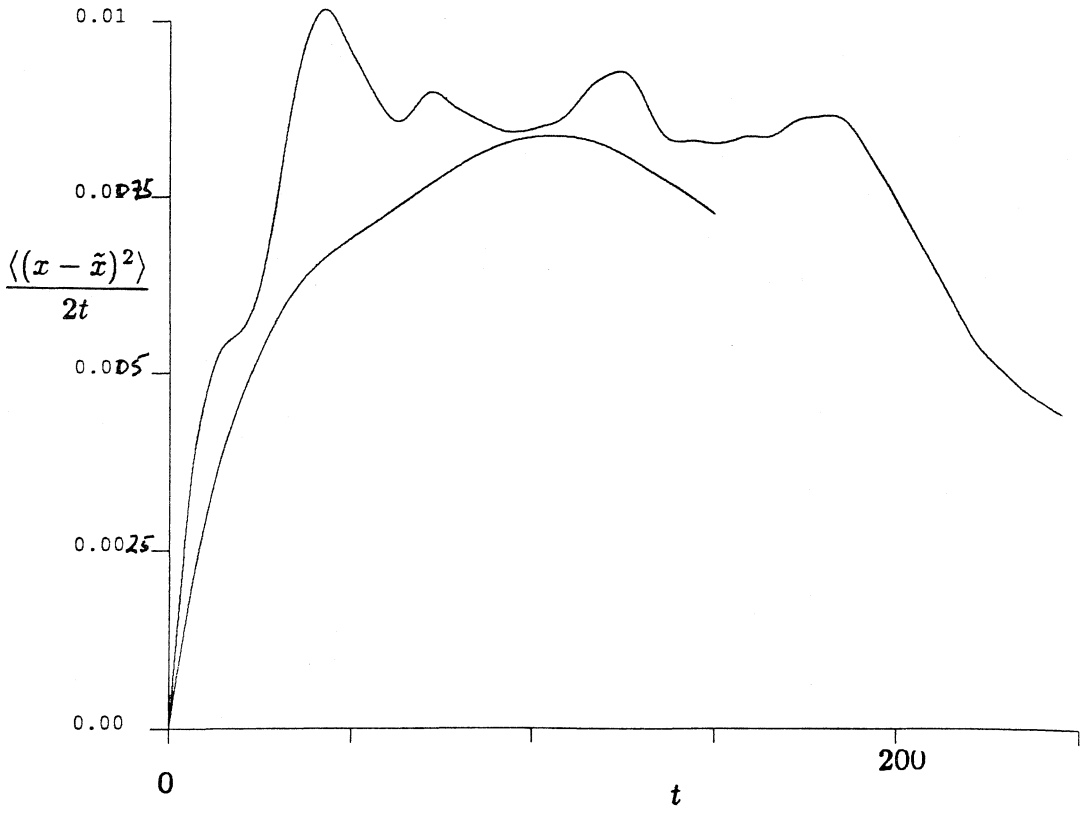

Figure B15.5 A $(D^s_\infty)_{xx}$-defining graph using displacement data from phi6efr3 (t= 250 – 500). The graph interval is 150 and 250 time units. The time between interval initial conditions is 0.01 time unit, except for the 250 time units curve where no averaging over initial conditions is done.

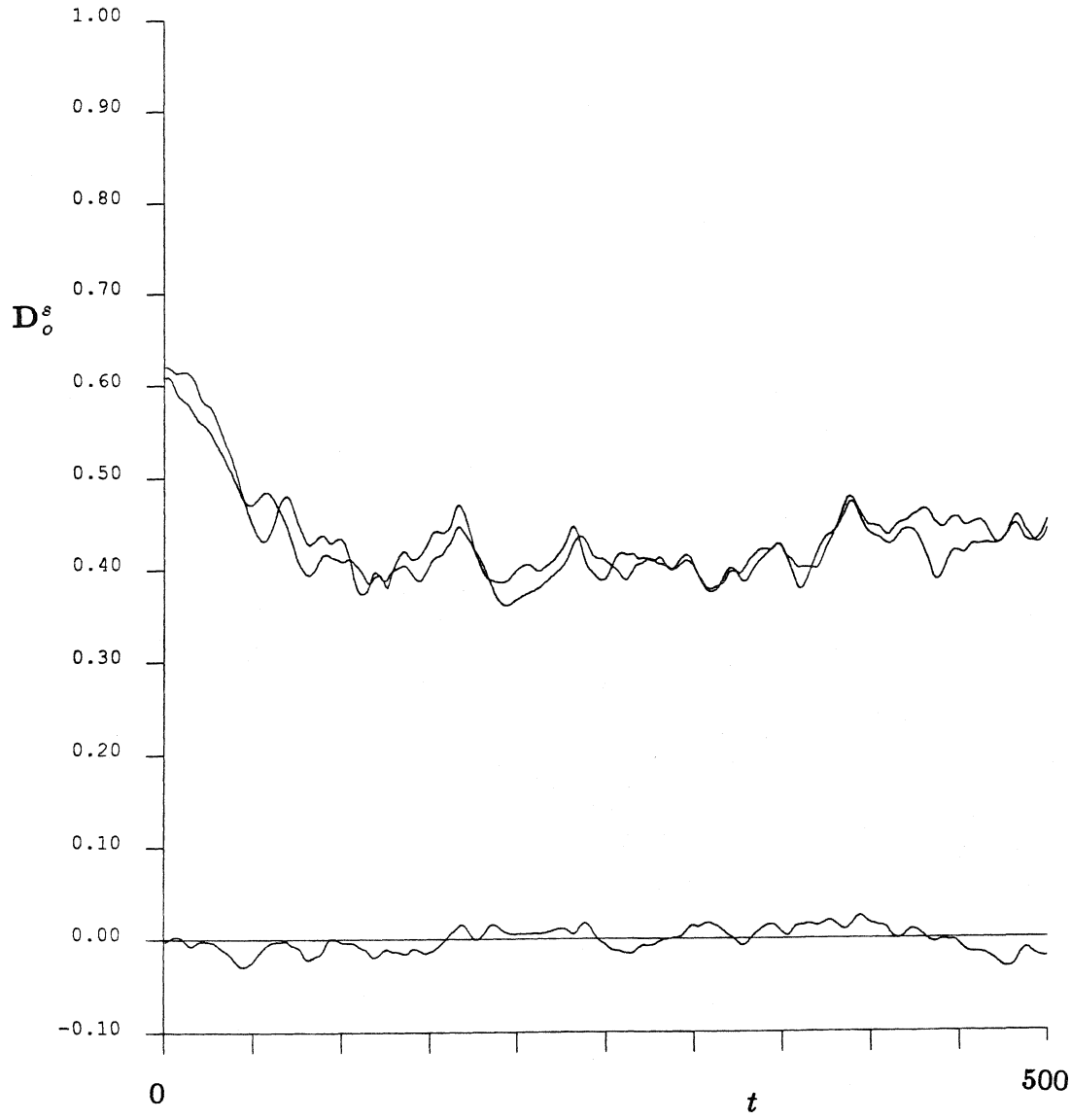

Figure B15.6 The time trace of $\mathbf{D}_o^s$ for the simulations phi6efr1 through phi6efr3. The upper two lines are the xx and yy components of this tensor. Of course, they should be equivalent for an infinite suspension – the slight variation occurs because of the finite number of spheres used in our simulation. The trace that fluctuates about the zero y-axis is the xy component of the short-time, self-diffusion tensor. Again, for an infinite number of spheres, this quantity would be exactly zero.

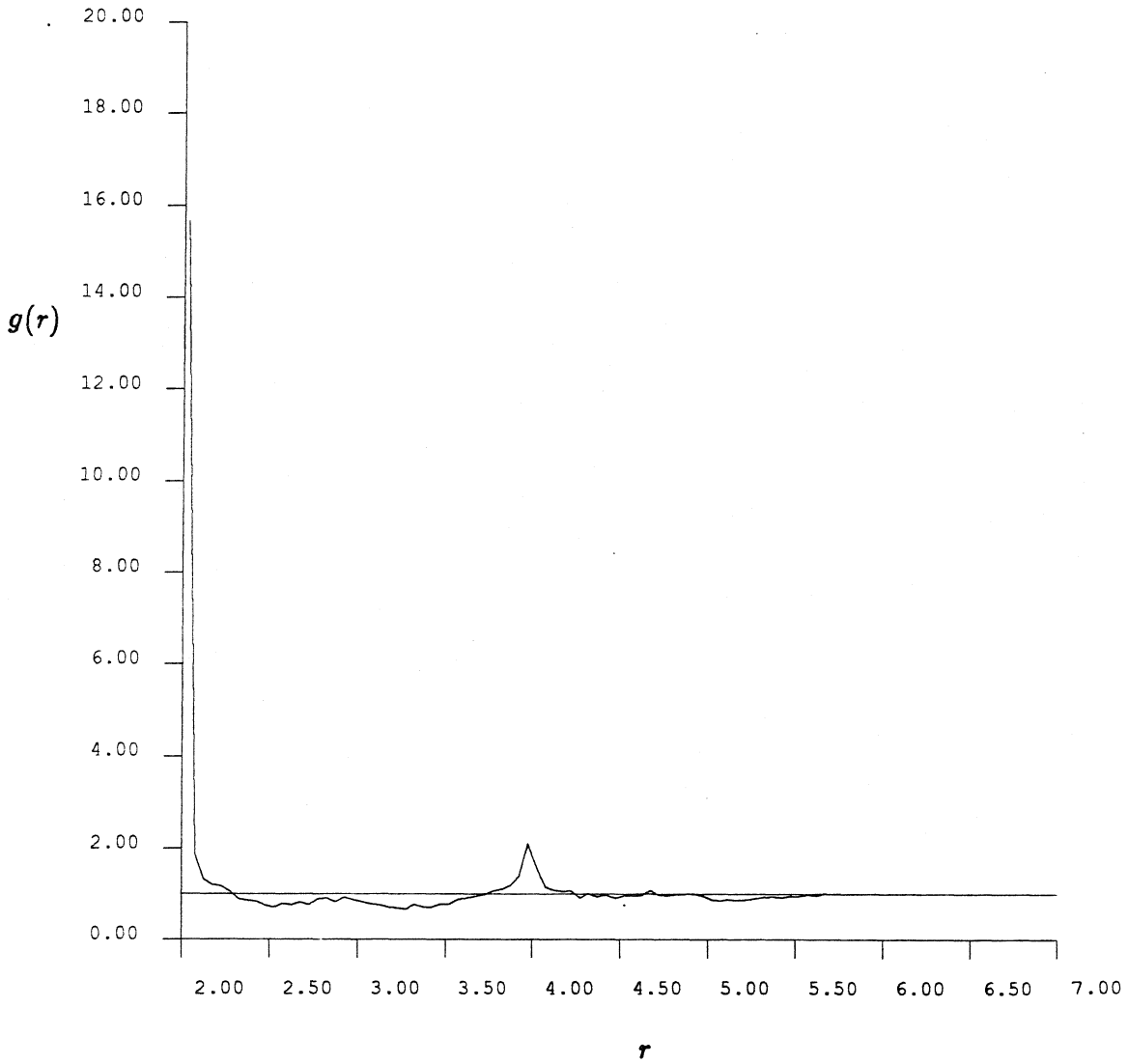

Figure B15.7 The radial pair-distribution function, $g(r)$, for the phi6efr3 run (t = 250 – 750).

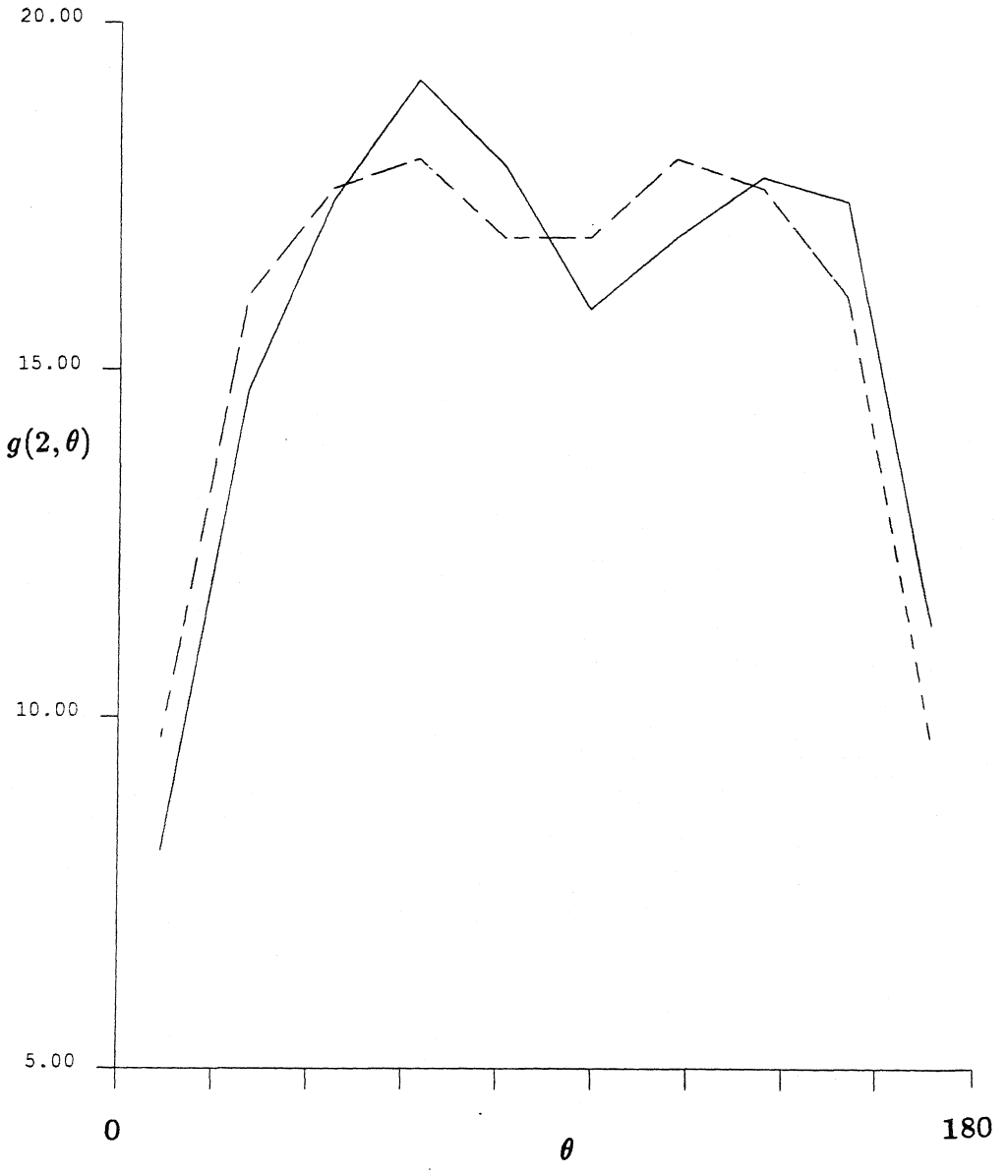

Figure B15.8 The full pair-distribution function for spheres whose surfaces are separated by less than 0.05 radii using data from the phi6efr3 run ($t = 250 - 750$). The dashed curve represents this function when it is forced to be symmetric about $\theta = 90°$.

APPENDIX C: TABULATION OF FIRST-ORDER INTEGRATOR RESULTS

This appendix simply reports the diffusion-related properties of early simulations that used a first-order, Euler integrator to advance the sphere positions. As is discussed in Chapter 2, Section 4, this integrator does not accurately capture the curved trajectories of spheres moving around each other. Despite this, these simulations still deserve some attention. Diffusive sphere motion is seen in these simulations at all concentrations (ϕ_A = 0.01, 0.1, 0.4, and 0.7). A compilation of these simulations' results can be found in another volume, but this appendix will report the velocity variance and long-time, self-diffusion coefficient for these simulations.

Table C.1 The simulation conditions for the first-order sedimentation runs. The first column is the memnonic case name for the method used in that simulation – 'f', 't', and/or 's' denotes the level of approximation. The mobility matrix was inverted every 'T invert' time units.

Case	Method	Ewald(?)	N	dt	ϕ	T invert
FTSn1	FTS	no	25	0.0025	0.4	1.0
FTS1	FTS	z_l=1.0	25	0.0025	0.4	1.0
FT1	FT	z_l=1.0	25	0.0025	0.4	1.0
F19	F	z_l=10.0	25	0.0025	0.4	1.0
F24	F	z_l=1.0	25	0.0025	0.4	2.0
F49	F	z_l=1.0	49	0.0025	0.4	1.0
F17	F	z_l=1.0	25	0.0025	0.4	1.0
F25	F	z_l=1.0	25	0.0025	0.4	1.0
F23	F	z_l=1.0	25	0.05	0.01	1.0
F22	F	z_l=1.0	25	0.01	0.1	1.0
F21	F	z_l=1.0	25	0.001	0.7	1.0

Table C.2 The time-averaged v_y variance and $(D^s_\infty)_{yy}$ for the first-order sedimentation runs. The final column is the ratio of the diffusion coefficient to the variance, which should be proportional to the time scale of the diffusive sphere motion.

Case	ϕ_A	v_y variance	$(D^s_\infty)_{yy}$	$(D^s_\infty)_{yy}$ / v_y variance
FTSn1	0.4	0.02123	0.49	23.1
FTS1	0.4	0.02718	0.85	31.3
FT1	0.4	0.03847	0.52	13.5
F19	0.4	0.01456	0.29	19.9
F24	0.4	0.02881	0.31	10.8
F49	0.4	0.05597	0.34	6.1
F17	0.4	0.02493	0.32	13.0
F25	0.4	0.02678	0.25	9.3
F23	0.01	0.05945	9.6	161.5
F22	0.1	0.09080	2.4	26.4
F21	0.7	0.00038	0.023	59.9

Table C.5 The time-averaged v_x variance and $(D^s_\infty)_{xx}$ for the first-order sedimentation runs. The final column is the ratio of the diffusion coefficient to the variance, which should be proportional to the time scale of the diffusive sphere motion.

Case	ϕ_A	v_x variance	$(D^s_\infty)_{xx}$	$(D^s_\infty)_{xx}$ / v_x variance
FTSn1	0.4	0.01242	0.095	7.6
FTS1	0.4	0.00636	0.048	7.3
FT1	0.4	0.00839	0.052	6.2
F19	0.4	0.00380	0.069	18.2
F24	0.4	0.00602	0.050	8.3
F49	0.4	0.00799	0.080	10.0
F17	0.4	0.00466	0.042	9.0
F25	0.4	0.00525	0.054	10.3
F23	0.01	0.00438	0.26	59.3
F22	0.1	0.01299	0.17	13.1
F21	0.7	0.00008	0.0019	23.0